Proceedings of the Seventh Symposium on Containment of Underground Nuclear Explosions—Volume 2

September 13–17, 1993
Auditorium: Boeing Space Center East
Kent, Washington

Clifford W. Olsen, Scientific Editor

MASTER

DISTRIBUTION OF THIS DOCUMENT IS UNLIMITED

DISCLAIMER

This report was prepared as an account of work sponsored by an agency of the United States Government. Neither the United States Government nor any agency thereof, nor any of their employees, make any warranty, express or implied, or assumes any legal liability or responsibility for the accuracy, completeness, or usefulness of any information, apparatus, product, or process disclosed, or represents that its use would not infringe privately owned rights. Reference herein to any specific commercial product, process, or service by trade name, trademark, manufacturer, or otherwise does not necessarily constitute or imply its endorsement, recommendation, or favoring by the United States Government or any agency thereof. The views and opinions of authors expressed herein do not necessarily state or reflect those of the United States Government or any agency thereof.

DISCLAIMER

Portions of this document may be illegible in electronic image products. Images are produced from the best available original document.

Preface and Acknowledgments

This is Volume 2 of two unclassified volumes of the Proceedings of the Seventh Symposium on Containment of Underground Nuclear Explosions. The Symposium, held September 13–17, 1993, at the Boeing Space Center East in Kent, Washington, was a meeting of workers at all levels in the science and technology of containment. Papers on containment and related geological, geophysical, engineering, chemical, and computational topics were included. The Seventh Symposium was quite possibly the last of the containment symposia, and we sincerely hope that these proceedings and those from earlier meetings will preserve some of the vast experience and expertise that was a part of the containment community.

We express our sincere thanks to Boeing for hosting the Symposium, and we give special thanks to Dr. Hal Ahlstrom and Ms. Debbie Petersen for their splendid cooperation in providing such fine facilities. Special thanks are due to S-Cubed and Raytheon Services Nevada for underwriting the Tuesday evening reception. Finally, we give our sincere thanks to Karen Roland and Marie Kaye for their invaluable support.

The Program Committee wishes to thank all presenters and attendees for their support, and gives special thanks to the session chairpersons: Ray Cornell, Hal Goldwire, Mel Hatch, Barbara Harris-West, Roger Jacobson, Jim Kamm, Willy Moss, Bill Proffer, Rachel Sandmann, Bob Swift, and Rick Warren.

We would also like to remember John Kalinowski of EG&G, who lost a battle with cancer in July 1993. John was not widely known, though he chaired a session at the Fifth Symposium, since most of his many years of work on containment were behind the scenes. His expertise on diagnostics and his unfailing good humor will be missed.

The Program Committee

Bob Deupree, LANL
Les Hill, Sandia
Cliff Olsen, LLNL
Paul Orkild, USGS
Roger Thompson, DNA

Organizers

Jack House, LANL
Cliff Olsen, LLNL

Symposium Attendees

Hal Ahlstrom, Boeing Defense and Space Group, P.O. Box 3999, MS85-85, Seattle, WA 98124-2499
Brian M. Allen, Raytheon Services Nevada, P.O. Box 328, Mercury, NV 89023
Gylan C. Allen, U.S. Department of Energy, P.O. Box 98518, Las Vegas, NV 89193-8518
Fredrick N. App, Los Alamos National Laboratory, P.O. Box 1663, M/S F659, Los Alamos, NM 87545
Margaret J. Baldwin, Raytheon Services Nevada, P.O. Box 328, M/S 940, Mercury, NV 89023
Harold A. Begley, Raytheon Services Nevada, P.O. Box 328, Mercury, NV 89023
Max J. Bennett, Raytheon Services Nevada, P.O. Box 328, M/S 940, Mercury, NV 89023
Thomas Bergstresser, Sandia National Laboratory, P.O. Box 5800, Orig. 9311, Albuquerque, NM 87115
Robert P. Bradford, Raytheon Services Nevada, P.O. Box 328, Mercury, NV 89023
Robert R. Brownlee, Raytheon Services Nevada, 4879 North Franklin Street, Loveland, CO 80538
Grant T. Bruesch, Raytheon Services Nevada, P.O. Box 95487, Las Vegas, NV 89193
Norman R. Burkhard, Lawrence Livermore National Laboratory, P.O. Box 808, L-221, Livermore, CA 94551
Ernest P. Buskirk, Raytheon Services Nevada, P.O. Box 328, M/S 258, Mercury, NV 89023
Richard C. Carlson, Lawrence Livermore National Laboratory, P.O. Box 808, L-221, Livermore, CA 94551
James E. Carothers, Lawrence Livermore National Laboratory, P.O. Box 808, L-451, Livermore, CA 94551
Christine Carrier, Lawrence Livermore National Laboratory, P.O. Box 808, L-221, Livermore, CA 94551
Roderick D. Carroll, U.S. Geological Survey, Box 25046, M/S 913, Denver, CO 80225
Albert J. Chabai, Sandia National Laboratory, P.O. Box 5800, Div. 9311, Albuquerque, NM 87106
Gilbert F. Cochran, Desert Research Institute, P.O. Box 60220, Reno, NV 89506
Ray H. Cornell, Lawrence Livermore National Laboratory, P.O. Box 808, L-224, Livermore, CA 94551
Harry R. Covington, NTS—U.S. Geological Survey, P.O. Box 327, Mercury, NV 89023
Lee E. Davies, EG&G, 316 E. Atlas Circle North, Las Vegas, NV 89125
Robert G. Deupree, Los Alamos National Laboratory, P.O. Box 1663, MS-P947, Los Alamos, NM 87545
Tom N. Dey, Los Alamos National Laboratory, P.O. Box 1663, MS F-665, Los Alamos, NM 87545
Sanders R. Dolce, Sandia National Laboratory, P.O. Box 5800, Albuquerque, NM 87185
Carl W. Douglass, Raytheon Services Nevada, P.O. Box 328, Mercury, NV 89023
Sigmund L. Drellack, Raytheon Services Nevada, P.O. Box 328, M/S 940, Mercury, NV 89023
Gordon D. Duckworth, Lawrence Livermore National Laboratory, P.O. Box 808, L-221, Livermore, CA 94551
Russell E. Duff, S-Cubed, 2263 Caminito Preciosa Sur, La Jolla, CA 92037
Donald D. Eilers, Raytheon Services Nevada, 105 La Vista Drive, Los Alamos, NM 87544
Ruston J. Eleogram, U.S. Department of Energy, Mercury, NV 89023
Conrad W. Felice, Mission Research, 9 Exchange Place, Suite 900, Salt Lake City, UT 84111
Martha N. Garcia, U.S. Geological Survey, P.O. Box 25046, M/S 913, Denver, CO 80225
Robert G. Geil, Lawrence Livermore National Laboratory, P.O. Box 808, L-205, Livermore, CA 94551
Lewis A. Glenn, Lawrence Livermore National Laboratory, P.O. Box 808, L-200, Livermore, CA 94551
Henry C. Goldwire, Lawrence Livermore National Laboratory, P.O. Box 808, L-221, Livermore, CA 94551

Glenn S. Hale, U.S. Geological Survey, 6770 South Paradise Road, Las Vegas, NV 89119
Barbara L. Harris-West, FC DNA, P.O. Box 208, Mercury, NV 89023
Bernie V. Harter, Lawrence Livermore National Laboratory, P.O. Box 808, L-221, Livermore, CA 94551
Melton A. Hatch, Jr., EG&G, Amador Valley Operations, P.O. Box 8051, Pleasanton, CA 94588-8651
Ward L. Hawkins, Los Alamos National Laboratory, P.O. Box 1663, MS F-659, Los Alamos, NM 87545
Joseph R Hearst, Lawrence Livermore National Laboratory, P.O. Box 808, L-221, Livermore, CA 94551
Ray A. Heinle, Lawrence Livermore National Laboratory, P.O. Box 808, L-221, Livermore, CA 94551
Francois Heuze, Lawrence Livermore National Laboratory, P.O. Box 808, L-221, Livermore, CA 94551
Michael L. Higginbotham, S-Cubed, 3398 Carmel Mountain Road, San Diego, CA 92121
Gary H. Higgins, Raytheon Services Nevada, 875A Island Drive, #420, Alameda, CA 94502
Leslie R. Hill, Sandia National Laboratory, P.O. Box 5800, Orig. 9311, Albuquerque, NM 87115
Jack W. House, Los Alamos National Laboratory, P.O. Box 1663, M/S F-659, Los Alamos, NM 87545
Kevin R. Housen, Boeing Defense & Space Group, P.O. Box 3999, MS 87-60, Seattle, WA 98124-2499
Billy C. Hudson, Lawrence Livermore National Laboratory, P.O. Box 808, L-221, Livermore, CA 94551
Richard M. Ivy, Raytheon Services Nevada, P.O. 328, Mercury, NV 89108
Roger L. Jacobson, Desert Research Institute, P.O. Box 19040, Las Vegas, NV 89132-0040
Evan C. Jenkins, U.S. Geological Survey, 301 South Williams Street, Denver, CO 80209-2636
James R. Kamm, Los Alamos National Laboratory, P.O. Box 1663, M/S F-659, Los Alamos, NM 87545
Marie C. Kaye, Los Alamos National Laboratory, P.O. Box 1663, M/S F-659, Los Alamos, NM 87545
Carl E. Keller, Eastman Cherrington Environment, 1640 Old Pecos Trail, Suite H, Santa Fe, NM 87504
Thomas D. Kunkle, Los Alamos National Laboratory, P.O. Box 1663, M/S F-665, Los Alamos, NM 87545
Joseph, W. LaComb, Jr., Raytheon Services Nevada, P.O. Box 328, M/S 258, Mercury, NV 89023
Stephen H. Leedom, U.S. Department of Energy, P.O. Box 98518, Las Vegas, NV 89193-8518
Gordon MacLeod, Raytheon Services Nevada, P.O. Box 768, MS 940, Mercury, NV 89023
Wesley Martin, Terra Tek, 420 Wakara Way, Salt Lake City, UT 84108
Nancy L. Marusak, Los Alamos National Laboratory, P.O. Box 1663, MS F-665, Los Alamos, NM 87545
William B. McKinnis, Nevada Test Site—LLNL, P.O. Box 45, L-777, Mercury, NV 89023
Thomas O. McKown, Los Alamos National Laboratory, P.O. Box 1663, P-15-MS D406, Los Alamos, NM 87545
James H. Metcalf, Sandia National Laboratory, P.O. Box 5800, Albuquerque, NM 87185-5800
Albert E. Moeller, EG&G, 316 E. Atlas Circle North, Las Vegas, NV 89125
Bill Moran, Lawrence Livermore National Laboratory, P.O. Box 808, L-200, Livermore, CA 94551
Benoit Morel, Carnegie Mellon University, Dept. of Eng. & Pub. Policy, Pittsburgh, PA 15213
William C. Moss, Lawrence Livermore National Laboratory, P.O. Box 808, L-200, Livermore, CA 94551
Richard Navarro, U.S. Department of Energy, P.O. Box 98518, Las Vegas, NV 89193-8518
Michael D. O'Hagan, IT Corporation, 4330 South Valley View, #114, Las Vegas, NV 89103-4047
Clifford W. Olsen, Lawrence Livermore National Laboratory, P.O. Box 808, L-221, Livermore, CA 94551
Kenneth H. Olsen, LANL, GCS International, 1029 187th PL SW, Lynnwood, WA 98037
Paul P. Orkild, U.S. Geological Survey, P.O. Box 25046, Denver, CO 80225
Dan F. Patch, SAIC/Pacifica Technology, 10260 Campus Pt. Dr., MS C-2, San Diego, CA 92121-1578
Gayle A. Pawloski, Lawrence Livermore National Laboratory, P.O. Box 808, L-221, Livermore, CA 94551
Edward W. Peterson, S-Cubed, 3398 Carmel Mountain Road, San Diego, CA 92121

William J. Proffer, S-Cubed, 3398 Carmel Mountain Road, San Diego, CA 92121
John T. Rambo, Lawrence Livermore National Laboratory, P.O. Box 808, L-200, Livermore, CA 94551
Jo Ann H. Rego, Lawrence Livermore National Laboratory, P.O. Box 808, L-231, Livermore, CA 94551
William W. Richardson, Lawrence Livermore National Laboratory, P.O. Box 808, L-221, Livermore, CA 94551
Norton Rimer, S-Cubed, 3398 Carmel Mountain Road, San Diego, CA 92121
Byron L. Ristvet, FC DNA, 1680 Texas Street, SE, Kirtland AFB, NM 87117-5669
Karen A. Roland, Lawrence Livermore National Laboratory, P.O. Box 808, L-221, Livermore, CA 94551
Gary A. Russell, U.S. Geological Survey, 6770 S. Paradise Road, Las Vegas, NV 89119
Rachel A. Sandmann, S-Cubed, 3398 Carmel Mountain Road, San Diego, CA 92121
Dave P. Sawyer, U.S. Geological Survey, P.O. Box 25046, Denver, CO 80225
Carl W. Smith, Sandia National Laboratory, P.O. Box 5800, Orig. 9311, Albuquerque, NM 87115
Charles F. Smith, Lawrence Livermore National Laboratory, P.O. Box 808, L-231, Livermore, CA 94551
Lana Stewart, Raytheon Services Nevada, P.O. Box 95487, Las Vegas, NV 89193-5487
Theodore F. Stubbs, EG&G/Lawrence Livermore National Laboratory, P.O. Box 808, L-221, Livermore, CA 94551
Robert A. Swift, Los Alamos National Laboratory, P.O. Box 1663, MS F-665, Los Alamos, NM 87545
Venkatrao Thummala, Raytheon Services Nevada, P.O. Box 328, M/S 607, Mercury, NV 89023
Dean R. Townsend, Raytheon Services Nevada, P.O. Box 328, MS 940, Mercury, NV 89023
Bryan J. Travis, Los Alamos National Laboratory, P.O. Box 1663, MS F-665, Los Alamos, NM 87545
Bruce C. Trent, Los Alamos National Laboratory, P.O. Box 1663, MS F-664, Los Alamos, NM 87545
Doug A. Trudeau, U.S. Geological Survey, 6770 South Paradise Road, Las Vegas, NV 89119
Randall W. Unger, U.S. Geological Survey—WRD, 6770 South Paradise Road, Las Vegas, NV 89119
Michael E. Voss, Boeing Defense & Space Group, P.O. Box 3999, Seattle, WA 98124-2499
Richard G. Warren, Los Alamos National Laboratory, P.O. Box 1663, MS D462, Los Alamos, NM 87545
Hugh E. Watling, Lawrence Livermore National Laboratory, P.O. Box 808, L-113, Livermore, CA 94551

Contents

Volume 1

General Containment

A-1 *Did the Nuclear Test Moratorium of 1958 Teach Us Anything?*
R. R. Brownlee (Raytheon) 3

A-2 *The Containment Evaluation Panel: Background and Foreground*
J. E. Carothers (LLNL) 11

A-3 *My Thoughts about Containment*
R. E. Duff (S-Cubed) 47

A-4 *Site Selection and Containment Evaluation for LLNL Nuclear Events*
C. W. Olsen (LLNL) 85

A-5 *Experimental Determination of Containment Versus Burial Depth for Explosions in Sand*
R. M. Schmidt and M. E. Voss (Boeing) 121

A-6 *Scaling of Deeply Buried Explosions*
K. R. Housen (Boeing) 129

Tunnel and LOS Topics

B-1 *Low-Yield Event Design and Performance Review*
E. W. Peterson (S-Cubed); B. Ristvet, J. LaComb, B. Harris-West (DNA); R. Metcalf (SNL); and D. Patch (SAIC) 133

B-2 *Initial Cavity-Growth/Pipe-Closure Phenomena*
K. Lie, M. L. Higginbotham, and E. Peterson (S-Cubed) 153

B-3 *Do Analytic Models of Near Source Pipe Flow Compare to Measurement?*
M. L. Higginbotham and R. A. Sandmann (S-Cubed) 179

B-4 *The Second Pipe Flow in the Line-of-Sight Pipe*
T. Bergstresser (SNL) and R. C. Bass (Consultant) 189

B-5 *Close-In Shock Wave Diagnostics on MIDDLE NOTE and MISSION CYBER*
R. Duff (S-Cubed), T. McKown (LANL), D. Eilers (Raytheon), W. Storey (Northern New Mexico Consultants), and R. Bass (Consultant) 191

Cavity Conditions

C-1 *The Size of Underground Cavities Formed by Nuclear Devices: Implications of Point-Source Solutions for Geological Materials*
K. A. Holsapple (UW) 227

C-3 *GALENA Pressure History and a Proposed Sensor for Mean Residual Stress*
B. Hudson, S. Pratuch, and R. Heinle (LLNL); M. Hatch and T. Stubbs (EG&G) 229

C-4 *Cavity Gas Pressure Measurements on DIAMOND FORTUNE*
C. W. Smith and S. P. Breeze (SNL) 239

LYNER and Chemical Kiloton

D-2 *Containment and Safety Data Acquisition System for the LYNER Complex*
R. G. Deupree, F. R. Oblad, and W. J. Turner (LANL); P. Blain and
N. Khalsa (EG&G) 251
D-3 *Three-Dimensional Porous Flow Calculations of the LYNER Concept*
B. C. Trent and B. J. Travis (LANL) 259
D-4 *Containment Related Phenomenology from Chemical Kiloton*
N. Rimer, W. Proffer, E. Halda, and R. Nilson (S-Cubed) 305

Contents

Volume 2

Low-Yield Test Beds

E-1 *Testbed Design and Analytic Evaluation of a Proposed Very Low Yield DNA Horizontal Line-of-Sight Event*
M. L. Higginbotham, C. R. Dismukes, and R. A. Sandmann (S-Cubed) 3

E-3 *Response of Steel Vessels and Cavity Liners to Dynamic Loading*
C. M. Snell, R. P. Swift, and N. L. Marusak (LANL); L. R. Hill (SNL) 21

E-4 *Canonical Wall Loading Functions for Decoupled Cavities and Containment Vessels*
C. M. Snell, R. P. Swift, N. L. Marusak, and G. R. Spillman (LANL) 23

E-5 *Containing Repeated Low-Yield Nuclear Explosions in Steel-Lined Rock Caverns*
F. E. Heuze (LLNL); R. P. Swift (LANL); L. R. Hill and W. H. Barrett (SNL) 45

Modeling and Residual Stress

F-1 *Distinct Element Modeling of Late-Time Containment Phenomena*
W. J. Proffer and E. J. Halda (S-Cubed) 61

F-2 *Calculations of NTS Residual Stress Measurements and Some Implications for Models and Material Properties*
J. T. Rambo (LLNL) and N. Rimer (S-Cubed) 87

F-4 *Calculations of the FLAX Events with Comparisons to Particle Velocity Data Recorded at Low Stress*
J. T. Rambo (LLNL) 125

F-6 *Residual Stress Implications due to Variations of Yield and Depth-of-Burial of Two Nearly Simultaneous Explosions*
J. T. Rambo, W. C. Moss, and J. L. Levatin (LLNL) 145

Material Properties

G-1 *Recent Observations of Mechanical Properties and Microstructure of Shock-Conditioned Tuff*
J. W. Martin, J. T. Fredrich, and S. J. Green (TerraTek) 149

G-3A *Properties of NTS Tuff*
V. Thummala, J. G. Moore, and J. E. Aamodt (Raytheon) 175

G-4 *Dynamic Response of PCGC-1(0) Grout*
C. W. Felice (Mission Research) and B. Ristvet (DNA) 191

Collapse Phenomena and Shock Diagnostics

H-3 *YOCOL Measurement System for Cavity Collapse*
R. G. Deupree and W. J. Turner (LANL); P. Blain, P. Flores, N. Khalsa, and D. Macy (EG&G) 203

H-5 *A Radio Frequency Interferometer (RFI) System*
H. C. Goldwire, Jr. (LLNL) 209

Stemming Practices and Performance

I-1 *Review and Analysis of Stemming Practices at LLNL with Consideration of Slumping Phenomena*
R. H. Cornell (LLNL) 213

I-2 *Polyurethane Foam Cable Bundle Block*
J. A. Mercier, R. H. Cornell, S. M. Pratuch, and A. Lundberg (LLNL) 225

I-3 *Field Permeability and Strength Tests of LANL Grout and TPE Plugs*
B. C. Trent (LANL) 243

I-4 *A Summary of LLNL Containment: Diagnostics Data, 1985–1993*
B. Hudson (LLNL) and T. Stubbs (EG&G) 275

I-5 *More RAMS Data for Selected LANL Events*
B. C. Trent and N. L. Marusak (LANL) 297

Geophysics

J-1 *In Situ Convergence Measurements and Initial Analysis from Mine-By Experiments in U12p and U12n Tunnels at the Nevada Test Site, Nye County, Nevada*
B. L. Harris-West (DNA) and M. B. Fogel (SAIC) 315

J-2 *Use of a Simple Constitutive Model for Volcanic Rocks of the Southwestern Nevada Volcanic Field for the Determination of Hugoniots in Testing Media of the Nevada Test Site*
B. Olinger, J. N. Fritz, R. G. Warren, and S. J. Chipera (LANL) 363

J-3 *A Comparison of the Moisture Gauge and the Neutron Log in Air-Filled Holes at NTS*
J. R Hearst and R. C. Carlson (LLNL) 399

J-4 *Maximum Likelihood Borehole Corrections for Dual-Detector Density Logs*
R. C. Carlson (LLNL) 407

J-5 *An* In Situ *Check of the Epithermal Neutron Log Calibration*
N. R. Burkhard (LLNL) 413

Geosciences and Weapons Destruction

K-1 *Soil Mounds at the Nevada Test Site: Natural or Nuclear?*
M. N. Garcia and H. R. Covington (USGS) 429

K-2 *Water-Level Map of Eastern Pahute Mesa and Vicinity, Nevada Test Site, Nye County, Nevada*
M. D. O'Hagan (IT Corp.) 431

K-3 *Groundwater Levels from Well and Test-Hole Data, Yucca Flat, Nevada Test Site, Nye County, Nevada, 1959–91*
G. S. Hale and D. A. Trudeau (USGS) 433
K-4 *An Electromagnetic Hole Separation Survey Tool*
H. C. Goldwire, Jr. (LLNL) 435
K-5 *Destruction of Chemical Weapons by Underground Nuclear Explosions*
B. Morel and S. Black (Carnegie Mellon University) 437

Low-Yield Test Beds



TESTBED DESIGN AND ANALYTIC EVALUATION OF A PROPOSED VERY LOW YIELD DNA HORIZONTAL LINE-OF-SIGHT EVENT

by
M. L. Higginbotham*, C. R. Dismukes and R. A. Sandmann,
S-Cubed
A Division of Maxwell Laboratories, Inc.
P. O. Box 1620
La Jolla, CA 92038

ABSTRACT

Since the last symposium the DNA has considered the feasibility of a very low yield SREMP Horizontal Line-Of-Sight (HLOS) event. S-Cubed was asked to participate in the design and evaluation of early test-bed concepts. Non-traditional designs are required for a very low yield event because achieving total containment using mechanical closures alone is mandatory. The design goal was to decrease the threats on the closure hardware to ensure their survival.

In the earliest phase of the project, attention was focused on the region within a few meters of the source. Initial designs included unusual geometries and special materials whose purpose was to divert expanding device products away from the open LOS pipe. The plan was to use the diverted energy to obliquely close the LOS pipe well ahead of the device explosion products moving toward the LOS. Although progress was made and workable designs seemed conceptually feasible, the close proximity of the source and LOS resulted in designs that were extremely sensitive to device characteristics.

Early design studies were terminated and design emphasis was modified as a different testbed fielding possibility emerged. The concept involved utilizing the previously executed DIAMOND FORTUNE cavity volume in conjunction with a proposed reentry drift to be mined into the DIAMOND FORTUNE cavity. What emerged was an initial plan for a low yield event named MISTY HORIZON. Important testbed requirements included: 1) Rapidly transport as much device energy as possible into the DIAMOND FORTUNE cavity so as to mitigate pressure loads on mechanical closures. 2) Minimize device products reaching mechanical closures to facilitate possible reentry activities and prevent testbed contamination in the event of a mechanical or geologic failure. 3) Reduce significantly the customary violent LOS closure at its entrance to achieve a major reduction of the energetic LOS plasma threat to the closures. Nine conceptual designs were investigated and computationally analyzed prior to the event being placed on permanent hold.

Early flow diverting designs and analytic models are briefly discussed. Nine candidate MISTY HORIZON source region designs are described, critical design assumptions identified and comparisons of calculated design effectiveness presented.

1. INTRODUCTION

Numerous ideas were investigated in the definition phase of a very low yield (VLY) horizontal line-of-sight (HLOS). Initially, the event was envisioned as a very low-yield SREMP (Source Region EMP) test utilizing unique testbed design features applicable for protection of a partially or fully reusable test facility.

This report summarizes and documents S-Cubed's efforts supporting the DNA in the initial VLY testbed evaluation. These efforts included the design and analysis in the near source region and their effects in reducing the threat to proposed mechanical closures. The region near the source is commonly called the front-end (FE). The intent of this report is to provide guidance for future FE design efforts should the VLY concept be seriously considered. First we briefly review analyses of some early FE designs. Second is a description of a parametric study of the latest testbed concept considered. Included are results and comparisons from our numerical simulations. A final section presents some ideas concerning the next phase of investigations aimed at advancing the low-yield testbed concept.

2. SOURCE REPRESENTATION

For all of the calculations performed in this investigation, the nuclear source was modeled as a 20 ton spherical device with a mass of 68 kg (150 pounds). The device was represented simply as an expanding cloud of debris with equal amounts of internal and kinetic energy.

3. PRELIMINARY STUDIES

The VLY concept was an opportunity to evaluate features that might be utilized to successfully contain and insure reusability of a partially or fully reusable test facility. Areas of incomplete technical understanding presented a formidable challenge. Initial guidelines included using large mined drifts to provide an energy dump volume, a short LOS pipe with a large taper, and rough estimates of nuclear source characteristics. Testbed designs were refined throughout the study phase but source definition remained undefined.

Initial calculations modeled the source located near the end of a mined 6 x 6 x 230 m tunnel. The LOS pipe was simply appended to the large tunnel near the source. It was found that typical LOS closure could not be achieved. Without the motions generated in a standard front-end an unacceptable amount of device debris was injected into the LOS. This result would probably negate the reusability of any facility.

In an attempt to remedy the perceived deficiency of the initial test concept a more complicated type of system was studied next. The possibility was investigated of isolating device products from the open LOS by injecting mass downstream from the expanding device debris. The design was inspired by Mr. Summa, DNA-FC FCTT, based on a 1951 JAP article[1] describing a method for producing stable converging shock waves. The design described in the article was adapted for a nuclear driven system. A number of variations to the basic design were

calculated and the effectiveness of each was assessed. This work culminated in the configuration shown in Figure 1. The figure is a combination material position and density contour plot. The basic function of this FE is to divert the expanding debris through a channel around a massive object to produce a cylindrically convergent shock that will move mass into the LOS ahead of the expanding device products. It is assumed that radiation test environment requirements will permit a thin iron plate across the LOS opening acting to slow expanding device debris. Computer simulations indicated that additional material is needed to adequately impede the LOS device debris and low density polystyrene foam was placed in the LOS on either side of the iron plate, see Figure 1. It was also learned that the open channel behind the "top shaped" tuballoy portion, if air-filled, does not channel enough momentum to the iron pipe past the "top". A subsequent modification was to fill that region with low density polystyrene. Computer generated results are shown in Figure 2 at 0.3 ms for this, the last design studied. As in Figure 1 material position and density contours are displayed. Note that fairly high density iron is imploded into the LOS well ahead of the LOS device debris. These simulations suggest that a dynamic closure system driven by the expanding debris may be possible. However, additional work will be required to; improve system performance, determine sensitivities to source assumptions and confirm desired behavior to later times.

4. PARAMETRIC INVESTIGATION

Early design studies were terminated and design emphasis was modified as a different testbed fielding possibility emerged. The concept involved utilizing the previously executed DIAMOND FORTUNE cavity volume in conjunction with a proposed reentry drift to be mined into the DIAMOND FORTUNE cavity. What emerged was an initial plan for a low yield event named MISTY HORIZON. Important testbed requirements included: 1) Rapid transport of as much device energy as possible into the DIAMOND FORTUNE cavity to mitigate pressure loads on mechanical closures, 2) Minimization of device products reaching mechanical closures to facilitate possible reentry activities and prevent testbed contamination in the event of a mechanical or geologic failure, and 3) Significant reduction of the customary violent LOS closure near its entrance was required to achieve a major reduction of the energetic LOS plasma threat to the closures.

For MISTY HORIZON nine source configurations were considered and calculations evaluated phenomenological concerns associated with the designs. Testbed assumptions common to all nine investigations include:

- The SREMP event would be fielded in a proposed 3.4 x 3.4 m DIAMOND FORTUNE reentry drift.
- Device emplacement would be such that the DIAMOND FORTUNE cavity volume would be available as an energy dump volume.
- The device was the spherical 20 ton nuclear source described above.
- An LOS pipe taper, based on providing a 12.2 m OD beam at a range of 84.4 m, was 0.1444 m/m (on the ID).

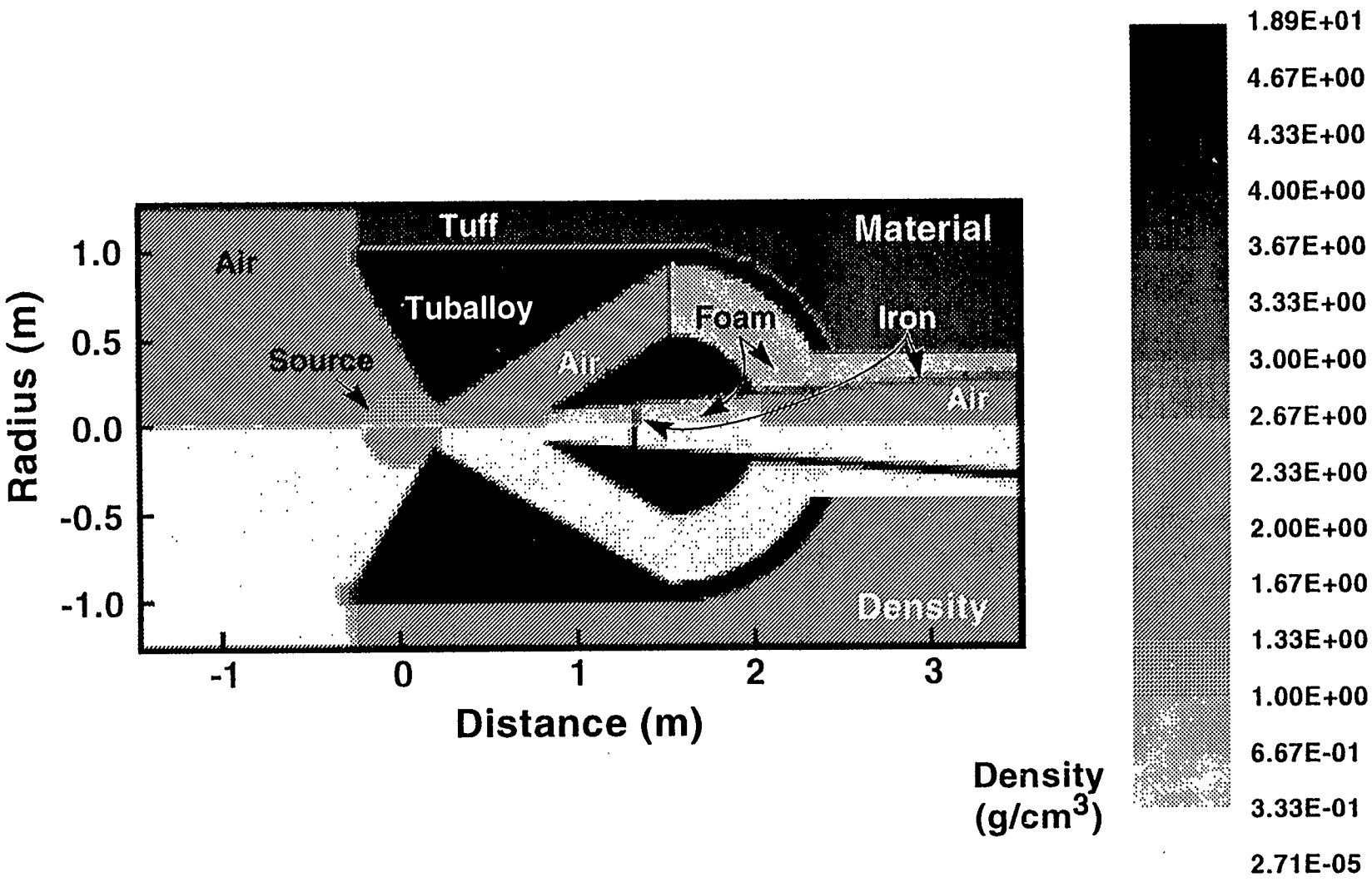


Figure 1. Density and material contours at t = 0.0 ms.

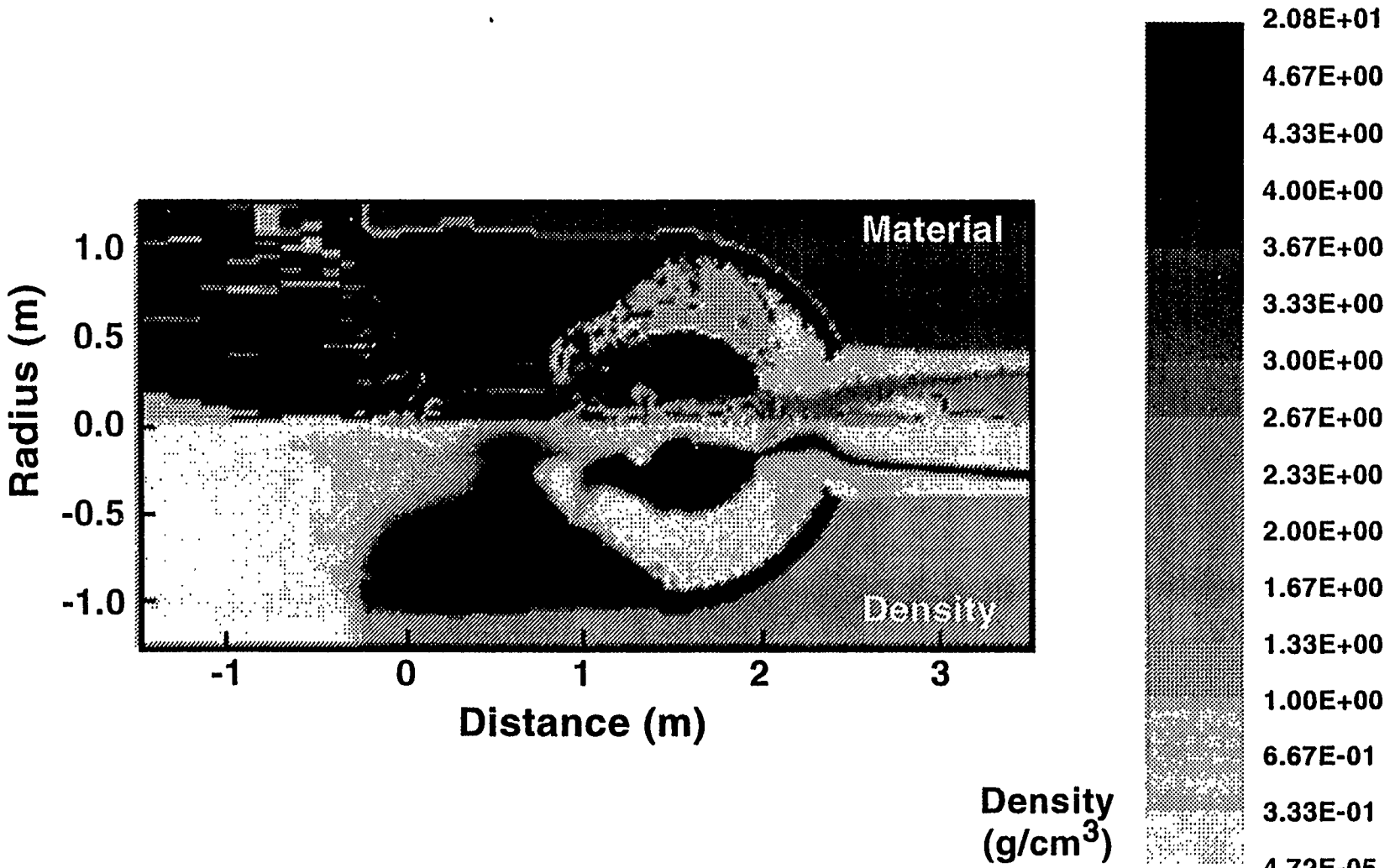


Figure 2. Density andmaterial contours at t = 0.3 ms.

SSS-DTR-92-13302

- To achieve purposed radiation environment signal levels the LOS would be evacuated to a tenth atmosphere maintained by a mylar vacuum window located at the LOS entrance.

- Containment would hinge on the survival of a 1.22 m OD high-strength iron "window", positioned 8.23 m from the WP, that would be designed to withstand dynamic and static loads.

A representation of the basic testbed and its relationship to the DIAMOND FORTUNE cavity is shown in Figure 3 along with a pictorial view of the calculational model of the cavity volume. The two barriers shown in the figure between the source and LOS pipe/sand region represent one of nine different calculated configurations. The basic testbed includes:

- A thick-walled (6 cm) iron LOS protruding 0.6 m into the air-filled reentry drift.

- 3 meters from the WP the reentry drift would be stemmed with a 2 m long sand column keyed to surrounding native wet tuff.

- A 2.1 m long high strength concrete (HSC) section beyond the sand column.

- A flow diverting open region in the reentry tunnel located between the HSC and the iron "window" at 8.23 m.

The nine variations of the basic design were modeled with the axisymmetric SOIL[2] code. Results were compared to determine the effectiveness of each design in displacing device energy into the DIAMOND FORTUNE cavity volume and to identify which configurations are most favorable for "window" survival. Each model included an equivalent-volume cylindrical DIAMOND FORTUNE cavity with identical stemming designs and the 8.23 m standoff between the WP and iron "window". The mylar vacuum seal was not included in the calculational configurations. HSC was modeled as wet tuff and the "window" was defined as a reflecting boundary at the 8.23 m location. The nine calculational models, displayed in Figure 4, are as follows:

Model 1 - The cavity to WP distance is 1 m and the reentry tunnel is open to 4.6 m from the WP.

Model 2 - Model 1 with a single 12.7 cm thick steel barrier located 1.5 m from the WP.

Model 3 - Model 1 with a reflective boundary located 0.61 m from the WP toward the portal.

Model 4 - A 3 m cavity to WP distance and two 12.7 cm thick steel barriers at 0.61 and 1.83 m from the WP.

Model 5 - Model 1 with barriers at 0.61 and 1.83 m.

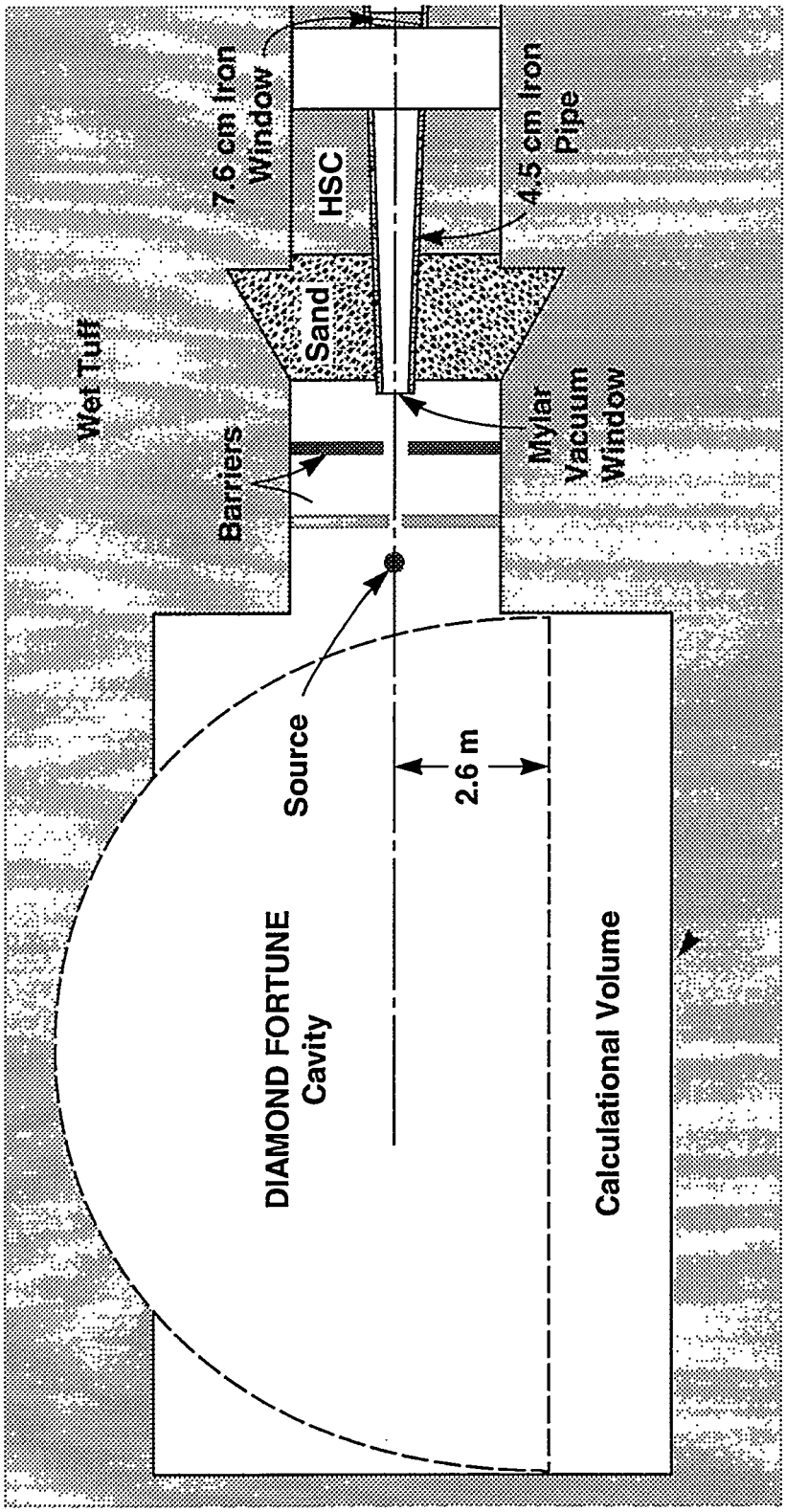


Figure 3. MISTY HORIZON calculational model.

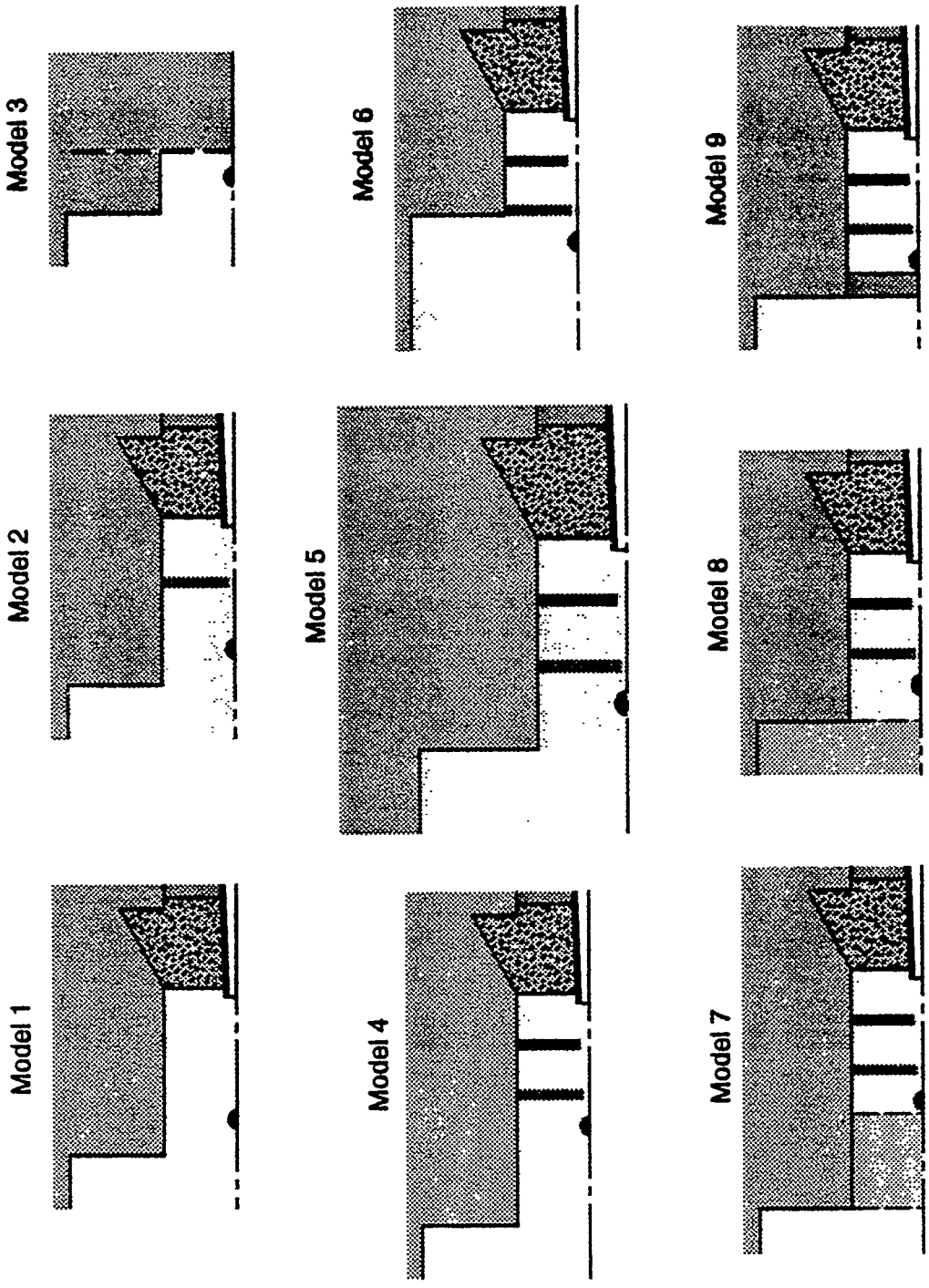


Figure 4. MISTY HORIZON calculational models.

Model 6 - Model 5 with the WP located 1 m into the DIAMOND FORTUNE cavity.

Model 7 - Model 5 with reentry tunnel filled with 0.03 g/cc polystyrene foam placed between the cavity and WP.

Model 8 - Model 5 with the cavity volume filled with polystyrene foam.

Model 9 - Model 5 with a 0.7 m pillar of grout between the cavity and WP.

SOIL calculations described device expansion and interaction with surrounding materials to 0.5 ms. To evaluate the effectiveness of each design in producing energy flow into the dump volume, the calculated shift of the energy center relative to the WP was compared. Energy center motion as a function of time is shown in Figure 5 for the nine simulations. When the configurations (Figure 4) and energy center shift (Figure 5) are compared the results appear reasonable. For example, the reduced energy shift found for Model 6 is expected since the WP began inside the cavity. If initially located at the cavity center the shift would be zero. Variations in device location in the tunnel up to a distance of 3 m appear unimportant since the 1 and 3 m results (Models 4 and 5) produce similar energy center shifts. The barriers on the portal side of the WP choke the flow toward the LOS and play a major role in directing energy back toward the cavity. It is important to note that the two barrier design produces nearly the same energy shift as a reflective boundary, presumably the maximum energy shift into the cavity that can be achieved.

Models 7, 8 and 9 addressed the desire (or necessity) to physically isolate the contaminated DIAMOND FORTUNE cavity from construction and fielding personnel. A foam-filled tunnel or cavity (Models 7 and 8), produced nearly identical energy center motion (see Figure 5), whereas the center remained nearly stationary when the grout curtain was utilized (Model 9). However, Model 7 was eliminated from further consideration because more energy was injected into the LOS than with Models 8 and 9 (see Figure 6). Figure 6 displays the amount of energy, relative to the 20 ton total, obtained by summing all grid energy from the "window" to the WP for Models 5, 7, 8 and 9. Model 5 is included in this comparison as representing the most effective design for moving energy into the dump volume and limiting energy injection into the LOS.

To examine the effectiveness of Models 5, 8 and 9 the calculations were continued to 2 ms. These three provide a comparison of two methods of isolating the contaminated cavity (Models 8 and 9) with the "best" design (Model 5). Density contours are shown in Figure 7 for these models at 2 ms. The remnants of the grout wall have expanded into the cavity in Model 9 and energy confinement near the WP has enhanced the motion of both barriers toward the sand section. Also, the reentry tunnel has undergone substantial expansion above the WP . Models 5 and 8 display similar contours but for Model 5 the high density LOS pipe has been scoured producing some additional mass (debris?) in the LOS near the 5 m location. Pressure, density and velocity along the LOS centerline for the three models are compared in Figure 8. The additional mass in the LOS for Model 5 significantly reduces the velocity of the LOS flow toward the "window" (reflect boundary). Note that by 2 ms the flow has reached the "window" location and material has begun to stagnate against it. The total energy summed from the

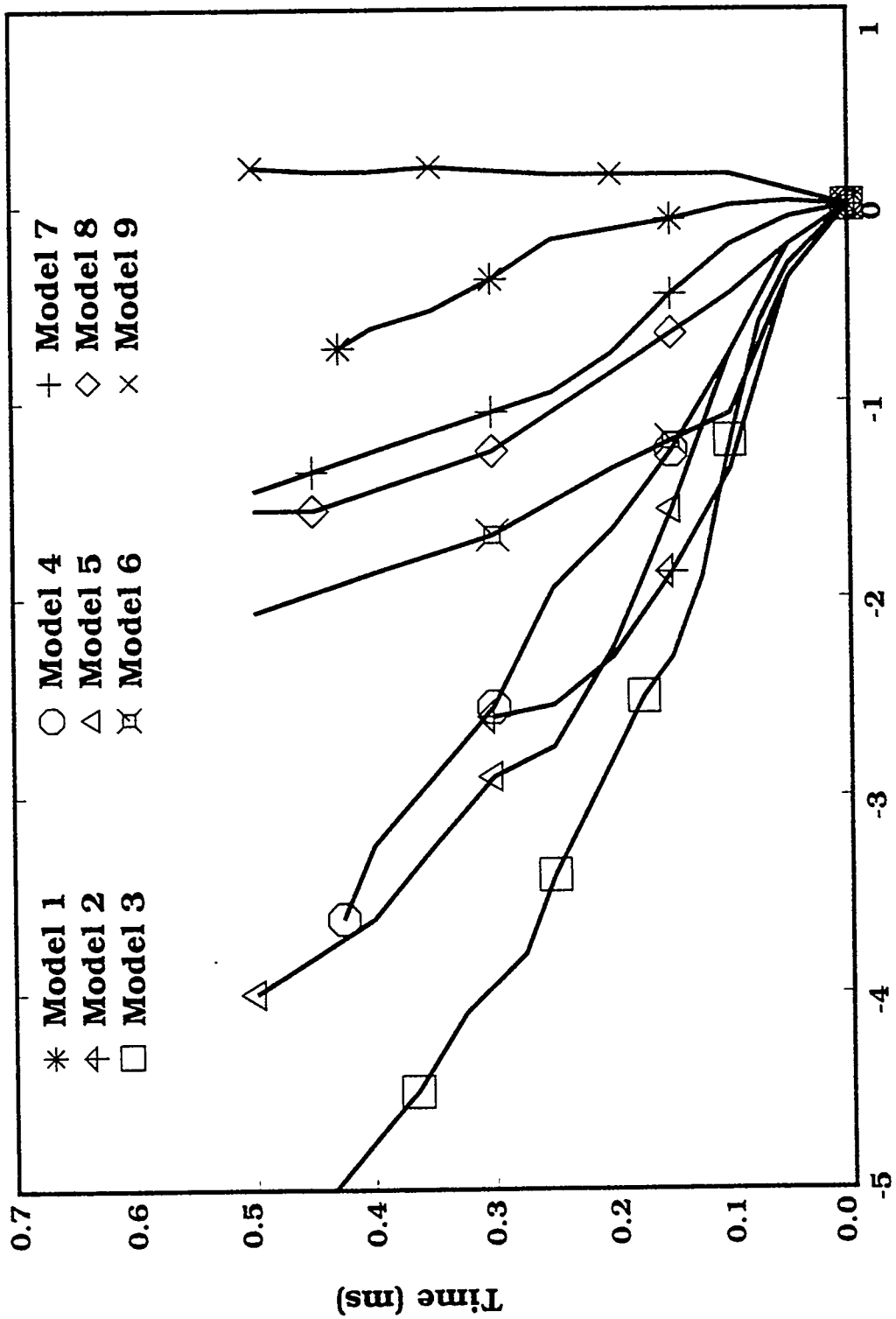


Figure 5. Energy center history.

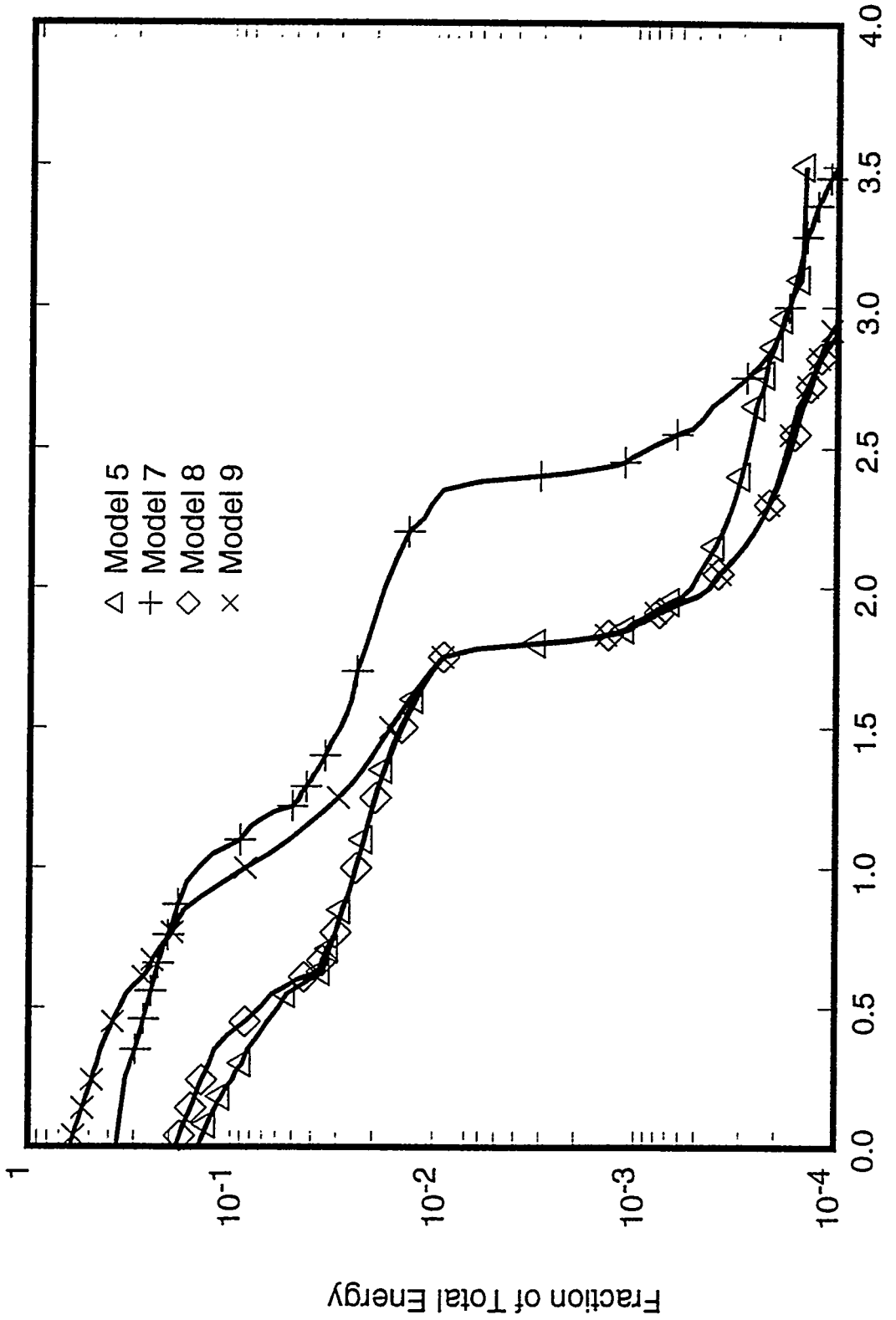


Figure 6. Window to WP integrated energy at 0.5 ms.

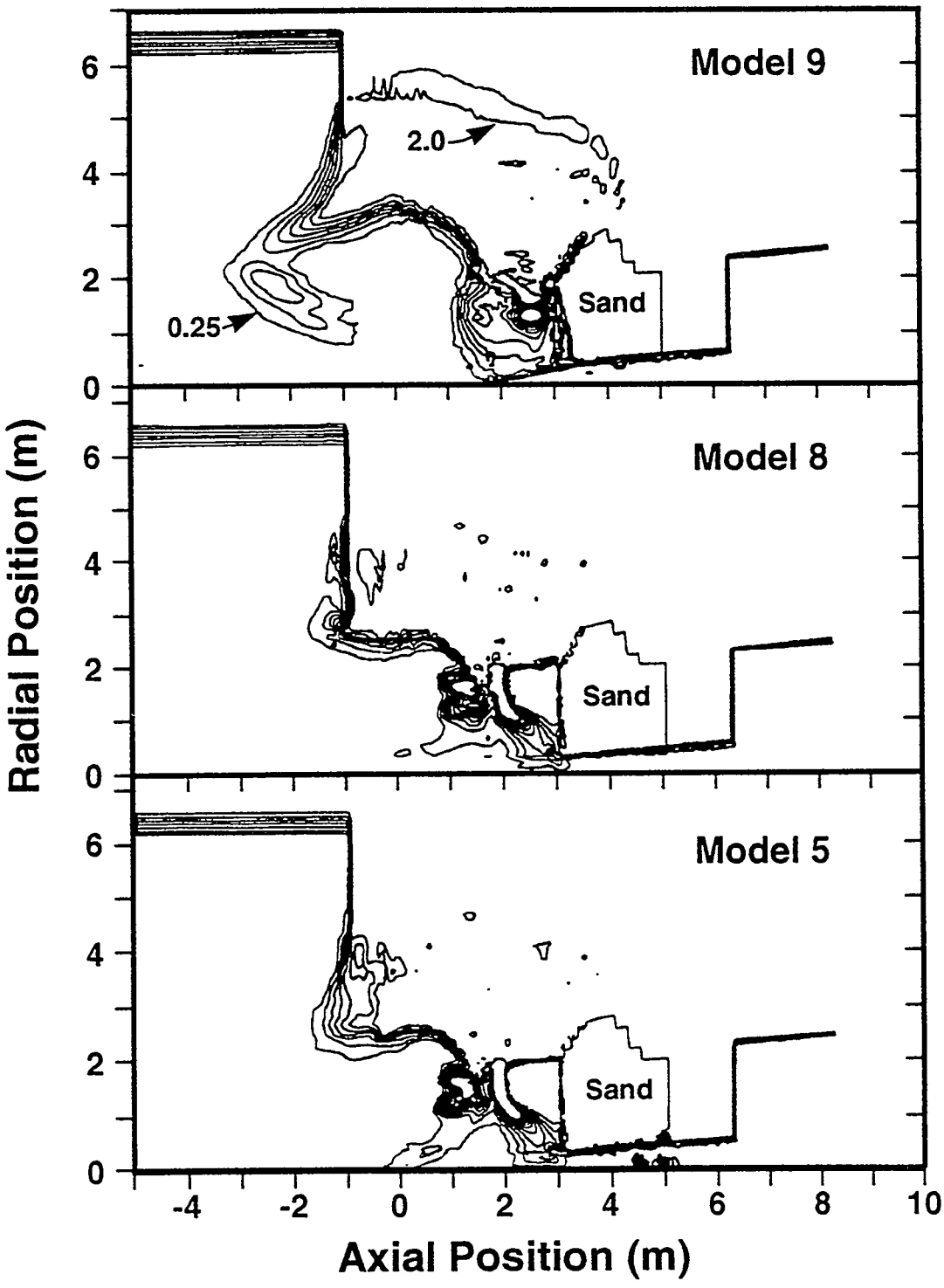


Figure 7. Density contours at 2 ms.

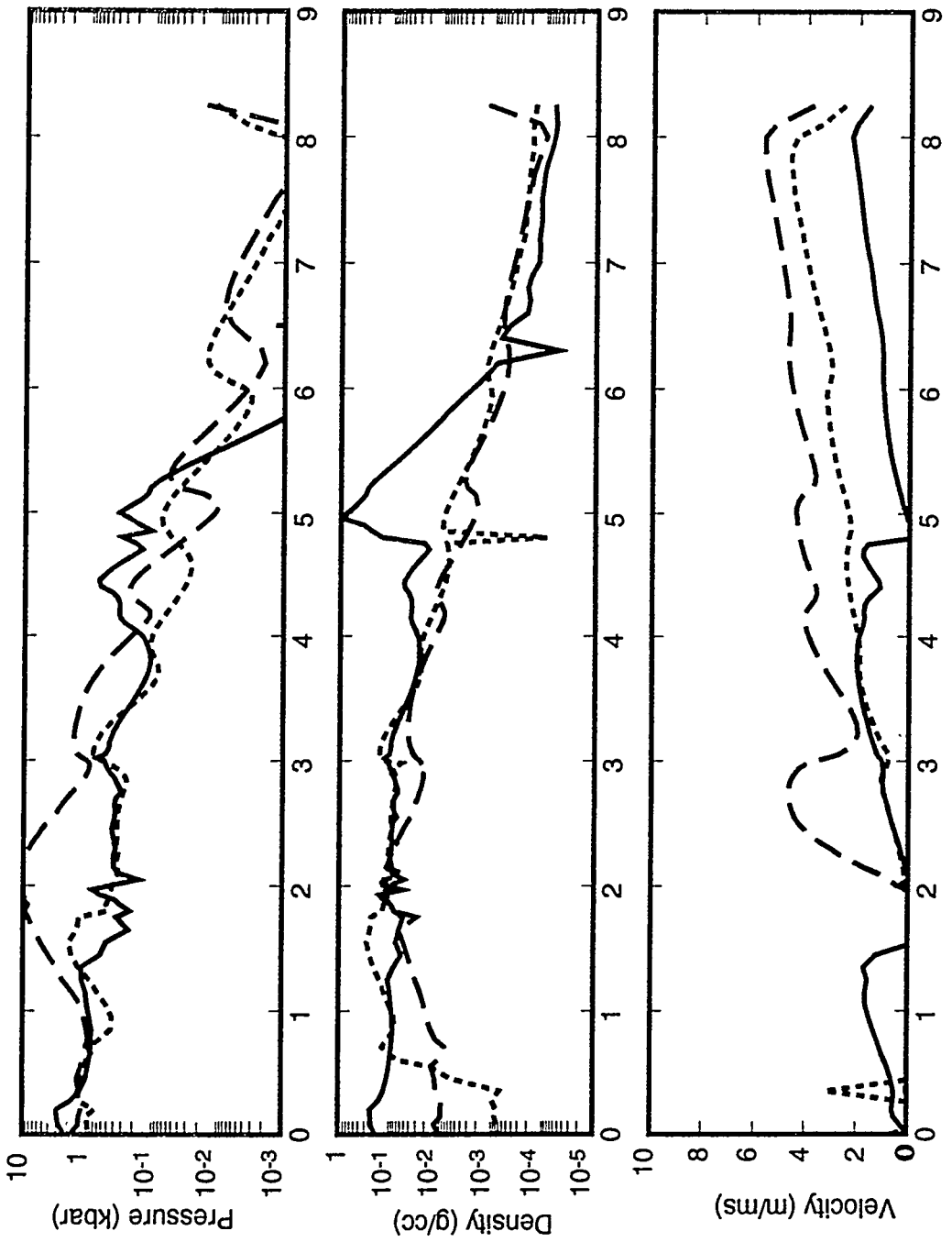


Figure 8. LOS centerline values at 2.0 ms. Solid line is Model 5. Dotted line is Model 8 Dashed line is Model 9.

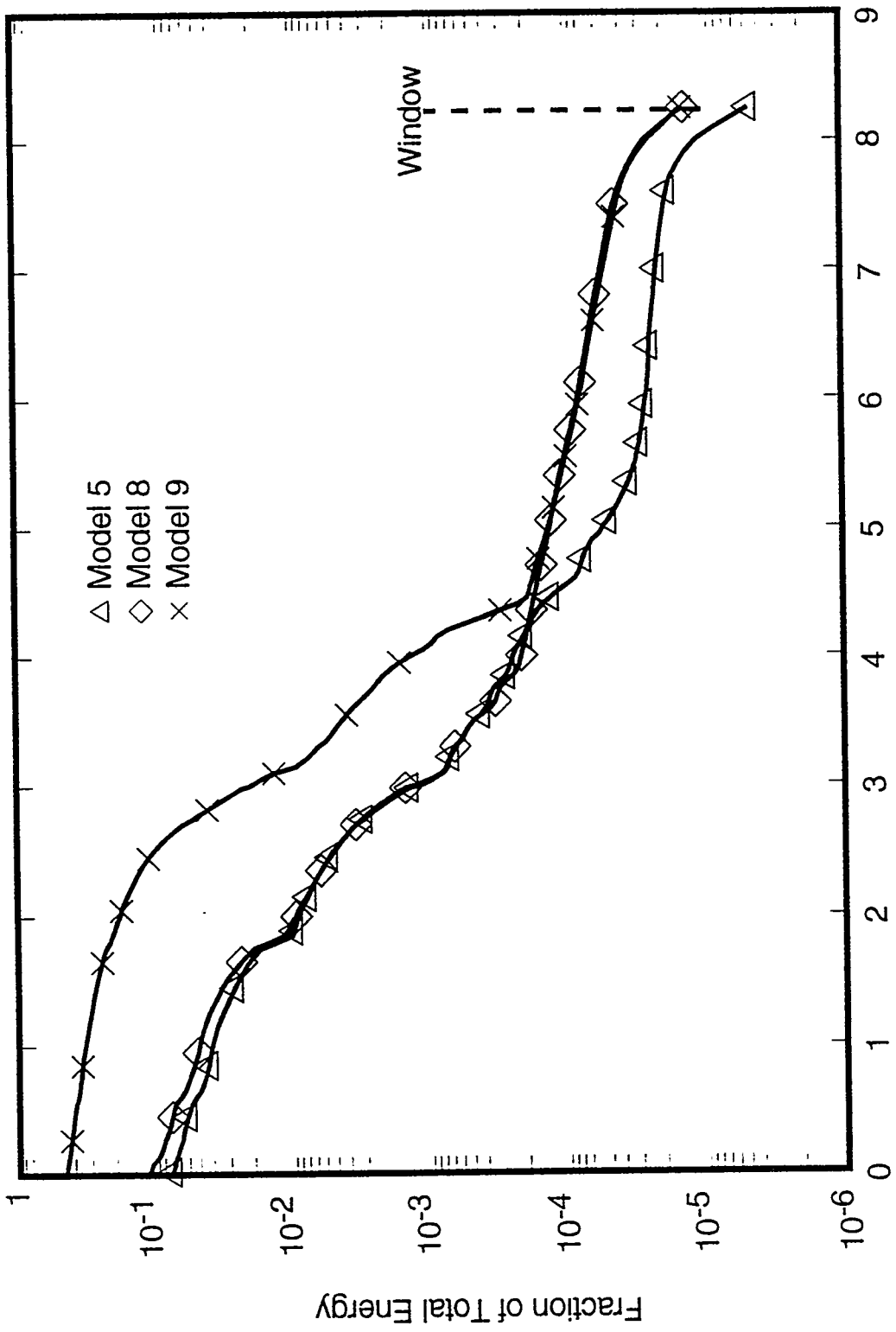


Figure 9. Window to WP integrated energy at 2 ms.

"window" toward the WP is compared in Figure 9 for the three cases. Model 9 energy deposition for the first few meters along the LOS is nearly an order of magnitude larger than the other two due to barrier impact on the sand stemming. All three models show that only about 5 pound HE equivalent energy has reached the "window" by 2 ms. The effectiveness of these three designs to move energy into the DIAMOND FORTUNE cavity is given in Figure 10. As expected, the design without cavity foam or the grout pillar has more direct access to the DIAMOND FORTUNE volume and therefore makes more effective use of the dump volume. If isolation of the contaminated cavity is necessary, these results indicate that filing the cavity with low density foam should lead to reduced early time loads on the high strength "window".

5. CRITIQUE

The representation of device characteristics and the possible influence of significant variations is a source of considerable uncertainty in this investigation. For the assumed device model the calculated energy coupling in barriers, tunnel walls, foam sections and LOS entrance are probably reasonable. Describing the cavity as a cylinder rather than a hemisphere whose floor is only a few feet below the device horizon may overestimate cavity flow since interactions along the floor are not included in the analytic simulation. However, evaluation of the relative merits of various designs seems justified. The capability of the Eulerian SOIL code to accurately describe LOS flow/pipewall interaction at very low stress levels, while not perfect, is felt to be a reasonable simulation. Other papers submitted to this symposium address this issue in more detail.

6. FUTURE PROGRAM: ISSUES/APPROACHES

To continue development of a VLY testbed some general concerns that must be addressed include:

- Device details are probably critical to system design. These include, non-spherical mass, geometry and total and radiated yield fractions.
- Dump volume geometry and limitations on volume accessibility will be important in maximizing dump volume effectiveness.
- Pipe taper and distances to a "window" or barrier, mechanical closure or test chambers or test cells are critical to hardware survivability.
- Geometric constraints on the size, shape and lengths of open volumes or tunnel size in the WP region will dictate close-in coupling and control energy flow into the dump volume.

Following satisfactory resolution of these issues the design development could continue. The next phase should include investigation of:

- Modified barrier designs to mitigate the flow toward the LOS.
- Detailed interactions of the expanding device debris with the LOS pipe entrance and the

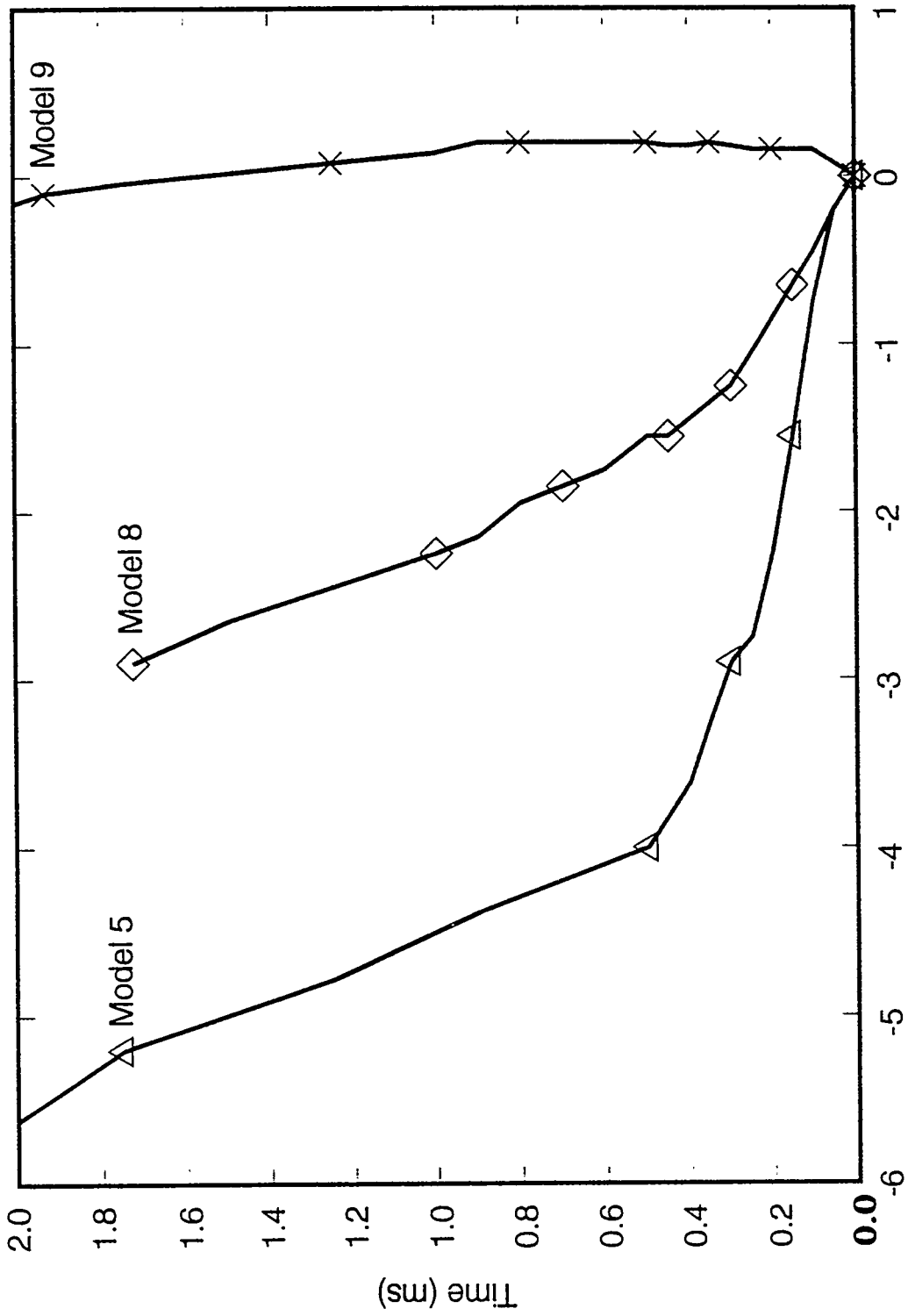


Figure 10. Energy center history.

mylar LOS vacuum window.

- The interaction of LOS flow and LOS pipe and characterization of dynamic and static loads on the proposed high strength steel barrier.

REFERENCES:

1. Perry, R.W. and A. Kantrowitz, "The Production and Stability of Converging Shock Waves," J.A.P., Volume 22, Number 7, July 1951. (U)

2. Johnson, W.E., "The SOIL Family of Codes" (U), Computer Code Consultants, Inc., DNA 295IT, 1982. (U)

Response of Steel Vessels and Cavity Liners to Dynamic Loading

C. M. Snell, R. P. Swift, and N. L. Marusak
Los Alamos National Laboratory, P.O. Box 1663, Los Alamos, NM 87545

L. R. Hill
Sandia National Laboratory, Albuquerque, NM 87185

Abstract

The use of steel vessels to fully contain explosion products is one approach for conducting high-explosive hydrodynamic experiments and zero-yield or low-yield nuclear tests. Such vessels could be free-standing, located above ground or underground, or a prestressed liner in a rock cavity utilizing the rock as an integral part of the containment system. We have performed a suite of one-dimensional calculations to define the dynamic response and assess containment capability of typical steel vessels. Performance was assessed as a function of the following parameters: (1) scaled vessel radius and wall thickness; (2) energy source type, i.e., high-explosive and nuclear; (3) initial air pressure inside the vessel; (4) elastic and elastic-plastic behavior of the vessel; and (5) external confinement, i.e., no confinement, soft rock, and hard rock. The energy source was modeled as a uniform "pill" of the appropriate mass and energy density. The pill approximation is shown to agree with more detailed source calculations, indicating that it is adequate for the regime of interest for the containment vessel response. Calculational results are presented in the form of scaled peak strains in the vessel wall *versus* energy density of the source. We find that impulsive loading tends to dominate the response for massive energy sources, e.g., high-explosive (HE), and for large initial air mass in the vessel, e.g., 1 atmosphere. The late-time quasi-static pressure becomes more important for low-mass nuclear sources and near-vacuum conditions. Peak strains are smaller for nuclear sources than for HE sources, and are significantly reduced by evacuating the vessel. Confining the vessel with rock also reduces the peak strains with best results obtained for hard rock backing. The rock confinement also serves to dampen late-time ringing of the vessel. This is important for asymmetric loading conditions and for multidimensional vessel designs. Two-dimensional calculations and experimental data show that such conditions can lead to strong bending modes in the vessel wall, with localized strain reinforcement on the order of two to four times larger than the initial peak. Adequate external damping can greatly reduce these undesirable late-time peaks. Finally, calculations are compared with the measured steel liner response for a recent cavity event.

CANONICAL WALL LOADING FUNCTIONS FOR DECOUPLED CAVITIES AND CONTAINMENT VESSELS

Charles M. Snell, Robert P. Swift, Nancy L. Marusak, George R. Spillman,
Groups EES-5 and P-DO, Los Alamos National Laboratory, MS F665,
Los Alamos, NM 87545

ABSTRACT

Airblast loading of a cavity wall by a nuclear or high-explosive detonation is of interest for containment of low-yield untamped explosions, dynamic response of containment vessels or liners, seismic decoupling by cavities, and other applications. Recent studies of the LYNER test concept and other cavity-related designs have highlighted the fact that there is no complete and internally consistent set of airblast loading functions to characterize the expected loading over a broad range of peak pressures. For cavity radii larger than about 10-15 $m/kt^{1/3}$, displacement of the wall during the loading pulse is generally small relative to the cavity radius. In this regime, the wall can be treated as a fixed or rigid boundary for the purpose of calculating the reflected airblast pressure history. We have performed a series of one-dimensional spherically symmetric calculations for typical nuclear and high-explosive energy sources in air-filled cavities with radii of 15 $m/kt^{1/3}$ to 295 $m/kt^{1/3}$. This encompasses a range of peak reflected pressures at the cavity wall from approximately 1000 MPa to 0.1 MPa. The calculations were run for durations of at least 0.07 $sec/kt^{1/3}$ for the smallest cavities, up to 0.9 $sec/kt^{1/3}$ for the largest cavities. This time period includes up to 25 cavity gas "bubble-bounce" oscillations for the smallest cavities. The calculational results were validated by comparison with nuclear and high-explosive free-air and reflected airblast data. These pressure-versus-time histories provide a convenient and accurate set of loading profiles that can be used for containment and cavity decoupling studies.

I. INTRODUCTION

One of the principal mechanisms that can cause mechanical damage to free-standing metal containment vessels or metal-lined cavities is the impulsive airblast load. In some regimes, this factor alone determines survivability of the structure. For other cases, quasi-static pressures and late-time thermal

effects become predominant. However, some of these mechanisms are amenable to mitigation schemes that will not reduce the impulsive load. Thus, the airblast load is always a significant consideration in design of explosive test containment structures with exposed walls.

Recently, several containment concepts have been proposed that involve vessels, lined cavities, or windows at a broad range of different distances from the explosive source and thus at dramatically different loading levels. Meaningful comparison of these concepts requires the use of airblast loading functions that are consistent and accurate over the entire span of distances in question. It has become apparent that there is no complete and internally consistent set of loading data suitable for use in these studies. To remedy this situation, we have performed a suite of one-dimensional calculations for nuclear and high-explosive airblast loading at a rigid wall. The source energy was assumed to be 20 tons (8.37×10^{10} J = 2×10^{10} cal). The calculations encompassed a range of wall radii "R_0" from 4 to 80 m, corresponding to scaled radii of 15 to 295 m/kt$^{1/3}$. Over this interval of distances, the peak reflected airblast overpressure at the rigid wall varies from about 1000 MPa (10 kb) to 0.13 MPa (1.3 bars). For loading pressures above this range, most metals will undergo dynamic failure at the shock front even before any stretching or bending of the window. Overpressures below 1 bar are not likely to be employed for dynamic containment applications. Our study therefore covers the loading range of interest for most containment concepts.

II. CALCULATIONAL ASSUMPTIONS

The key assumptions of the model are:

1) The geometry was one dimensional and spherically symmetric. A finite-difference zone size of 2.7 cm was employed in the nuclear energy source region, with a maximum zone size of 5.3 cm in the air for most calculations. Zone size and other comparison studies were also performed and are briefly discussed below.

2) The nuclear energy source was modeled using the adiabatic or "pill" source approximation, as an initially uniform spherical region of the appropriate energy content. The initial source radius was 27 cm. The mass of the source was assumed to be M_0 = 70 kg for most of the calculations, although several comparison runs were made for M_0 = 22 kg (low-mass source) and 124 kg (high-mass source). Radiation transport and details of the very-early-time dynamics in the source region were not included. More detailed source calculations that include these

effects show that radiation transport and source-region kinetics are unimportant and do not significantly affect the airblast at ranges beyond a few meters for low-yield sources. Some inaccuracy would be expected at high yields, however, see the discussion below for an indication these results remain accurate even at somewhat higher yields.

3) The blast propagation medium was assumed to be uniform air at an initial density of $\rho_0 = 0.00123$ gm/cc and an initial pressure of $P_0 = 1.013$ bars. This corresponds approximately to sea level air at a temperature of 15°C.

4) The outer boundary of the calculation was treated as an unmoving or perfectly rigid wall. This boundary condition is appropriate for steel vessels and similar applications because the wall undergoes peak excursions of about ± 2 cm or less for a typical containment vessel, resulting in a total volume change of about 1%. This small amount of wall motion has virtually no feedback effect on the blast reflections and dynamics of the gas inside the vessel. For the case of a cavity in rock or soil, significantly larger wall expansions may occur in some cases. However, these expansions typically require tens of milliseconds and will not have a major influence on the crucial loading during the first millisecond or so after blast arrival.

5) Turbulent mixing of the dense source material with the air is ignored. Mixing will have no effect on the calculated initial blast loading, but may eventually cause the late-time reflections occurring in the cavity to be damped and die out.

III. VALIDATION

Unfortunately, there is little or no nuclear airblast data on close-range reflected overpressures at a spherical rigid wall. There are, however, extensive measurements for high explosive and nuclear free-air and surface bursts that can be scaled for comparison with the present calculations. Figure 1 compares the present calculations with the best available high-explosive free-air data. The figure is taken from Baker [1], based on the work of Goodman [2]. In this case, we have plotted the peak overpressure normalized to the ambient pressure ($\Delta P/P_o$), versus the range normalized to high-explosive charge radius (R/R_{charge}). The calculated peak overpressures are slightly high but within the span of the data at close ranges, and are in excellent agreement at longer ranges (beyond about ten charge radii). Nuclear calculations are compared with experimental measurements in Figure 2, which is again taken from Baker[1] based on analysis of unclassified data by Kingery and others [3]. This graph displays peak

overpressure ΔP (in psi) versus cube-root scaled range R (in $m/kt^{1/3}$). The nuclear data are for surface bursts rather than free-air values, so it is necessary to apply an appropriate correction factor to the calculated results. We have scaled the calculations to a larger effective surface burst yield using the relation $W_{surface\text{-}burst} = 1.7 \times W_{free\text{-}air}$ (see reference [1] and discussion below). Also shown in Figure 2 is a fitted curve for high-explosive surface burst experiments scaled to an equivalent nuclear yield using the relation $W_{nuclear} = 0.5 \times W_{high\text{-}explosive}$ [1]. Again, the calculations are slightly high at small scaled ranges and in excellent agreement at longer ranges. More important, the calculations have been compared in detail with measured high-explosive and nuclear impulses, and with high-explosive data for reflected airblast at a rigid wall. The agreement is extremely close at all pressure levels. Finally, the entire calculated pressure-versus-time histories have been closely compared with measured nuclear waveforms at very high peak overpressure levels of ~0.1 - 0.5 GPa (1-5 kb). The nuclear data show significant scatter up to ±30% or more, but again excellent agreement is achieved within the limits of the measurement capabilities. This result is obtained despite the fact that most of the nuclear data are for larger yields W = 0.5 - 1 kt, rather than for the W = 0.02 kt yield employed for the calculations. It is clear that radiation and source mass effects are not very important at yields up to a kiloton or so. It follows that our calculated airblast loadings can be scaled and employed for larger yields, as well as for the low sub-kiloton range that was our first concern in this study.

Although experimental data are lacking for reflected nuclear airblast, simple tests have been made to assure that the calculations are accurate. Figure 3 shows pressure histories at several locations for a calculation with the rigid wall at R_0 = 60 m. The gradually decaying incident pulse approaches the wall (R = 50 m, 55 m, 57.5 m), and is subsequently reinforced by a reflection from the wall arriving on the tail of the pulse. The arrival of the inward-propagating reflection occurs progressively earlier at locations closer to the wall. Finally, at the wall position (R_o = 60 m), the initial and reflected pulses are simultaneous and the greatest reinforcement of peak overpressure occurs. The peak would be increased by a factor of two for an ideal, small-amplitude acoustic reflection. In this case, reinforcement is somewhat greater than a factor of two because of the finite amplitude of the incident pulse. Of course much larger reinforcement factors are experienced for the small-radius cavities with very high incident overpressures.

IV. EFFECTS OF ZONING, SOURCE MASS, AND ENERGY SOURCE TYPE

The computer time required for a one-dimensional calculation increases as the square of the number of zones. It is thus desirable to employ zoning that is fine enough to adequately resolve physical effects of interest but not excessively fine. Also, use of automatic rezoning to combine compressed zones behind the outgoing shock front can speed up the calculation by a factor of ten or more. For this study, we have adopted a maximum zone size in the air of 5.3 cm and have routinely used the rezoning capability. To check the effect of these choices, comparison calculations were performed with zone size decreased by a factor of five, and with the automatic rezone procedure suppressed. These comparisons were made for the nuclear case with a cavity radius of R_0 = 11 m. Results are displayed in Figure 4. The very-fine-zoned run (shown by the dotted curve) gives a slightly sharper definition of the shock front but otherwise closely tracks the standard case (solid curve). The calculation without rezoning (dashed curve) is almost indistinguishable from the standard case. Clearly, the finite-difference zoning and rezone procedures used here are adequate to provide reliable results for these calculations.

One physical parameter that can influence airblast coupling efficiency for nuclear events is the mass of the energy source. It is recognized that large differences in source mass and energy density can have a substantial impact, as for example the substantial difference between high-explosive and nuclear airblast at equal energy yields. To examine this factor, we made calculations for three source masses of M_0 = 124, 70, and 22 kg. The cavity wall was at a radius of 11 m and all other factors were kept identical among the three runs. The resultant airblast profiles at the wall are compared in Figure 5. The arrival times are earlier and the peak overpressures are slightly higher for higher mass sources. However, impulse is generally a more important criterion than peak overpressure for structural damage effects. To obtain a meaningful comparison, we have shifted the three waveforms to match arrival times, and integrated the pressure versus time to obtain impulse. Results are displayed in Figure 6 (impulse is in units of megabar-microseconds). During the first millisecond after blast wave arrival, the impulses are quite comparable. At later times, the impulses are actually slightly greater for the 70 kg and 22 kg sources (dashed and dotted curves) than for the high-mass source (solid curve). All of the calculated impulses lie within a narrow range of 3-7% over the entire time period of interest for mechanical response modeling. Clearly, source mass does not have a dramatic effect on impulse over the range of variation examined here. We have also performed calculations with a fully detailed model of the nuclear

energy source in place of the "pill source" approximation. Although the calculated waveforms very close to the source differ slightly, the impulse falls entirely within the range showing Figure 6. This result is fortunate, because it allows us to adopt a single source mass for parametric studies of airblast effects. In the calculations presented below, we have employed a source mass of 70 kg in all cases.

Typical examples of the calculated nuclear and high explosive airblast pressure profiles at the cavity wall are compared in Figure 7. For the smaller cavity radii, R_o = 8 and 11 m, the nuclear signal arrives earlier but is lower in amplitude than the HE pulse. The average pressures for the HE remain higher at late times and deliver a larger total impulse to the wall. It is interesting to note that the cavity reverberation frequency associated with reflection between the wall and the center of symmetry is higher for the nuclear source, because of the higher average temperature and sound speed in the nuclear cavity. At the large cavity radius of R_o = 25 m, the larger-amplitude HE signal has caught and passed the nuclear signal, and arrives earlier at the wall. Again, the higher peak pressure and impulse for the HE loading are evident.

V. CAVITY RADIUS STUDY

Table 1 lists the initial conditions for fourteen nuclear and twelve high explosive calculations included in the parameter study of wall loading as a function of cavity radius "R_o". The pressure profiles at the cavity wall for the nuclear source are displayed in Figure 8-11; those for the high-explosive source are presented in Figures 12-15. The pressure and time axis scales are logarithmic for the small cavity radii (Figures 8 and 12), because of the early arrival times and high peak amplitudes of the signals. For the larger cavities, the peak amplitude decreases and becomes comparable to the 1-bar ambient pressure. Linear axis scales are employed in these cases (Figures 9-11, 13-15). Comparison of the blast waveforms clearly shows the expected decay of peak reflected airblast pressure with increasing cavity size, as well as the increase in the cavity reverberation period. Also evident are the progressive changes of the waveforms with cavity radius and energy source type. For example, both nuclear and HE events show the double peak structure associated with the initial airblast arrival and the subsequent arrival of the shock caused by the debris-air interface [4]. However, the second peak for nuclear sources arrives relatively late, is smaller than the initial peak, and is most evident for cavity radii of R_o = 8 - 14 m (Figures 8 and 9). At smaller radii, the late-arriving second peak is overwhelmed by the cavity reverberation arrival. At larger radii, the second peak is largely merged with

the initial airblast pulse. The high-explosive sources display a much stronger second peak, which is very prominent for cavity radii of R_o = 6 - 20 m and is larger in peak amplitude than the initial arrival for radii up to about 11 m. The calculations show a number of other interesting features, which will not be further discussed here. All of the calculated pressure-time waveforms are available in digital form; to obtain the data, see Section VII.

Impulse delivered to the cavity wall is often the most important physical quantity for structural response applications. The time interval over which impulse is effective in inducing motion will depend on the characteristic response period of the structure. A small, stiff, high-frequency structure will respond over a shorter interval than a large structure. Also, local details of the response may be quite sensitive to temporal features of the waveform and to interaction of higher modes excited in the structure. These factors are obviously specific to a given loading profile and structure, requiring detailed response predictions for each individual case. However, it is possible to get a useful idea of relative effects by comparing the wall impulse for various profiles. We have integrated the waveforms shown in Figures 8-15 to obtain the impulse over intervals of 1 millisecond and 5 milliseconds after the initial airblast shock arrival. The results are displayed as a function of cavity radius in Figure 16. For both integration intervals the impulse for high explosive is approximately a factor of two higher than the corresponding nuclear impulse. It is apparent that there are several kinks or irregularities in these impulse curves. Close examination has shown that these effects are caused by physical features present in the loading waveforms. For example, in the nuclear (1 msec) case, the smallest cavity radii of 4 and 5 m appear somewhat high because the 1-msec integration period includes the first cavity reverberation arrival only for these two cases. The high explosive (1 msec) point at a cavity radius of 14 m appears to drop off steeply because the 1-msec integration excludes the debris shock arrival at this radius. Likewise, the nuclear (5 msec) point at a cavity radius of 11 m is low because the 5 msec period again excludes the cavity reverberations (the closer nuclear points include two or more reverberation periods). The presence of such features will cause inaccuracies when attempting to use simple models for the impulse delivery. Although estimates can be made based on general impulse criteria, accurate predictions require the use of realistic loading waveforms and calculation of the complete temporal response of the structure.

VI. SCALING AND OTHER APPLICATIONS OF THE RESULTS

These calculations are specifically directed toward the low yield nuclear energy source in air. However, results can be straightforwardly extended to

other energy yields by use of Hopkinson scaling [1]. The Hopkinson scaling law states that, for a given ambient medium, range scales as the cube root of energy yield:

$$R = R_0 (W/W_0)^{1/3} \quad (1)$$

where R = range;
W = energy yield;
R_0 = range from the reference energy source;
W_0 = yield of the reference energy source
(W_0 = 0.02 kt for these calculations).

Time likewise scales as the cube root of yield:

$$t = t_0 (W/W_0)^{1/3} \quad (2)$$

where t = time;
t_0 = time for the reference energy source.

And the peak overpressure at a given scaled range scales directly (scaling factor of 1.0):

$$\Delta P(R/W^{1/3}) = \Delta P_0(R_0/W_0^{1/3}) \quad (3)$$

From these results, it is clear that impulse at a given scaled range also scales as the cube root of yield.

Hopkinson scaling applies only for fixed ambient conditions, i.e., air at an initial pressure of 0.1013 MPa (1.013 bar) in these calculations. The more general Sachs law allows blast scaling for different ambient conditions. However, this scaling law has restrictions and is valid only over a certain range of ambient conditions. More thorough discussions in [1] and other references therein review the applicability and limitations of the scaling laws.

Our calculations are also limited to spherical one-dimensional geometry. There are no general scaling procedures for different energy source types or for multidimensional effects. However, some empirically developed rules-of-thumb allows estimates to be made for certain cases. Past work indicates that a surface burst in hemispherical geometry produces airblast roughly equivalent to a spherical (free-air) burst of 1.7 times the energy yield: $W_{surface\text{-}burst} = 1.7 \times W_{free\text{-}air}$. Substituting this increased "apparent yield" into the above scaling laws will allow the results to be used for a surface burst (hemispherical geometry). The situation becomes much more complex

for elevated bursts or other multidimensional geometries, and simple estimates no longer apply. More elaborate analyses or multidimensional calculations are generally required to predict the loading for these cases.

VII. AVAILABILITY OF THE DATA

The airblast pressure profiles have been saved in digital form to facilitate computer calculations of vessel or cavity dynamic response. The loading histories can be employed as pressure boundary conditions to drive finite-difference or finite-element calculations. The data are available as UNIX text files in a Los Alamos universal-access Common File System (CFS) directory called /AIRBLAST/WALL. The individual files are named as indicated in Table 1: NUC04, NUC05, etc. (nuclear calculations), and PBX06, PBX08, etc. (Pbx9404 high-explosive calculations). Comments at the beginning of each file describe the data format.

To reduce the size of these files, data more than a few hundred microseconds preceding the initial shock arrival have been truncated in most cases. The pressure before this time is equal to the ambient pressure in the air. Also in the interest of reducing file size, very fine time resolution is employed for the initial peak, with somewhat coarser resolution at late times. This approach does not significantly affect the quality of the data, because adequate resolution has been retained to resolve the later-arriving features in the signal.

In the calculations for larger cavity radii, the initial airblast shock does not arrive at the wall for several tens of milliseconds. It would be wasteful to run mechanical response calculations through this long quiescent period before the signal arrives. For this reason, it is often desirable to shift the pressure profile backward in time so that the blast wave arrival occurs just after zero time. Likewise, it is sometimes useful to drive response calculations with a pressure profile starting at zero pressure (rather than the 1.013-bar ambient pressure). In this case, it is necessary to shift the calculated pressure downward by an amount equal to the ambient pressure. A small code called PROFILE has been written to allow temporal and pressure shifting of the pressure profiles. It is available from the same CFS directory, /AIRBLAST/WALL. The PROFILE code can also multiply the times and pressures by any specified factors. This capability is useful for two purposes: (1) to convert the times and pressures from units of microseconds and megabars to any desired system of units, and, (2) to scale the times from 0.02 kt to any desired energy yield (see Eqn. 2, Section VI above). PROFILE runs on the Unix Cray computers. Operation is interactive, with self-explanatory prompts for input.

References

[1] W. E. Baker, Explosions in Air, University of Texas Press, Austin, Texas (1973).

[2] H. J. Goodman, "Compiled Free-Air Blast Data on Bare Spherical Pentolite", Ballistic Research Laboratory Report BRL #1092, Aberdeen Proving Ground, Maryland (1960).

[3] C. N. Kingery, "Parametric Analysis of Sub-Kiloton Nuclear and High Explosives Blast," Ballistic Research Laboratory Report BRL #1393, Aberdeen Proving Ground, Maryland (1968).

[4] R. R. Karpp, T. A. Duffey, and T. R. Neal, "Response of Containment Vessels to Explosive Blast Loading", Los Alamos National Laboratory Report LA-8082 (June, 1980).

Table 1. Suite of Nuclear and Pbx 9404 He Calculations for Different Cavity Radii. All Calculations Used a Source Energy E_0 = 20 Tons and an Initial Air Pressure P_0 = 1.013 Bars. The Nuclear Calculations Used a Source Mass M_0 = 70 kg.

Nuclear Calculations	Wall Radius R_0 (m)	Termination Time (microseconds)
NUC04	4.0	15000
NUC05	5.0	15000
NUC06	6.0	20000
NUC08	8.0	20000
NUC11	11.0	20000
NUC14	14.0	30000
NUC17	17.0	40000
NUC20	20.0	50000
NUC25	25.0	66000
NUC30	30.0	82000
NUC40	40.0	114000
NUC50	50.0	146000
NUC60	60.0	178000
NUC80	80.0	242000
HE Calculations		
PBX06	6.0	8000
PBX08	8.0	20000
PBX11	11.0	20000
PBX14	14.0	30000
PBX17	17.0	40000
PBX20	20.0	50000
PBX25	25.0	66000
PBX30	30.0	82000
PBX40	40.0	114000
PBX50	50.0	146000
PBX60	60.0	178000
PBX80	80.0	242000

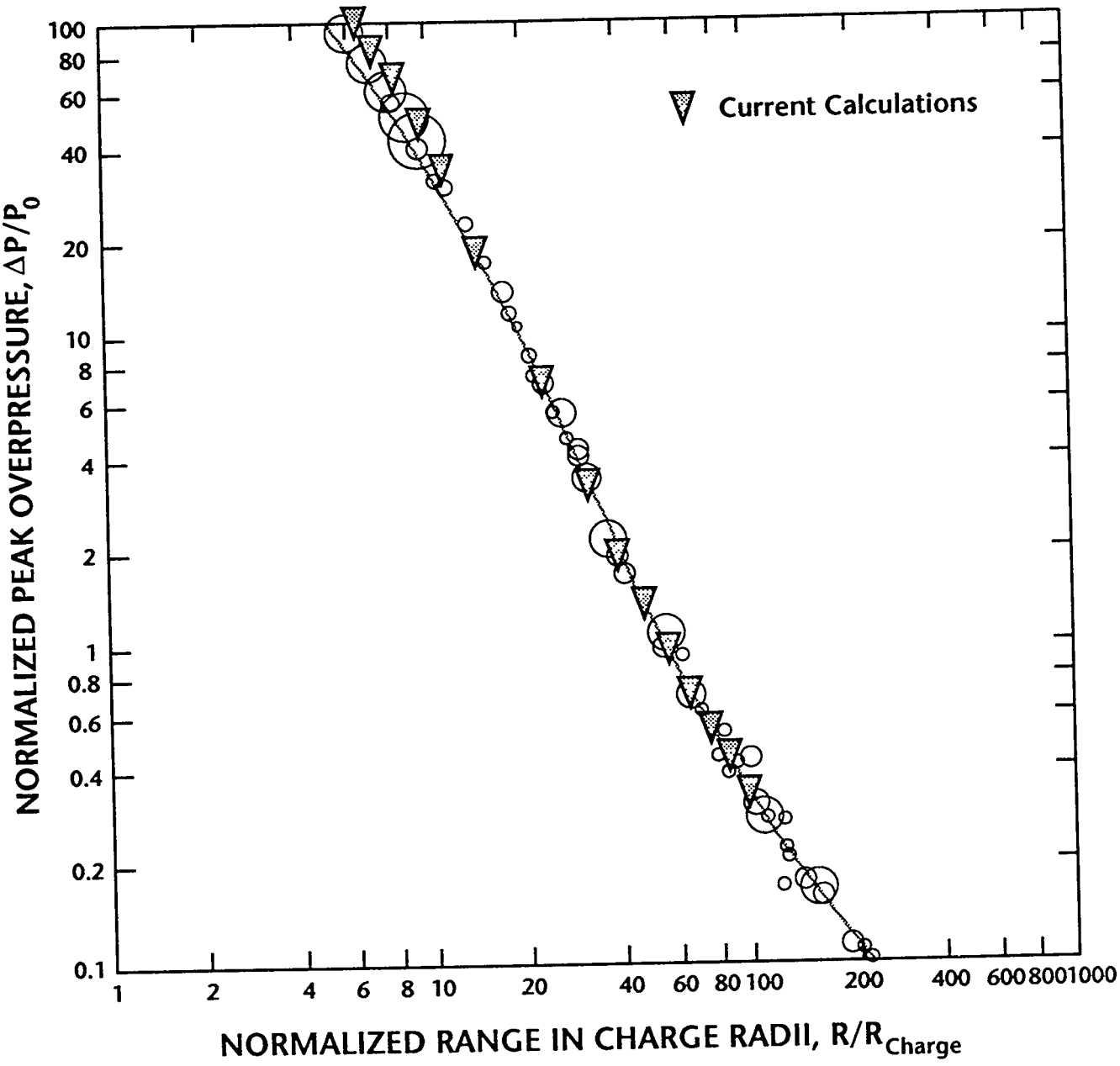


Fig. 1. High explosive free-air peak airblast overpressure versus range. Calculations are shown as inverted triangles. (Data taken from ref. [1], Figs. 5.4a-b; for readability, only selected data points are plotted, see original reference for all data.)

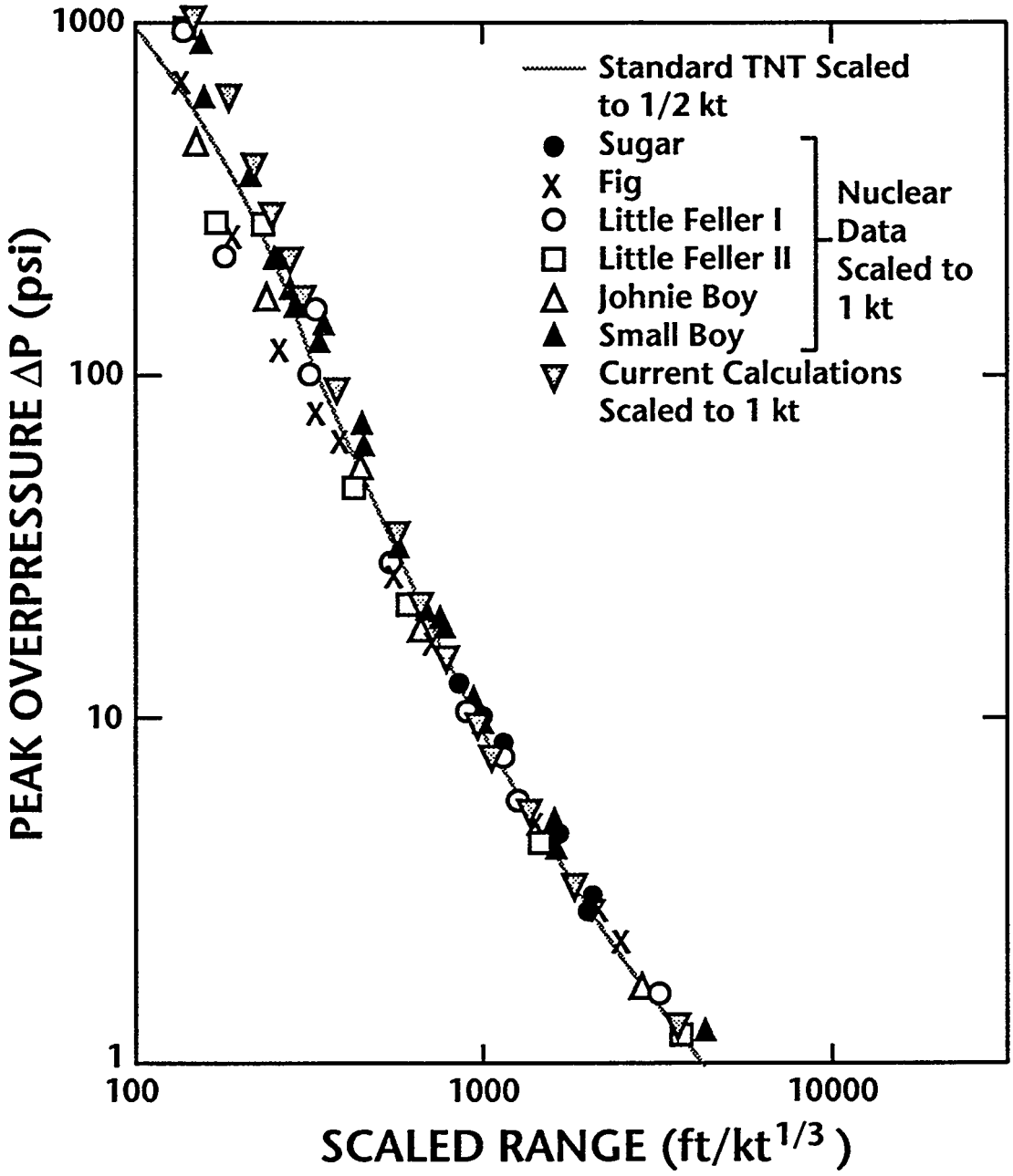


Fig. 2. Nuclear surface burst peak airblast overpressure versus range, scaled to 1 kt. Calculations are shown as inverted triangles. Also shown is an experimental high-explosive curve scaled to 0.5 kt (Data taken from ref. [1], Fig. 5.9).

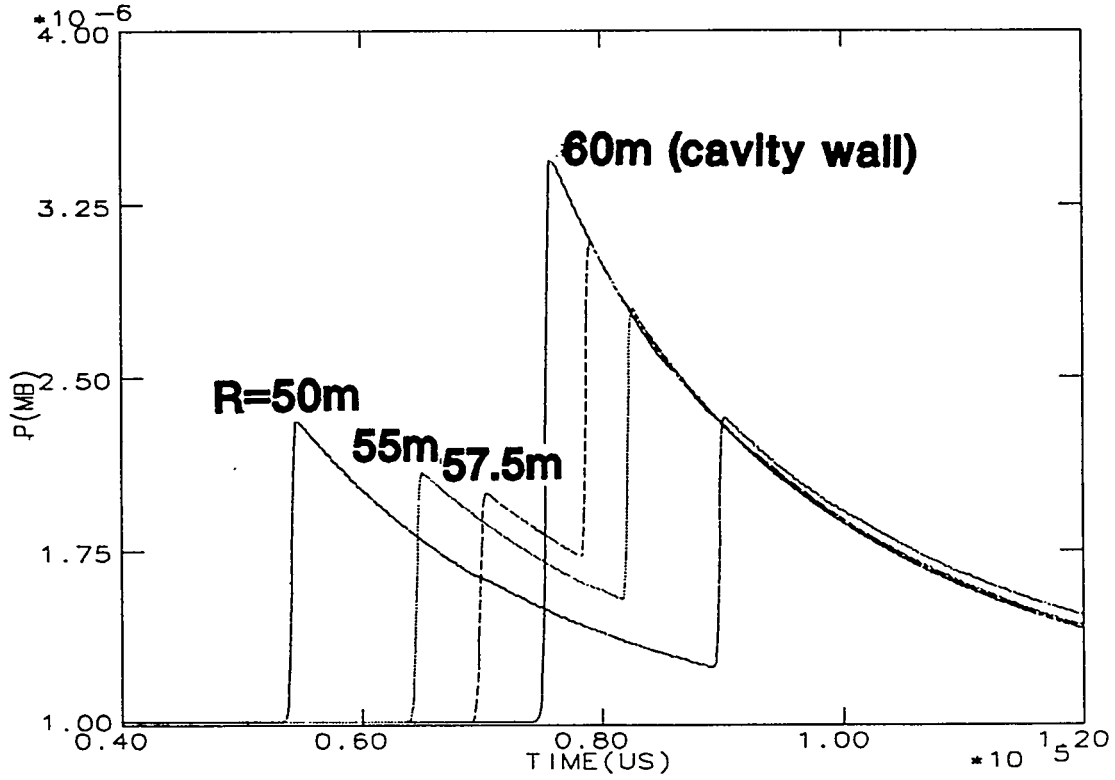


Fig. 3. Reinforcement of airblast pressure pulse due to reflection at the rigid wall (nuclear event, cavity radius R_0 = 60 m).

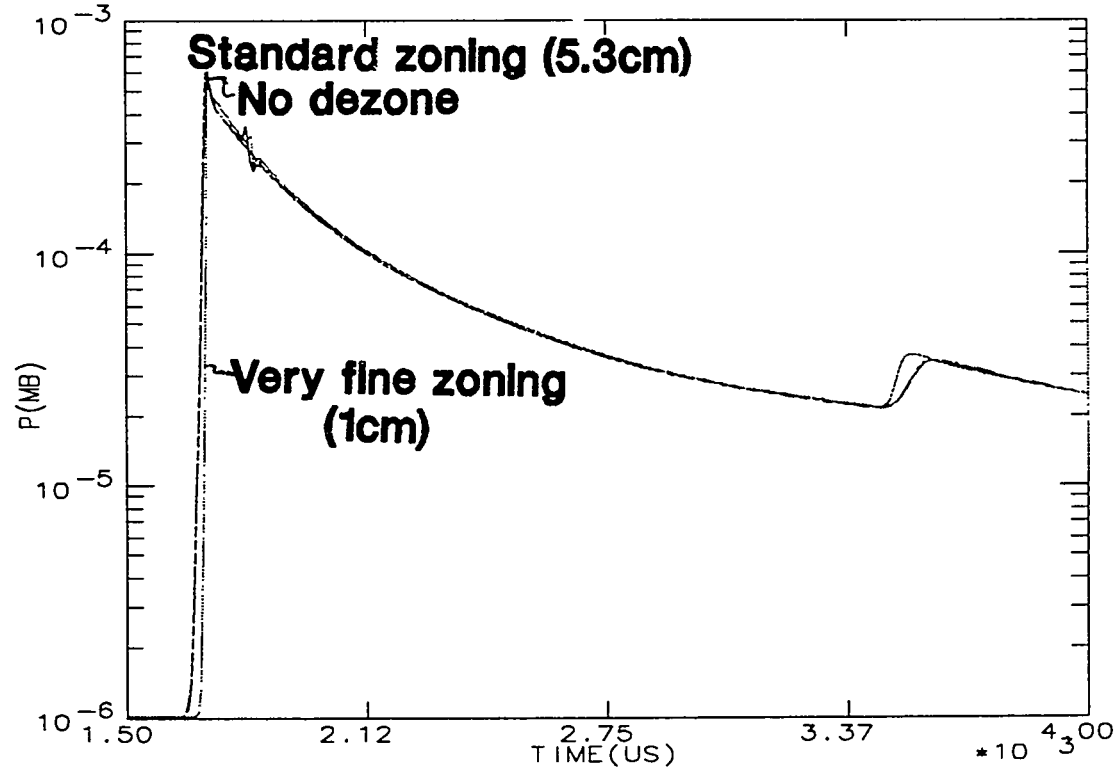


Fig. 4. Influence of zoning on the calculated airblast pressure profiles at the rigid wall (nuclear event R_0 = 11 m): normal zoning (solid), no dezoning (long dash), and very fine zoning (short dash).

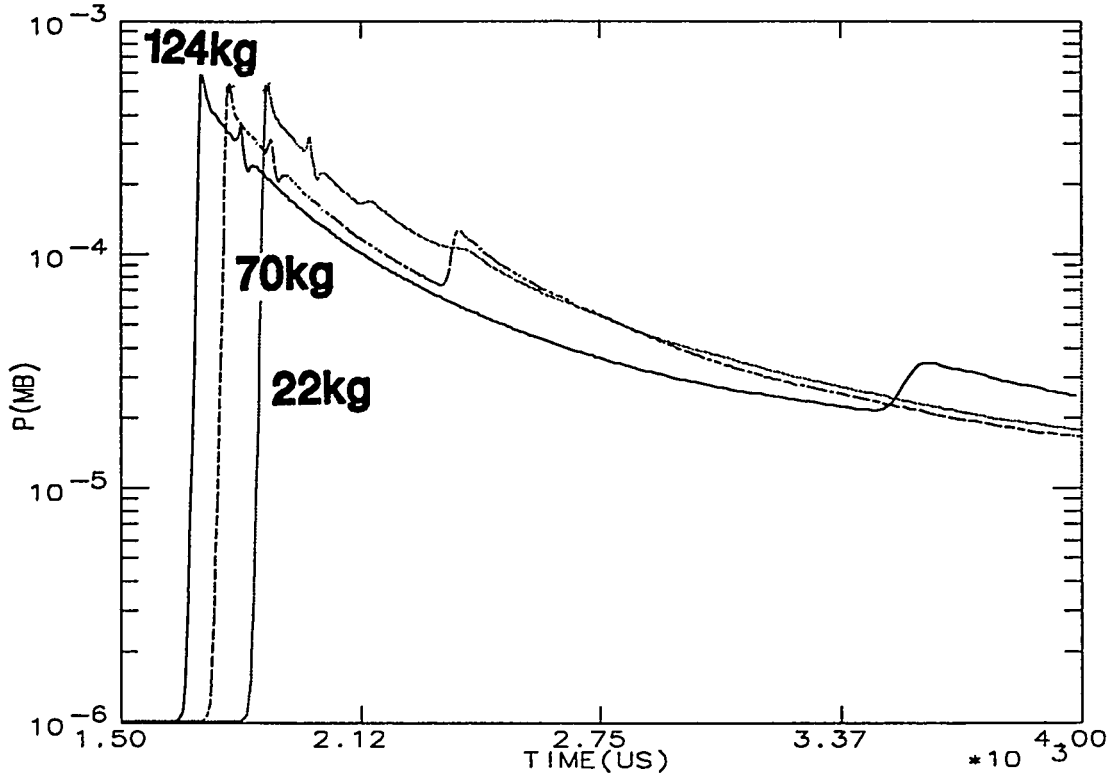


Fig. 5. Influence of source mass M_0 on the calculated airblast pressure profiles at the rigid wall (nuclear event R_0 = 11 m): for masses of M_0 = 124 kg (solid), 70 kg (long dash) and 22 kg (short dash).

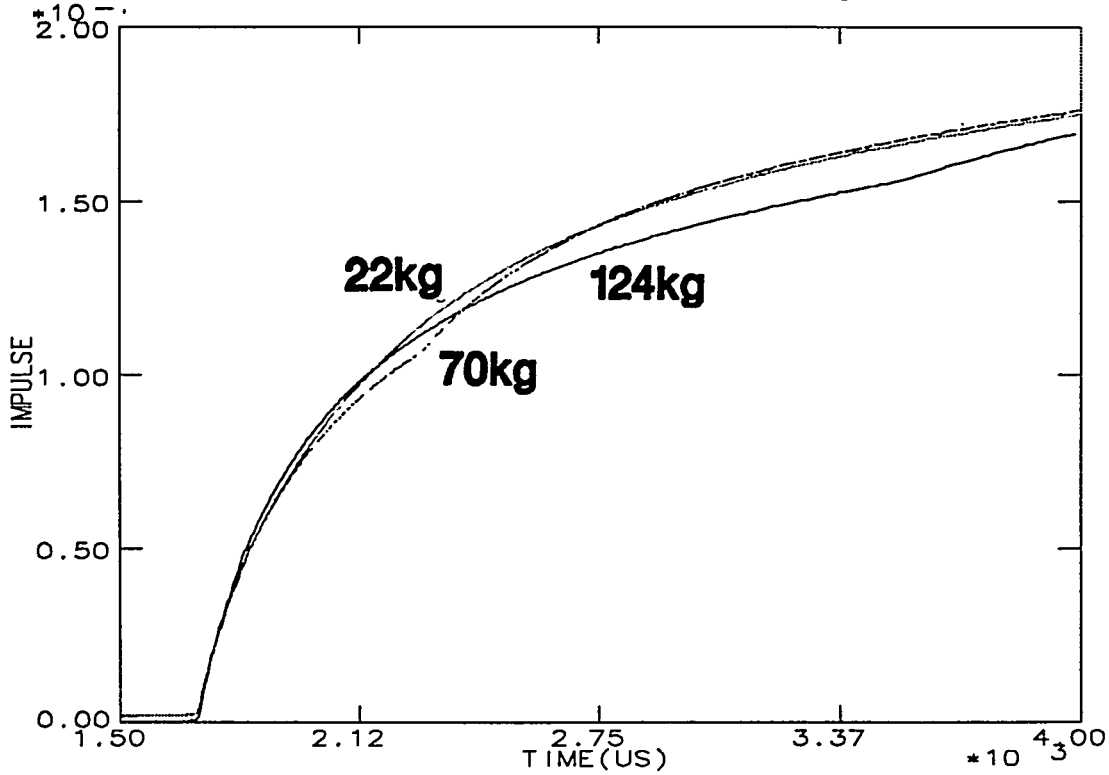


Fig. 6. Integrated impulses at the rigid wall with the pressure profiles time shifted to match the arrival times. Cases are the same as for Figure 5.

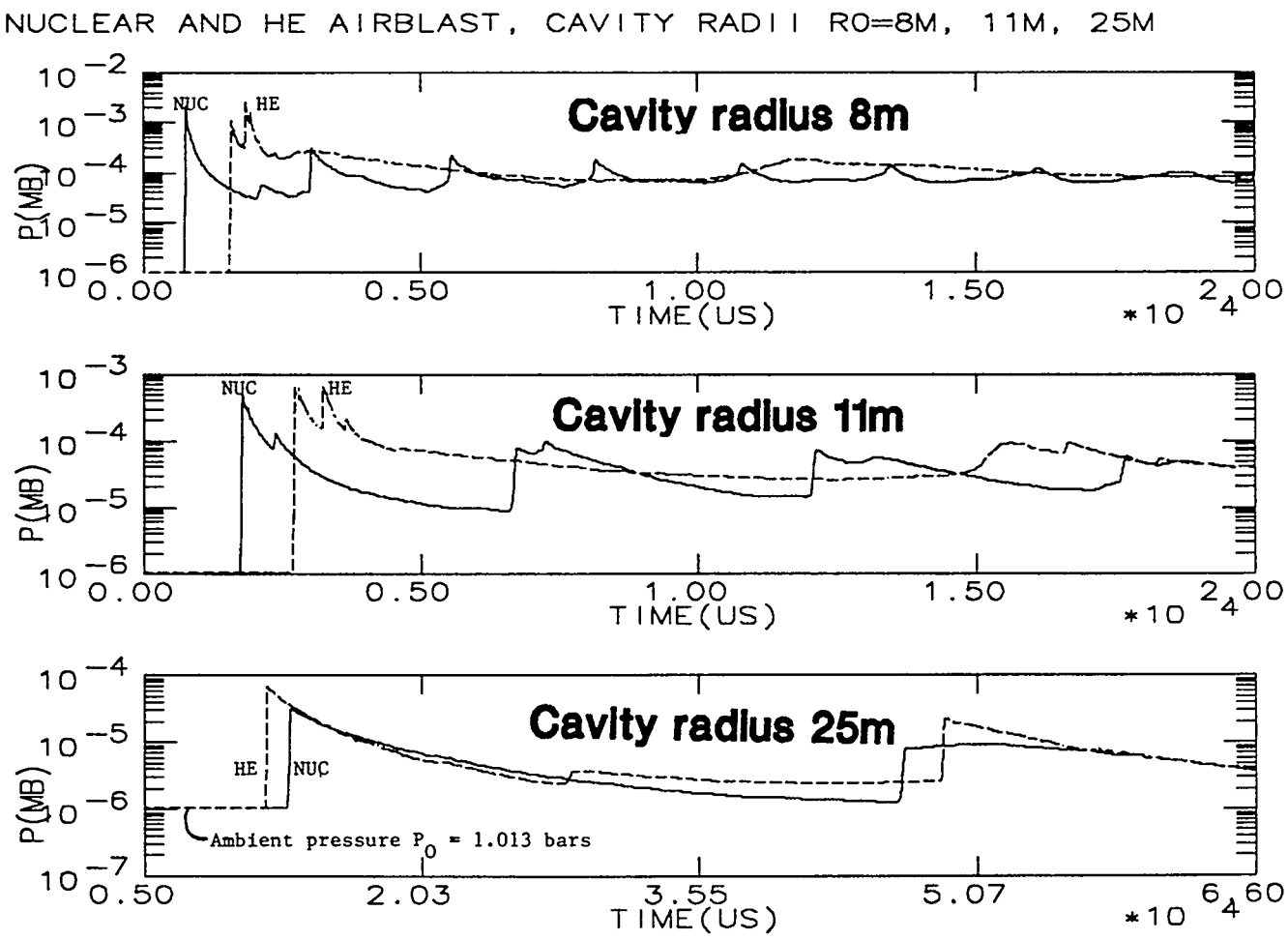


Fig. 7. Examples of reflected pressure-time histories at the wall, for nuclear events (solid) and HE (dashed). For cavity radii of R_0 = 8 m, 11 m, and 25 m.

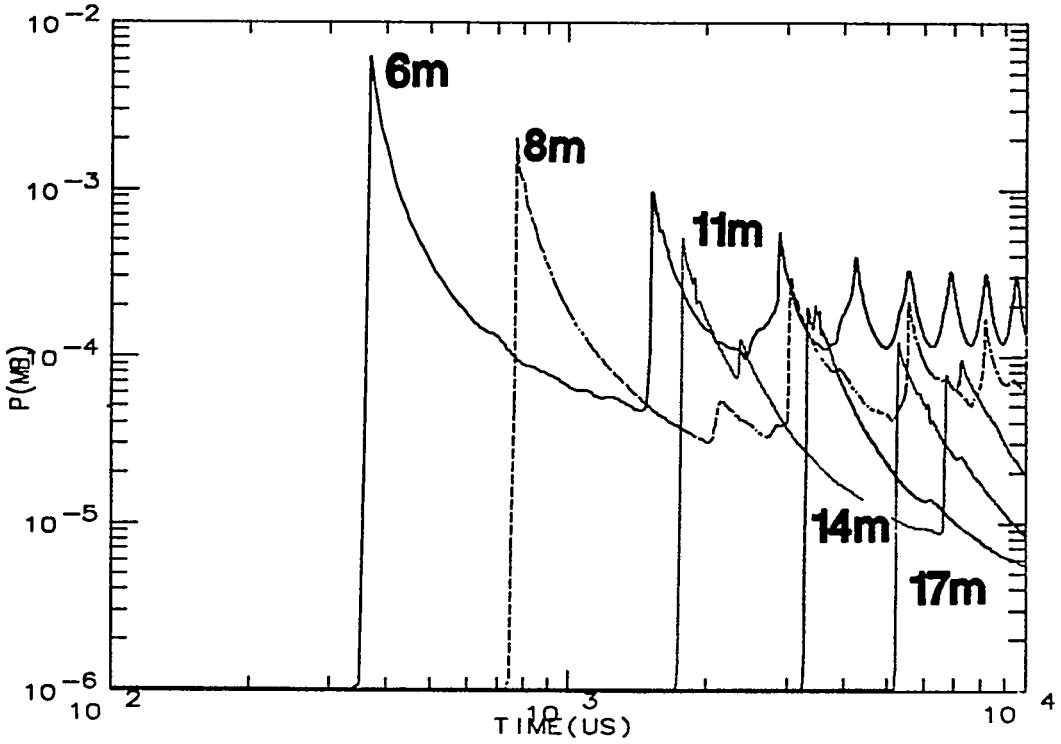


Fig. 8. Calculated nuclear airblast pressure profiles at the rigid wall, for radii of R_0 = 6 m (solid), 8 m (dashed), 11 m (dotted), 14 m (dashed), and 17 m (dotted).

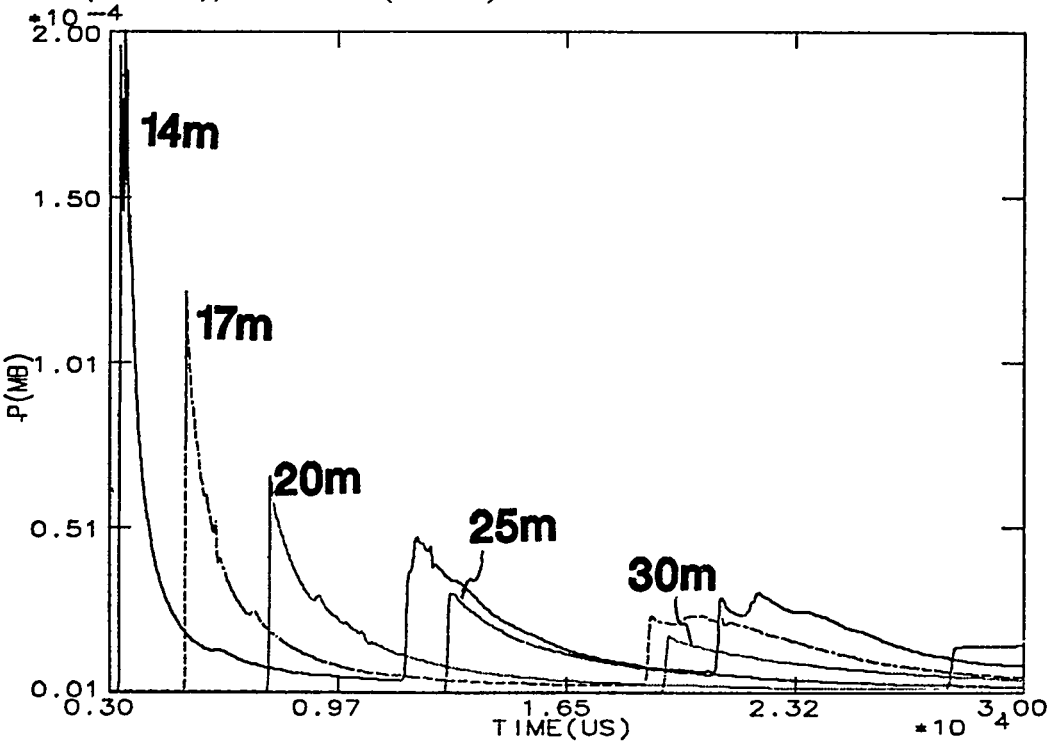


Fig. 9. Calculated nuclear airblast pressure profiles at the rigid wall, for radii of R_0 = 14 m (solid), 17 m (dashed), 20 m (dotted), 25 m (dashed), and 30 m (dotted).

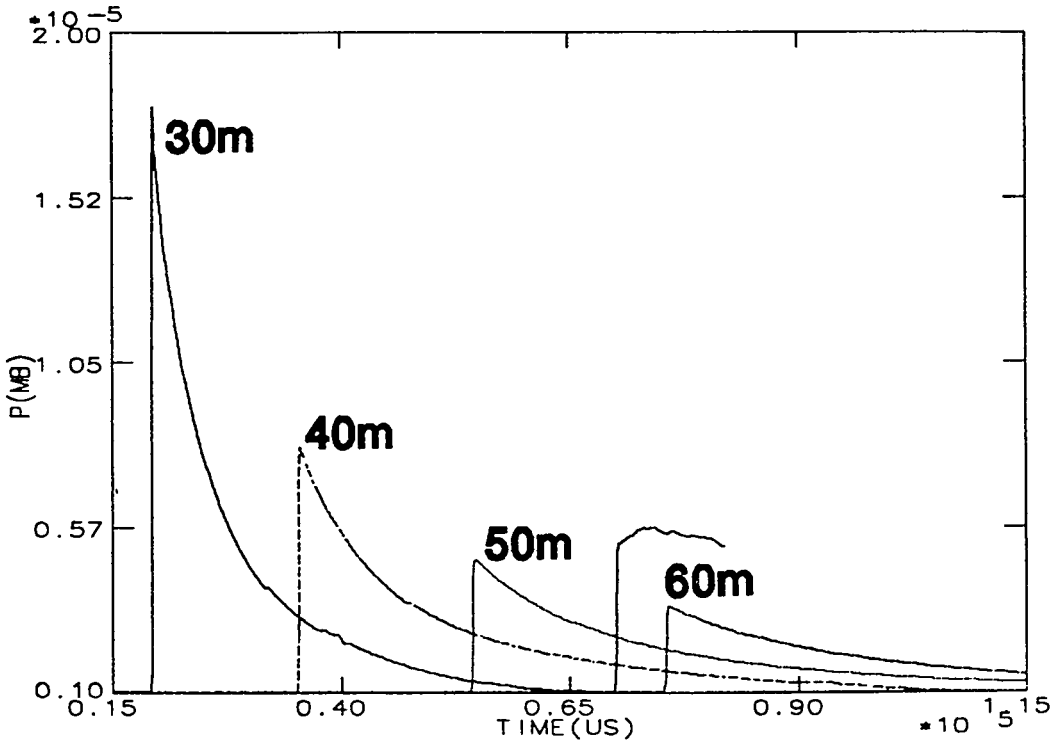


Fig. 10. Calculated nuclear airblast pressure profiles at the rigid wall, for radii of R_0 = 30 m (solid), 40 m (dashed), 50 m (dotted), and 60 m (dashed).

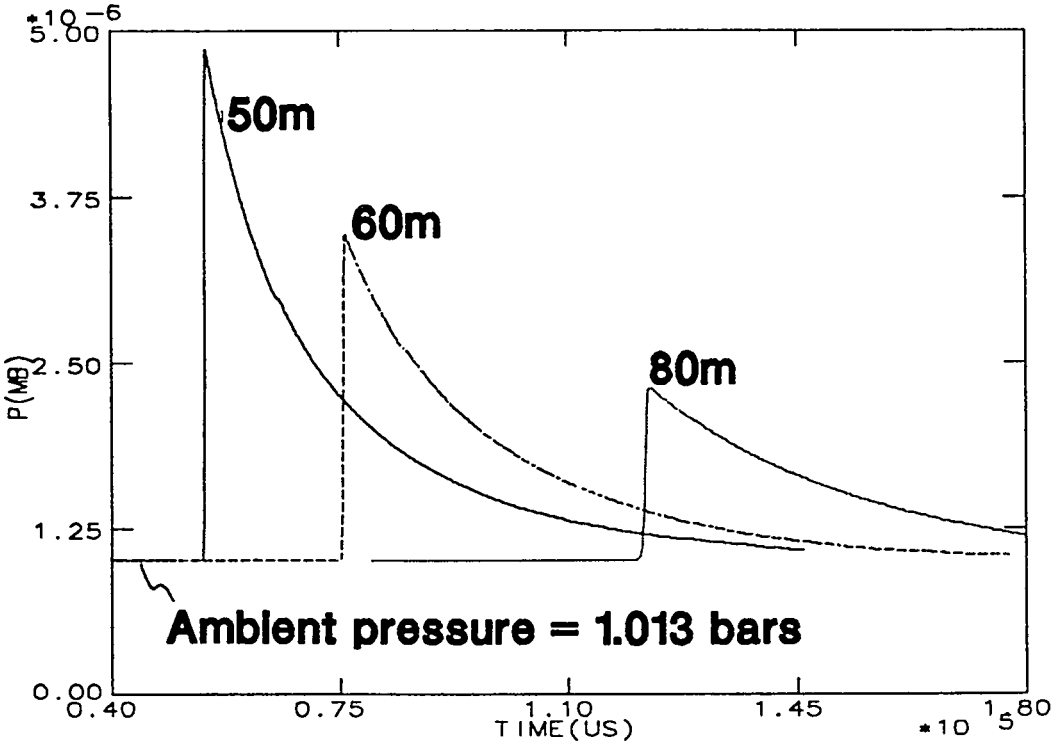


Fig. 11. Calculated nuclear airblast pressure profiles at the rigid wall, for radii of R_0 = 50 m (solid), 60 m (dashed), and 80 m (dotted).

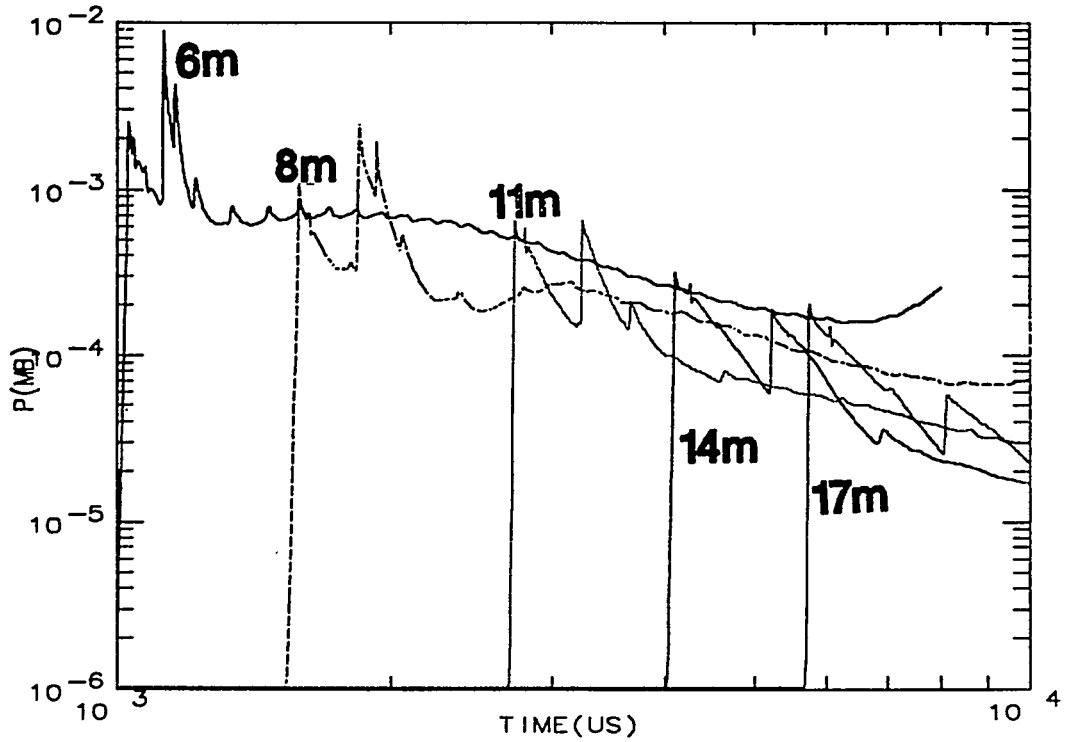


Fig. 12. Calculated high-explosive airblast pressure profiles at the rigid wall, for radii of R_0 = 6 m (solid), 8 m (dashed), 11 m (dotted), 14 m (dashed), and 17 m (dotted).

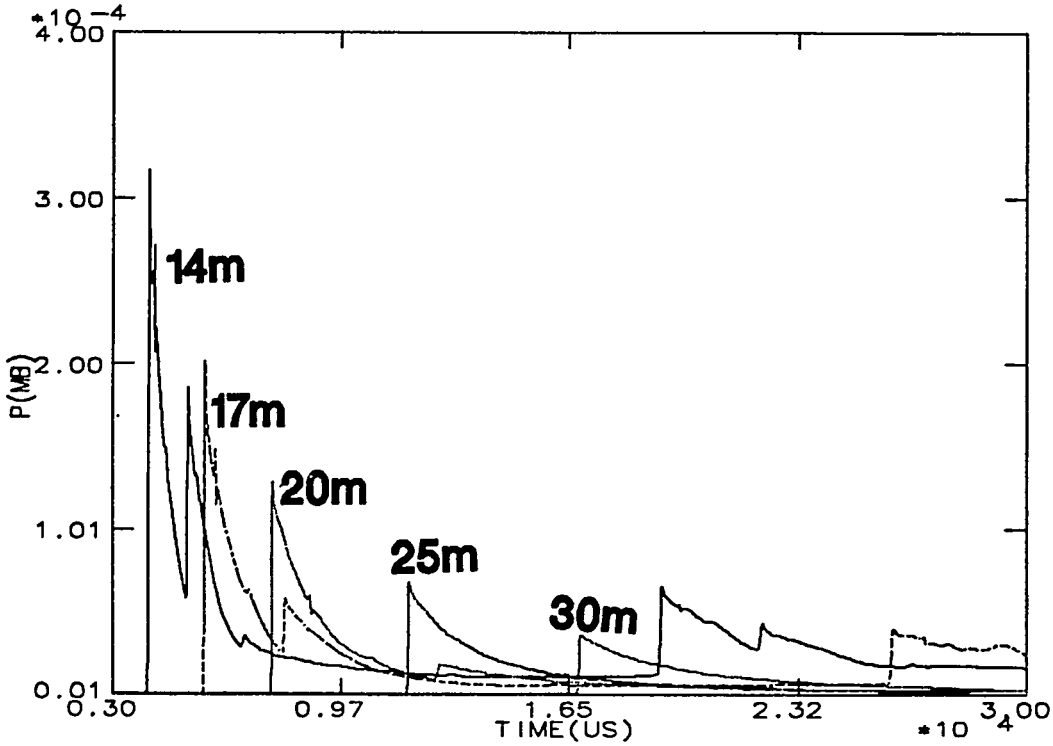


Fig. 13. Calculated high-explosive airblast pressure profiles at the rigid wall, for radii of R0 = 14 m (solid), 17 m (dashed), 20 m (dotted), 25 m (dashed), and 30 m (dotted).

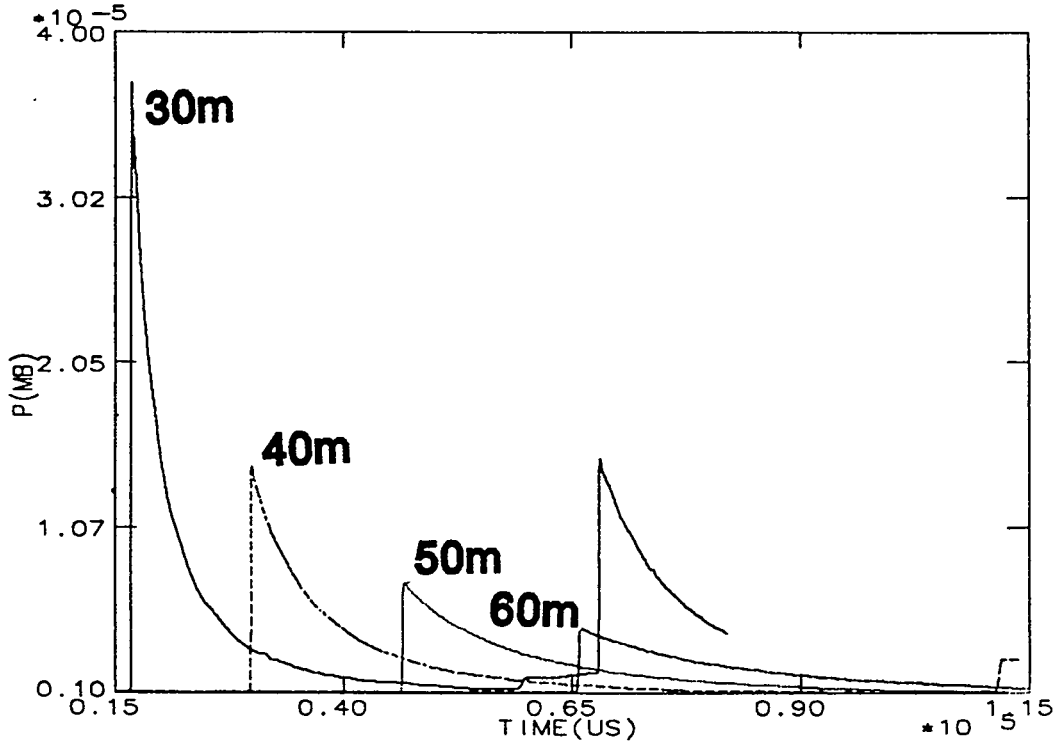


Fig. 14. Calculated high-explosive airblast pressure profiles at the rigid wall, for radii of R_0 = 30 m (solid), 40 m (dashed), 50 m (dotted), and 60 m (dashed).

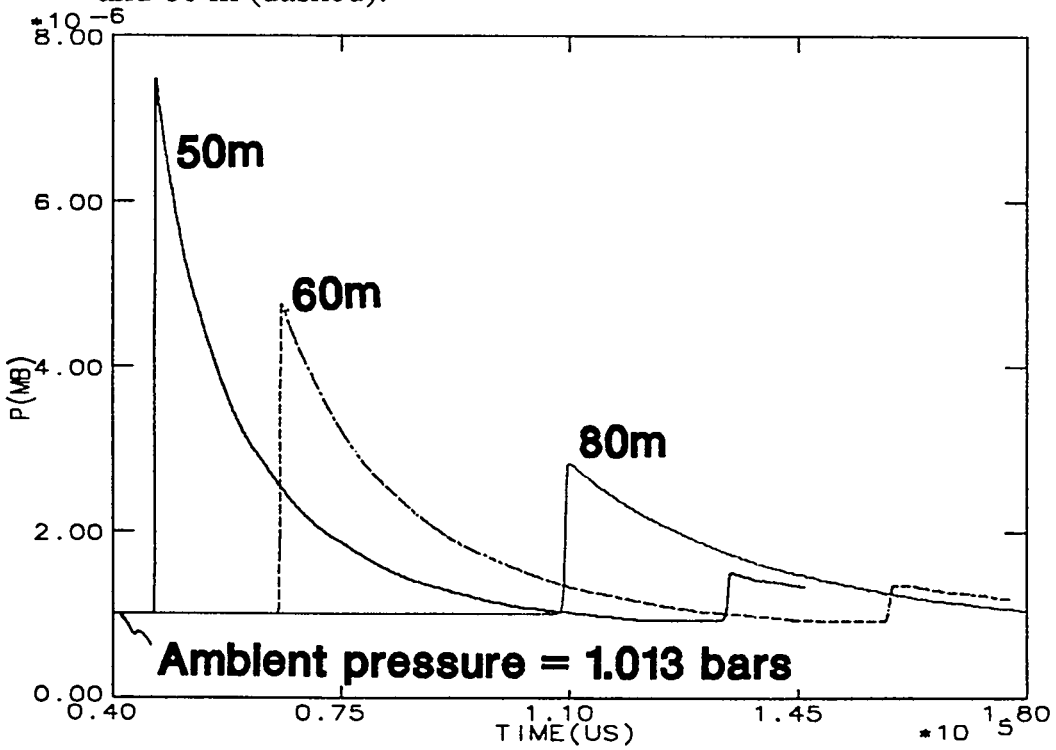


Fig. 15. Calculated high-explosive airblast pressure profiles at the rigid wall, for radii of R_0 = 50 m (solid), 60 m (dashed), and 80 m (dotted).

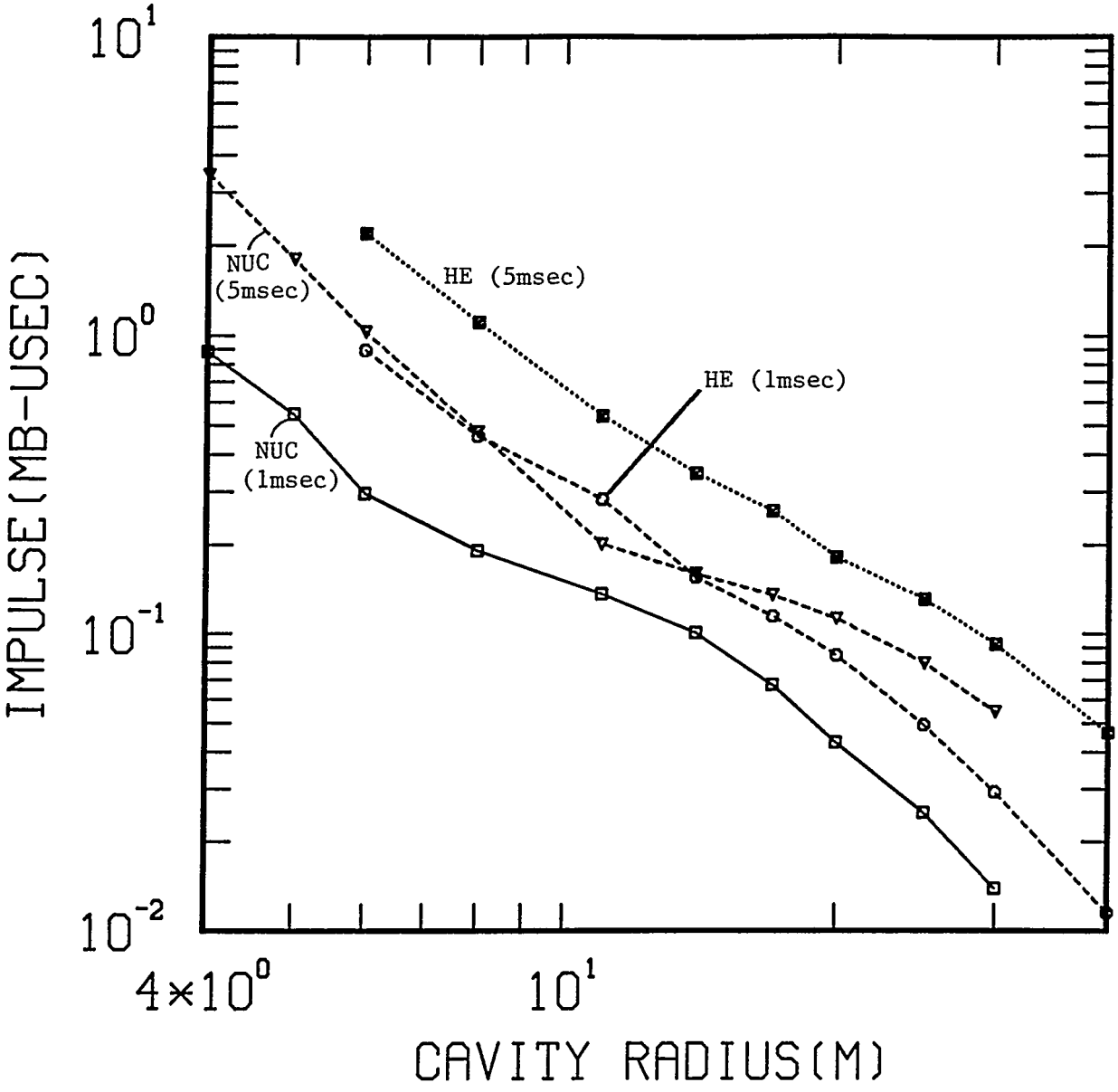


Fig. 16. Comparison of nuclear and high-explosive impulses at the cavity wall, integrated over time intervals of 1 millisecond and 5 milliseconds after the initial airblast arrival: nuclear integrated to 1 msec (squares), HE to 1 msec (circles), nuclear to 5 msec (inverted triangles), HE to 5 msec (filled squares).

Containing Repeated Low-Yield Nuclear Explosions in Steel-Lined Rock Caverns

F. E. Heuze, and R. P. Swift*
Lawrence Livermore National Laboratory, Livermore, CA

Leslie R. Hill, and William H. Barrett
Sandia National Laboratories, Albuquerque, NM

ABSTRACT

This work involved the response of a liner-bolt system installed on the wall of the DIAMOND FORTUNE cavity, a 22-m diameter nearly semi-spherical chamber in tuff, at the Nevada Test Site. DIAMOND FORTUNE is a low-yield nuclear test of the Defense Nuclear Agency which was performed in April, 1992. A 1.4-m square, 2.5-cm thick steel plate was anchored by 9-m long bolts: four 2.5-cm diameter bolts at the corners and a 5-cm diameter bolt at the center. The bolt ends daylighted in a tunnel surrounding the cavity, and were tensioned from there. The system was equipped with 20 data channels for strain, acceleration, contact pressure, and temperature. We relate the thermal analyses and the 3-dimensional dynamic analyses performed for this project, and we present the test results which indicated the excellent response of this system to the high dynamic loads and temperatures.

Introduction and Overview

In the early 1980's, the idea was put forth to provide a reusable underground cavity in which a series of low-yield nuclear explosions could be performed for the purpose of research in weapons physics and non-weapon high-energy physics. The concept, now designated as CONVEX (COntained Nuclear Vessel EXperiment), is a joint effort of three DOE laboratories (LANL, LLNL, SNLA), and the Defense Nuclear Agency (DNA). Early studies by Heuze (1983) on HEDEF (High-Energy Density Experimental Facility), a precursor of CONVEX, concluded that a steel-lined rock cavity would offer containment advantages over a free-standing steel vessel. In addition, the steel liner would be pre-stressed against the rock by bolts that daylight in tunnels adjacent to the cavity, as proposed by Heuze and Thorpe (1983). This concept was tested recently, as an add-on to the low-yield nuclear test of the DNA, DIAMOND FORTUNE, executed in an 11-m radius hemispherical underground chamber in tuff, in April 1992. Our experiment was called the CONVEX Liner Add-on.

This paper presents a summary of the data obtained on the CONVEX Liner Add-On, describes numerical simulations of the experiment, and gives comparisons of the measured data and results of calculations. The data analyzed include strains on the tensioned bolts and on the steel liner plate, stresses in the grout/rock backing the liner, temperature on the back of the plate, and accelerations on the plate and in the rock pillar. The quality of the data obtained is very good, and the response features captured by the different data sets are quite similar and reveal the complex nature of the flow field inside the cavity. Calculations were performed using three-dimensional, static and dynamic, finite-element codes, developed at LLNL. NIKE3D, described by Maker et al. (1991),

---

* Now at Los Alamos National Laboratory, Los Alamos, NM

was used to simulate the pre-test bolt tensioning condition. DYNA3D, described by Whirley and Hallquist (1991), provided the dynamic response of the bolt/liner/rock system. Pre-test calculations were performed to guide instrument choice, location and recording ranges, to set the tensioning of the bolts, and generally to produce confidence that the liner system would survive the environment and remain operational. Post-test calculations were performed with the best estimate of the actual cavity pressure history at the liner plate, obtained from measurements and flow field calculations. Experimental measurements showed that the bolts remained in a tensioned state throughout the duration of the test. Hence, the bolt tensioning used (about 330 Mpa) was sufficient to offset the compressive air blast loading. They also showed that the liner plate maintained firm contact with its grout-rock backing, thus fulfilling the main operational objective of the test.

LINER EXPERIMENT

Configuration and Instrumentation

The liner experimental configuration consisted of a steel plate anchored vertically to the cavity wall by four corner bolts and a centerbolt, with the bolts daylighting in an adjacent "run-around" drift (Figure 1). The cavity rock consisted of volcanic tuff located in the P-tunnel complex at the Nevada Test Site. The rock quality was quite variable, as indicated by RQD and in-situ modulus NX jack tests in the pillar between the cavity and the drift (Figure 2). The plate is 1.4 m square, 2.54 cm thick, and made of A36 steel. The bolts, 2.54 cm and 5.08 cm in diameter at the corners and center, respectively, are about 9 m long and made of 1045 steel. A thin layer of rock-matching grout, about 5 cm thick, was used between the plate and rock to provide a smooth bearing surface for the plate. The bolts were tensioned to about 330 Mpa, less than 50% of their yield strength. This initial pre-tension load was selected on the basis of preliminary calculations indicating that the bolts would remain in tension during the dynamic loading. The corner bolts were grouted in their boreholes after tensioning. The centerbolt was encased in a 10 cm diameter schedule 40 pipe casing. The annulus between the casing and the bolt was filled with *Vistanex* (an inert non-toxic hydrocarbon polymer made by EXXON Chemical Company) for containment purpose. The casing was cemented in the pillar.

The set of diagnostics, shown in Table 1, was adapted to a 20 data channel allotment to provide the mechanical and thermal response of the liner/bolt/rock system. The desired measurements included: horizontal and vertical strains, acceleration, and temperature on the back of the plate; axial strains and bolt loads for the centerbolt and corner bolts; contact pressure between the plate and the rock; cavity wall pressure; and acceleration inside the 9 m rock pillar separating the cavity and run-around drift.

The cavity side and drift side of the system ready for testing are shown in Figures 3 and 4.

Summary of Test Results

As indicated in Figures 5 and 6, the salient feature of the test was the fact that the instruments showed the whole system retaining strong tension and contact with the rock throughout the dynamic phase. Figure 5 is the time history of 4 longitudinal strain gauges on the center bolt within a 30-cm section. The first aspect to note is the excellent reproducibility of the strain records. The second is the fact that the bolt quickly regained up to 80 percent of its original tension, after the first few milliseconds. Such behavior was also true of the only strain-gauged corner bolt (not shown), which retained over 85

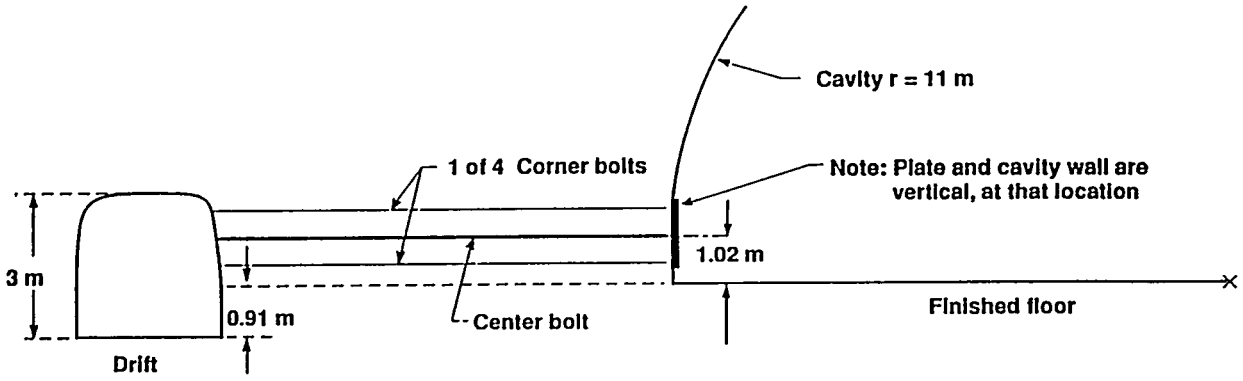


Figure 1: Geometric lay-out of CONVEX Liner Add-On; elevation.

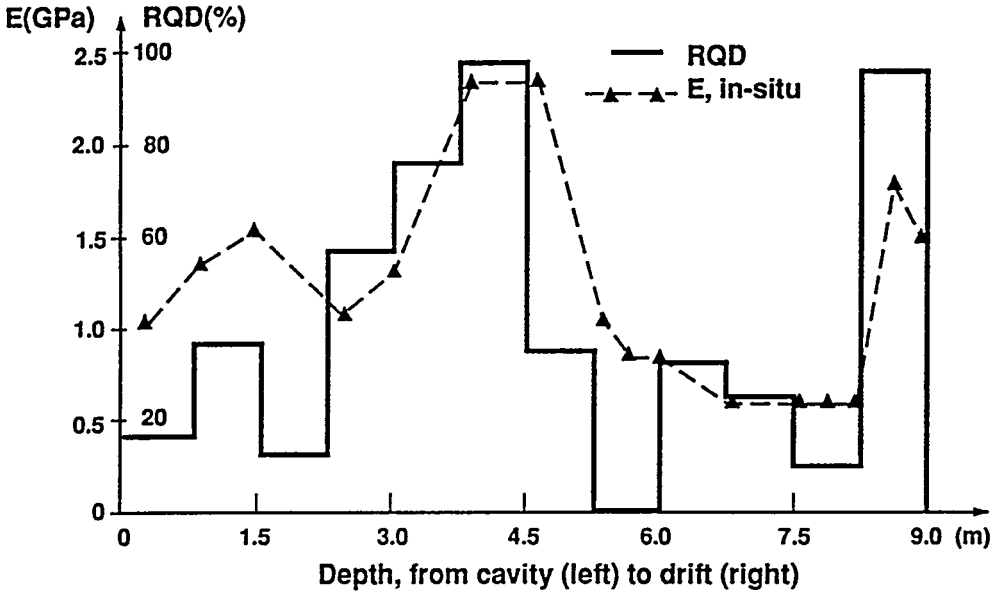


Figure 2: RQD and In-Situ Modulus, of Tuff in Cavity Wall. Note the good correlation between E and RQD.

Table 1. Instrumentation for the CONVEX Liner Add-On.

		Strain	Stress	Accel.	Pressure	Temperature
Plate:	4 Strain Gauges	√				
	1 Accelerometer			√		
	1 Thermocouple					√
Plate/Rock:	2 Toadstools				√	
Center bolt:	4 Strain Gauges	√				
	1 Load Cell		√			
Corner bolt:	2 Strain Gauges	√				
	1 Load Cell		√			
Rock Pillar:	3 Fluid-Coupled Plates				√	
	1 Accelerometer			√		

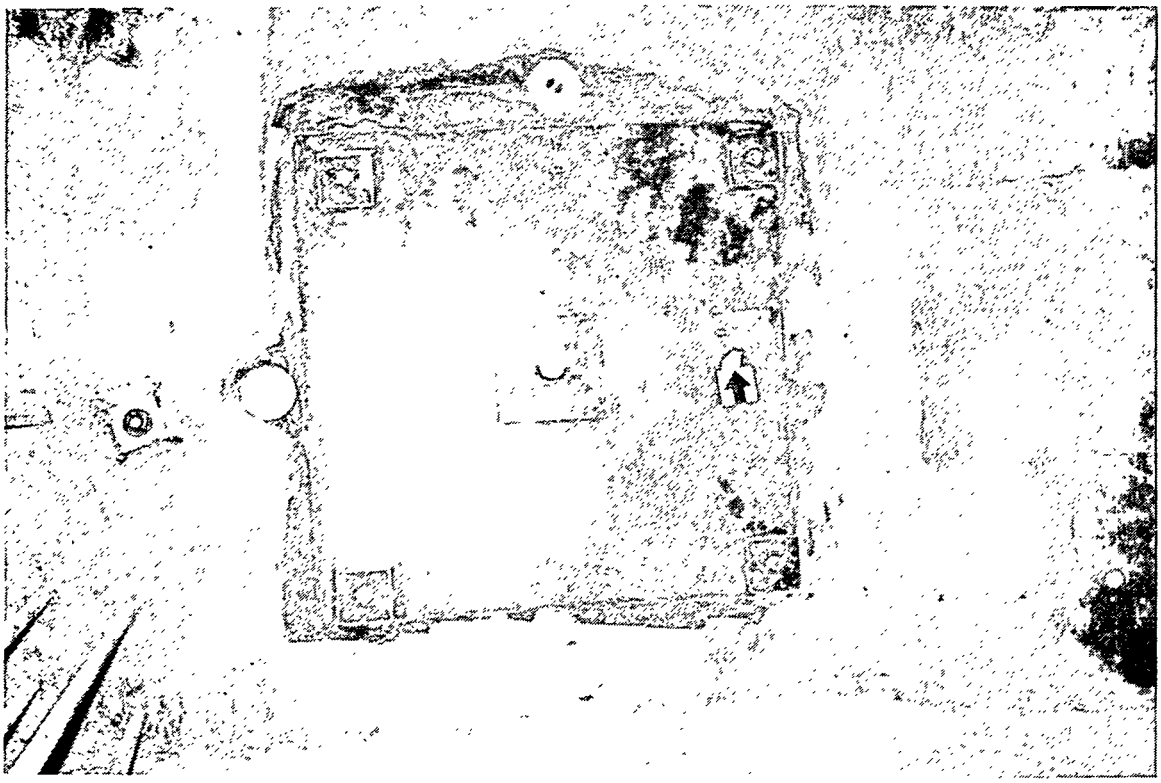


Figure 3: CONVEX liner plate, cavity side.

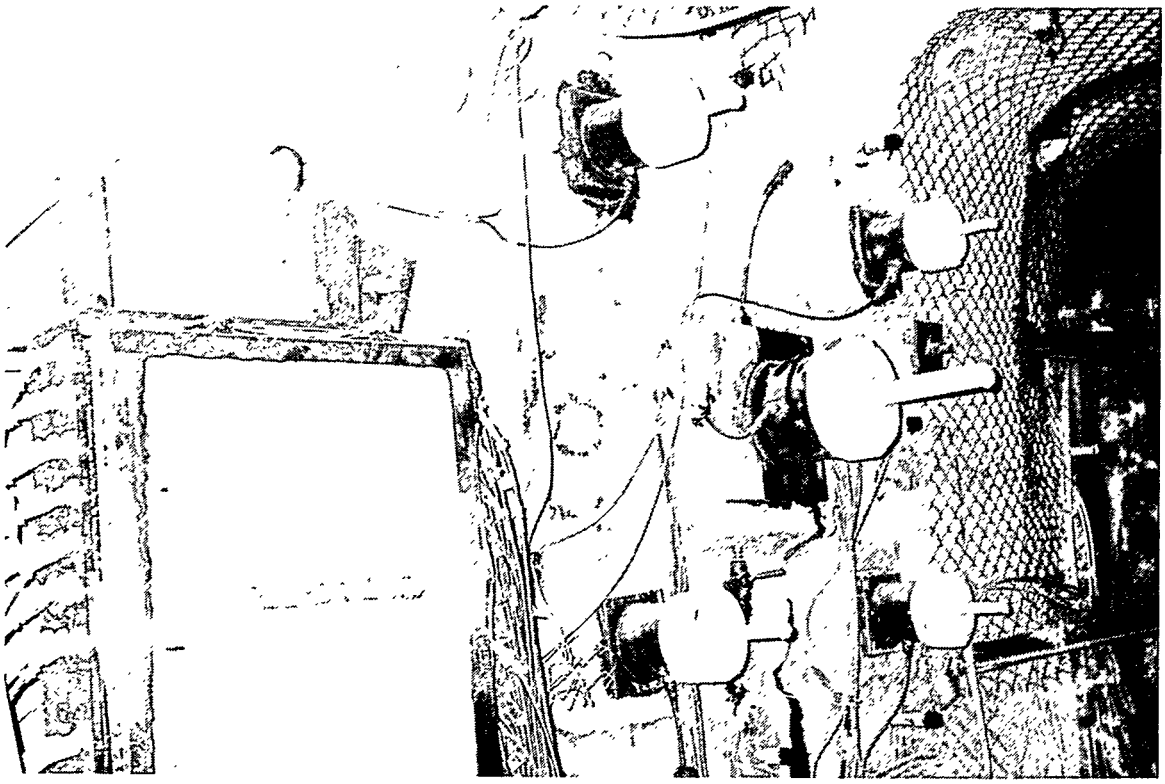


Figure 4: Bolts, load cells, and junction box, drift side.

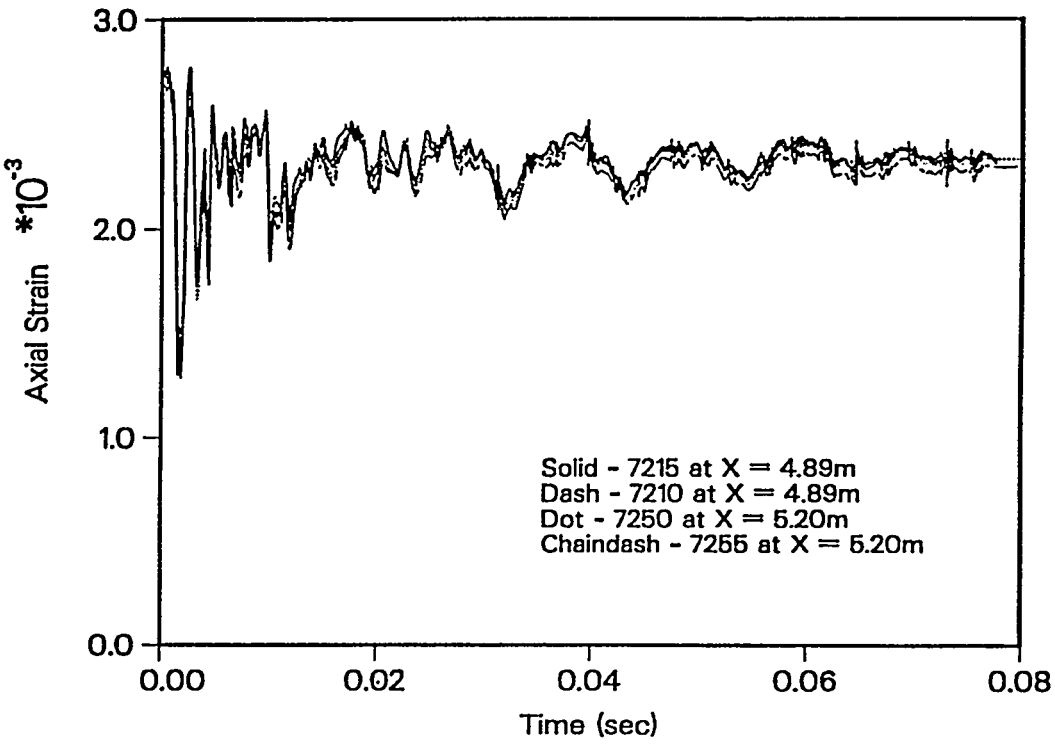


Figure 5: **Measured responses of axial strain gauges on the centerbolt.**

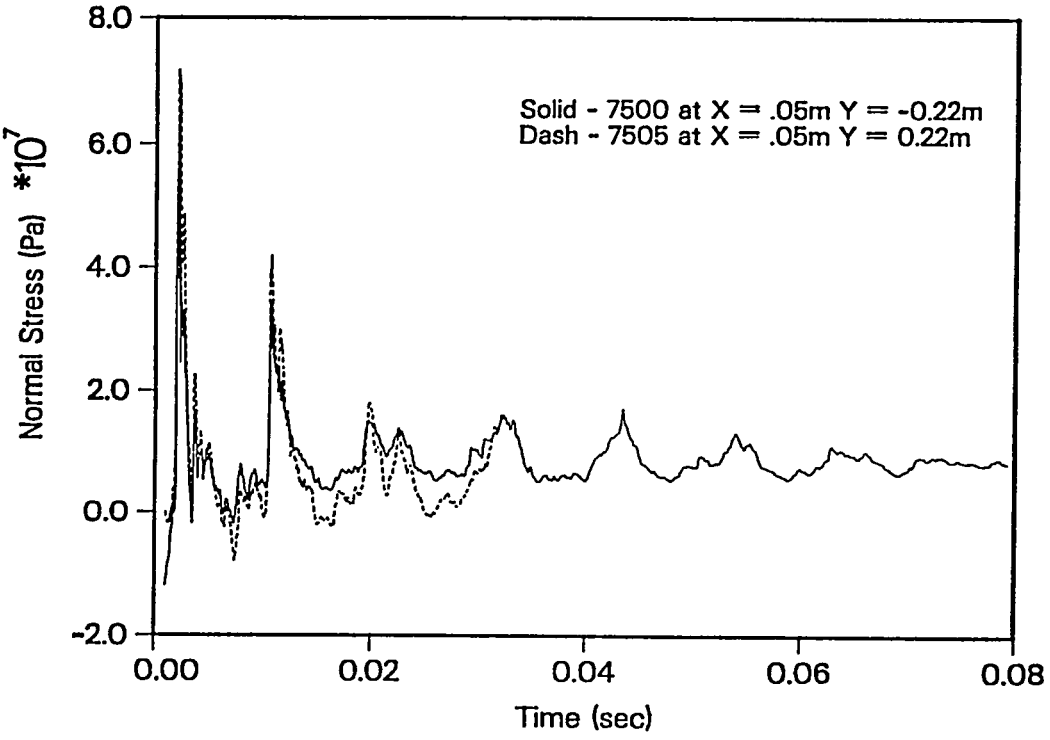


Figure 6: **Measured responses of pressure gauges in grout between the liner plate and the rock.**

percent, of its original tension. Figure 6 shows the time history of the two "toadstool" gauges measuring the stress in the grout perpendicular to and behind the plate. The two instruments again gave consistent results, and the remaining gauge at 80 ms shows a strong contact pressure. Another remarkable feature of the test data is the consistency of various stress and strain records in showing the history of cavity pressure oscillations (Figure 7).

CALCULATIONS

Thermal Calculations

Regarding the thermal environment, the strain-gauges could operate up to a maximum of 175 C. The TOPAZ2D finite element code (Shapiro, 1986) was used to estimate the temperatures in the plate, grout, and rock. For simplicity, the grout and rock were given constant thermal temperatures, although temperature-dependent properties of the grout are available (Moss et al, 1982; Zimmerman, 1982). The rock, grout, and steel thermal properties used in the calculations are summarized in Table 2. Figure 8 shows the input temperature in the cavity, i.e. on the front side of the liner plate (A), and the expected histories on the back of the plate (B), and in the middle of the grout (C). Clearly the temperature gradients are very high. The actual temperature record (D) was well within the range of expectations, even with a simple model. More than 10 seconds elapsed before a temperature of 175 C was reached on the back of the plate. There was no need for temperature correction of gauge readings in the dynamic phase.

Table 2: Properties for Thermal Calculations

	Density (g/cm3)	Heat Capacity (cal/g.°c)	Thermal Conductivy (cal/s.cm.°c)	Melting Temperature (°c)	Latent Heat of Fusion (cal/g)
Steel	7.85	0.116	0.121	n/a	n/a
Rock, or Grout	1.75	0.250	3.58 E-3	1000	80

The 3-D Mechanical Model

The approach to numerically simulate the CONVEX plate/bolt/rock system consisted of defining the equilibrium state due to bolt tensioning, using NIKE3D, and mapping the equilibrium conditions into DYNA3D as initial conditions for the dynamic response calculations. Views of the three-dimensional model are given in Figures 9 and 10, showing the upper-right quadrant of the system that extends back from the cavity face into the rock. The quadrant geometry reflects the symmetry of the experiment about the axis of the centerbolt. The model extends axially outward, 9 m, to the run-around alcove where the wall buffer plates and holding nuts for the centerbolt and cornerbolt are secured. A total of 22,706 solid-brick elements were used in the static model along with 19 slide surfaces. The dynamic model is identical to the NIKE3D model, plus 2139 additional elements and 4 slide surfaces extending the rear of the model into the grout-enclosed run-around region and beyond into the rock to a range of 50 m. Slide surfaces include the steel bolt-steel plate, steel plate-buffer plate, steel plate-grout, steel bolt-grout, and rock-grout interfaces. Both the centerbolt and the cornerbolts were tied to the nuts

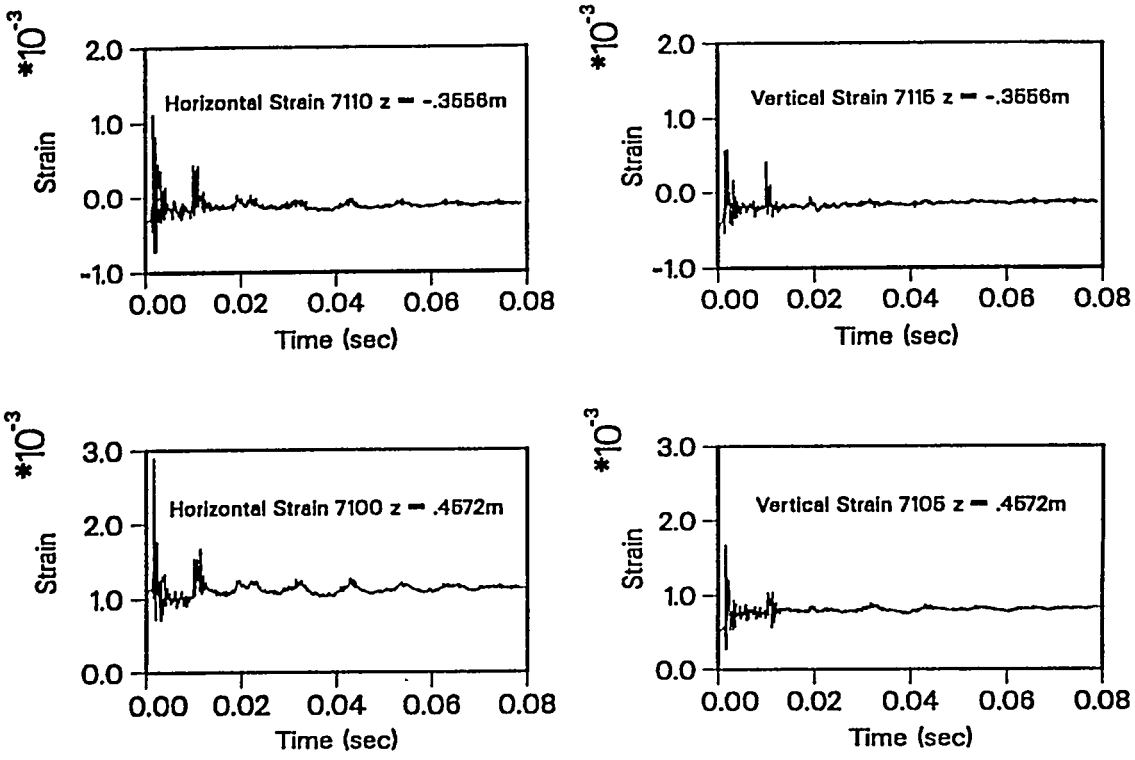


Figure 7: Data sets were consistent in showing cavity pressure oscillations.

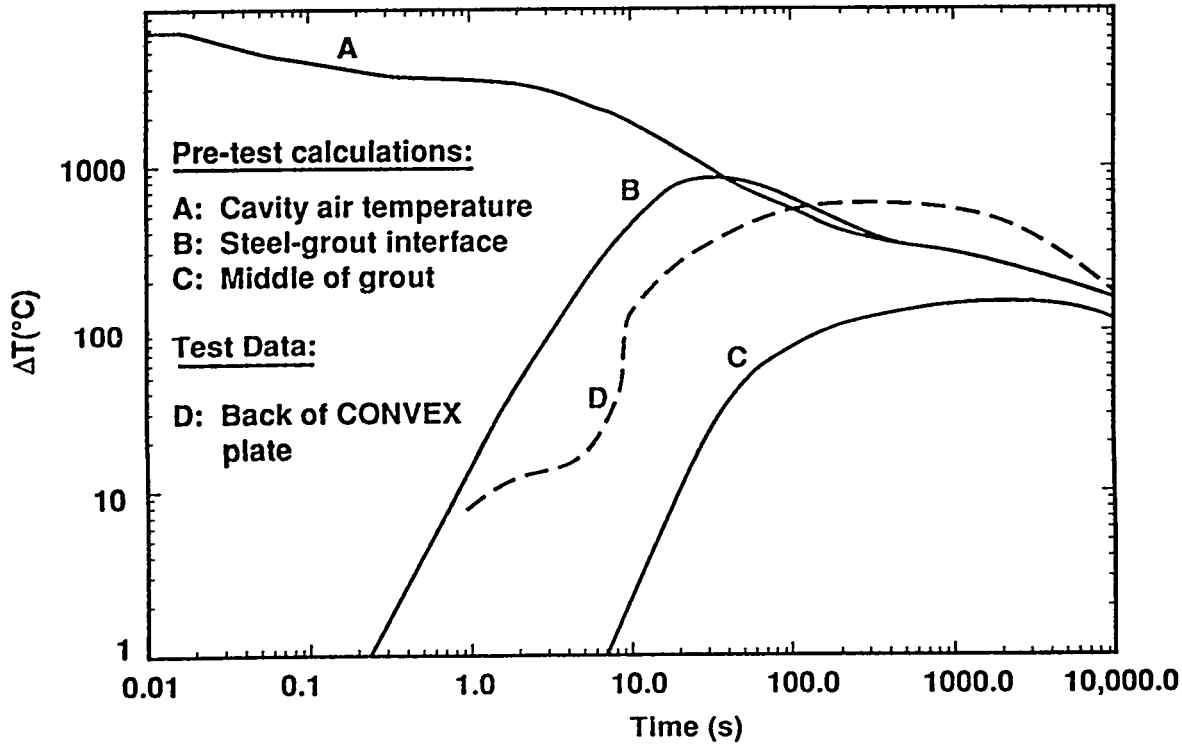


Figure 8: Measured and calculated temperature histories.

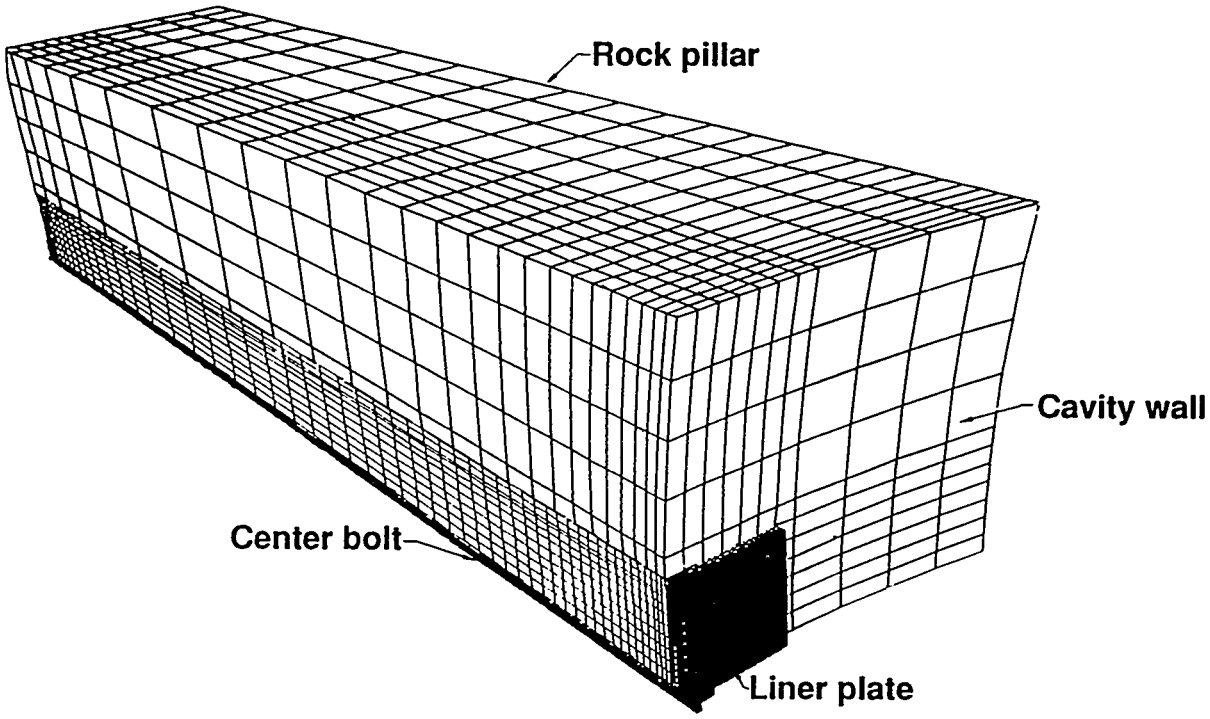


Figure 9: Complete model for 3-D mechanical analysis. Note the double curvature of the cavity wall.

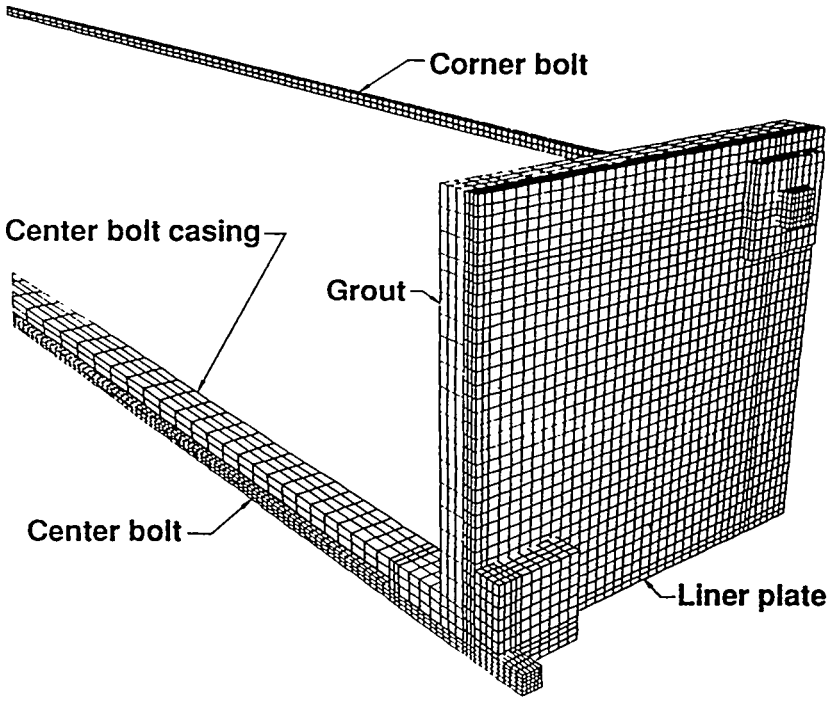


Figure 10: Details of plate, bolts and grout model.

and plates at the cavity and rear surfaces. The boundary conditions on the top and right outer rock surfaces allowed no vertical and no horizontal motion, respectively.

Estimates for the rock material properties required for numerical modeling were obtained from in-situ borehole-jack tests in one of the cable holes of the pillar, along with wave speed and strength measurements on core samples from the pillar. Wave speed and strength measurements also were obtained on core samples of the HLNCC grout used behind the plate.

The values retained for mechanical analysis were:

Rock:	modulus:	1.70 GPa
	Poisson's ratio:	0.45
Grout:	modulus:	4.0 GPa
	Poisson's ratio:	0.35
A36 Steel:	modulus:	200 GPa
	Poisson's ratio:	0.30
	density:	7.85 g/cm^3
	yield stress:	250 MPa
1045 Steel:	modulus:	200 GPa
	Poisson's ratio:	0.30
	density:	7.85 g/cm^3
	yield stress:	760 MPa

Equilibrium Condition

The equilibrium outward displacements calculated with NIKE3D for the rear surface of the plate adjacent to the grout, and caused by pre-tensioning the centerbolt and cornerbolt, are shown in Figure 11. The pretensioning was done by using initial thermal strains. The maximum displacement is about 0.45 mm in the elements next to the centerbolt. The stress distribution for the centerbolt and plate indicated maximum compressive and tensile axial values of about -300 Mpa and +430 Mpa, respectively, in the region where the nut fastens the bolt to the plate. These stress levels are well below the elastic yield stress, and the entire system is linear. Just behind the plate, at a distance of about 8.5 cm along the length of the bolt, the stress becomes uniform with an axial tension of 325 Mpa (Figure 12) and remains at this level until in the immediate vicinity of the run-around drift wall. This configuration is mapped into DYNA3D as the initial state for the dynamic response calculation. The pseudo-thermal model approach is believed to simulate the stress and strain states associated with bolt tensioning quite realistically. The same conditions would be very difficult to obtain using mechanical force or pressure prescriptions for the bolts, plate and rock exterior surfaces.

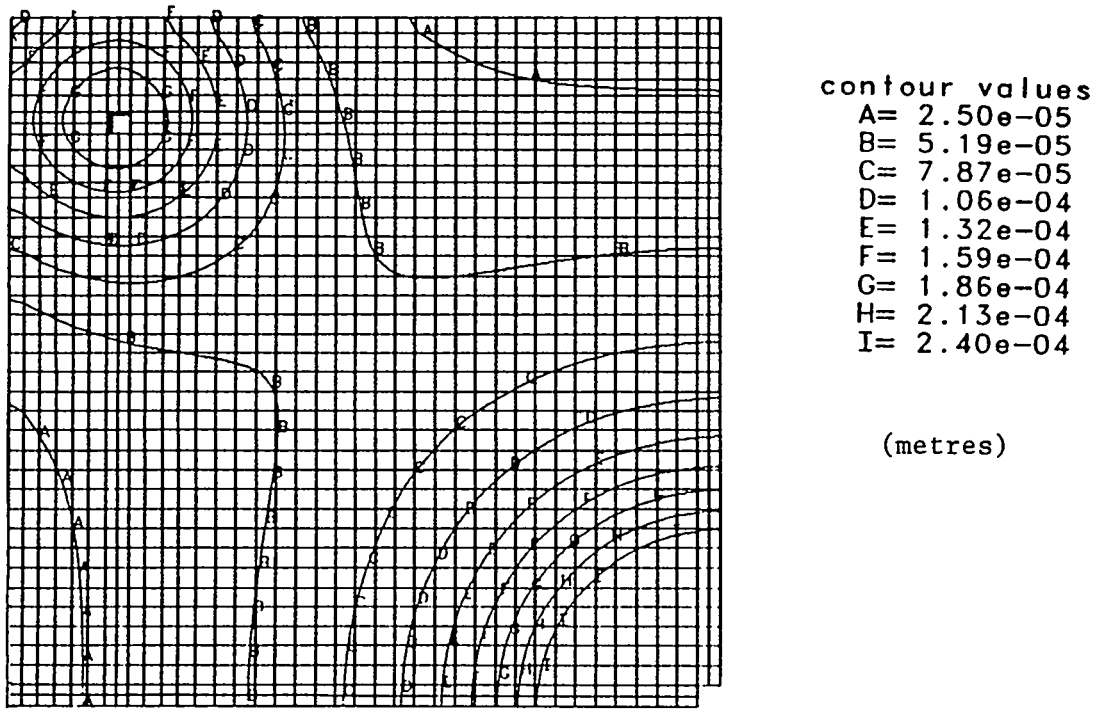


Figure 11: Calculated equilibrium displacement on back of plate, caused by 325 Mpa tension in bolts.

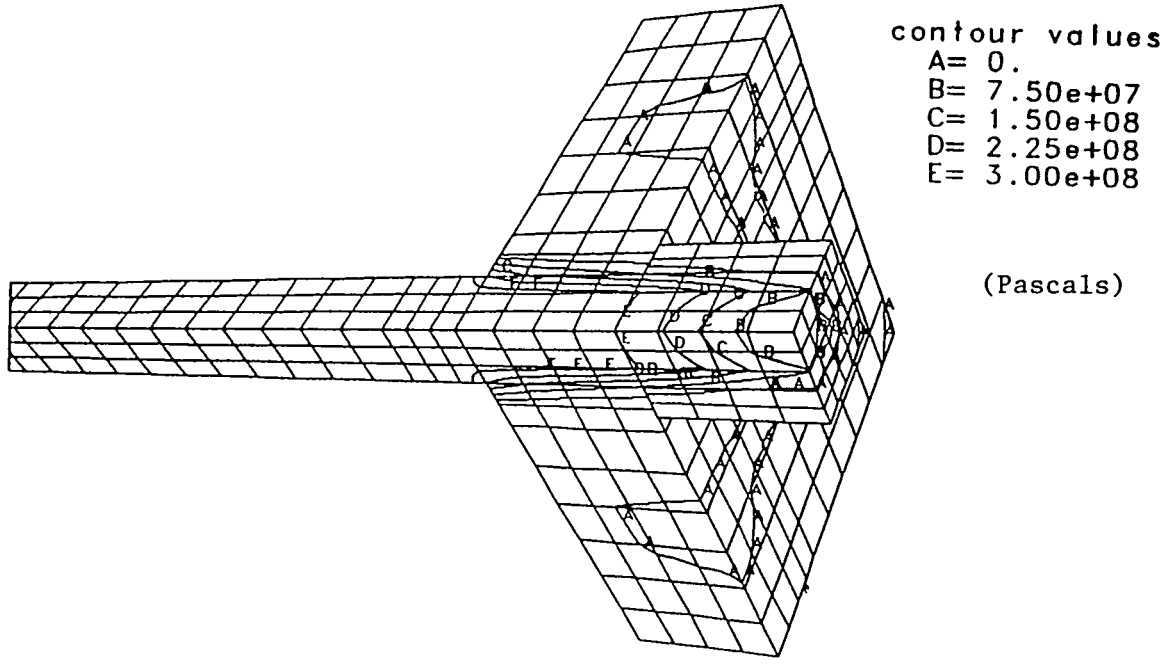


Figure 12: Axial stress distribution in center bolt and plate, at pretensioning.

Dynamic Response

The dynamic response calculations were carried out to a time of 40 ms. The normal pressure loading function on the plate is given in Figure 13. This function was applied uniformly to the cavity surface and to the plate and bolt surfaces facing toward the cavity.

The comparison of calculation results and test data, shown in Figures 14 to 17, highlights the successes and shortcomings of the calculations. Figure 14 shows that the horizontal (as well as vertical) strains on the back of the plate could be estimated satisfactorily, for the purpose of establishing the type and range of strain gauges to be used. Figure 15 shows that the prediction of center bolt axial-strain history at mid-length was pessimistic in terms of the negative effect of the loading on the retained tension. Basically, it is thought that the rock model in DYNA3D did not damp out the shock energy in the liner system as the real rock did. The comparison of calculated and measured axial strain at mid-length on one of the corner bolts (not shown) indicated an even grater disparity between calculations and observations. This also reflects the difficulty in modeling the sequence of bolt tensioning, bolt grouting, and selecting a bolt-grout interface condition after grout curing. Figures 16 and 17 relate to accelerations. The comparison for the back of the plate is satisfactory (Figure 16). But Figure 17, again, clearly indicates a lack of material damping in the calculations.

SUMMARY AND CONCLUSIONS

This combined experimental and modeling project was very successful in proving the validity of the concept of a prestressed steel liner and bolt system, for the reinforcement of rock cavities subjected to extreme thermal and dynamic mechanical loading. The instrumentation performed extremely well and provided the essential diagnostics to determine the residual tensions and liner-rock contact pressure. The two-dimensional thermal modeling was very adequate in predicting the plate temperature. The extensive 3-D mechanical modeling highlighted both the power and some of the shortcoming of these models. The comparison of calculational results and test data suggests the need for improvements in the rock material models and in the handling of linked static (pretensioning) and dynamic analyses.

REFERENCES

Heuze, F. E., "Preliminary Structural Investigations for a High-Energy Density Facility", Lawrence Livermore National Laboratory Report UCID-19575 Rev. 1, 37 p., (June, 1983).

Heuze, F. E., and Thorpe, R. K., "Geological Engineering Considerations for a High-Energy Facility, and a Cost Estimate for the Related Conceptual Design", Lawrence Livermore National Laboratory Report UCID-19848, 40 p., (July, 1983).

Maker, B. N.,. Ferencz, R. M, and. Hallquist, J. O, "NIKE3D - A Nonlinear, Implicit, Three-Dimensional Finite Element Code for Solid and Structural Mechanics- User's Manual", Lawrence Livermore National Laboratory Report UCRL-MA-105268, (January, 1991).

Moss, M., Koski, J. A., Haseman, G. M., and Torney, T. V., "The Effect of Composition, Porosity, Bedding Plane Orientation, Water Content, and a Joint, on the Thermal

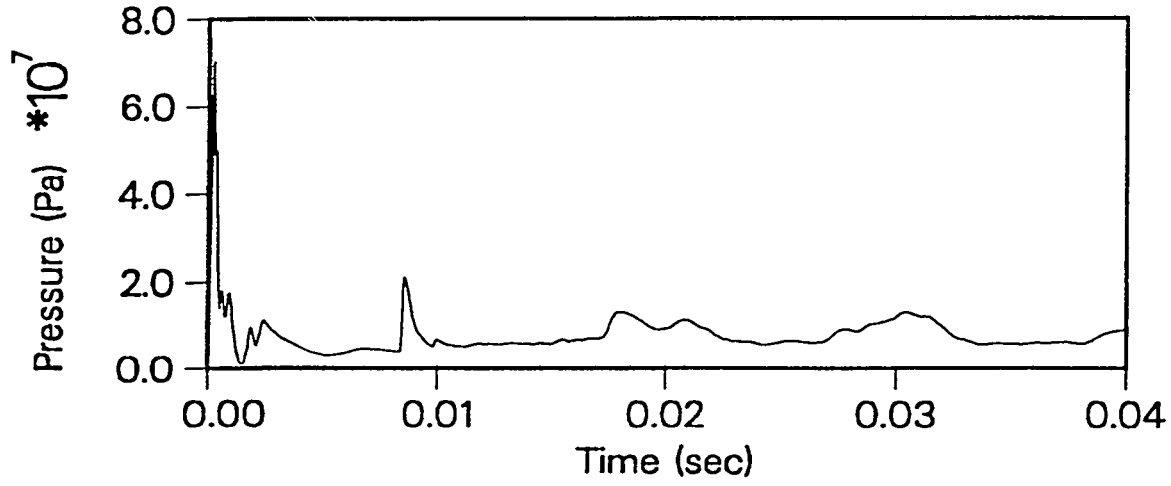


Figure 13: Pressure loading function used for dynamic response calculations.

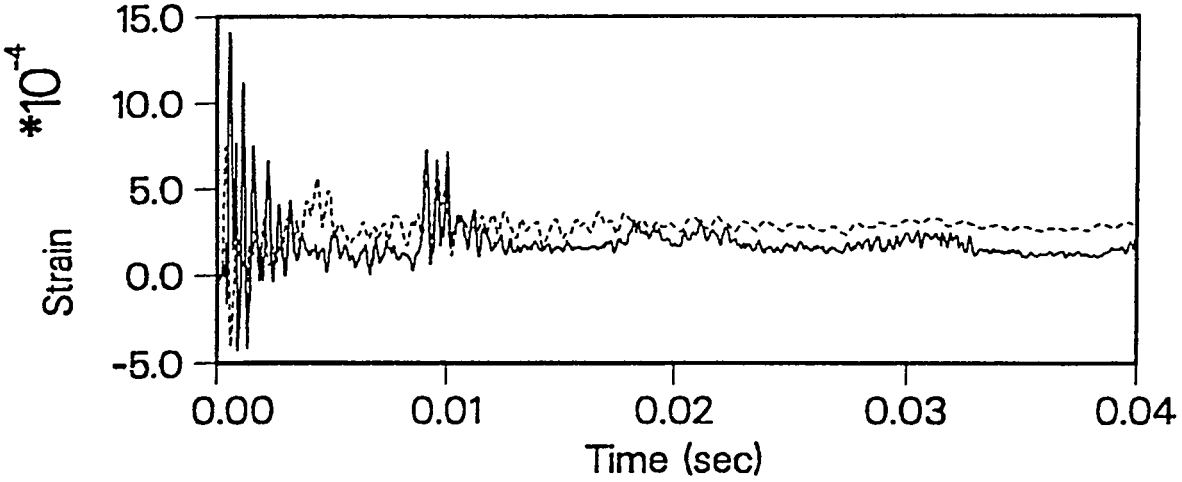


Figure 14: Horizontal strain on back of plate: calculated (dash) vs measured (solid).

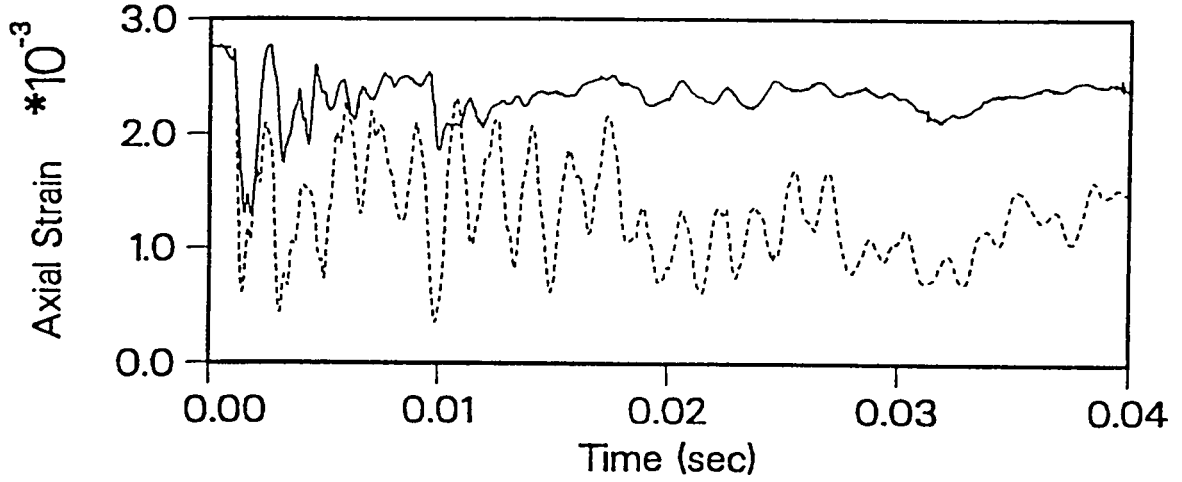


Figure 15: Axial strain on centerbolt, mid length, calculated (dash) vs measured (solid).

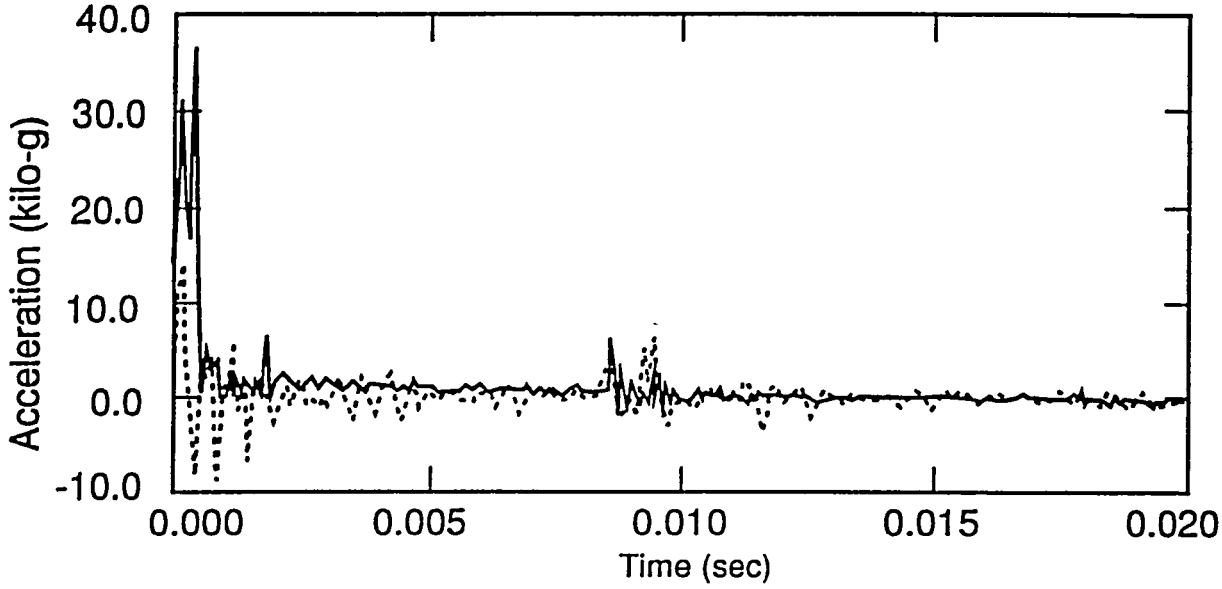


Figure 16: Acceleration on back of plate: calculated (dash) vs. measured (solid).

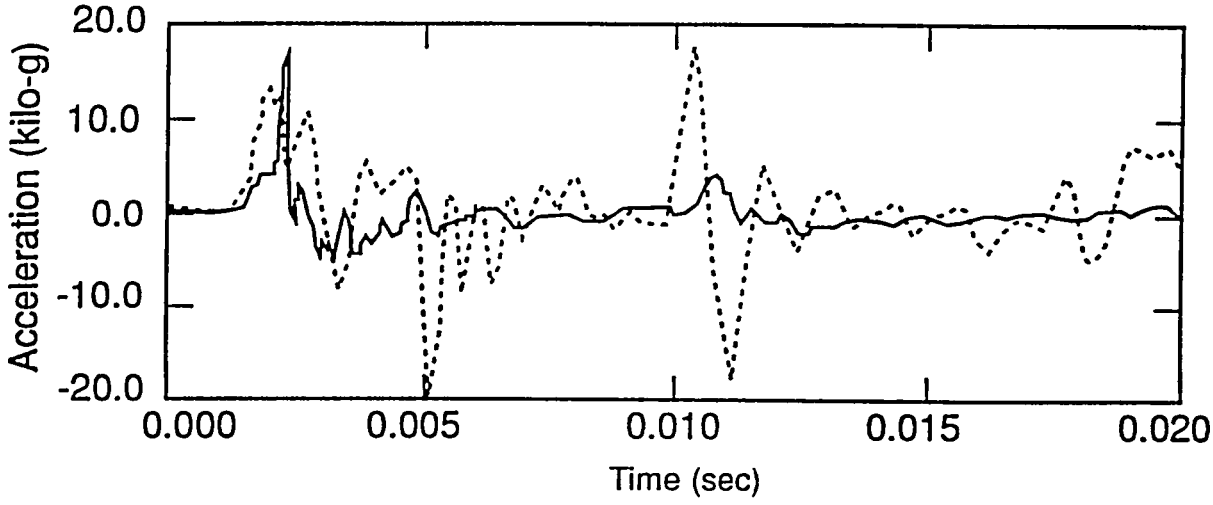


Figure 17: Acceleration at mid-pillar: calculated (dash) vs. measured (solid).

Conductivity of Tuff", Sandia National Laboratories, Albuquerque, NM, SAND 82-1164, 28 p., (November, 1982).

Shapiro, A. B., "TOPAZ2D: A Two-Dimensional Finite Element Code for Heat Transfer Analysis, Electrostatic, and Magnetostatic Problems", Lawrence Livermore National Laboratory Report, UCID-20824, 110 p., (July 1986).

Whirley, R. G., and Hallquist, J. O., "DYNA3D - A Nonlinear, Explicit, Three-Dimensional Finite Element Code for Solid and Structural Mechanics - User's Manual", Lawrence Livermore National Laboratory Report, UCRL-107254, 314 p., (May, 1991).

Zimmerman, R. M., "Conceptual Design of Field Experiments for Welded Tuff Rock Mechanics Program", Sandia National Laboratories, Albuquerque, NM, SAND 81-1768, (October 1982).

ACKNOWLEDGMENTS

This work was supported in part by the Department of Energy under contract W-7405-Eng-48 with the Lawrence Livermore National Laboratory. Sandia National Laboratory, Albuquerque, NM and the Defense Nuclear Agency were partners in this project. We thank C. Snell, Los Alamos National Laboratory, who provided cavity flow field estimates. V. Peterson and S. Uhlhorn skillfully typed the manuscript.

Modeling and Residual Stress



Distinct Element Modeling of Late-Time Containment Phenomena

by

W. J. Proffer* and E. J. Halda

S-Cubed, A Division of Maxwell Laboratories, Inc.
P.O. Box 1620, La Jolla, CA 92038-1620

ABSTRACT

Ground motion predictions for underground nuclear tests are traditionally performed using finite difference models based on continuum mechanics. Calculations performed with these models show that in tamped events the plastic work done on the surrounding rock during cavity growth should produce compressive residual hoop stresses which are large enough to contain the cavity gases.

Small scale laboratory and field experiments have verified that such residual stress fields are formed by explosions conducted in homogeneous materials. However, the few successful measurements obtained within the severe environments produced by nuclear events suggest that the actual residual stresses may be weaker than calculated or may decay very rapidly. It has been conjectured that the absence or reduction of residual stresses might be a consequence of the faults and joints which are present in the geologic host medium.

Shear displacements of faults and joints, sometimes exceeding a meter, are routinely observed on reentry. Since these non-homogeneous discrete motions occur within the confines of the residual stress fields calculated by the continuum models, they clearly have the potential to significantly alter the formation of a confining stress field.

To evaluate the influence of joints and faults on the residual stress field formation, two-dimensional calculations have been performed using a coupled version of the UDEC and CRAM codes. The UDEC distinct element model (DEM) used for this work considers sliding interactions between blocks of material as well as the material deformation occurring within the blocks. The CRAM Lagrangian finite difference coding is used to model the extreme deformation of the rock in the immediate vicinity of the cavity.

This paper describes: (1) some typical observations of block motions following HLOS events, (2) the modifications and extensions required to use the distinct element model to analyze dynamic motion involving very large deformations associated with cavity formation, and (3) some preliminary results which indicate that residual stress may be significantly degraded by the observed fault slippage.

1. INTRODUCTION

Over the past quarter century, numerical simulations of the ground motion caused by underground nuclear explosions have been performed by numerous investigators employing many different methods to represent the physics of wave propagation in solid rock. The majority, if not all, of these calculations were performed using finite element or finite difference discretions of a continuum mechanics representation of the rock mass. Since these models usually included some form of plastic flow in the rock response; not surprisingly, a residual compressive hoop stress formed at some later time after the cylindrically- or spherically-symmetric explosive loading was applied.

Small scale laboratory and field experiments done with chemical explosives at very small yields have verified that such residual stresses are indeed formed in homogeneous geological materials [Smith, 1987] . Observations and measurements obtained in the nuclear case suggest that the compressive stress field formed in a UGT may be weaker than current continuum models indicate. Or, perhaps, some relaxation mechanism causes a rapid decay of an initially competent residual stress. One suggested hypothesis is that the presence of non-homogeneities, such as faults and joints in the rock, may either inhibit the initial formation of a strong, uniform residual stress or may provide a stress redistribution mechanism which degrades it subsequent to it's formation.

Evidence for this theory comes from post-shot reentry observations of event-induced shear displacements along faults and joints. These offsets sometimes exceed a meter and are seen within the ranges of the calculated residual stresses. Because these joints represent potential discontinuities in stress, they have the potential to alter adversely the formation of a compressive, confining stress field. "Traditional" calculations of ground motion do not contain a mechanism to model the existence of these joints.

In the second section of this paper some of the recent "block motion" observations are briefly discussed. The third section of the paper summarizes previous work by other authors to include joint movement in ground motion simulations, and describes the calculational methods used in the current study. Results of a series of calculations of the resultant residual stress field are presented. In the fourth section, calculations of a single fault, two faults, and a network of multiple faults approximating those seen in the MIGHTY EPIC UGT were in turn modeled. The perturbation in the residual hoop stress field caused by each of these cases is graphically compared to the case with no included faults. Some comments on the geometric constraints of the current work, and suggestions for future work conclude the discussion.

2. BLOCK MOTION OBSERVATIONS

Visual observations made during post-shot reentry of areas near underground nuclear explosions in tuff beneath Ranier Mesa reveal that block motions occur on most, if not all, of these UGTs. Block motion is defined as the explosive-induced, permanent,

relative displacement in rock along the pre-existing planes of weakness [Bedsun, 1987]. Various forms of evidence exists to substantiate event-induced fault motion. A compendium of relevant observations was published in 1987 by Bedsun, Ristvet and Tremba [Bedsun, 1987]. Observations from the more recent events are included in the various Containment Summary Reports. To provide some background for the current study, fault motion observations from two recent events will be briefly discussed below.

Sandia National Labs instrumented a fault plane where it crossed the access drift approximately 350 feet from the working point of MISTY ECHO prior to the shot. Displacement and velocity records versus time were obtained on both sides of the fault. Additional post-shot reentry observations of motion adjacent to intersected faults were made for this interface and others visible along the reentry path. Figure 2-1 shows a tunnel plane view of the MISTY ECHO fault geometry. The magnitude and locations of the observed post-shot displacements are noted on the figure. The MISTY ECHO records are of particular interest because they provide information on the fault motion that occurred during the time of passage of the explosive stress wave. This gives a useful metric against which to compare the response of calculational fault models.

Another recent event in which the joint displacements were particularly well characterized, and thought to be typical, was MIGHTY EPIC. Post-shot measurements were made at thirteen locations to determine the differential shear displacements of eight prominent faults. These measurements are summarized and their corresponding locations are indicated on the tunnel plane schematic in Figure 2-2.

The database of these, and other, observations provides a means to make quantitative estimates of the influence of jointed rock on the residual stresses postulated to exist around a post-event cavity. Calibration of models with these observations allows subsequent careful extrapolation to other geometries and geologies. Without mining out the entire mountain, detailed knowledge of the exact extent and configuration of the faults will never be known. Additionally, the complexity of the rock fabric and the non-uniformity of the joints makes complete knowledge of the insitu frictional characteristics of individual joints impossible. However, one can formulate a model whose response matches observed fault characteristics in the field by adjusting the frictional parameters of the simulation model.

Admittedly, these frictional characteristics will vary from one fault to the next, and the displacement-matching procedure is necessarily based on just a few post-shot point measurements. Nevertheless, a simulation should provide a reasonable indication of the first order effects of block motion on residual stress. Qualified predictions for future events might be made, based on pre-shot inspection of exposed faults, use of model frictional characteristics consistent with successful post-dictions, and the exercise of the modeling procedure through the range of a physically reasonable parameter space.

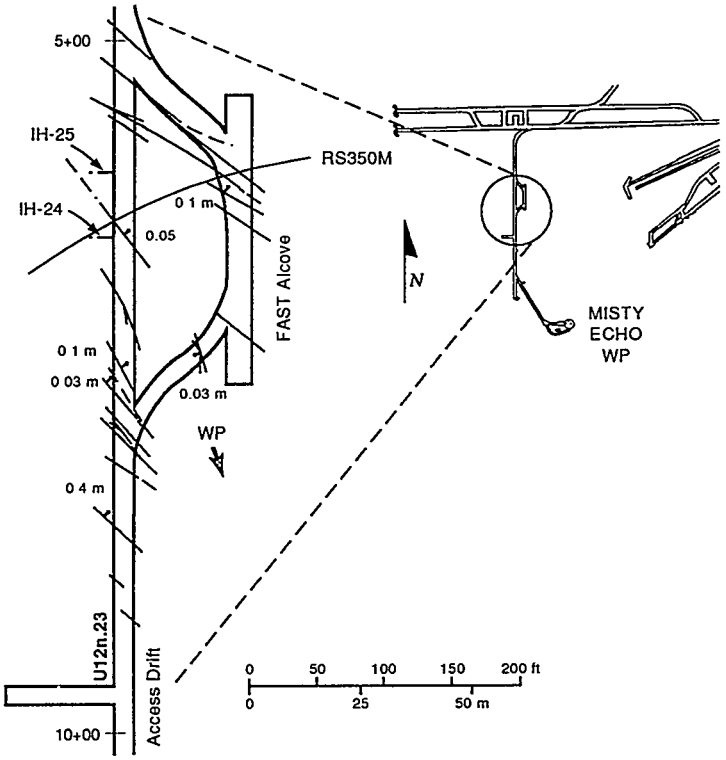


Figure 2-1. MISTY ECHO fault geometry showing magnitudes and locations of the observed post-shot displacements.

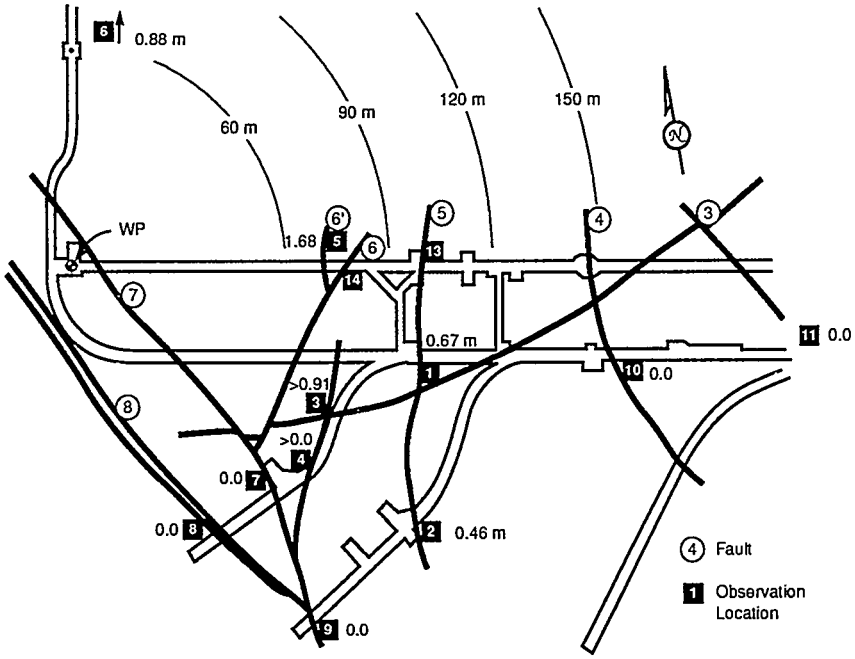


Figure 2-2. MIGHTY EPIC fault geometry with magnitudes and locations of the observed post-shot displacements.

2.1 Results of Previous Simulations

During the past two decades, the Defense Nuclear Agency (DNA) has funded a number of research programs to investigate underground block motion caused by nearby nuclear explosions. The primary motivation for this work was to determine the influence of joint motion on the survival of underground structures subject to ground level explosions. Various experiments were fielded during HLOS UGT's to characterize this motion and provide data for the characterization of joint properties and the validation of calculational techniques, among which was the distinct element method. Results of previous block motion studies are briefly summarized below and the data pertinent to containment science is extracted and discussed.

2.1.1 Analytical Modeling of Joints

In 1976, Johnson and Schmitz investigated analytically the fault motion driven by a spherical explosion in a boundless elastic medium [Johnson, 1976]. This analysis, limited to defining the onset of shear failure, showed that at certain orientations of the fault, even relatively close to the source, initiation of failure was inhibited. Fault movement for events of this type should not be expected for those faults oriented nearly perpendicular to the radial direction or parallel to the radial direction. More interestingly here, however, the method provides a means of exercising a block motion code against simple analytic solutions. It also provides some information (when compared against observed block motions) for calibrating the computational joint model. The major limitations of this analytic method are that it only defines the potential onset of movement (it gives no information about the magnitude of the fault motions) and clearly overestimates the wave propagation, since the region of interest undergoes considerable plastic work in the real case.

To address these shortcomings, Short and Kennedy [Short, 1978] modified the method to account for the inelastic behavior of the rock near the cavity. They also extended the analysis using some early work done by Rinehart [Rinehart, 1975] allowing estimation of the magnitude of the fault slippage. A method for calculating the relative velocities of each side of the fault, given an incoming plane wave, is constructed in his work. Short and Kennedy extended this analysis to include the effects of friction in the fault model. The resulting block motion prediction methodology was applied to the DIABLO HAWK event [Short, 1982]. Although the assumption of ideal planar and spherical wave forms limits the general applicability of the prediction methodology, the availability of analytical forms provides a useful yardstick against which to benchmark the current computational work.

2.1.2 Itasca Block Motion Research

Given the limitations of the early analytical work, DNA funded research during the mid-1980's to further investigate the effects of block motion due to UGT's on structures. This effort culminated in a prediction of the block motion for the MIGHTY OAK event using Itasca's discrete element code, UDEC [Hart 1987]. Although, again, the

research was not concerned with containment issues, and no attempt was made to calculate resultant residual stress fields, the work performed provides a wealth of information about the response of the block motion models, definition of material and fault property parameters, and sensitivity of the models to various geometric and constitutive values. Of special interest are results showing the interaction of the joints in models with multiple, intersecting faults and the subsequent "lockup" of the joints at the intersections and the effect on the surrounding stress field. Since containment questions were not investigated, the material models used for the tuff in the Itasca analysis were relatively simple (*e.g.* Mohr-Coloumb elastic-plastic and no treatment of either volumetric crush-up nor damage mechanisms). Additionally, since the available computer capacity was limited, the zone dimensions were large and approximations were made to the applied velocity boundary condition to avoid Courant condition caused computational problems. The region around the cavity was not modeled, but rather the velocity boundary condition was applied to the grid at some distance from the edge of the final cavity dimension. Because these results could be reproduced using the current version of the UDEC code, they are noted here.

3. CALCULATIONAL METHOD

3.1 Distinct Element Method

Distinct Element Methods (DEM) are specifically designed to model the behavior of media composed of individual particles or blocks; of which granular materials and jointed rock masses are familiar examples. Traditionally, computational and analytical modeling of stress wave propagation and stress states underground has been done primarily using techniques which treat the domain as a continuum. That is to say, although layers of different materials are allowed, the equations of motion and the stress fabric across these materials are treated as continuous. In DEM analysis, the motion of each material block is calculated by determining the contact forces which act on it's boundaries and then applying Newton's laws of motion. Customary finite difference (FD) and finite element (FE) models represent the material as continuous and largely devoid of joints and interfaces. Although these techniques (FD and FE) can be used to model jointed materials (usually through the introduction of special "slip lines" between the zones or elements), they are normally restricted to simple cases which have only a few non-intersecting joints. Because of the observed joint complexity of the rock matrix around a typical UGT, this restriction makes them of limited use for modeling the domain of interest.

Of equal importance in modeling discontinuous systems is the representation of both the mechanical behavior of the discontinuities and that of the solid material. For the purposes of our study, the modeling of the discontinuities must handle wave propagation at relatively high stress levels and frictions. This requires that the contact stiffness be included in order to obtain correct wave speeds across the joints. A fairly sophisticated treatment of the contacts, including a means of handling the interpenetration of point contacts into blocks, is necessary. Second, since the region of interest

undergoes extensive volumetric crushing and plastic deviatoric deformation, simple solid block models are inadequate and the method must provide for modeling nonlinear deformation within blocks.

The distinct element method falls taxonomically within a suite of analysis techniques which treat the domain as a discontinuous medium. Contacts and joints between multiple discrete bodies which make up the domain are modeled using physical laws of motion. Differences between DEM models arise from the way that they treat the interaction of the contacts and the representation of the "blocks" numerically.

The Universal Distinct Element Code (UDEC), used for the calculations in this report, resides in the subclass of the DEM comprising computer codes denoted "discrete elements" [Itasca, 1992]. These implement numerical algorithms allowing the representation of multiple, intersecting discontinuities explicitly. Finite displacements and rotations of the discrete bodies, including complete detachment, are allowed, and new contacts are automatically created as the calculation progresses. Representative alternative codes with different capabilities include DIBS [Walton, 1980], 3DSHEAR [Walton, 1988] and BLOCKS3D [Taylor, 1983]. A complete taxonomy of DEM methods and codes is presented in [Cundall, 1989].

Conceptually, in the distinct element method, joints are interfaces between distinct bodies and the rock mass is viewed as an assembly of discrete blocks. Equivalently speaking, the discontinuity is treated as a boundary condition. An algorithm calculates the movement of the blocks via the contact forces and displacements at the interfaces of the stressed assembly of blocks. The propagation of disturbances caused by the applied loads or body forces is a dynamic process where the speed of propagation depends on the physical properties of the blocks and the joints.

Dynamic response of the block assembly is controlled by a timestepping calculation wherein the size of the step is limited by an assumption of constant velocity and acceleration within the timestep. The timestep is limited to be sufficiently small that disturbances cannot propagate between zones in less than a single step. This algorithm is identical to the calculational scheme used in the explicit finite difference method employed for continuum analysis, except that in the DEM, the timestep restriction applies to both the contacts and the blocks. For the case in which deformable blocks are used, the zone size of the finite difference zone controls the timestep and the stiffness of the system involves both the intact rock moduli and the contact stiffness.

Figure 3-1 shows schematically the calculation cycle for the distinct element method. The calculational sequence cycles between application of a force-displacement law at all of the contacts and application of Newton's second law to all of the block motions. For deformable blocks (*e.g.* those which are zoned with internal finite difference zones), the motion is calculated at the gridpoints of the triangular finite-strain zones within the block. Application of the block material constitutive laws then gives new stresses within the zones.

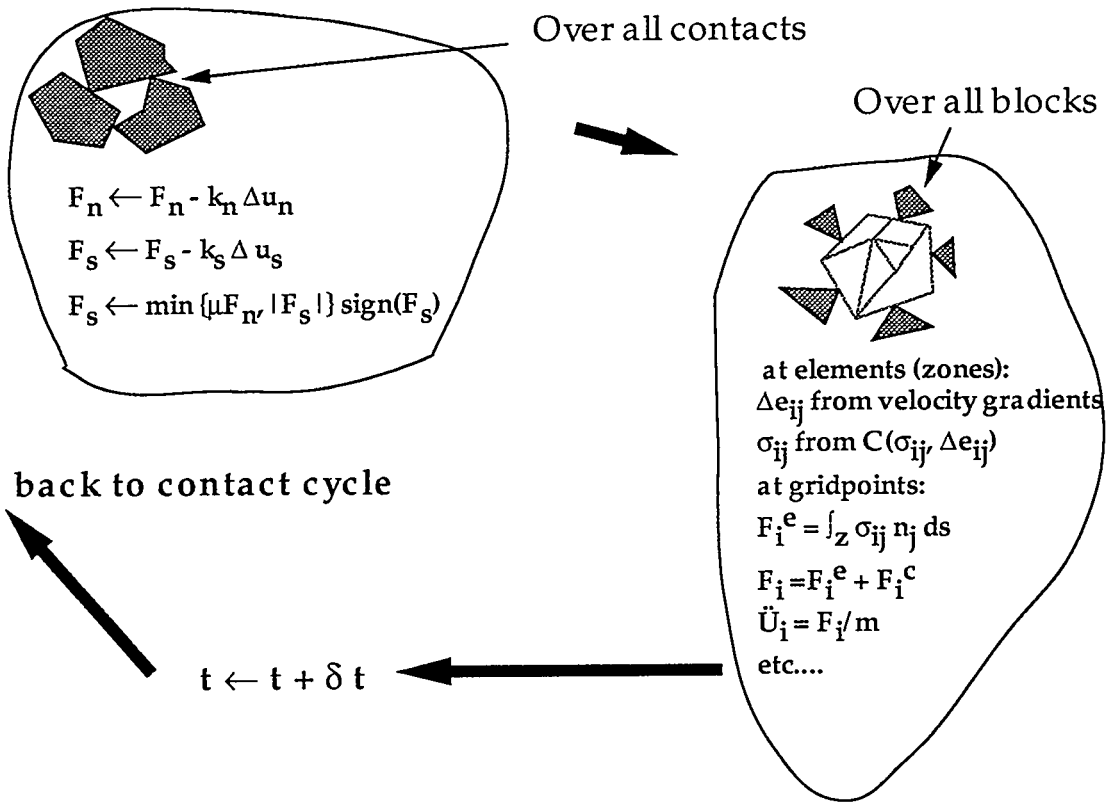


Figure 3-1. Schematic of the calculational cycle for the UDEC code.

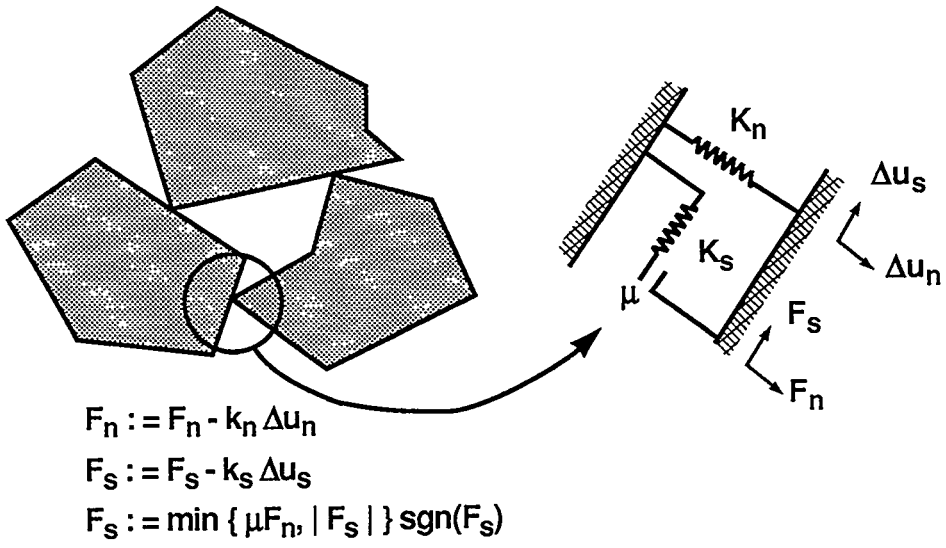


Figure 3-2. Representations of contacts in the UDEC code.

The distinct element method can be shown to satisfy conservation of momentum and energy provided the error introduced by the numerical integration process is kept small through the use of suitable timesteps and sufficient numerical precision in storing grid coordinates and motion information. Verification of the code's accuracy has been done by comparison to various closed-form solutions [Itasca, 1992].

In UDEC, a rock joint is represented numerically as a contact surface formed between two block edges. In the code, adjacent blocks can touch along a common edge segment at discrete points where a corner meets an edge or another corner. Figure 3-2 shows the scheme for representation of contacts. For rigid blocks, a contact in UDEC is created at each corner interacting with a corner or edge of an opposing block. If the blocks are deformable (*e.g.* internally discretized), point contacts are created at all gridpoints located on the block edge in contact. The corners are rounded so that the blocks can slide past one another.

Contact points are updated automatically as block motion occurs. Contact updating is forced by significant relative motion within a domain. A fictitious displacement is accumulated for each domain, and this displacement is related to the incremental motion that has taken place in the domain since the last update. When the displacement exceeds a given tolerance, an update is triggered. This insures that contacts are detected before physical contact occurs.

For block motion involving large shear displacements, contact updating must ensure that contact forces are preserved when contacts are added or deleted so that a smooth transition will exist between neighboring states. This is particularly important for dynamic analysis with high stress gradients. The contact update logic in UDEC has been tested for explosion-driven motion involving large displacements [Hart, 1987].

3.2 CRAM/UDEC Coupling

Calculation of underground explosions in tamped or untamped cavities which release the energy inherent in the nuclear case severely, and nonlinearly, deform the media surrounding the cavity. Volumetric crushup of the region immediately adjacent to the explosive source far exceeds that computable using linearized elastic formulations of the governing stress-strain relations and creates numerical situations in finite difference schemes which can drive the effective timestep toward zero in order to satisfy Courant stability in the time domain. The standard solution employed in finite deformation codes is to employ some sort of rezoning scheme during the initial part of the calculation to remove the smallest zones at predetermined intervals such that a reasonable Δt is maintained. The trick is to delay the rezones until a major portion of the explosive energy has been imparted to the surrounding rock so that the effect of the rezoning on the accuracy of the calculation is minimized.

Since the standard discrete element formulation available in UDEC does not provide any mechanism for conveniently rezoning the finite differenced-blocks, the

problem of modeling the explosive source and subsequent massive deformation of the grid must be handled in some other manner. Previous investigations of block motion around nuclear cavities were done ignoring the inner region of material around the cavity and supplying instead a velocity history to the edge of the grid at some "safe" (*e.g.* computationally possible) radial distance from the cavity. The velocity history in this case was obtained from an S-Cubed 1D calculation. This is one approach, but there are some drawbacks. First, any non-symmetric response of the model due to wave reflections off faults, etc. cannot be modeled correctly, as the inner boundary of the grid is forced to conform to the symmetric driving function. Second, modeling of block response inside of the "safe" radius is impossible. Additionally, the magnitude of the applied velocity history (derived from a spherical calculation) has to be artificially lowered in order to correct it for differences in attenuation due to the cylindrical geometry used in the block motion calculation.

A second approach, and the one used for the majority of the calculations in the study, is to marry a "special block" (in this case the CRAM code was used to avoid extensive recoding of UDEC) to the existing UDEC code to allow rezoning of the inner ring of material. Again, there is no modeling of the block response inside of the CRAM grid, however, all motions and stresses are correctly represented at the interface. The CRAM/UDEC grid is pictured in Figure 3-3.

(CRAM is a 2D finite difference wave propagation code containing appropriate physical models and an extensive history of successful use in containment simulations.) As time progresses, and after the majority of the explosive energy has been imparted into the grid, concentric rings of the CRAM zone are removed and their nodal and zonal properties interpolated into the resulting larger zone. The problem here was in devising a coupling scheme which correctly interpolated nodal velocities and accelerations and zonal strains, stresses, and material model parameters between the two codes.

Since both codes use basically the same differencing and time marching algorithms, the problem reduced down to assuring that the codes interpolated between CRAM's rectangular zones and UDEC's triangular zones properly and that the zonal material models corresponded. A scheme was devised which overlays the outer ring of CRAM zones onto the innermost ring of UDEC zones. Nodal velocities for the overlaid zones are synchronized between the codes at each time step. The UDEC zoning is constrained such that the inner ring of zones are composed of diagonally-opposed triangles, resulting in a rectangular mesh corresponding to the CRAM zoning at this location. The code which computes the smallest time step is allowed to control the time step for both codes. Initially, because of the compression of the interior CRAM zones before the first rezone, the CRAM time step is usually smaller than the one calculated for the UDEC zones. Later, as joint movement occurs, UDEC usually controls the time step.

The inside of the CRAM grid is driven by a pressure loading function computed from a previously determined energy loading density for a nuclear explosive.

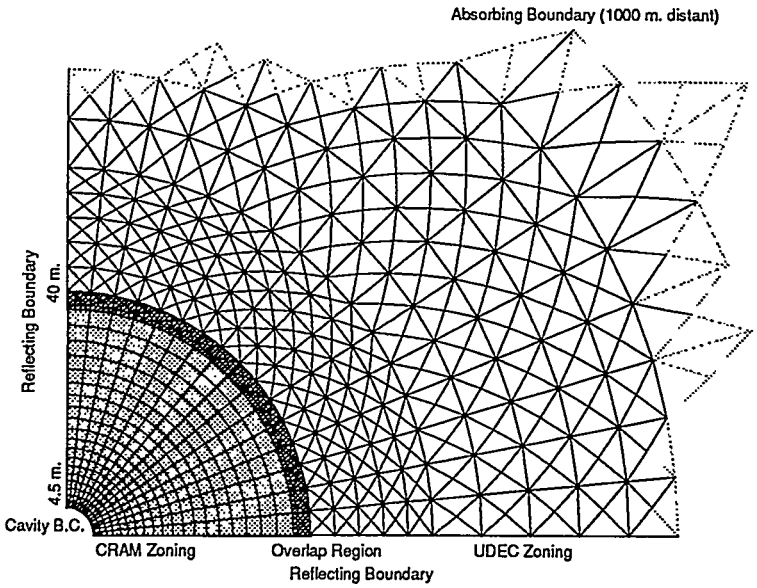


Figure 3-3. CRAM-UDEC coupling and calculational geometry used.

The interface location between the CRAM and UDEC codes was chosen as a compromise between assuring "safe" deformation in the UDEC grid (since there are no rezones available) and allowing placement of joints as close as possible to the cavity (since CRAM has no joint modeling capability).

3.3 Continuum and Joint Material Response Models

Discrete element model codes must provide constitutive models for both the non-linear response of material interior to the blocks and representations of the interaction of the blocks with each other. UDEC usually treats, as it's default option, the blocks as simply (*e.g.* elastically) deformable. For this study, it is clearly necessary to choose the other option available, which is to model each of the blocks as a fully deformable finite difference domain with appropriate non-linear constitutive models for both volumetric and deviatoric response.

From a containment analysis standpoint, the standard material models available in UDEC for the block response are not appropriate for characterizing the features of tuff dynamic material response necessary for computing residual stress fields. Although the existing models could perhaps be coerced into approximating the desired response, it was felt that a better approach was to install the "standard" S-Cubed material models used for containment calculations into the UDEC code. This was done and verification of the correct installation was determined using the test problems described below. The standard UDEC joint model was employed. It is described below and a justification for it's use is presented.

3.3.1 Block Response Models

3.3.1.1 Volumetric

Volumetric response was modeled using an implementation of the P-alpha model installed into the "stock" UDEC code. A description of the model, and justification for it's use in these wave propagation problems is presented in Rimer, 1985 and is not repeated here. Figure 3-4 shows the shape of the crush curve used in these calculations. The parameters used result in a generic model for Nevada Test Site tuff and are not intended to reproduce the response of tuff for a specific event.

3.3.1.2 Deviatoric

Mohr-Coloumb

The default model for representing the non-linear deviatoric response of the deformable blocks in UDEC is the Mohr-Coloumb failure surface [Chen, 1985]. This model represents the elastic-plastic response of the individual zones as a function of the material's cohesion and friction angle (Figure 3-5). The model has been extensively applied to soil plasticity, but suffers from the shortcoming that the corners are numerically troublesome in three dimensional stress states. (*e.g.*, the hexagonal shape of the failure surface in principal stress space.) The model also neglects the effects of the intermediate principal stress and does not model dependence of the failure surface on the third deviatoric invariant. Although usable for the 2D calculations done here, because of our familiarity with the Peyton formulation of the failure surface, and it's availability in existing codes, we chose to implement it and use it instead in UDEC [Rimer, 1985]. The Peyton model addresses the Mohr model's shortcomings.

Previous comparisons with available experimental data have shown that the residual stresses and ground motion waveforms calculated using only a failure surface obtained from laboratory tests do not result in good fits. Consequently, ground motion calculators, armed with field observations and experimental evidence, have developed extensions to the deviatoric response which include the effects of damage on the material. These models result in reduced material strength in regions which have undergone extensive volumetric strain "Old Damage" or strain difference "New Damage". For use in this study, both of these damage models were coded into UDEC, although the majority of the calculations were performed using the New Damage model. The models are described in detail in [Proffer, 1990]. Figure 3-6 shows the initial and damaged failure surfaces used in the New Damage model for these calculations.

3.3.1.3 Tensile

The tensile failure model in UDEC checks for tensile stresses which exceed either the plastic apex limit or the tensile strength. If the major principal compressive stress (σ_1) exceeds the plastic apex, then all three principal stresses are set to the apex value. If the tensile strength is smaller than the apex value, the tensile strength value is cut to

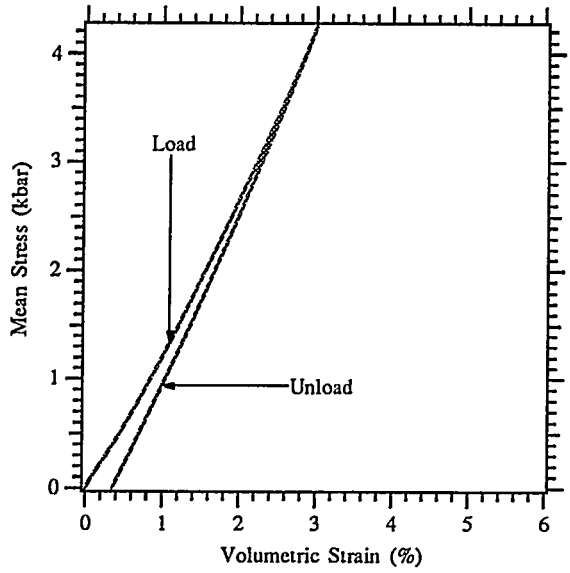


Figure 3-4. P-α volumetric crush re-rsponse model.

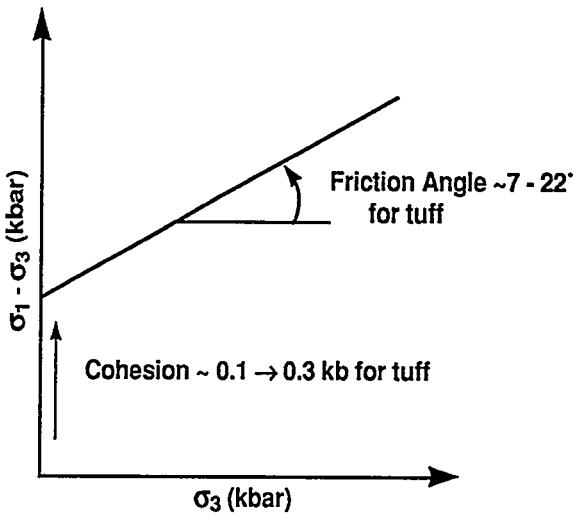


Figure 3-5. Mohr-Coloumb failure surface.

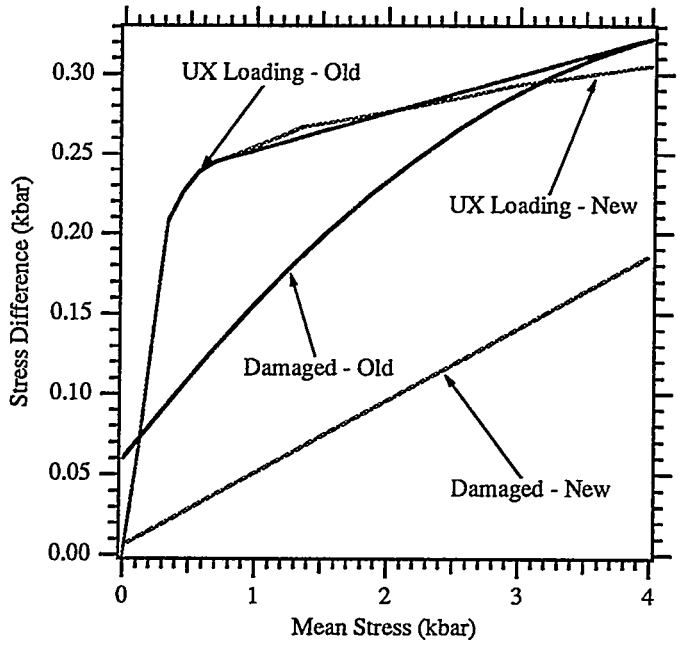


Figure 3-6. Strength model used in the calculations.

zero, and all three principal stresses are set to zero. In this case, the zone has failed in tension and can no longer sustain tensile stresses. CRAM employs a Maenchen-Sack tension failure model. Here, inelastic crack strains are used to model tensile fractures. These open whenever a principal stress exceeds the tensile strength in the material. For these calculations, a very small value of tensile strength (10 bars, 1.0 MPa) was used to represent the minimal strength of tuff. This was suggested by [Hart, 1987] as a way to make the plane strain model wave attenuation resemble that of an axisymmetric one.

The use of a small tensile strength for tuff is physically acceptable as shown in [Tillerson, 1984].

3.3.2 Joint Response Models

As discussed above, there are only two types of contacts required by the code's data structure to represent the assemblage of blocks: corner-to-corner and edge-to-corner. A third type of contact, edge-to-edge, is physically important, however, as it represents a rock joint closed along its entire length which is necessary here for representing the behavior of faults. Various constitutive models for simulating the physical response of joints can be envisioned. Three successively more complex joint models are available in the stock UDEC code [Itasca, 1992, Barton, 1982].

Because so little insitu and experimental data is available for the response of joints in tuff, and that which is available is characterized by wide sample variation, the simplest UDEC model was used in this study. It nevertheless exhibits a number of the features representative of actual joint response. Stress-displacement in the normal direction is modeled using a linear "spring" equation:

$$\Delta\sigma_n = k_n \, \Delta u_n$$

where $\Delta\sigma_n$ is the normal stress increment and Δu_n is the normal displacement increment during a time step. k_n is a joint stiffness coefficient with units of stress/displacement (length). The tensile strength of the joint is limited to a value of T and if it is exceeded σ_n is zeroed. In shear, the linear response is modeled by

$$\Delta\tau_s = k_s \, \Delta u_s^e$$

Here the shear stress (τ_s) is limited by a combination of cohesive (C) and frictional (ϕ) strength:

$$\text{abs}\,(\tau_s) \le C + \sigma_n \tan\phi = \tau_{max}.$$

If

$$|\tau_s| \le \tau_{max},$$

then

$$\tau_s = \text{sign}(\Delta u_s)\, \tau_{max}.$$

Here:

Δu_s^e is the elastic part of the incremental shear displacement, Δu_s is the total incremental shear displacement, and u_s is the shear stiffness.

Joint dilation may also occur at the initiation of joint slippage and is controlled by the input of the dilation angle, ψ, into the model. Dilitation is restricted such that if:

$$|\tau_s| \le \tau_{max},$$

then,

$$\psi = 0,$$

and if,

$$|\tau_s| = \tau_{max}$$

and

$$|u_s| \geq u_{cs},$$

then

$$\psi = 0.$$

Where u_{cs} is a limiting value on the accumulated shear displacement.

The model approximates the displacement-weakening behavior which is observed in real joints by setting the tensile strength and the cohesion to zero when either the tensile or shear strength is exceeded.

Hart, Lemos and Cundall [Hart, 1987] review the available insitu and experimental data available for joints in tuff. Some recent information for tuff from quasi-static and dynamic laboratory experiments on jointed tuff blocks is reported in [Baktar, 1990]. A reasonable range of values for cohesion (C) suggested by these sources seems to be 30 to 80 bars (3 to 8 MPa). A baseline value of 34.5 bars (3.45 MPa) was chosen for the majority of calculations performed. Credible values for the friction angle range from 5 degrees to 39 degrees. The baseline was chosen as 11 degrees ($\mu = 0.194$). Although Baktar and Barton [Baktar, 1990] propose that dilation is an important phenomena in the cyclic dynamic response of tuff joints, to simplify the analysis herein, the dilation angle was maintained at zero.

Shear and normal stiffness for the joints were chosen consistent with recommendations set forth in [UDEC, 1992]; namely within an order of magnitude of the stiffness of the neighboring block zones, *e.g.* $k_n=k_s=1x10^5$ MPa. Unnecessarily larger values of stiffness cause run times for the code to increase due to timestep requirements.

4 RESULTS OF CALCULATIONS

4.1 CRAM/UDEC Code Verification Comparisons with 1D Skipper Calculations

Since the implementation of new material models into an existing code is fraught with potential bugs, and the UDEC code was initially unfamiliar to the authors, it was deemed prudent to exercise both the existing code and the coding of the new models against results obtained using a familiar, and less complex, code. Since 1D SKIPPER code results are used as a check against the coding changes and extensions required to move new material models and numerical techniques into the CRAM code, it was also employed to validate the UDEC models. S-Cubed has extensive experience calculating one-dimensional nuclear explosion calculations using the SKIPPER code [Rimer, 1987]. SKIPPER is also used as a testbed for the implementation of new material models and

thus has available a large database of carefully studied results for various material models and parameters [Rimer, 1987]. Since SKIPPER can be run in both 1D cylindrical and spherical configurations, it can also be employed to compare the effects of geometry on the resulting waveforms and residual stresses.

The following test calculations were run using CRAM/UDEC and verified against the results obtained using the SKIPPER and CRAM codes:

- 1D quasi-static elastic-plastic sphere and cylinder to verify correct implementation of the Peyton deviatoric failure model.
- 1D P-alpha sphere and cylinder to verify correct implementation of the P-alpha volumetric crush-up model.
- 1D damage model sphere and cylinder to verify the coding of the Rimer damage models.
- 1D spherical explosion calculation, using the above material models, to verify the coupling scheme between the CRAM and UDEC codes.
- 1D cylindrical explosion calculation, to investigate the effects of geometry on the UDEC calculational results.
- Generation of residual stress fields, to verify the capability of the CRAM/UDEC code to do containment-type calculations.

A difficulty in the current two-dimensional analysis is representing realistic fault geometries within the constraints of plane strain or axisymmetric idealizations of a three-dimensional body. Although a three-dimensional version of the UDEC code exists, it was not available for this analysis, and the current version of CRAM is a two-dimensional code. For simplicity the current study was limited to 2D representations of the block motion. These qualitative analyses should show whether faults can degrade residual stress fields.

For accurate representation of the wave propagation, attenuation and strain paths caused by a spherical source, the axisymmetric (r, z, θ) formulation is preferable. Both CRAM and UDEC provide the capability to run in this geometry. Our version of UDEC, however, does not appear able to treat the joint interactions correctly for joints intersecting the z axis. In addition, in axisymmetry, joints become surfaces of revolution about the z axis, resulting in cylindrical and cone shaped faults. The blocks associated with these are "donuts" and are consequently artificially constrained in possible movement.

Alternatively, a plane strain representation requires joints of infinite extent in the z coordinate direction and results in a cylindrical, or line charge explosive source. The pulse attenuation from such a source does not decay rapidly enough with distance, resulting in higher waveform peaks at locations away from the cavity. This effect must be considered when interpreting the results, as it affects both the magnitude of the fault

displacements and the response of the block material (due to the different strain path seen by the constitutive models).

For current study, the plane strain model was chosen as the more realistic approximation to the actual three dimensional geometry. Comparisons of the SKIPPER calculations done in both geometries reveal that the difference in the final form of the residual stress field is not that important for our purposes here. Further comparisons of the calculated final residual stress between SKIPPER and CRAM/UDEC (with any faults) validate the accuracy of the 2D CRAM/UDEC stress field.

4.2 Single Fault Calculations

Effect of different joint orientations on fault motion.

Because the previous analytical investigations identified a dependence of both the onset and magnitude of joint displacements as a function of orientation to the incoming wave motion, two different fault orientations were zoned for the single fault simulations. The geometries of these calculations are shown in Figure 4-1. Results showing the relative displacement of the interface versus position are shown in Figure 4-2. In this figure the relative shear displacement of the fault is indicated by the width of the dark plotted line at a given position. As expected from the aforementioned analytical work, the displacements along the horizontal fault are much larger than those for the diagonal fault. The displacements seen along the horizontal fault are approximately $^1/_3$ of those reported in the Itasca study for the same single fault geometry and fault properties. The difference here is that the damage mechanism in the current

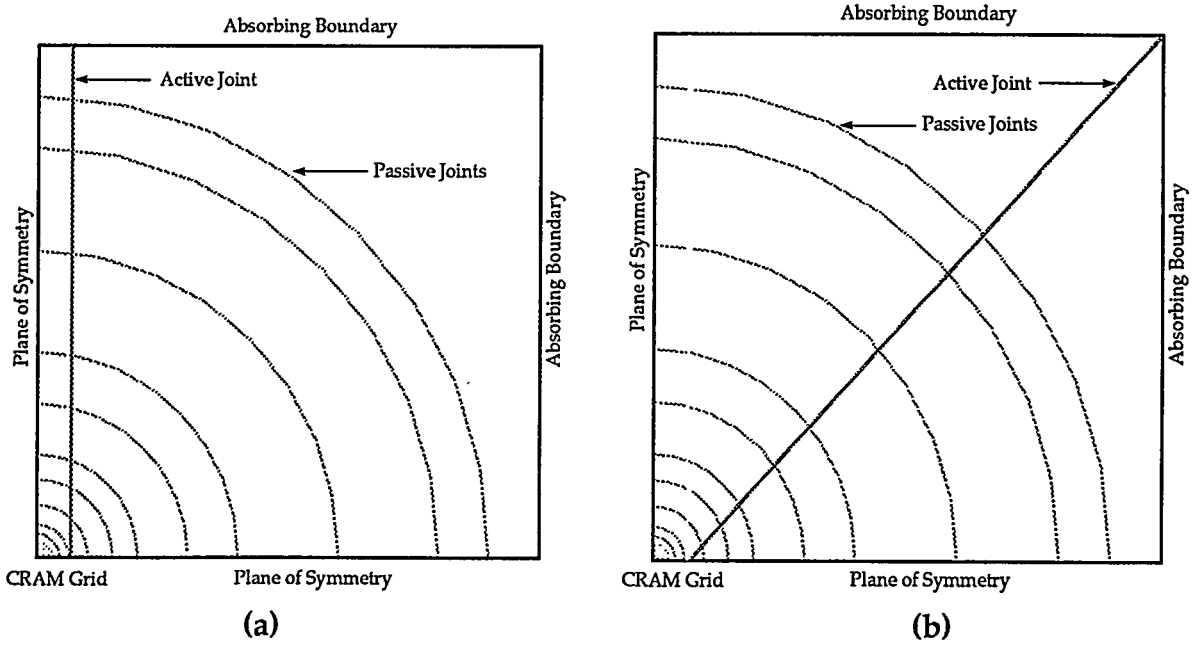


Figure 4-1. Orientation of faults for single fault calculations.

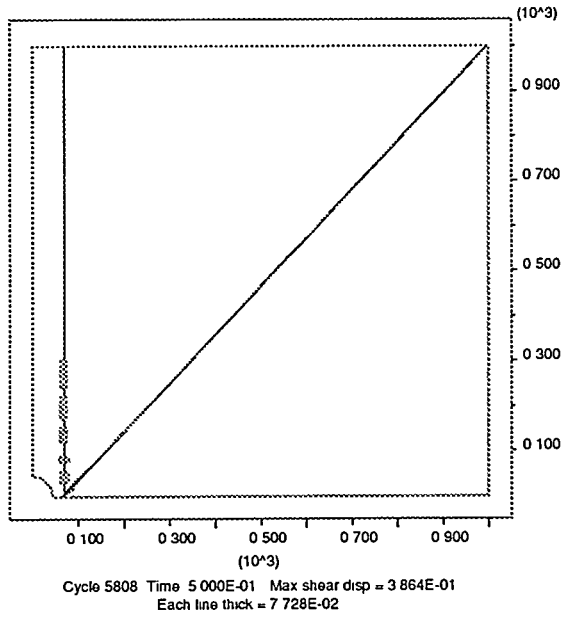


Figure 4-2. Relative displacement of interface for single fault calculations.

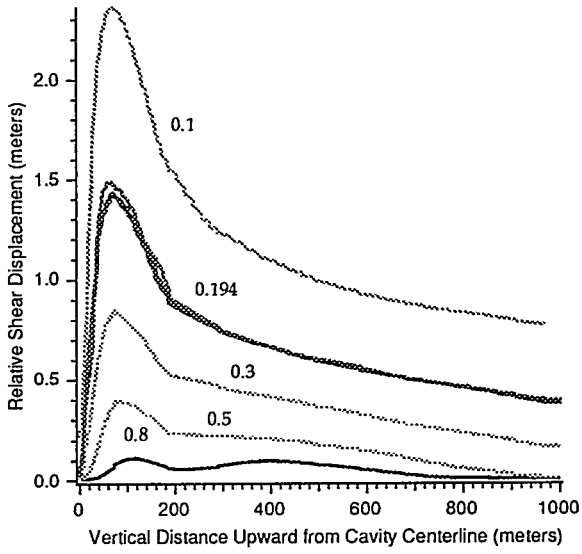


Figure 4-3. Effect of joint properties on fault motion.

failure model for the intact rock reduces the apparent strength of the rock in this area. Consequently, the relative ratio of rock strength to joint strength is reduced considerably when compared to the Itasca case using the Mohr failure surface. This results in reduced slippage along the fault.

Effect of joint properties on fault motion.

Since the parameters for the joint model are not well constrained by the available insitu and experimental data, a second suite of calculations (using the single fault orientation exhibiting the largest relative displacement) was done, varying the joint cohesion and friction angle over the range indicated by the experimental data. Results of this parameter study are plotted in Figure 4-3 for values of tan θ from 0.1 to 0.8. It can be seen that variations in the friction angle have a significant effect on maximum joint motion. Also investigated, but not shown here, was the effect of the cohesion on joint motion. For a reasonable range of cohesion values (30 to 80 bars, 3 to 8 MPa), little effect was seen. These results echo those previously obtained in the analytical studies of Johnson and Schmitz and Short and Kennedy.

Effect of single fault on calculated residual stress field.

Figure 4-4 graphically illustrates the local perturbation in the residual stress field caused by an intersecting fault plane. For this calculation, the joint properties and orientation resulting in the maximum amount of joint movement was used. The introduction of a discontinuity in stress and displacement at this location adversely affects the formation of the residual stress field. Originally a color contour plot, this figure has been modified to show the stress ranges as shades of grey. The feature to note is the region of reduced compressive stress (light color is highest compressive stress) above

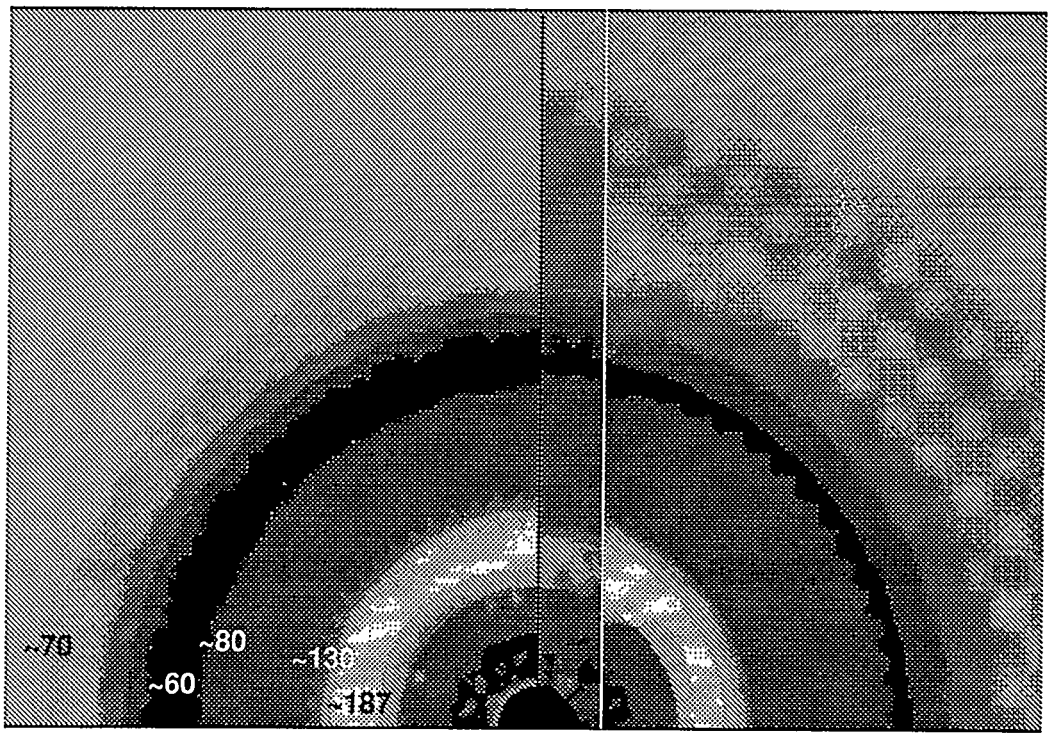


Figure 4-4. Effect of single fault on residual hoop stress. (Approximate compressive stress in bars, left side: no faults, right side: 1 fault case.)

the cavity for the case with the single fault (on the right side of the figure). The reduction in this area is on the order of 20 to 40 bars, compared to the competent residual stress peak (approximately 180 bars) seen on the left hand side of the figure.

4.3 Multiple Fault Calculations

Since there are many faults in the actual insitu case, an attempt was made to at least qualitatively investigate the effects on the residual stress of multiple joints. Although an almost infinite number of possible orientations for two (or more) faults can be contemplated, an interesting configuration wherein two faults either intersected or not was chosen (Figure 4-5). The corresponding contour plots of the residual stress for the intersecting and non-intersecting cases are shown in Figure 4-6. Again, there is considerable reduction (20-40 bars) in both the peaks and the fidelity of the residual stress field in both cases with included faults.

A final calculation of a multiple-fault case representative of a slice of the MIGHTY EPIC event fault locations was performed. Figure 4-7 shows the fault geometry used in this calculation. Here again the concentric rings are "inactive" faults included for zoning convenience. The active faults where chosen to match a calcula

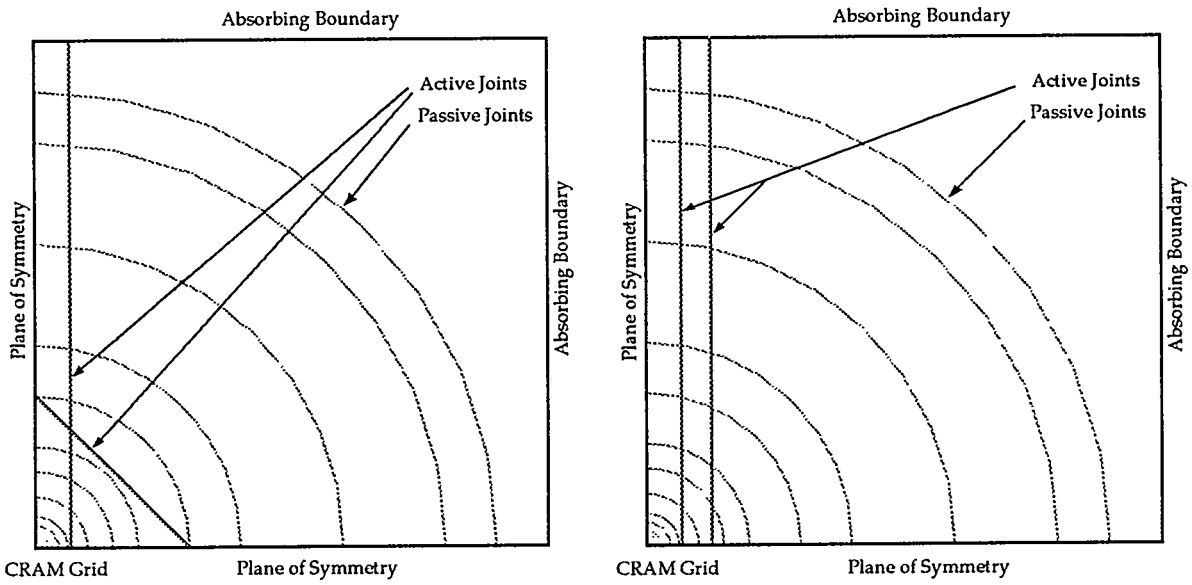
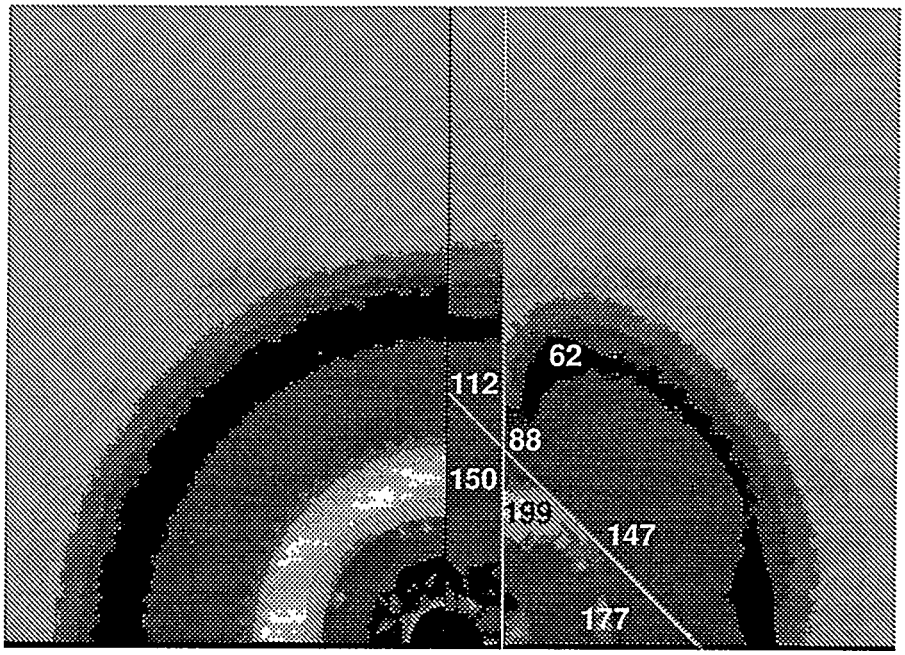


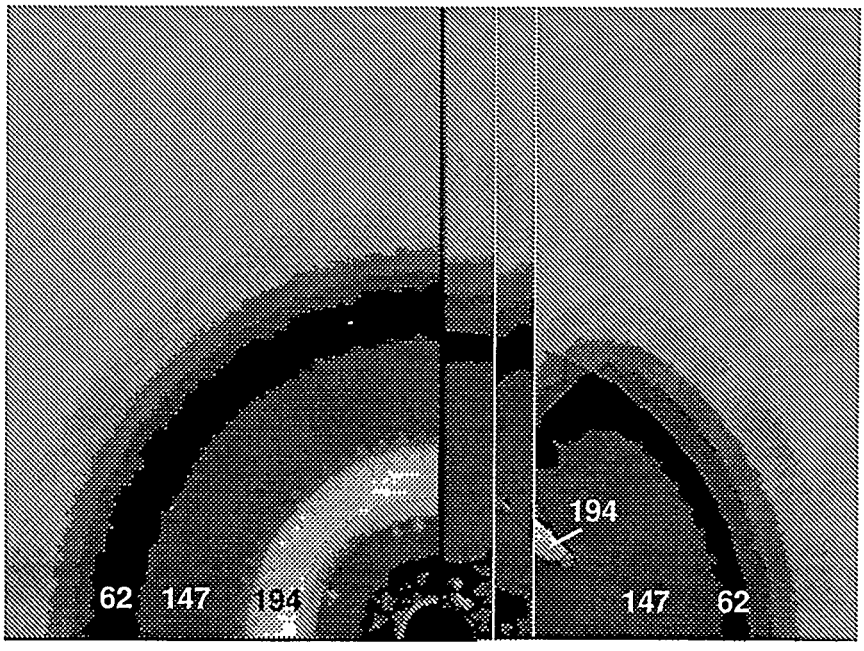
Figure 4-5. Two fault case, (a) intersecting, (b) not intersecting.

tional geometry previously used in the Itasca study [Hart, 1987] and roughly represent the spatial orientation of the observed faults as viewed vertically through the line of sight (LOS) pipe drift. The displacement calculated in the current study are shown in Figure 4-8 (the magnitudes are represented by the thickness of the lines). Also shown are the locations of the two relevant observations from the ME reentry. Our current study shows no displacement at location 10, consistent with reentry observations. The reentry found a dip-slip movement of 1.68 meters at location 5, however. Our calculation shows a displacement of only approximately 0.1 meters in the correct direction here. The previous Itasca study had a displacement of 0.33 meters here. The difference in displacement between the Itasca study and ours can be explained by the reduced block material strength. However, although the calculations provide the correct directional movement of the faults, they underestimate the magnitude considerably.

Figure 4-9 shows the residual stress field calculated for the ME case. The stress field in the area around the intersection of the three faults to the right of the cavity is significantly modified by their presence and interaction. Also, the area above the cavity has seen it's peak stress reduced by the presence of the fault.



(a)



(b)

Figure 4-6. Residual hoop stress (approximate compressive stress in bars). Left side: no faults, top right: two intersecting faults, bottom right: two non-interesting faults.

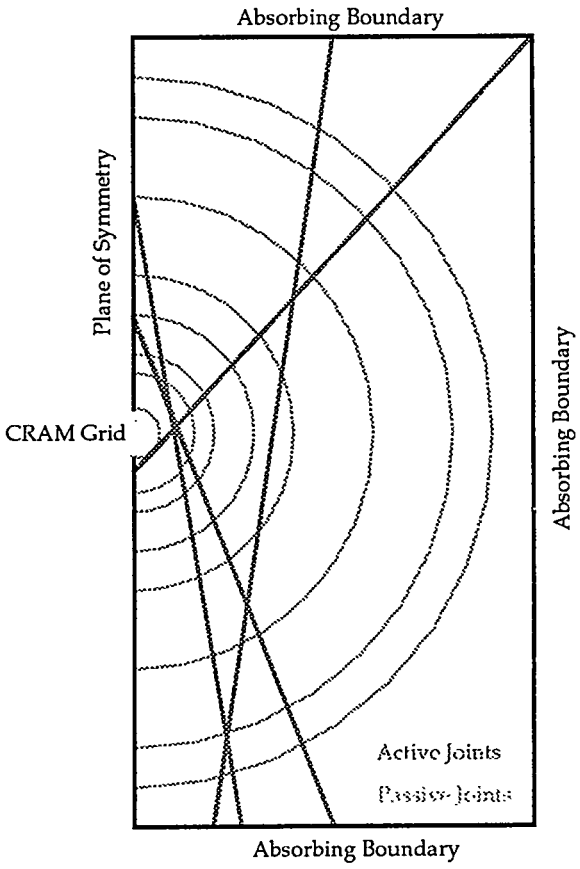


Figure 4-7. MISTY ECHO geometry.

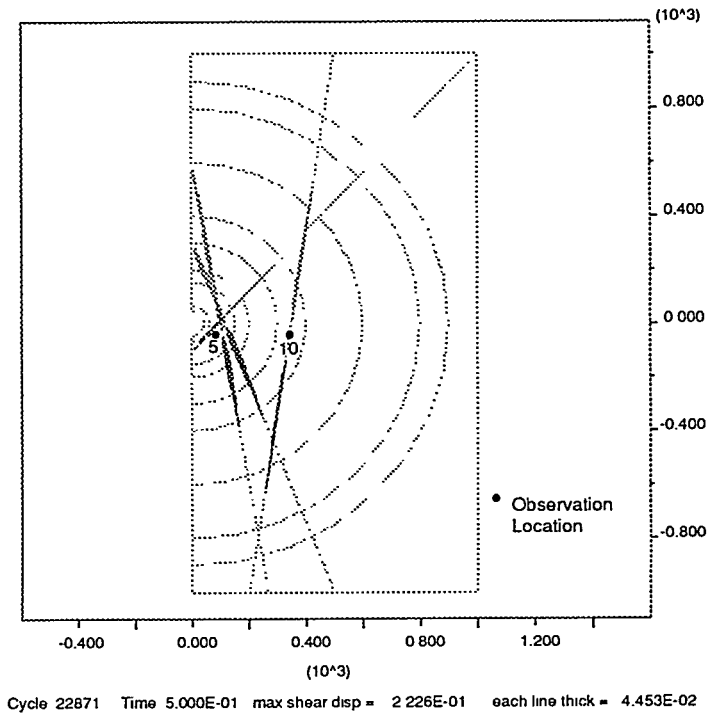


Figure 4-8. MISTY ECHO fault displacements.

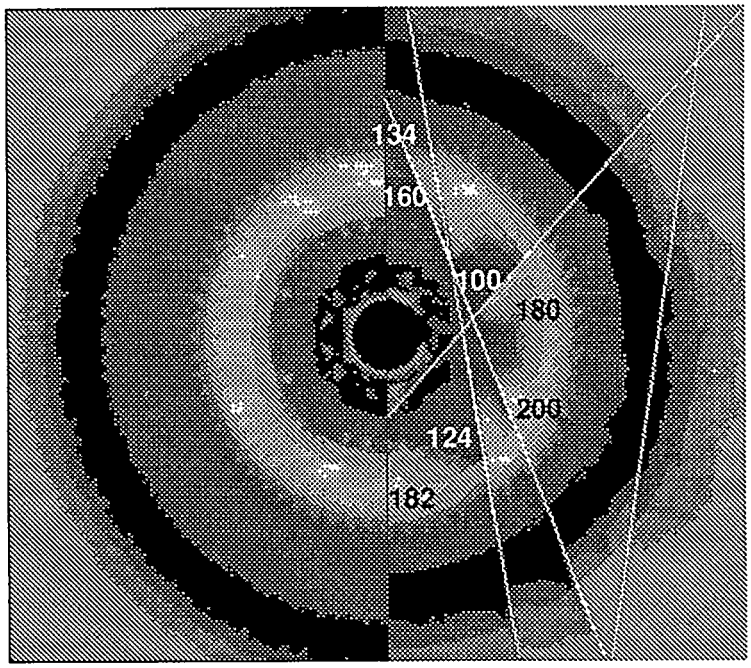


Figure 4-9. MISTY ECHO residual stresses (approximate compressive stress in bars). Left side: no faults, right side: idealized vertical fault locations.

5. SUMMARY AND FUTURE WORK

The preliminary results presented here suggest that the discontinuous block motion resulting from the passage of the stress wave from an underground nuclear explosion could affect the formation of the residual stress field postulated to exist subsequent to the event. Using joint models with parameter choices with the range of experimental evidence and a two dimensional approximation of the actual underground configuration of joints, localized degradation of the magnitude and uniformity of the residual stress is shown.

Even given the uncertainties in available material and joint mechanical response data, further 2D simulations which investigate different fault orientations and configurations are probably useful to better define geometric effects. It is unclear at this point whether the differences in fault displacement magnitudes between the reentry observations and the calculations is attributable to either geometric effects or incorrect modeling of the joint properties, or both. Additional work is necessary to improve the finite difference model and zoning used in UDEC for dynamic wave propagation calculations. At least a small number of full three dimensional UDEC calculations should be performed to investigate the effects of the two dimensional geometry approximations and ultimately determine the effects of block motion on stemming plug formation.

6. REFERENCES

Barton, N. "Modeling Rock Joint Behavior From Insitu Block Tests: Implications for Nuclear Waste Repository Design," Technical Report ONWI-308, Sept., 1982.

Bedsun, D.A., B.L. Ristvet and E.L. Tremba, "A Summary of Observations of Block Motion for Explosive Events in Rock," Technical Report DNA-TR-87-277, Defense Nuclear Agency, Alexandria, VA.,1 August 1987.

Chen, W. F. and G. Y. Baladi, Soil Plasticity: Theory and Implementation, Elsevier, 1985.

Cundall, P.A. and R.D. Hart, "Numerical Modeling of Discontinua," Keynote Address, in Proceedings of the 1st Conference on Discrete Element Methods (Golden, Colorado, October 1989), CSM Press, 1989.

Cundall, P.A., "Formulation of a Three-Dimensional Distinct Element Method - Part I: A Scheme to Detect and Represent Contacts in a System Composed of Many Polyhedral Blocks,", Int. J. Rock Mech., Min. Sci. & Geomech. Abstr., 25 107-11, 1988.

Hart, R.D., J. Lemos, and P.Cundall, "Block Motion Research: Volume II-Analysis with the Distinct Element Method,", Technical Report DNA-TR-88-34-V2, Defense Nuclear Agency, Alexandria, VA., 14 December 1987.

Heuzé, F E., O.R. Walton, D.M. Maddix, R.J. Shaffer and T.R. Butkovich, "Analysis of Explosions in Hard Rocks: The Power of Discrete Element Modeling,", LLNL Report UCRL-JC-103498, March, 1990.

Johnson, J. N. and D. R. Schmitz, "Incipient Fault Motion Due to a Spherical Explosion," TerraTek Topical Report DNA 3948T, February, 1976.

Peterson, E., et. al., "Containment Program Support," Final Report DNA-TR-92-158-RW, Defense Nuclear Agency, Alexandria, VA., July 1993.

Proffer, W. and N. Rimer, "Another Computational Model for Tuff,", S-Cubed Report SSS-DTR-90-11961, October 1990.

Rimer, N. and K. Lie, "Numerical Predictions of the Ground Motions from a ONETON Insitu High Explosive Event in Nevada Test Site Tuff," S-Cubed Report SSS-R-6493, January, 1984.

Rimer, N. and K. Lie, "Numerical Simulation of the Velocity Records from the SRI Grout Spheres Experiments," Technical Report DNA-TR-82-54, Defense Nuclear Agency, September 1982.

Rimer, N., "The Effects of Strain Paths Calculated for Spherically Symmetric Explosions on Measured Damage in Tuff," S-Cubed Report SSS-R-88-8988, Sept. 1987.

Rimer, N., H.E. Read, S.K. Garg, S. Peyton, & S. M. Day, "Effect of Pore Fluid Pressure on Explosive Ground Motions in Low Porosity Brittle Rocks," DNA Report TR-85-245, 1985.

Rinehart, J. S., Stress Transients in Solids, Hyperdynamics, Santa Fe, May 1975.

Short, S.A. and R. P. Kennedy, "Interim Report 3, MIGHTY EPIC/DIABLO HAWK Block Motion Program - Prediction of DIABLO HAWK Block Motion," EDAC Topical Report 177-020.3, July 1978.

Short, S.A. and R.P. Kennedy, "MIGHTY EPIC/DIABLO HAWK Block Motion Program, Volume II - Block Motion Prediction," Technical Report DNA-TR-6230-F-2, Defense Nuclear Agency, December 1982.

Smith, C.W., "Residual Stress Fields - Results from High-Explosive Field Tests,", 2nd Symposium on Containment of Underground Nuclear Explosives, 87-107, 1983.

Taylor, L.M. "BLOCKS: A Block Motion Code for Geomechanics Studies", Sandia National Laboratories, Report SAND82-2372, March 1983.

Tillerson, J. R., and F. B. Nimick, "Geoengineering Properties of Potential Repository Units at Yucca Mountain, Southern Nevada," SAND84-0221, Dec. 1984.

UDEC: Universal Distinct Element Code, Version 1.8 User's Manual", Itasca Consulting Group, Inc., Minneapolis, MN., June 1992.

Walton, O.R., "Particle Dynamic Modeling of Geological Materials," Lawrence Livermore National Laboratory, Report UCRL-52915, 1980.

Walton, O.R., R.L. Braun, R. G. Mallon and D. M. Cervelli, "Particle Dynamics Calculations of Gravity Flows of Inelastic, Frictional Spheres," Micromechanics of Granular Material, Amsterdam, Elsevier Science Publishers, 1988.

CALCULATIONS OF NTS RESIDUAL STRESS MEASUREMENTS AND SOME IMPLICATIONS FOR MODELS AND MATERIAL PROPERTIES

JOHN RAMBO, Lawrence Livermore National Laboratory, P.O. Box 808, Livermore, California 94551; and

NORTON RIMER, S-Cubed, A Division of Maxwell Laboratories, Inc., P.O. Box 1620, La Jolla, California 92038

ABSTRACT

Residual stress measurements have been obtained from several events, in particular LLNL's QUESO and ORKNEY in NTS Area 10, and DNA's HUNTERS TROPHY event in Area 12. These events employed different types of stress gauges to measure radial- and tangential-stress components. The Area 10 events show the development of compressive residual stresses.

For ORKNEY, with a working point in alluvium, just above the alluvium/tuff interface, radial- and tangential-stress gauges were located at 36 and 44 m range, respectively. Since direct comparisons between the two stress measurements are complicated by stress attenuation across the 6 m separation between the two gauges, ground motion calculations were employed to aid in the evaluation of the measurements. The calculated and measured peak-stress attenuations were found to be consistent as were the times of residual stress setup and rebound, also inferred from velocity gauges located further from the working point.

The radial and tangential gauges for QUESO were located in the satellite hole at about the same 22 m range from the working point (1 to 2 cavity radii). Comparison of both stress components showed the failure surface up to about the time of residual stress rebound. Residual stress measurements in the Area 10 material appear to be in qualitative agreement with the calculations.

In contrast, measurements to date of the residual stresses predicted for tunnel events in Area 12 tuff are inconclusive. Stress gauges on HUNTERS TROPHY generally showed a final state of tension. This study discusses the possible influence of material properties differences between the geologic areas.

INTRODUCTION

The question of the existence of residual stress or the reliance on a compressive residual-stress field as a protective mechanism that

prevents the prompt release of radioactive gases is still being debated[1]. It is appropriate to study all or any available residual-stress data since the concept of residual hoop stress is basic to containment science. One of the purposes of the study is to bring available data to the scrutiny of interpretation with calculations. We wish to establish the key observables in the data that imply shear strength (a model parameter that is central to simulations of residual hoop stress). The agreements and differences between data and simulations are intended to emphasize model implications or possibly limitations in the validity of the data. However these data are very sparse because of the rare success in obtaining late time data from gauges that must survive close to the working point.

There are three nuclear events where stress data are recorded for sufficient time duration at locations close enough to the working point to record residual stress before and after rebound. The events we are considering for this part of the study are ORKNEY, QUESO and HUNTERS TROPHY. There are a few other data sets for other events that could eventually be considered, but they have not been identified as having as high a potential for residual-stress field (RSF) information as the events being considered.

For this study the data will be emphasized and preliminary calculations mentioned as they relate to strength models. This is work in progress and future calculational efforts are required to finalize our conclusions.

PURPOSE

The purpose of the paper is to check for consistency between types of residual-stress field measurements and discuss the implications for calculational models.

DATA CONSISTENCY

If complete RSF data recovery was possible for any event, then radial- and hoop-stress, particle-velocity and laboratory-strength measurements would all be available as close to the same radial location as possible. The integration of the particle velocity (double integration of the acceleration) shows the point of maximum displacement of the material around the cavity just prior to rebound (rebound time). A spherical convergent phase follows in which the compressive hoop stress increases as material adjusts into a smaller volume. The expectation is that the hoop stress increases some time after the rebound time as depicted is Figure 1a. A second internal check is that at some locations within three cavity radii, the hoop stress should increase above the radial stress after rebound time. A

third check is to compare the laboratory measured stress difference to the stress difference of the compared waveforms of radial and hoop stress. Calculations indicate that the peak hoop stress and a portion of the stress after the peak are controlled by the shear failure surface, i.e. the maximum allowed stress difference for a given pressure. Thus the pre-event laboratory strength measurement should be in general agreement with the difference in the hoop- and radial-stress measurement as shown in Figure 1b. This will be more true in the earlier part of the wave before the in-situ material is damaged significantly by ground motion.

MODEL IMPLICATIONS

Assuming, again, that all residual-stress data are from the same location, some portions of a strength model could be implied from the radial- and hoop-stress measurements (Figure 2a). A calculation using the strength model would provide a cross check to the model by comparing the calculation to other measured data such as the measured rebound time (Figure 2b), the rebound distance (Figure 2c), and the final value of hoop stress (Figure 2d). Each of these is sensitive to the strength model that is used. Ultimately, on further iterations, we could attempt a single strength model, likely with a damage component, that is consistent with all the residual-stress data (Figure 2e).

LIMITATIONS

The available data are sketchy at best. In some cases the radial- and hoop-stress data are not at the same radial locations, there are no particle velocity data at other stress data locations and some data may have been recorded for locations outside the residual-stress field. Gauge inclusion effects have not been considered. There is no overburden stress on the stress gauge prior to the stress arrival. Overburden may be sensed some time after the initial stress arrival. There may be errors in the proper functioning of the instrument or recording. However, we have given the benefit of the doubt to the data to explore possible implications for models.

This is work in progress and thus far we have performed scoping calculations primarily to test that reasonable models provide results similar to the recorded data.

EVENT PARAMETERS COMPARED

Table I shows a comparison of event parameters between ORKNEY, QUESO, and HUNTERS TROPHY. Selected parameters are chosen for relevance to calculations and the data. There are similarities between ORKNEY[2] and QUESO[3] in that they were fired in porous alluvium that is granular in nature. HUNTERS TROPHY was fired in a nearly saturated tuff which is likely stronger than the alluvium and is faulted.

For each event there are calculational difficulties. The gauges on ORKNEY were located in the gypsum aggregate plug in the stemming column. This geometry required 2-D KDYNA[4] calculations to properly model the stemming column and surrounding alluvium. The working point region on QUESO contained a slump of material that extended from the work point upward 9 m prior to backfilling the hole (Figure 3). The process of backfilling the hole may have have left a void near the top of the original void[5]. Although this is a 2-D setting, 1-D[6] scoping calculations were used to simulate sand backfill and surrounding alluvium for gauges located in the satellite hole. However, future attempts to model the hoop-stress measurement in the emplacement hole will require a 2-D simulation. On HUNTERS TROPHY block motion may be in evidence near the gauge locations and finite difference continuum calculations do not handle this phenomena.

Post event radiation measurements on ORKNEY were excellent. Only a trace of radiation occurred after ten hours above the lowest plug where the residual-stress gauges were located. The bottom of the plug was challenged with radiation and pressure. No collapse occurred above the bottom of the plug, and most of the residual stress instruments in the plug survived until they eventually were turned off[7]. Radiation occurred in the stemming column on QUESO after a subsurface collapse at 20 minutes. Radiation arrival occurred at about 1 hour[8]. Radiation was expected and observed in the stemming on HUNTERS TROPHY[9].

ORKNEY

Figure 4 shows the ORKNEY configuration for gauges located in the exploratory hole (UE10 ITS #5) and the emplacement hole (U10be). Hole UE10 ITS #5 is located about 15.2 m from U10be. The radial-stress record in the exploratory hole displayed data to a time just past the peak as shown in Figure 5a. Figure 5b shows the integrated accelerometer data with a rebound time of 0.103 s. These gauges

were located in a ground matching grout of about 6.4 MPa unconfined compressive strength[10] in a 0.22 m diameter hole. Since the diameter is small and the strength is low, the gauge response may be mostly from the free field. These data have not yet been incorporated into the calculational study analysis.

The locations of radial-, and hoop-stress gauges and accelerometers in the lowest gypsum aggregate plug in U10be are shown in Figure 4. The Sandia gauges include a ytterbium (Yb) element for radial-stress measurement and an accelerometer in the same gauge housing[11]. They were located closest to the bottom (33 m range) and top (45 m Range) of the plug and the record from each gauge are shown in Figures 6a and 6b, respectively. Between these two are two experimental torpedo gauges fabricated by Dynasen: a radial-stress gauge at 38 m range and a hoop-stress gauge at 44 m range[12]; the stresses from these gauges are shown in Figure 6c. They used a fluid cavity with a stress sensing element oriented perpendicular to the stress component of interest. Unfortunately these two gauges were not at the same range, so that a stress difference comparison was not directly available for the torpedo gauges. The strength of the gypsum aggregate cement is known, and an estimate of the in-situ strength of the cement near the gauges can be made by comparing the hoop and an estimate of the tangential stress at the same location as shown in Figure 7a. Since the peak particle velocity versus range tends to be linear in log-log coordinates, the peak value of radial stress at 44 m can be estimated from the value at 38 m assuming a linear attenuation based on the site simulation of peak radial stress. The difference between the projected peak radial stress and the measured peak hoop is about 27 MPa. An alternate way of estimating the strength uses the radial-stress measurement from the Sandia radial-stress gauge, which was only about a meter above the Dynasen hoop-stress gauge. The difference between the line connecting the two Sandia radial-stress measurements and the hoop-stress measurement is about 16 MPa. Although we think it is more appropriate to compare the torpedo gauges with each other, the Sandia-Dynasen comparison provides a lower limit. Figure 7b shows that the two estimates span the strength measurement for gypsum aggregate cement. The confining pressure at the time of peak stress is between 27 and 40 MPa depending on the value of radial stress and the possible addition of overburden during the shock passage. The gypsum aggregate strength is flat above 20 MPa confining pressure (Pm), and the static strength is within the limits of the dynamic measurement.

The rebound time can be observed from velocity gauges and the hoop-stress gauge. The maximum outward extent of displacement occurs where the velocity trace is zero and precedes the negative velocity and displacement of rebound. A hoop-stress increase is observed at or shortly after this time in calculations as the material contracts in the rebound phase. What we observe in Figures 8a, 8b, and 8c seems to refute our expectations. Figures 8a and 8c represent velocity gauges below and above the hoop-stress gauge in the plug. The rebound times are 0.125 and 0.132 s, respectively. However, the rebound time of the hoop stress appears to occur about 0.084 s, a time much earlier than the motion would indicate. The rebound time from the velocity gauge located at 40 m in the satellite hole is also later (0.103 s) and may be more indicative of the surrounding alluvium at that location. The strengths estimated from the rebound times[13] are about 40 MPa for the hoop-stress gauge and about 20 MPa from the particle velocity gauges in the plug. The value of 40 MPa appears high for both the alluvium and the gypsum concrete. The value of 20 MPa is a reasonable average strength value for both the plug and the alluvium. Figures 9a and 9b show unconfined compressive strength values of indurated and non-indurated surface alluvium taken at the AGRINI site, U2ev[14]. The value of 20 MPa is high but not unusual compared to this data set. The tests of failed material do not show severe weakening of the alluvium as well.

1-D simulations used the measured static-strength properties of the plug to assess the importance of the stress path on the apparent rebound time of the hoop-stress gauge. Further 2-D simulations were run with alluvium strengths of 20 and 40 MPa to assess the late time stress and rebound phenomena of the plug due to the surrounding alluvium.

Two simulations showed that the damage surface upon unloading controlled the unloading of the hoop stress. A 40 MPa strength model is shown in Figures 10a and 10b. This high strength model was based on the apparent rebound time at 0.08 s. Figure 10a shows the loading path to the right of the tension line. As the radial divergence increases near the peak, the hoop stress decreases abruptly to the tension line where the hoop stress is zero. This is observed in time in Figure 10b and shows the hoop stress dropping to zero (tension) immediately following the peak at 0.044 s and is very different from the measured stress following the peak in Figure 10a. The high strength model was replaced with 20 MPa alluvium and a model of the plug. The 1-D simulation modeled the length of the plug and

material strength of the concrete. A simple damage model was used, and the shear failure surfaces are shown in Figure 10c. The failure model and the damage surface prevent the hoop stress from going into tension as in Figure 10a and 10c. A brief hoop-stress increase is seen at about 0.06 to 0.07 s. The hoop-stress increase appears independent of the radial velocity rebound that takes place at about 0.100 s in the calculation. Agreement between the simulated and measured hoop stress was reasonable (Figures 10d and 10e) until the strong increase in hoop stress occurs at 0.08 s in the data. The simulation showed accumulated shear strains reached values of 12 to 17%. This amount is sufficient to cause damage, but it is not known what type of damage strength model is appropriate. Further work might resolve failure models that simulate better agreement. The value of the simulations was to show there can be independence between the rebound times of velocity and hoop stress and that the damage model has a dominant influence.

Observation of the late time stresses are important to assess the decay time of the residual-stress field. It is useful to know how long cavity gases may be prevented from quickly seeping into the stemming column or other undesirable locations. Carl Smith of Sandia National Laboratory had the foresight to view the radial-stress data out to late times. Although the data were recorded to much later times, his radial-stress data are shown out to 500 s[11] in Figures 11a and 11c. The gauge at 36 m range shows a radial-stress decay to about 1 MPa compared to about 4 MPa at the 45 m range. Until this report the Dynasen stress data has not been viewed out to late time; these data are shown in Figure 11b located in a relative position between Figures 11a and 11c that is in the same position sequence as the gauges in the plug. The Dynasen radial-stress gauge at 38 m shows a more rapid decay than the Sandia gauge at 36 m. There are many sources of gauge error and media inhomogeneities that would cause differences and either or both gauges could be correct.

From a computer modeling viewpoint the hoop-stress measurement was classical. To our knowledge no other hoop-stress gauge has ever recorded a nearly static hoop stress out to times of 500 s. Following the peak hoop stress the decay is only about 1.5 to 2.0 MPa. This sort of decay, or lack of, is similar to stress conditions predicted by simulations. Simulations usually show a hoop-stress build up following the rebound which stays relatively static through the termination of the simulation at about 1 to 2 s. They, however, ignore slow mechanisms such as creep and stress relaxation observed at late time.

Two 2-D simulations were run to look at late time stresses. As mentioned earlier the alluvium shear strengths used were 20 and 40 MPa. Figures 12a and 12b show comparisons of the radial and hoop stress, respectively, through the plug for both simulations. Although there is significant variation in calculated post-rebound stress through the plug, the simulated hoop stress is not unreasonable compared to the measured value of about 12.5 MPa at a matching time of 1.0 s. Unexpectedly, the high-strength alluvium resulted in better agreement. We emphasize that these are only preliminary simulations to see if the data were in reasonable agreement to simulations, and we make the judgement that further simulation work would probably bring better agreements or understanding without unusual modifications to material models.

QUESO

The instrumentation on QUESO, U10bf, was somewhat different than ORKNEY. The gauge locations are schematically shown in Figure 13. Two flat-pack stress gauges, oriented hoop and radial, were located in the satellite hole, UE10bf, at 22 m range from the emplacement hole working point. These gauges were in a small diameter hole, 0.305 m, and were located as near to a simultaneous range as possible. The Waterways Experiment Station (WES) ground matching grout in the satellite hole has 6.4 MPa unconfined compressive strength[10]. Three other particle velocity (uv) and accelerometer (av) gauges were located some distance above the stress gauges. The emplacement hole data came from one surviving hoop-stress gauge also at 22 m range, but located in a very different material of LLNL stemming mix. This material is dry and likely more porous than the surrounding alluvium. The gauge was a Dynasen ytterbium-carbon composite and a different type from the satellite hole flat-packs.

Figure 14a shows an overplot of the flat-pack hoop and radial stresses versus time. The hoop stress appears initially below the radial, and the difference increases until the peak stresses occur at about 0.018 s. This corresponds to the spike that is observed above 30 MPa in Figure 14b. Figure 14c shows a plot of stress difference plotted versus mean stress. The initial rise shows a relatively linear relationship between stress difference and mean stress which reaches about 40 MPa. If uniaxial strain is assumed, a Poissons ratio of 0.16 is estimated. The stress difference appears unusually high for alluvium at 40 MPa and the Poissons ratio of 0.16 is also representative of stiff material as well. We do not know if this portion of the data is believable or is some function of gauge

response. Both gauges are subject to fast rise times during this excursion and we do not know if minor positional errors could have influenced the stress difference. Is it possible that material under high strain rate appears stronger? If there were a broader experience base with the flat-packs, it would be easier to assess errors in the rise times. The stress difference immediately following the peak drops to about zero and gradually increases to about 20 MPa by 0.03 s. 1-D simulations of the flat-pack location indicate the stress difference is on the failure surface along the back side of the stress pulse. This part of the data is less susceptible to the gauge dynamics and is more believable. Figure 14c shows the data tracing out what we believe to be part of the failure envelope as the stress difference decreases below 20 MPa. Below 10 MPa, the material may no longer be on the failure surface, that is, the stress difference may be controlled more by the dynamics of the ground motion. Figure 14a shows the hoop-stress rebound time appears to be about 0.06 s but there are no velocity gauges at the same location to further analyse the observation, as there was on ORKNEY. The hoop stress crosses above the radial stress at about 0.07 s and remains at about 5 MPa above this value at later times.

Our preliminary 1-D simulations showed a reasonable agreement to the radial-stress peak. The simulation used a strength model similar to the failure path traced out by the data below 20 MPa in Figure 14c. The stress difference versus time in the calculation was in reasonable agreement to the data below 20 MPa. The rebound time in the calculations depended on variations of the strength model implied by the data. However, agreement between data rebound time and our preliminary simulations could be obtained from reasonable strength model variations. We overpredicted the final hoop stress by about 5 MPa. The calculation showed 10 MPa compared to 5 MPa measured. The data shown in Figure 14c indicated an initial state of being in tension and appeared physically incorrect. When corrections are made to shift the data, the final hoop stress is more like 10 MPa. This correction is somewhat ad hoc but was considered a reasonable correction by the data specialist[15]. The adjusted data are presented in Figures 15a, 15b, and 15c. Our preliminary 1-D simulations did not capture the apparent high stress difference during the initial rise of the stress or the low stress difference just after the peak.

We did not compare the hoop-stress data from the emplacement hole in the preliminary 1-D study. 2-D simulations for these data might be necessary to capture the response in the stemming surrounded by

alluvium. There was some difficulty in obtaining agreement to the velocity measurements located higher in UE10bf. Some previous work[5] expressed similar difficulties, and 2-D effects are suggested by unusual initial conditions of sloughing around the working point.

HUNTERS TROPHY

Radial stress, hoop stress, and material motions were measured at three locations at about 62, 90 and 106 m range[16] and are shown in Figure 16. These locations were selected based on S-Cubed residual-stress simulations[17] and the avoidance of nearby faults which might subject the measurements to non-radial motions. Each location was instrumented with duplicate sets of ytterbium and pancake stress gauges as well as accelerometers. Two transverse holes were located at each range to provide primary and backup measurements.

Figure 17a shows a plot of all the peak stresses which includes radial-stress locations closer to the working point than the selected hoop-stress locations. The hoop- and radial-stress measurements appear more erratic at lower stress ranges. One peak hoop stress at 63 m is higher than the radial stresses and violates our expectations based on simulations. Reference 16 has a detailed description of all the data and we show one radial and hoop-stress comparison at 62 and 106 m and two comparisons at 90 m range. Comparisons are shown for gauges located in the same transverse hole. Figure 17b is the lower hoop and radial stresses compared at 63 m range. The stress differences vary between about 55 to 65 MPa. This pair shows relatively constent stress difference until the hoop stress reaches zero at 0.03 s and remains. This is a reasonably good indication that area around the gauge has gone into tension. That is, radial trending cracks may have occurred which relieve the hoop stresses. The gauges located at 106 m range (Figure 17c) show constant stress difference of about 9 MPa following the peaks. The hoop-stress gauge goes into tension at about 0.04 s. Two sets of traces from the 90 m gauges are shown in Figures 18a and 18b and exhibit variation that can occur at the same radial range. In Figure 18b the stress difference varies from about 20 to 28 MPa, then appears to drop into tension at about 0.04 s. At later time (0.075 s) the hoop increases above the radial and is followed by stages of hoop equal to radial and radial greater than hoop. Figure 18a shows stress difference that is much less than in Figure 18b. The stress difference is 4.5 MPa at the peak and about zero thereafter except for two hoop-stress excursions above the radial at 0.04 and 0.08 s. The hoop stress appears to go into tension at 0.065 and 0.115 s. The two sets of compared stress

data are very unlike in the peak values and late time character. About the only similarity is the increase in hoop at 0.08 s. These different characteristics may be due to the gauges being in very different strength media that are local to the gauges. There were no laboratory strength measurements made for the specific locations of the residual-stress measurements. However, there are laboratory strength measurements made closer to the working point along the U12n.24 GI-1 hole. Figure 18c shows the suite of TerraTek uniaxial strain tests in which the stress differences span most of the observations of stress difference at the gauges. There is also some evidence of non-radial motions in this area[18], and it may be that block motions may have influence on the late time stresses as well.

The rebound time is taken from the peak displacement shown in Figure 19. They occur for the residual-stress region at times between 0.10 and 0.12 s. The hoop stresses have all reached zero stress before the rebound takes place. This is reminiscent of the observations on ORKNEY and the calculations which implied that higher strengths could cause the hoop stress to drop into tension before rebound occurs.

Two 1-D simulations of HUNTERS TROPHY were performed. One strength model was uniform over the entire range of interest and was used originally to predict the residual stress (Rimer's model 57)[17]. This model showed quite reasonable agreement to peak radial stress (Figure 17a) and very good agreement to peak displacement and rebound time (Figure 19). However the calculated peak hoop stresses are usually much higher than the data and the calculated hoop stress did not go into tension. The close agreement to calculated displacements and rebound time were arrived at using an average strength similar to uniaxial strain curve 6 in Figure 18c. However, some of the stress difference measurements indicate higher strengths similar to curve 3 in Figure 18c. We suspected that most of the gauges were located in a higher strength region and developed a second model which combined the first model with a higher strength beyond 40 m range. We assumed that pre-existing cracks are in the vicinity of the gauges so the higher strength segment of the model has no tensile strength. This model showed closer agreement to peak hoop stresses (Figure 17a), and calculated hoop stresses drop into tension. However there is much poorer agreement to displacement and rebound time (Figure 19). The residual hoop stresses are calculated to exist closer toward the working point for the higher strength model.

One possible interpretation of these two calculations is that the material is like strong blocks surrounded by weakened planes. The weakened planes allow larger radial motions of the material assemblage. Gauges located in the strong blocks would show large stress differences and hoop stresses measured in the stronger blocks would quickly unload due to the greater outward radial motion of the blocks. We have not run this type of model in 2-D and do not know the generic affect on the residual-stress field.

SITE DIFFERENCES AND RESIDUAL-STRESS MEASUREMENTS

There has been a great deal of difficulty obtaining good residual-stress records in the DNA tunnel complex. It was only recently before HUNTERS TROPHY that reliable armored cable survived the stresses near the gauge to late times that included rebound time. Yet, there had been reasonably good results without the special cable each time the residual-stress measurement was attempted on the two vertical shaft events. DNA radial-stress instrumentation survived quite well on ORKNEY, but in their tunnel usage prior to HUNTERS TROPHY, gauge failure was common before the residual-stress rebound time. Although the residual-stress-measurement sampling is not large, it shows a trend. We suspect that the material properties in the high-stress environment have a great deal to do with gauge survival. The tunnel areas usually have low air voids of 1 to 2 %. compared to the higher air voids of the NTS flats and the stress attenuates much less through the nearly saturated residual-stress region. There is further complication in that relatively harder tuffs with faults and joints likely lead to non-radial motions of various sized blocks. Some multiaxis accelerometers for HUNTERS TROPHY and other tunnel events show displacements that are greater in the non-radial directions[18]. In general, the material in the working points of the NTS flats are weaker, more granular and less faulted. The strengths are usually more homogeneous and less likely to produce the block motions observed on the tunnel events. These differences in site properties would favor successful residual-stress measurements in the NTS flats.

The difficulty in observing the residual stress in the tunnel events and the observation of radiation at various locations in the post event tunnel complex have led to serious debate over the presence and necessity of the residual hoop-stress concept. One of the main purposes of this paper is to show that the classical residual hoop stress does exist in a dryer and in a strengthwise more homogeneous setting. Although the residual hoop stress may not be robust in the

tunnel setting, it is likely present in a number of locations and its presence has been confirmed by experimental post-shot hydrofracture measurements. Although we welcome criticism of the concepts, we believe that it would be a mistake to abandon the residual-stress concept that is useful in simulations and the resulting containment analysis. There have been simulations, such as BANEBERRY[19] and BARNWELL[20], that have been successfully used to associate a calculated poor residual hoop stress to the observed post-event radiation. We believe that 1-D and 2-D simulations can be used as a tool that in some situations could help to identify unsafe containment. Until better calculational tools, such as 3-D finite difference, 3-D finite element or distinct element modeling[21], have been successfully adapted to containment applications, the 1-D and 2-D simulations can still provide insights into containment phenomena. They can still be particularly useful in simulating sites with relatively homogeneous layers.

SUMMARY

After reviewing the available residual hoop-stress data with some preliminary simulations, can a case be made for the residual hoop-stress concept?

The ORKNEY data showed a good case for residual hoop stress in the emplacement plug. The hoop-stress data remained high out to late times while the nearby radial stresses decayed. This is the classical expectation of a stable residual-stress field[19,22] and is the only very late-time residual-stress measurements that we know of. There was some validation of the hoop-stress data in that the estimated stress difference is similar to the strength of the plug material around the gauges.

The QUESO data showed some features that are typical of residual-stress simulations. We observed the crossover of the hoop stress above the radial stress which is similar to those observed in calculations. The dynamic stress difference versus pressure data was used for the strength model in the simulations which in turn gave reasonable agreement with some of the data. The agreement between the calculated final stress state and the data after the data were shifted to remove the initial tensile state was reasonably good.

The residual hoop stress on HUNTERS TROPHY was not observed. However there is sufficient data to imply a different strength model that would show similar calculated hoop stress to the data. The implication is that the data region quickly went into tension and

relieved the stress state. Simulations indicate that a residual hoop stress would be located closer to the working point.

Initially, we considered the question of achieving agreement with all the data from one event. Where there are very uniform media, this may be a possibility. However, the geologic mediums we deal with have variations in properties that can give very different answers. There are the global response measurements such as velocity rebound time and rebound distance that are sensitive to an average strength of the medium and an average damage model close to the working point. At the other extreme are the measurements that are sensitive to the local response of the medium around the measuring instrument. The hoop stress and stress-difference measurements appear very dependent on the local strength near the gauge. It is not an easy task to combine global and local strength models into a single calculation.

Some areas of the initial modeling we did poorly. The rebound distance was usually underestimated by the calculations. The rebound distance can influence the velocity waveform as far away as the ground surface. There is a sensitivity of rebound distance to the damage model that is used in the cavity region and a completely different model may be needed farther from the cavity. It is very difficult to capture the nuances of damage with range from the energy source. However, reference 17 discusses one possible computational algorithm for doing this and we continue to search for the correct model input data. Further calculations to compare to the QUESO data would be useful but might also require 2-D simulations due to the complexity of the stemming and sloughing around the working point. Ideally, a future event in relatively uniform media with hoop-stress, radial-stress, and velocity measurements at many radial locations would be useful to study damage versus range in the free field.

Most of the data observations were within reasonable modeling capabilities of calculations. Exceptions are the high-strength, low-strength response near the peak of the velocity on the QUESO data, the rebound distance, and the gauge showing hoop stress greater than radial stress on HUNTERS TROPHY. We express the caveats that we may not be able to model all observables within the same calculation and there are not enough residual-stress data for generic models to be developed. The data explored thus far suggest that the residual-stress concept is not a remote calculational concept, but that there is evidence of its reality.

ACKNOWLEDGEMENTS

We wish to acknowledge the work of Carl Smith from Sandia National Laboratory for providing stress data on ORKNEY and HUNTERS TROPHY and for useful discussions on the subject. We thank Ted Stubbs from EG&G for providing QUESO and ORKNEY data processing. We are indebted to the EG&G policy of maintaining data archives that could retrieve and process the ORKNEY hoop-stress data out to late times. We acknowledge Cliff Olsen for his comments in reviewing this paper. We thank John Mercier for obtaining strength data for satellite hole grouts for QUESO and ORKNEY.

REFERENCES

1. R. E. Duff, "Thoughts about Containment", 7th Symposium on Containment of Underground Nuclear Explosions", September 13-17, 1993, Auditorium: Boeing Space Center East, Kent, Washington.

2. N. W. Howard, "U10be Site Characteristics Report," Lawrence Livermore National Laboratory, Livermore, California, Internal Report, CP-83-107, November 3, 1983.

3. N. W. Howard, "U10bf Site Characteristics Report," Lawrence Livermore National Laboratory, Livermore, California, Internal Report, DM-82-20, March 17, 1982

4. J. L. Levatin, A. V. Attia, and J. O. Hallquist, "KDYNA USER'S MANUAL", Lawrence Livermore National Laboratory, Livermore, California, UCRL-ID-106104, 1990.

5. S. R. Taylor, J. T. Rambo, and R. P. Swift, "Near-Source Effects on Regional Seismograms: An Analysis of the NTS Explosions Pera and Queso", Bulletin of the Seismological Society of America, Vol. 81, No. 6, pp 2371-2394, December 1991.

6. J. F. Schatz, "SOC73, A One-Dimensional Wave Propagation Code for Rock Media", Lawrence Livermore National Laboratory, Livermore, California, UCRL-51689, Nov., 1974.

7. B. C. Hudson, Lawrence Livermore National Laboratory, Livermore, California, Private Communication, 1992.

8. H. D. Glenn, T. F. Stubbs, J. A. Kalinowski, and E. C. Woodward, Containment Analysis for the QUESO Nuclear Event", Lawrence Livermore National Laboratory, UCRL-89410, August, 1983.

9. B. Ristvet, Defense Nuclear Agency, Albuquerque, New Mexico, Private Communication, 1993.

10. J. Mercier, Lawrence Livermore National Laboratory, Livermore, California, Private Communication, 1993.

11. C. W. Smith, "Orkney Document", Albuquerque, New Mexico, Sandia National Laboratory, Internal Report, 7112, September 5, 1984.

12. J. A. Charest, "Field Stress Measurements", Dynasen, Inc., Goletz, California, Internal Report, 1984.

13. R. W. Terhune, and H. D. Glenn, "Estimated Shear Strength of Earth Media at Nevada Test Site", Lawrence Livermore National Laboratory, Livermore, California, UCRL-52358, 1977.

14. B. C. Hudson, J. T. Rambo, J. L. Wagoner, and W. E. Lowry, "AGRINI Post-Shot Containment Report", Third Symposium on Containment of Underground Nuclear Explosions, CONF-850953-VOL1, Idaho Operations Office of the DOE, Idaho Falls, Idaho, September 9-13, 1985.

15. T. Stubbs, EG&G Inc., San Ramon, California, Private Communication, 1993.

16. C. W. Smith, and R. E. Peppers, "Residual Stress and Motion Fields (U), Experiments 0441, 0442, 0443, 0451, 0452, 0453, 0461, 0462, 0463, 0471, 0472, 0473, 0481, 0482, 0483, 0491, 0492, and 0493", Sandia National Laboratory, Albuquerque, New Mexico, Internal Report, 1993.

17. N. Rimer, and W. Proffer, "Containment Phenomenology Using a New Shear-Strain-Based Computational Model for Tuff", 6th Symposium on Containment of Underground Nuclear Explosions, CONF-9109114-VOL1, Lawlor Events Center, University of Nevada, Reno, Nevada, September 24-27, 1991.

18. C. W. Smith, Sandia National Laboratory, Albuquerque, New Mexico, Private Communication, 1993.

19. R. W. Terhune, H. D. Glenn, D. E. Burton, H. L. McKague, and J. T. Rambo, "Calculational Examination of the BANEBERRY Event", Lawrence Livermore National Laboratory, Livermore, California, UCRL-52365, December 5, 1977.

20. J. T. Rambo and W. C. Moss, "BARNWELL Residual Stress Simulations", 6th Symposium on Containment of Underground Nuclear Explosions, CONF-9109114-ABS, Lawlor Events Center, University of Nevada, Reno, Nevada, September 24-27, 1991.

21. W. J. Proffer and E. J. Halda, "Distinct Element Modeling of Late-Time Containment Phenomena", 7th Symposium on Containment of Underground Nuclear Explosions", September 13-17, 1993, Auditorium: Boeing Space Center East, Kent, Washington.

22. N. Rimer, "The Relationship Between Material Properties, Residual Stresses, and Cavity Radius Due to a Nuclear Explosion", Systems Science and Software, Rept. SSS-R-76-2907, May, 1976.

*Work performed under the auspices of the U. S. Department of Energy by the Lawrence Livermore National Laboratory under contract number W-7405-ENG-48.

TABLE I

COMPARISONS OF EVENT PARAMETERS

	ORKNEY	QUESO	HUNTERS TROPHY
SPONSOR	LLNL	LLNL	DNA
AREA	10be[b]	10bf[b]	12n.24
YIELD	Low	Low	Low
DOB	210 m	216 m	385 m
MEDIUM	Alluvium[b]	Alluvium[b]	Wet Tuff
DENSITY	2.02 Mg/m^3	1.60 Mg/m^3[a]	1.94 Mg/m^3
TOTAL POROSITY	30 Vol %	45 Vol %[a]	36 Vol %
GAS POROSITY	12 Vol %[b]	23.1 Vol %[a,b]	1 Vol %
MEAS. STRENGTH	Yes (In Lower Plug)	No	Yes (WP Region)
MATERIAL CHAR.	Granular[b]	Granular[b]	Higher Str., Faulted
OVERBURDEN	4.3 MPa	4.5 MPa	6.9 MPa
CALC.. PROBLEM	Hoop to Radial Separation, Gauges in Plug	Above Slough	Block Motion
STEMMING RAD.	Trace	Yes	Yes

a includes low density slough region

b Significant differences from HUNTERS TROPHY

Data Consistency

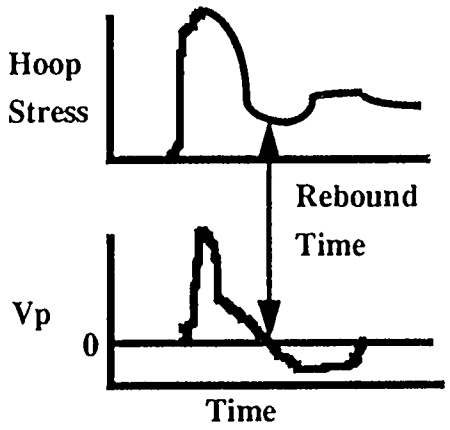


Figure 1a

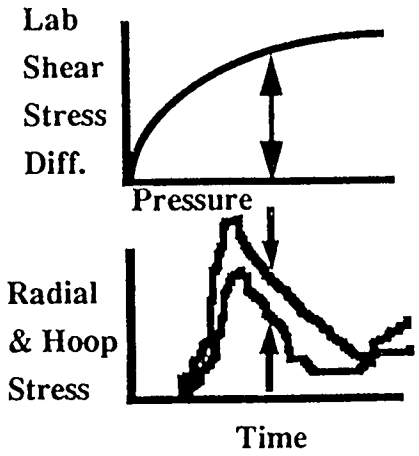


Figure 1b

Constructing a Strength Model Consistent with All the RSF Data

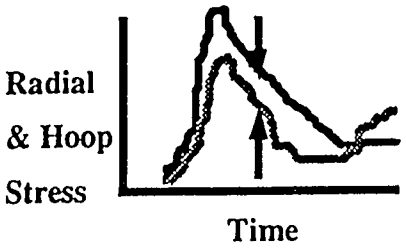


Figure 2a

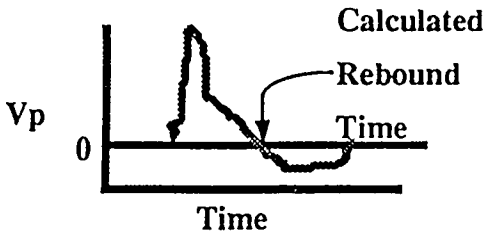


Figure 2b

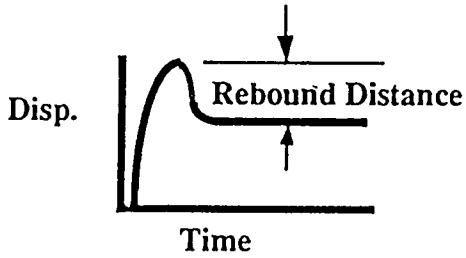


Figure 2c

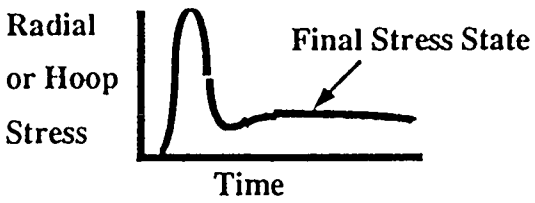


Figure 2d

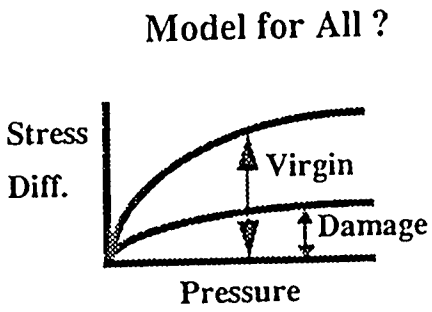


Figure 2e

QUESO Slough Region

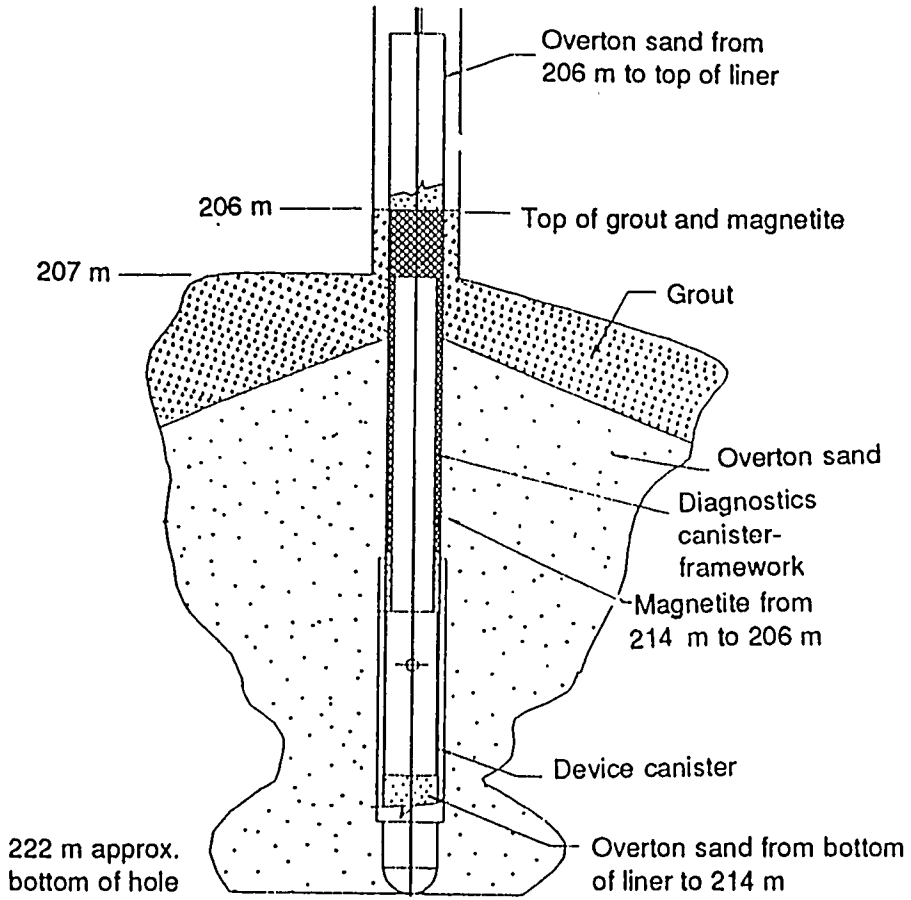


Figure 3

ORKNEY Gauge Location Schematic

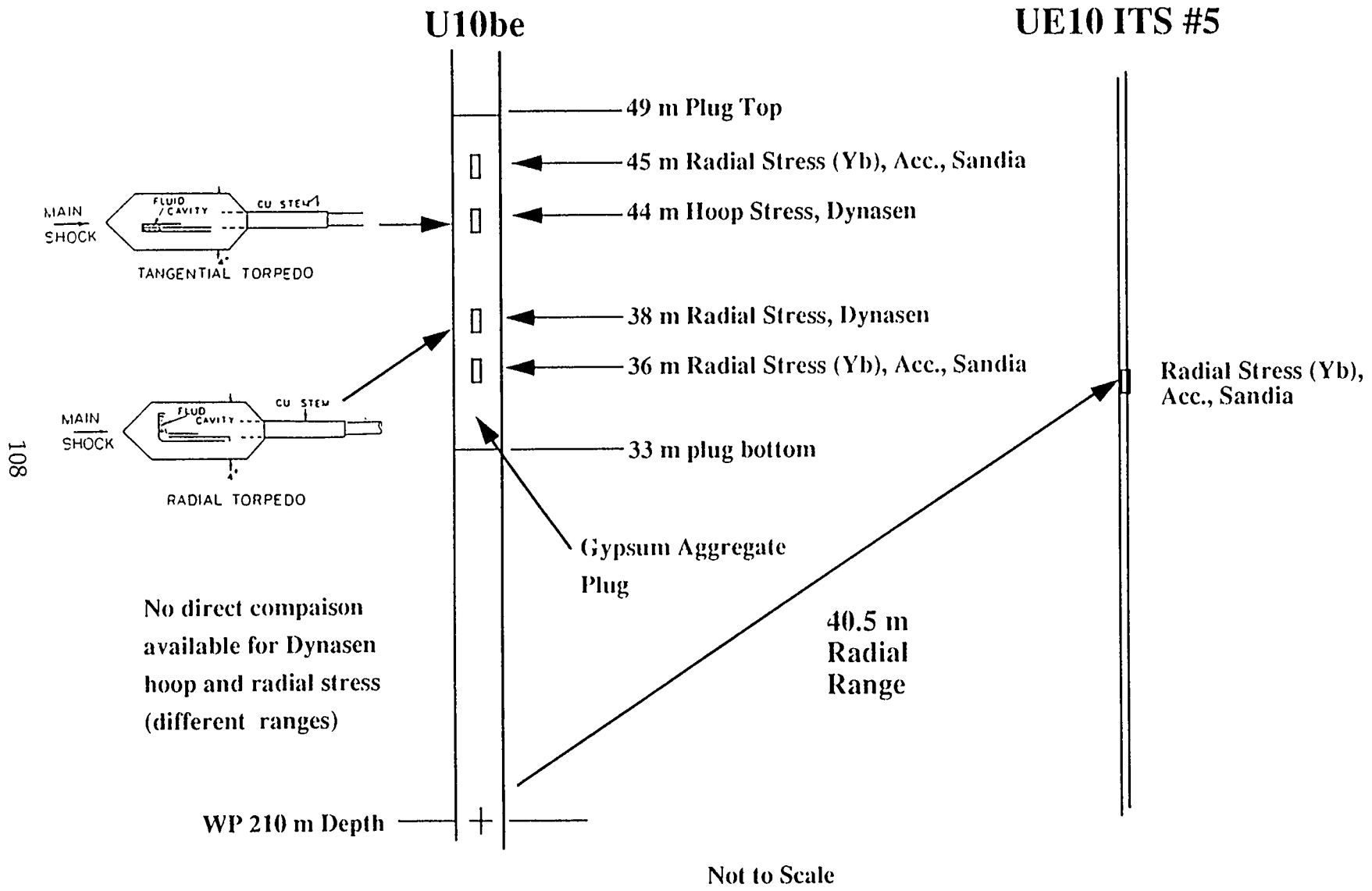


Figure 4

ORKNEY Satellite Hole Radial stress and Radial Particle Velocity

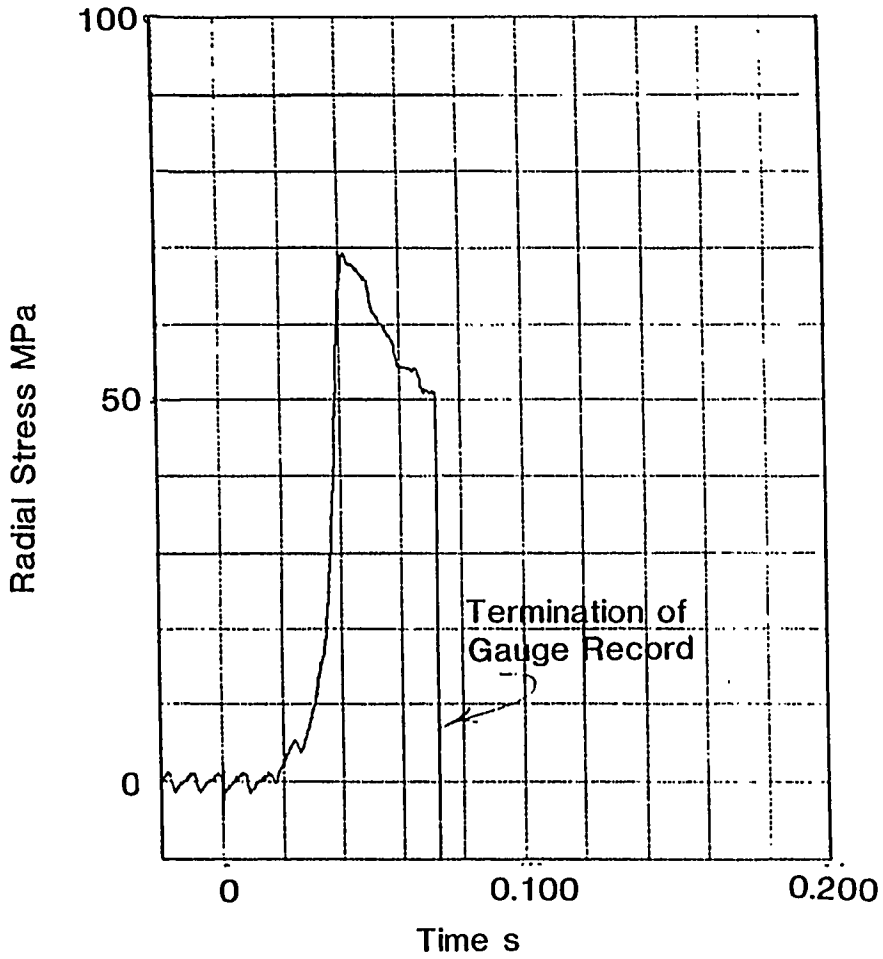


Figure 5a

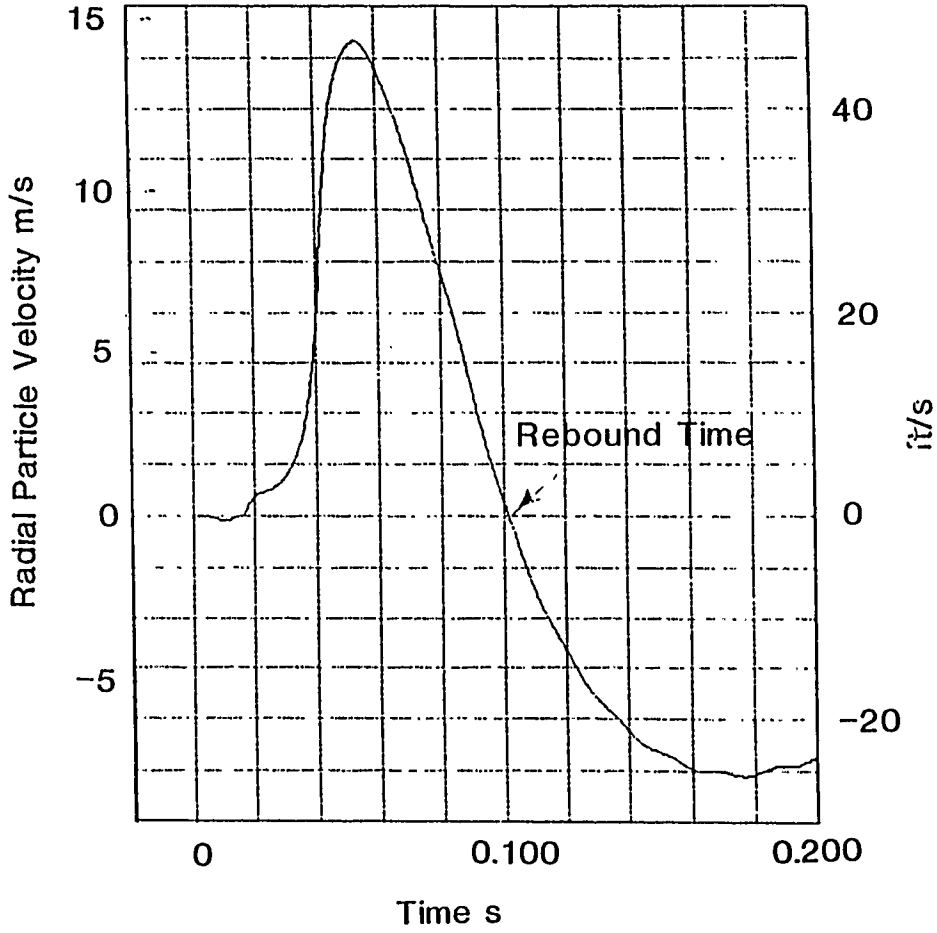


Figure 5b

ORKNEY Emplacement Hole Stresses in the Plug

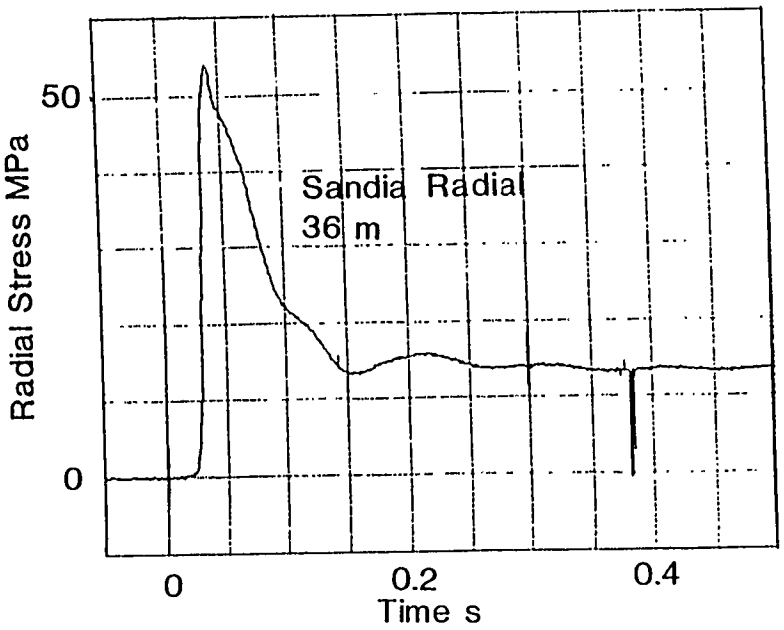


Figure 6a

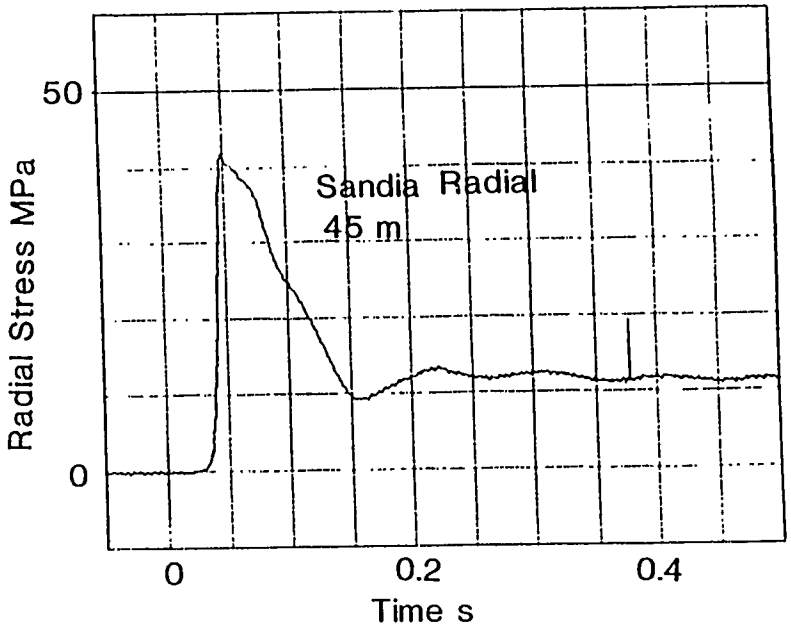


Figure 6b

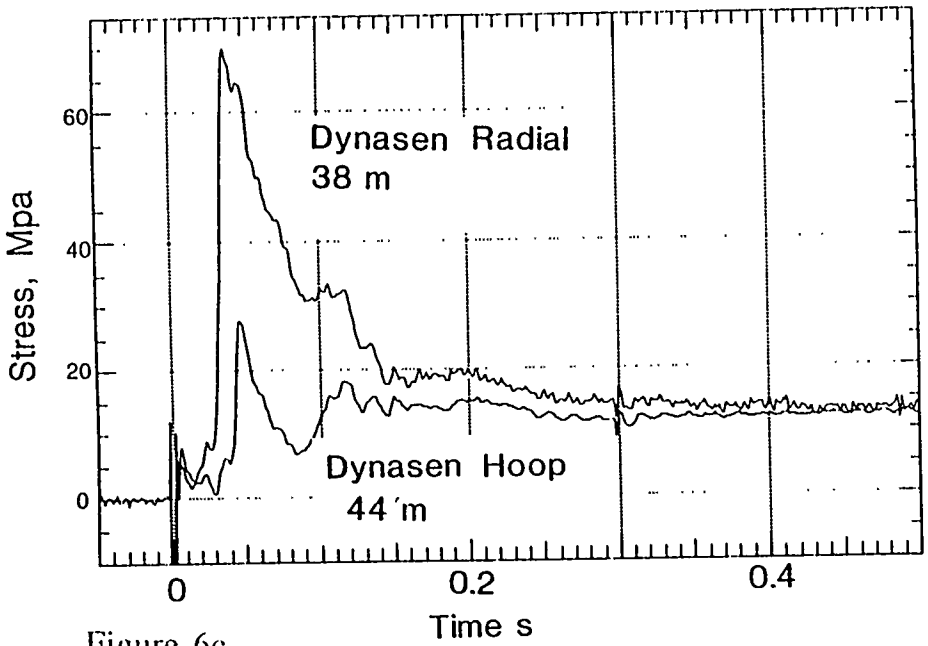


Figure 6c

Method of Comparison Between Laboratory Shear Strength and Dynamic Measurements

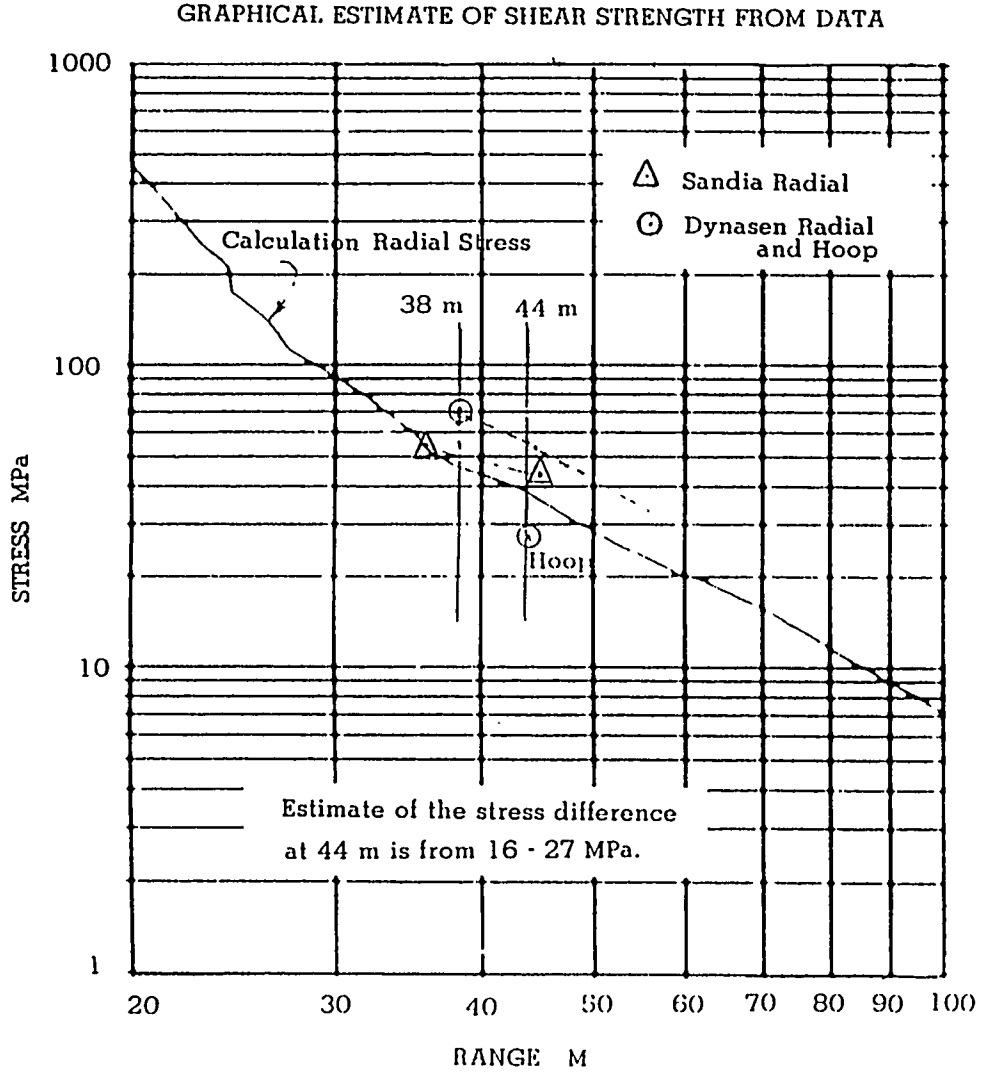


Figure 7a

Gypsum Aggregate Strength Compared to Estimate of Dynamic Measurements

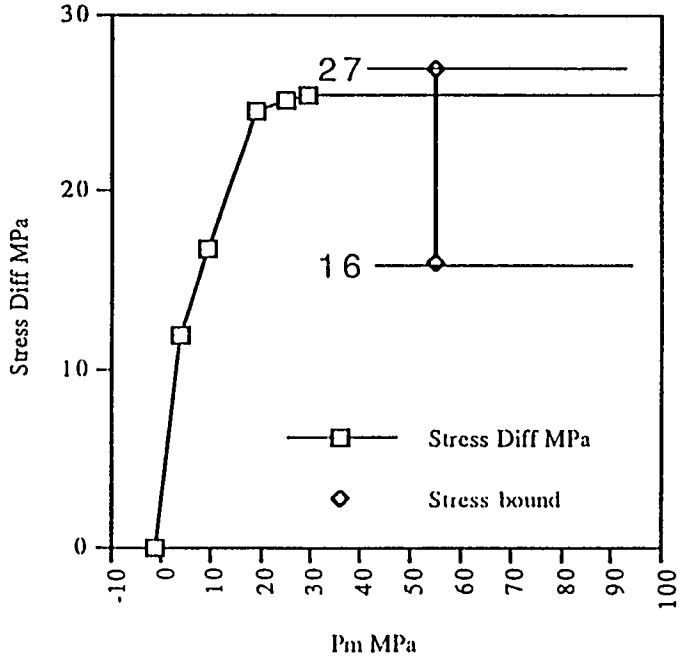


Figure 7b

Comparison of Plug Rebound Times

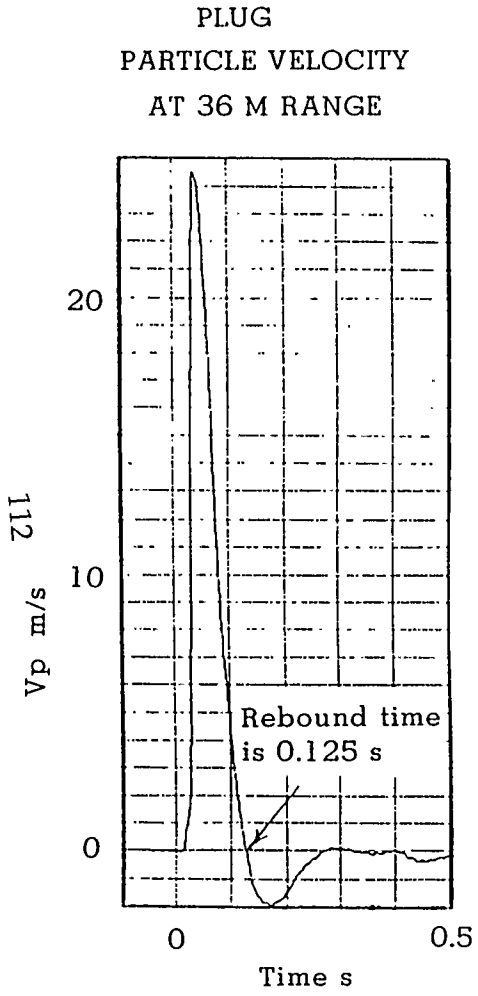


Figure 8a

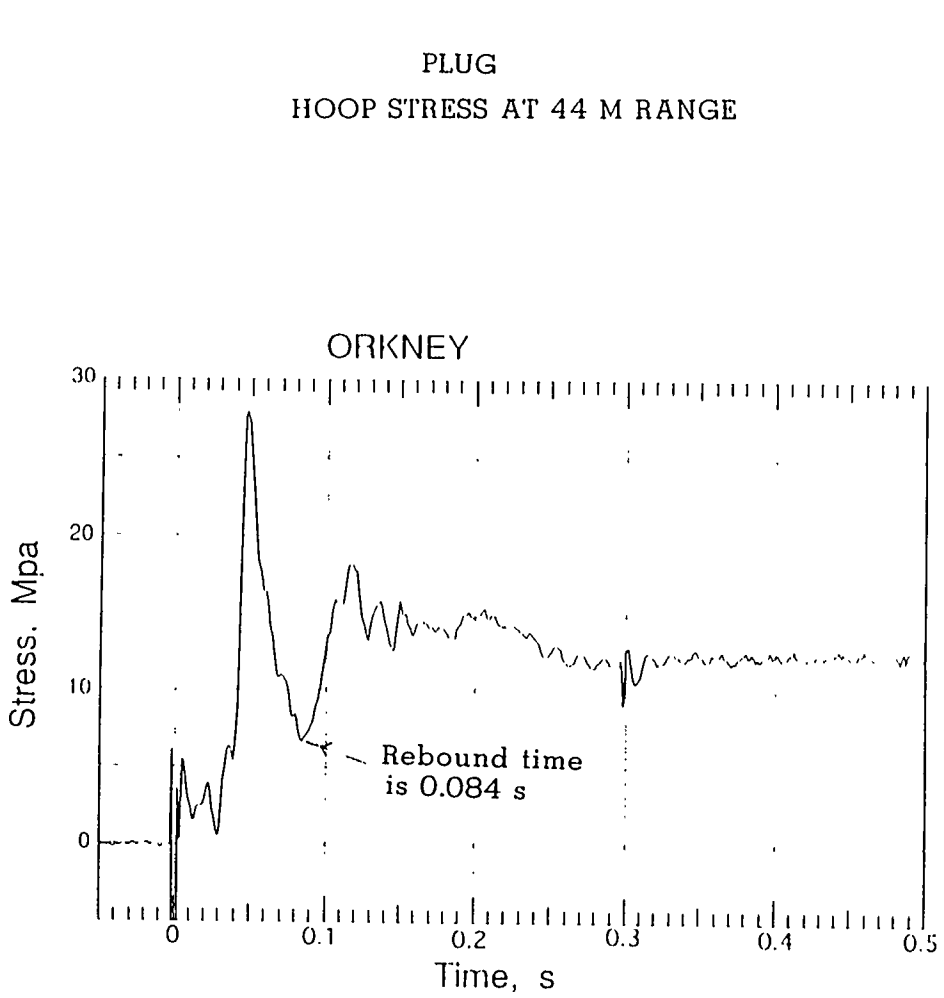


Figure 8b

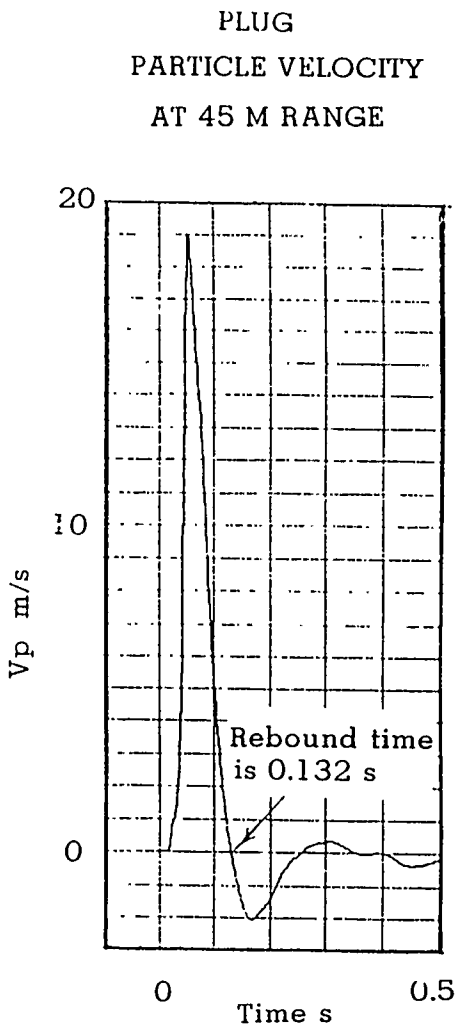


Figure 8c

Unconfined Compressive Strengths of U2ev Near Surface Alluvium

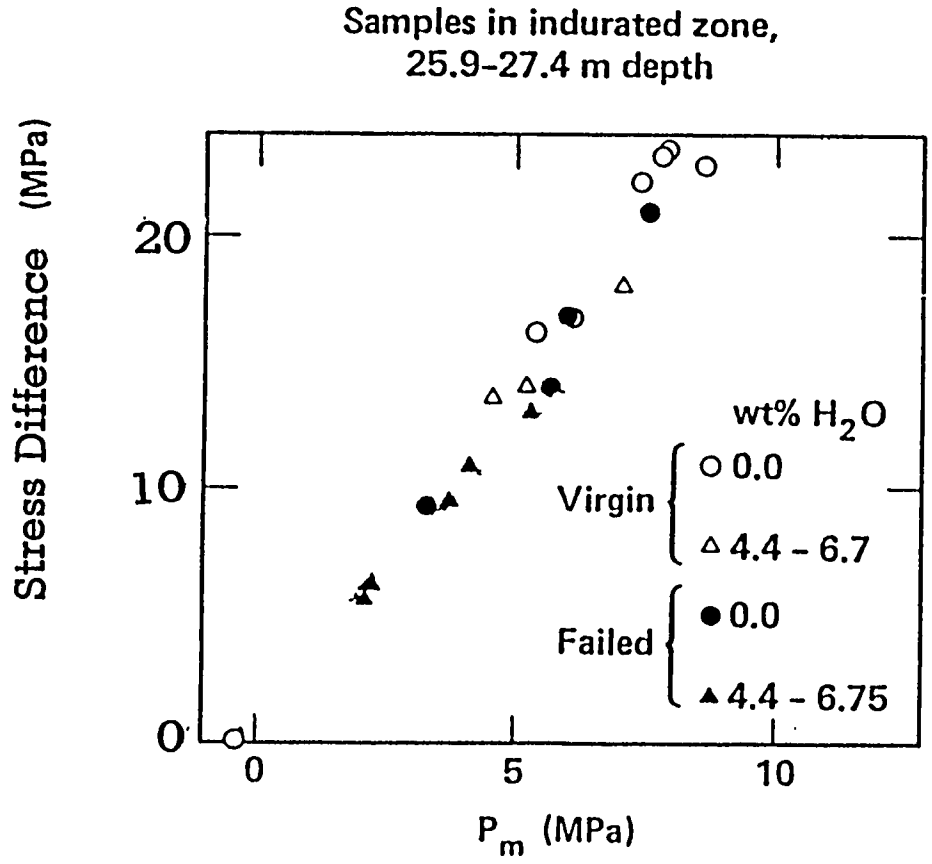


Figure 9a

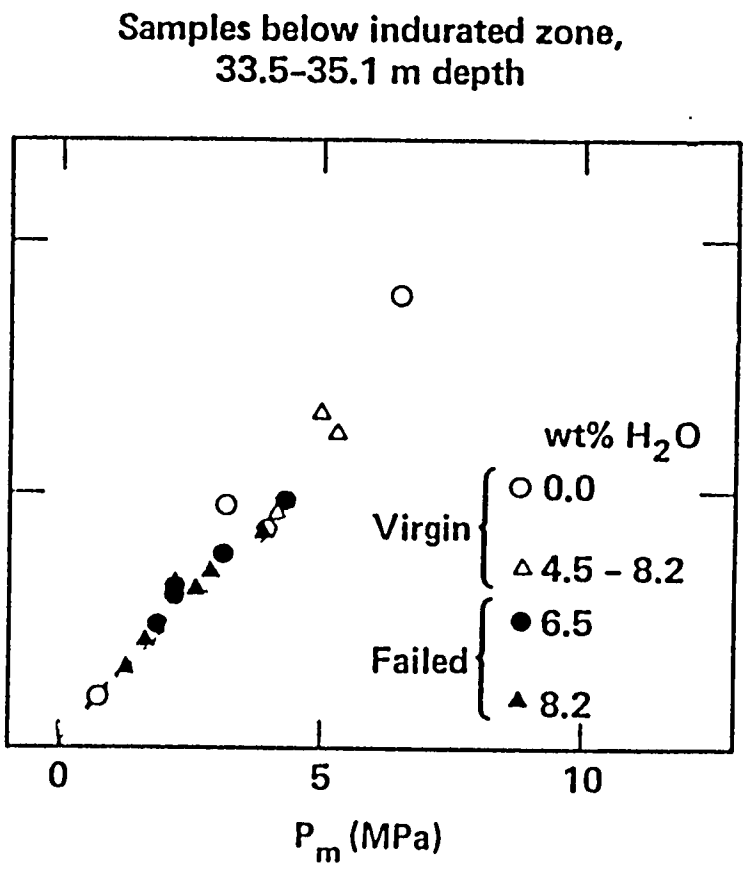


Figure 9b

Stress Rebound Sensitivity to Shear Strength and Damage Model

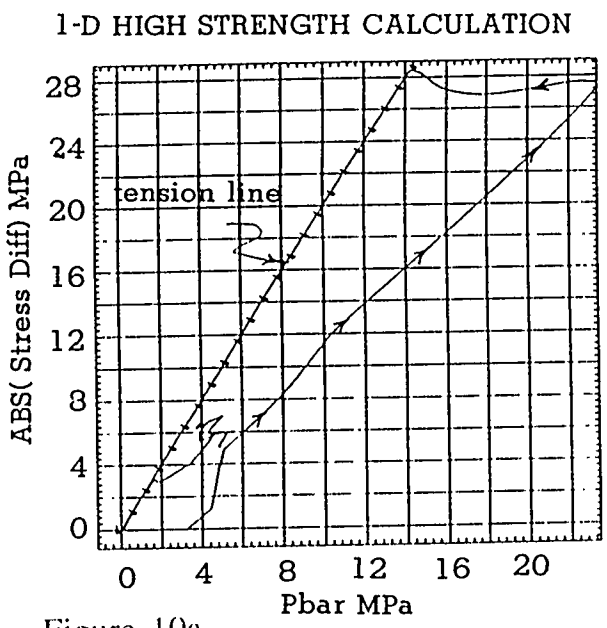


Figure 10a

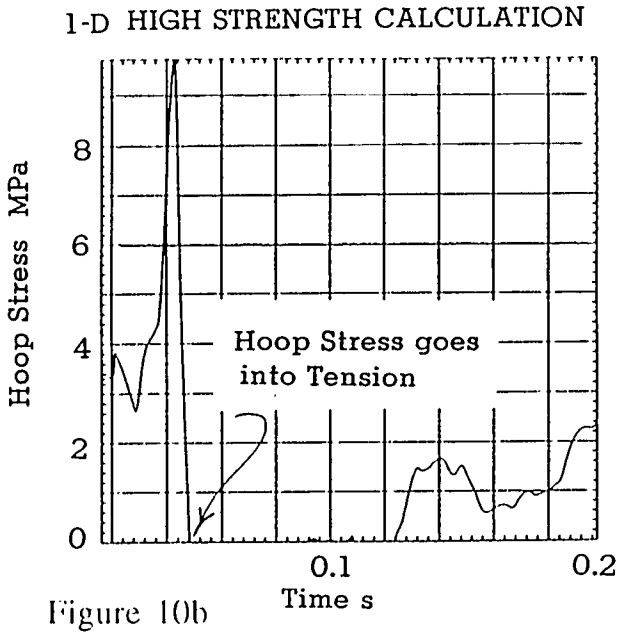


Figure 10b

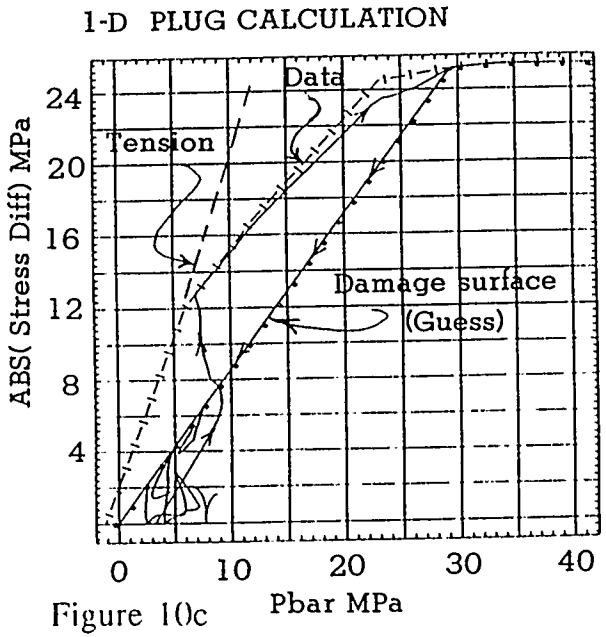


Figure 10c

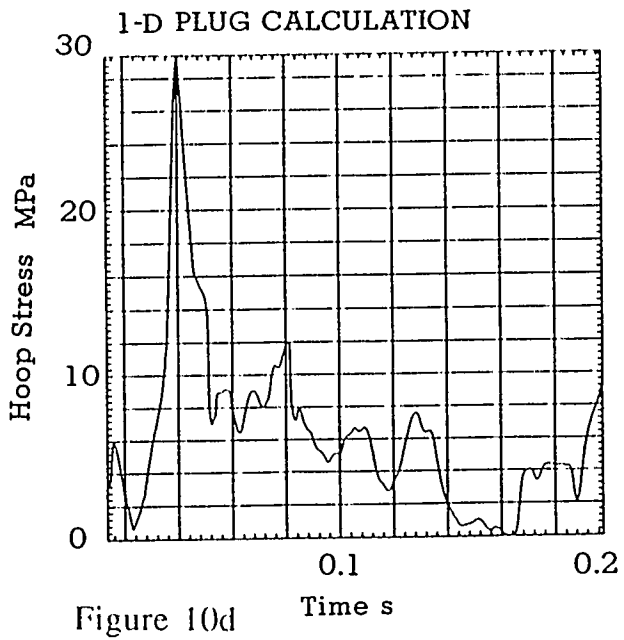


Figure 10d

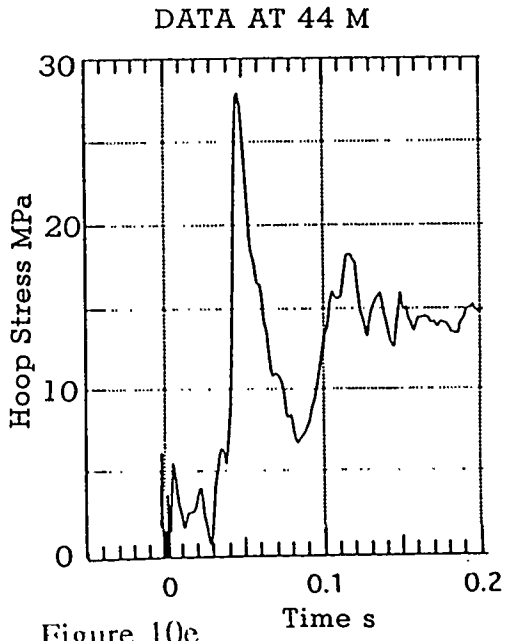
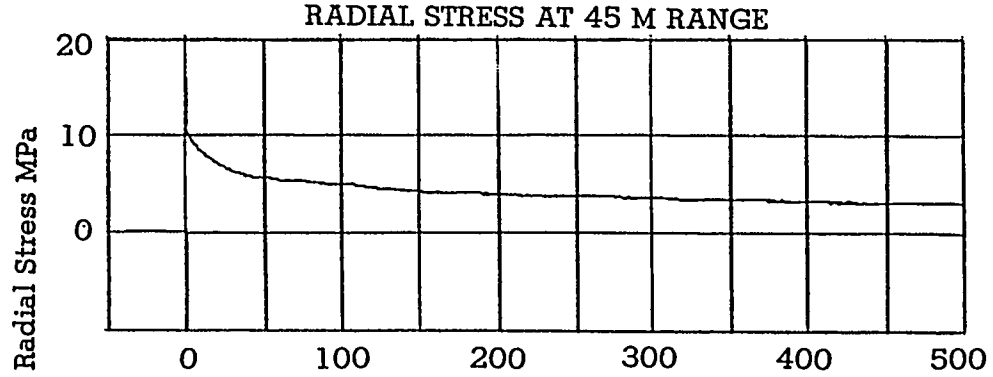


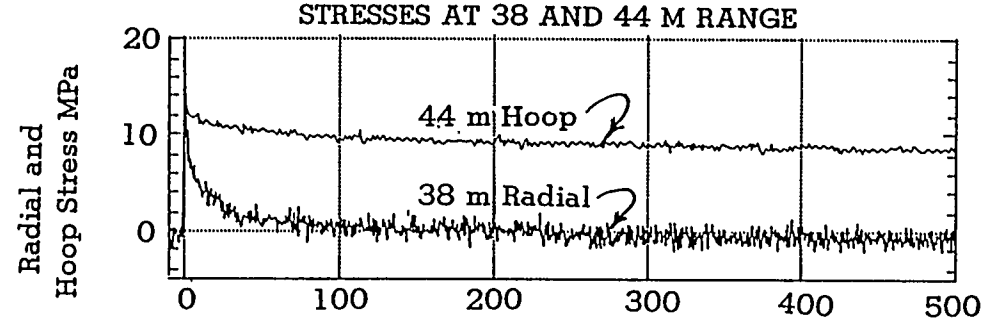
Figure 10e

Hoop and Radial Stresses to 500 s



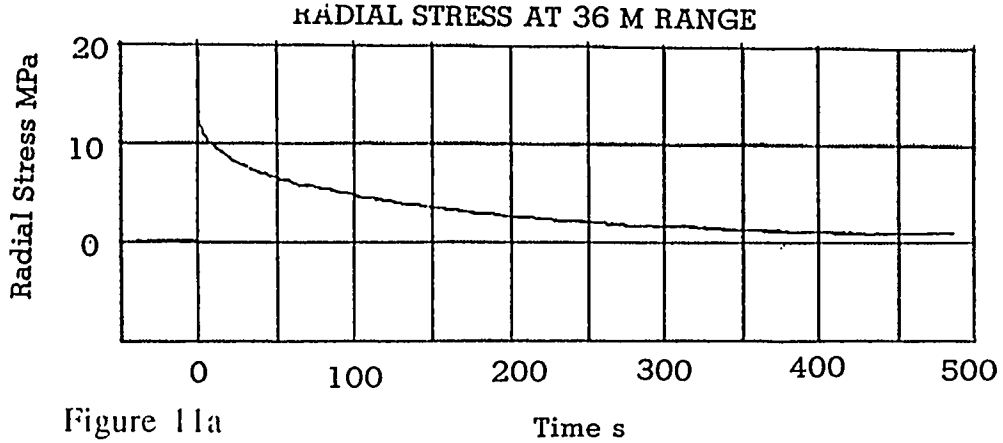
SANDIA GAUGE

Figure 11c



DYNASEN GAUGES

Figure 11b



SANDIA GAUGE

Figure 11a

2-D Simulations of Residual Stress in the Plug Compared to Data at 1 s

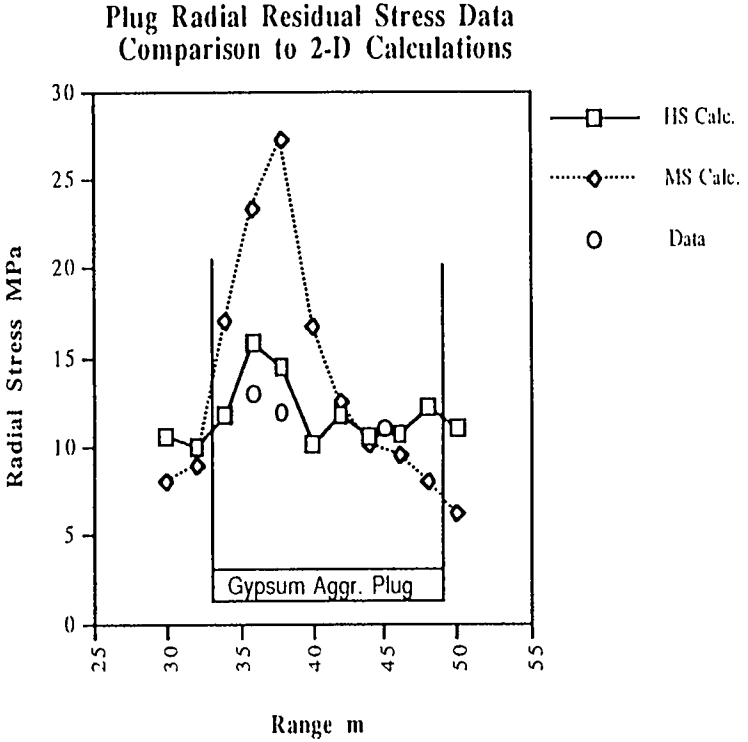


Figure 12a

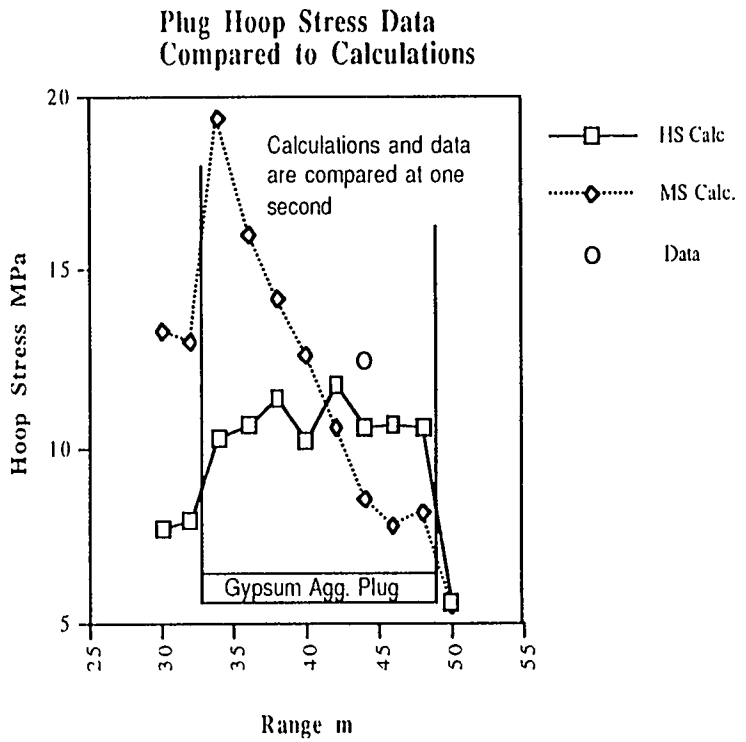


Figure 12b

QUESO Gauge Location Schematic

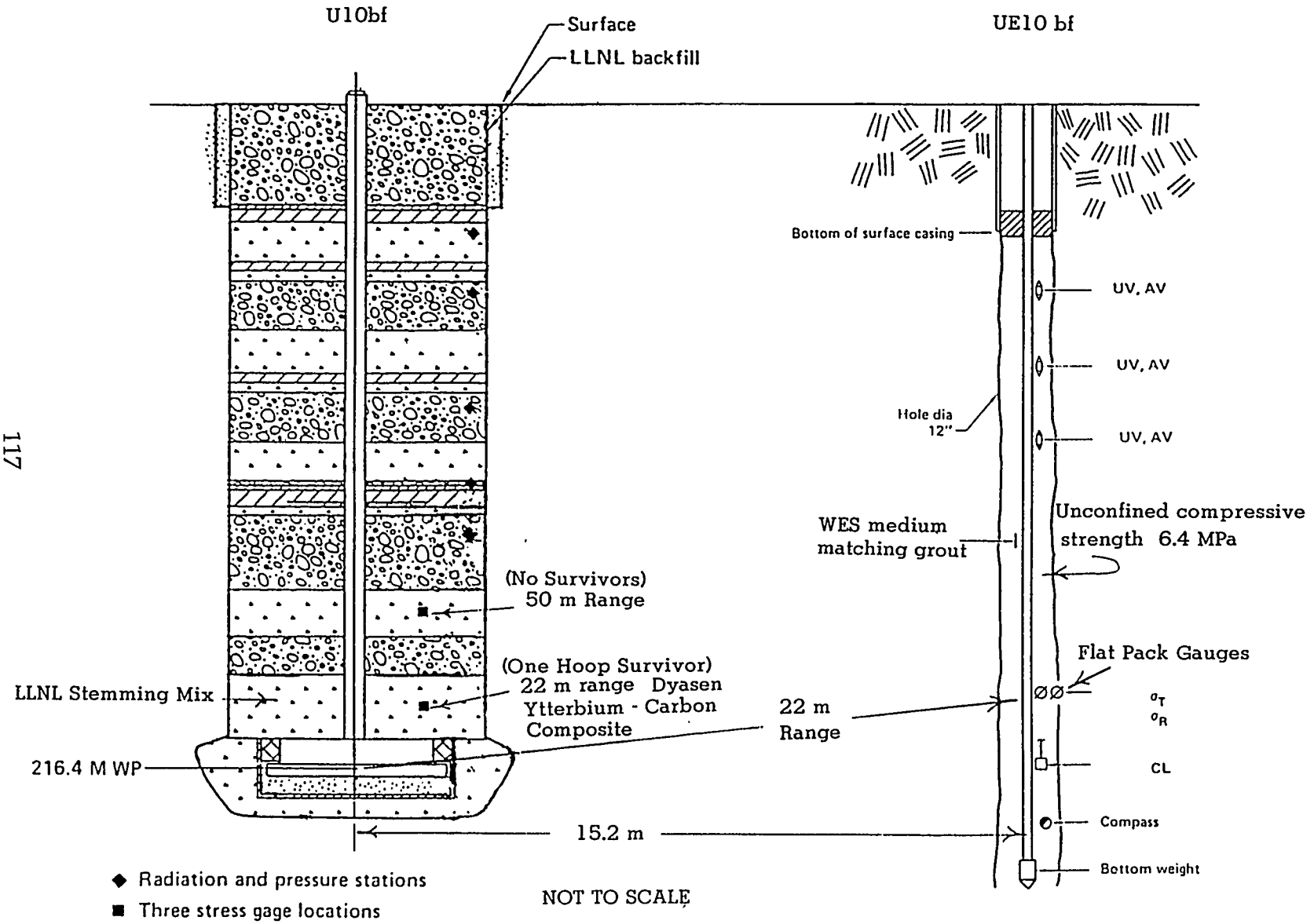


Figure 13

QUESO Hoop and Radial Stresses Compared

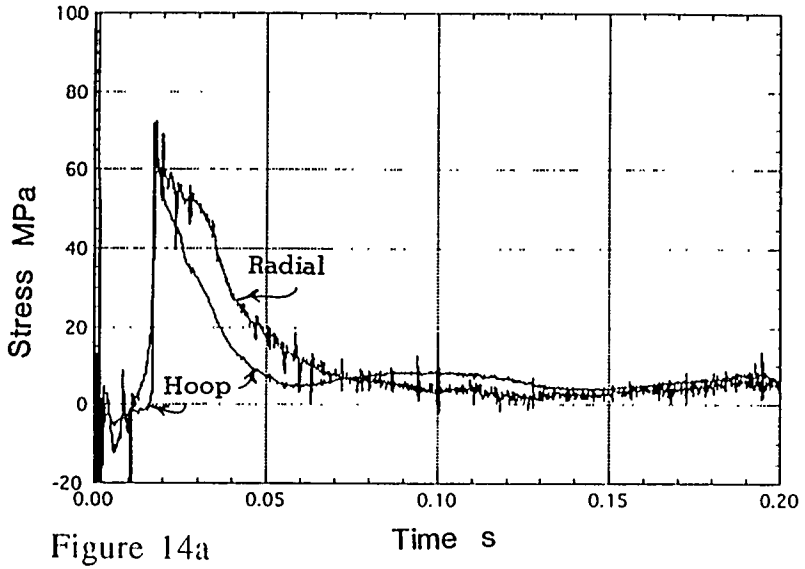


Figure 14a

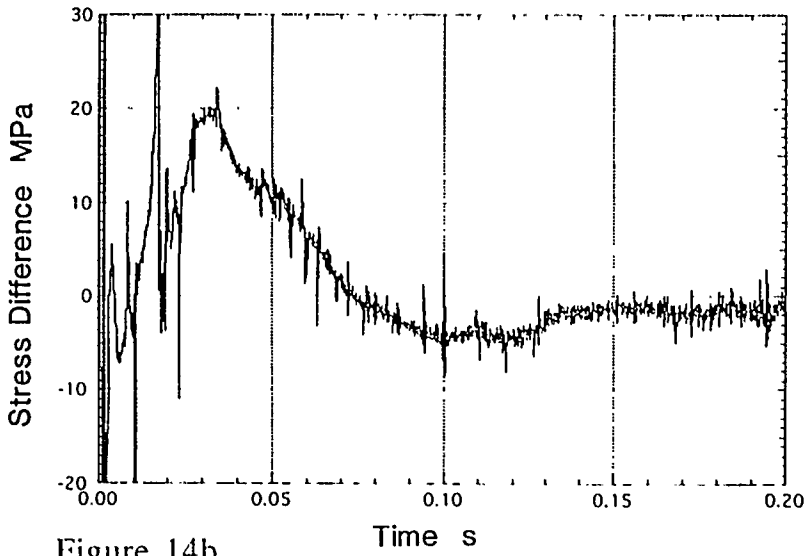


Figure 14b

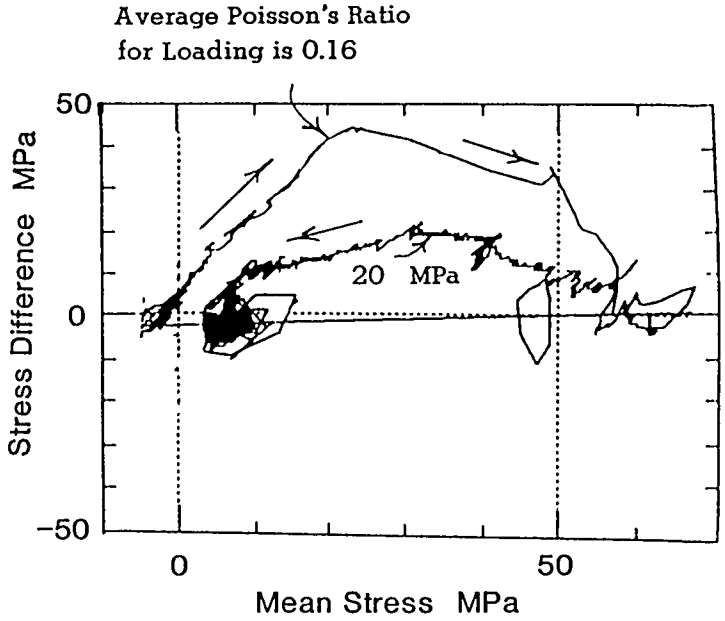


Figure 14c

QUESO Flat-Pack Data Corrected to Zero Tension

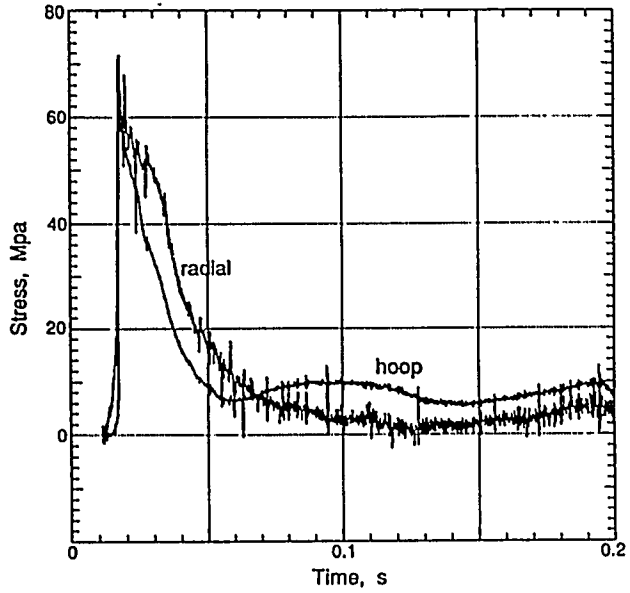


Figure 15a

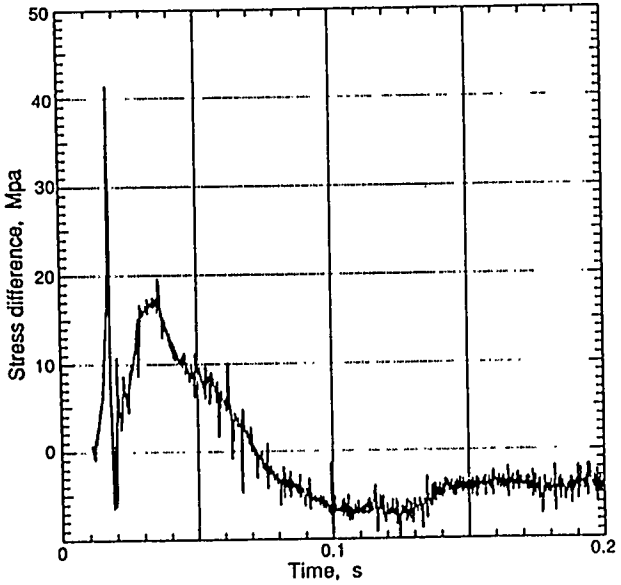


Figure 15b

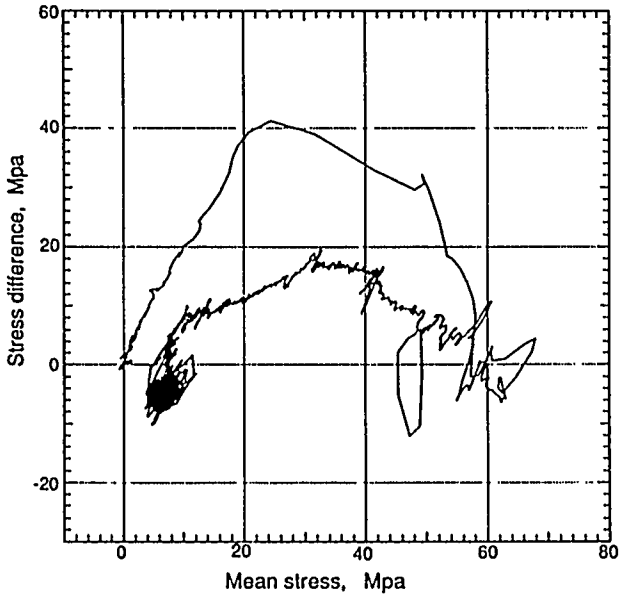


Figure 15c

HUNTERS TROPHY Gauge Location Schematic

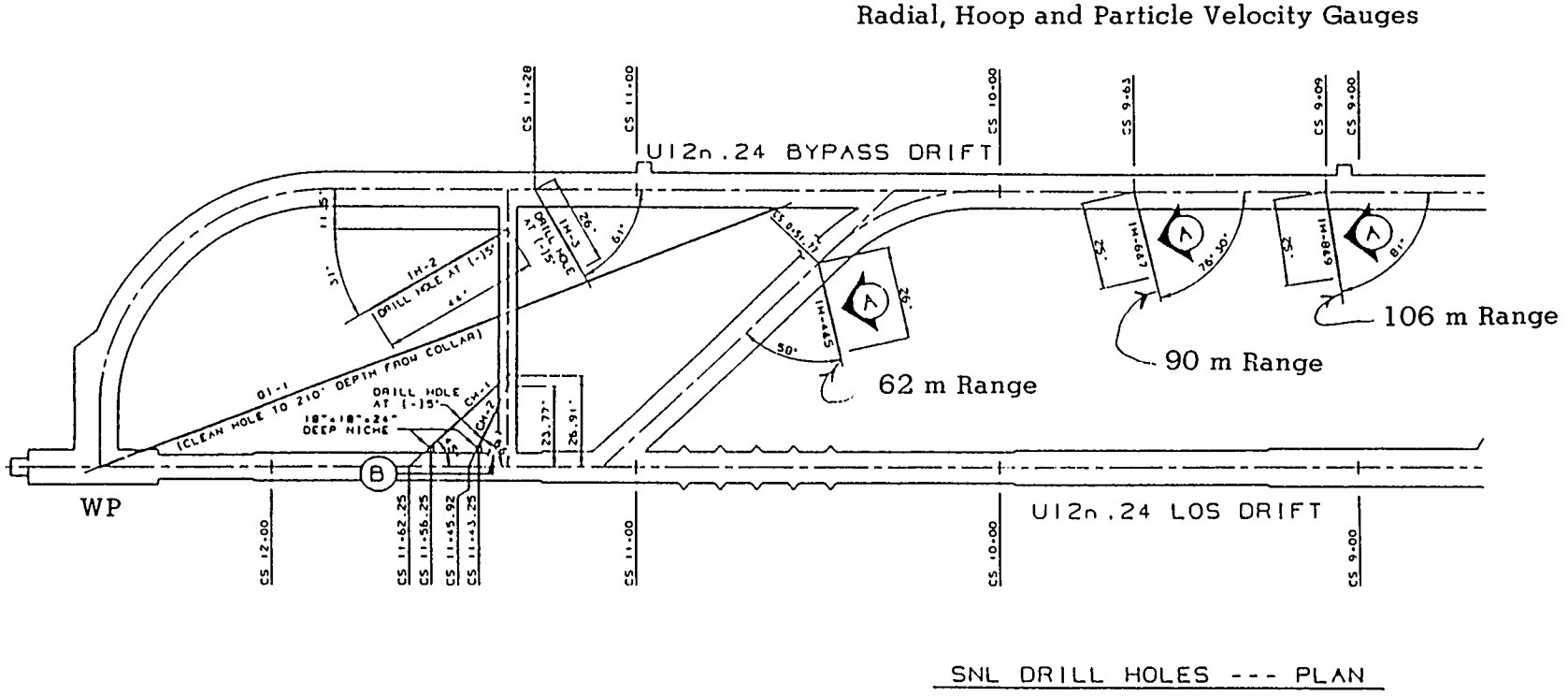


Figure 16

HUNTERS TROPHY Data Comparisons

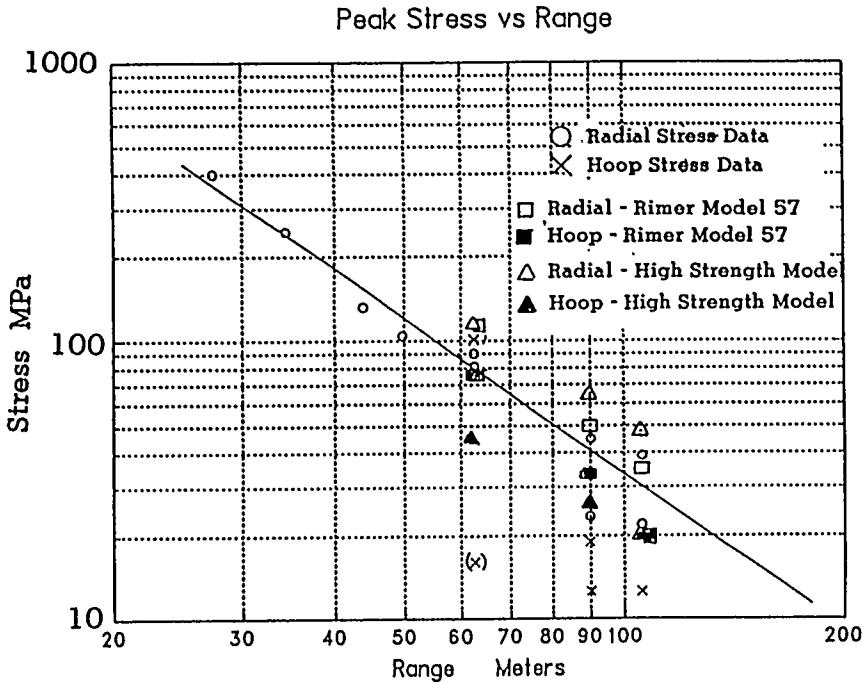


Figure 17a

Rebound Time from Particle Velocity is 0.10 to 0.12 s

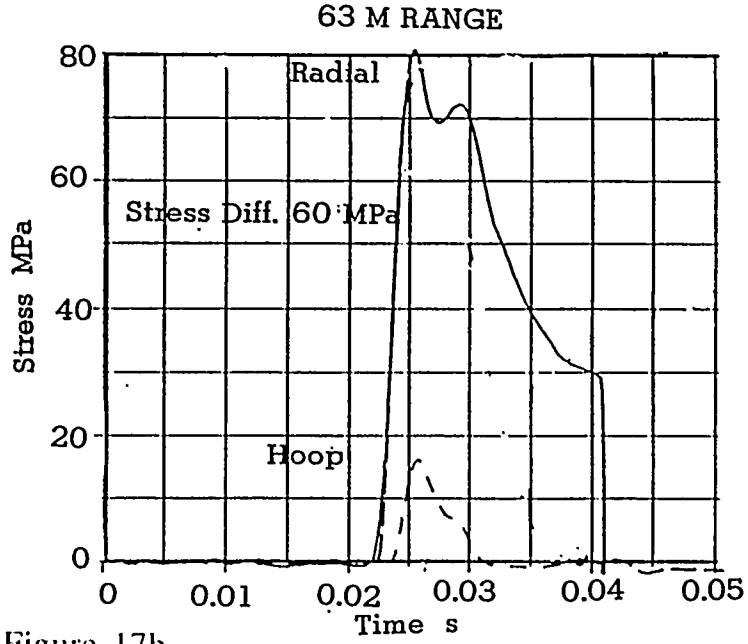


Figure 17b

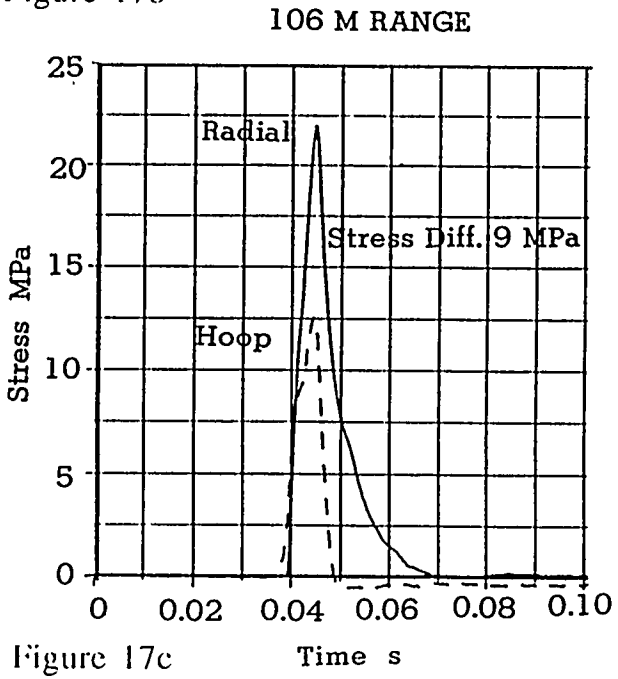


Figure 17c

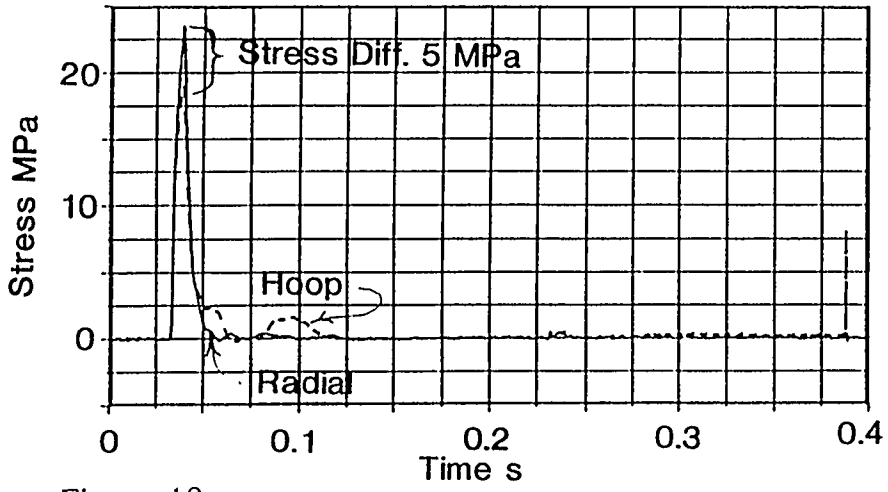


Figure 18a

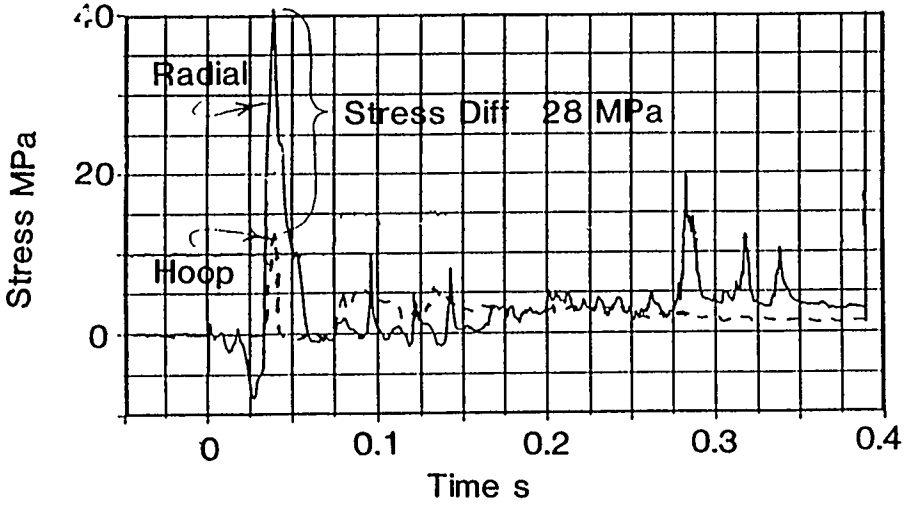


Figure 18b

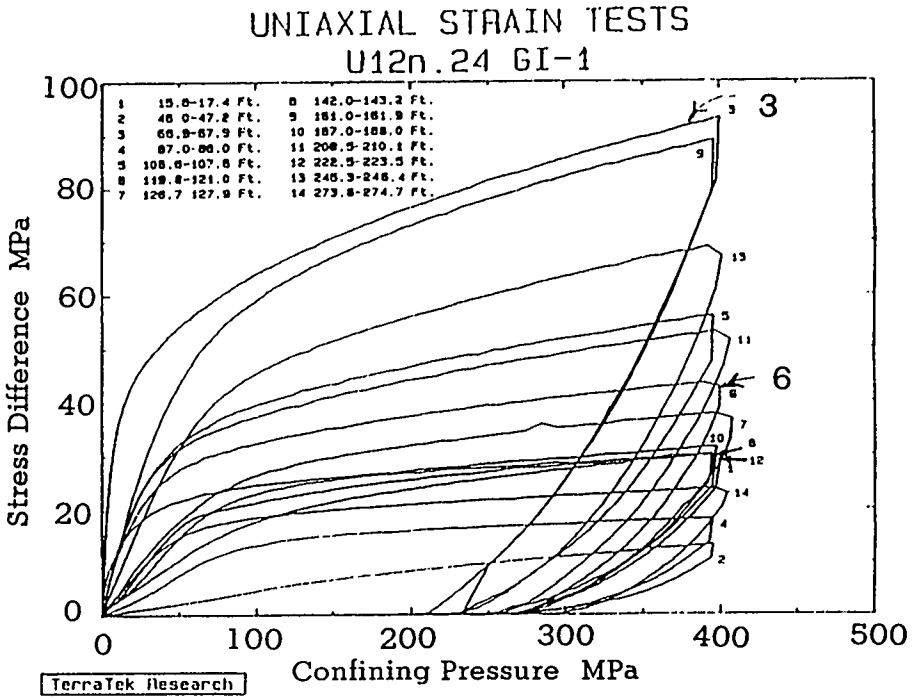


Figure 18c

Rebound Times from Radial Displacements

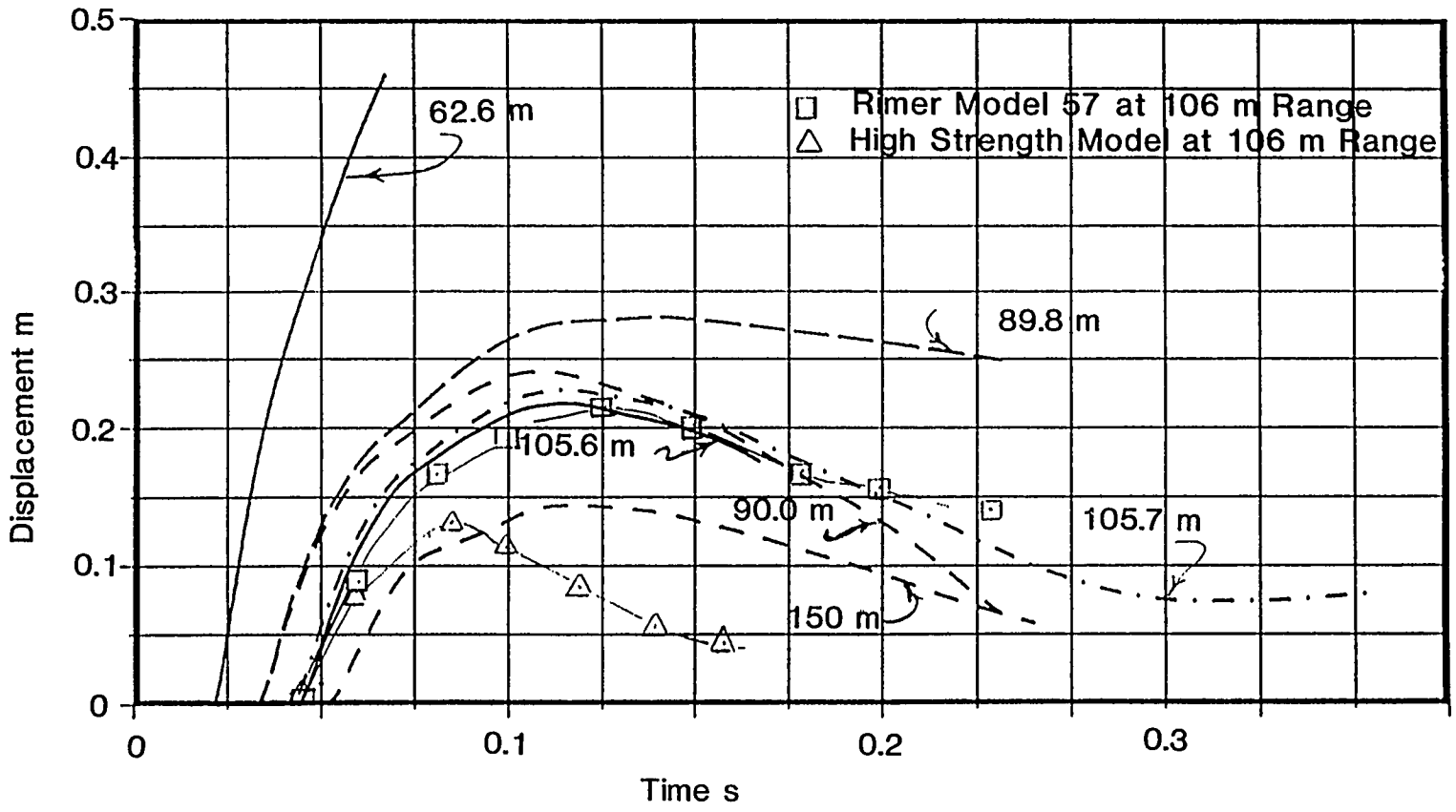


Figure 19

Calculations of The FLAX Events with Comparisons to Particle Velocity Data Recorded at Low Stress

John Rambo, Lawrence Livermore National Laboratory

ABSTRACT

The FLAX event, fired in 1972, produced two particle velocity data sets from two devices in the same hole, U2dj. The data are of interest because they contain verification of focusing of a shock wave above the water table. The FLAX data show the peak velocity attenuation from the device buried in saturated tuff are different from those emanating from the upper device buried in porous alluvium. The attenuations of the peaks are different in regions traversed by both waves traveling at the same sound speed and measured by the same particle velocity gages. The attenuation rate from the lower device is due to 2-D effects attributed to wave focusing above the water table and is a feature that should be captured by 2-D calculations. LLNL's KDYNA[1] calculations used for containment analyses have utilized a material model initially developed by Butkovich, which estimates strength and compressibility based on gas porosity, total porosity, and water content determined from geophysical measurements. Unfortunately, the material model estimates do not correctly model the more important details of strength and compressibility used for matching the velocity data. The velocity gage data contain information that can be related to the strength properties of the medium, provided that there are more than two gages recording in the stress region of plastic deformation of the material. A modification to Butkovich's model incorporated approximate strengths derived from the data. The mechanisms of focusing will be discussed and will incorporate additional information from the TYBO event.

INTRODUCTION

Calculations used for containment analyses utilize a material model initially developed by Butkovich[2], which estimates strength and compressibility based on gas porosity, total porosity, and water content determined from geophysical measurements. We used this model to simulate ground motion for two nuclear detonations (the FLAX event) conducted in the same drill hole and separated in time by an amount that was sufficient to record separate ground motion features.

For the FLAX devices, the peak particle velocity attenuations are different in regions traversed by both elastic waves and measured by the same

*Work performed under the auspices of the U. S. Department of Energy by the Lawrence Livermore National Laboratory under contract number W-7405-ENG-48.

particle velocity gages. The wave propagation from the lower device is enhanced by the water saturation and by effects attributed to wave focusing above the water table. These are features that should be and are simulated by 2-D calculations. The velocity gage data contain information independent of yield that can be related to the strength properties of the medium provided that there are more than two gages recording in the stress region of plastic deformation of the material. A modification to Butkovich's model incorporated approximate strengths derived from such data. The strength modifications result in a better matching of the particle velocity data than using the default strengths from Butkovich's model.

FLAX PARTICLE VELOCITY OBSERVATIONS

The FLAX peak free surface velocities were unusual. FLAX was composed of two devices. The lower event with depth-of-burial, DOB, of 689 m was detonated about 30 s before the upper event with DOB of 435 m. The upper event which was about 3 times the yield of the lower device and closer to the surface gave a lower peak surface velocity (1.01 m/s) than the lower placed event (1.43 m/s). Figure 1 shows a symbolic representation of the relationship.

Limited data were available for analysis of this event. There were few velocity gages and some areas of the satellite hole had no coverage[3,4] as shown in Figure 2. However, the available gages revealed important phenomena. The gages above the upper device recorded velocities from both events and the attenuations of the peak velocities were measured through the same medium. Geophysical logs (1972)[5] were crude by todays standards. Review of recent events near the FLAX site, U2dj, show consistently higher grain density measurements[6,7]. The methodology for this measurement has improved over the years, and L. McKague[8] has suggested using measured grain density values from one of the nearby recent events. Some strength and compressibility measurements on cores were performed for only a few locations[9]. They did not provide a complete representation of the geology and were not used in this analysis.

Time-of-arrival (TOA) of the outgoing waves are useful to evaluate material crushing caused by the lower event that could change the material properties for the upper event. Where the peak of the particle velocity is propagating at near the sound speed, we assume that elastic or almost elastic behavior is in effect and either purely elastic compression or minimal crush and/or damage to the material is occurring. The elastic onset (the time of the first positive detectable particle velocity) and the following time of the peak particle velocity arrival are shown for each event in Figure 3.

The slopes of the TOA values in Figure 3 translate to velocity of the wave between points. The onset velocities represent the elastic sound speed of the material between the measurement points. The slope of the peaks can be compared to the slope of the elastic onset to determine where the peaks are undergoing large amounts of plastic failure. Above the standing water level (SWL) where the gas porosity is high, the lower event peak velocities travel slowly indicating plastic failure. Further above the SWL the peak abruptly increases to a sound speed similar to the speed of the elastic onset. Some minor time spread of the two parts of the wave occurs upward to a location just below the upper device. Above the upper working point the onset and peak travel parallel (the same sound speed) until just below the surface where spall obscures the timing of the peak. The fact of the same sound speed for both onset and peak velocity indicates very little crush up of the material has occurred above the upper device. The peak wave velocity from the upper device shows a similar slow velocity for the pore-crush followed by a higher sound speed velocity to the surface. The onsets and peaks from both devices travel with about the same sound speed through the same upper region of the FLAX site.

Attenuation of the peak particle velocity is material dependant. The most important factors are usually gas porosity and strength, where the peak of the wave is undergoing plastic failure. Where the wave is truly elastic, the attenuation should be R^{-1}. Particle velocity attenuations from calculations usually show an abrupt change in attenuation to R^{-1} when the stress falls below plastic failure into the elastic regime. This is accompanied by a sudden change to elastic sound speed at the same location. However, the data for the quasi-elastic attenuations do not follow the calculations in quite the same way.

A comparison of peak velocity vs range for both devices is shown in Figure 4. The range axis of the log-log plots is referenced to the depth-of-burial, DOB, of each device and the attenuation is determined from a power fit to the data, $Up=aR^b$, where b is the attenuation exponent and Up is the peak particle velocity. The upper event attenuation, b, is about -2.9 and uses three data points above 9 m/s and one point almost in the spall zone (0.7 m/s). There is no information on the attenuation between 0.7 and 9 m/s. However, the attenuation of -2.9 compares well with a more recent nearby event, CORNUCOPIA in hole U2gaS, with the value[10] of -3.2. The upper FLAX particle velocity values above 9 m/s were scaled to the particle velocities of CORNUCOPIA and resulted in a yield estimate very near the official yield.

INTERPRETATION OF THE FLAX DATA

From the scaling and the similarity in attenuations, the upper FLAX data are interpreted as "normal" for an alluvium event and the material was not significantly changed by the lower device. The porous alluvial events experience strong energy attenuation because of the material failure and PdV work that accompany pore-crush. This dissipates the wave's kinetic energy in the source region, and this decoupling is observed at seismic distances as well.

The lower device data show some unusual attenuations. Data from both devices have about the same particle velocity value at about 110 m range. Velocity (as a function of range) from the upper device attenuates steeply in porous material at a higher yield while the lower device velocities attenuate less steeply in a saturated material at a lower yield to get to about the same particle velocity at 110 m range. Above the 110 m range, the lower device data attenuation exponent is about -9.0 due to the gas porosity above the water table. The attenuation changes to -1.4 at about the place where sound speeds occur for the peak. An interesting observation is that the attenuations in the regions traversed at similar sound speeds are different for both peak velocity data sets as shown by the thickened lines of Figure 4. Since the upper data are normal and the material was not significantly changed by the lower event, then the lower device attenuation of -1.4 appears unusual. The objective was to understand this unusual attenuation.

MODEL

A material model which was first developed by Butkovich, estimates compressibility based on density, water content, grain density, Poisson's ratio, and longitudinal velocity. Strength in terms of the compressive elastic limit is estimated, and the user can estimate shear strength from the compressive elastic limit and Poisson's ratio if uniaxial strain is assumed. Additionally, strength can be estimated from particle velocity data where gage records are relatively close together and the peak velocities indicate plastic failure. Fortunately, both FLAX device data sets show plastic failure.

The calculational model consisted of several horizontal layers designed to capture some of the nuances of elastic properties and the gas porosity. Figure 5 shows some of the logging data that were the source of material properties used in the model. The trace of the density, longitudinal velocity

(DHAL)*, acoustic impedance, and wt% of H_2O are shown next to the rock type. The units are mixed between English and SI because the original logs are in English units from an unpublished document[11]. The depths of the layers are given in meters and the working points are shown in the left margin. The calculated value of gas porosity was derived from density (U2dj)[5], wt% H_2O (U2dj, UE2dj, U2ge), and grain density (U2ge)[6]. The most significant modeling of gas porosity was the water table interface at 574 m depth. Above the interface the gas porosity is 13 vol% and it has a large influence on the wave attenuation. The default elastic limit strengths from Butkovich's model are shown, as well as the modified strengths derived from the particle velocity data. The modified strengths are considerably weaker than the default values and were used only in the layers for which the strengths could be estimated from the data.

MODIFICATIONS TO DEFAULT STRENGTHS

The modified strength and compressibility relationship near the linear elastic region was modified from the default values of the Butkovich model values. Figure 6 shows schematically some of the process to refine the model. Two adjacent particle-velocity waveforms located above the water table were compared. The average elastic limit is selected based on the observance of a constant time difference between equivalent parts of the wave. Constant difference suggests those parts to be traveling at the same sound speed and are considered to be linear elastic in the model. Above this point equivalent parts of the wave spread in time as they represent higher pressures subjected to the porous crush-up of the material. The radial stress (σ_r) can be estimated from the highest particle velocity of constant time difference (U_p), the sound speed (U_s) calculated from the gage separation distance divided by the time separation, and the initial state density (ρ_0) by the conservation of mass equation for the jump condition, $\sigma_r = \rho_0 . U_s . U_p$. Assuming a Poisson ratio, the mean elastic pressure (P_m) and strength (τ) can also be estimated from the formulas shown in Figure 6, assuming the condition of uniaxial strain.

Above the elastic limit a qualitative picture of the shape of the P vs mu relationship was estimated from the incremental application of the conservation of mass formula. Since the velocities (Us) over the interval between the estimated elastic limit and the peak were increasingly slower, this equation was not quite appropriate, but more useful to give the approximate curvature in the low pressure regime than the default. Figure 6 shows a comparison with the default higher strength P vs mu

* Dry Hole Acoustic Log

compressional relationship compared to the derived lower strength relationship that is suggested from data. For the material just above the water table the two P vs mu curves tended to merge at higher pressures.

The P vs mu relationships below and above the water table are shown in Figure 7. This shows a large increase in compressibility that occurs across the water table at this site. The sound speed is related to the slope of the P vs mu relationship. As the pressure wave crosses the water table the velocity slows considerably as the wave travels into the more porous material.

AGREEMENT OF CALCULATED PEAK SURFACE VELOCITY TO DATA

Using the actual FLAX yields the agreement between calculations and the peak free surface velocity data from both devices was good. The tables in Figure 8 show the agreement. However, considering the simplicity and approximations of the model, the very close agreement was fortuitous. The upper device data did not model the near surface spall region very well and wave forms in this region were not well matched. The data from the lower device showed much better agreement with wave forms.

FOCUSING ABOVE THE WATER TABLE

The calculations were useful for explaining the high surface velocity from the lower FLAX device. Shock waves usually travel slow in porous material and more rapidly in the saturated material, for plastic stresses less than 500-MPa. The slope of the compressibility relationship, P vs mu, is quite different for saturated and porous alluvium for the pressure ranges occurring near the water table. The shock wave travels at high velocity and low attenuation up to the water table interface and with slow velocity and high attenuation above. The effect of slowing down can be seen in velocity contours of Figure 9. A circular contour line has been plotted over the second contour line to emphasize the shape difference below and above the water table (SWL). The wave is generally spherical in the calculation relative to the center of the explosion below SWL and has flattened considerably above.

The wave above the SWL is spherical as well but relative to a geometric center below the actual center as depicted schematically in Figure 10a. This is partially due to a Snell's Law effect at the SWL and has the analogy of focusing of light by a lens. The spherical divergence changes above the SWL as shown schematically with the solid radial lines from both geometric sources. Both 1-D and 2-D calculations have been compared using the same model parameters. The 1-D[12] calculations produce a spherical interface which eliminates the Snell's Law effect on the

calculation. The attenuation effect of divergence above the SWL is shown in the schematic comparison of Figure 10b. The 2-D calculation agrees well with the 1-D calculation radially to the SWL. Above the SWL the 2-D calculation shows higher velocities and lower attenuations.

AXIAL PREFERENCE OF PORE COLLAPSE FLATTENS THE WAVE FRONT

There is a second effect that contributes to focusing. The path between the lower device and the water table is shortest in the axial (vertical) direction. The stress at the water table is greatest at that point and diminishes horizontally along the water table as the wave takes longer paths (with more attenuation) to arrive. The highest stress, axial path at the SWL takes the longest porous crush-up time and distance to attenuate to elastic stress above the water table. The other paths take less crush up time and distance as shown in Figure 11. The crush up distance between the SWL and the curved line representing the location of elastic stress diminishes with horizontal distance. The decreasing time in the crush up has been observed from surface gages on the TYBO event[13]. The particle velocity vs time from locations along the ground surface showed greatest time separation between the elastic portion of the wave and the remnant of the plastic peak at surface ground zero (SGZ). Other observations on TYBO were very high SGZ surface velocity and a pronounced reduction of the peak surface velocities with horizontal distance.

SUMMARY

The surface velocities from both FLAX devices at first appeared anomalous. Comparisons with nearby alluvium event data indicate the upper FLAX device is a "normal" alluvium event and the velocity peak attenuation is similar. The sound speeds indicate that the alluvial material was not significantly changed by the passage of the stress wave from the lower FLAX device prior to the detonation of the upper event. The lower FLAX event has high peak surface velocity because of lower peak attenuation in the saturated medium below the water table and the 2-D effect of wave focusing above the water table. The focussing is attributed to two effects; Snell's Law and the preference of the shock to run slowly for a longer time during the pore-crush in the axial direction.

Significant improvements to the default FLAX modeling were due to well placed velocity gages from which strengths could be estimated. Further improvements for the FLAX modeling are possible, but most involve model changes based on the calculator's experience and are not easily justified without core measurements. There are measured strength data from core at some FLAX locations which could be incorporated in simulations. This

might resolve the issue of the importance of core samples. Other models developed for nearby events could be employed (such as a damage model)[14] to examine their sensitivity.

Improvements in the general process for a new event would require more velocity gages coupled with simulations to further develop material models. Perhaps analysis of Lagrangian measurements[15] (multiple velocity gages) could be employed to obtain better in-situ material properties. Core measurements at appropriate locations which include strength and compressibility would also be valuable.

ACKNOWLEDGEMENTS

I wish to thank J. White for reviewing the paper and for general technical discussions. Discussions about the wave propagation above the water table were very useful. I also thank Ted Butkovich for his help with the computer calculations and post processing, and C. Olsen for reviewing the paper.

REFERENCES

1. Levatin, J. L., Attia, A. V., and Hallquist, J. O., "KDYNA USER'S MANUAL", Lawrence Livermore National Laboratory, Livermore, CA, UCRL-ID-106104, 1990.
2. Butkovich, T. R., "A Technique for Generation Pressure-Volume Relationships and Failure Envelopes for Rocks", Lawrence Livermore National Laboratory, Livermore, CA, UCRL-51441, Nov., 1973.
3. Wheeler, V. E., Lawrence Livermore National Laboratory, private communication, May, 1973.
4. Preston, R. G., Lawrence Livermore National Laboratory, private communication, May, 1973.
5. LLN-N Geology, "Geology of Emplacement Hole U2dj (FLAX)", Lawrence Livermore National Laboratory internal memorandum, GN-6-72, April, 28, 1972
6. Clarke, S. R., and McKague, L., "U2ge Site Characteristics Summary", CP 87-36, April, 1987
7. Howard, N., "U2fa Preliminary Site Characteristics Summary", AGTG 77-39, April 29, 1977
8. McKague, L., Lawrence Livermore National Laboratory, 1992, private communication, (Currently with Southwest Research Institute, San Antonio, Texas)

9. Brandt, H., and Chu, H., "Triaxial Tests of Alluvium, Final Report", University of California Department of Mechanical Engineering, Davis California, Contract Order Number 2100603, 1977
10. Hudson, B., Lawrence Livermore National Laboratory, private communication, Sept., 1992.
11. Ramspott, L., "U2dj Site Characteristics Report", Lawrence Livermore National Laboratory, Internal Memorandum, Unpublished, March 30, 1972
12. Snell, C. M. and Austin, M. G., "SOC Code: Lagrangian, Finite-Difference Calculational Technique in One-Dimensional Symmetry", Lawrence Livermore National Laboratory, Livermore, CA, UCID-18220, July, 1979.
13. Rambo, J. T., and Bryan, J. B., "Calculation of High Surface Velocity Due to Focusing in the TYBO Event", Proceeding of the Second Containment Symposium, Kirkland AFB, Albuquerque, NM, August 2-4, 1983.
14. N. Rimer, and W. Proffer, "Containment Phenomenology Using a New Shear-Strain-Based Computational Model for Tuff", 6th Symposium on Containment of Underground Nuclear Explosions, CONF-9109114-VOL1, Lawlor Events Center, University of Nevada, Reno, Nevada, September 24-27, 1991.
15. Aidun, J. B., and Gupta, Y. M., "Analysis of Lagrangian Gauge Measurements of Simple and Nonsimple Plane Waves", J. Appl. Phys. 69 (10), May 15, 1991.

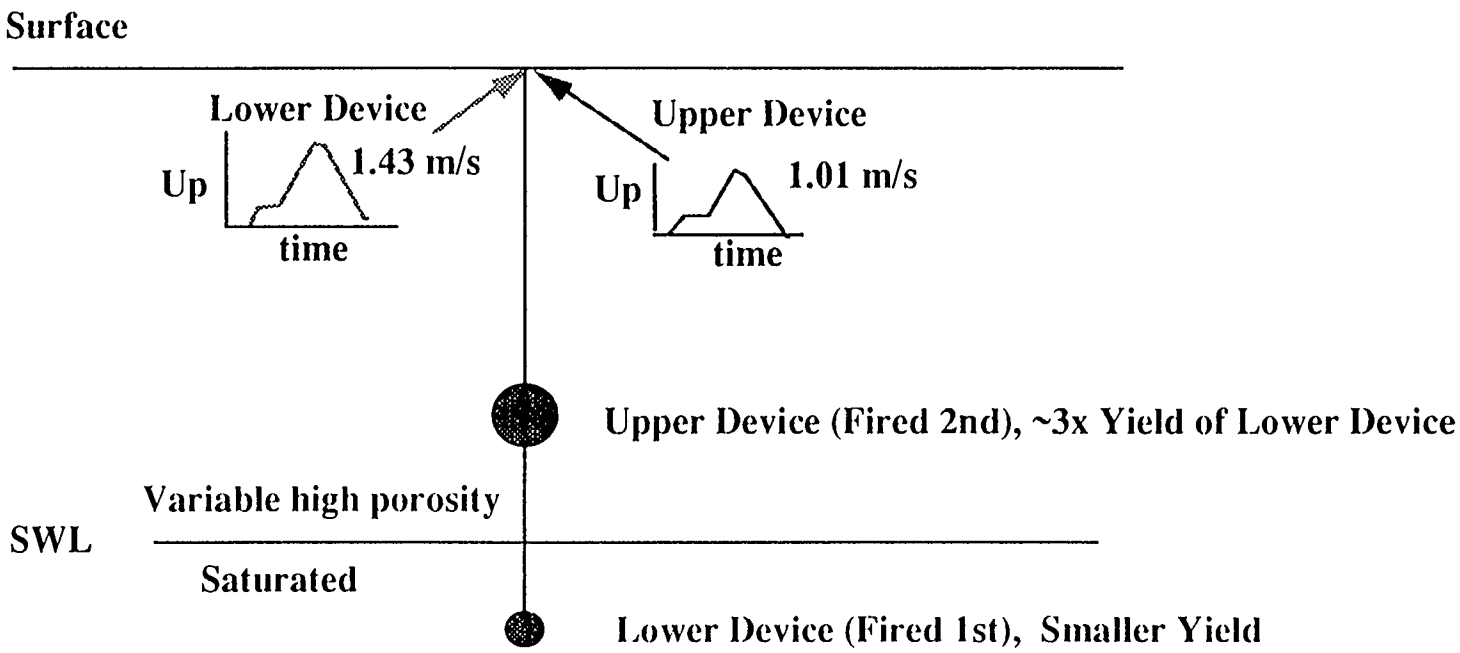


Figure 1. Schematic of device position and particle velocity results. Lower device is buried below the standing water level (SWL) and gives a higher peak surface velocity than the shallower, larger yield event.

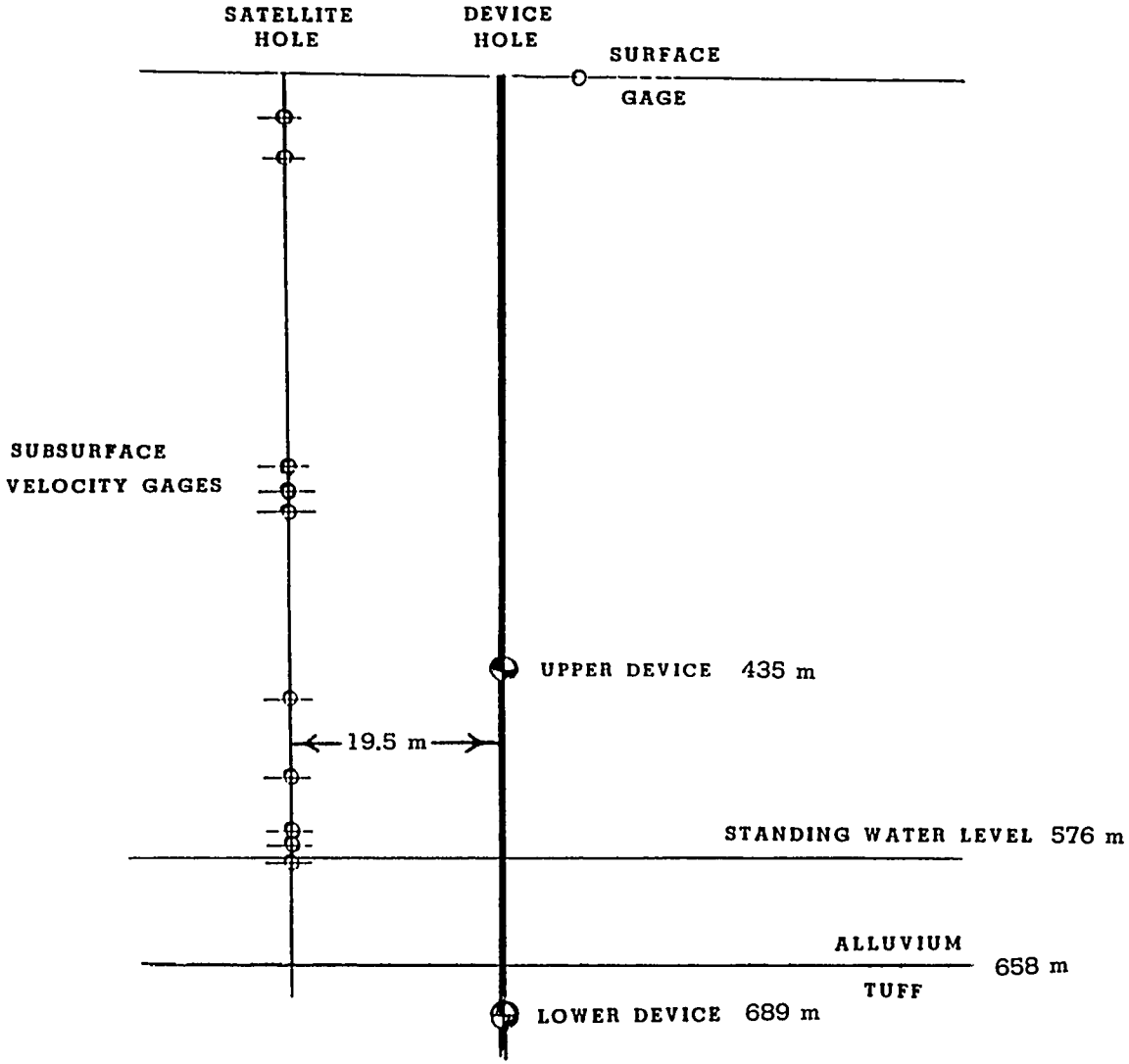


Figure 2. Schematic of gage locations relative to device locations. Gages above upper device recorded data from both devices.

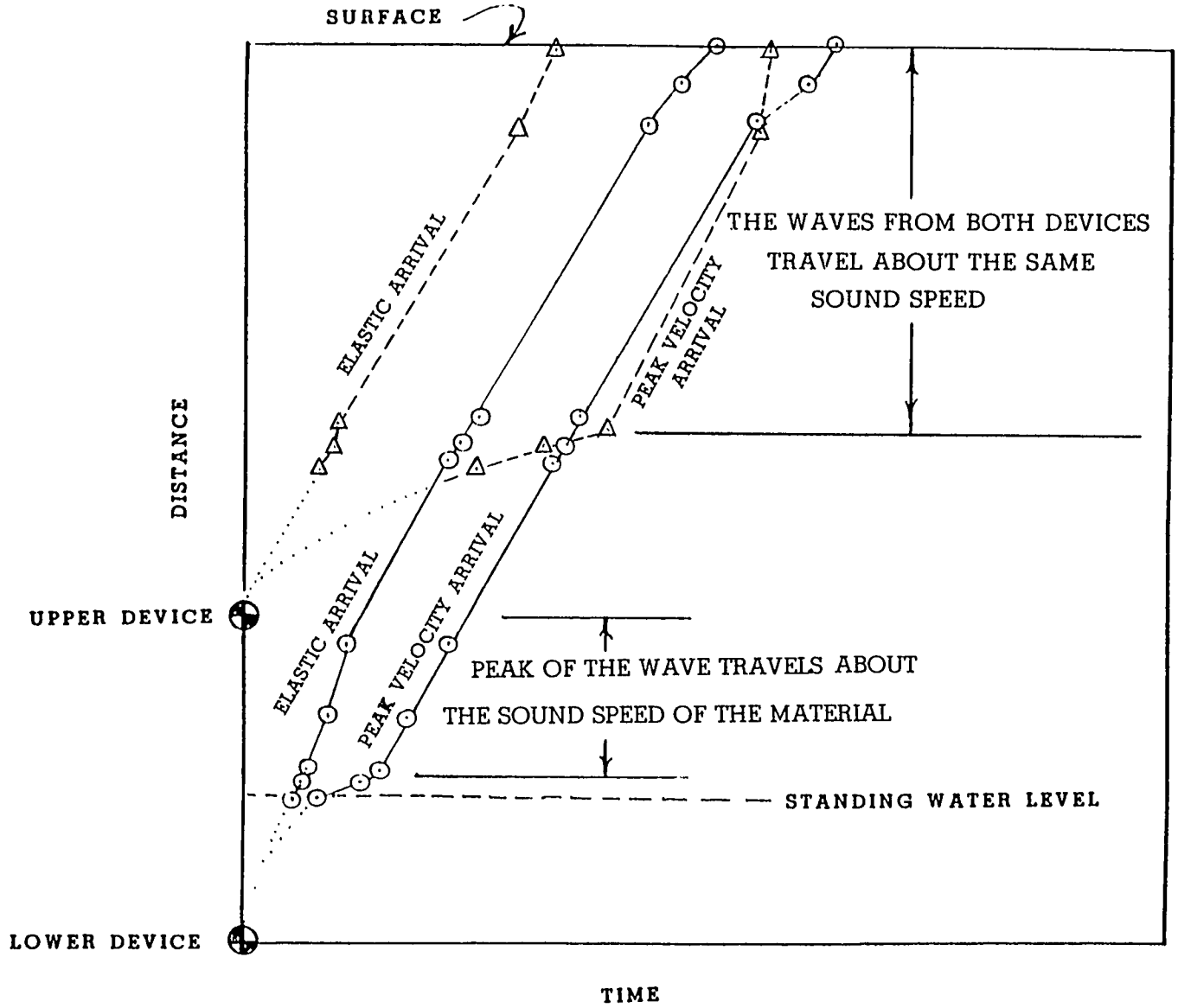


Figure 3. Time-of-arrival of elastic onset and the peak of the velocity wave from both devices. The peak velocity wave from the lower device (solid lines) travels at the sound speed before it passes the upper device. The peak particle velocity wave from the upper device (dashed lines) travels at about the same sound speed as does the lower one.

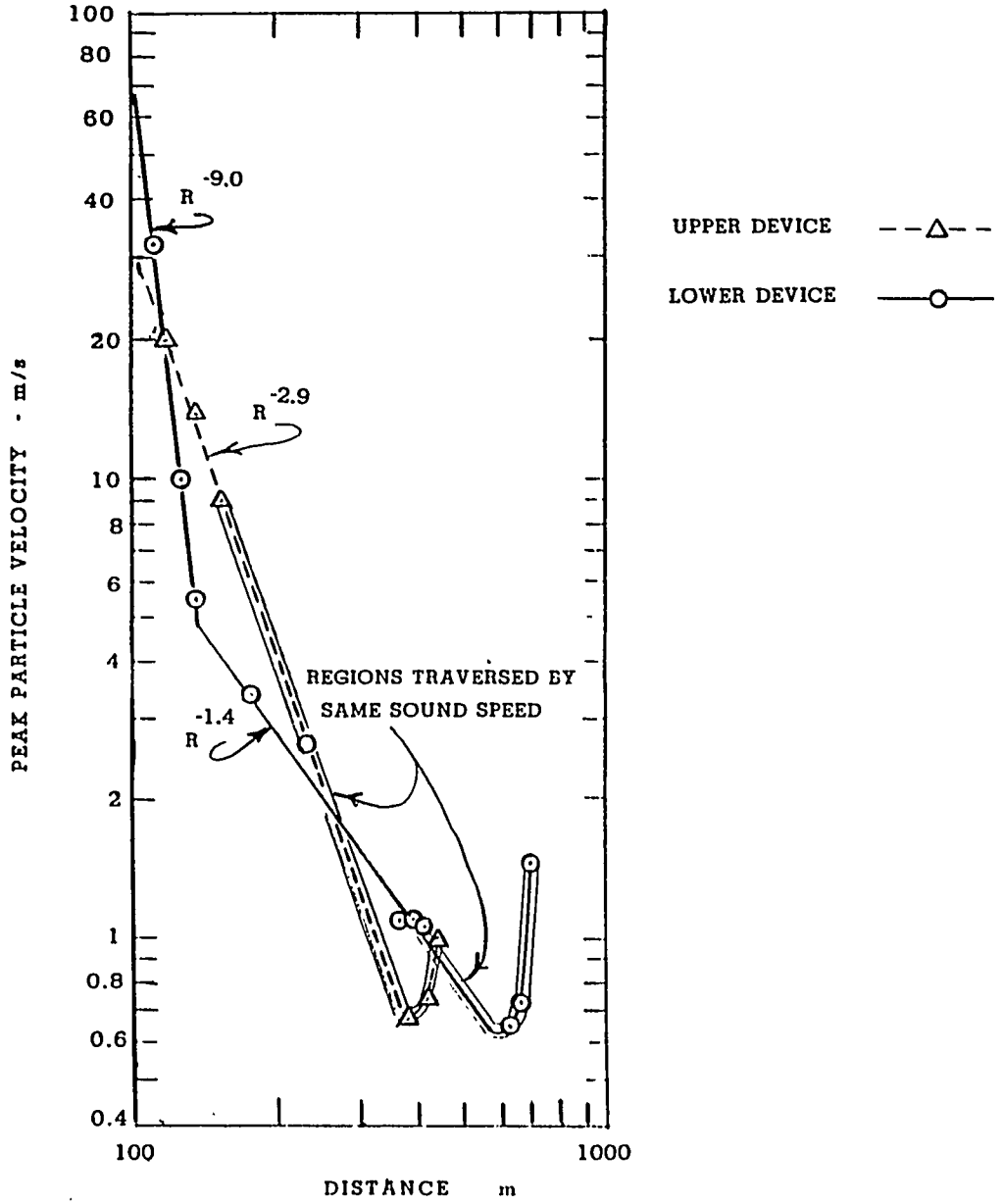


Figure 4. Peak particle velocity vs attenuation from both devices. Thick lines are areas traversed by waves from both devices at the same sound speed but both have different attenuation exponents.

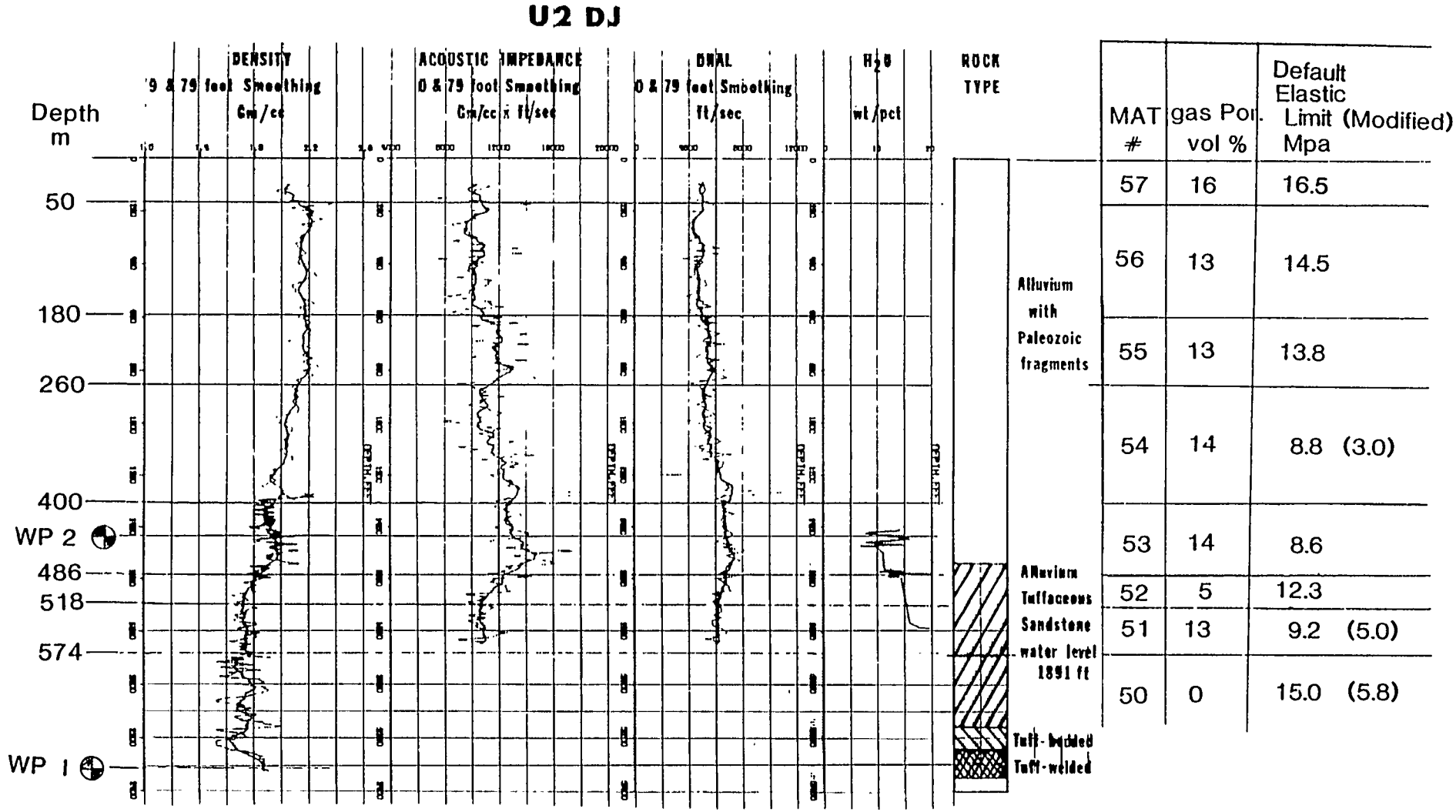


Figure 5. Geophysical model showing geophysical logs, selected layers, gas porosity, rock type and strength. Modified strengths are shown in parentheses. Gas porosity above water table (574 m depth) and strengths are the most important aspects of the model.

Estimation of the elastic limit

For the elastic case

$\sigma_r = \rho_o \cdot U_s \cdot U_p$

Assuming uniaxial strain and a

Poisson's ratio, ν, mean stress, P_m,

and shear strength, τ, can be estimated.

$$P_m = \frac{\sigma_r}{3}\left[\frac{1+\nu}{1-\nu}\right]$$

where $\tau = \frac{\sigma_r - \sigma_\theta}{2}$

$$\tau = \frac{\sigma_r}{2}\left[\frac{1-2\nu}{1-\nu}\right]$$

Assumes τ relatively constant over

P_m of interest.

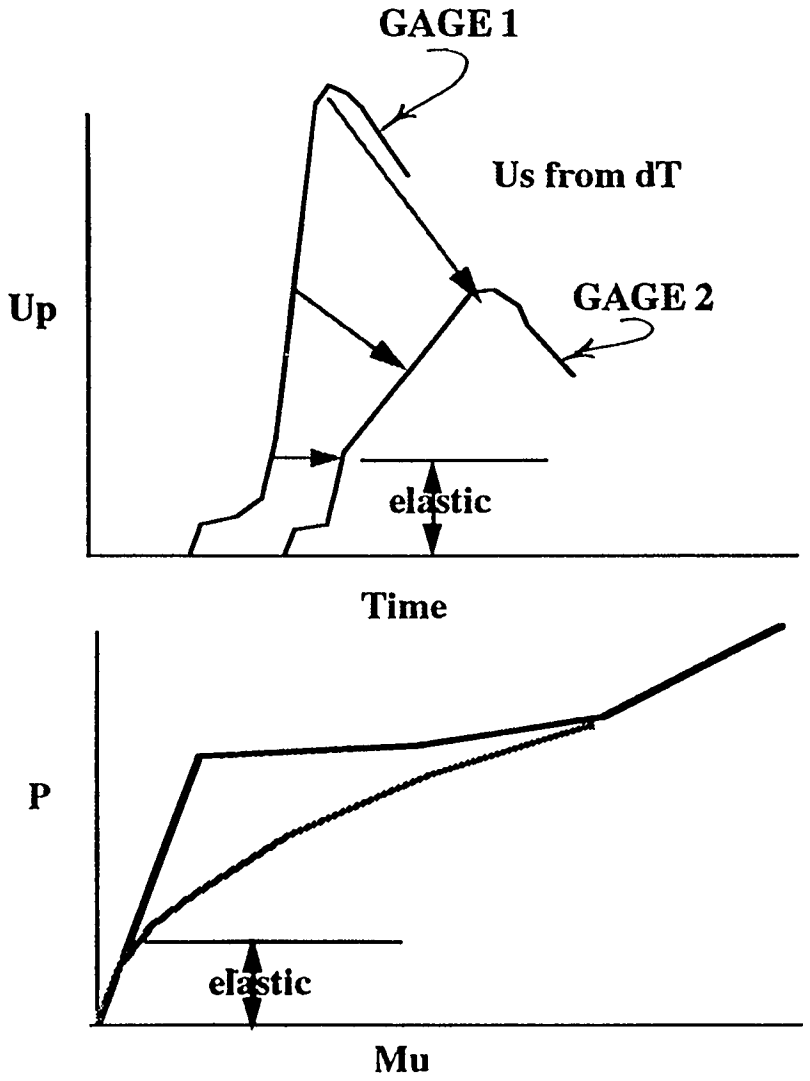


Figure 6. Method of establishing the elastic limit and shape of the P vs mu relationship.

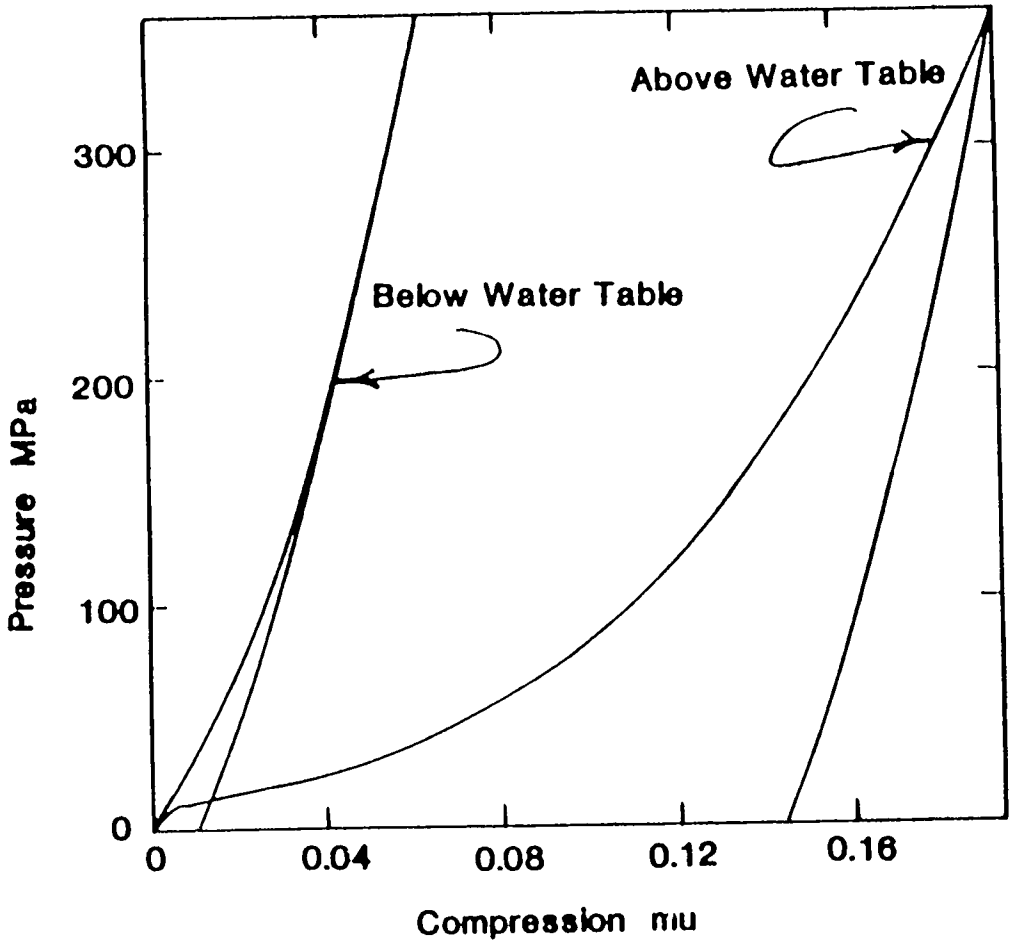


Figure 7. Comparison of the P vs mu relationships below and above the water table.

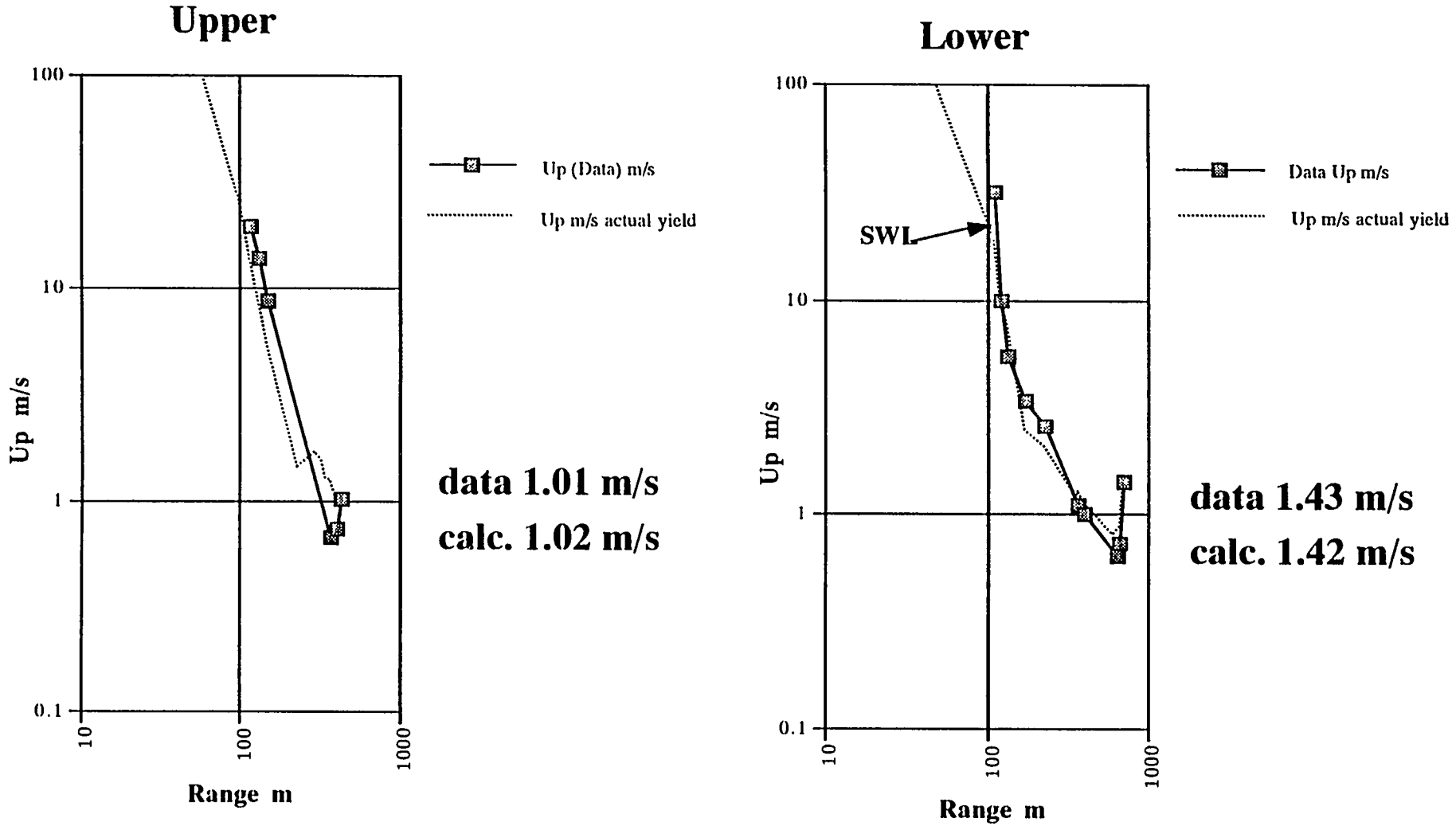


Figure 8. Free surface velocity has good agreement to modified-strength calculation run at actual yield. The upper event calculation shows poor agreement to the near surface data and the agreement at the surface may be fortuitous.

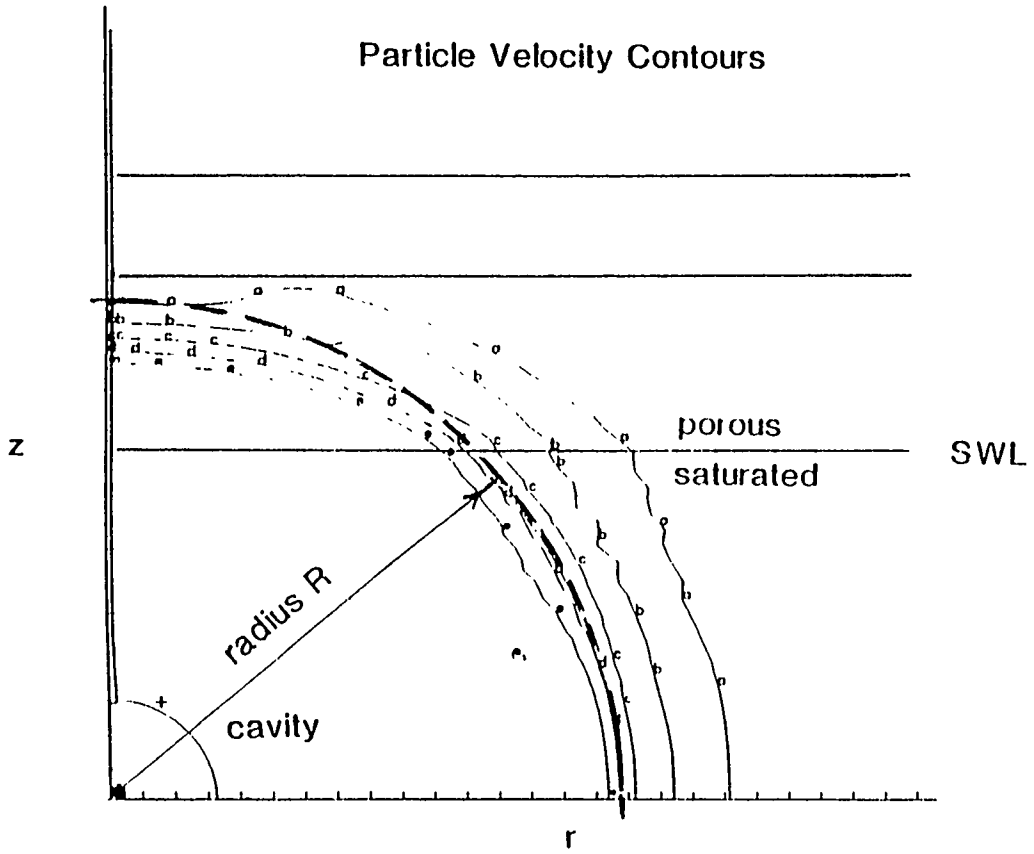


Figure 9. Flattening of the particle velocity wave above the water table is shown by comparison to a circular contour of radius R. Above the SWL the circular contour crosses over the velocity contours indicating a flatter wave front.

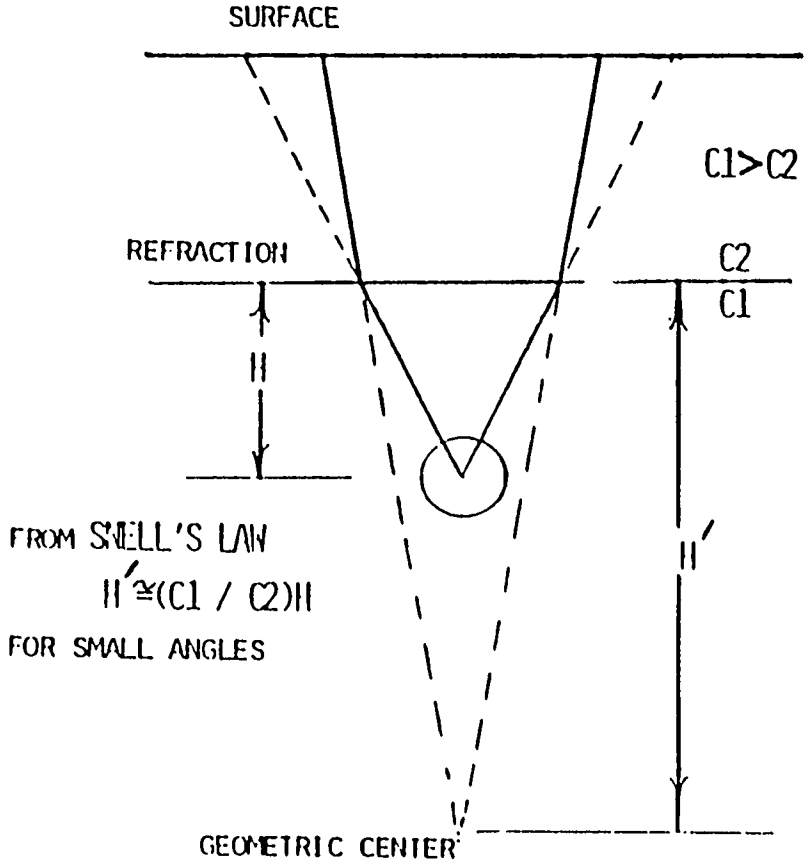


Figure 10 a. Schematic of Snell's law focussing. The solid line shows the change in radial divergence from the actual source center H below the SWL to an apparent source center H' above the SWL.

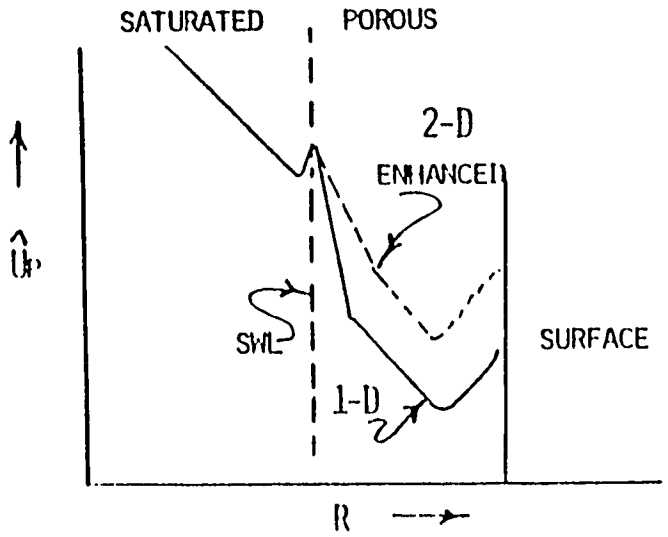


Figure 10 b. Schematic of attenuation difference between 1-D and 2-D calculations. Above the SWL the 2-D calculations show higher "enhanced" peak velocities due to the reduced radial divergence.

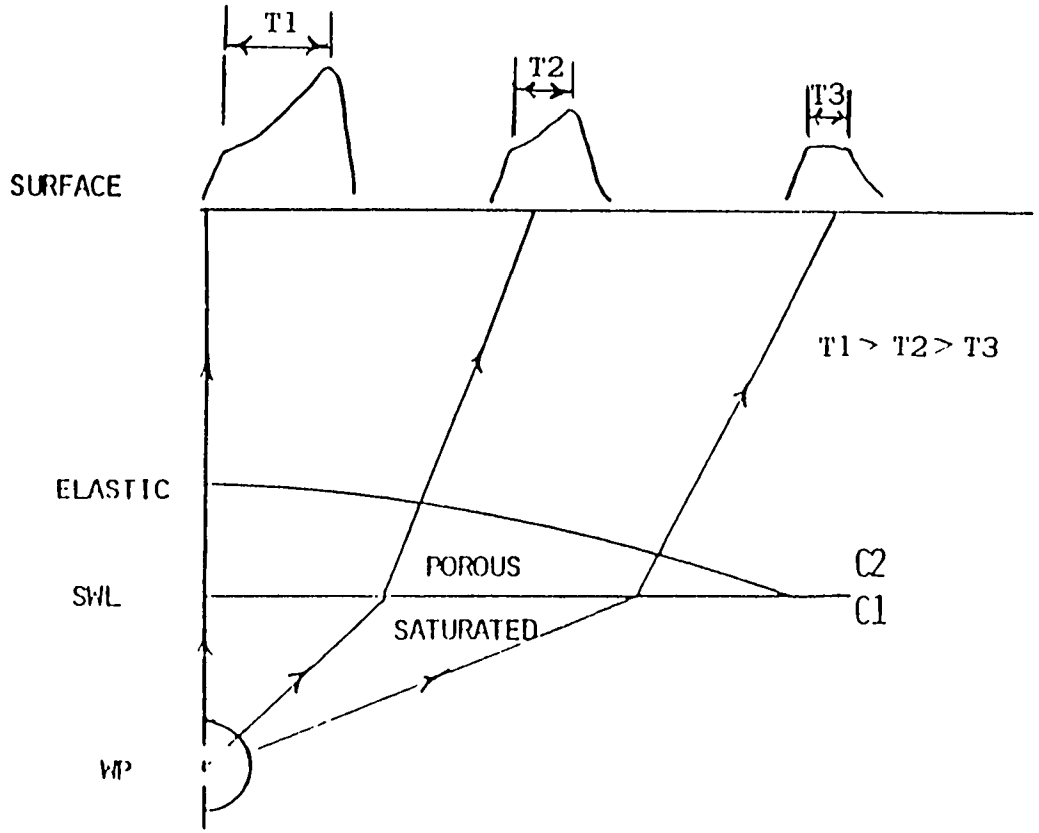


Figure 11. Schematic shows axial preference of porous crush and evidence found from surface velocity gages observed at he TYBO event. The peak of the wave travels slowly in the pore crush phase above the SWL and below the elastic curved line. Axially, the incident wave has the highest stress at the SWL than any other path. The axial stress takes longer and a greater distance for the peak to attenuate to elastic stress. Observations on TYBO showed wave forms along the surface which verified the diminishing time between elastic portions of the wave and the remnant of the plastic peak.

Residual Stress Implications due to Variations of Yield and Depth-of-Burial of Two Nearly Simultaneous Explosions

J. T. Rambo, W. C. Moss, and J. L. Levatin
Lawrence Livermore National Laboratory, P.O. Box 808, Livermore, CA 94551

Abstract

Underground tests of two nearly simultaneous explosions in the same vertical hole have often been done by placing a very low yield device below a normally buried higher yield device. However, there are economies to detonating higher yield combinations in the same hole and especially to placing the lower yield device above a normally buried higher yield device. We have calculated the residual stress fields (RSF) for various combinations of yields and vertical device separations where the lower yield device was placed above the higher yield device.

Two types of scale depth-of-burial (SDOB) criteria and various separation criteria were considered. Initially, large separation distances greater than four times the lower final-cavity radius were used to prevent contamination of tracers (nuclear chemistry requirement). Possible atypical collapse scenarios provide additional constraints that restrict the upper device to a SDOB equal to or greater than 250 $m/kt^{1/3}$. These calculations showed a poor RSF. When the nuclear chemistry constraint was relaxed (i.e., 1, 2, and 3 final-cavity radii separation), a better RSF was calculated. However, for smaller separations, our previous work suggests these closely spaced devices can develop high cavity pressures. Cavity merging, which could occur, but was not included in our previous calculations, would alleviate the high cavity pressures. Our recent calculations with closely spaced devices used a separation of 40 m, (approximately a diagnostic canister length), with various yield combinations surrounded by a generic NTS flats tuff. The close spacing required software development to merge cavities and will be discussed. Calculations that demonstrate weaknesses in the RSF will be shown. The calculations provide some general emplacement guidelines but site-specific material properties and geologies of actual events should be calculated for an appropriate containment analysis.

Material Properties



RECENT OBSERVATIONS OF MECHANICAL PROPERTIES AND MICROSTRUCTURE OF SHOCK-CONDITIONED TUFF

J.W. MARTIN, J.T. FREDRICH, and S.J. GREEN, TerraTek, Inc.
University of Utah Research Park, 420 Wakara Way, Salt Lake City, UT 84108

EXECUTIVE SUMMARY

"Shock-Conditioning" as used herein is a term used to indicate changes in geologic material resulting from the passage of an explosively driven stress wave through the material. A detailed understanding of shock-conditioning may aid the containment design of underground nuclear tests, assessment of the vulnerability of underground structures, design of tunnel support, and development of constitutive models for shock damaged media.

This paper documents the results of a research effort which focused on three related issues: (1) the effect of shock-conditioning on the physical and mechanical properties of NTS tuff; (2) the identification and quantification of microstructural damage in shock-conditioned tuff; and (3) the comparison of microstructural damage resulting from field (dynamic) versus laboratory (quasi-static) loading. Laboratory and microscopy studies performed on two suites of tuff retrieved from the P-tunnel complex prior to and immediately following the DISKO ELM event reveal that: (1) the shock-conditioning caused no significant change in physical properties (i.e. porosity and saturation); (2) the shear strength and the stiffness moduli of shock-conditioned tuff are significantly lowered for peak stresses of 200 MPa and higher; (3) this degradation is believed to be associated with measurable microstructural damage consisting of new microcracks; (4) the microstructural damage in the form of microcracks and crushed pores which is present in tuff exposed to approximate shock levels of 200 MPa and greater increases with shock level; (5) the degradation caused by shock-conditioning (i.e. dynamic loading) is greater than that caused by quasi-static laboratory loading following the postulated field-loading path; and (6) the shock-conditioned tuff shows a more homogeneous distribution of new microcracks than the laboratory-loaded samples which exhibit strain localization (microcrack coalescence along a single shear-oriented plane) for samples loaded to approximately the same peak radial stress. A clear difference between shock-conditioned and laboratory loaded samples is shown by a new technique of metal injection and microscopy analysis.

The poroelastic response of pristine versus shock-conditioned tuff during undrained uniaxial strain loading was investigated and characterized by the pore pressure coefficient (B), defined as the increase in pore pressure caused by an increase in applied mean normal stress. The material shocked to stresses of 200 MPa and greater has a B value close to unity at applied mean stresses greater than 25 MPa, whereas pristine tuff is characterized by B values close to unity only at applied mean stresses greater than 150 MPa. Thus, the tuff shocked to stresses of 200 MPa and greater is characterized by an undrained Poisson ratio close to 0.5. Testing of the pristine tuff indicated that B values at the same mean applied normal stress are lower for hydrostatic loading than for uniaxial strain loading, demonstrating the effect of shear (deviatoric) stress on deformation.

Scanning electron microscopy (SEM) of fracture surfaces reveal the occurrence of a

marked discontinuity in microstructure at shock levels of 150 to 200 MPa. Tuff shocked to stresses up to 150 MPa exhibit a cohesive matrix with little or no evidence of microcracking or pore collapse. Tuff shocked to higher stresses (greater than 150 MPa) display a high density of microcracks and a granular, poorly cohesive matrix. Damage was quantified using high resolution optical microscopy on planar polished sections whose pore space was impregnated with a low melting point alloy (Cerrosafe®). Microstructural damage in the shock-conditioned tuff is homogeneously distributed with no signs of incipient localization. The microcrack structure is anisotropic and the microcrack density increases systematically with shock level. The microstructural analysis is consistent with the mechanical data in that a dramatic increase in damage is observed for tuff subjected to shock loading to stresses of 200 MPa and higher.

Additional microscopy was performed on pristine samples which had been deformed in the laboratory following a biaxial strain path after loading in uniaxial strain to peak radial stresses of 200, 300, and 400 MPa. The data indicate that significant differences exist between field (dynamic) and laboratory (quasi-static) loading. Quantitative characterization of the microcrack structure of the laboratory-versus-field damaged samples reveals three distinct differences in the damage structure. First, the field-shocked samples contained a markedly higher density of microcracks than the laboratory-damaged samples for identical values of the peak radial stress. Second, damage is homogeneously distributed in the field-shocked tuff, but localized in shear zones in the laboratory-damaged tuff. Finally, whereas the density of microcracks increases with stress level for the field-shocked samples, the laboratory-damaged samples exhibit similar damage structures with increasing stress.

1.0 INTRODUCTION

Shock-conditioning is a term used to describe changes in geologic materials resulting from the passage of an explosively driven stress wave. Previous work related to shock-conditioning has focussed on quantifying the physical properties (density, porosity, and saturation) and ultrasonic velocity of tuff at the Nevada Test Site (NTS) as a function of distance from the working point (WP) [1,2,3]. Many of these studies showed no systematic variations in physical properties, although decreases in velocity with approach to the WP have been documented for some events [4]. In many cases, the interpretation of the data is uncertain because possible variations introduced by pre-existing lithologic contrasts were not considered.

Our preliminary study [2] demonstrated that the strength and constrained modulus of shocked tuff was less than that observed for pristine tuff, whereas the undrained Poisson's ratio was typically greater for the shocked material. Scanning electron microscopy (SEM) revealed that the microstructure of shocked tuff differs significantly from that of pristine tuff, with shocked tuff exhibiting extensive zeolite damage, microcracking, and collapsed pores. The size and frequency of fractures appeared to be a function of both the proximity to the WP and the material composition.

Here we present measurements of physical and mechanical properties for two suites of nearly saturated tuff ("shock-conditioned" and "pristine equivalent") in an attempt to quantify the effect of damage caused by an underground nuclear test. In addition, microstructural damage was directly observed using both optical and SEM techniques. Although these are standard damage assessment methods in rock mechanics, only limited analysis using these techniques have been previously applied to NTS tuff. Our objectives were to: (1) determine the effect of shock damage on physical and mechanical properties; (2) identify and quantify

damage in shocked tuff; and (3) determine differences in damage resulting from field (dynamic) versus laboratory (quasi-static) loading. The primary goal of the research is to facilitate the evaluation of containment potential of possible sites for future underground nuclear detonations. A detailed understanding of shock-conditioning will also aid the assessment of the vulnerability of underground structures, the design of tunnel support, and the development of constitutive models for shock-conditioned media.

To meet these objectives, a test program was designed to specifically assess shock-conditioning using standard techniques and new innovative approaches consisting of microstructural observations of the pore structure and the measurement of induced pore pressure during mechanical testing. The material requirements consisted of obtaining a homogeneous suite of NTS tuff which had been dynamically loaded in the field to a range of stress levels along with their pristine counterparts. The pristine material fulfilled three purposes. First, the effect of slight lithologic variations which may mask the influence of shock-conditioning were identified from similar tests conducted on the pristine material. Second, an understanding of the microstructure of the preshocked material was used to assess damage in the field-shocked samples. Finally, selected pristine samples were quasi-statically loaded along a strain path intended to simulate that imposed on the field-shocked samples, and the resultant damage was analyzed and compared to the field-shocked samples.

The test program was divided into three phases. The first phase involved routine physical property measurements. The second phase involved routine undrained uniaxial strain tests with a specially designed transducer for measuring the induced pore pressure. The third phase consisted of microstructural observations of shocked and pristine material using standard (SEM) techniques and a new impregnation procedure to in-fill the pore structure of the undamaged and damaged (both field and laboratory induced) samples with a metal alloy. Analysis of the metal-impregnated tuff was performed using laser scanning confocal microscopy (LSCM). Material damage was quantified by counting observed microfractures (low-aspect ratio pores) and statistically determining fracture density. The complete testing program is described elsewhere [5].

2.0 TEST MATERIAL AND PROCEDURES

A suite of shock-conditioned core from P-tunnel (DISKO ELM event) was used for this investigation. Seven intervals of shocked core from U12p.03 RE-3 (with approximate field shock levels of 50, 75, 100, 150, 200, 250, and 300 MPa) and their pristine equivalents from U12p.03 IH-2 and U12p.03 GI-2 were obtained (Table 1) from dominantly zeolitized tuff beds (Figure 1) [6]. The orientation of the post-shot drill hole (RE-3) is nominally horizontal (2° above horizontal) and elevations of the two pre-shot drill holes and their proximity to the DISKO ELM WP are shown in Figure 2 [6].

Undrained mechanical tests following the uniaxial strain path ($\varepsilon_{radial}=0$) were conducted on 50 mm diameter by 100 mm long cylindrical samples of the shock-conditioned and pristine material. Samples were tested with their *in situ* moisture content (94.2% to 99.7% saturation) and induced pore pressure was measured using a miniaturized transducer (note that the conventional effective stress law, P_c effective = P_c applied - αP_p, with $\alpha=1$, [e.g. 7] is assumed). Test samples were placed between polished steel endcaps (of the same diameter as the test sample), jacketed with polyurethane to prevent the confining fluid (odorless mineral spirits) from entering the pore space, instrumented with strain-gauged axial and radial cantilever-beam transduc-

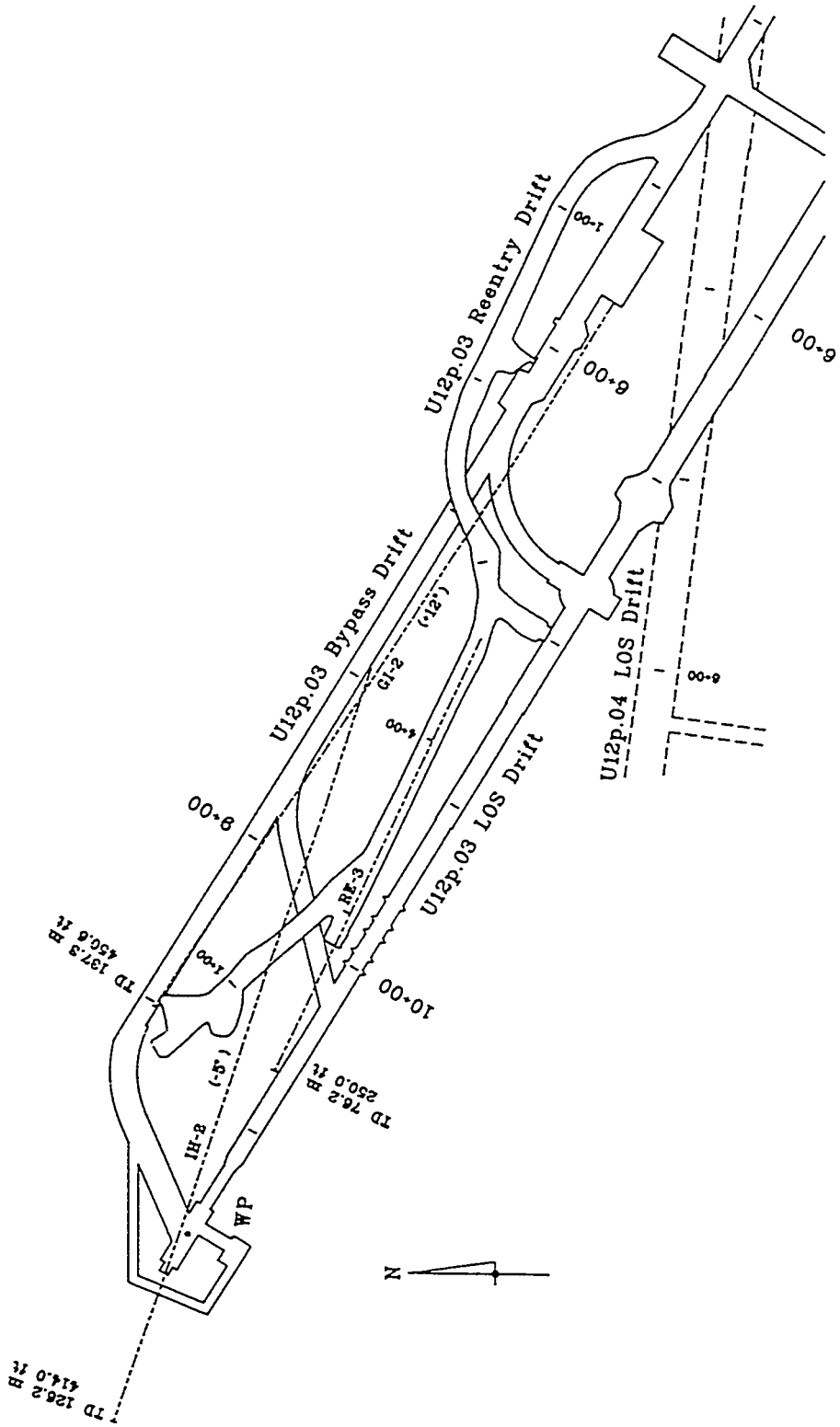


Figure 1. Location of Drill Holes U12p.03 IH-2, GI-2 and RE-3 [6].

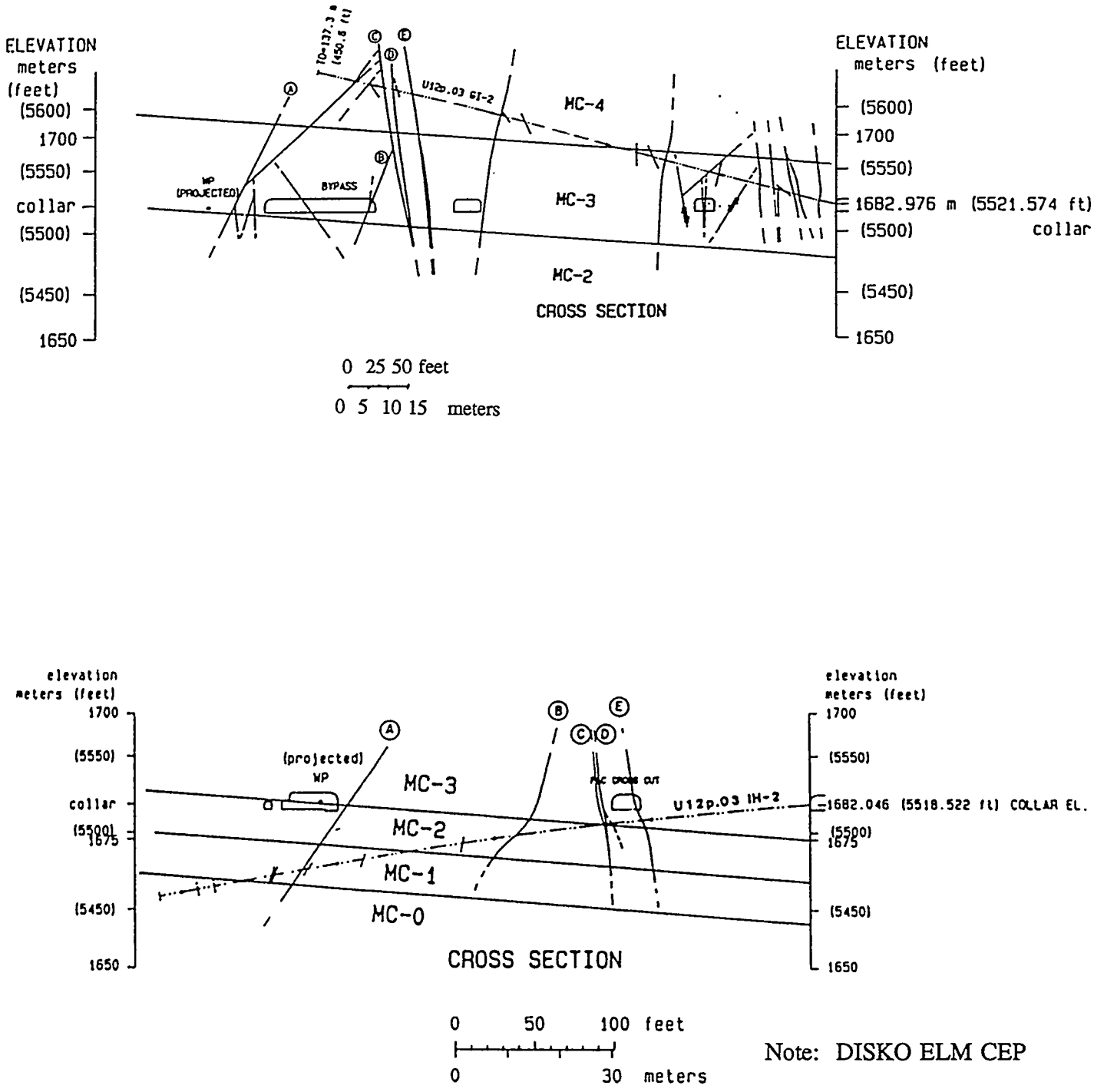


Figure 2. Elevations of drill holes U12p.03 IH-2 and GI-2 [6].

Table 1. Shock-conditioned material and their pristine equivalents from U12p.03.

Corehole	Depth Interval (ft)	Approximate Stress Level (MPa)
U12p.03 RE-3	NA	50
U12p.03 IH-2	14.2-15.2 18.2-19.3	Pristine
U12p.03 RE-3	NA	75
U12p.03 IH-2	50.3-50.8 51.5-52.2	Pristine
U12p.03 RE-3	NA	100
U12p.03 IH-2	56.7-57.2 61.7-62.7	Pristine
U12p.03 RE-3	NA	150
U12p.03 IH-2	76.9-77.4 77.9-78.6	Pristine
U12p.03 RE-3	NA	200
U12p.03 GI-2	127.9-128.9 129.6-130.6	Pristine
U12p.03 RE-3	NA	250
U12p.03 GI-2	103.9-104.7 106.0-106.6	Pristine
U12p.03 RE-3	NA	300
U12p.03 GI-2	97.2-97.8 99.7-100.5 101.9-102.5	Pristine

ers, and placed inside a pressure vessel equipped with an internal load cell. The uniaxial strain condition was applied by increasing the axial stress such that a constant axial strain rate of 10^{-4} s^{-1} was maintained while the confining pressure was servo-controlled to maintain an average of zero radial strain along two perpendicular directions. Unloading to a hydrostatic stress state occurred in uniaxial strain. A small number of additional tests in which the uniaxial strain loading was followed by biaxial strain unloading were conducted on the pristine material. During the biaxial strain unloading, the confining pressure was reduced while the axial stress

was varied such that the condition $\Delta\varepsilon_{axial}=0$ was maintained (note that the condition $\Delta\varepsilon_{radial}=0$ did not apply during the unloading).

Fresh surfaces for SEM were prepared by breaking the sample either by hand or with a chisel. Because the existence and properties of microcracks are more readily identified via microscopy on plane polished sections, rather than on rough fracture surfaces, additional characterization was performed using optical microscopy. To quantify damage, observations were made on pristine and shocked tuff following impregnation with Cerrosafe® metal [8]. Cerrosafe® consists of 42.5% Bi, 37.7% Pb, 11.3% Sn, and 8.5% Cd, has a melting point range from 71.1 to 87.8°C, and is solid at room temperature. Dried, heated and evacuated tuff samples were submerged in the molten metal which, with a surface tension of 400 mN/m, penetrates cracks with apertures of only 0.8 μm under a pressure of 10 MPa [8].

The central portion of the field-shocked and laboratory-damaged samples were cut in two orthogonal directions (perpendicular and parallel to the core axis), polished using 600 grit silicon carbide paper, and photographed. Detailed analysis was performed using high resolution optical microscopy (laser scanning confocal microscopy - LSCM). The primary advantage of LSCM for the present study is that the Cerrosafe® metal used to impregnate the pore space fluoresces when illuminated by a laser, whereas the rock matrix is only weakly fluorescent. Following preliminary examination, sample surfaces were etched with hydrofluoric acid in order to eliminate fluorescence generated by the solid rock matrix. A parallel study was performed on samples of pristine tuff which were subjected to uniaxial strain loading followed by biaxial strain unloading in order to directly compare damage induced by dynamic (field) loading versus quasi-static (laboratory) loading.

For some samples, the density of microcracks was quantified using standard stereological techniques [9]. Measurements were made on mylar crack tracings prepared from photomosaics taken at magnifications ranging from 6 to 7×. Additional measurements were made at a magnification of 17 to 27×. The test grid for the low magnification photomosaics of the field-shocked samples consisted of 32 to 70 parallel lines of 18 mm to 34 mm length and spaced by 0.35 mm to 0.42 mm. The test grid for the low magnification photomosaics of the laboratory-damaged samples consisted of 32 to 70 parallel lines of 20 mm to 40 mm length and spaced by 0.42 mm to 0.45 mm. The test grid for the higher magnification crack tracings consisted of 32 to 70 parallel lines with dimensions of 3.8 mm to 7.85 mm and spaced by 0.09 mm to 0.15 mm. The number of crack intersections for each line was determined, and a set of 32 to 70 such measurements was then statistically analyzed to determine the mean and standard deviation.

3.0 RESULTS

3.1 Lithology, Mineralogy and Physical Properties

The tuff may be broken down into four compositionally distinct textures: groundmass, pumice fragments, phenocrysts, and lithic fragments. The groundmass (i.e., fine-grained matrix material) was originally composed of vitric ash and pumice fragments less than 1 mm in size. Depending upon the severity of the devitrification, the vitric material (ash and pumice) may be

partially to completely altered to zeolite, clay, and/or silica. Pumice fragments, ranging in size from one to tens of millimeters, were originally frothy, highly porous vesicular glass fragments which, like the vitric ash, is susceptible to devitrification and alteration. Phenocrysts are conspicuous crystals (typically quartz, potassium and plagioclase feldspar, biotite, and amphibole) that are relatively large with respect to the groundmass and are derived from the source of the ash and pumice. Lithics are fragments of the surrounding country rock incorporated into the tuff during deposition.

Lithologies determined by optical microscopy for the shocked and pristine tuff are shown in Figure 3. Lithologies determined for the 50, 75, 150, and 250 MPa shocked samples agree well with those determined for their pristine counterparts. However, the 100, 200, and 300 MPa shocked samples contain fewer lithics and phenocrysts and more pumice and groundmass than their pristine equivalents. Also, note that both the 150 and 200 MPa shocked samples contain higher amounts of groundmass (>70%) than the other test samples. The 150 MPa shocked sample is unique for two reasons. First, this sample contains more groundmass than all of the other test samples. Second, the groundmass of this sample is significantly "harder" (more difficult to scratch with a knife) than that of the other samples and may be partially silicified.

The texture of the samples shocked to lower stresses (50, 75, 100, and 150 MPa) differs substantially from that of the samples shocked to the three highest stresses (200, 250, and 300 MPa). Samples stressed to the lower levels exhibit a cohesive, moderately to well indurated matrix whereas the matrix of the samples subjected to high stresses is granular, highly friable, and poorly to moderately indurated. With the exception of the 300 MPa shocked sample, the tuffs are classified as zeolitized-crystal tuff (calcalkaline). The 300 MPa shocked sample

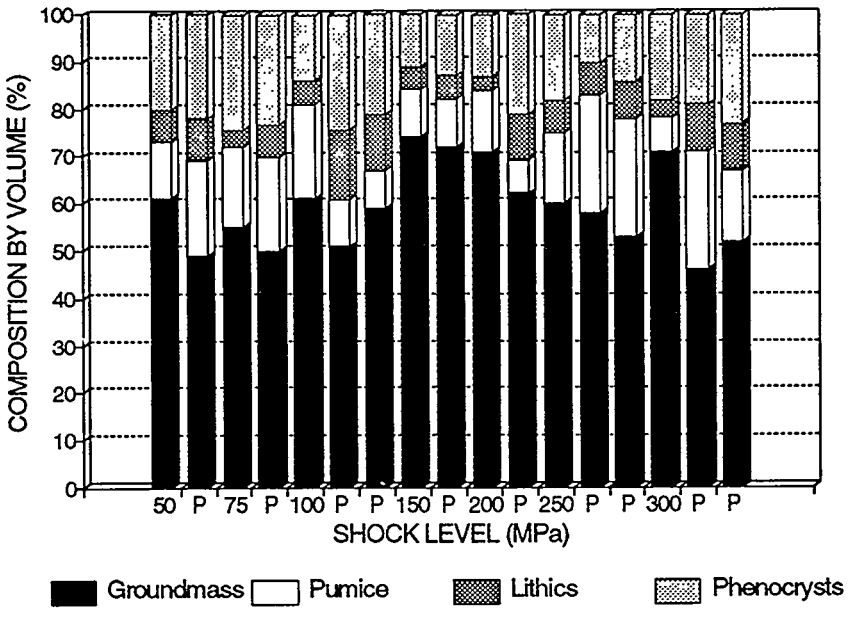


Figure 3. Lithologic profile of shocked and pristine equivalent (P) tuff.

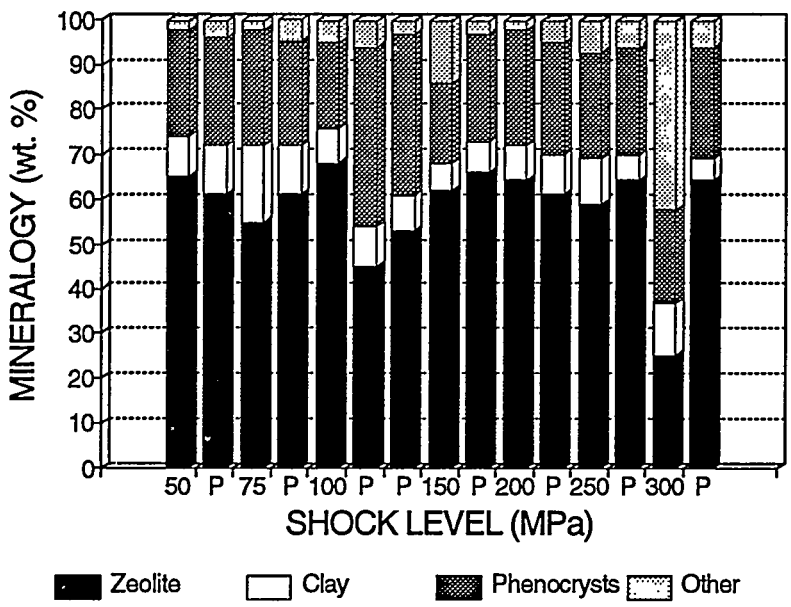


Figure 4. XRD mineralogy of shocked and pristine (P) tuff. Note consistent zeolite content (except for the 300 MPa shocked sample).

contains a high percentage of unaltered to partially altered glass shards and is classified as a vitric tuff.

The P-tunnel material exhibits good mineralogic correlation (see Figure 4) with one exception: the 300 MPa shocked sample has a significantly lower zeolite content (25%) and higher amorphous content (41%) than all of the other intervals. Zeolite content for the 300 MPa pristine equivalent and the remaining six intervals ranges from 45% to 68%, and averages 61±6%.

Slightly higher phenocryst content appears to be correlated with a lower zeolite content. This is exemplified by the pristine sample corresponding to the 100 MPa shocked tuff (56.7 ft), which has a low zeolite content of 45% and a fairly high apparent phenocryst content of 40% (apparent phenocryst content is defined as the sum of the quartz, feldspar and biotite). In contrast, the 100 MPa shocked sample contains a higher zeolite content of 68% and a lower apparent phenocryst content of 19%. Excluding the 300 MPa shocked sample, the remaining samples fall within these limits.

Other mineralogic constituents such as clay and secondary silica are also consistent amongst the intervals. Clay content (smectite) ranges from 5% to 17% and averages approximately 9±3% while secondary silica (Opal-CT) averages approximately 4±2%. Macroscopic examination of the 300 MPa shocked core indicates a high density of vitric fragments, thus suggesting that the amorphous material of the 300 MPa sample is probably unaltered to moderately altered volcanic glass. Possibilities for the amorphous content of the remaining intervals are poorly crystalline secondary silica (Opal-A), amorphous oxides (limonite, organics), or material below the detection limit of the XRD apparatus.

Grain densities determined via water pycnometry (Figure 5) for both the shocked-conditioned and pristine material are consistent. This is expected since the mineralogies determined from XRD (Figure 4) are relatively consistent for tuff with the exception of one sample.

The grain densities determined for the 300 MPa shocked sample and pristine counterpart are virtually identical. This is somewhat surprising since the XRD mineralogies are quite dissimilar. This suggests that the amorphous material (presumably volcanic glass), which makes up the difference in zeolite content relative to the other intervals, may have a grain density similar to that of the zeolite clinoptilolite. This is noteworthy since silicic glass has a grain density of approximately 2.4 gm/cm^3 whereas clinoptilolite has a reported density of 2.16 gm/cm^3 [10]. The density of clinoptilolite has been disputed in the past [11]; our data may indicate a clinoptilolite density between 2.3-2.4 gm/cm^3.

The physical properties of the shocked and pristine tuff are illustrated with respect to shock level in Figures 6 to 9. Moisture content and porosity for the shocked samples varies randomly from 15.0% to 24.6% and 31.4% to 44.2%, respectively. Similar fluctuations are evident for the pristine equivalents. This coincides with results from some previous studies [2,12]. The variation is probably more likely due to slight changes in lithology as opposed to an influence from shock loading. Also, the discrepancy between the saturation and calculated air-void content for the shocked and pristine samples appears to be slightly larger at shock levels less than 200 MPa (Figures 8 and 9).

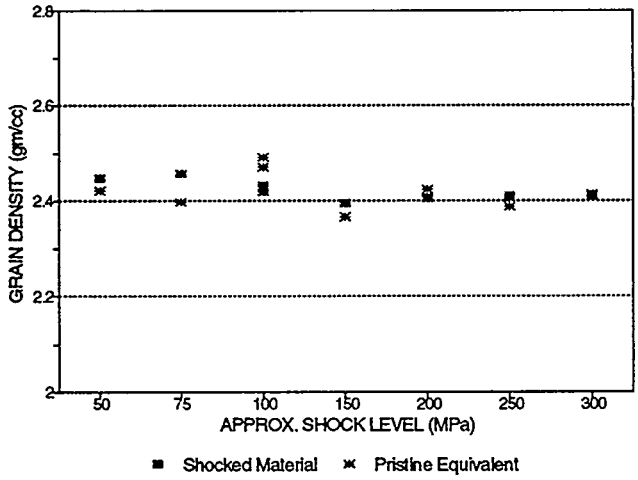


Figure 5. Grain density of shocked and pristine tuff from U12p.03.

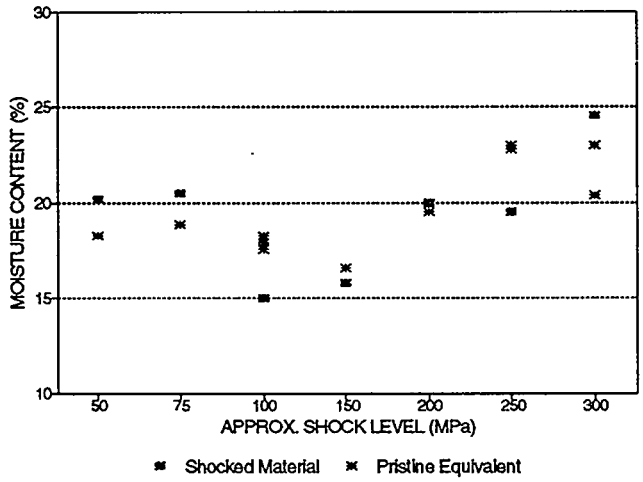


Figure 6. Water content of shocked and pristine tuff from U12p.03.

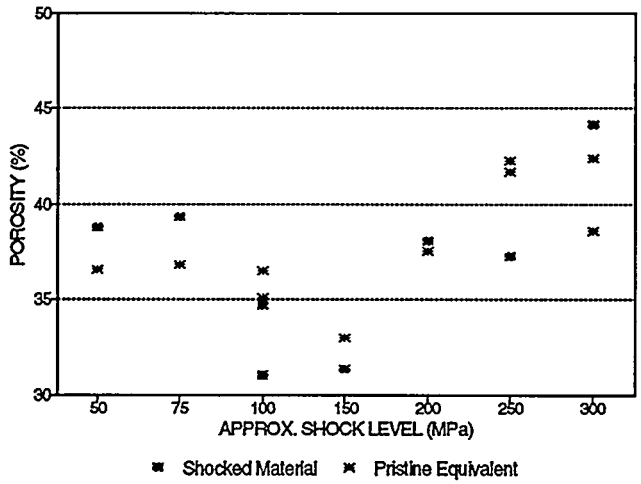


Figure 7. Porosity of shocked and pristine equivalent tuff from U12p.03.

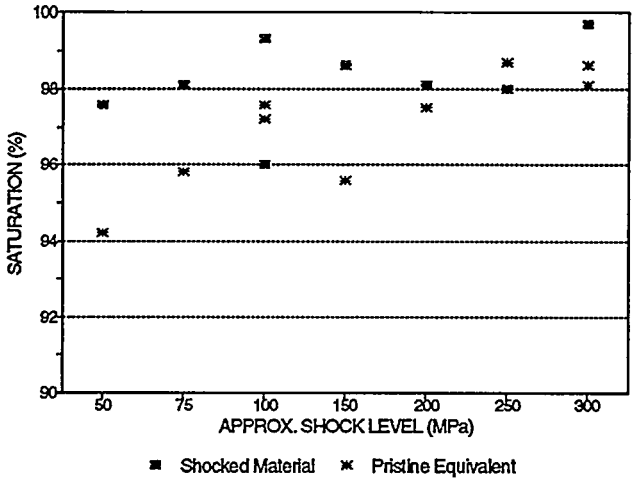


Figure 8. Saturation of shocked and pristine equivalent tuff from U12p.03.

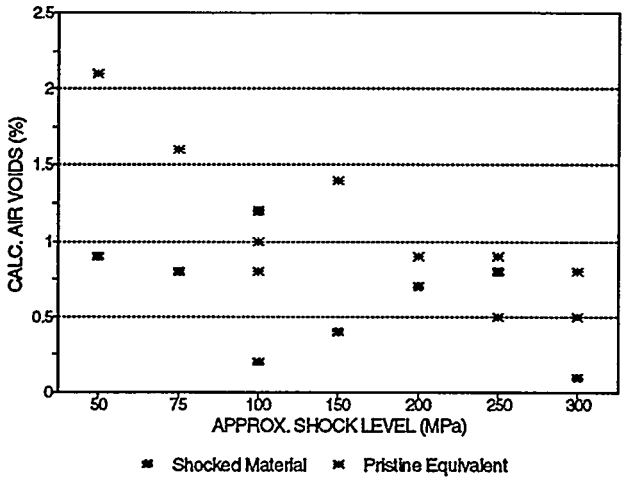


Figure 9. Air-void content of shocked and pristine equivalent tuff from U12p.03.

3.2 Mechanical Properties

Uniaxial Strain: The mechanical behavior determined from uniaxial strain loading/unloading for the pristine equivalent material is similar with the exception of the 100 and 150 MPa samples (Figures 10 and 11). The shock-conditioned material exhibits significant variability. Material shock-conditioned to stresses below 200 MPa is similar to the pristine material. The stress difference-confining stress response (Figure 11) of the material shocked to 100 and 150 MPa is similar to that observed for the material shocked to lower levels; however, material strength is significantly greater. Samples shock-conditioned to stresses of 200 MPa and greater are characterized by a significantly degraded strength and higher undrained Poisson ratio.

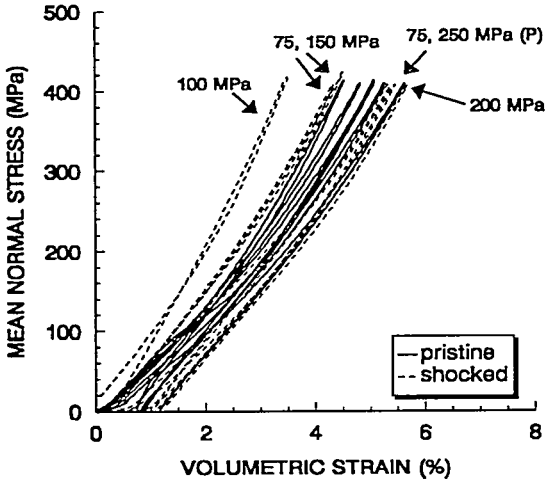


Figure 10. Mean applied normal stress versus volumetric strain for pristine (P) and shocked material, loaded in uniaxial strain.

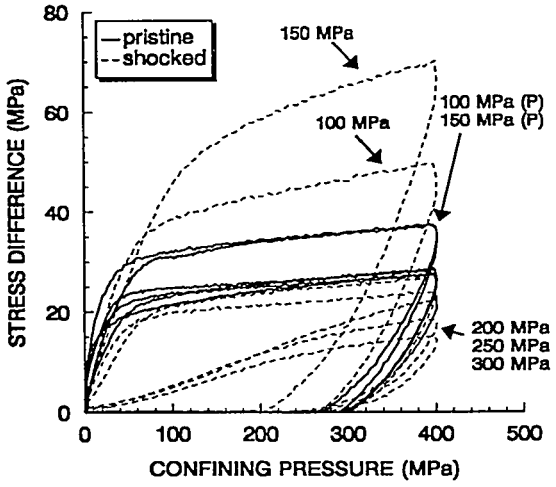


Figure 11. Stress difference versus applied confining pressure for pristine (P) and shocked material, loaded in uniaxial strain.

Additional insight may be obtained if one considers the material response in terms of effective stress, defined as σ_{ij}-$\alpha P_P \delta_{ij}$, where σ_{ij} is the applied stress, α is a constant which is approximately equal to one, P_P is the pore pressure, and δ_{ij} is the Knonecker delta. For α=1, the principal effective stress components are σ_1-P_P, σ_2-P_P, and σ_3-P_P, where σ_1, σ_2, and σ_3 are the total applied principal stresses. Note that the magnitude of the stress difference σ_1-σ_3 is the same regardless of whether one considers effective or total stress. The volumetric strain response of stratigraphically pristine matches for the 100 MPa and 150 MPa shocked material, when considered in terms of effective stress (Figure 12), is now seen to deviate substantially from that observed for the other depth intervals, consistent with what one might expect based on the greater differential stress supported by this material (Figure 11). Similarly, that the material shocked to stresses of 200 MPa and above is characterized by a significantly enhanced compressibility is readily apparent when the volumetric strain data is analyzed in terms of effective mean normal stress (Figure 13).

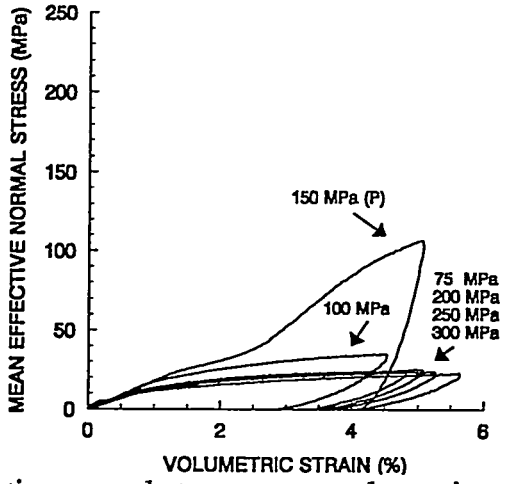


Figure 12. Mean effective normal stress versus volumetric strain for pristine material loaded in uniaxial strain.

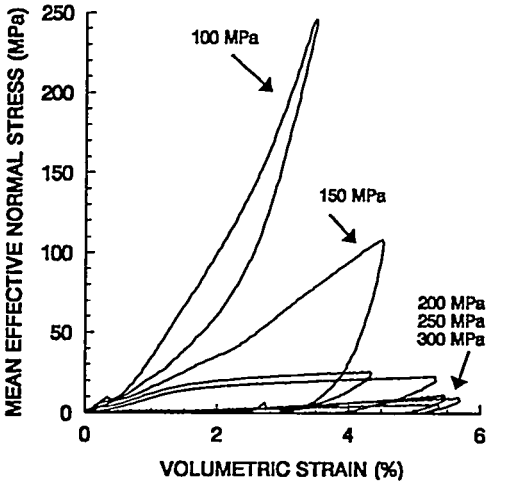


Figure 13. Mean effective normal stress versus volumetric strain for shocked material loaded in uniaxial strain.

The differences in mechanical behavior are thus more appropriately considered in the context of poroelasticity theory [13]. For undrained deformation, a fundamental parameter is the Skempton ratio B (a.k.a. pore pressure coefficient), defined as the increase in pore pressure P_P due to an increase in applied pressure P_C [14]. For loading in uniaxial strain, B is defined as

$$B=\frac{\partial P_P}{\partial \sigma_N} \tag{1}$$

where σ_N is the mean normal stress and equal to $\frac{1}{3}(\sigma_1 + 2\sigma_3)$.

The difference in mechanical behavior for the pristine versus shocked samples is highlighted when data are analyzed to determine the Skempton ratio B as a function of applied pressure. The pristine samples (Figure 14) show essentially identical behavior, with the exception of the 150 MPa shocked equivalent. Pore pressure coefficients close to 1 are not realized until applied mean normal stresses of about 200 MPa. Duplicate testing of the 150 MPa pristine equivalent material suggests that the lower B values observed for this material are genuine and not an artifact caused by, for example, inadequate communication between the sample and transducer. Duplicate tests performed on samples from four other depth intervals indicate excellent repeatability. The large variation in B observed at applied mean normal stresses of 0-25 MPa is attributed to the slight variations in original saturation (Figure 8) and the averaging procedure used to calculate B. For incompletely saturated media, no pore pressure buildup can occur until the air-filled porosity is closed; this will yield deceptively low B values over the stress range 0-25 MPa.

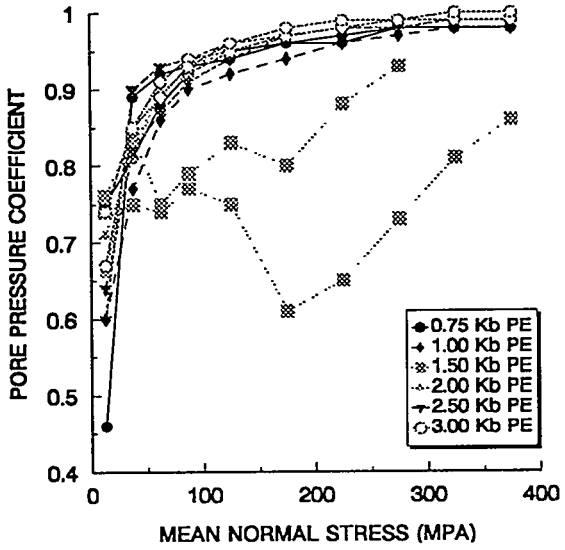


Figure 14. Pore pressure coefficient versus mean normal stress for pristine material.

Behavior of samples field-shocked to stresses of 200 MPa and greater differs markedly from that observed for the pristine material. Pore pressure coefficients close to 1 are realized at applied mean normal stresses as low as 25-50 MPa (Figure 15). Samples shocked to stresses of 50 and 75 MPa show behavior similar to that observed for the pristine samples. Samples shocked to intermediate stresses of 100-150 MPa show lower B values. The samples field-shocked to stress levels of 200 MPa and greater exhibit poroelastic behavior characteristic of

unconsolidated sediments at applied stresses significantly less than those observed for the pristine material. The implications of the higher B values for samples field-shocked to stresses of 200 MPa are that at the same applied confining stress, preshocked material will see a lower effective confining stress than pristine material, and thus possibly exhibit a lower strength than the pristine material.

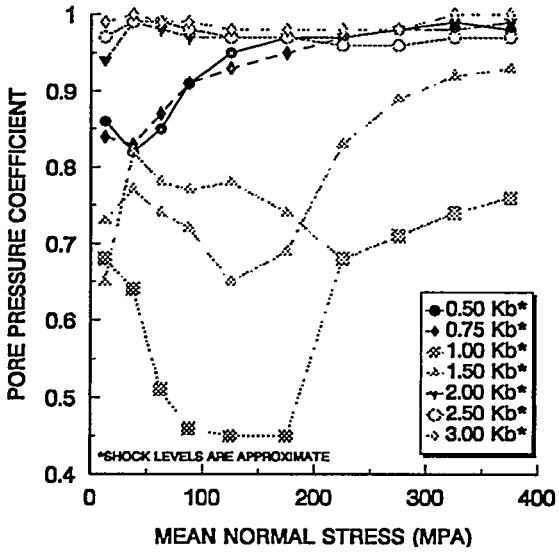


Figure 15. Pore pressure coefficient versus mean normal stress for shocked material.

Biaxial Strain: To qualitatively compare the effects of laboratory (quasi-static) versus field (dynamic) loading, several pristine samples were loaded in uniaxial strain and then unloaded along the biaxial strain path ($\Delta e_1=0$). The biaxial strain path is considered similar to that occurring following an underground nuclear test [15]. Through-going shear fractures formed in the samples unloaded along the biaxial strain path after uniaxial strain loading to peak applied confining pressures of 200, 300, and 400 MPa. Mechanical data are summarized in Figures 16 and 17.

The biaxial strain unloading curve lies below the uniaxial strain loading curve in stress difference-confining pressure space; however, the unloading curve lies above the loading curve in stress difference-effective confining pressure space (Fig. 17). Because the uniaxial strain path follows the yield surface (which lies below the failure surface), the occurrence of shear localization (failure) can only be rationalized by consideration of the effective stress behavior.

3.3 Microstructural Observations

Scanning Electron Microscopy (SEM) of Field-Shocked Tuff: The microstructure of the field-shocked tuff subjected to approximate stresses of 50 to 150 MPa is characterized by large (>100 microns) intact pores, a cohesive fine-grained groundmass, and well formed zeolite crystals (clinoptilolite) which are typically intergrown and line the perimeter of the pores. Secondary silica (opal-CT) occurs in the four samples subjected to field stresses of 150 MPa and less; however, the mode of occurrence and relative abundance varies considerably between

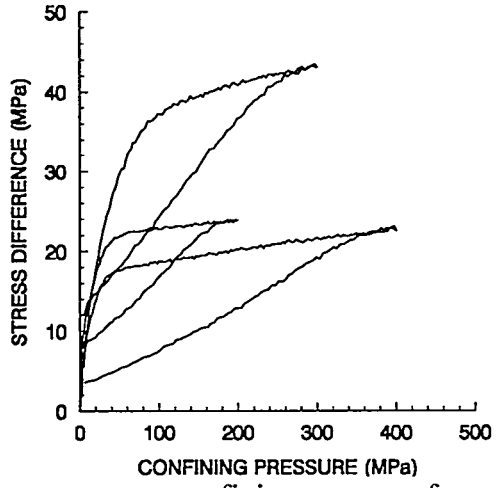


Figure 16. Stress difference versus confining pressure for uniaxial strain load-biaxial strain unload.

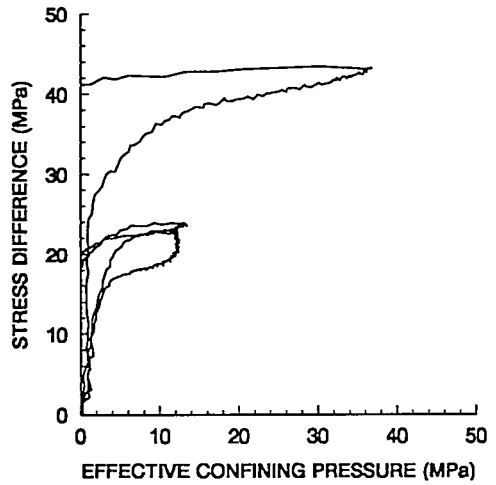


Figure 17. Stress difference versus effective confining pressure for uniaxial strain load-biaxial strain unload.

the samples. For example, the 50 MPa sample exhibits minor amounts of secondary silica in some pores, whereas the 75 MPa sample contains some regions in which pores are dominated by secondary silica. Secondary silica appears more uniformly distributed in both the 100 MPa and the 150 MPa samples and occurs as cement (Figure 18). Minor damage in the form of fractures is observed in the 75 MPa and 100 MPa samples. Fractures extending through large pores and into the groundmass are present in the 75 MPa sample, and cracked zeolite crystals are present in a few pores in the 100 MPa sample. In both cases, the damage is minor and may be an artifact of sample preparation. No obvious damage is observed in either the 50 or 150 MPa samples.

Substantial differences in the microstructure are found for the shocked samples subjected to stresses of 200, 250, and 300 MPa. Figure 19 illustrates the most obvious microstructural differences in the samples subjected to low versus high field stresses. The three samples

subjected to higher stresses (≥200 MPa) exhibit a granular, poorly cemented matrix and lack pores larger than 50 microns in diameter. The matrix appears to be fairly cohesionless. Pores (Figure 19) lack the intergrown chain-like structures formed by zeolites which are observed in the shocked samples subjected to field stresses ≤150 MPa. Zeolites in the samples shocked to peak stresses in excess of 200 MPa are fragmented and appear, along with debris from the surrounding groundmass, to in-fill pores. Fractures are commonly observed in the matrix of the 200, 250, and 300 MPa shocked samples. In a few areas, fractures have propagated through phenocrysts and lithic fragments and extended through the groundmass. Larger scale fractures are more prevalent in the 200 and 250 MPa samples as compared to the 300 MPa sample. This difference may be due to the vastly different composition of the 300 MPa shocked core which is a vitric tuff containing unaltered to moderately altered glass shards (Figure 4).



Figure 18. SEM micrograph of secondary silica (opal-CT) dominating a pore space in the 150 MPa shocked sample.

Note that the validity of the SEM damage observations are limited by the sample preparation technique which may induce additional damage. Depending upon the competency of the sample, fresh surfaces for SEM are obtained by either breaking the sample by hand or with a chisel. Thus, the path of the exposed fracture surface may be influenced by the pre-existing microcracks.

Optical Microscopy of Field-Shocked and Laboratory-Damaged Tuff

Field-Shocked Samples. Impregnation of the samples with Cerrosafe® metal reveals the presence of fractures to the naked eye. At this scale, there is a clear absence of fractures in samples subjected to stresses up to 150 MPa, whereas fractures are common in samples shocked to stresses of 200 MPa and greater. There is an apparent increase in fracture density with increasing stress level for samples shocked to stresses of 200 MPa and greater. Also, fractures clearly propagate through competent fragments such as lithics. As previously noted, these microcracks were not evident either during macroscopic examination of the whole core nor during SEM examination of rough fracture surfaces.

Polished sections oriented both perpendicular and parallel to the core axis for the tuff samples subjected to the three highest shock levels (200, 250, and 300 MPa) were studied in detail using LSCM. For comparison, the sample subjected to a stress of 150 MPa was also analyzed.

The pore morphology in the 150 MPa sample differs markedly from that present in the 200, 250, and 300 MPa samples. There is a marked absence of fractures in the 150 MPa sample, whereas fractures dominate the porosity of the 250 MPa sample. Porosity in the 150

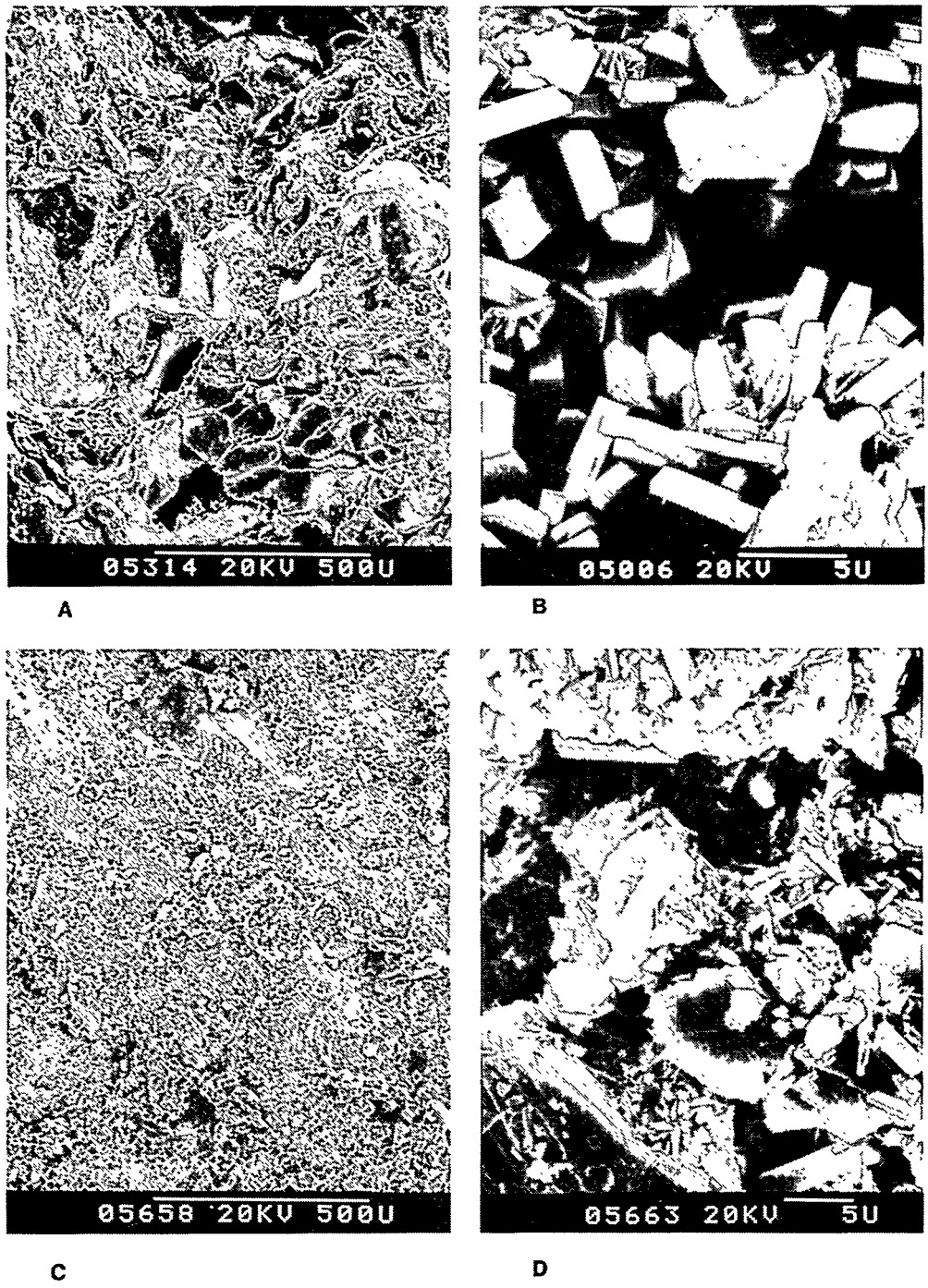


Figure 19. Scanning electron micrographs illustrating microstructural differences of shocked and pristine tuff. The typical microstructure of pristine tuff and tuff shocked to 150 MPa is shown in (A) and (B). Pores larger than 100 microns across are evident in the pristine material (A). The lack of damage in samples stressed to ≥150 MPa is apparent in this pore containing intact well-formed prismatic-tabular crystals (clinoptilolite) and extremely small bladed secondary silica (B). In contrast, the microstructure of tuff subjected to field stresses of 200 MPa and higher exhibit a granular friable matrix (C) lacking large pores. Zeolite fragments and groundmass debris infill pores (D), which show signs of collapse.

MPa sample is dominated by high aspect ratio pores, many of which are larger than 100 microns. Porosity in the 200 MPa sample is a combination of both high aspect ratio pores and low aspect ratio microcracks. Porosity in the 250 and 300 MPa samples is dominated by low aspect ratio microfractures. The microcrack distribution in the 250 and 300 MPa shocked samples is clearly anisotropic, with microcracks preferentially oriented at approximately 30° to the core axis.

Damage in the samples subjected to field stresses of 200, 250, and 300 MPa was quantified using stereological techniques. As noted above, the microcrack structure of the field-shocked samples exhibits a pronounced anisotropy oblique to the axis of the core. The orientation for the first set of measurements was chosen such that the measured crack density would be maximized, and the second set of measurements was performed in a direction perpendicular to the first set. Note that since the core was unoriented, the exact alignment of these two sets of measurements in space is unknown. That the preferred orientation of cracks in the field-shocked samples is oblique to the axis of the core (which is oriented normal to the shock wave front) is difficult to rationalize since crack propagation in rocks generally occurs in Mode I [7]. The reason for this is unknown, but such a distribution may possibly result from anisotropy in the pre-existing microstructure.

The crack density data obtained from the tracings (Figure 20) is summarized in Table 2. Also shown in Table 2 is the approximate crack aperture, determined by averaging measurements of crack width made at random. Both the density and anisotropy of microcracks increases with stress level (Figure 21). The average crack aperture determined for the sample loaded to 300 MPa is markedly smaller than that found for the samples stressed to 200 and 250 MPa; this may in part be due to the differing initial composition and microstructure of the 300 MPa sample.

Table 2. Crack density data for field-shocked samples (magnification: 6 to 7×)

Sample ID	Crack Density (mm^{-1})		Aperture Range (μm)	Estimated Average Aperture (μm)
	O1*	O2*		
200 MPa	0.43 ±0.12	0.37 ±0.14	11 to 166	49.7 (19 observations)
250 MPa	0.81 ±0.14	0.55 ±0.19	14 to 195	47.6 (23 observations)
300 MPa	1.32 ±0.22	0.57 ±0.14	14 to 66	30.0 (20 observations)

* O1 = Orientation of traverse normal to the major alignment of microcracks
O2 = Orientation perpendicular to O1

Laboratory-Damaged Tuff: A parallel study was performed on the samples of pristine tuff which were subjected to uniaxial strain loading followed by biaxial strain unloading in order to directly compare damage induced by dynamic (field) versus quasi-static (laboratory) loading. The shear zones formed during the biaxial unload are characterized by a high density of micro-

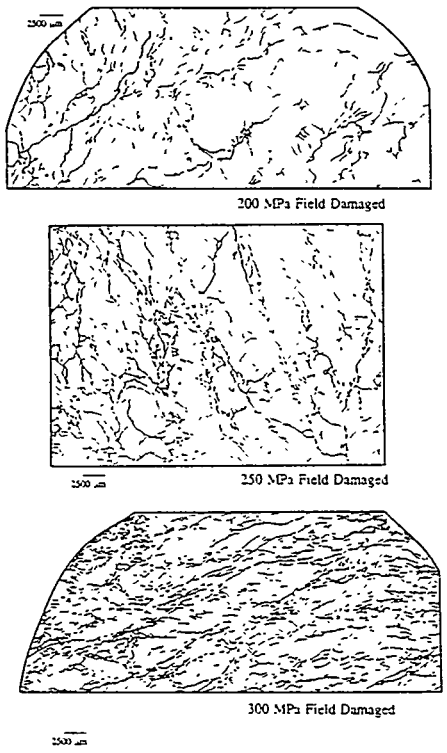


Figure 20. Fracture traces from planes perpendicular to the shock front. Tracings are not oriented and note equidimensional porosity is not shown.

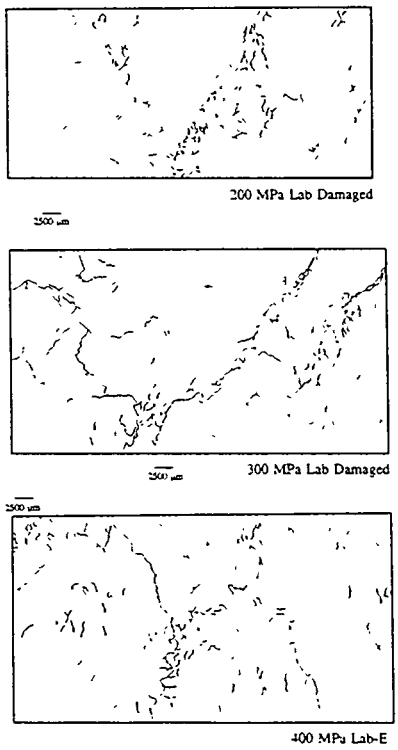


Figure 22. Fracture traces of laboratory-damaged samples. Equidimensional porosity is not shown.

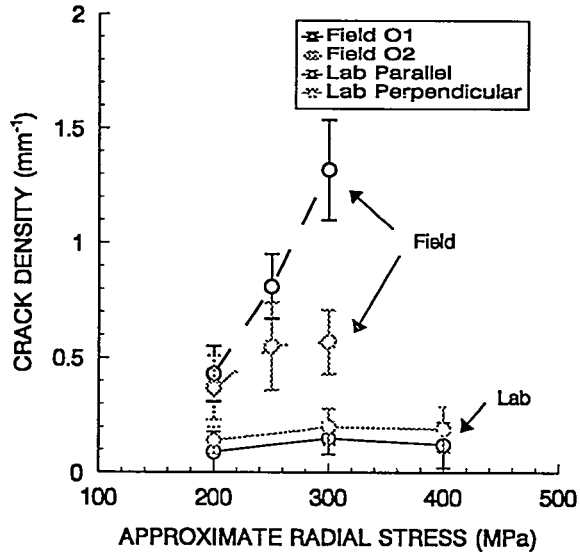


Figure 21. Fracture density as a function of stress for field and laboratory-damaged tuff.

cracks, many of which propagate through lithic fragments. Microcracks are rarely observed to propagate through lithics outside of the shear zone. There is no strong correlation between crack density and peak radial stress for the laboratory-damaged samples (Figures 21 and 22 and Table 3). The marginally higher degree of damage in the 300 MPa sample may be attributable to a variance in composition relative to the other laboratory tested samples (Figure 3).

Table 3. Crack density data for laboratory-damaged samples (magnification: 6×)

Sample ID	Crack Density (mm^{-1})		Aperture Range (μm)	Estimated Aperture Average (μm)
	Parallel to Loading Axis	Perpendicular to Loading Axis		
200 MPa	0.09 ±0.09	0.14 ±0.06	21 to 30	24.9 (8 observations)
300 MPa	0.15 ±0.07	0.20 ±0.08	7 to 180	46.2 (21 observations)
400 MPa	0.12 ±0.10	0.19 ±0.10	15 to 128	48.9 (20 observations)

4.0 DISCUSSION AND CONCLUSION

4.1 Effect of Shock-Conditioning on Physical and Mechanical Properties

The results of the laboratory test program comparing the properties of shock-conditioned and pristine tuff clearly indicate that the passage of the shock wave with a stress level of 200 MPa and greater generated by the underground detonation of a nuclear device significantly alters the properties of NTS tuff. Whereas the physical properties of the shock-conditioned tuff do not vary systematically in comparison to those characteristic of the pristine tuff, the mechanical properties (modulus, strength) of tuff subjected to shock waves of 200 MPa and greater exhibit clear degradation.

The absence of a marked variation in physical properties is consistent with the results of previous studies [12]. Density and ultrasonic velocity depend on both the mineralogy and pore structure. We interpret the lack of a systematic variation in density and ultrasonic velocity to result from three factors: first, changes in crack density may be offset by pore collapse and have a negligible effect on bulk density; second, changes with shock level may be masked by the small variations in the composition and initial microstructure of the tuff as a function of distance from the WP; and finally, the effects of the change in damage structure which may result from shock loading may be overshadowed by the effects of the variable mineralogy and initially high porosity.

Analysis of the mechanical data for the pristine and shock-conditioned tuff in terms of effective stress indicates that the poroelastic response is altered dramatically by exposure to shock loading of 200 MPa and greater. Tuff subjected to these higher stress levels exhibit pore pressure coefficients (B) close to 1 at applied mean stresses of 25 MPa whereas pristine tuff is characterized by B values close to 1 only at applied mean stresses greater than 150 MPa. Because the strength of brittle rock increases with effective confining pressure [7], this implies that for loading in undrained conditions, shock-conditioned tuff may be weaker than pristine tuff at identical values of the applied confining stress. The higher B values for the tuff shock-conditioned to stresses of 200 MPa and greater imply an enhanced compressibility which is corroborated by the mechanical data. The lower B values of samples shock-conditioned to 100 and 150 MPa may be due to the variation in the initial lithology. The higher percentage of secondary silica, along with its occurrence as cement, may account for the different mechanical behavior observed for the 150 MPa shock-conditioned sample.

It is difficult to comment on the relative strength and failure behavior of the pristine versus shock-conditioned tuff due to the absence of triaxial test data in which the effective confining pressure is controlled. For example, although the stress difference-confining pressure data suggest a reduced yield surface for the highly stressed samples, interpretation is complicated because of the small range covered in stress difference-effective confining pressure space. However, because damage (parameterized in terms of crack density) is a key factor in models for the failure of brittle rocks, it is not unrealistic to expect the tuff dynamically loaded to stresses of 200 MPa and greater to be weaker than the pristine tuff.

4.2 Identification and Quantification of Microstructural Damage in Shock-Conditioned Tuff

The microstructural analysis is consistent with the mechanical data in that a dramatic increase in damage (in the form of microcracks) is observed for tuff subjected to shock loading to stresses of 200 MPa and greater. In particular, SEM reveals a dramatic textural change between the 150 MPa and 200 MPa shocked samples. All three of the highly stressed samples exhibit low aspect ratio cracks and a granular, poorly cemented (almost cohesionless) matrix. It is difficult to differentiate the degree of damage sustained by the three highest shocked samples using SEM techniques on fracture surfaces alone. In particular, the microstructure observed with SEM for the 200 and 250 MPa shocked samples appears almost identical. Analysis performed utilizing the Cerrosafe® impregnation technique provides a means to effectively quantify damage. Damage observed in the field-shocked samples is homogeneously distributed with no evident signs of incipient localization. The microcrack density is anisotropic and increases systematically with shock level. Microcracks are preferentially oriented at approximately 30° to the core axis; however, this distribution is at odds with that expected based upon the geometry of loading since the core axis is oriented normal to the shock wave front. The reason for this is unknown, but such a distribution may possibly result from anisotropy in the pre-existing microstructure. Limited measurements of crack aperture indicate that cracks in the tuff loaded to 300 MPa are narrower than those observed in the tuff loaded to stresses of 200 and 250 MPa. Again, the explanation for this is uncertain, but the distribution may be a function of the differing composition of the 300 MPa tuff. SEM observations provided evidence that the 300 MPa shocked sample is a vitric tuff dominated by poorly cemented glass shards. In comparison, all of the other test samples, both pristine and field-shocked, are zeolitized tuff lacking any unaltered vitric material. In previous work [16], substantial "crush-up" strain occurs at low stresses during uniaxial strain loading for vitric tuff. This material behavior is significantly different than the material response observed for zeolitized tuff. The completely different microstructure observed for vitric tuff relative to zeolitized tuff may contribute to differing failure mechanisms (more volumetric strain is typically observed at low stresses for vitric tuff [16]). Hence, the narrower apertures and the magnitude of the crack density determined for the 300 MPa shocked sample may be attributed to its unique microstructure.

4.3 Field (Dynamic) versus Laboratory (Static) Damage

The microscopy study reveals three main differences in the damage structure of the dynamically (field) and quasi-statically (laboratory) stressed samples. First, the field-shocked samples contain a markedly higher density of microcracks than the laboratory-damaged samples for identical values of the peak radial stress. Second, damage is homogeneously distributed in the field-loaded samples, but is localized in shear zones in the laboratory-damaged samples. Finally, whereas the density of microcracks increases with stress level for the field-shocked samples, the laboratory-damaged samples exhibit virtually identical damage structures over the same applied (radial) stress range.

The first two observations are qualitatively consistent with the previous studies concerning dynamic versus quasi-static loading. The brittle failure of rock results from the activation and propagation of flaws inherent in the virgin material [7]. When load is applied slowly

(quasi-statically) only those flaws activated at low stress levels contribute to the fracture process. However, when load is applied rapidly (dynamically), the local stresses in the rock are significantly higher, resulting in the activation of a greater number of flaws. Thus, a greater number of microcracks participate in the damage process for dynamic than static loading [17]. The participation of a greater number of flaws in the dynamic fracture process may tend to promote widespread disaggregation, rather than shear localization which is thought to result from the interaction of microcracks [18]. Note that an alternative explanation for both observations is simply that the uniaxial-biaxial laboratory loading path does not satisfactorily represent that realized during the propagation of a shock wave due to the underground detonation of a nuclear device.

The third observation concerning the lack of a correlation between peak radial stress and crack density in the laboratory-damaged samples can only be rationalized by considering the material response in terms of effective stress. That is, although the peak applied radial stresses for the samples differs by as much as 200 MPa, the peak effective radial stress prior to the initiation of the biaxial unload for the three samples is nearly identical. Again, this response is a consequence of a B value close to one for pristine tuff at applied mean pressures greater than about 150 MPa. For B=1, an increase in applied stress is exactly countered by an increase in pore pressure so that the effective stress remains unchanged. Thus, a nearly identical damage structure in the three laboratory-damaged samples is expected since the samples supported similar differential stresses and were unloaded at close to the same peak effective radial stress.

This interpretation highlights the significance of the induced pore pressure measurement. Similarly, although the biaxial strain unloading curve lies below the uniaxial strain loading curve in stress difference-confining pressure space, the unloading curve lies above the loading curve in stress difference-effective confining pressure space. The occurrence of shear localization (failure) during the biaxial unload would be difficult to rationalize if the stress difference-confining pressure behavior represented the true material response and can only be understood if the material response is considered in terms of effective stress.

Note that although the occurrence of a constant damage structure in the laboratory samples unloaded in biaxial strain is physically rationalized, that the field-loaded samples exhibit increasing damage with increasing stress level further implies that the loading path in the field may differ significantly from that simulated in the laboratory.

ACKNOWLEDGEMENT

The authors would like to express their appreciation to Mr. Robert Clayton for performing the mechanical property tests, Mr. Jim Marquardt for performing the Cerrosafe® impregnation, assembling the photomosaics, and assisting with the lithologic descriptions, Mr. Greg Davis for assisting with the Cerrosafe® impregnation and performing the physical property measurements, and Ms. Lizette Haddad for aid in helping acquire and present the data needed to complete this report. The authors also appreciate the procedural information on Cerrosafe® impregnation conveyed by Dr. Ziqiong Zheng, the assistance of Dr. Edward King with LSCM, and valuable discussions/comments from Dr. Arfon H. Jones and Dr. John D. McLennan. Special thanks are given to Dr. Byron Ristvet and Mr. Joe LaComb of DNA for their valuable comments made during several meetings over the course of this study. This work was supported by DNA under contract No. DNA 001-90-C-0169.

5.0 REFERENCES

1. Lupo, J.F., Martin, J.W., and Klauber, W., *Characterization of Tuff from U12n.17 RE-2,* TerraTek Report TR87-84, 1987.

2. Torres, G.T., Tester, V.J., and Martin, J.W., *Characterization of Pristine and Shock-Conditioned Tuff from the T-Tunnel Complex,* TerraTek Report TR89-67, 1989.

3. Torres, G.T., et al., *Characterization of Shock-Conditioned Tuff from Drill Hole U12p.-02 RE-1,* TerraTek Report TR88-73, 1988.

4. Butters, S.W., et al., *Effects of Shock Loading on Rock Properties and In-Situ Stress States,* TerraTek Report TR79-25, 1979.

5. Martin, J.W., Fredrich, J.T., and Felice, C.W., *Effect of Shock-Conditioning on Properties of NTS Tuff,* DNA report DNA-TR-92-141-V1, 1993.

6. RSN's Geology/Hydrology Division.

7. Paterson, M.S., *Experimental Rock Deformation - The Brittle Field,* Springer-Verlag, New York, 1978.

8. Zheng, Z., Cook, N.G.W., and Doyle, F.M., A new technique to observe three dimensional cracks in rocks. *EOS, Trans. AGU,* **68**, 1477 (1987).

9. Underwood, E.E., *Quantitative Stereology,* Addison-Wesley, Reading, MA, 1970.

10. Mumpton, F.A., "Mineralogy and Geology of Natural Zeolites," *Reviews of Mineralogy,* Vol. 4, Washington Mineralogical Society of America, 1986.

11. McKague, H.L., personal communication, 1990.

12. Torres, G.T., et al., "Characterization of Shock-Conditioned Tuff," *Fifth Symposium on the Containment of Underground Nuclear Explosions,* Santa Barbara, CA, 1989.

13. Kumpel, H.-J., "Poroelasticity: parameters reviewed," *Geophys. J. Int.,* 105, 783-799, 1991.

14. Skempton, A.W., "The pore-pressure coefficients A and B," *Geotech.,* 4, 143-147, 1954.

15. Rimer, N., Green, S.J., and Klauber, W., "The Effect of Strain Paths Calculated for Spherically Symmetric Explosions on Measured Damage in Tuff," *Fourth Symposium on the Containment of Underground Nuclear Explosions,* 1987.

16. Torres, G.T., et al., *Material Properties of Cored Tuff from Vertical Borehole UE-12n#14,* TerraTek Report TR88-43, 1988.

17. Grady, D.E., Kipp, M.E., "Dynamic Rock Fragmentation," *Fracture Mechanics of Rock*, p. 429-475, Academic Press, 1987.

18. Trapponier, P., and Brace, W.F., "Development of stress-induced microcracks in Westerly Granite," *Int. J. Rock Mech. Min. Sci. Geomech. Abstr.*, **13**, 103-113, 1976.

PROPERTIES OF NTS TUFF

V. Thummala, J. G. Moore, J. E. Aamodt
Raytheon Services Nevada
Materials Testing Laboratory
P.O. Box 328, Mercury, NV 89023

Abstract:

The Raytheon Services Nevada (RSN) Materials Testing Laboratory (MTL) located at the Nevada Test Site (NTS) in Mercury, Nevada has been conducting rock testing for DOE, DOD/DNA, LLNL, and LANL and for other special projects. Various NTS tuff (a volcanic rock formation) samples were tested using different methods over the years.

Welded and non-welded tuff physical, mechanical, hydrologic and thermal properties are presented. The properties are sorted and summarized according to the general NTS tuff stratigraphic units. Drill holes UE19P, UE18E and samples from G-Tunnel rock property summaries and general test methods are discussed.

Introduction:

The Materials Testing Laboratory (MTL) at the Nevada Test Site is operated by Raytheon Services Nevada (RSN). The MTL is equipped with state of the art test and data acquisition equipment to conduct the rock, soil, and other materials physical, chemical, mechanical, hydrologic and other special testing.

In the past 25 years, the MTL conducted a variety of properties tests for several DOE programs. Some of the rock properties of the NTS tuff and test procedures are discussed in this presentation.

The properties discussed in this paper give a profile of various properties of NTS tuff. Most of the samples tested at the MTL were core samples which were generally foil wrapped and waxed

for moisture and saturation measurements.

Physical Properties:

In general, the physical property tests consist of bulk density, grain density (specific gravity), moisture content and porosities. The bulk densities are determined on wax coated cores and grain densities on dried and ground powder samples. Bulk and grain densities are also used to calculate the sample porosities and saturations based on moisture levels.

Typical physical properties of various tuff units are given in Tables 1 and 2 for holes UE19P and UE18E#1. Dry bulk densities given in Table 1 and 2 vary from 2.51 g/cc to 1.35 g/cc which is typical for welded to nonwelded tuff cores. Welded and bedded tuff samples have higher densities. Porosities of the welded to nonwelded tuff samples ranged from 1% to 45%.

Dynamic Properties:

Dynamic rock properties of tuff core samples are determined by measuring the compressional and shear wave sonic velocities. The dynamic elastic moduli and Poisson's ratios were computed using the sonic velocities. The velocities of the welded samples are generally higher due to the low porosities and better propagation of the sonic waves. Details are given in Table 1. The velocities ranged from 625 to 5200 m/sec. The dynamic elastic properties for various tuff units are given in Table 1.

Mechanical Properties:

Tuff core samples were used to obtain the various mechanical properties and they are summarized in Tables 2 through 4. Uniaxial compression strengths varied from 750 to 11,320 psi for the samples from core hole UE18E#1. The core samples were instrumented with deformation jackets for measuring the axial and transverse strains

TABLE 1
PHYSICAL AND DYNAMIC PROERTIES OF TUFF CORES, UE19p

Group	Unit	Depth m	Bulk Density (dry) g/cc	Grain Density g/cc	Percent Porosity	Comp. Velocity m/sec	Shear Velocity m/sec	Young's Modulus GPA	Bulk Modulus GPA	Shear Modulus GPA	Poisson's Ratio
Timber Mountain (Tm)	Rainier Mesa (Tmr)	305	2.18	2.41	9.2	5294	2970	45.0	29.9	18.1	0.249
	Holmes Road (Tmrh)	343	1.36	2.39	43.2	1165	625	1.5	1.2	0.6	0.284
Paintbrush (Tp)	Pahute Mesa (Tpcm)	369	2.37	2.40	1.4	4088	1851	11.8	6.5	4.9	0.195
	Rhyolite of Echo Peak (Tpe)	432	2.33	2.37	1.8	3978	1687	11.6	12.7	4.3	0.347
Area 20 (Tra)	Calico Hill (Tacp)	506	1.45	2.32	37.4	2912	1452	4.8	2.7	2.0	0.200
	Rhyolite of Sled (Tcps)	553	1.51	2.35	35.8	3389	1660	16.3	7.2	7.3	0.123
	Mafic-rich Bull frog (Tcblr)	608	2.17	2.61	16.9	3248	1651	19.4	15.4	7.5	0.290
	Mafic-poor Bull frog (Tcblp)	650	1.63	2.44	33.2	2918	1493	7.9	4.5	3.3	0.203

TABLE 2
PHYSICAL AND MECHANICAL PROPERTIES, UE18e #1

Unit	Depth Ft	Bulk Density (dry) g/cc	Grain Density g/cc	Porosity Percent	Comp. Strength psi	Young's Modulus psi	Shear Modulus psi	Poisson's Ratio
Rhyolite, brown flowbanding	61	2.23	2.62	14.8	5420	1.360E+06	5.820E+05	0.168
	179	2.09	2.62	20.4	5200	2.360E+06	8.850E+05	0.333
Vitrophyre, black flowbanding	212	2.15	2.61	17.7	8790	3.750E+06	1.457E+06	0.287
Tuff intermixed ash-fall grayish-yellow	238	2.51	2.63	4.6	11320	5.150E+06	2.237E+06	0.151
	270	2.22	2.60	14.6	3240	1.760E+06	7.620E+05	0.155
	281	2.36	2.39	1.1	4500	2.930E+06	1.117E+06	0.311
	301	1.38	2.35	41.3	750	5.530E+05	2.190E+05	0.260
	327	1.35	2.38	43.2	790	3.780E+05	1.600E+05	0.178

TABLE 3
MECHANICAL PROPERTIES UNDER CONFINING PRESSURES, UE18e #1

Unit	Depth Ft	Conf. Pressure psi	Axial @ failure psi	Young's Modulus psi	Poisson's Ratio
Rhyolite, brown flowbanding	94.4	1000	23030	3.408E+06	0.241
	94.7	2000	29500	3.332E+06	0.221
	95.1	3000	33650	3.588E+06	0.214
Rhyolite, brown flowbanding	144.3	1000	5140	2.115E+06	0.174
	144.9	2000	6350	2.778E+06	0.400
	140.4	3000	19000	2.159E+06	0.191
Vitrophyre, black flowbanding	212	1000	14760	3.550E+06	0.232
	213.8	2000	19290	3.140E+06	0.289
	213.5	3000	12620	4.140E+06	0.292
Tuff intermixed ash-fall grayish-yellow	281.8	1000	13170	2.340E+06	0.137

TABLE 4
PROPERTIES OF NONWELDED TUFF FROM G-TUNNEL DRIFT

Sample #	Bulk Density (dry) g/cc	Grain Density g/cc	Porosity Percent	Tensile Strength psi	Comp. Strength psi	Young's Modulus psi	Poisson's Ratio
1	1.52	2.43	37	177	1354	3.360E+05	0.129
2	1.56	2.51	38	206	1880	8.280E+05	0.188
3	1.42	2.45	42	30	1870	4.150E+05	0.131
4	1.53	2.51	39	171	2410	7.540E+05	0.184
5	1.60	2.52	37	241	3000	7.140E+05	0.141
6	1.60	2.47	32	135	4230	1.065E+06	0.231
7	1.67	2.39	30	105	3480	7.960E+05	0.194
8	1.51	2.37	36	75	2445	6.170E+05	0.223
9	1.43	2.39	40	150	2625	6.560E+05	0.185
10	1.60	2.49	36	207	3342	8.690E+05	0.196
11	1.61	2.50	36	45	1986	7.020E+05	0.261
12	1.59	2.48	36	119	3046	8.320E+05	0.224
13	1.48	2.32	37	59	5404	8.770E+05	0.168
14	1.57	2.55	39	65	1619	3.340E+05	0.189
15	1.68	2.44	31	324	4185	1.059E+06	0.262
16	1.62	2.43	33	140	3464	8.530E+05	0.314
17	1.69	2.43	30	178	3150	6.600E+05	0.317
18	1.60	2.47	35	162	6298	1.470E+06	0.250
19	1.57	2.48	37	147	2707	6.390E+05	0.217
20	1.51	2.49	39	162	2501	6.300E+05	0.321
21	1.64	2.57	36	37	2060	5.630E+05	0.234
22	1.62	2.54	36	103	2325	6.720E+05	0.248
23	1.55	2.38	35	66	1589	3.090E+05	0.145
24	1.53	2.49	39	103	1471	5.190E+05	0.181

Average	1.57	2.46	36.0	134	2852	7.154E+05	0.214
Std.dev	0.07	0.06	3.0	69	1201	2.542E+05	0.054

and tested in uniaxial loading. The strength, elastic moduli and Poisson's ratios for various geologic units are in Table 2. Static, elastic and failure loads for the same geologic units under confining pressures (up to 3000 psi) are given in Table 3. The Young's moduli are comparable at various confining pressures. The mechanical properties of the nonwelded tuff from G-Tunnel main drift are summarized in Table 4. The results of the porosity from densities averaged about 36% and it is very typical for nonwelded tuff samples. The average tensile strength of 134 psi is low in comparison to sandstone for example. The Young's moduli and Poisson's ratios given in Table 4 are typical for most of the nonwelded tuffs.

Hydrologic Properties:

Porosities and permeabilities of the tuff samples from G-Tunnel are given in Tables 5 and 6. The porosities given in Tables 5 and 6 were calculated from the bulk and apparent densities. The apparent densities were determined for the intact samples by water, helium and mercury saturation methods. These densities for the welded tuffs are comparable as given in Table 5 and averaged about 2.6 g/cc for samples obtained from both dry and wet drilling methods. The density results of the nonwelded tuff samples from the water, helium and mercury methods varied from 2.19 to 2.40 g/cc. These types of variations were observed on several nonwelded tuff samples mainly due to the water reaction with zeolites which are present in nonwelded tuffs. In most cases, grain densities using water are about 5% higher compared to those determined by using helium. The densities by mercury in Tables 5 and 6 were measured by mercury injection by using a mercury porosimeter.

The water permeability for the tuffs ranged from 0.37 to 0.015 millidarcies and the results are given in Tables 5 and 6. These permeabilities were measured on 3.8 cm diameter x 3 cm long cores using NTS well water. The confining pressure around the sample ranged from 50 psi to 150 psi during testing.

TABLE 5.
HYDROLOGIC PROPERTIES OF WELDED TUFF SAMPLES
HOLE U12G.12

DRY CORING METHOD

Depth (approx.) (ft)	Apparent Porosity to Water (%)	Apparent Porosity to Helium (%)	Apparent Skeletal density by Water (g/cc)	Apparent Skeletal density by Helium (g/cc)	Apparent Skeletal density by Mercury (g/cc)	Water Permeability (millidarcys)
1	16.2	16.5	2.62	2.63	2.62	0.006
4	16.4	16.3	2.61	2.61	2.60	0.010
8	15.6	18.4	2.62	2.71	2.60	0.007
13	15.1	16.1	2.62	2.65	2.60	0.003
19	13.2	13.8	2.62	2.64	2.59	0.038
20	18.0	18.7	2.62	2.64	2.58	0.024
21	18.4	18.4	2.62	2.62	2.60	0.035
23	16.6	16.8	2.62	2.63	2.61	0.012
Average	16.2	16.9	2.62	2.64	2.60	0.017
Std. dev.	1.5	1.5	0.00	0.03	0.01	0.013

WET CORING METHOD

Depth (approx.) (ft)	Apparent Porosity to Water (%)	Apparent Porosity to Helium (%)	Apparent Skeletal density by Water (g/cc)	Apparent Skeletal density by Helium (g/cc)	Apparent Skeletal density by Mercury (g/cc)	Water Permeability (millidarcys)
1	14.7	16.8	2.62	2.68	2.60	0.006
4	17.2	18.6	2.62	2.66	2.61	0.020
12	16.9	17.8	2.62	2.65	2.61	0.067
14	14.0	15.2	2.62	2.65	2.62	0.002
16	15.9	16.3	2.61	2.62	2.61	0.005
18	15.8	16.5	2.62	2.64	2.63	0.006
19	16.5	16.3	2.62	2.61	2.61	0.008
21	16.7	16.3	2.61	2.60	2.63	0.007
22	17.1	17.7	2.62	2.64	2.62	0.010
Average	16.0	16.7	2.62	2.64	2.62	0.015
Std. dev.	1.0	1.0	0.00	0.03	0.01	0.020

TABLE 6.
HYDROLOGIC PROPERTIES OF NONWELDED TUFF SAMPLES
HOLE U12G.12

DRY CORING METHOD

Depth (approx.) (ft)	Apparent Porosity to Water (%)	Apparent Porosity to Helium (%)	Apparent Skeletal density by Water (g/cc)	Apparent Skeletal density by Helium (g/cc)	Apparent Skeletal density by Mercury (g/cc)	Water Permeability (millidarcys)
7	40.5	38.5	2.44	2.36	2.21	3.302
8	22.9	20.0	2.43	2.34	2.27	0.133
13	29.8	27.1	2.42	2.33	2.20	0.801
16	42.8	39.3	2.39	2.26	2.14	2.891
17	46.9	44.9	2.41	2.32	2.22	2.934
22	33.5	31.7	2.37	2.31	2.17	0.189
24	35.7	34.0	2.36	2.30	2.14	1.551
29	51.0	47.7	2.40	2.25	2.17	1.539
30	49.6	44.9	2.40	2.20	2.19	1.052
Average	39.2	36.5	2.40	2.30	2.19	1.599
Std. dev.	8.9	8.6	0.02	0.05	0.04	1.127

WET CORING METHOD

Depth (approx.) (ft)	Apparent Porosity to Water (%)	Apparent Porosity to Helium (%)	Apparent Skeletal density by Water (g/cc)	Apparent Skeletal density by Helium (g/cc)	Apparent Skeletal density by Mercury (g/cc)	Water Permeability (millidarcys)
2	48.3	46.0	2.43	2.32	2.24	0.037
7	43.9	40.4	2.45	2.30	2.19	0.417
8	38.2	36.1	2.44	2.36	2.18	0.161
13	28.6	26.3	2.43	2.35	2.22	0.044
17	43.3	40.6	2.40	2.29	2.15	0.211
22	29.6	26.3	2.35	2.24	2.15	0.323
24	46.6	42.9	2.40	2.24	2.17	0.305
29	45.7	42.8	2.41	2.28	2.14	1.105
30	42.8	39.9	2.40	2.28	2.15	0.717
Average	40.8	37.9	2.41	2.30	2.18	0.369
Std. dev.	6.8	6.7	0.03	0.04	0.03	0.326

The mercury injection at various pressures was measured for welded and nonwelded tuff samples and typical results are shown in Figures 1 and 2. These tests were conducted by using the Micromeritics mercury porosimeter. Small 1/2" to 3/4" rock pieces or cores are dried and then subjected to mercury injection to determine pore size, and pore volume by measuring the volume of mercury injected at various pressures up to 60,000 psi. The mercury volume is recorded by measuring the capacitance of the mercury column and the pressures by a transducer.

The mercury injection and pore volume data were used in hydrologic modeling to determine the fluid flow in various formations. The injection curves in Figures 1 and 2 are given for densities measured by using water, helium and mercury. Typical data reduction used to prepare figures 1 and 2 are given in Table 7 where mercury saturations were calculated. The porosity variations by using different test methods can be seen in Figure 1 for nonwelded samples and they are very minimal for the welded tuff samples shown in Figure 2.

Thermal Properties:

Typical nonwelded tuff thermal conductivity properties are given in Table 8. The results are given for two saturation levels and thermal conductivities are a little higher at higher saturations. Their values ranged from 0.008 to 0.01 watts/cm/°C. For comparison, NTS soil thermal conductivities are given in Table 9 which were measured at various temperatures. The results indicate that once the moisture is driven out, the thermal conductivities will stay consistent at various temperatures.

Thermal Conductivity Tests:

Transient thermal conductivity testing of solids follows the method described in U.S. Bureau of Mines Report of Investigations

Figure 1. Injection Pressure Curves

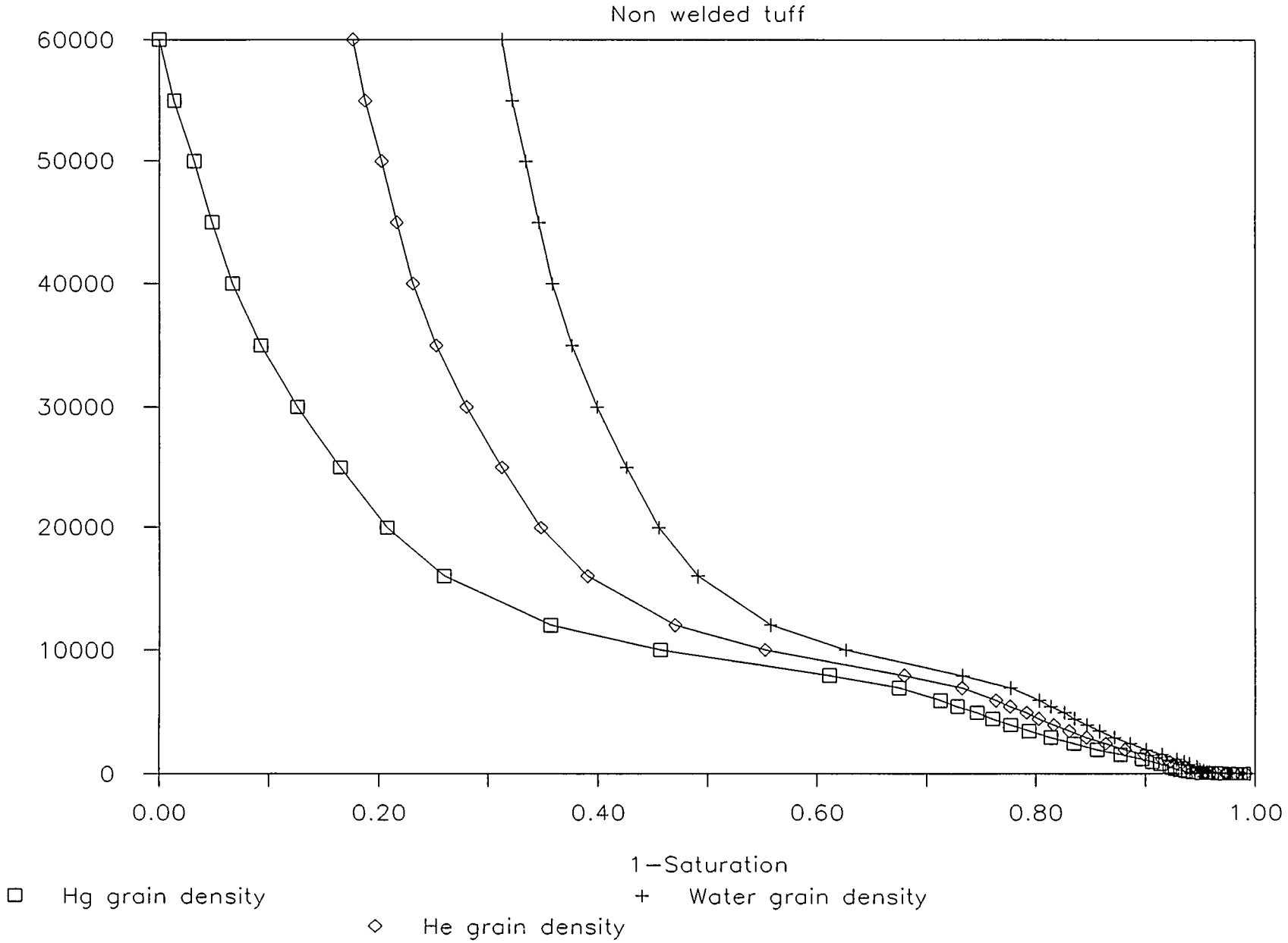


Figure 2. Injection Pressure Curves

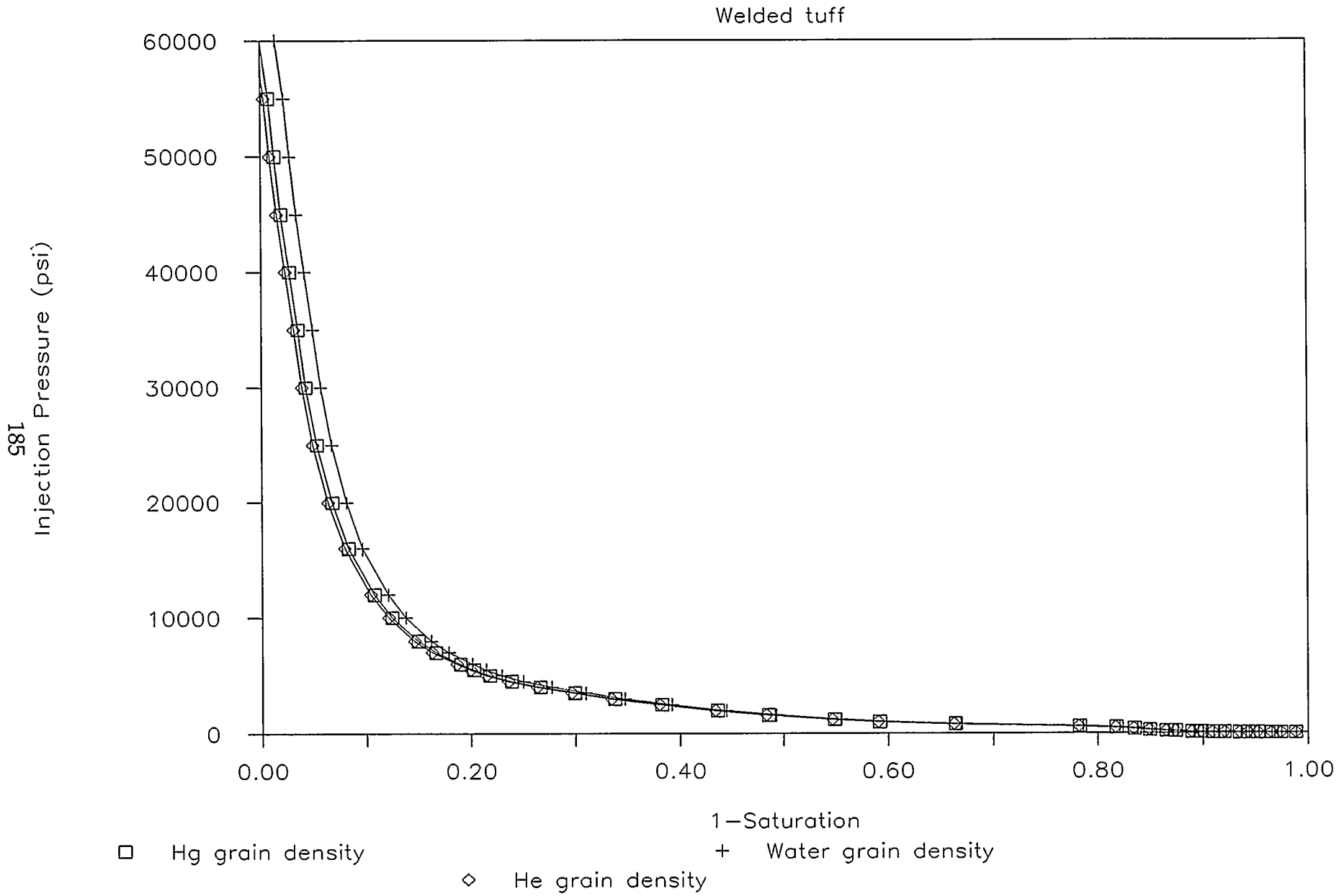


TABLE 7
MERCURY POROSIMETER CAPILLARY PRESSURE CURVE DATA

Mercury Injection Pressure (psia)	Cumulative Injected Mercury (ml/g)	1–Porosimeter Mercury Saturation	1–Water basis Mercury Saturation	1–Helium basis Mercury Saturation	Core Properties
2.00	0.0007	0.989	0.993	0.991	2781 = RSN Lab #
5.00	0.0011	0.983	0.989	0.986	18.56 = Dry sample weight (g) from Hg data
10.00	0.0014	0.979	0.985	0.983	1.97 = Bulk density (g/cc) from Hg data
20.00	0.0020	0.970	0.979	0.975	2.27 = Grain density by porosimeter (g/cc)
30.00	0.0021	0.968	0.978	0.974	2.43 = Grain density by water
40.00	0.0022	0.967	0.977	0.973	displacement (g/cc)
60.00	0.0028	0.958	0.971	0.965	2.34 = Grain density by helium
80.00	0.0032	0.951	0.967	0.960	displacement (g/cc)
100.0	0.0035	0.947	0.963	0.956	1.22 = Porosimeter pore volume (ml)
120.0	0.0037	0.944	0.961	0.954	1.78 = Water basis pore volume (ml)
160.0	0.0040	0.939	0.958	0.950	1.49 = Helium basis pore volume (ml)
200.0	0.0042	0.936	0.956	0.948	
300.0	0.0045	0.932	0.953	0.944	
400.0	0.0048	0.927	0.950	0.940	
500.0	0.0050	0.924	0.948	0.938	
600.0	0.0051	0.923	0.947	0.936	
800.0	0.0057	0.914	0.941	0.929	
1000.0	0.0062	0.906	0.935	0.923	
1,200	0.0068	0.897	0.929	0.915	
1,600	0.0081	0.877	0.916	0.899	
2,000	0.0095	0.856	0.901	0.881	
2,500	0.0109	0.835	0.886	0.864	
3,000	0.0123	0.813	0.872	0.846	
3,500	0.0136	0.794	0.858	0.830	
4,000	0.0147	0.777	0.847	0.816	
4,500	0.0158	0.760	0.835	0.803	
5,000	0.0167	0.747	0.826	0.791	
5,500	0.0179	0.728	0.813	0.776	
6,000	0.0189	0.713	0.803	0.764	
7,000	0.0214	0.675	0.777	0.733	
8,000	0.0256	0.612	0.733	0.680	
10,000	0.0358	0.457	0.627	0.553	
12,000	0.0424	0.357	0.558	0.470	
16,000	0.0488	0.259	0.491	0.390	
20,000	0.0522	0.208	0.455	0.348	
25,000	0.0550	0.165	0.426	0.313	
30,000	0.0576	0.126	0.399	0.280	
35,000	0.0598	0.093	0.376	0.253	
40,000	0.0615	0.067	0.358	0.232	
45,000	0.0627	0.049	0.346	0.217	
50,000	0.0638	0.032	0.334	0.203	
55,000	0.065	0.014	0.322	0.188	
60,000	0.0659	0.000	0.313	0.177	

TABLE 8
THERMAL CONDUCTIVITY OF NONWELDED TUFF CORES

Core Source	Saturated Density g/cc	Thermal Conductivity @ 15°C K, w/cm/°C	
		Saturation 100%	Saturation 90%
G-Tunnel	1.81	0.00985	0.00946
G-Tunnel	1.92	0.01150	0.01030
G-Tunnel	1.80	0.00885	0.00860
G-Tunnel	1.75	0.00899	0.00843
G-Tunnel	1.81	0.01030	0.00974
G-Tunnel	1.75	0.00938	0.00878
G-Tunnel	1.71	0.00904	0.00851
G-Tunnel	1.69	0.00974	0.00861
G-Tunnel	1.75	0.00964	0.00914

TABLE 9
THERMAL CONDUCTIVITIES OF SOIL SAMPLES

Soil Source	Measured at Temperature °F	Thermal Conductivity K, w/cm/°C		
		Depth 5 ft	Depth 10 ft	Depth 15 ft
AREA 25	ROOM	0.008067	0.009000	0.008882
AREA 25	100.00	0.006469	0.006062	0.009077
AREA 25	200.00	0.004289	0.004257	0.006045
AREA 25	300.00	0.004382	0.004444	0.004654
AREA 25	400.00	0.004202	0.004420	0.004582
AREA 25	500.00	0.004273	0.004461	0.004600
AREA 25	600.00	0.004325	0.004226	0.004742
AREA 25	700.00	0.004005	0.003999	0.004536

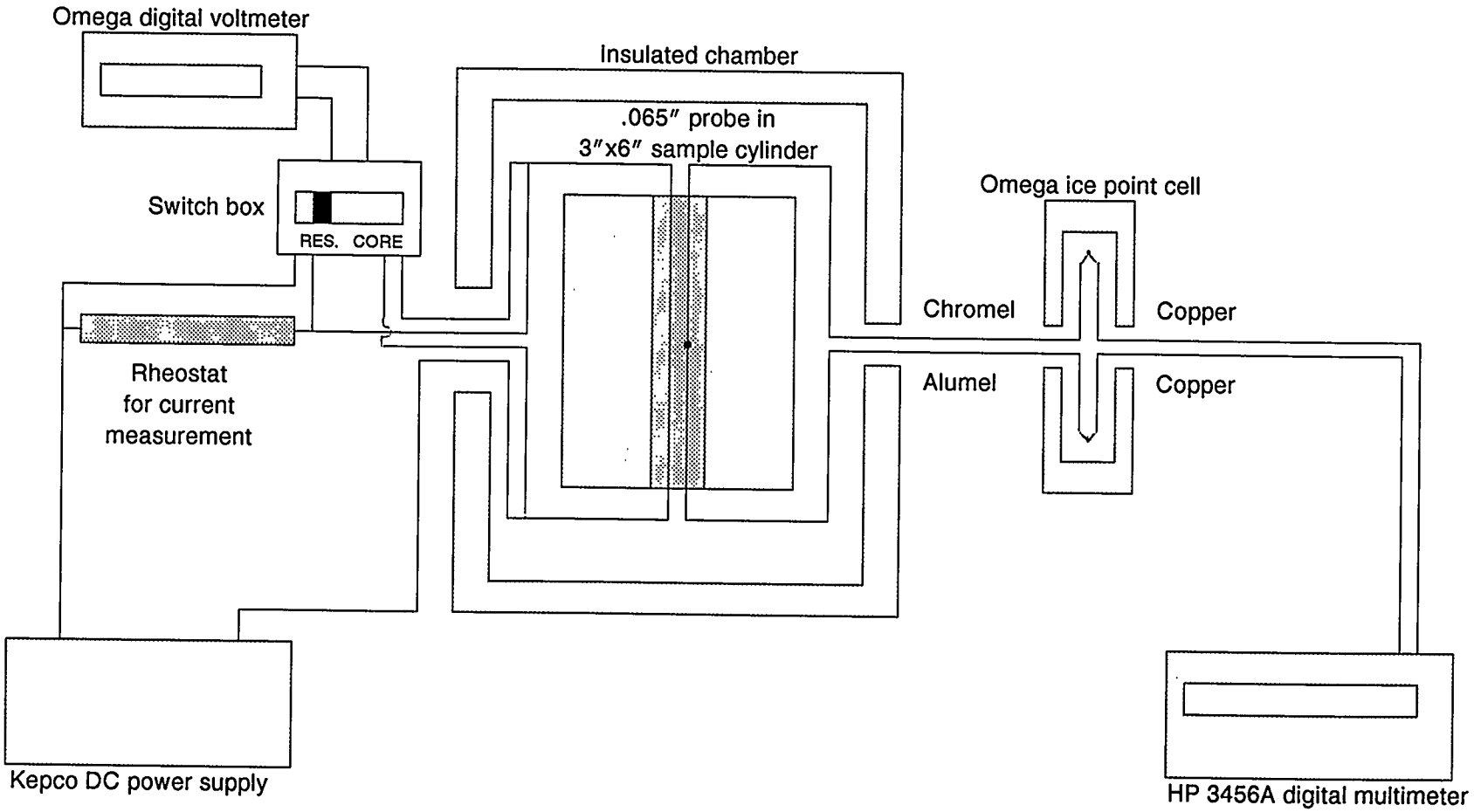
#6604.

A probe consisting of a 1/16" diameter fused alumina rod containing the heater and Type K thermocouple wires is axially mounted in the center of the sample. A hole is drilled in rock or concrete cores for the probe; bulk solids or pourable slurries are compacted around the probe in a cylindrical mold. The instrumented sample is then placed on its side in an insulated box or oven and the heater and thermocouple connections are made as shown in Figure 3.

The thermocouple circuit is completed in an ice point cell containing copper-chromel and copper-alumel junctions to avoid thermal offsets. A regulated DC power supply provides current to the probe connected in series with a wire-wound rheostat and the probe. A Hewlett-Packard voltmeter featuring 100 nanovolt resolution and data logging capability measures thermocouple output during the tests.

Thermocouple voltages are converted to temperature using a NIST power series expansion and then plotted versus the natural logarithm of elapsed time. The log linear portion of each graph is used in the conductivity calculation. A Lotus Symphony spreadsheet developed at the MTL facilitates data reduction and plotting.

Figure 3. Schematic of Heater and Thermocouple Circuits



Acknowledgments

The information presented in this report was from various DOE and DOD/DNA projects. The MTL would like to acknowledge Mr. Harold E. Begley, Mr. Ernest Buskirk, and Mr. Richard Ivy for their support of the MTL in development and research programs.

DYNAMIC RESPONSE OF PCGC-1(O) GROUT

By C. W. Felice[1], and Byron Ristvet[2]

ABSTRACT: This paper presents the results from a limited series of split-Hopkinson pressure bar (SHPB) experiments on PCGC-1(O) grout. The purpose of the experiments was to qualitatively observe the damage induced in the grout specimens due to the dynamic, high strain rate load. Besides the qualitative observations, stress-time data are presented and compared with the response obtained under static loads. In a traditional SHPB experiment, the load is generated by the impact of a projectile against the incident pressure bar. Instead of a projectile, the loading pulse in these experiments was initiated by an explosive. The explosive detonation produces a half sine wave pulse shape. The pulse is assumed to be one-dimensional, elastic and nondispersive. The explosive consisted of a blasting cap with a 0.4 gram base charge of PETN plus a 0.5 gram booster of PETN. The explosive produced a nominal incident stress of 250 MPa. The specimens were prepared from tube samples of PCGC grout supplied by the U.S. Army Engineers Waterways Experiment Station. The tube samples were nominally 50 mm in diameter. The SHPB specimens were cored to be the same diameter as the pressure bars and end ground to produce three nominal length/diameter (l/d) ratios; 0.2, 0.5 and 1.0. Two specimens were prepared at each l/d ratio. Qualitatively, the observed behavior ranged from pulverizing a zone around the edge of the specimens with the smallest l/d ratio, to slabbing at the intermediate l/d, and finally axial splitting of the specimens with the l/d ration of 1.0. The axial splitting was similar to what is observed in a static unconfined compression test.

INTRODUCTION

This paper presents the results of six explosively driven split-Hopkinson pressure bar experiments (SHPB) on PCGC-1(O) grout. The purpose of this limited series of experiments was to qualitatively observe the damage sustained by the specimens due to the dynamic load.

Over the past several years the Geomechanics Division at the U. S. Army Engineers Waterways Experiment Station (WES) has been developing mixes and conducting static laboratory tests on a gypsum based grout designated PCGC-1(O) for the Defense Nuclear Agency (DNA). For convenience, the grout will referred to as PCGC in the remainder of the paper. The purpose of the WES development effort is to characterize the material in enough detail to determine if it can be used as a stemming material and therefore become an integral component of a containment design for an underground nuclear test. A particular characteristic of the PCGC grout is that its strength decreases with increasing confining pressure. In addition, at large strains, it was expected that a through-going shear will develop leading to failure of the specimen. However, at axial strains up to 18 percent, through-going shear planes did not appear [1]. Also, under confinement, the grout does not damage like a Portland cement based grout and it has been suggested that the grout may "heal" with confining pressure. These characteristics are in general different from the behavior trends exhibited by most geologic materials. For example most geologic materials tend to exhibit an increase in strength with increasing confining pressure in triaxial compression.

---

[1] Mission Research Corporation, 9 Exchange Pl, Suite 900, Salt Lake City, Utah 84111

[2] Defense Nuclear Agency, 1680 Texas St. SE , Kirtland AFB, NM, 87117-5669

Presented in this paper is a description of the SHPB apparatus and the experimental procedure that was followed in performing the experiments. A description of the PCGC grout is included which is followed by the experimental results.

EXPERIMENTAL TECHNIQUE

Description of Apparatus

Figure 1 is a schematic of the explosively driven SHPB apparatus and blasting chamber used to perform the experiments reported in this paper. The apparatus is the property of the University of Utah, College of Mines. The main components of the SHPB system are the reaction I beam, and the incident and transmitter pressure bars. The pressure bars are fabricated from Durafox-250 alloy steel with the nominal dimensions of 31.75 mm in diameter and 1.295 m in length. The steel bars are heat-treated to an average Rockwell hardness of 76 with a tensile yield strength of 1.7 GPa. The measured static Young's modulus and bulk density of the bar are 1.893×10^5 MPa and 7813 kg/m^3, respectively. The bar velocity is 4,992 m/s. The pressure bars ride in

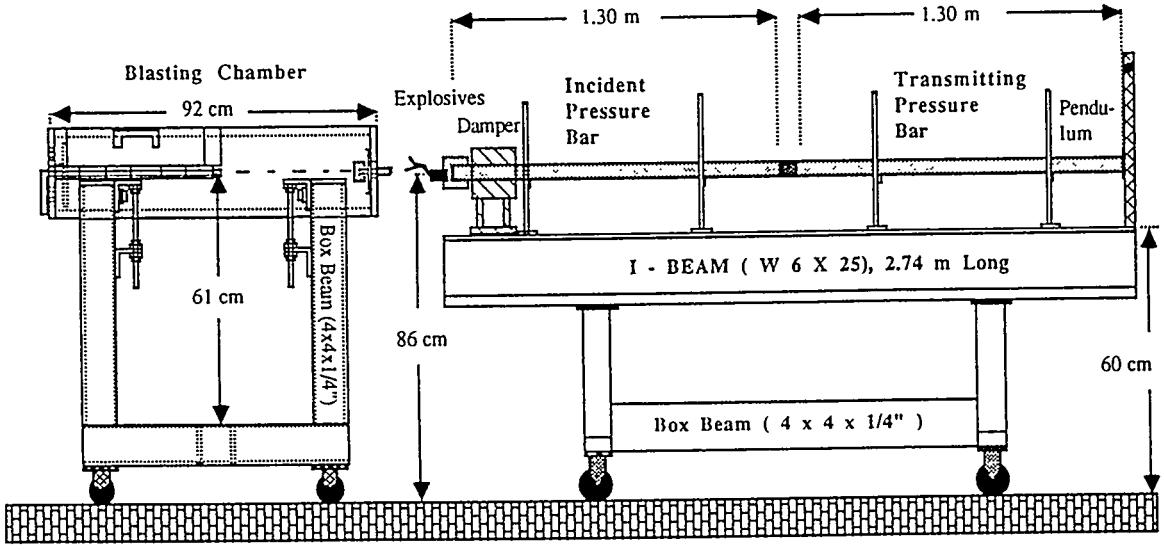


Figure 1. Schematic of explosively driven SHPB [2].

nylon bearings within aluminum supports. The load is generated by an explosive detonation at the end of the incident bar. The resulting pressure pulse is monitored by pairs of strain gages bonded to the incident and transmitter pressure bars. Kim [2] provides a more detailed description of the apparatus.

Explosive application of load

As mentioned above, an explosive detonation is used to generate the stress pulse. An explosive driver was used by Kolsky [3] when he modified the experimental procedure to allow

the average response of the specimen to be determined by indirect measurements. This is an alternative to perhaps a more common approach which is to generate the loading pulse by launching a striker bar or projectile using a gas gun that impacts the incident bar [e.g., 4]. When using a projectile, the amplitude of the pulse is proportional to the impact velocity of the projectile with the incident bar and the duration is proportional to the projectile length. The projectile generates a nearly rectangular wave with observable Phochhammer-Chree oscillations [5,6]. With the explosive driver, both the pulse width and amplitude are a function of the amount and type of explosive used. The explosive detonation produces a pressure pulse shaped like one half of a sine wave. The pulse is assumed to be one-dimensional, elastic, and non-dispersive as it propagates.

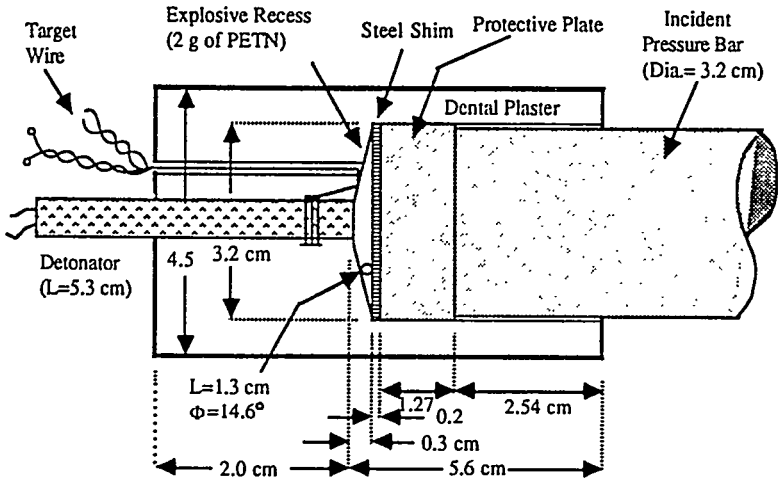


Figure 2. Schematic of explosive driver [2].

Figure 2 shows a schematic of the explosive driver. The explosion is initiated by detonating a blasting cap which contains a base charge of 0.4 grams of PETN. The detonator is placed against a recess which can accommodate approximately 2 grams of additional PETN. For these experiments, an additional booster of 0.5 grams of PETN was added. The additional amount of explosive was held in place by a steel shim. A plaster cast was poured around the explosive fixture to ensure proper placement against the incident bar. To protect the incident bar from being damaged by the detonation, a protective plate was placed between the shim and the incident bar. Kim [2] provides additional details on the explosive driver system. The total amount of explosive was selected to produce a target incident stress of 300 MPa.

Procedure

The experiment is conducted by detonating the explosive that generates a compressive stress wave which propagates down the incident bar. The amplitude of the incident stress wave is dependent on the total amount of explosive used and was selected from a predefined calibration curve [7]. Upon reaching the specimen, the wave is partitioned with a portion being reflected back into the incident bar and a portion passing on into the specimen and through it into the transmitter bar. If the impedance of the bars is higher than that of the specimen, a compressive wave is set up in the specimen that increases in amplitude with each traverse. An experimental

assumption is that the pulse width is sufficiently long compared to the wave travel time in the specimen such that there will exist a uniform distribution of stress over the length of the specimen. Therefore, the average specimen response can be obtained.

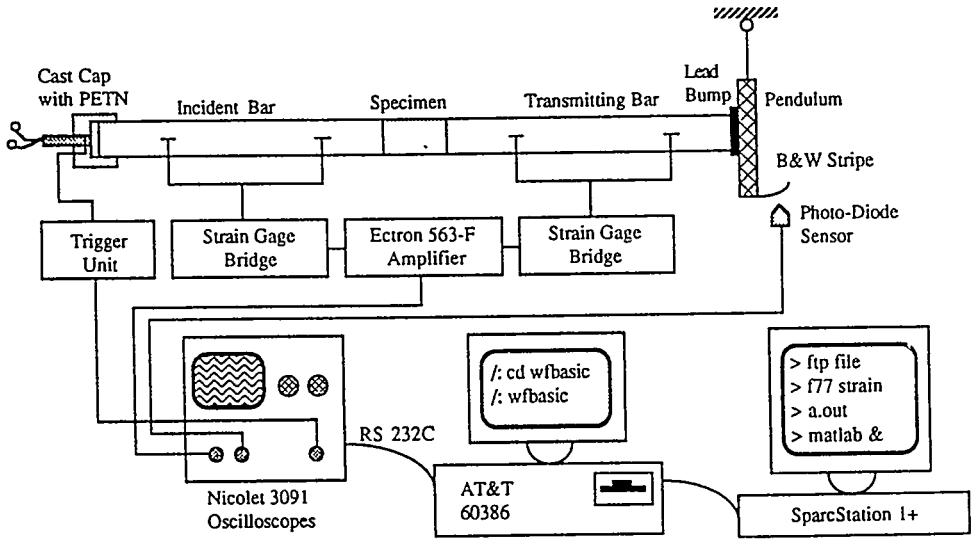


Figure 3. Schematic of complete system [2].

The incident (σ_i), and resulting reflected (σ_r), and transmitted (σ_t) stress waves (e.g., rise-time, amplitude and width) are recorded by strain gages mounted on the surface of the cylindrical pressure bars. The strain gages are mounted in pairs on opposite sides of the respective bars and connected in a half bridge configuration to nullify bending strains. Figure 3 shows a complete schematic of the apparatus with the recording and data reduction systems. Data were recorded at a rate of 1μs per data point and the total recording time was 4ms. Most of the signals that were obtained in the experiments were relatively clean. However, all the reflected waves required filtering due to signal noise. To maintain a consistent data analysis, signal analyses were performed with a 70 kHz low pass digital filter. Filtering did not change the magnitude or shape of the original waveforms.

For these experiments, the specimens were subjected to uniaxial stress (i.e., unconfined compression). However, uniaxial strain and triaxial compression experiments are also possible.

Data Analysis

The waves recorded by the strain gages are used to compute the average specimen response as follows:

$$\sigma_{avg} = \frac{E\,A_p}{2\,A_s}\left(\varepsilon_I + \varepsilon_R + \varepsilon_T\right), \tag{1}$$

$$\dot{\varepsilon}_{avg} = \frac{C_b}{L_s}\left(\varepsilon_I - \varepsilon_R - \varepsilon_T\right). \quad (2)$$

where σ_{avg} is average stress in the specimen, $\dot{\varepsilon}_{avg}$ is the average strain rate in the specimen, E is Young's modulus of the bar material, C_b is the elastic wave velocity in the bar, L_s is the initial specimen length, A_p is the area of the pressure bar, A_s the area of the specimen, and ε_I, ε_R, ε_T are the absolute magnitudes of the incident, reflected, and transmitted strains, respectively. The reflected wave is tensile. The average strain in the specimen at any time is computed by taking the integral of the strain rate.

DESCRIPTION OF PCGC GROUT

The experiments were conducted on a gypsum based grout designated PCGC-1(O). The samples of the PCGC grout were provided by the WES. The grout mixture is given in Table 1 [8]. For a typical batch, the wet density is 2.13 gm/cm^3, with a grain density of 2.48 gm/cm^3 and

Table 1 Materials and mix for PCGC-1(O) grout.

Material	Lbs for 1 ft^3 batch
Super X gypsum cement	49.0
Overton sand	61.35
Sodium citrate	0.09
Water	21.0

wave velocity of 3,300 m/s [1].

The specimens were prepared from tube samples that were nominally 50 mm in diameter. The SHPB specimens were cored to be the same diameter as the pressure bars and end ground to produce three nominal length/diameter (l/d) ratios; 0.2, 0.5 and 1.0. Two specimens were prepared at each l/d ratio for a total of six experiments. To minimize friction effects, a thin layer of high vacuum grease was placed between the specimens and the pressure bars.

To examine the response of the PCGC grout, WES conducted a series of static triaxial compression tests. The results are presented in Figure 4. The nominal peak strains for the specimens in Figure 4 is 10 percent. Figure 4 serves to illustrate several features of the grout behavior. The most notable is the decrease in strength with increasing confining pressure. Also, there is a quantitative difference in behavior, however, qualitatively, the response is very similar from batch to batch. What cannot be observed, but has been reported by Akers [1] is that at confining pressures greater than 100 MPa the specimens did not develop a through-going shear plane, whereas at confining pressures less than 100 MPa, some specimens did develop a through-going shear plane, however the specimens remained in one piece. This behavior suggests that

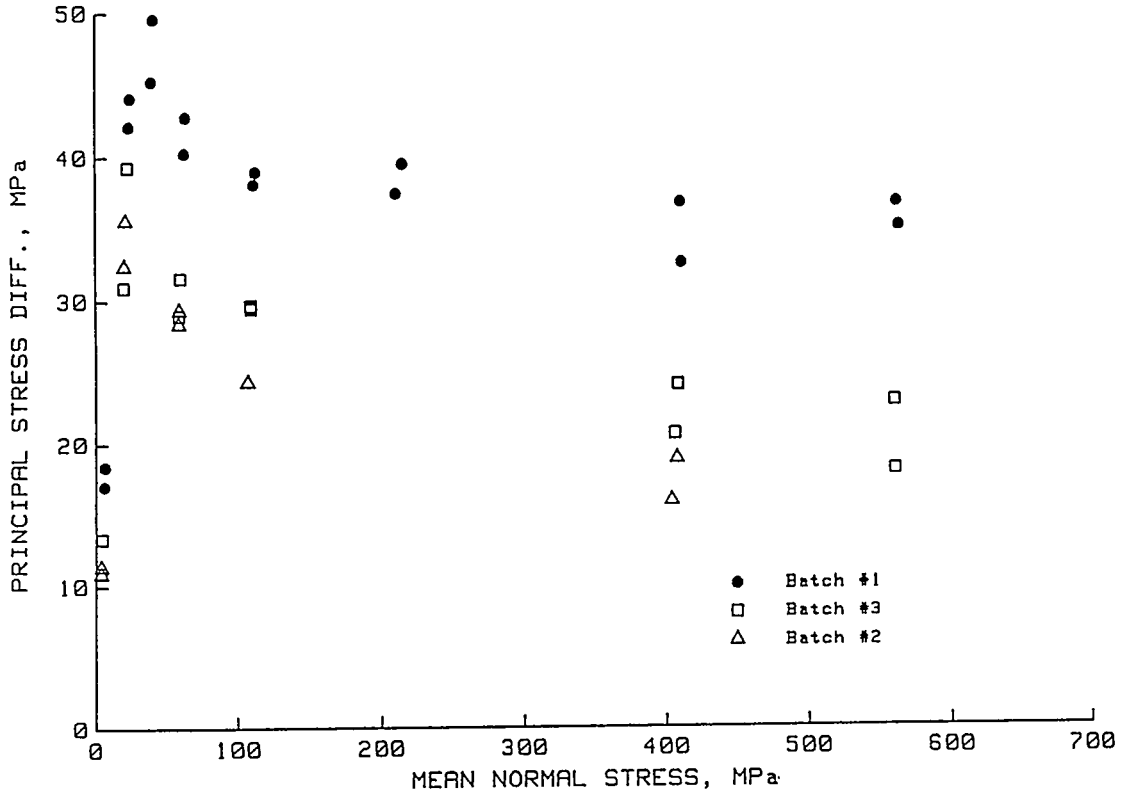


Figure 4. Failure data obtained from static triaxial compression tests [1].

under the influence of confining pressure, a chemical process within the grout is activated that acts as a healing agent for internal fractures.

For reference, this grout mix was fielded as a test section in the DISTANT ZENITH weapons effects test. The test section was approximately 3 meters by 3 meters and was subjected to stress levels in the range of 200 MPa to 300 MPa. Upon examination during reentry, the grout was observed to behave in a ductile manner, i.e., no fracturing was observed.

EXPERIMENTAL RESULTS

Table 2 lists the quantitative results for each of the six experiments. Figure 5 shows a sketch of the condition of each specimen post-test. Although the purpose of these tests was to qualitatively observe damage, several records were reduced to estimate the stress-time response. Figure 6 presents representative stress-time results for each l/d ratio.

Qualitatively the observed behavior ranged from pulverizing a zone around the specimens with the smallest l/d ratio, to slabbing at the intermediate l/d, and finally axially cracking for the specimens with the l/d ratio of 1. These dynamic compression experiments were conducted in unconfined compression, therefore these observations are in general what was expected. Although some amount of ductile behavior may be inferred, it would be more appropriate to compare the static results with dynamic results obtained under uniaxial strain or triaxial compression boundary conditions.

Table 2. Quantitative results from the six experiments.

Specimen	L/D	σ_I (MPa)	t_r (μs)	σ_{avg} (MPa)	ε_{avg} (%)	$\dot{\varepsilon}_{avg}$ (s^{-1})
A	0.155	250	23	29	2.9	2500
B	0.161	240	21	33	2.4	2300
C	0.511	230	23	30	0.75	700
D	0.507	240	22	29	0.81	750
E	1.019	240	21	25	0.40	360
F	1.021	250	21	26	0.40	370

(σ_I is the peak incident stress, t_r is the rise time to peak stress, σ_{avg}, ε_{avg},and $\dot{\varepsilon}_{avg}$ are the average specimen stress, strain and strain rate, respectively)

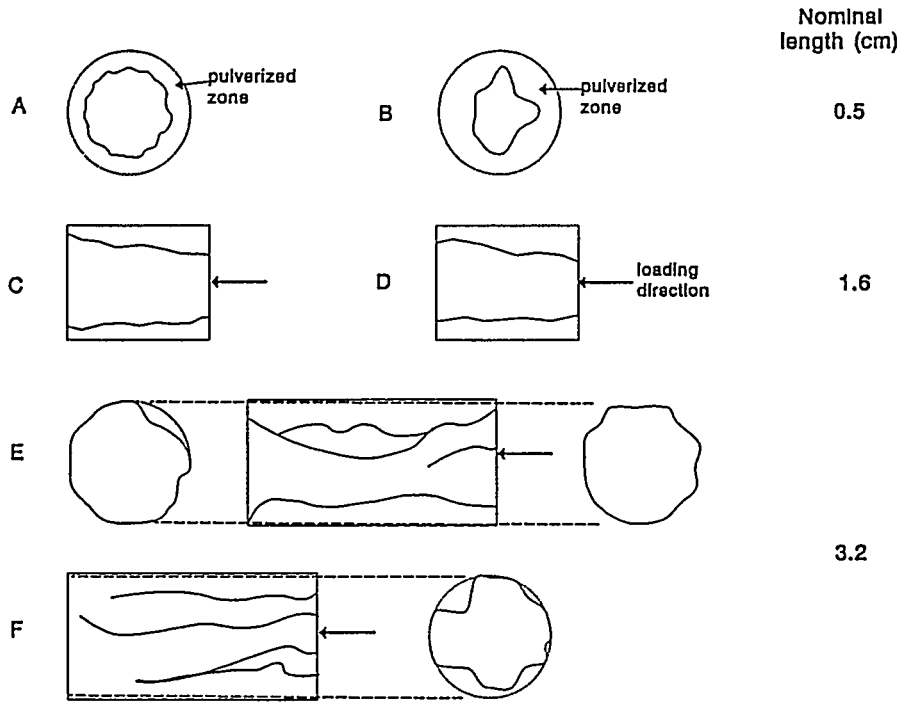


Figure 5. Observations of specimen damage.

Using the average wave velocity in the grout, the number of times the stress wave traversed a specimen before the peak stress was reached ranged from about 13 in the short specimens to 2 in to the longer specimens. Therefore, according to the Davies and Hunter criteria [9], uniform stress was achieved in the short specimens, but not the longer specimens. However, because the strengths were very similar, the data from the longer specimens have been determined to be

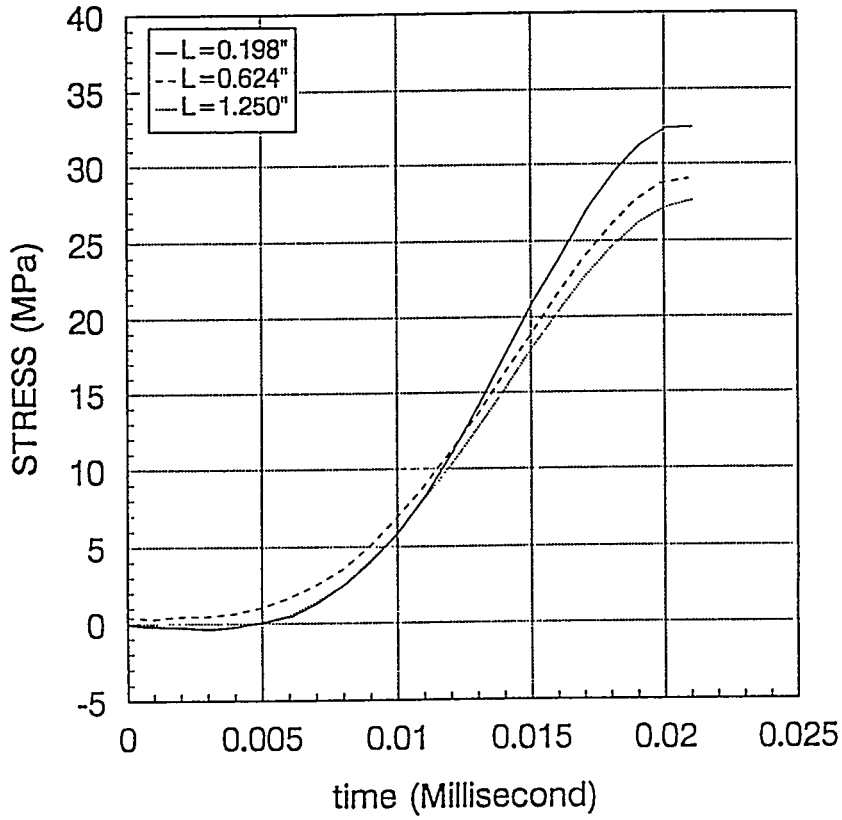


Figure 6. Representative stress time response at each l/d ratio.

acceptable.

An interesting observation is the potential rate dependence that is suggested by the comparison of the peak stresses obtained in the SHPB experiments and those reported by WES (i.e., see Figure 4). The unconfined compressive strength reported by WES ranged from 10 MPa to 20 MPa. The average peak stress from the SHPB experiments was 28 MPa. Unfortunately there is not enough data, both in quantity and over the needed range of strain rates to form any conclusions. Further investigation will be needed to quantify the rate dependence of the PCGC grout.

SUMMARY

The results from a limited series of SHPB experiments on PCGC-1(O) grout specimens has been presented. The purpose of the experiments was to qualitatively observe the damage sustained by the specimens due to dynamic loading under uniaxial stress boundary conditions. Qualitatively the observed behavior was as expected. Although some amount of ductile behavior may be inferred, it would be more appropriate to compare the static results with dynamic results obtained under uniaxial strain or triaxial compression boundary conditions. In addition, a moderate rate dependence was observed, but will require further investigation to substantiate this behavior.

ACKNOWLEDGEMENT

The authors would like to recognize the assistance of Dal Sun Kim who conducted the explosive SHPB experiments and Dr. M. K. McCarter for allowing us access to the apparatus and his useful guidance and comments. We are grateful to Mr. Stephen A. Akers for taking the time to review the manuscript, his comments and suggestions were greatly appreciated.

REFERENCES

1. Akers, S., and P Reed, *Selected Mechanical Responses of PCGC-1(O) Grout*, Briefing Package Presented to the SubCAT, U.S. Army Waterways Experiment Station, Vicksburg, Mississippi, 12 November, 1992.

2. Kim, Dal Sun, "The Effect of Shock-Induced Damage on Comminution of Rock Materials," dissertation presented to the University of Utah in 1993, in partial fulfillment of the requirements for the degree of Doctor of Philosophy.

3. Kolsky, H., "An Investigation of the Mechanical Properties of Materials at Very High Rates of Loading." *Proceedings of the Physical Society*, Section B, Vol. 2, 1949, pp. 676-700.

4. Felice, C. W., E.S. Gaffney, J. A. Brown, and J. M. Olsen, "Dynamic High Stress Experiments on Soil," *Geotechnical Testing Journal*, ASTM, Vol. 10, No. 4, December, 1987, pp. 192-202.

5. Pochhammer, L. "On the Propagation Velocities of Small Oscillations in an Unlimited Isotropic Circular Cylinder," *Journal fur die Reine und Angewandte Mathematik*, Vol. 81, 1876, pp. 324-326.

6. Chree, C., "The Equations of an Isotropic Elastic Solid in Polar and Cylindrical Coordinates, their Solution and Applications," *Transactions of the Cambridge Philosophical Society*, Vol. 14, 1889, pp. 250-369.

7. Kim, Dal Sun, *Memo for Record*, to M.K. McCarter, University of Utah, July 13, 1992.

8. Akers, S., *Personal Correspondence*, 23 July, 1993.

9. Davies, E. D., and S. C. Hunter, "The Dynamic Compression Testing of Solids by the Method of the Split-Hopkinson Pressure Bar," *Journal of the Mechanics and Physics of Solids*, Vol. II, 1963, pp. 155-179.

Collapse Phenomena and Shock Diagnostics



YOCOL Measurement System for Cavity Collapse

Robert G. Deupree, W. J. Turner
Los Alamos National Laboratory
and
Philippe Blain, Paul Flores, Noor Khalsa, and Don Macy
EG&G/Los Alamos Operations

ABSTRACT

There are currently two ways in which the process of cavity collapse is measured on Los Alamos National Laboratory nuclear weapons tests: 1) using backfill packages to measure the gas pressure and radiation (and infrequently the acceleration) in the stemming material, and 2) using CACOL units to measure the subsurface breaking of coaxial cables. Both of these are indirect measurements of cavity collapse and occasionally give incompatible results. This has led us to devise a more direct measurement of the stemming motion with a technique called YOCOL. The experiment follows the motion of a weight at the end of a wire from a linear transition transducer, which we expect to be tightly coupled to the motion of the stemming material.

I. INTRODUCTION

Knowledge of the vertical extension of cavity collapse is useful to containment for determining likely escape paths and how closely a new hole can be sited to an expended hole. For surface collapses there is of course no uncertainty, but we need some diagnostics to determine the location of the end of cavity collapse downhole for those events which do not collapse to the surface. Los Alamos has relied on downhole radiation and pressure packages and on CACOL (Deupree, Neergaard and Turner 1992) units to measure the subsurface crushing of cables by the collapse (e.g., Deupree, Noel, and Watson 1987).

The backfill radiation and pressure sensors measure the radiation levels and the drop in pressure sensors measure the radiation levels and the drop in pressure associated with the cavity at selected places in the stemming. The CACOL time domain reflectometer measurements continually pulse coaxial cables to determine both the process of the collapse up the hole and the final

location of the cable crush. Note that all of these measurements are only indirect measures of the motion of the stemming material.

Very often the results of these measurement techniques agree, or at least are consistent with each other. However, there have been some events for which the data appear contradictory (Kunkle 1992). The most recent of these was the JUNCTION event, on which the all CACOL (and other) cables showed the end of cable crush to be below he plug at approximately 1000', while the radiation and pressure sensors at 495' detected radiation and the drop in pressure associated with the cavity. This difference in distance is sufficiently large that it is difficult to reconcile all the data.

We were tasked with trying to resolve this difficulty. After deciding that we did not have sufficient information to do this for the JUNCTION event, we began an examination to find some approach which would be more closely coupled to the stemming motion during cavity collapse. In the next section we outline the experiment we proposed. All of the hardware and software were designed, constructed, and tested between July and September 1992 because of a great rush to field the system on the DIVIDER event. Although we did not collect interesting data on this event, we did learn a lot about the system and we have made and tested a number of modifications in the event that we need to carry out this experiment. The results from the DIVIDER event and the modifications are given in section III.

II. THE YOCOL SYSTEM

The YOCOL (for YOyo COLlapse) system is composed of a number of downhole linear position transducers (called "yoyos") attached to spreader bars in various locations and an uphole controller and power supply. The uphole controller is in communication with a personal computer in the Monitor Room at the CP via either the microwave link or the fiber optic backbone.

A downhole yoyo includes a variable resistance whose value is proportional to how much cable has been rolled off a spool. The constant input voltage to the circuit is supplied from uphole, and the variable output voltage is recorded and translated into how much cable has rolled off the spool.

The initial concept was to attach a weight to the end of the spool and lock the weight in place until stemming was complete. The electronic lock would then be unlocked and the weight would drop a small distance into the stemming. It would remain in position through ground shock until cavity

collapse reached that location. Once this happened the weight would fall with the stemming and the changing output voltage recorded. Complications would ensue if the spreader bar to which the spool was attached broke and the spool began to fall, but there should be a time lag between when the weight starts to fall and the spool begins to fall. This measurement should give a fairly accurate picture of the stemming motion at this location. On any given event we would expect to field two or three of the downhole units in a fines layer not too far above a plug.

Beginning in July 1992 we began developing the packaging which would enable the commercial yoyo to survive downhole, the hardware and software fabrication of the uphole controller, and the software for the personal computer to communicate with the uphole controller. A picture of the final downhole package is shown in Figure 1. Figure 2 shows one of the two downhole packages attached to a spreader bar on the DIVIDER event.

We discovered that we had a design problem when we put one of the downhole units on a shaker table to see if the unit could experience a simulated ground shock and still function. As long as the weight was locked there was no problem. However, when the weight was dropped and then hit, we found that the release of the weight tension allowed the cable to come off the spool and tangle. This rendered it useless. Under considerable time pressure, we decided to keep the weight locked until after ground shock had passed and then drop the weight. This required us either to drop the weight remotely from the Monitor Room or to have it drop automatically a set time after it received the fidu trigger. Both options required considerable reprogramming. This also required that the power source to supply the voltage signal to drop the weight be permanently hooked up.

III. THE DIVIDER EVENT

The downhole units fielded on the DIVIDER event were located at depths of 575' and 810' below the surface. These locations were about 50' above a plug. Each unit was calibrated several times before emplacement by pulling out the cable several set distances and reading the corresponding voltages. These were fairly reproducible and highly linear. The major difference among calibrations was a constant offset.

Each unit was fastened to the spreader bar using two U bolts and then covered and taped with rubber sheeting (see Figure 2). The interruption to downhole operations while mounting took place was about ten minutes for each package.

Both downhole units were monitored during the downhole operation and the early part of the stemming. At some time during an hour and a half period, the weights for both yoyos were released accidentally. This was believed to have been caused by a programming error in the uphole controller software which allowed access to the unlocking part of the code when not desired. Once that part of the code was accessed and a fidu occurred during a dry run in this time interval, the weights would be released. With the weights fully extend before stemming reached their location, it was clear that very little useful information would be obtained. However, we were able to assure ourselves that the lower yoyo failed just after zero time (as did the two backfill packages near the same location), presumably due to ground shock, but that the upper yoyo survived.

This premature releasing of the weights caused us to reexamine out approach. The uphole controller had been programmed in assembly language on a chip with limited memory. We felt that most of the problems we encountered would be alleviated by using a higher level language and some different hardware. This development effort is being completed. In addition, it was felt that we needed to devise a mechanism which would allow us to unlock the weights after stemming is completed but before we no longer have personnel access to the trailer. We have tried to accomplish this by adding a short beaded chain between the end of the yoyo wire and the weight. This significantly reduces the impulse traveling up the cable to the flywheel and prevents the cable from coming off the flywheel. The beaded chain arrangement significantly improves the problem, but extensive shaker table tests have shown that the cable can still come of the spool. Fixing this problem is an active area of research.

We have not completed development and testing of the YOCOL system. We believe that we could successfully obtain this data on any future event as long as the yoyo is sufficiently far from the source to survive ground shock.

REFERENCES

Deupree, R. G., Neergaard, J., and Turner, W. J. 1992, "Cavity Collapse Safety System:, Proceeding of the Sixth Symposium on the Containment of Underground Nuclear Explosions, 1, 311.

Deupree, R. G., Noel, S. D., and Watson, C. A. 1987, "Trends in Cavity Collapse Data", Proceedings of the Fourth Symposium on the Containment of Underground Nuclear Explosions, 2, 430.

Kunkle, T. D. 1992, private communication.

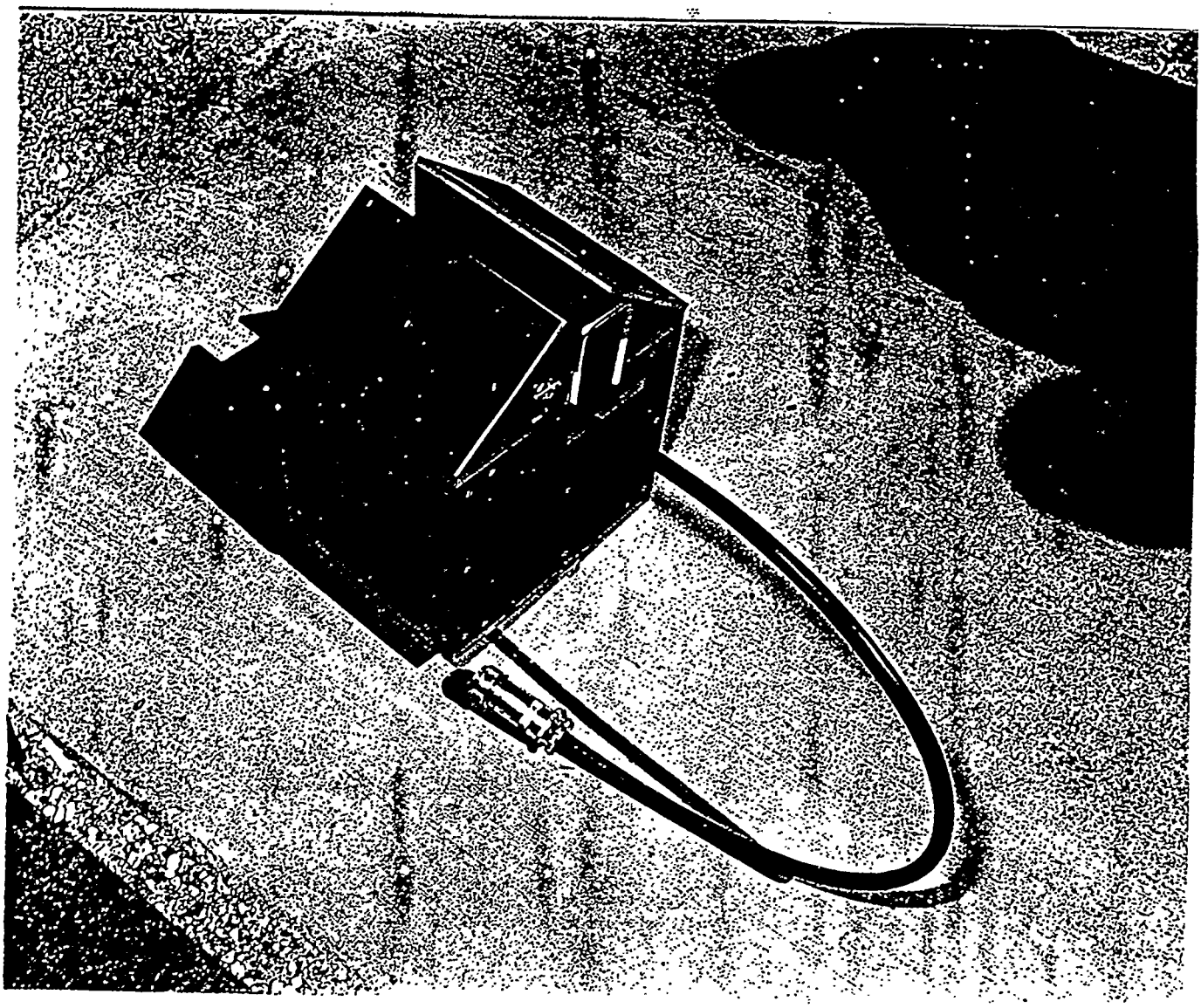


Figure 1. Downhole YOCOL package.

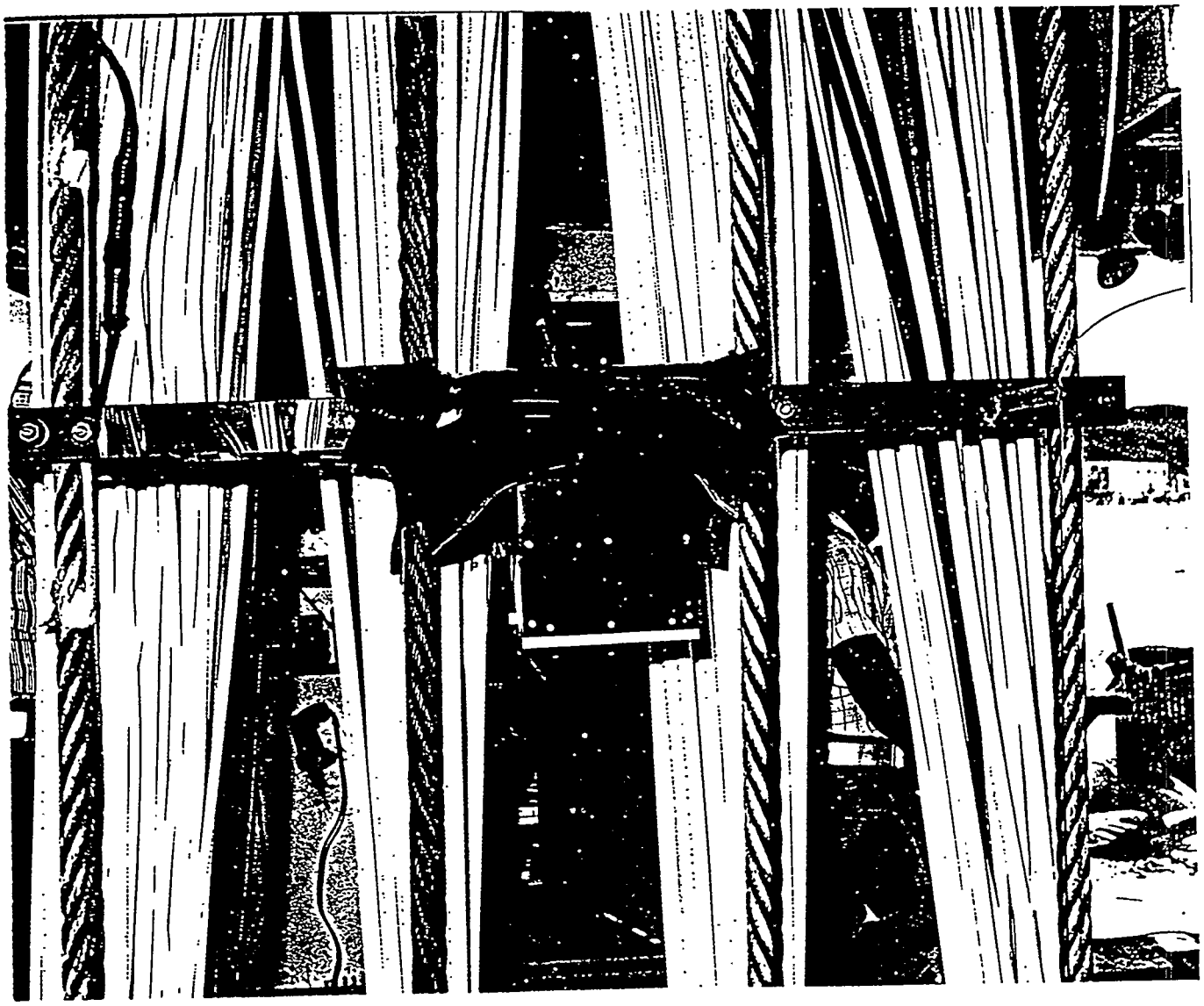


Figure 2. Downhole YOCOL package attached to a spreader bar.

A Radio Frequency Interferometer (RFI) System

H. C. Goldwire, Jr.
Lawrence Livermore National Laboratory, P.O. Box 808, Livermore, CA 94551

Abstract

We describe a radio frequency interferometer (RFI) system developed and tested by Lawrence Livermore National Laboratory over the last several years. The basic theory of operation, sample data, and analyzed results will be presented and compared to results obtained by conventional TDR means (CORRTEX).

A typical shock location measurement used for hydro-yield determination or for energy flow diagnostics comprises a coaxial sensing cable extending from the detonation region to a CORRTEX recording instrument. Our single digitizer-based RFI system uses an identical sensing cable installation technique. Recording equipment consists of a CAMAC digitizer module, which produces a sinusoidal probing signal (the signal sent downhole) for each sensing channel (cable), while also coherently sampling the phase of the reflected signal. Each channel is recorded using a single digitizer, providing maximal temporal and spatial resolution, but independent of channel gain or quadruture errors inherent to dual digitizer systems. Interpolation software with suitable look-ahead logic permits determination of complete quadruture information using a single digitizer. This RFI system provides several times better spatial resolution and two orders of magnitude better temporal sampling density than does CORRTEX. It also is less susceptible to electromagnetic pulse distortion and provides a direct means for identifying (and rejecting) any data so contaminated.

Stemming Particles and Performance



Review and Analysis of Stemming Practices at LLNL with Consideration of Slumping Phenomena*

Ray H. Cornell
Lawrence Livermore National Laboratory
Livermore, California 94550

Abstract

Established LLNL practices for stemming and granular materials do not seem to be completely based on analytical or measured criteria. However, data from field experiments and analytical work by a number of investigators indicate that the established standards are conservative regarding stemming induced over-pressure and granular stemming flow past restrictive annuli. Experimental data indicates that the falling speed of granular stemming is materially less than the expected terminal velocity. This implies the existence of significant wall energy losses for falling stemming.

It is difficult to assess how stemming rates effect the potential of slumping. Increasing the stemming rate has been observed to increase the emplaced bulk density of the stemming bed. Higher bulk densities reduce the potential size of a slump. However, increased stemming rate increases downhole air pressure. Increased air pressure is thought to be a factor in the production of slumps. These competing characteristics form a subject for further study and experiment. The need exists to develop a method for selecting an optimum stemming rate that will minimize or eliminate slumping potential while still keeping within maximum pressure and restricted area flow allowances.

Introduction

This review of granular stemming practices at LLNL was prompted by the apparent stemming slump** that occurred two days into the stemming of the GALENA event. Strain gages detected this "Slump" just above the nuclear test package, as a sudden 65000 pound load increase in the emplacement pipe. A drop in the sand stemming by, as much as, 24 feet under the bottom grout plug was speculated. The presence of this apparent void in the stemming column was worrisome and caused the CEP to reconvene to review the implications to nuclear containment.

We re-checked the GALENA stemming plans and conducted our own investigation at LLNL. We confirmed that established standards for materials and procedures were followed. We followed LLNL specifications for stemming mass flow rates which were, purportedly, designed to minimize slump producing bridging and downhole pressure buildup. We even included an extended waiting-time procedure during the stemming of GALENA, specifically, to avoid a slump occurring during subsequent stemming and grout plug emplacement. Still the slump occurred.

The validity of our stemming standards, which were derived from work and experience dating as far back as the late 1960s, were questioned during the GALENA investigation. A review of past documents uncovered most of the analytical models and explanations used to develop our present practices. This research also unearthed inconsistencies between some of this past work and the sparsely available data from actual measurements.

---

* This work was performed under the auspices of the U.S. Department of Energy by Lawrence Livermore National Laboratory under contract No. W-7405-Eng-48

** Slumping is the sudden drop, or consolidation, of the granular stemming mass some time after it has been emplaced in the nuclear test borehole.

This paper gives a review of LLNL's granular stemming standards and a history of their development. In addition, these standards and their supporting theories are compared with the results of experiments and analytical work of others to form criteria used in the conclusions. Finally, a description of how environmental regulations and the search for economies in nuclear testing will effect future stemming materials and processes.

LLNL Granular Stemming Standards

Material Standards - LLNL granular stemming material requirements are described in formal LLNL materials specifications. These standards define permissible particle sizes, allowable moisture content and, in some cases, allowable or desirable chemical constituents. Table-1 lists properties for the most common LLNL stemming materials.

Table 1 - Properties of LLNL stemming materials

Material	LLNL Specification	Particle Sizes	Mass Percent	Allowable Moisture	Comments
Coarse Fill	MEL78-001400	> .625" .5"-.625" .079"-..5" <.079"	0 0-5 93-100 0-7	No Spec.	-
10-200 Sand	MEL76-001292	>.079" .003"-.079" <.003"	0 95-100 0-5	≤0.2%	<0.5% CO_2
Stemming Fines	MEL75-001282	> .625" .5"-.625" .375"-.5" .079"-.375" .006"-.079" <.006"	0 0-5 0-10 15-35 45-65 10-15	≤3.5%	-
Magnetite	MEL76-001300	>.094" .023"-.094" .006"-.023" <.006"	0 0-50 25-100 0-25	≤0.7%	Iron Content ≥55% Particle Density ≥4.5 g/cm^2
Boron Rich	MEL86-001761	>.5" .006"-.5" <.006"	0 75-100 0-25	≤1.5%	Boron Content ≥5.5%

Coarse Fill stemming gravel is, by far, the most used stemming material. Coarse Fill is naturally occurring gravel from the NTS shaker plant in Area-1. A sieving process eliminates particle sizes that are too large or too small. Approximately 80% of a normal nuclear test stemming column is composed of Coarse Fill gravel. The purpose of Coarse Fill is to fill volume. It provides very little impedance to gas flow.

The next, most important, granular stemming material is 10-200 Sand.* This silica sand has the ability to fill small cross section volumes without clogging or bridging. It is, also, used for stemming past narrow restrictions such as are found between the nuclear test package and borehole wall. These clearances may be less than 5 inches. LLNL used 10-200 sand to stem the 360 feet of borehole below the top GALENA experiment.

The remaining LLNL stemming materials are used for more restricted applications. Stemming Fines material is used in thin layers as a bed for pouring grout plugs. Magnetite and Boron Rich materials are

---

* 10-200 sand was formerly designated Overton sand.

The remaining LLNL stemming materials are used for more restricted applications. Stemming Fines material is used in thin layers as a bed for pouring grout plugs. Magnetite and Boron Rich materials are sometimes used in the annulus between the nuclear test package and the walls of the borehole because of their ability to effect nuclear radiation transport.

Stemming Rate Standards - Stemming rate standards are described in the LLNL Nuclear Test Engineering Division (NTED) Design Guide[1] (Section 7.) These standards were derived from original work by Kleck[2] and Hamilton[3] and are based, partly, on the calculated downhole pressure rise caused by falling stemming. Downhole pressure rise is calculated by:

$$\Delta P/\Delta H = R/[A(V_T)] \quad [1]$$

Where: ΔP = Pressure rise.
ΔH = Depth over which pressure rise is calculated.
R = Stemming rate (stemming mass/unit time.)
A = Cross-section area of the flow passage.
V_T = Average terminal velocity of falling stemming. Values for average terminal velocity are listed in Table-2.

Table 2 - Values of average terminal velocity for various stemming materials. These values were determined by Hamilton[3] and are included in the NTED Design Guide.[1]

Material	Terminal Velocity (ft./s)
Coarse Fill (Pea Gravel‡)	32
NTS Fines (Stemming Fines‡)	15
10-200 Sand (Overton Sand‡)	8

‡ Material names in the NTED Design Guide.

In 1970 Karpenko produced curves[4] for determining acceptable stemming rates. In 1975 Karpenko made these curves LLNL stemming rate standards.[5] Present LLNL stemming rate limit curves evolved from these early standards. See Figure-1. The stemming rate maximum of 200 tons/hr, shown in Figure-1, is felt to be a reasonable maximum capacity for stemming equipment.

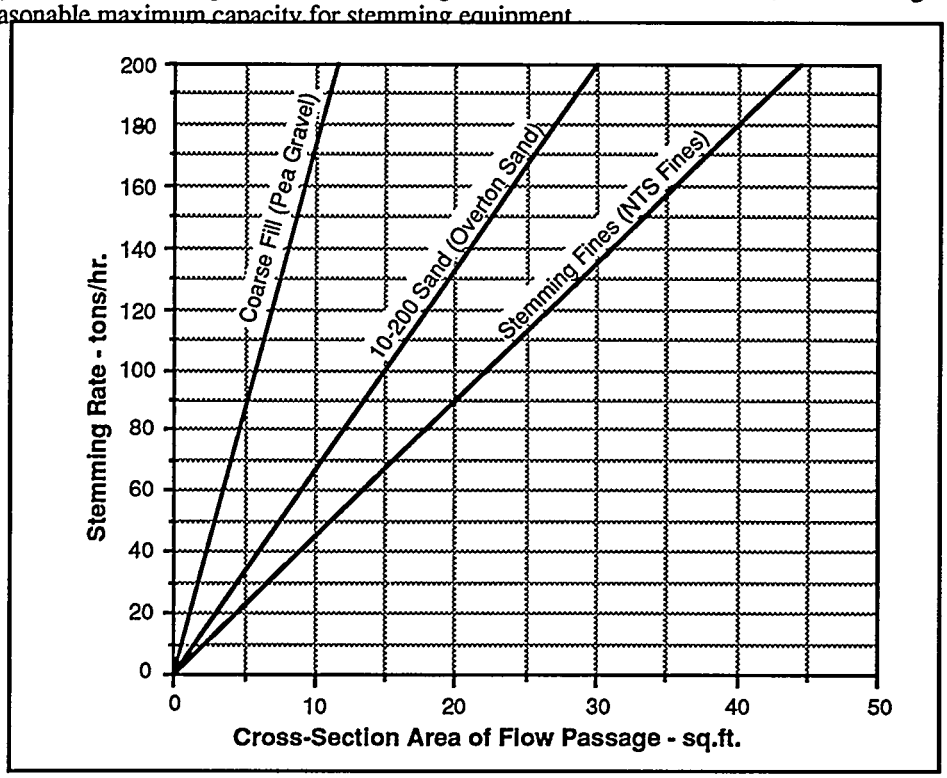


Figure 1 - Established stemming rate limits vs flow area for Coarse Fill, 10-200 Sand and Stemming Fines. Material names in parentheses are obsolete nomenclature.

Stemming Rate Standards - (continued)

Karpenko's 1970 memorandum[4] states that there is a direct relationship between bridging and stemming rates. He cites Klecks work[2] as evidence for this although Kleck makes no references to bridging in his paper. Karpenko also states in his 1970 memorandum that stemming materials with small particle size such as sand and fines have relatively high bulking factors* and tend to consolidate slowly. Because of this, he recommends keeping stemming rates at, or below, those shown in his curves. Finally, in this paper Karpenko refers to Hamilton's paper[3] regarding air pressure rise due to falling stemming. Hamilton defines this pressure in the terms similar to Equation [1] above.

In his 1975 memorandum,[5] Karpenko shows the derivation of his stemming rate curves.

$$Rv \leq A\,(V_T)/2 \quad \text{..... [2]}$$

Where: Rv = Volume stemming rate (yds/hr).
A = Cross-section area of the smallest flow passage in the column (sq.ft.).
V_T = Average terminal velocity of falling stemming (ft./s).

The value chosen for the area (A) is the area of the smallest restriction that the stemming must pass through in its flow path. Depth corrections to stemming rates are given in Karpenko's 1975 paper. For holes deeper than 1000 feet the stemming rate must be multiplied by 1000/hole depth.

Present stemming rate curves are given in tons/hr. Present depth correction standards are 2000/(hole depth) when stemming with Coarse Fill in holes over 2000 feet deep. Depth correction for all other stemming materials are the same as given by Karpenko (1000/hole depth).

Karpenko also recommends stemming for 15 minutes followed by 15 minutes of wait time when stemming small annuli. He also recommends a waiting period of 8 hours before pouring a plug. This timing and waiting in the stemming process seems to have been practiced for a number of years but was eventually abandoned because of its the apparent lack of correlation to bridging, slumping or other deleterious effects.

We included a 16 hour wait during the stemming of the GALENA event. This wait-time commenced after the pouring of the final 10-200 Sand lift and just before the pouring of the bottom grout plug. The apparent slump occurred ~2 days later.

Comparisons of Theory, Standards and Measured Data

Stemming Flow Past Restrictions - Karpenko's memoes[4-5] describe the basis for LLNL's stemming rate standards for flow past restricted areas in the nuclear test borehole. However, research into past documentation does not uncover technical reasons for selecting Equation-[2].

In 1978 Morrison[6] described some work he did on flow through annular orifices below a bed of Overton sand. He derived an equation for this flow and did some confirming tests.

$$Q = C\,g^{1/2}D(D-d)^{3/2} \quad \text{..... [3]}$$

Where: Q = Volume flow rate.
C = Flow coefficient (C=0.74 for d/D≥ 0.47).
g = Acceleration of gravity.
D = Outer diameter of annulus.
d = Inner diameter of annulus.

---

* Bulking factor is the percent bulk volume increase, caused by disturbance or flow.

Stemming Flow Past Restrictions - (con't)

$$w = Q/\gamma \quad \text{.....} \quad [4]$$

Where: w = Weight flow rate.
γ = Emplaced weight-bulk-density of Overton sand (~100 lb/cu.ft.)

Stemming flow in an annulus is assumed to be diffusely distributed as it flows downward. Leung etal[7] predicts the onset of flow choking when the solid volume concentration of particles in air approaches 3% of the total volume. Solid volume concentration can be determined by:

$$K = w/((\Gamma A U_S) \quad \text{.....} \quad [5]$$

Where: K = Volume concentration of solids.
w = Stemming rate (weight/time).
Γ = grain density of solids (weight/volume)
A = Cross-section area of the annulus.
U_S = Downward velocity of solids.

LLNL's Overton sand stemming rate standard (Figure-1) is compared to Overton sand flow rates calculated using Morrison's annular flow equation and the 3% concentration choking line in Figure-2. Note that LLNL's stemming rate limits for Overton sand are well below the others.

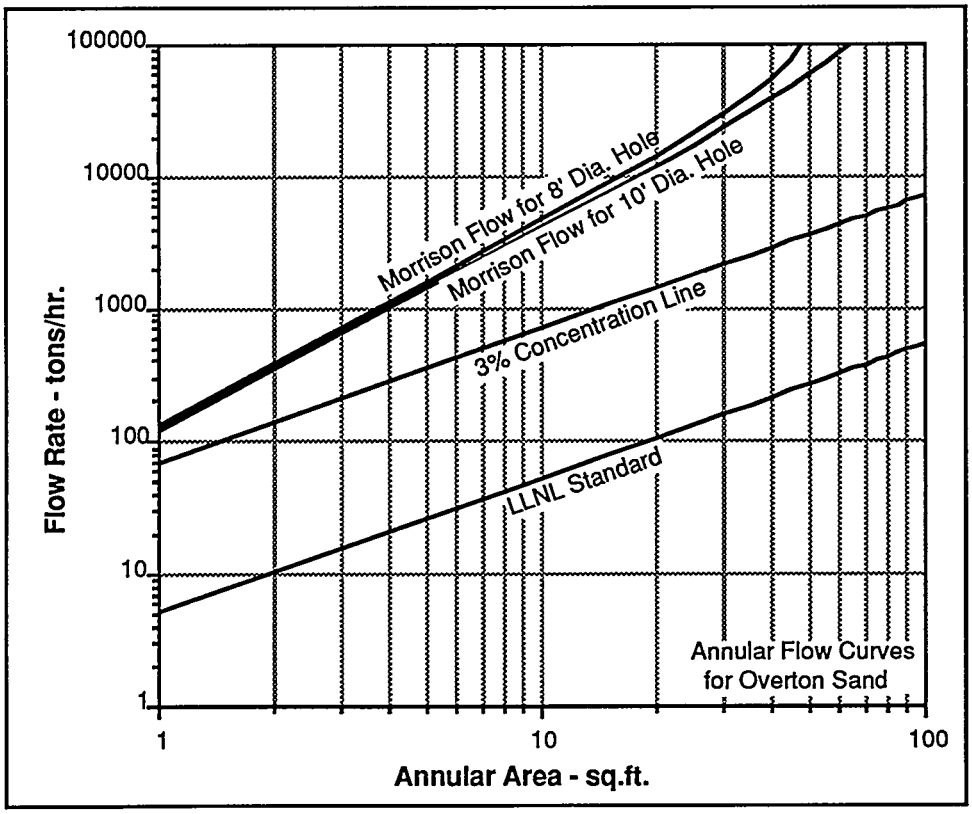


Figure 2 - Comparisons of various flowrate limits for Overton Sand(10-200 sand). The bottom curve is the flowrate limit described by Karpenko and the NTED Design Guide. The next curve (up) is the 3% volume concentration line that Leung describes as onset of choking. Above the 3% curve are flowrates (from a bed of sand) calculated from Morrison's Equation [3].

U2ar Stemming Experiment - In November, 1976, LLNL conducted a comprehensive stemming experiment in hole U2ar at NTS. During this experiment two different stemming materials were poured down the 4 feet diameter-cased hole while various measurements were made. Stemming rates were also varied during the experiment. Air pressure and stemming stress measurements were made at a number of depths. Load on the downhole cable was also measured.

The U2ar stemming experimental data was reported by Freynik etal[8] in January of 1978. However little use has been made of this information except for some permeability analysis. Included in the U2ar experiments were measurements taken at the time a 16 feet slump occurred. This is probably the most comprehensive slump data ever recorded.

Emplaced Bulk Density - Karpenko[4-5] indicated that because small particle stemming materials have high bulking factors it is important to keep stemming rates low to avoid low density emplacement. However, the opposite seems to be true. Zaslawsky[9] observed that emplaced densities were increased by increased stemming rates during the stemming of the BANON event. The U2ar stemming experiment also showed increased density with increased stemming rate. See Figure-3.

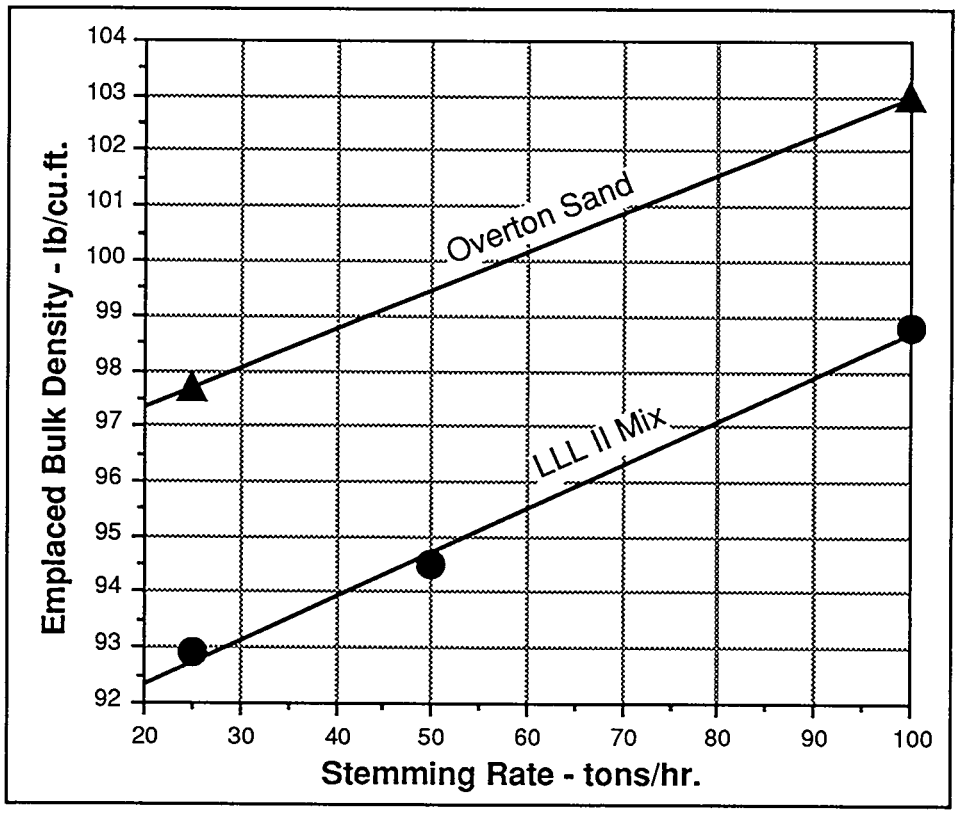


Figure 3 - Measured bulk densities vs stemming rates for the U2ar stemming experiment. Note the obvious increase in emplaced density at higher stemming rates.

Air Pressure Rise Gradients - Air pressure transducers were installed at several depths in hole U2ar for the stemming experiment. Air overpressures induced by falling stemming were measured and overpressure gradients were determined. A free data point ($\Delta P/\Delta H = 0$) exists at zero stemming rate. Comparisons of overpressure gradient data and gradients calculated with Equation [1] are given in Table-3. This data is also plotted in Figure-4.

U2ar air pressure gradient data deviates downward, away from the Equation [1] curve as stemming rate is increased. This phenomena is different from what we expect from stated theories. However, hardware designed to survive pressures calculated with Equation [1] will have a built in conservatism.

Material	Stemming Rate (tons/hr)	Overpressure Gradient from Test Data (psi/ft)	Calculated‡ Overpressure Gradient (psi/ft)
Overton Sand	100	.002116	.003838
Overton Sand	25	.000881	.000959
Overton Sand	0	0	0
LLL II Mix	100	.002332	‡‡
LLL II Mix	50	.001519	‡‡
LLL II Mix	25	.000919	‡‡
LLL II Mix	0	0	0

‡ Overpressure gradients calculated with Equation-1 using standard or estimated values for average terminal velocities.
‡‡ Terminal velocity for LLL II Mix stemming material has not been estimated. Pressure gradients cannot be calculated

Table-3 - Air overpressure gradient data from the U2ar stemming experiment. Overton sand induced gradients are compared with pressure gradients calculated using Equation [1].

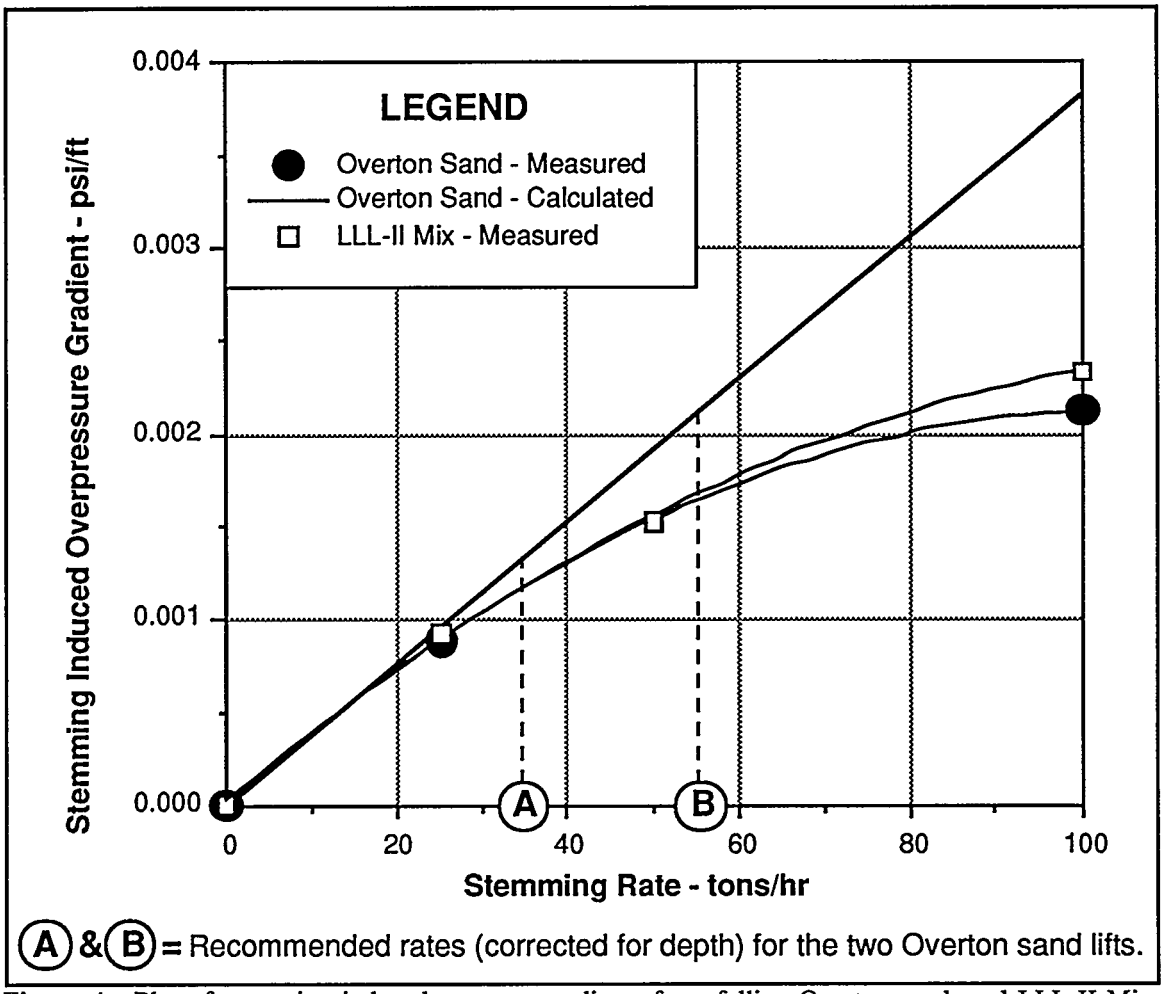


Figure 4 - Plot of stemming induced pressure gradients from falling Overton sand, and LLL-II Mix, measured during the U2ar stemming experiments. Overton sand data is compared with gradients calculated using Equation-1 and terminal velocity from Table-2. Measured overpressures are less than calculated overpressures. Note that zero stemming rate produces zero overpressure.

Velocity of Falling Stemming - Measured air overpressure gradients do not obey Equation [1]. It is, therefore, reasonable to assume that the velocity doesn't follow the accepted theory that stemming falls at terminal velocity.

Terminal velocity only occurs when all the potential energy loss of stemming, falling from one elevation to another, is transferred into dissipative aerodynamic drag. It is known, however, that some of the falling stemming energy is lost to the walls of the hole, the emplacement pipe and cables. Wall loss takes from the same energy source as aerodynamic drag. Therefore, there is not enough energy available for stemming to attain terminal velocity.

Aerodynamic drag is proportional to velocity squared, and since air overpressure gradients are proportional to drag, the following relationship should apply:

$$(\Delta P/\Delta D)/(\Delta P/\Delta D)_{max} = V^2/V_T^2 \quad \text{..... [6]}$$

where: $(\Delta P/\Delta D)$ = measured air overpressure gradient data
$(\Delta P/\Delta D)_{max}$ = pressure gradient calculated from Equation [1]
V = Estimate of real stemming velocity
V_T = Terminal velocity

Equation [6] was used to estimate the U2ar stemming velocities from overpressure gradient data. See Figure-5.

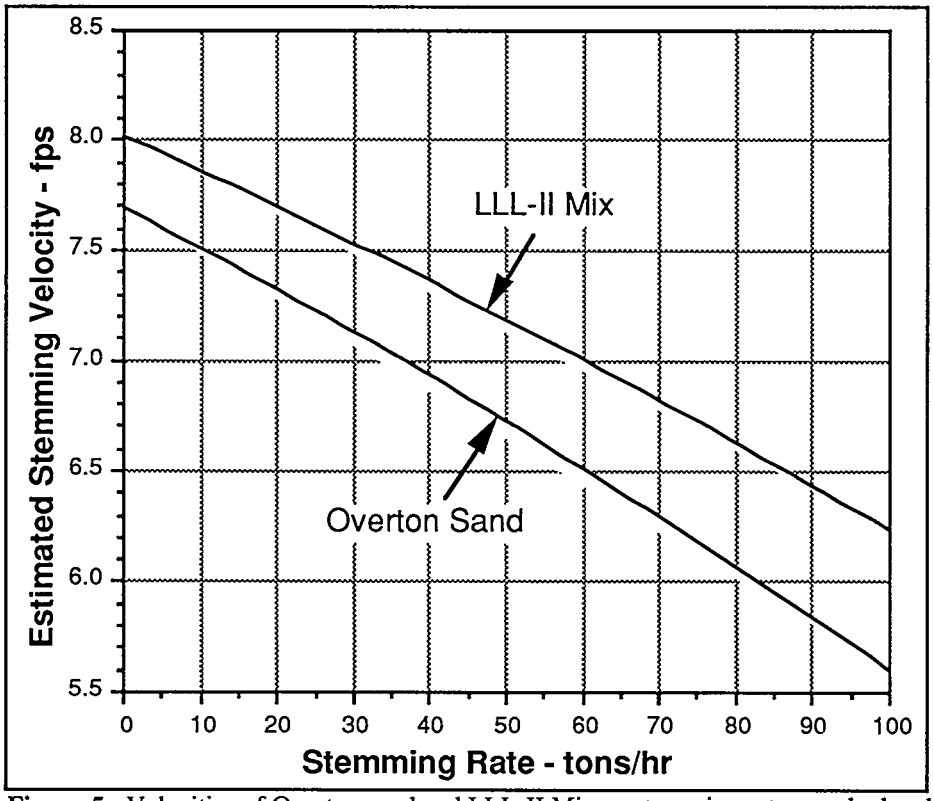


Figure 5 - Velocities of Overton sand and LLL-II Mix vs stemming rate as calculated using pressure gradient data from Figure-4 and Equation [6]. Note the drop in velocity with increased stemming rate. Velocity at zero stemming rate is probably the true terminal velocity.

Velocities calculated at zero stemming rate must be at terminal velocity because there can be no wall losses at this rate. Terminal velocity of Overton sand (10-200 sand) is 7.7 fps and LLL-II Mix is 8.0 fps when calculated using Equation [6] and the U2ar air overpressure data. In the past, estimates for average terminal

velocity of stemming were obtained from measured particle size distribution and estimated values for drag coefficients. See Hamilton's work[3].

The U2ar experiment gaveuseful air overpressure and stemming velocity data for Overton sand and LLL-II Mix falling in a four feet diameter borehole. However, velocities for most of the contemporary granular stemming materials have not been experimentally determined. Velocities calculated from the U2ar experiment don't address the eight and ten feet diameter holes, in use today. Hole size is probably a parameter that affects stemming velocity.

Slump Phenomena

The U2ar Stemming experiment provided a window into a sudden 16' slump. The following is a description of the changes that took place during this slump which occurred 8+ hours after the third layer of stemming was placed.

Pore Air Pressure - Air pressure was continuously monitored during stemming and after stemming was emplaced. During the 16' slump the buried air pressure transducers showed a sudden pressure rise in the two LLL-II Mix layers. See Figure-6. This sudden pressure increase is, no doubt, due to reduction of the pore volume caused by slump induced consolidation of the stemming.

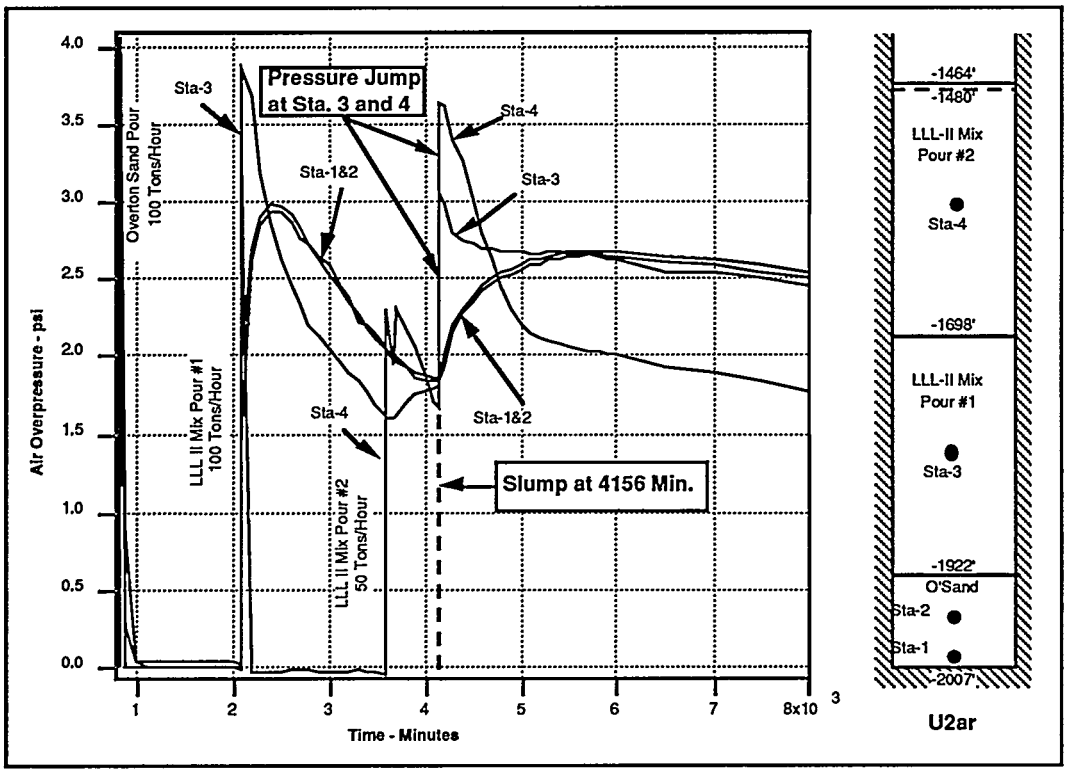


Figure 6 - Plot of air overpressure data from the U2ar stemming experiment before, during and after the 16' slump. Note the sudden increase in pressure at stations 3 and 4. This indicates collapse of pore volume of the LLL-II Mix stemming. The bottom stemming layer (Overton sand) does not exhibit a jump in pressure but instead rises slowly. This indicates that slumping did not occur in the sand but must have started somewhere near the bottom of the LLL-II Mix stemming

Estimation of stemming slump height is possible using a combination of the measured stemming pore pressure, emplaced stemming weight, length of the emplaced stemming bed and stemming-grain-density. The estimation method utilizes the ideal gas law pressure-to-volume relationships at constant temperature.

$$\Delta L = [1 - P_1/P_2][L - 4W/(\pi D^2 \Gamma)] \quad \text{.....[7]}$$

Where: ΔL = Height of the drop in stemming due to slump.
L = Length of the emplaced stemming bed
P_1 = Absolute air pressure in stemming bed just before the slump
P_2 = Absolute air pressure in stemming bed just after the slump
W = Weight of stemming in stemming bed
D = Borehole diameter
Γ = Stemming particle density

Pore pressure measurements are a positive way for detecting slumps and determining their extent. The strain gage load shift method that was used during the GALENA event is more difficult to analyze.

Stemming Stresses - Internal stemming stresses are caused by the overburden load. Only about two diameters worth of overburden pressure acts downward because almost all of the stemming load is supported, by friction, by the vertical walls of the hole, the emplacement pipe and signal cables. LLNL calculates stemming loads on vertical and horizontal surfaces by a method developed for storage bins. This method is described in the NTED Design Guide.[1]

Both horizontal and vertical stemming stresses were measured during the U2ar stemming experiment. These stresses changed dramatically during the 16' slump (See Figure-7). Horizontal stemming stresses dropped off, in the slumped layers, while the vertical stresses increased significantly. Horizontal stress reduction reduces frictional loads on vertical walls pipes and cables.

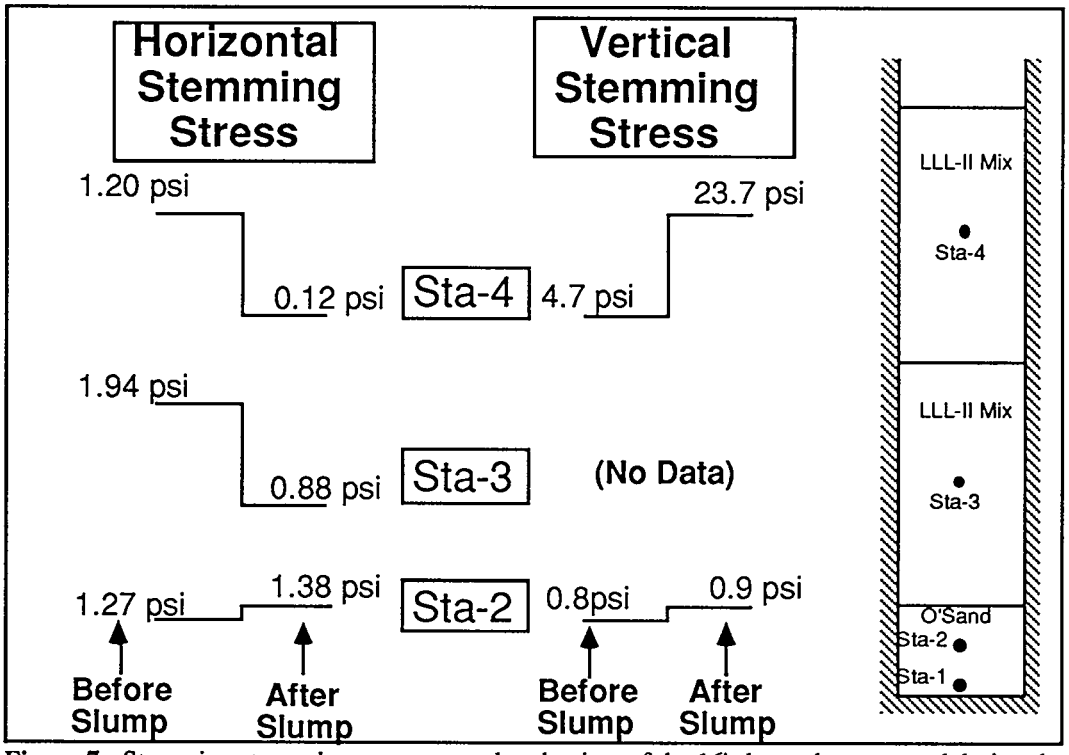


Figure 7 - Stemming stress changes measured at the time of the 16' slump that occurred during the U2ar stemming experiment. Notice how horizontal stresses decrease while vertical stresses rise dramatically at Stations 3 and 4. Also note the very small stress changes at Station 2. This helps to confirm that slumping occurred in the two LLL-II Mix layers but not in the Overton sand layer.

Slumping mechanisms

The U2ar stemming experiment didn't reveal much about what causes slumping or what role entrapped air plays in slumping. A full understanding of the conditions that promote slumping is necessary before methods for avoidance can be determined. However, a paper by Comfort and Cowin[10] gives insight into how a slump might move through a stemming column and Johanson and Jenike[11] derived a method for analyzing the effects of air pressure on settlement in a column of granular material. These papers may be a good starting point for further investigation into slump phenomena.

Summary and Conclusions

This review uncovered the following:

- Stemming rate limits are based on vague reasoning.
- Air overpressures are less than calculated.
- Velocity of falling stemming is probably less than terminal velocity.
- Specified LLNL stemming rate limits for Overton sand are well below the rates that cause choking.
- Increasing the stemming rate increases emplaced density which may reduce slumping potential.
- Air pressure measurements are a good way to obtain parameters useful for setting stemming rate standards and determining stemming velocity.
- Monitoring pore air pressure in stemming is an excellent way for detecting a slump and obtaining information for estimating the extent of a slump.
- Horizontal stresses decrease while vertical stresses increase in the stemming column during a slump.
- There is still a general lack of knowledge about downhole stemming flow and slumping.

Future Challenges

The Area-1 deposit is rapidly running out of coarse-sized-stemming gravel. New gravel sources or less expensive crushed gravel will have to replace what is now used. Crushed gravel causes higher stemming loads[12] and increases cable erosion.[13]

Airborne dust generated by gravel plant operations and downhole stemming is now prohibited. New, low-fines stemming materials, or enclosed handling systems, must be developed.

References

1. LLNL Nuclear Test Engineering Division, *NTED Design Guide*, M-186 Revision-1 (Internal Document), May, 1993.

2. Kleck, W. Jr., *Terminal Velocity of Stemming Materials*, **ENN** 70-23 (Internal Engineering Note), May 19, 1970.

3. Hamilton, W. A., *HANDLEY, U20m, Stemming Material Velocity, Add-On Experiment, Preliminary Results*, **ANS** 4-3574 (Internal Memo), April 29,1970.

4. Karpenko, V. N., *Rates of Stemming Emplacement Holes*, **NTE** 32-70 (Internal Memo), June 22, 1970.

5. Karpenko V. N., *Stemming and Polymer Plug Emplacement Criteria*, **NTED** (Internal Memo) 75-254, October 23, 1975.

6. Morrison, F. A. Jr., *The Flow of Granular Solids Through Annular Orifices*, **ENN** 78-27 (Internal Engineering Note), April 24 1978.

7. Leung, L. S., Wiles, R. J., Nicklin, D. J., *Correlation for Predicting Choking Flowrates in Vertical Pneumatic Conveying*, **Ind. Eng. Chem. Process. Des. Develop.**, V 10, No. 2, (1971) 183 - 189.

8. Freynik, H. S. etal, *Measured Air Overpressures, Soil-Particle Pressures and Slumps During the Pre-Asiago U2ar Stemming Experiment*, **UCID**-17619, January 4, 1978.

9. Zaslawsky, M., *Effects of Stemming Rate on Stemming Material Consolidation*, **ENN** 76-97 (Internal Engineering Note), March 17,1977.

10. Cowin, S. C. and Comfort W. J. III, *Gravity Induced Density Discontinuity Waves in Sand Columns*, **UCRL**-85920, April 1981.

11. Johanson, J. R. and Jenike, A. W., *Settlement of Powders in Vertical Channels Caused by Gas Escape*, **J. of Applied Mechanics, V**13 (1972) 863 - 868

12. Clay, J. and Biesiada, T., *A Recommended Method of Predicting Stemming Loads*, **ENN** 91-903 (Internal Engineering Note), March 17,1993.

13. Cornell, R. H., *Cable Abrasion Test Results and Analysis*, **ENN** 93-3 (Internal Engineering Note), June 15,1993.

Polyurethane Foam Cable Bundle Block*

John A. Mercier, Ray H. Cornell, Steve M. Pratuch, and Andy Lundberg
Lawrence Livermore National Laboratory
P.O. Box 808
Livermore, CA 94550

Abstract

Blocking the flow of radioactive gas in the emplacement hole requires attention to three items: the stemming materials, the cables, and the spaces between the cables. This paper deals with an improvement in the latter; that is, filling the spaces between the cables and, thus, forming a bundle block.

We have tested a two-part polyurethane foam in the field with apparent success. Field tests included recovery of sample cable bundles from a nuclear test in a tunnel. The foam creates a bundle block that survives the shock loading and improves the resistance to gas flow by as much as a factor of 3.

Introduction

In the last twenty years, several issues concerning containment have been studied extensively. Geology, or site selection, is fundamental. Methods of blocking gas flow in cables have been developed. Improved materials maintain the integrity of the stemming column. However, the cable bundle, i.e., the space between cables, is not easily filled with the correct material during stemming. A cable bundle block is a needed feature of containment design. The foam method discussed here is shown to be an improvement over past practices.

*This work was performed under the auspices of the U.S. Department of Energy by Lawrence Livermore National Laboratory under contract No. W-7405-Eng-48.

Typical LLNL Stemming Design

Figure 1 shows a typical stemming plan employed by LLNL. Most of the hole above the device canisters is filled with coarse granular material. At four locations (E-1), there are gas blocks in the cables. These cable gas blocks are located so as to be encapsulated by gypsum concrete plugs, which serve to block the hole and provide structure for the stemming. The cables are held apart or fanned out at these places, as shown in Figure 2, to allow the plug materials to flow through the bundle and around every cable.

One problem with the typical fanout and plug is that when the plug is placed, the fanout may be partially filled with some of the preceding granular material. Another feature is the dust on every cable, further weakening confidence in this arrangement as an obstacle to gas flow.

We have concluded that forming the bundle block at the surface during emplacement will improve confidence in the ability of the bundle block to perform as desired.

Polyurethane Foam as a Bundle Block

The material that could be used for a cable bundle block had to meet the following criteria:

- Easy to install
- Compound to be reliable and of long term stability
- Bonds to various surfaces (cable jacket, steel pipe)
- Easily removable in the event of reverse process
- Temperature in curing should not affect the electrical cables
- Withstand high gas pressure (125 psi)
- Environmentally acceptable
- Cost not prohibitive
- Not susceptible to damage by water, cement, and gypsum (stemming material)
- Survive zero time shock loading
- Not interfere with normal stemming procedures

A polyurethane foam at density 2 lb/ft^3 was found to have the desire characteristics. This material is mixed and dispensed by special equipment at the time

of emplacement, and requires little time for the operation. Laboratory experiments were encouraging, but we knew field tests were necessary.

Figures 3, 4, 5, and 6 illustrate the process in the field. First, the cable bundle is wrapped with a plastic sheet, which is secured by means of tape. Hoses carry the components to a mixing nozzle, which is inserted into the cable bundle. The finished product can be unwrapped (Fig. 6) in about 5 minutes. Foam that is outside the cable bundle is eroded away by later gravel stemming material, and thus minimizes interference with stemming.

We had earlier tested the foam for its effect on the cables. As shown in Figures 7 and 8, the effect is negligible. Although the foam shows a peak temperature well over 300°F, it has a very low heat capacity compared to the cables. Figure 8 shows a peak cable temperature a little over 110°F, well below the allowable temperature for any of the cables.

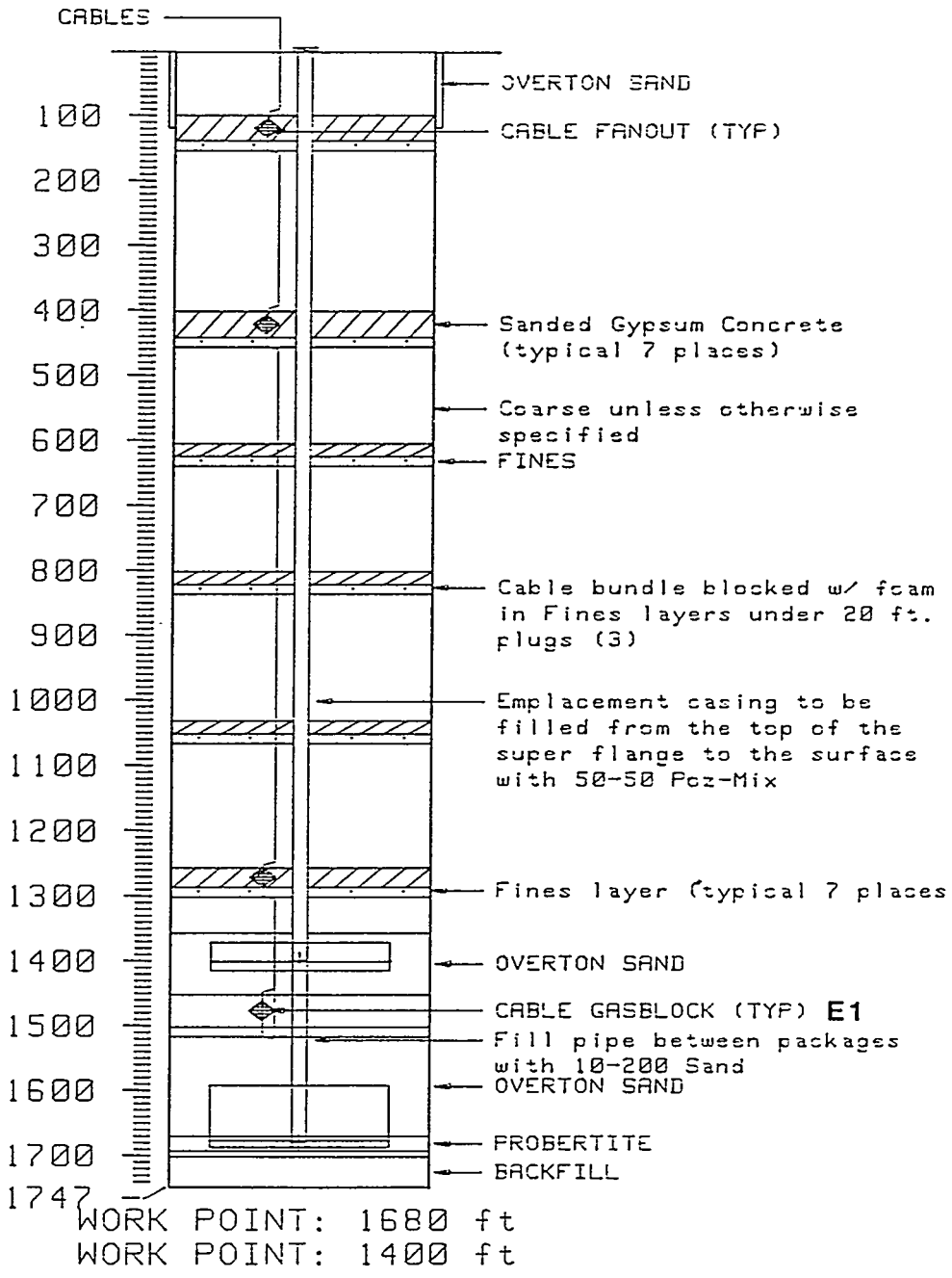


Figure 1. Standard stemming plan.

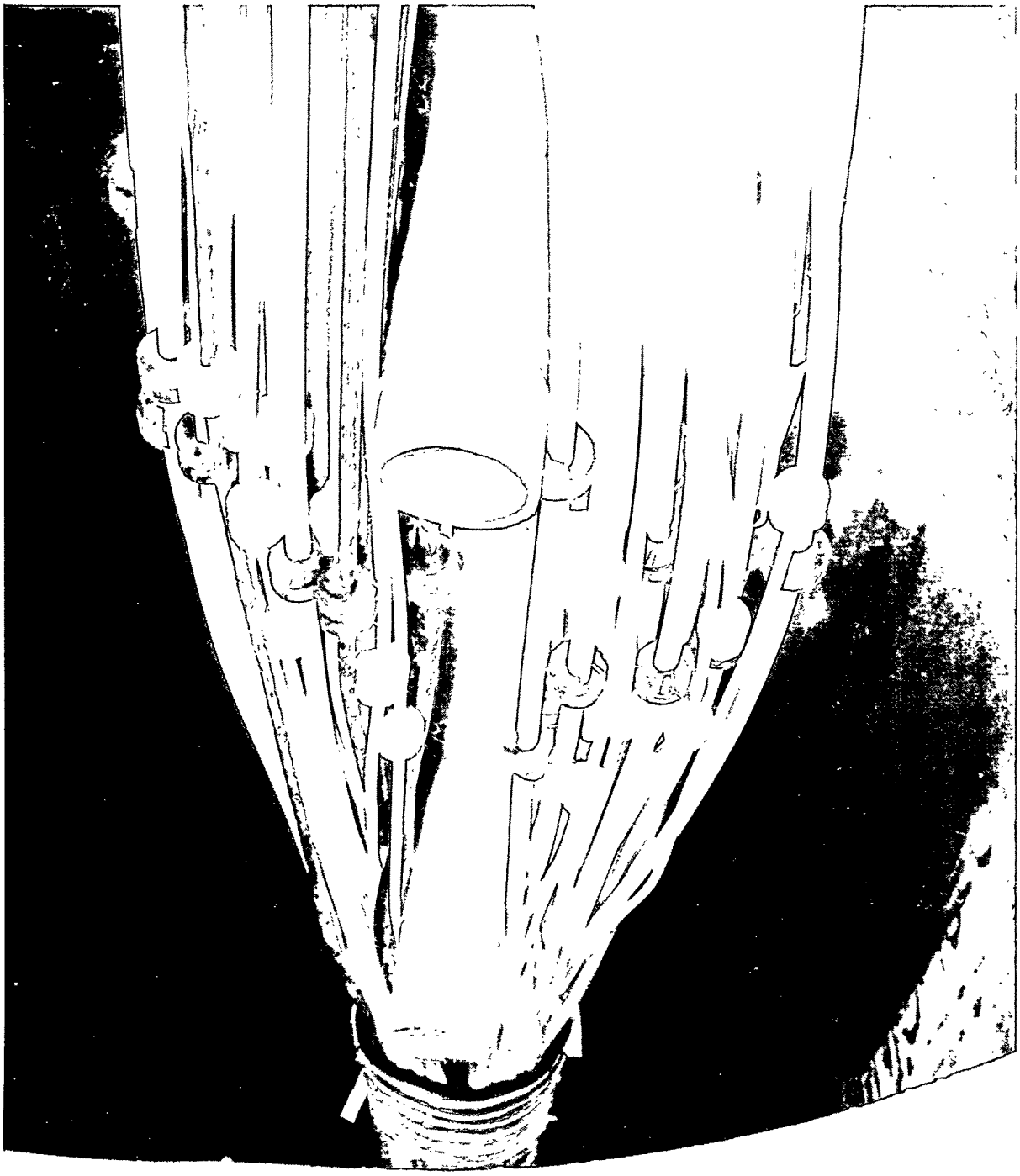


Figure 2. Typical cable fanout.



Figure 3. The cable bundle is wrapped with a plastic sheet,.



Figure 4. Hoses carry the components to a mixing nozzle, which is inserted into the cable bundle.

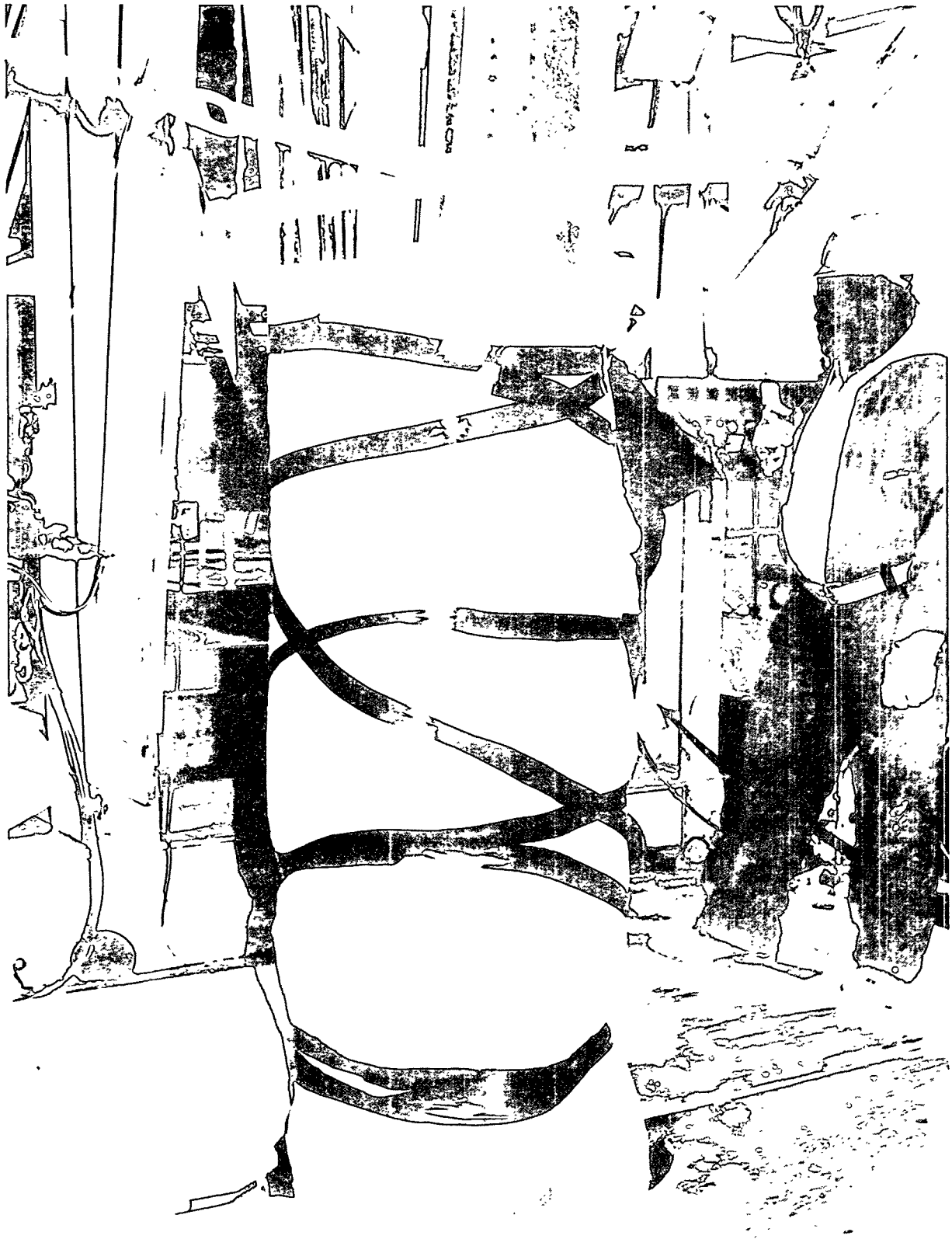


Figure 5. Plastic around the cable bundle is secured with tape.



Figure 6. The finished foam-filled cable bundle is unwrapped.

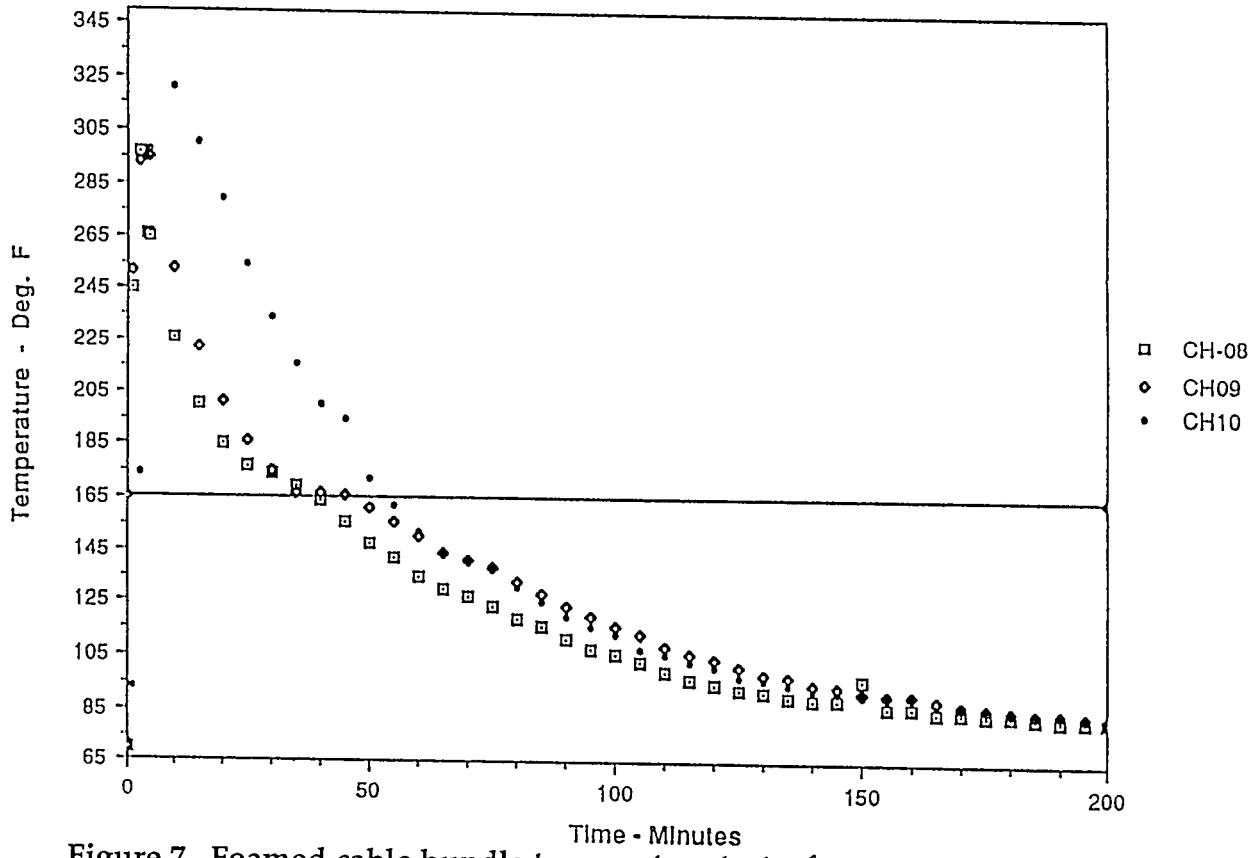


Figure 7. Foamed cable bundle temperature test—foam temperature vs time.

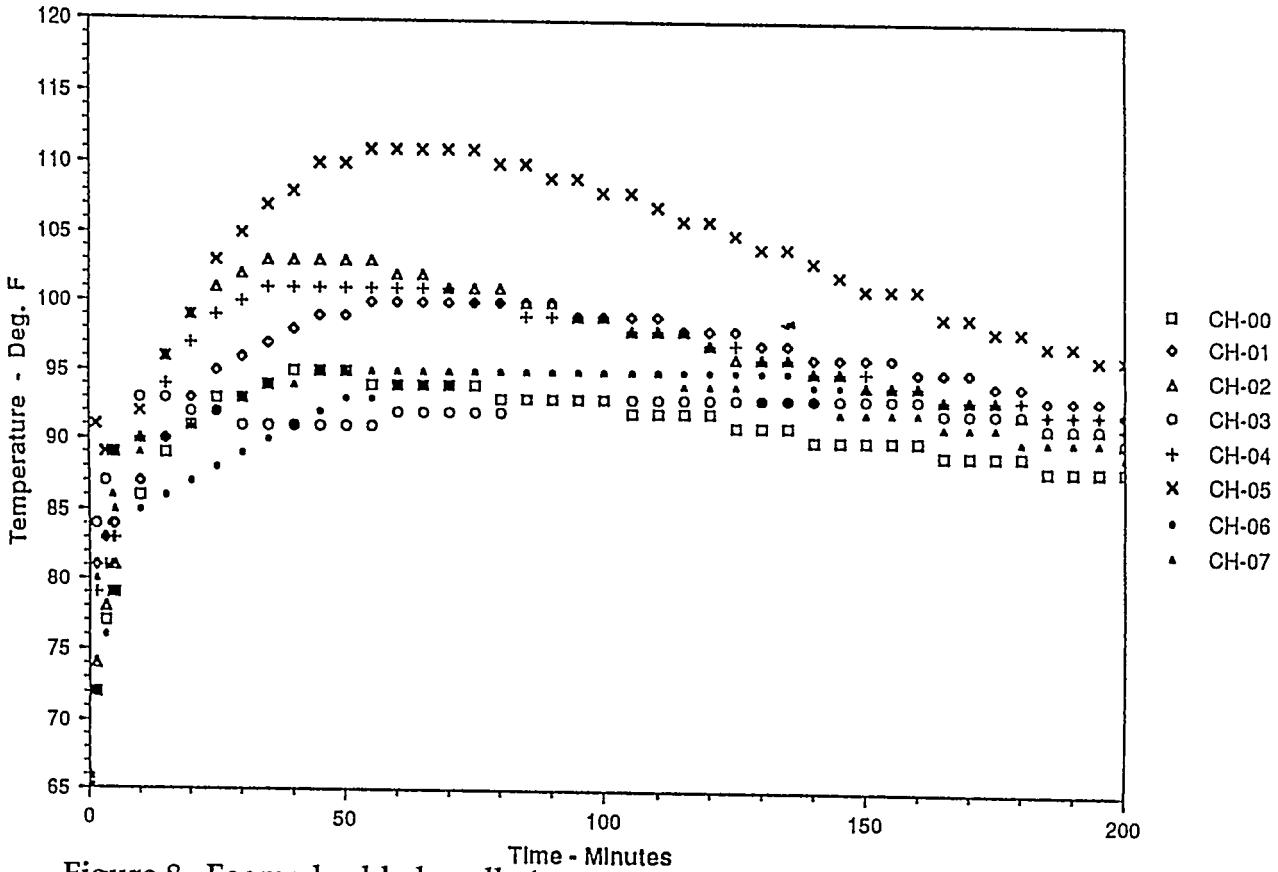


Figure 8. Foamed cable bundle temperature test—cable temperature vs time.

Field Tests

As described briefly above, the foam bundle block was tested for ease of installation. These tests, on the Hoya and Bristol events, were satisfactory and met all expectations. However, these events did not include instrumentation to allow assessment of performance.

A test of performance was done on a tunnel event (Distant Zenith). We placed samples of representative stemming and bundle materials at about 140 ft from the shot point. (See location 29 in Figure 9.) At this location the estimated peak radial stress is 2.7 Kbar.

Each of the four samples was placed inside a 50-gal drum. Cable bundles were filled with foam in three samples; the fourth had gypsum concrete to represent typical LLNL stemming practice. The sample drums were surrounded by the normal stemming material (sanded gypsum) for this location in a tunnel event.

Figure 10 shows a portion of an LLNL stemming design, a plug of sanded gypsum concrete with fines below and coarse gravel above. The roman numerals show the four regions represented by the tunnel samples.

I. Foam bundle block in coarse
II. Foam bundle block in fines
III. Foam bundle block in plug
IV. Cable fanout in plug

Figure 11 shows the typical cross section of a foamed bundle. Note the complete filling, even where cables appear to be touching. Since the foam is applied over a length of three or four feet, no two cables are straight enough or so tightly held together so as to form a barrier to the foam mixture.

Figure 12 shows Sample II after the tunnel test. Though not easily seen in this photo, the foam does not show any cracks or voids, which would later be pathways for gas. All four samples are shown in Figure 13. Recovery operations did not damage the samples.

Figure 14 includes a table of results of the tunnel experiments. Note that the two assemblies with porous stemming materials experienced significant permanent compression. Those with the gypsum concrete, even the one with a foam bundle block, had little permanent compression.

Gas pressure tests were done on the assemblies, as shown in the table in Figure 13. The typical LLNL plug with a fanout (Sample IV) is the reference design; it started to leak at about 5 psi. All others were better by a factor of three or four, except that Sample I began to leak in the interface between pipe and bundle at 5 psi.

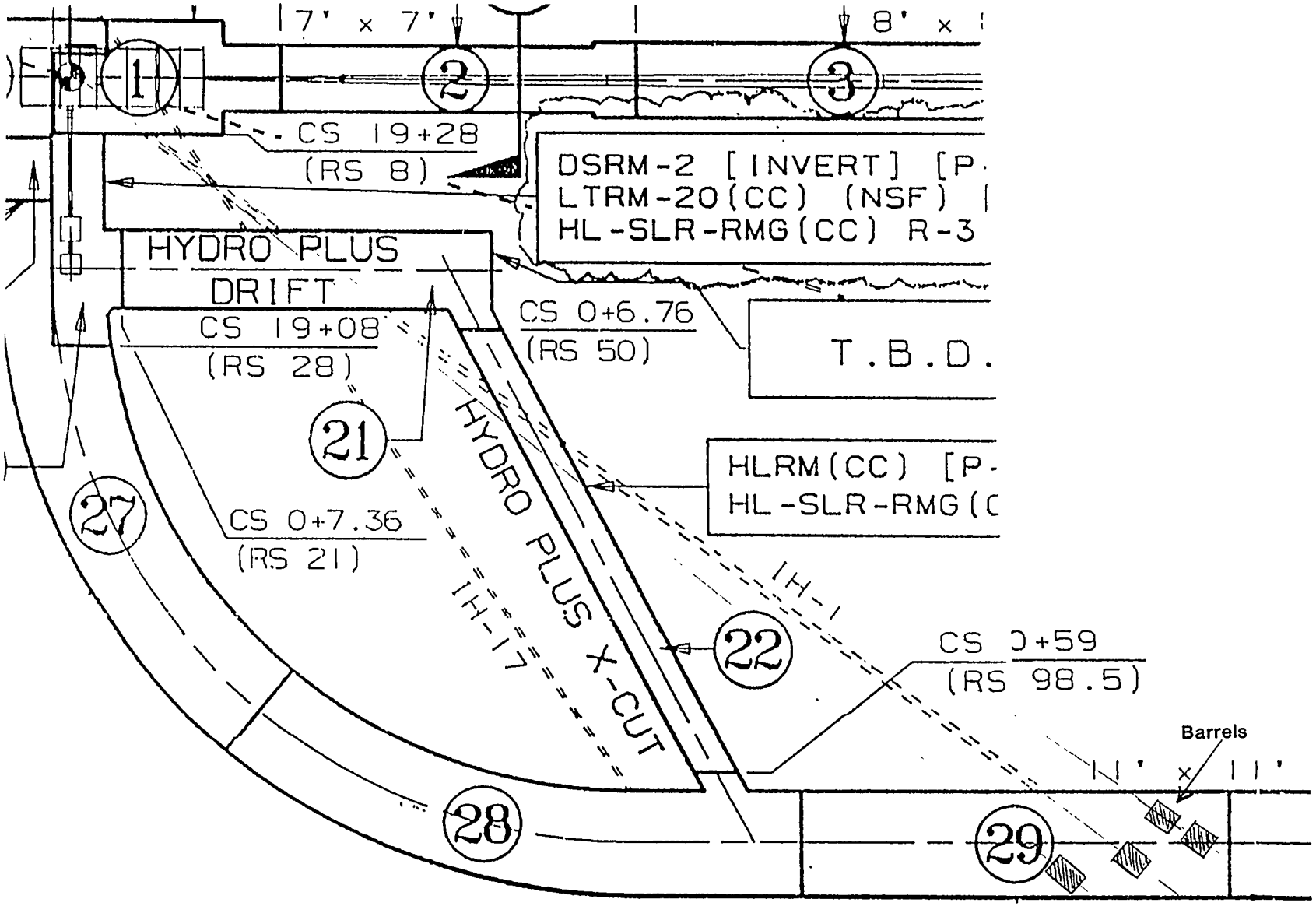


Figure 9. Samples were placed in location 29.

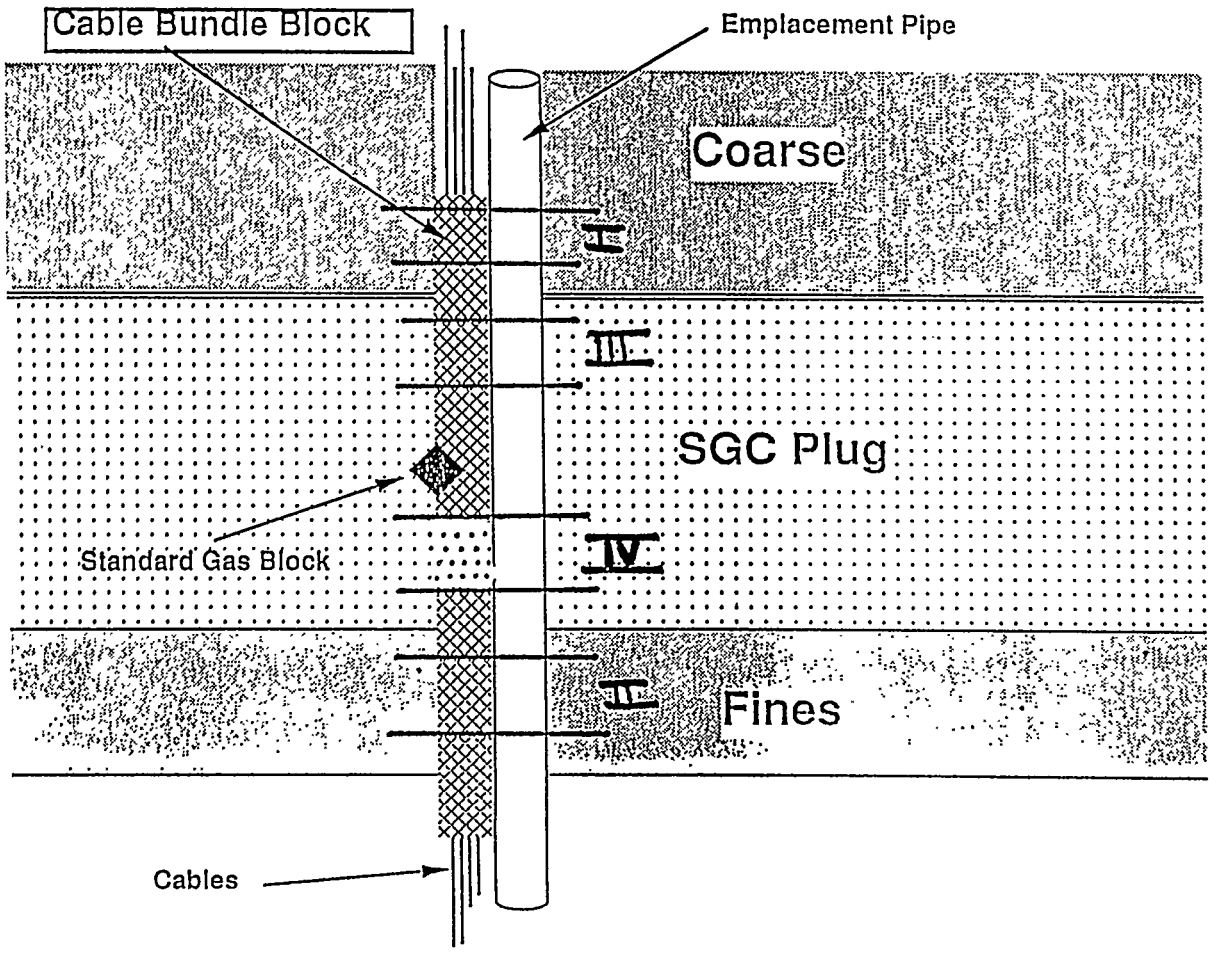


Figure 10. LLNL stemming design.

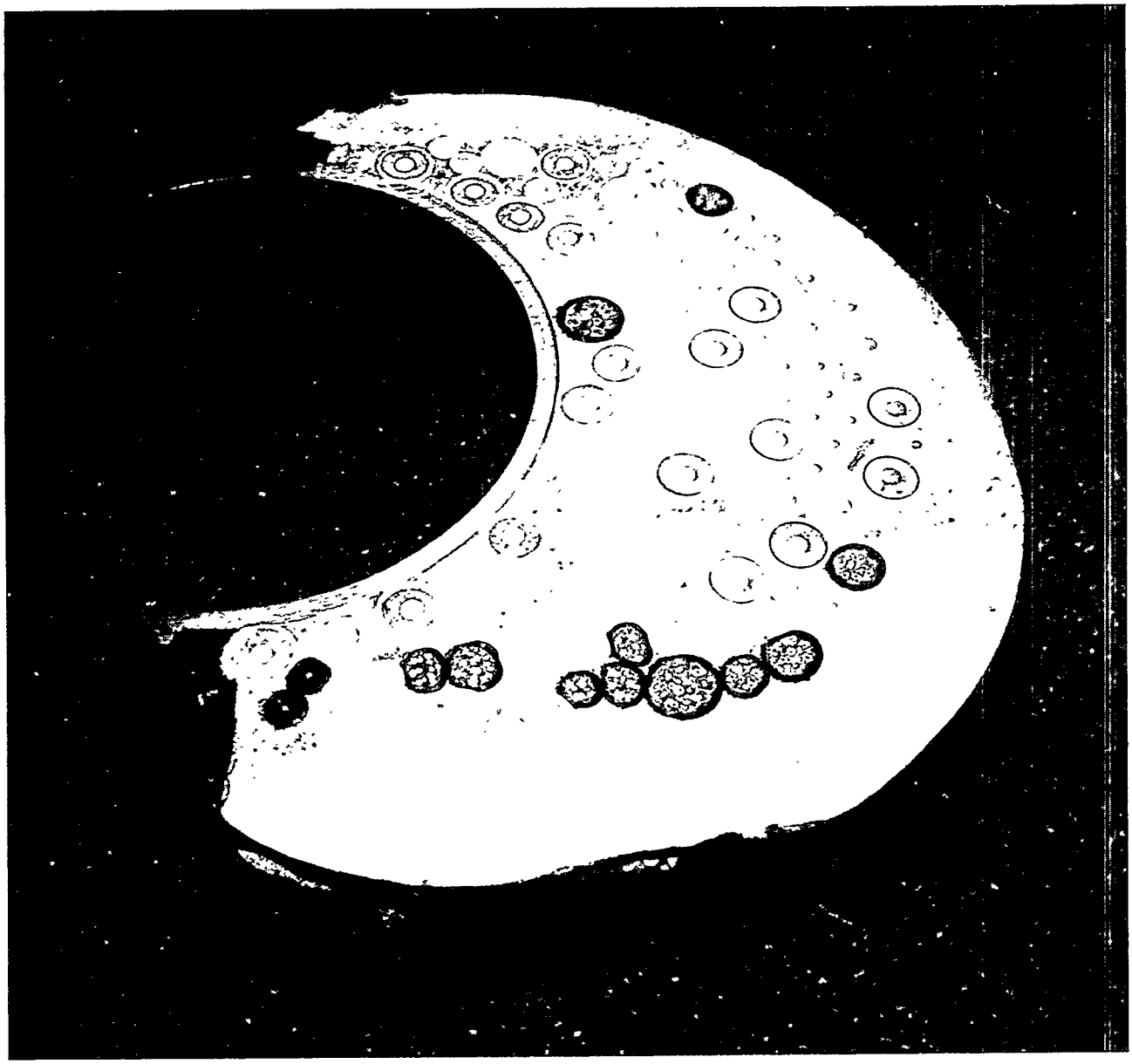
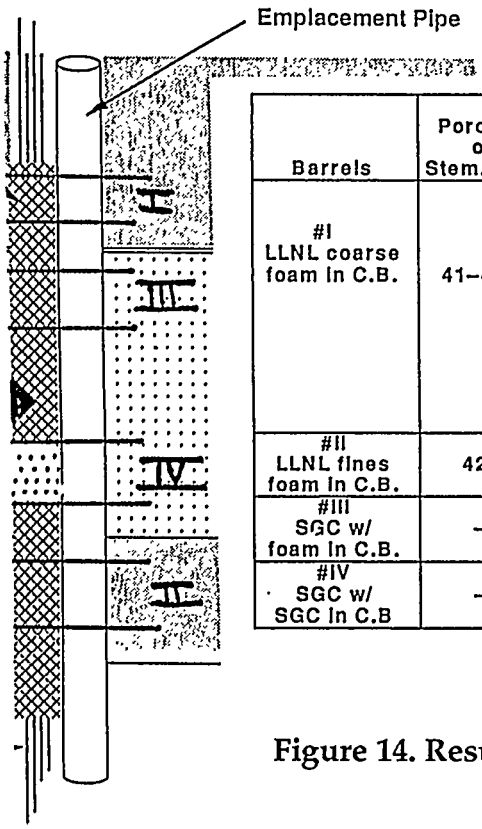


Figure 11. Typical cross-section of a foamed bundle.



Figure 12. Sample II after the tunnel test.

Figure 13. All four samples after the tunnel test.



Barrels	Porosity of Stem. Mat.	Surf. Area of Barrel (in^2) before/after	Circum. of Barrel (inches) before/after	Area % Reduction	Leak Press. (psi)	Where
#I LLNL coarse foam in C.B.	41–47%	535/346	82/66	35%	5 20 40	Interface cables/pipe (foam bundle o.k.) Edge of barrels & coarse Leak at edge of barrel due to shock damage & around pipe
#II LLNL fines foam in C.B.	42%	535/424	82/73	21%	15	Start leaking around 7/8 cables
#III SGC w/ foam in C.B.	—	535/499	82/79	7%	20	Start leaking around cables in bundle
#IV SGC w/ SGC in C.B	—	535/507	82/80	5%	5	Leak around edge of CB w/SGC

Figure 14. Results of cable bundle block leak tests.

Conclusions

Filling the cable bundle with foam has been shown to produce an effective resistance to the flow of gas in the stemming column. The process of filling the bundle at the surface allows effective control of the process, giving confidence that the bundle is filled. With experience, the operation can be done in less time than the conventional fanout.

Field Permeability and Strength Tests of LANL Grout and TPE Plugs

B. C. Trent, X-4, MS F664, LANL
Los Alamos, NM 87545

ABSTRACT

Several full-scale pressurization experiments were performed on LANL rigid plug materials to determine resistance to gas pressures. In particular, a new candidate grout, HPNS-5, has been proposed to replace certain applications of two-part epoxy (TPE) plugs. The testing procedure consisted of placing pressure transducers within coarse and fines layers between two rigid plugs. Air was then forced into the coarse layer and the resulting time-dependent pressures were monitored. During emplacement of the test plugs and layers of fine and coarse stemming materials, every effort was made to follow as closely as possible actual stemming procedures used full scale emplacements. The effects of ground shock and slap down were investigated by performing a similar series of experiments in the rack assembly hole for the JUNCTION event. To determine the strength characteristics of HPNS-5, a structural frame was used to load the wire harnesses after the permeability tests were completed. The experimental data from all these experiments are presented and their implications for underground nuclear testing are discussed.

INTRODUCTION

These experiments were planned to determine near-surface characteristics of LANL rigid plug materials. Modern LANL stemming designs usually include a TPE plug in contact with the surface conductor to serve as a last line of defense against radioactive gas flow toward the surface within the emplacement hole. The high cost of TPE as well as the requirement to maintain a separate capability for this material, has resulted in the search for an alternative material that would serve the same purpose. A new grout, HPNS-5, has been developed with support from the U. S. Army Engineer Waterways Experiment Station to fill this need. The ability of the plug material to support significant loads through the harness cables during and especially after detonation is also an issue that is receiving significant attention. It was decided to test the harness cables (one with and one

without a connecting pin) through the HPNS-5 to determine the ability of the new grout to adequately secure loads associated with stemming operations and post-shot phenomenology. This was done after the field permeability experiments so as not to affect those measurements.

This paper will address the four experiments in different sections: the HPNS-5 bulk permeability; the HPNS-5 permeability subject to ground shock and slapdown; the TPE bulk permeability; the pull tests of the harness cables in HPNS-5. Each section will discuss the details of the given experiment, and a separate section will address how the different experiments are related and the resulting implications for containment.

BULK FIELD PERMEABILITY FOR AN HPNS-5 PLUG

General

The purpose of these experiments was to determine the permeability characteristics of a rigid HPNS-5 plug in contact with a surface conductor. This would include sources of enhanced permeability such as cable bundles, wire rope harnesses and shrinkage or cracking near the grout/conductor interface. The geologic material, alluvium in this case, does not affect the measurement since flow is confined within the surface conductor. The hole U3jz was selected as the experimental site. It is a 98" diameter hole but was only drilled to a depth of 117 feet. The entire length was cased with a one inch thick steel emplacement pipe. This was considered an ideal site because several full-size permeability experiments could be conducted, one after another, under equivalent, controlled conditions.

Experimental Diagnostics and Stemming Operations

The stemming diagram for the first series of permeability tests is shown in Fig. 1. The depths shown are design values. The actual as-built lengths are provided and analyzed in a later section where the bulk permeabilities are calculated. The bottom of the hole was "sealed off" from the alluvium with a 8 foot length of HPNS-5 grout. The field diagnostics consisted of low pressure (20 psia) and higher pressure (30 psia) transducers in each of the coarse and fines layers. Temperature sensors were embedded within the upper grout plug to monitor the exothermic reaction. No measurements were made in the lower grout plug which was essentially only an exercise of mixing and pouring the new

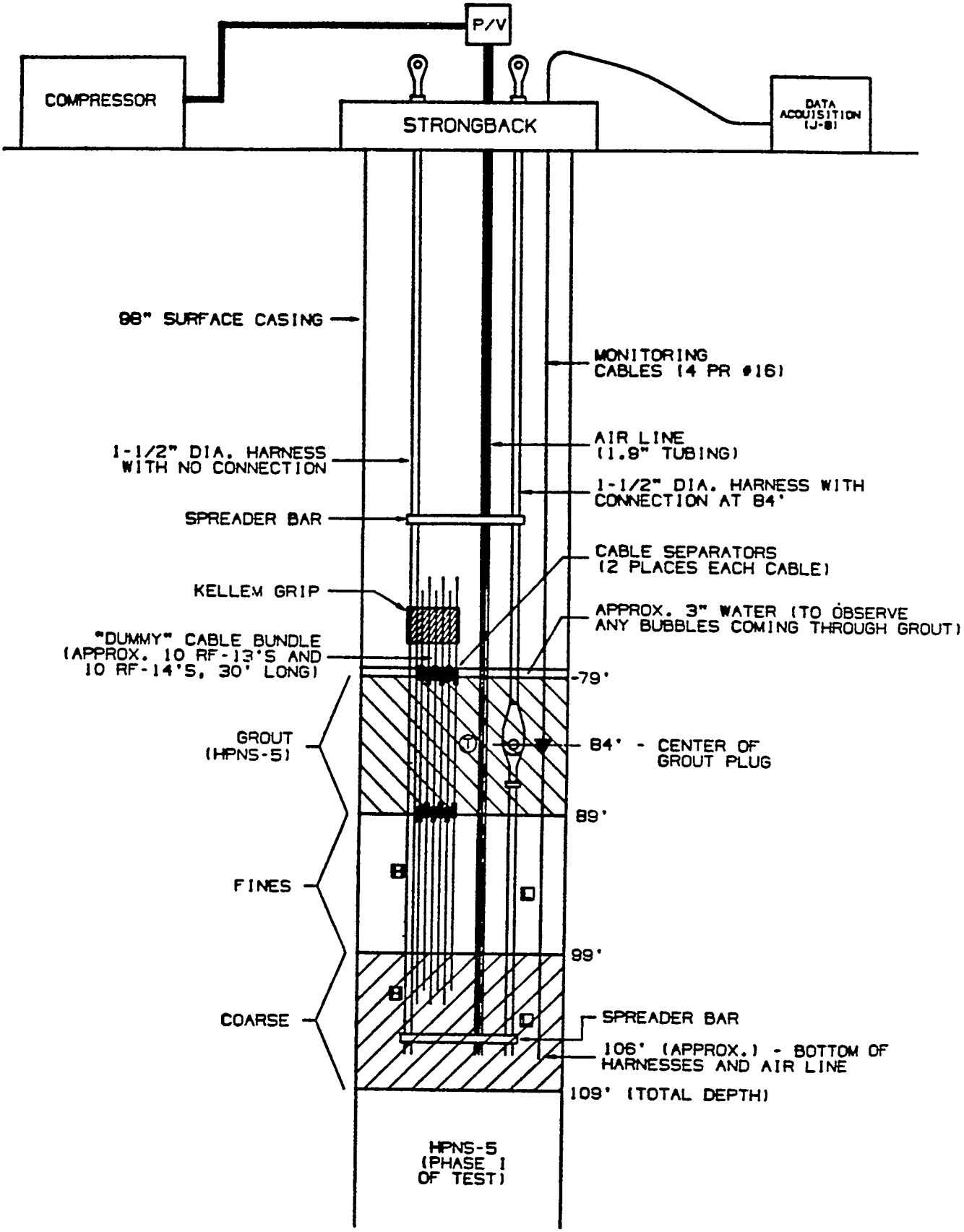


Figure 1. Stemming diagram (as designed) for field permeability test of HPNS-5 grout in U3jz.

grout. A pressure transducer was also attached uphole to the air supply pipe to monitor compressor pressures and detect any losses to the gauges down hole. Finally an air velocity gauge was mounted in the air flow pipe to determine the volume of air injected. The gauges were bundled together and attached to the wire rope harnesses. Spreader bars were used to separate the harnesses and this entire assembly was then lowered down hole.

A 10 foot section of standard coarse material was placed on top of the lower grout plug, followed by an 11 foot (as-built) length of standard LANL fines. This was accomplished by using a front end loader which dropped the material into a funnel equipped with a sifting grate. Finally, a 9 foot section of HPNS-5 was poured on top of the fines. Notice in Fig. 1 that several "typical" features common to LANL emplacements pass through the upper plug and fines layer and terminate in the coarse. These include two standard 1.5 inch wire rope harnesses (one with and one without a connecting pin at the center of the plug), and a mock cable bundle, consisting of approximately 20 cables. Some of the cables were left over from sections that had passed factory gas block pressurization tests. Other cables were fitted with field-installed gas blocks. They were fanned out with standard LANL cable separators. In addition, a steel pipe (1.9" i.d.) was placed so as to terminate within a few inches of the top of the lower plug. A compressor at the surface provided air to this pipe in order to "challenge" the upper most plug with pressurized air. Finally, several inches of water were placed on top of the upper grout plug and a TV camera, provided by Sandia, was lowered to observe any bubbles as air passed through the plug.

Experimental Procedure and Results

The original plan called for the first series of pressurization experiments to begin three days after the upper grout plug had been poured. This would correspond to the minimum time between completion of stemming operations and detonation of the nuclear device. After completion of the pressurization experiments, a second series of experiments was to be conducted after a delay of approximately one week. This would correspond to the maximum time between stemming and detonation under ordinary circumstances.

Surprisingly, after three days the temperature at the top of the plug was continuing to increase. Figure 2 shows the temperature time histories for two temperature sensors in the upper portion of the grout plug. The temperature initially drops to nearly freezing since the grout is mixed with ice to keep the material from setting up in the mixer during

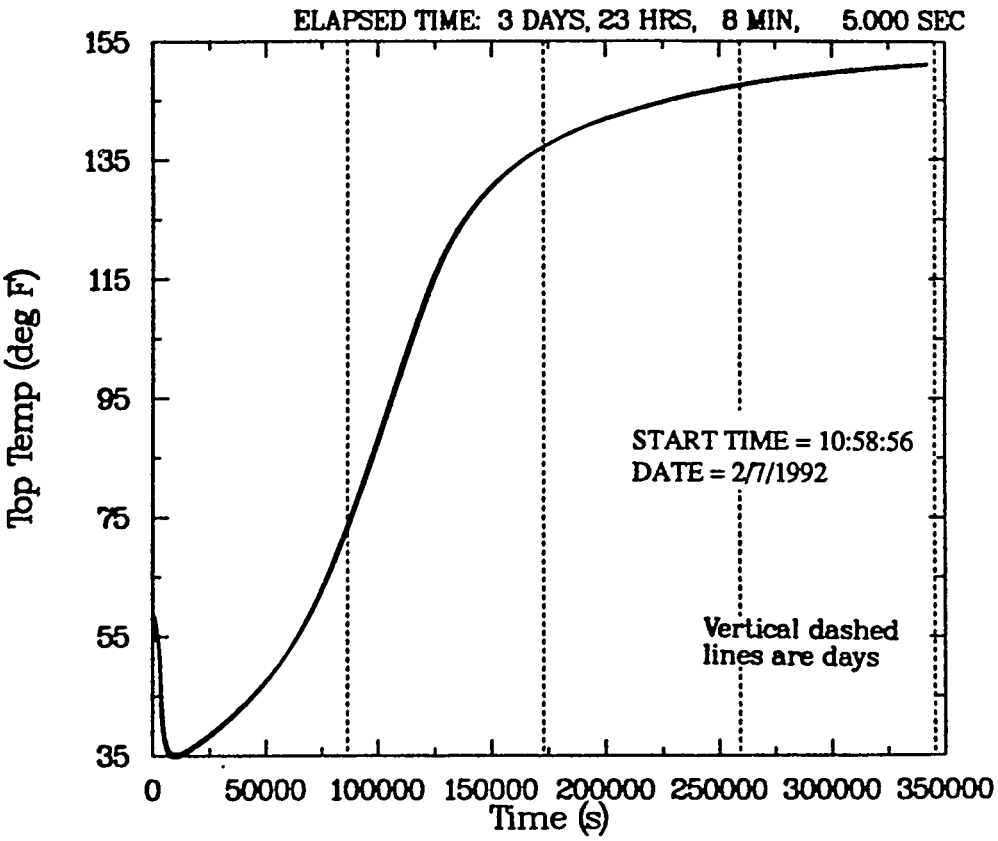


Figure 2. Temperature time histories in upper portion of top HPNS-5 plug ins U3jz.

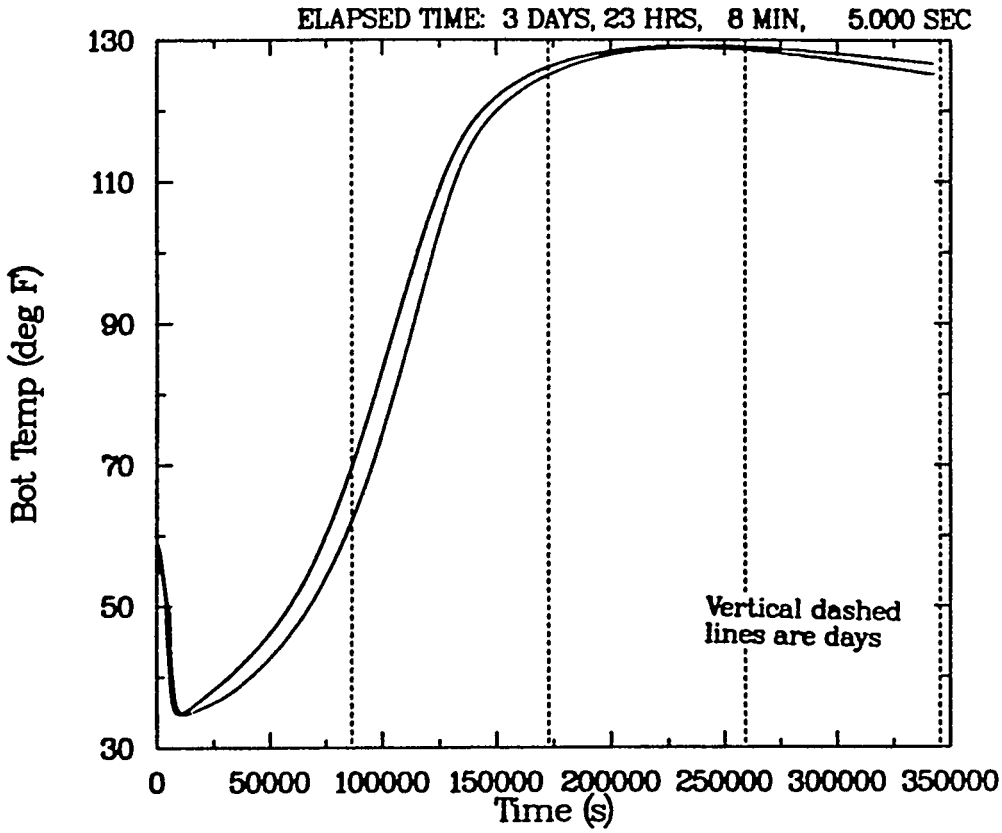


Figure 3. Temperature time histories in lower portion of top HPNS-5 plug in U3jz.

the trip from the batch plant to the field-site. Notice the temperature was still increasing, even after waiting an additional day, although two sensors in the lower portion of the grout plug had started to drop as illustrated in Fig. 3.

The decision was made to proceed with the experiment since curing was essentially complete. The actual pressurization could have been done two ways. One method would have been to inject air very slowly, e.g., 25 cubic feet per minute, to obtain data at low pressures and to avoid damage to the plug from a high pressure pulse. It was decided, however, that if pressure were to challenge the grout, it would likely result from a channel with moderately high pressure. Therefore, the first permeability test consisted of multiple injections of air at approximately 50 cubic feet per minute for seven minutes until a pressure of 23 psia (10 psig over ambient conditions) was reached.

Air was injected as shown in Fig. 4. The solid line shows the velocity in the pipe coming from the compressor. The scale for this curve is on the left. The dashed line is the integration of this curve multiplied times the cross-sectional area of the pipe (1.9 inch diameter) to give the net volume of air injected. The scale for this curve is on the right. Nearly 700 standard cubic feet (scf) of air were injected in this first experiment. Figure 5 shows the pressure time histories of the gauges. The initial pressures at each gauge have been subtracted out to show gauge pressure (psig) rather than absolute pressure (psia) as actually measured. In this way, the curves may all be plotted on the same graph and small calibration differences are all canceled out. All the pressure gauges responded essentially uniformly, indicating rapid communication through the coarse and fines.

During the first 5 minutes of the first injection no bubbles were observed in the water on top of the grout plug. Shortly thereafter, however, significant amounts of bubbles were seen around the circumference of the emplacement pipe and a few bubbles were coming up through the cable bundle (between the cables) and outside of the air supply pipe. For the next 140 minutes the pressure dropped at a fairly constant rate of approximately 3.8 psi per hour, after which the pressure decayed asymtotically to ambient conditions.

The pressure was than increased to 3 psig and allowed to decay for 30 minutes. The pressure was then increased up to 5 psig and allowed to bleed off for 30 minutes. Finally, the pressure was again increased to 10 psig and was monitored overnight. Generally, the same rate of pressure loss was observed in all the experiments, with slightly higher rates at the highest gauge pressures, and nearly flat response as the pressure difference in the

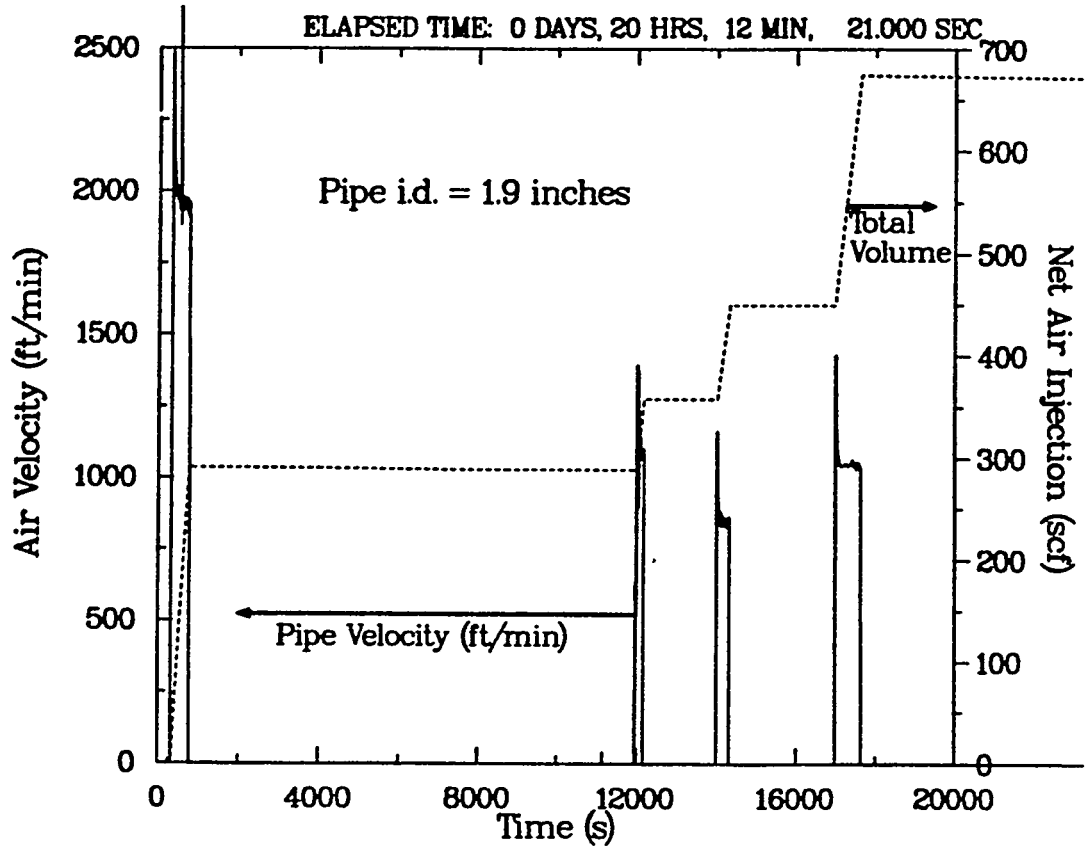


Figure 4. Velocity of air from the compressor (solid) and the volume of air resulting from this flow (dashed). This test was performed after 4 days of curing.

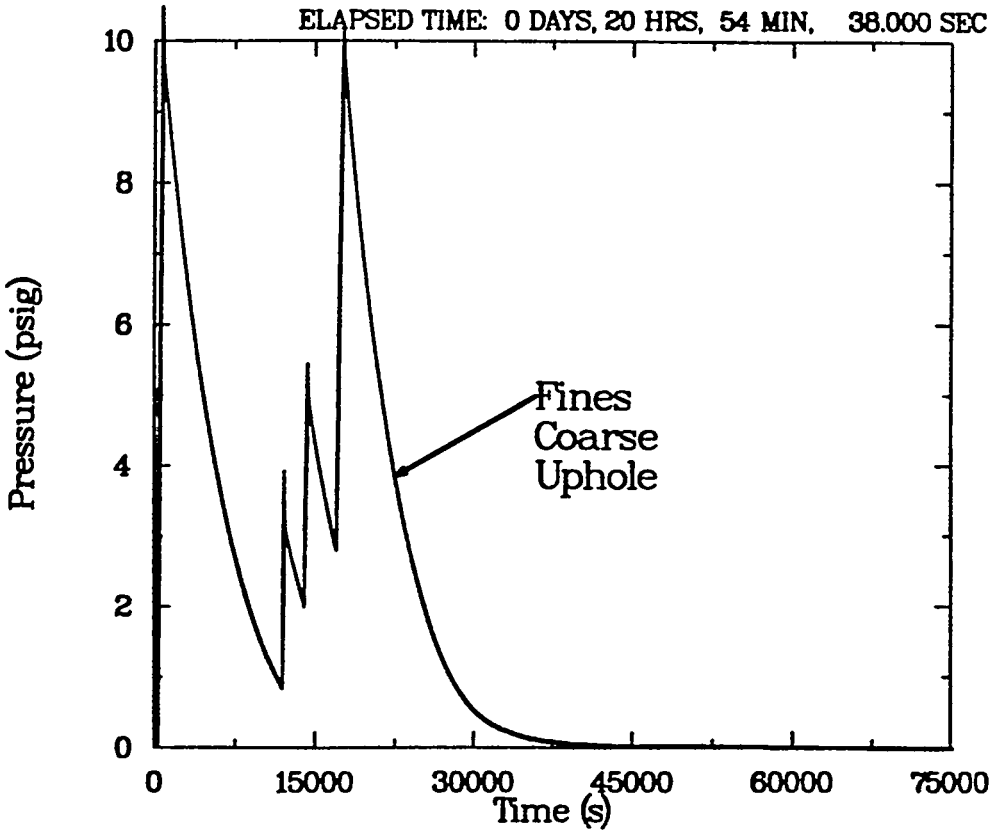


Figure 5. Pressure time histories for gauges in the fines, coarse and in the pipe from the compressor. This corresponds to the first pressurization test of HPNS-5 in U3jz.

stemming and the atmosphere approached zero. It took about seven hours for the final test to lose all of the overpressure. A calculation of permeability is given in the discussion following the experimental results.

Eight days later a second series of tests were performed with the same configuration. Figure 6 shows the air velocity and the resulting volume of air injection (dashed line). The pressure time histories are shown in Fig. 7. The results were similar but the rate of air loss increased to approximately 4.5 psi per hour, possibly indicating an increase in bulk permeability of the plug due to grout cracking or shrinkage (although this grout mixture had been promoted as having very little shrinkage or expansion during curing). The final permeability test involved pressurization to 30 psig and was monitored overnight. It only took six hours to reach equilibrium with the atmospheric pressure, compared to seven hours when the pressure was initially only 10 psig during the early series of tests, further indicating some permeability enhancement had occurred from 4 to 12 days of curing. In addition, the video camera showed bubbles actually coming up through the middle of the grout plug, far away from any hardware features, i.e. the cable bundle, the wire rope harnesses and the air pipe. This was observed at the first pressurization, only 2 psi above ambient. However, most of the air bubbles, as before, were concentrated around the circumference of the air injection pipe.

PERMEABILITY TESTS IN THE JUNCTION RACK ASSEMBLY HOLE

General

The rack assembly hole for the JUNCTION event was utilized for the second location of pressurization tests of the HPNS-5 grout. The plan was to perform similar permeability tests before the execution of the underground nuclear test and again after the test was completed to determine the effect of ground shock and surface spall on the permeability characteristics of the grout. The rack assembly hole was within 20 meters of surface ground zero, thereby subjecting the single grout plug used in the experiment to severe loading.

Experimental Procedure and Results

The actual implementation of the plug environment differed in many significant ways from the U3jz tests. First, the hole was only 74 inches in diameter and the bottom of the 17 foot emplacement pipe was welded into place, thereby prohibiting flow in the

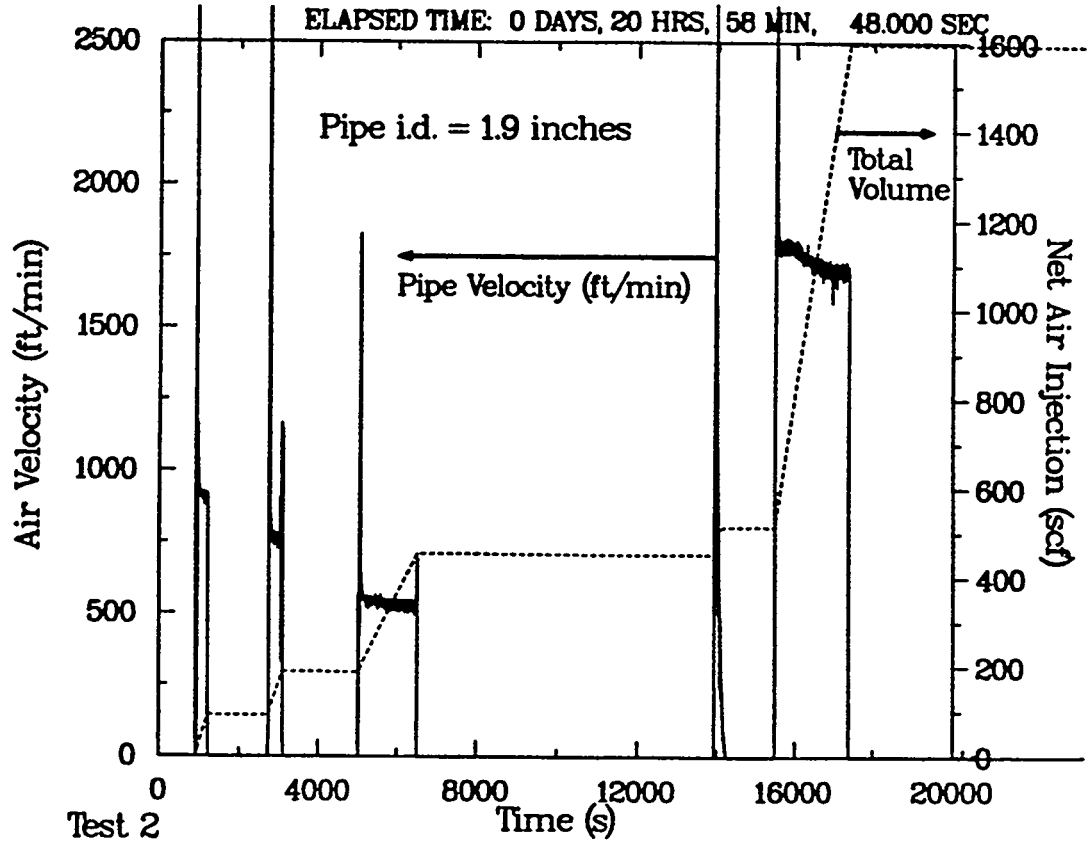


Figure 6. Velocity of air from the compressor (solid) and the volume of air resulting from this flow (dashed) after 12 days of grout curing.

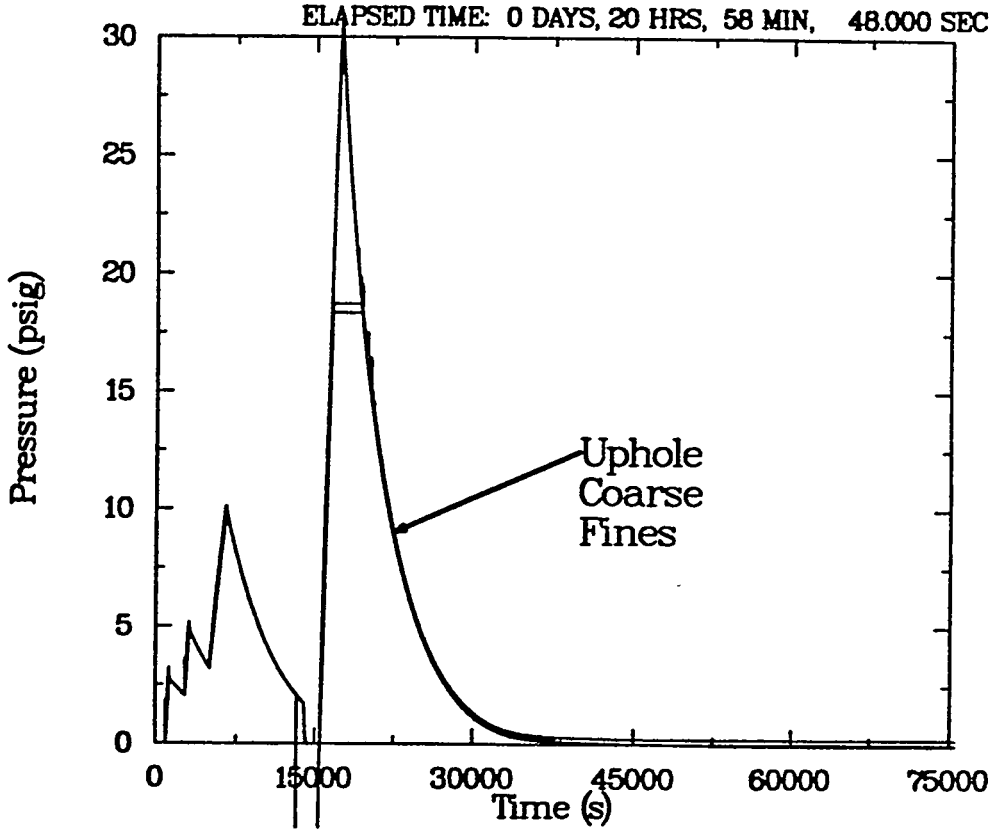


Figure 7. Pressure time histories for gauges in the stemming after 12 days of grout curing. The gauges in the coarse and fines are saturated at about 18 psig (30 psia).

downward direction. There were only four feet of fines and four feet of coarse below the eight foot long grout plug, providing a smaller reservoir of pressurized gas to act against a shorter plug. More importantly, there was no cable bundle and no wire rope harnesses and there were only two pressure transducers downhole. The temperature in the grout plug was monitored and performed essentially the same as the plug in U3jz, i.e. peaking after four days at about 150 degrees F. The time histories of the three temperature sensors in the grout are shown in Fig. 8. Notice once again the initial drop in temperature due to the ice present during mixing.

Since the void volume in the stemming was only about one fourth of that available in the U3jz tests (because of the smaller diameter and shorter lengths) the pressure increases were much more sensitive to the output from the compressor. Figure 9 shows the pre-shot pressurization and the resulting volume of air injected. Notice that only about one tenth of the volume of air was injected as compared to the first portion of the test in Fig. 4. The resulting pressures are shown in Fig. 10. Again, all three gauges indicated very similar performance, although the close-up view in Fig. 11 seems to show the uphole pressure slightly lower than the other two gauges. This would indicate that air is being lost "up stream" from the stemming due to a leak either in the valve, in the flexible tubing from the compressor or in the air injection pipe. The pressure difference, however, is so small that it may be simply the resolution of the gauges. Still, it is possible that without all the usual stemming features, the most permeable path is back through the injection system. The resulting bulk permeability would therefore be an upper bound.

The coarse and fines were pressurized to 16 psia (4 psi over ambient) and allowed to bleed off through the grout. The drop in pressure was only 0.5 psi per hour over the two hour test, a substantial improvement over the tests in U3jz study. No bubbles were observed at the top of the grout (covered with 1 to 2 inches of water) indicating the pressure loss might be in the very long length of the high pressure rubber tubing from the experiment (near SGZ) out to the perimeter fence where the compressor was located.

Ten days later, the post-shot pressurization experiment was conducted. The velocity/volume curves are shown in Fig. 12. Notice that the air is injected for a longer period of time to reach the same pressures as in the pre-shot experiment, but at a lower rate. This is a reflection of the lack of control over the valve on the compressor. It can be seen, however, in Fig. 13 that the pressure in fines is about 4.5 psia, the same as the

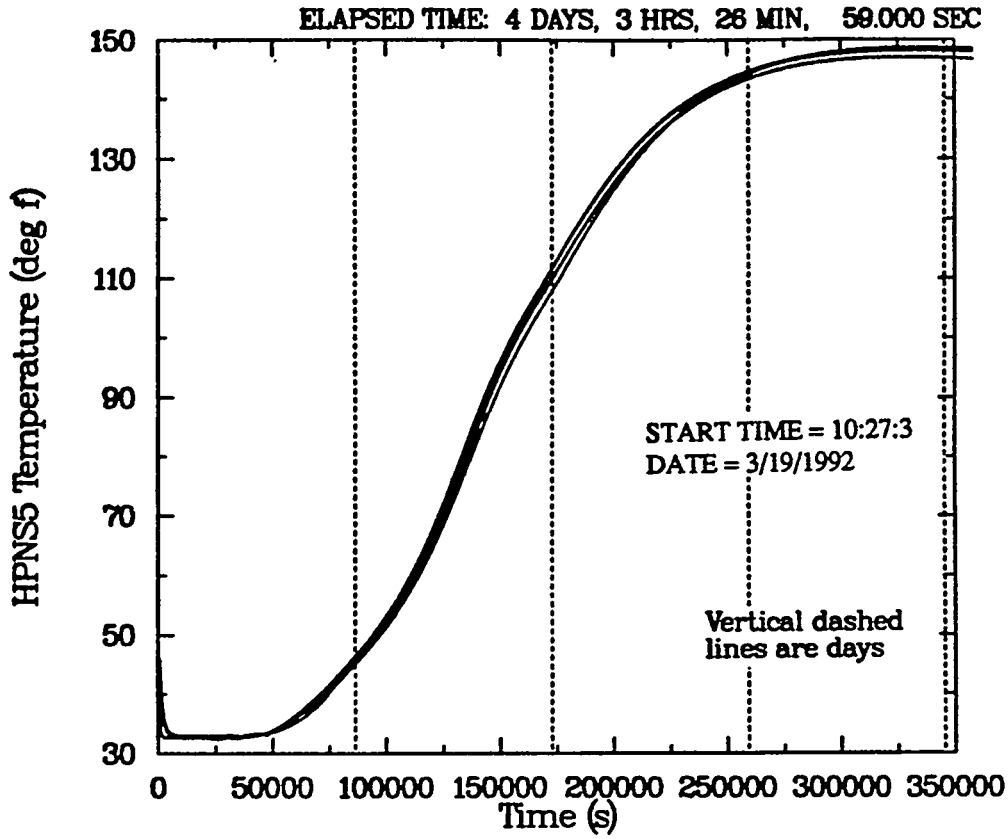


Figure 8. Temperature time histories for the permeability test of HPNS-5 grout in the rack assembly hole for the JUNCTION event.

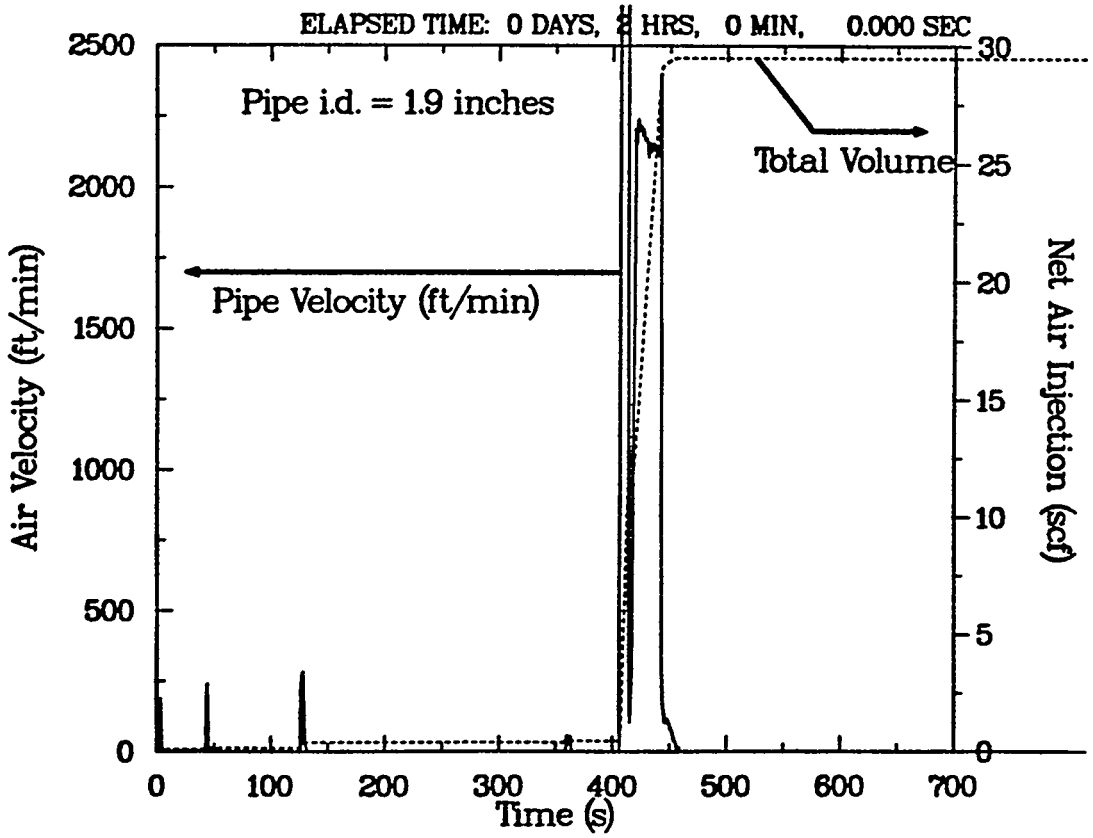


Figure 9. Velocity of the air in the pipe from the compressor and the net volume of air injected. This was the pre-shot test in the JUNCTION rack assembly hole.

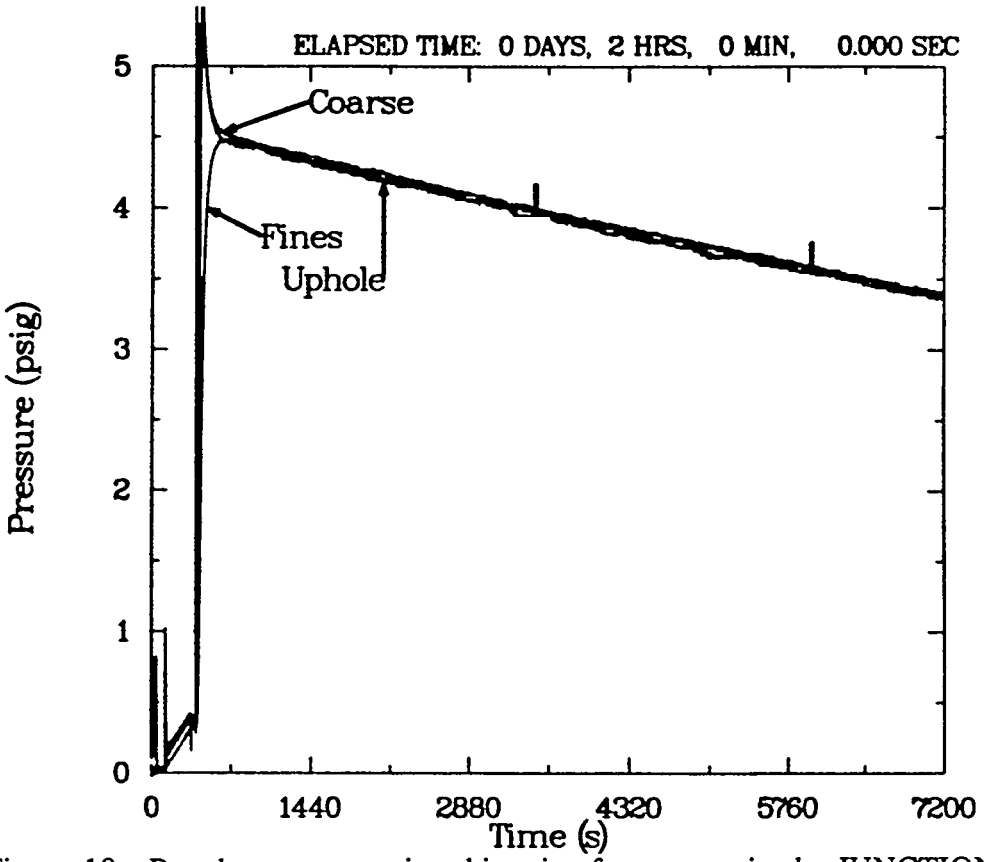


Figure 10. Pre-shot pressure time histories for gauges in the JUNCTION rack assembly hole stemming. Notice that all gauges show nearly the same response and the rate of pressure drop is fairly constant.

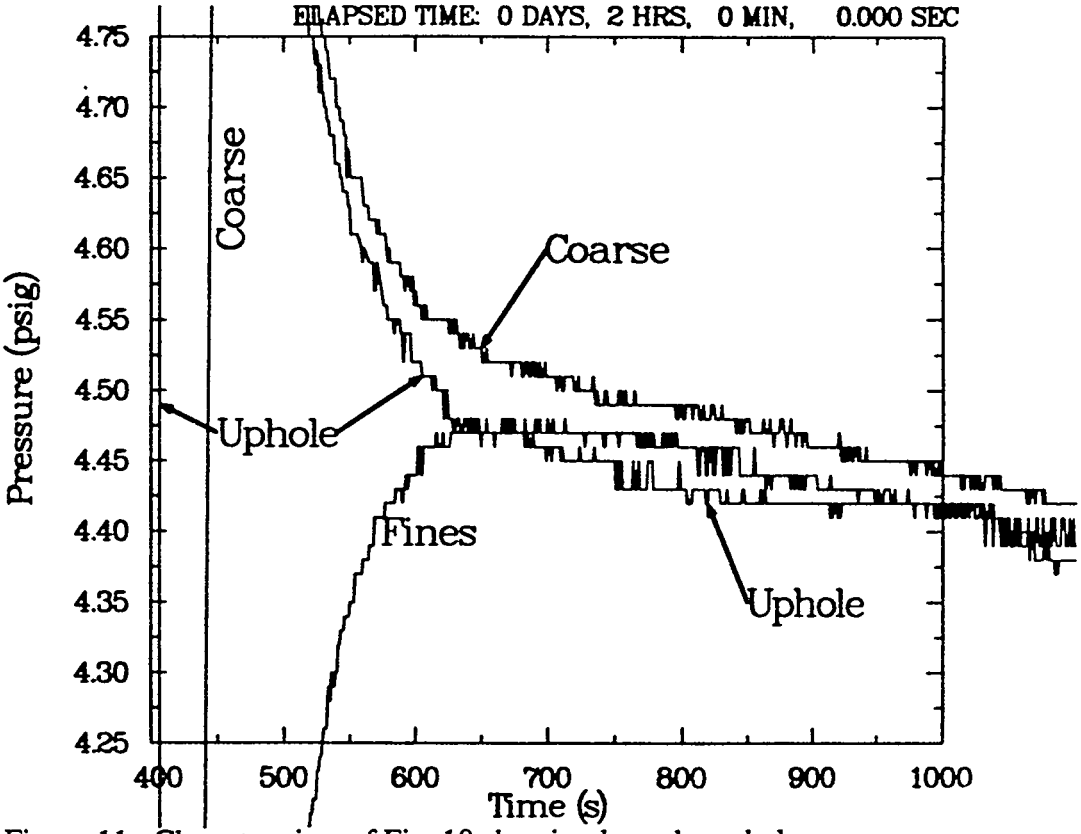


Figure 11. Close-up view of Fig. 10 showing how the uphole gauge pressure seems to drop below the other two, indicating the injection system may be leaking faster than this HPNS-5 plug (which has no cable harnesses, etc).

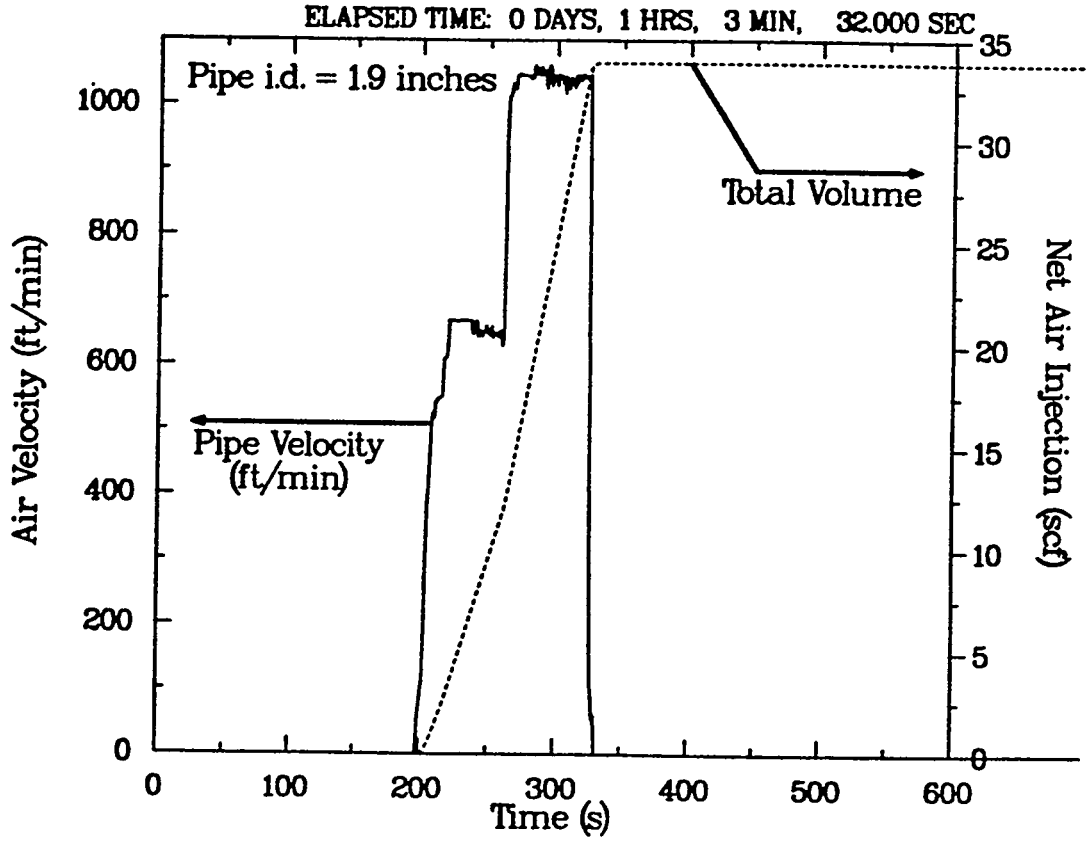


Figure 12. Air velocity and net volume curves for the first post-shot test of HPNS-5 in the JUNCTION rack assembly hole.

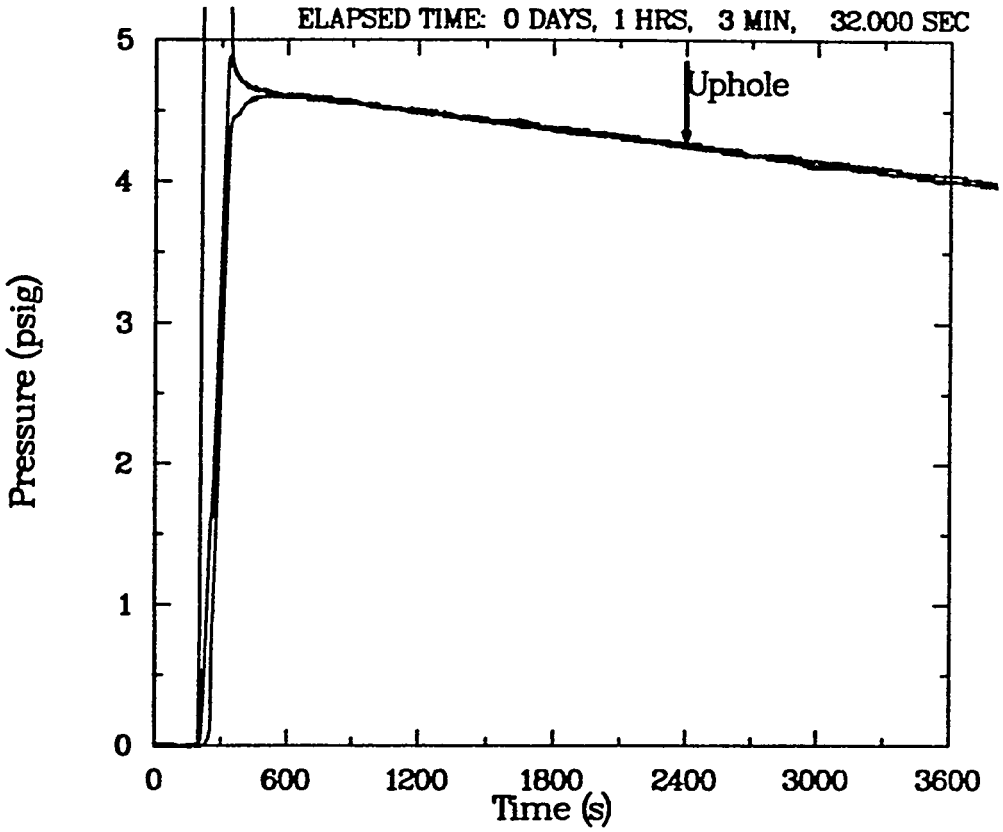


Figure 13. Pressure time histories from the first post-shot pressurization of the stemming in the JUNCTION rack assembly hole.

previous test. The close-up view in Fig. 14 shows that the pressure at the uphole gauge is now lagging the other two gauges, indicating that the effects of the nuclear test and/or the additional curing have made the HPNS-5 plug slightly more permeable. This is discussed further in a following section. Notice in Fig. 13 that the rate had increased to 0.75 psi per hour after an initial pressurization to 4.5 psig.

The next series of experiment in U3jz was performed well after all excess pressure below the plug had escaped (see Fig. 7). The injection rate and volume shown in Fig. 15 were used to pressurize the voids in the coarse and fines materials to over 9 psig as shown in Fig.16. The rate of pressure decay increased to 1 psi per hour. A close-up view is shown in Fig. 17. No visual observation of the grout was possible due to the collapse hazard inside the perimeter fence. Interestingly, the pressure in the fines layer followed almost exactly the pressure in the uphole gauge until about 3150 sec. Then it dropped and followed the pressure decay curve for the coarse material for the remainder of the test.

PERMEABILITY TESTS OF A TPE RIGID PLUG

General

Although significant data had been collected for the new candidate grout, HPNS-5. We could not make an evaluation of its potential effectiveness until similar tests had been performed on the two part epoxy (TPE) plugs currently in use at the bottom of the surface conductors for most NTS events. The depth of U3jz allowed for additional tests of this type so an experimental program was set up to test TPE.

Experimental Procedure and Results

In order to seal off the damaged HPNS-5 plugs in the lower portion of U3jz, a 2 foot section of TPE was poured on top of the upper HPNS-5 plug and allowed to cure. Next a dummy cable bundle was fabricated and green and yellow (for different sized cables) separators were installed and the assembly was tied to spreader bars. Unlike an actual NTS test, the cable bundle was bound together between the fanouts - a procedure which does not allow the plug material to freely flow between the cables along the entire length between fanouts. This could potentially increase the risk of gas flow through the plug, but the decision to proceed was made, since this deficiency was present on the HPNS-5 test in U3jz and we could be assured that the plug material would extend to cover both

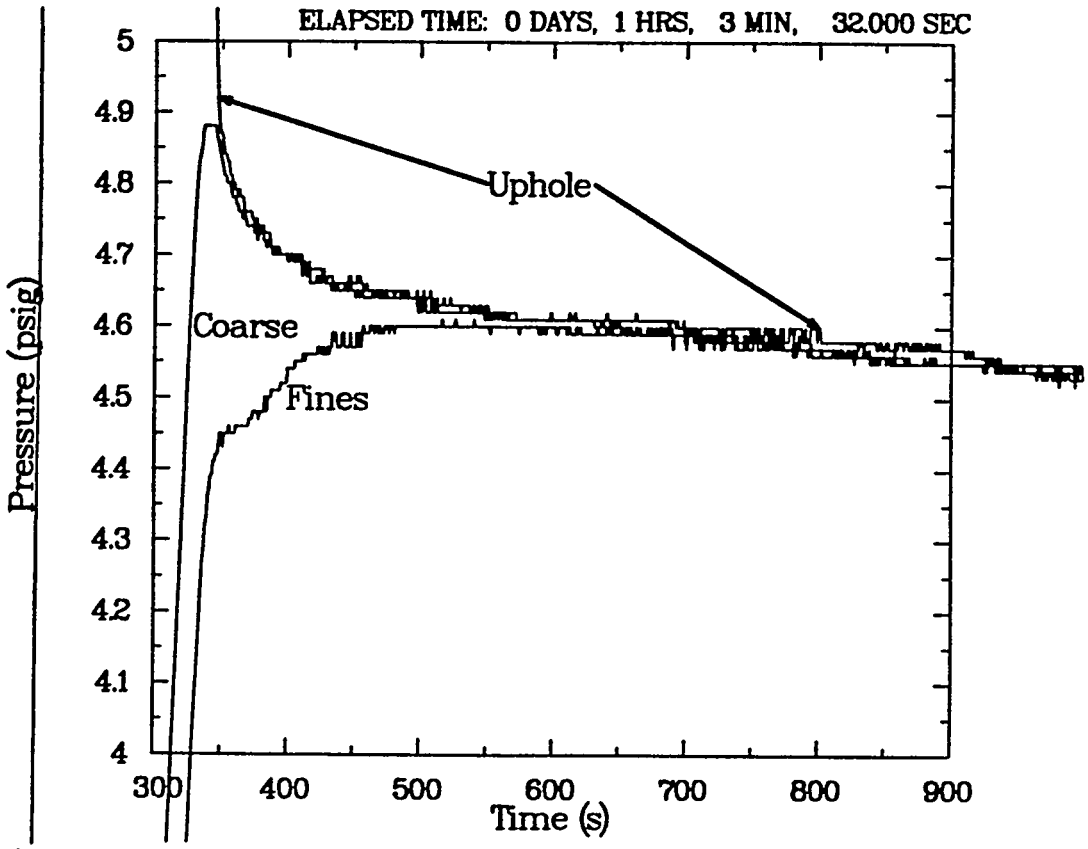


Figure 14. Close-up view of the pressures in Fig. 13. Notice that the pressure in the uphole gauge is now lagging the other two.

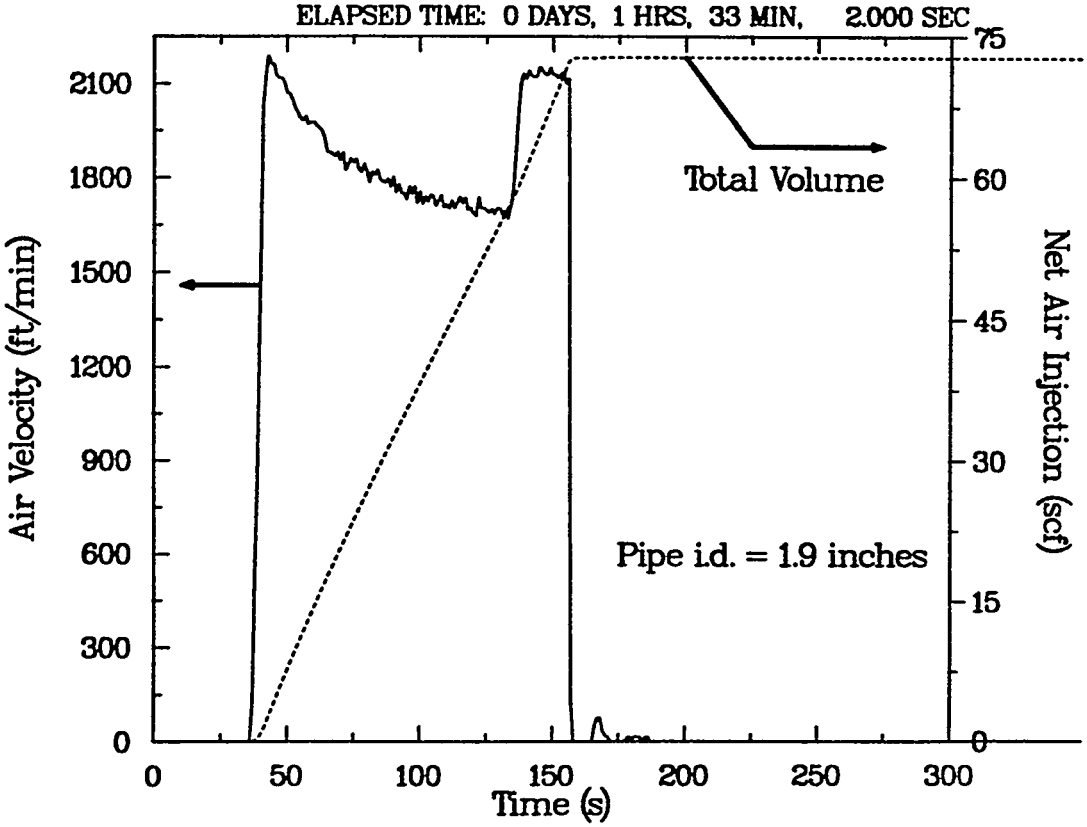


Figure 15. Air velocity and volume injected for the high pressure post-shot experiment in the rack assembly hole for JUNCTION.

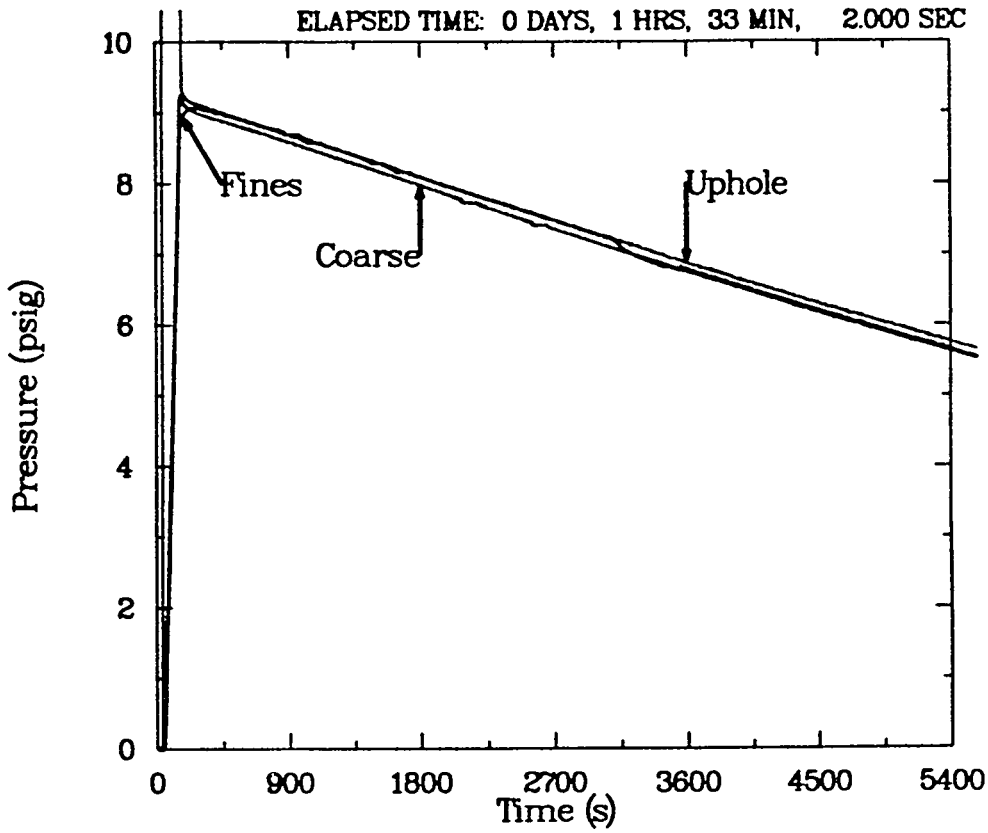


Figure 16. Pressure time histories for the high-pressure test of the HPNS-5 grout post-shot permeability experiment in U19bg.

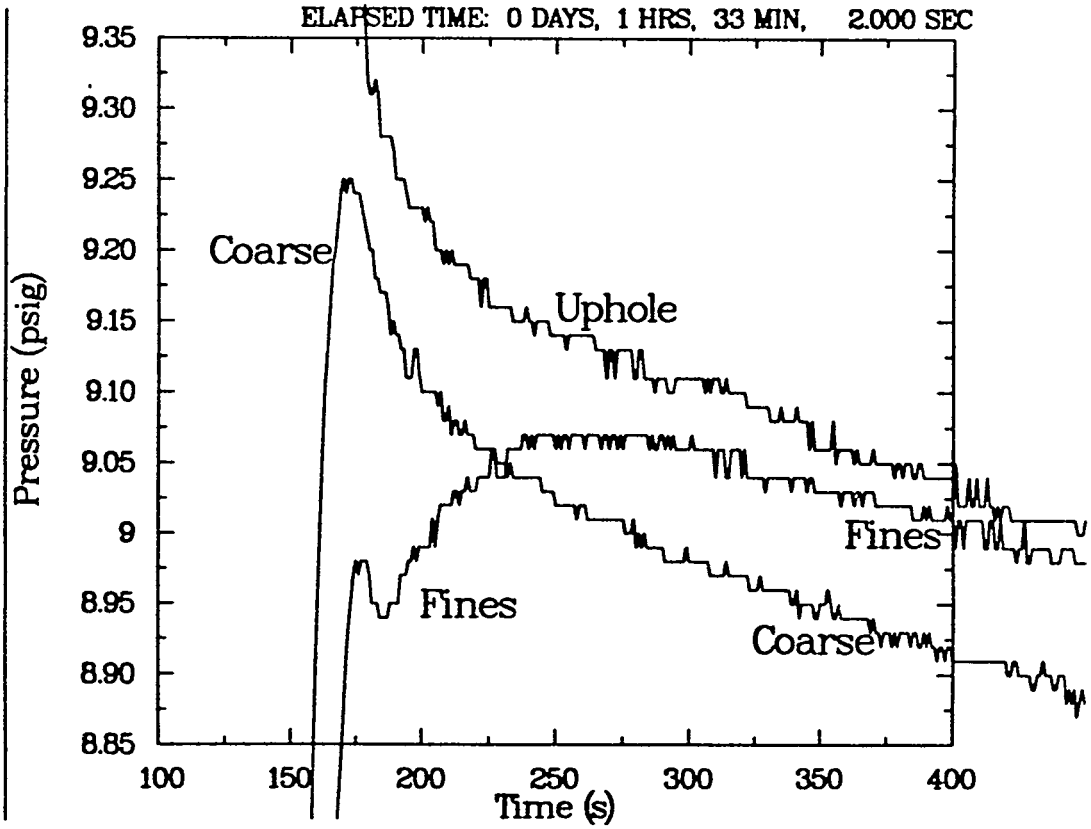


Figure 17. Close-up view of the pressures in the stemming from the post-shot high pressure test. Note the uphole gauge is well above the other two.

fanouts. The spreader bar assembly with pressure gauges attached was lowered into the hole and a new air pressure pipe was lowered to within a few inches of the top of the lower TPE plug. The wire rope harnesses from the HPNS-5 test in U3jz were still intact. Next a 10 feet length of standard LANL coarse material was poured, and by a 9 foot length of fines was poured on top. All sections of different stemming material were intended to be 10 foot long (except the lower 2 foot section of TPE seal) but the as-built dimensions were sometimes different by ±1 foot. Finally an 11 foot section of TPE was poured on top of the fines. The curing of this plug is revealed in Fig. 18 which shows the temperature time histories for two sensors. Notice several differences from the HPNS-5 temperature profiles: there is no large initial drop since the TPE is not mixed with ice; peak temperature exceeds HPNS-5 by at least 10°F; the temperature begins to drop after 17 hours versus 4 days for HPNS-5.

The pressurization plan for the TPE experiment was to raise the pressure beneath the plug in 2 psi increments, with a pause after each increment to scan the upper surface of the water-covered plug for leaks (bubbles) with the down hole camera. The flow velocities and air volume injected curves are shown in Fig. 19 for the first series. The 2 psi increments were followed until 10 psig was attained. No leaks were observed. The pressure time histories for gauges in the fines, coarse and uphole at the value closing off the compressor are shown in Fig. 20. During each pause of approximately 5 minutes the pressure dropped about 0.1 psi resulting in a pressure drop rate of 1.2 psi per hour. The next increment was 5 psi, resulting in an overpressure of 15 psig. A few bubbles were observed (1 every 2-3 sec.) at one location that was well removed from the edge of the plug and any penetrations. Air just seemed to be percolating up through the TPE matrix. The plug was left in this condition for about one hour. The pressure declined about 2 psi (to about 13 psig) over the one hour time interval, indicating that some leakage was occurring somewhere, but it seems doubtful that the single leak observed on the surface could account for the observed pressure decay.

Figure 21 shows the 3 pressure histories during one of the pauses after a 2 psi increment. Notice that the uphole pressure is greater than both the fines and the coarse during pressurization, but drops below the fines pressure when the compressor is isolated. As shown in Fig. 22 the pressurization was restarted with the intent of reaching 20 psig (and eventually above that if conditions warranted). The rate of increase in pressure (under a constant inflow rate) markedly decreased during this stage, indicating increased leakage (somewhere). The flow rate was increased to 5000 ft/min, which was the maximum

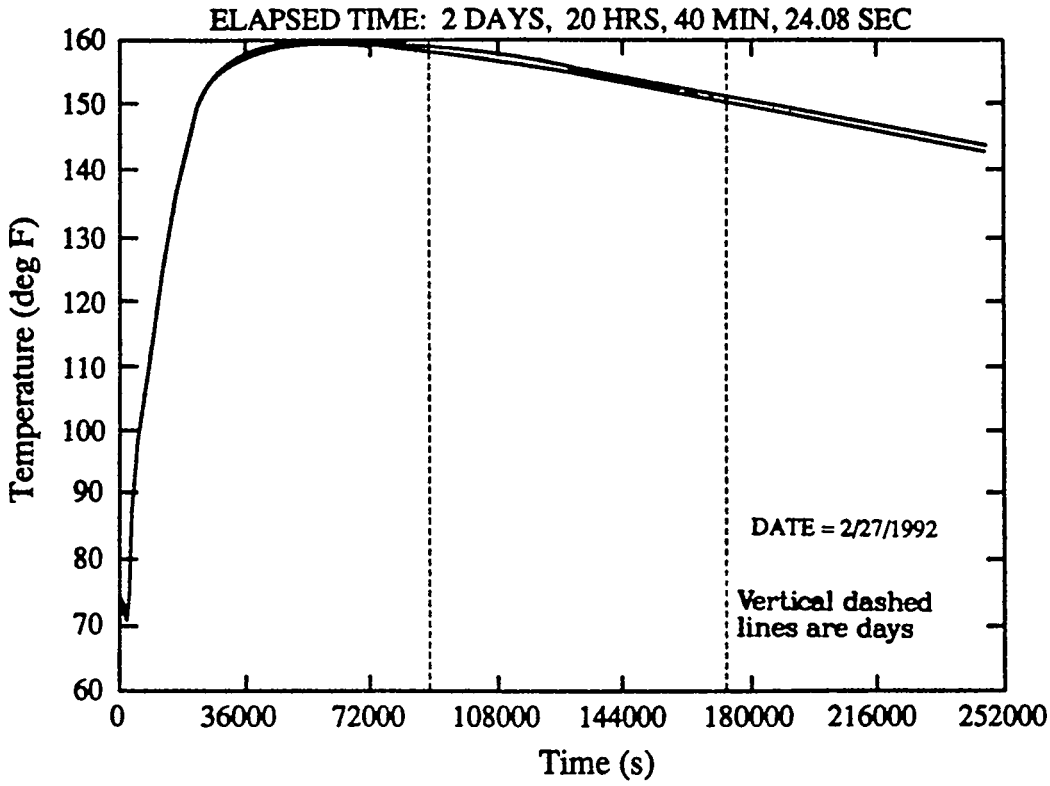


Figure 18. Temperature time histories in the upper TPE plug in U3jz.

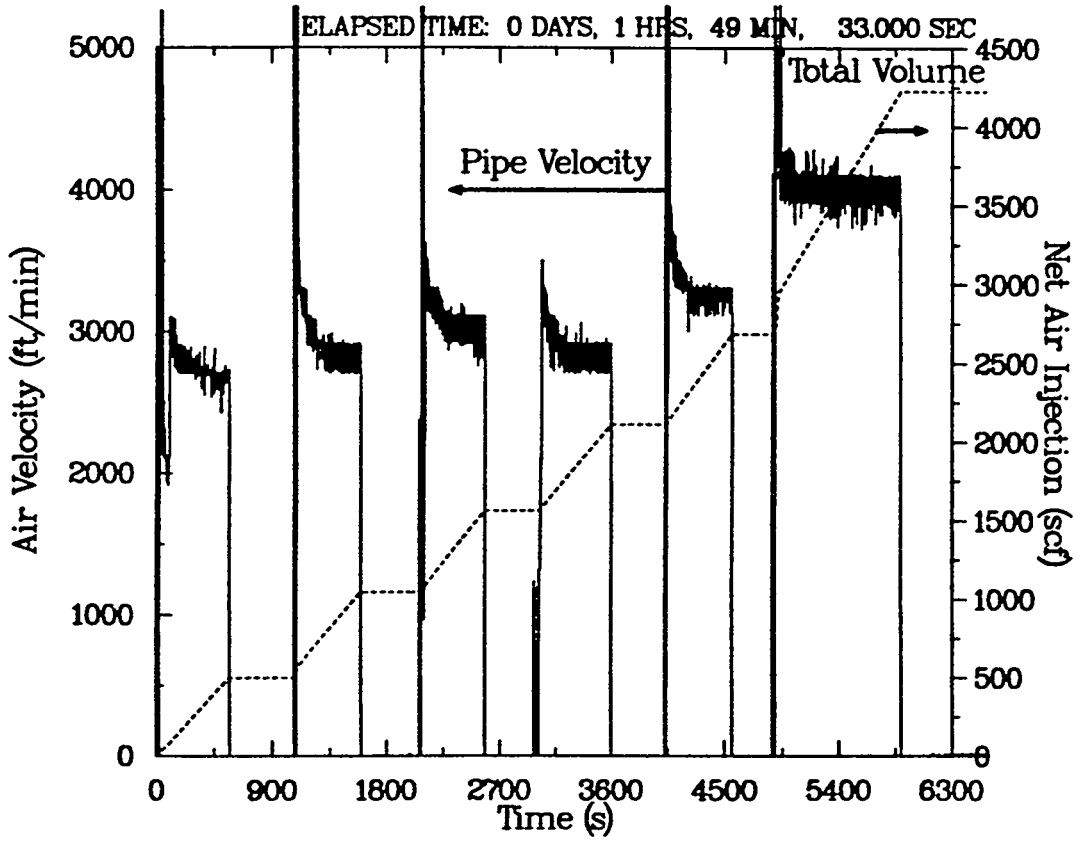


Figure 19. Air velocity (solid) and net air volume injected (dashed) for the initial phase of the TPE pressurization experiment in U3jz.

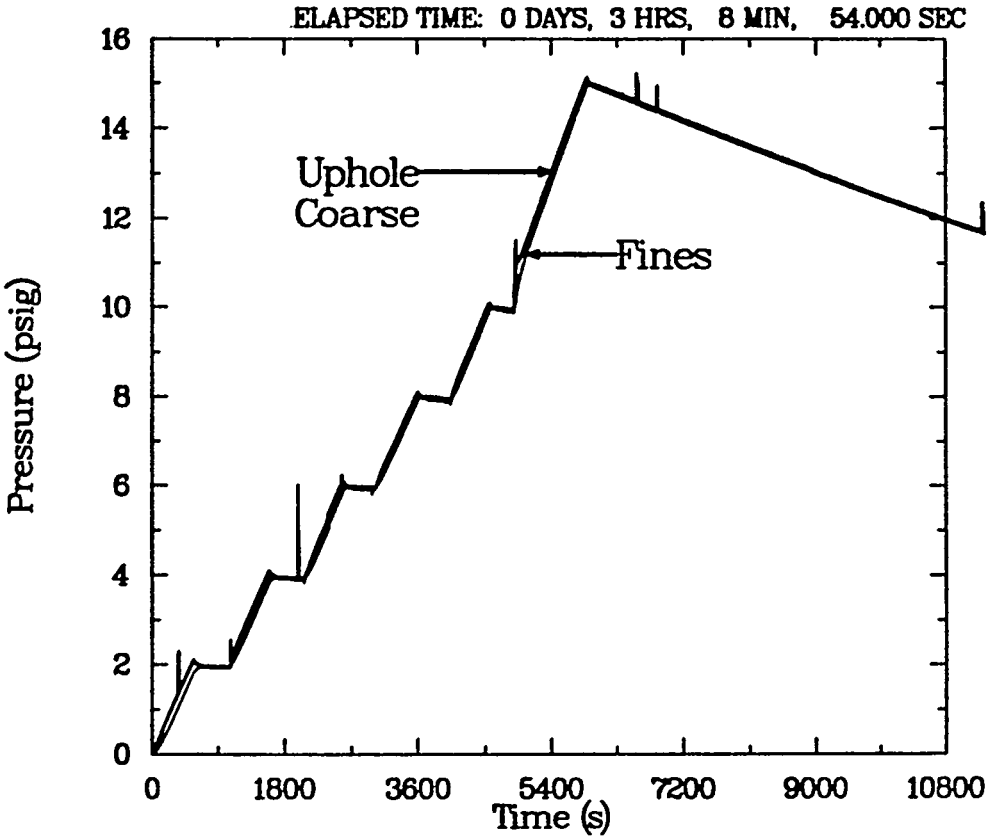


Figure 20. Pressure time histories showing the response in the fines, coarse and uphole during five 2 psi increments and one 5 psi increment below the TPE plug.

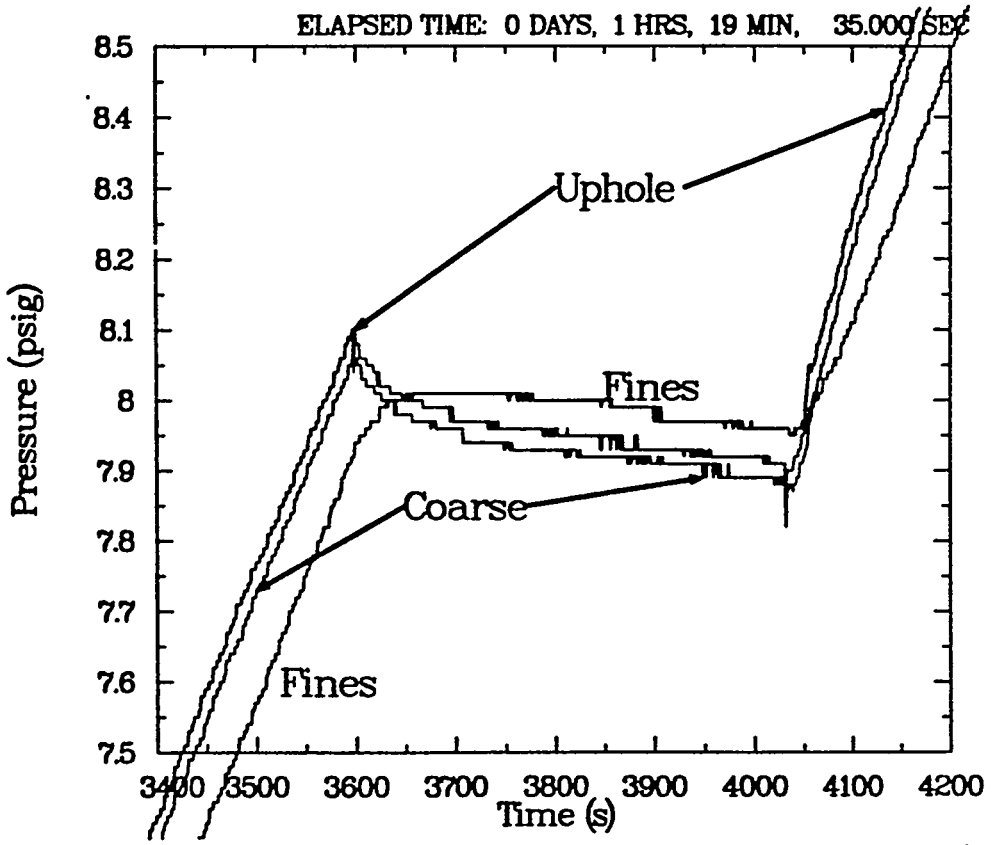


Figure 21. Close-up of pressure from Fig. 20 showing the uphole pressure dropping below the fines pressure when the valve to the compressor is closed.

possible for accurately measuring flow with the particular gage being used. During this stage, the bubbling was no longer observed.

The pressure time-histories shown in Fig. 23 indicate that there was a pause at 18.5 psig, during which there was significant decay (but still no bubbles). It seems reasonable that leakage was either down through the previously tested grout plug (capped with a 2 ft thick layer of TPE) and/or through the insides (within the jackets) of the cables. The cut ends of the cables varied from a few inches to about 2 ft above the water level, so gas escaping through any cable would not have caused bubbling. The cables were checked for leaks by dumping more water onto the top of the plug to cover at least some of the cable ends. The air flow was turned back on. The first cable ends to become submerged were five RF-13s. Although the ends of the cables could no longer be observed through the muddy water, it appeared that one of the cables was leaking. Bubbles were fairly continuous and always at the same location. Another small, slow bubbling occurred on the other side of the cable bundle at 8-20 sec interval. The active part of the test was terminated at this point since it appeared there was little more to be learned by further pressurization (water was not added to cover all of the cable ends - 5 were covered, 7 uncovered). At the end of the pressurization, 19.5 psig had been attained.

The pressure decay was recorded through the night (with a larger sampling interval). The on-site REECo representative was questioned about the continuously gas blocked RF-13 cables. He said that they had checked a ten foot section from the roll from which the test cables were taken, and it passed the test. The actual cable sections used in the test were not individually tested for gas tightness. Another source of possible leakage is that the old pressurization pipe for the HPNS-5 plug test was uncapped at the top. If gas were leaking through the lower 2 foot TPE seal into the region beneath the grout plug, it would have a free run to the surface through the open pipe.

TPE seem to be excellent material for plugging the surface conductor in underground nuclear tests. No leaks were observed around the perimeter of the plug (at the plug-steel interface), through the cable bundles or along any other penetrations through the plug. The bubbling observed during the 15 psig pause later mysteriously disappeared, and those bubbles, and the ones mentioned as being "on the other side of the cable bundle", were probably caused by gas that was previously trapped within the TPE, escaping when the plug was "loaded" from below. It does not seem likely that the bubbles were from a leak through the plug (why would it stop?). There was probably leakage downward through

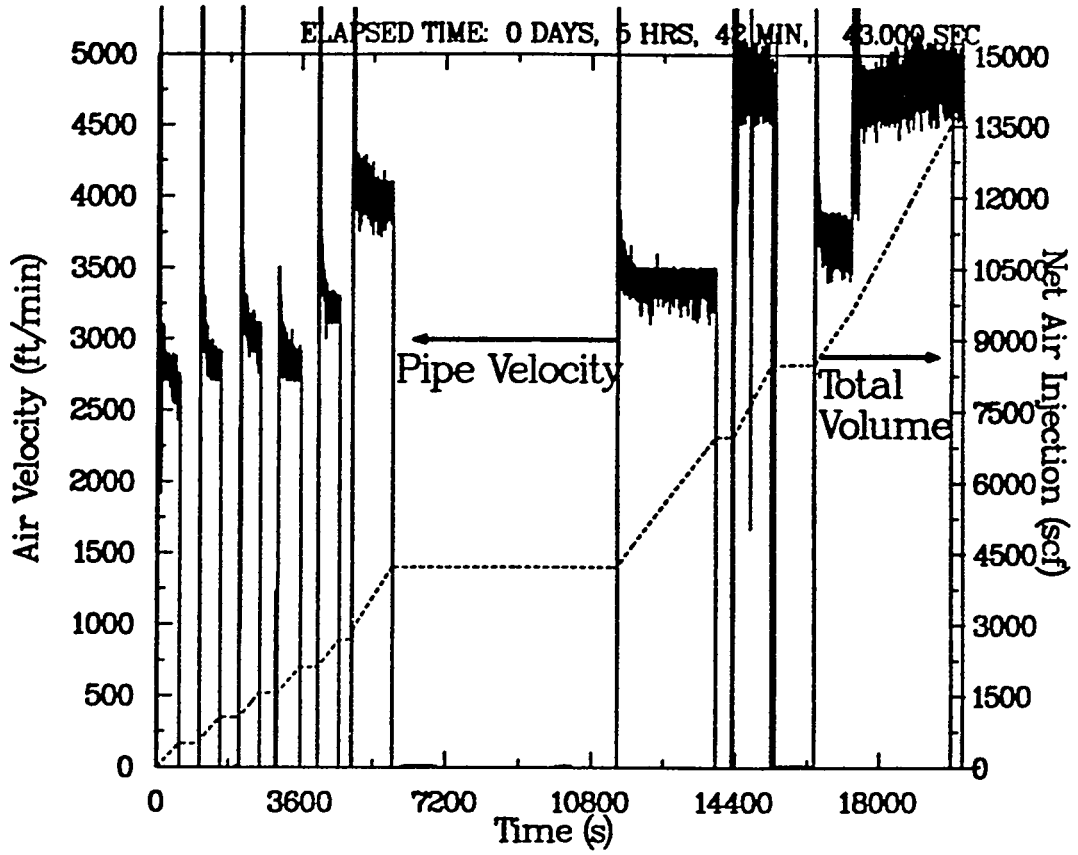


Figure 22. Velocity and volume injection curves for the high pressure loading portion (after 10800 sec) of the TPE field permeability tests.

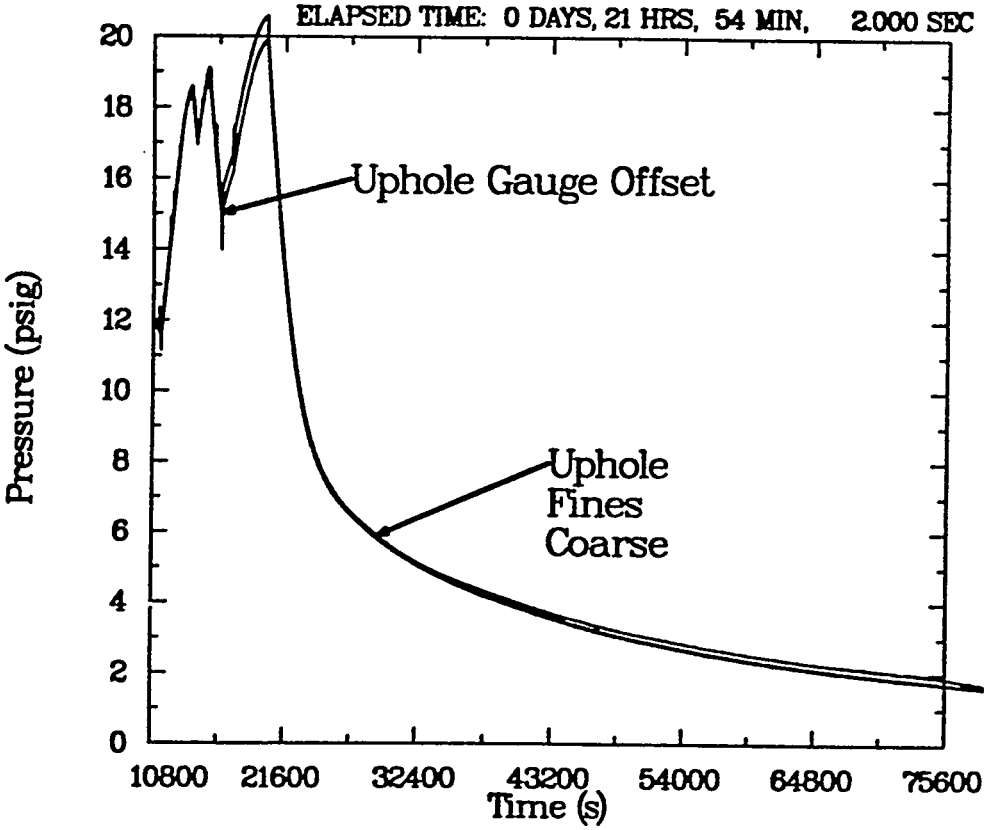


Figure 23. Pressure time histories in the fines, coarse and uphole portion of the pressurization system during the high pressure TPE testing.

the old, previously failed, HPNS-5 plug. The 2 ft thickness of TPE on top of the plug may have been inadequate to effect a proper seal. It is clear that there was leakage through at least one of the factory gas blocked cables.

DISCUSSION OF RESULTS FROM THE PERMEABILITY TESTS

The previous sections have shown the results of three different rigid plug permeability experiments. Many aspects of each test were quite different. In order to compare the results of a given series of tests with itself and with the other experiments, the bulk permeabilities of the rigid plugs are calculated at various times during the testing process. In particular, the pressure decay time history, after the compressor was turned off, in the fines layer was chosen, since this pressure is the closest measure of the conditions at the bottom of the plug.

To calculate the permeability:

$$\text{Rate of air loss} = \underbrace{\frac{\partial \rho}{\partial t} \cdot A \cdot L_{CF} \cdot \varepsilon_{CF}}_{\text{pressure decay}} = \underbrace{- A \cdot u \cdot \rho}_{\text{flow thru plug}}$$

where:

L_{CF} = length of coarse and fines layers
ε_{CF} = porosity of coarse and fines layrs
A = cross-sectional area
ρ = density - $B \cdot P$, where P is the pressure
u = the air velocity through the plug

Now, Darcy's law states

$$-u = \frac{k}{\mu} \frac{\partial P}{\partial x}$$

where:

k = the permeability of the plug
μ = the viscosity of air

so:

$$+ Au\rho = + A \frac{k}{\mu} \frac{\partial P}{\partial x} \cdot B \cdot P = B \cdot \frac{\partial P}{\partial t} \cdot A \cdot L_{CF} \cdot \varepsilon_{CF}$$

since A and B cancel out:

$$\frac{k}{2\mu} \frac{\partial P^2}{\partial x} = \frac{\partial P}{\partial t} \cdot L_{CF} \cdot \varepsilon_{CF}$$

During a portion of the experiment where the decay is nearly constant:

$$\frac{\partial P}{\partial t} \cong \frac{\Delta P_B}{\Delta t}$$

and

$$\frac{\partial P^2}{\partial x} \cong \frac{P_T^2 - P_B^2}{\Delta x} = \frac{P_T^2 - P_B^2}{L_P}$$

where:

L_P is the length of the plug

P_T is the (ambient) pressure at the top of the plug

P_B is the pressure at the bottom of the plug (in the fines)

Finally, the equation for permeability may be written:

$$k = \frac{- \frac{\Delta P_B}{\Delta t} \cdot L_{CF} \cdot \varepsilon_{CF} \cdot 2 \mu L_P}{P_B^2 - P_T^2}$$

This equation was used to evaluate several different portions of different decay curves.

The following properties are the same for all cases:

$$\text{air viscosity} = 1.9 \times 10^{-4} \frac{\text{dyn} \cdot \text{s}}{\text{cm}^2} \quad (\text{at } 40^\circ \text{ C})$$

porosity of coarse/fines = 0.35.

Table 1 gives constant material properties.

Table 1. Properties Which Are Constant for a Given Series

Series	Hole	Plug Material	Length of Coarse & Fines	Length of Plug
1	U3jz	HPNS-5	640 cm	274 cm
2	U19bg	HPNS-5	244 cm	244 cm
3	U3jz	TPE	579 cm	335 cm

The following table summarizes the selected experiments chosen for analysis.

Table 2. Selected Experiments Analyzed for Plug Permeability

Series	Cure (Days)	Description	$\Delta P/\Delta t$ (psi/sec)	P_B (psi)	P_T (psi)	k (darcy)
1	4	10 psig	3.20/2319	22.40	12.81	0.138
1	4	3 psig	0.98/1780	15.85	12.81	0.214
1	12	3 psig	0.65/1453	14.96	12.88	0.261
1	12	5 psig	1.55/1806	17.65	12.88	0.199
1	12	10 psig	2.95/1695	22.78	12.88	0.168
2	4	5 psig Pre-shot	0.73/3800	16.12	11.62	0.016
2	14	5 psig Post-shot	0.46/2410	16.31	11.71	0.016
2	14	13 psig Post-shot	1.88/2798	24.77	11.71	0.015
3	3	10 psig	0.08/256	22.34	12.33	0.034
3	3	15 psig	1.54/2399	26.95	12.33	0.042
3	3	19 psig	2.82/781	31.39	12.33	0.162
3	3	20 psig	2.25/470	32.25	12.33	0.202
3	3	4 psig	0.73/7197	16.60	12.33	0.031
3	3	2 psig	0.32/9600	14.23	12.33	0.025

The last column in Table 2 allows all the experiments to be compared to each other. Several conclusions may be drawn:

1) The lowest permeability plug was the HPNS-5 in the U19bg rack assembly hole (Series 2). This is understandable since there were no through-going features, e.g. no cable bundle or wire rope harnesses, and the lower boundary rather than a possibly porous plug was a steel lid which had been welded to the surface conductor, to impede flow downward.

2) The ground shock and slapdown from the JUNCTION event apparently had no effect on the bulk permeability (not to mention the additional 10 days of curing).

3) The permeability of this plug seems to be fairly independent of pressure, at least up to 13 psig.

4) The TPE plug in U3jz (Series 3) is the next best performing plug at low pressures, but the permeability of the plug increases dramatically with increasing pressure.

5) The HPNS-5 plug in U3jz (Series 1) is also a very low permeability section, at least it is significantly lower permeability than most alluvium, particularly near the surface. Notice the permeability of the plug decreases with increasing challenge pressure, just the opposite of the TPE plug.

6) The permeability of the HPNS-5 plug in U3jz (Series 1) increased 22% for both the 3 psig and the 10 psig experiments after 8 days of additional curing.

IN SITU STRENGTH TESTS OF HPNS-5

General

The strength of any plug material is an important issue for several reasons. In addition to the usually accepted strength role of any rigid plug, namely to support the layers of coarse and fines above it in the event of a stemming fall, below it, there are two other scenarios which have recently been considered. The "LaComb Scenario" is one in which the entire stemming column above a given plug can effectively load that plug if there is significant seismic activity present. This assumes that all the adhesion and bridging action of the

coarse and fines layers (and any upper plugs) is lost due to violent dynamic shaking. The "Keller Scenario" suggests that the sudden release of harness cable tension after event execution, perhaps in conjunction with a stemming fall up to the base of a plug (well after ground shock), could yank the cables vertically upward and then out of the plug, thereby establishing a highly permeable path for cavity gases.

Both of these special scenarios, with variations, are probably only remotely credible; however, they illustrate the importance of high strength, as well as low permeability, for any candidate grout which is being considered as a replacement for any rigid plug material currently in use.

Experimental Procedure and Results

The tests which are described below simply load the grout by placing the harness cables in tension. The grout will either fail, by allowing the cables to pass through, or the grout will hold. In fact the grout held in both tests, so it is not a "strength test" since no ultimate breaking value was achieved. Rather, this was a performance test whereby loads equivalent to actual field conditions were applied and met satisfactorily. The only true "strength" data is from the small scale laboratory samples, presented below. Estimates of the loads required to fail the grout are given in Figs. 24a and 24b. A general cone failure through the grout would require a load in excess of 5,000,000 lbs, well beyond the capabilities of the loading frame and the wire rope. As a worst case, failure through the grout above the pin (4 ft. vertical section) would require over 450,000 lbs. If failure is due to a simple adhesive failure of the cable (with no pin connector) through the 10 ft grout section, the load required is only 280,000 lbs, assuming the adhesive strength is equal to the shear strength of the grout. Note that all these loads are based on the 4 day unconfined compressive strength of 1000 psi (twice the shear strength) and could increase by 50 to 100% depending on how long the grout cures. Since all these loads were greater than the capabilities of the wire rope, failure of the grout was not expected.

At the conclusion of the HPNS-5 permeability tests in U3jz, an A-frame assembly was installed above the wire rope harnesses and loaded with four high pressure hydraulic jacks at the corners of the frame. Pre-test calculations based upon laboratory compression tests, indicated that neither cable would fail during the field test. The cables were tensioned to a high percentage of their breaking strength, and neither cable failed, although the cable without the pin connection experienced a slight unloading midway

$$A_{cone} = \sqrt{2}\,\pi\,(4\text{ ft})^2 = 71.086\text{ ft}^2$$

since $\tau_{max} = \dfrac{\sigma_{uc}}{2}$ and $\sigma_{uc} = 1000$ psi

then $\tau_{max} = 500$ psi $= 72000$ psf

Finally, $S = \tau \cdot A = (72000)(71.068)$

$= \underline{5{,}118{,}200\text{ lbs}}$

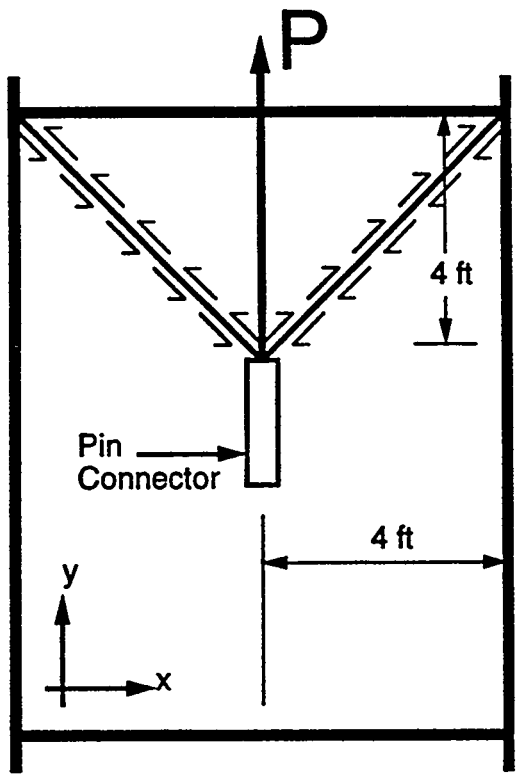


Figure 24a. Estimate of the load required for shear cone failure through HPNS-5 grout plug.

Cylindrical Failure Above Pin

$A_{cyl} = 2\,\pi\,(0.25)(4) = 6.28\text{ ft}^2$

if $\tau_{max} = 72000$ psf

$P_{max} = (72000)(6.28) = \underline{452400\text{ lbs}}$

Grout Adhesion Failure (no pin)

$$A_{wire} = 2\pi\,\frac{(1.5/2)}{12}\,(10) = 3.93\text{ ft}^2$$

$P_{max} = \tau_{max} \cdot A_{wire} = (72000)\,(3.93)$

$= \underline{282700\text{ lbs}}$

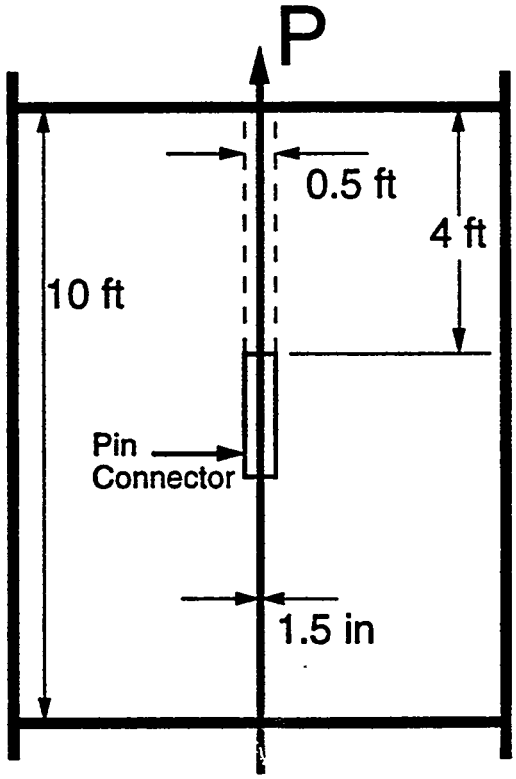


Figure 24b. Estimates of loads required for cylindrical grout failure above pin and for adhesive failure of wire rope through entire 10 ft section.

towards its final load, causing some excitement in an otherwise dull experiment. This probably resulted from a slightly eccentric loading on the cable from its initial position. The cable was reloaded and experienced no further loss of tension. The Sandia camera was recording the downhole environment during this experiment.

The jacks were connected together and the load on harness cable #1 (with no pin connector) was calculated to be 150,000 lbs. resulting in a cable stretching of 7 inches. After the load had been released, the downhole camera showed that the cable had been stretched out of shape, indicating inelastic deformation, i.e., yielding of the cable. Only a few measurements of stretching were taken, but they seem to indicate that non-linear behavior began at approximately 100,000 lbs. Inelastic behavior in those cables does not imply incipient failure and is expected at these loads. Also, dynamic strengths (which would be appropriate for event-related scenarios) are typically much greater than the static values tested here (both for the cables and for the grout). The second harness (with a pin connector) was loaded to a total of 210,000 lbs and experienced 7.5 inches of stretch, indicating significantly stiffer behavior, or more likely, uncertainty in the deformation measurements. At any rate, the harness cables performed satisfactorily and seem to meet the strength requirements for a rigid plug.

The manufacture specifies a breaking strength of 228,000 lbs for the 1 1/2 inch diameter wire rope and inelastic stretching is expected at 60% of this value. A "typical" LANL rack weighs 300,000 lbs and is lowered into the emplacement hole with four 2 inch cables, in 80 foot lengths to a depth of 500 feet. A safety factor of at least 4:1 is always maintained. A transition to 2 1/4 inch cables is then made for the next 500 feet. The deepest holes finish with a pair of 3 inch cables which are linked to four 2 inch cables at the surface which are attached to the strongback. The total weight of the rack plus the wire rope harnesses and the diagnostic cables can be as much as 500,000 lbs. LLNL total weights often approach 1,000,000 lbs and are lowered on a structural steal pipe. One reason the LLNL rack is so much heavier is that the magnetite is in place around the experiments prior to lowering the rack downhole. LANL emplacements drop most of the magnetite from the surface after the rack has been lowered to the proper depth.

Laboratory compressive tests were performed on samples from each of the three plugs. The TPE samples were tested at 3, 5 and 7 days. The strengths seemed to be independent of these curing times (which is expected since the temperature had begun to drop after

only 17 hours). The mean strength of 14 samples was 1416 psi with a standard deviation of 151 psi. The unconfined compression tests on HPNS-5 are summarized in Table 3.

Table 3. Summary of HPNS-5 Compressive Strength Tests (in psi)

(standard deviation in parentheses)

	4 days	7 days	14 days	21 days	28 days
U19bg: (4 samples)	1077 (240)	1095 (160)	1532 (34)	1610 (85)	2035 (122)
U3jz: (6 samples)	1063 (63)	1220 (80)	1578 (101)	1773 (48)	2000 (115)

From Table 3, it is clear that the HPNS-5 has reached over 50% of its 28-day strength after only 4 days. The upper grout plug was poured 13 days prior to the field harness cable test, so the result may have been different if tested after only 4 days. Still, the HPNS-5 grout seems to be a reasonable replacement to TPE based on strength as well as permeability requirements.

SUMMARY

The conclusions drawn in the section where the plug permeabilities were calculated are shown graphically in Fig. 25. Although the HPNS-5 grout seems to be more permeable than the TPE (in U3jz) the relevant question is, "how impermeable does this plug need to be?" A permeability of less than 0.3 darcy would almost certainly be significantly less permeable than the surrounding alluvium near the surface. It is also important to emphasize that it is extremely rare to observe even a 1 psi increase in challenge pressure at an upper plug location. Therefore, this series of field experiments tends to support the notion that the new candidate grout, HPNS-5, would be an acceptable substitute for TPE at the surface conductor. The strength of HPNS-5 after 13 days (and perhaps even 4 days) appears to be sufficient to meet the strength requirements for the uppermost plug in contact with the surface conductor.

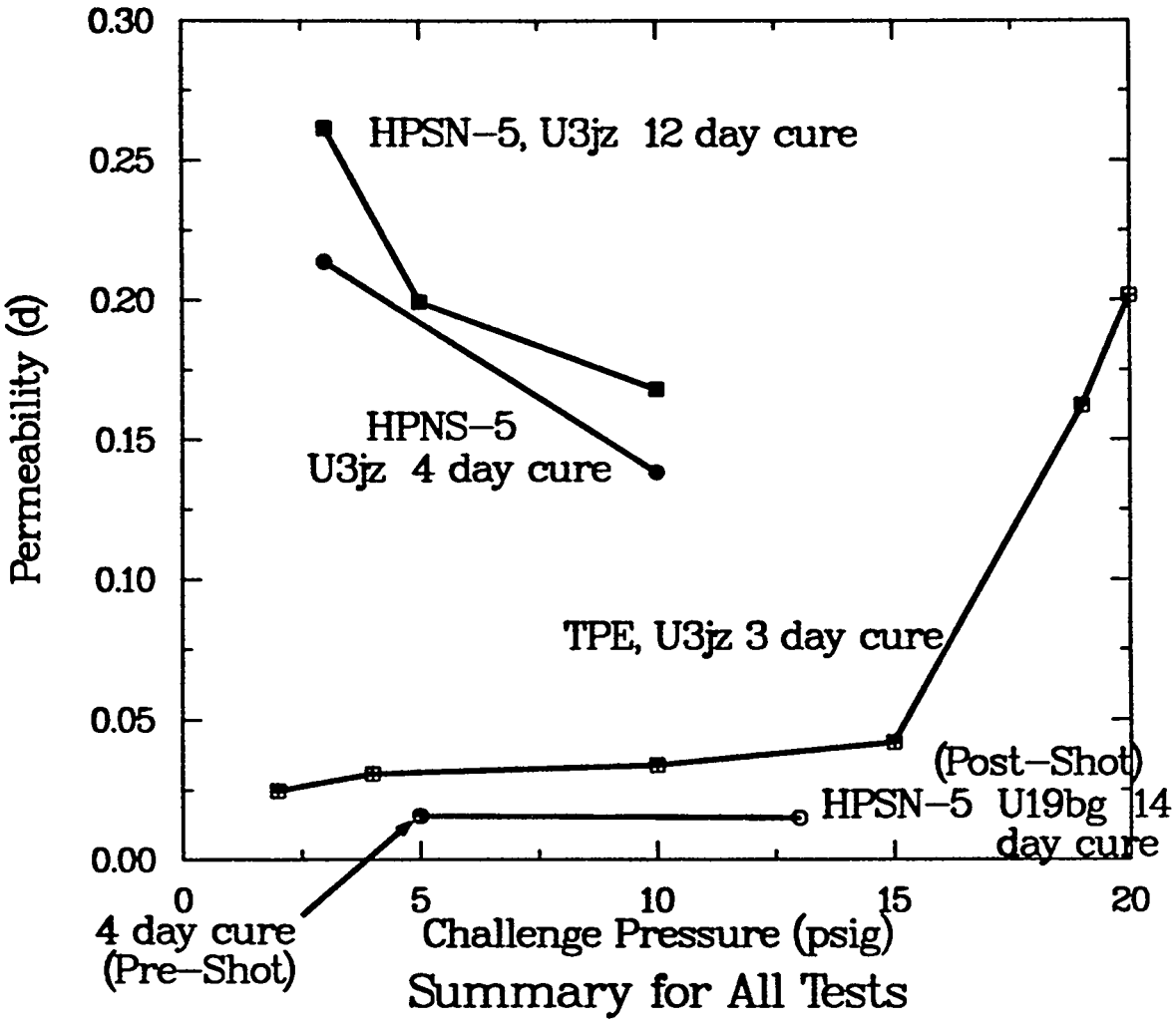


Figure 25. Summary of field permeability tests on HPNS-5 grout and two-part epoxy (TPE). The grout plug in U19bg is the least permeable and was not affected by ground shock and slapdown resulting from the detonation of JUNCTION. This plug had no wire rope harnesses and no mock cable bundles running through it. The TPE plug also had a very low permeability, which seems to increase with increases in pressure. The HPNS-5 grout showed a higher permeability (but still very low when compared to alluvium near the surface) and indicates a tendency toward increased permeability as the curing time increased from 4 to 12 days.

ACKNOWLEDGMENTS

Many individuals made these field tests possible. Barry Bailey and Joe Spoeneman of J-6 were responsible for the field operations. Barry also provided the information on cable strengths and emplacement details. Willie Jim Turner from J-8 ran the data acquisition hardware and software and made the data available in an easily retrievable format. Richard Laverty of Raytheon Services Nevada made detailed written documentation of every phase of the experiments and organized the compression tests. Fred App and Wendee Brunish helped design the pressure loading sequences for the TPE experiments and provided a significant portion of the write-up of that experiment in this paper. Bryan Travis derived the formula for bulk permeability, which gave meaning to the seemingly endless mountain of data. Finally, many thanks to Jack House who recognized the need for these experiments and provided the political clout to assure the effort was successful. This work was performed under the auspices of the U. S. Department of Energy.

MISC-

A Summary of LLNL Containment: Diagnostics Data, 1985–1993

(LLNL SGC Stemming Plug Performance)



B. Hudson
T. Stubbs

Introduction

For normally buried underground nuclear tests, the site and depth of burial are chosen so that no radioactive material is expected at the surface as a result of leakage through the surrounding overburden media. Concurrently, the emplacement hole is stemmed so that it is not expected to provide a leakage path to the surface. Beginning with the GOLDSTONE event (12/85), the LLNL has used a system of granular stemming layers and sanded gypsum concrete (SGC) plugs for stemming emplacement holes. The major objective of this report is to summarize the containment-related performance of these plugs.

A typical stemming plan is shown in Figure 1a. Two types of diagnostics are used to confirm that plugs have been emplaced and have performed as designed: conductivity and temperature for emplacement; pressure and radiation for performance. The conductivity and temperature probes are used to monitor plug location, thickness, and temperature histories. The latter provides information concerning the strength of the plug material. While probe data have, on occasion, shown deviations between the designed and the as-built stemming column, no deviation indicated a compromise which would degrade SGC plug performance. Consequently, these data will not be discussed in this report. Pressure and radiation sensors are placed between the plugs to indicate impedance to gas flow; EXCOR (EXtended CORrtex, a continuous, time-domain reflectometer) and motion sensors are used to indicate plug structural integrity (as a stemming platform) during collapse.

Containment experience since beginning the use of SGC plugs has been satisfactory, i.e., no radioactive material has been detected at the surface during the first 24 hours after a detonation[1]. We therefor conclude that currently employed methods and materials used for stemming emplacement holes have been adequate. However, performance-related data suggest that significant improvements in stemming reliability might be achievable. There is also a desire on the part of Test Program to reduce the cost of stemming materials and/or emplacement procedures. The purpose of this paper is to summarize the containment performance-related data so that informed decisions can be made with regard to *improvements* or potential *cost savings*.

SGC Stemming Plug Performance

The currently used LLNL stemming design comprises a series of SGC plugs and granular layers as shown in Figures 1a–b. The purpose of each plug is two-fold: to impede the flow of gas up the emplacement hole; and act as a structural bridge to support the stemming above a plug, should the stemming below that plug be lost into an apical chimney void.

In practice, plug performance can be gauged when diagnostics data indicate a pressure change or an arrival of radioactive material in the stemming column (gas impedance challenge), or sub–surface subsidence (stemming support challenge). The following discussion includes relevant data from the stemming columns on all LLNL events having SGC plugs and containment performance-related instrumentation (GOLDSTONE through GALENA, see Table 1). Figures 2c–d and 3a–b show measured radiation arrival times and extent of the collapse for each of these events. Beginning at the bottom of the stemming column, the performance of each plug may be summarized as follows.

Plug one ("deep" plug, typically 50 feet in thickness)

The primary purpose of the deep plug is to impede the flow of gas up the stemming column before collapse. The optimum position for this plug is believed to be between one and two cavity radii distant from the planned working point where explosion-induced residual stress in the surrounding medium is expected to be higher than cavity pressure. Diagnostics data have shown that, without a deep plug, radioactive material can be expected to travel a significant distance up the stemming column (perhaps one third to one half the distance to the surface) within the first minute after detonation[2]. After introducing the use of a deep fines plug on the CABOC event (12/16/81), early arrivals above this location were observed in five of eight events[3] (see Figures 2a–b). The subsequent replacement of fines by somewhat more expensive gypsum concrete (for the deep plug) was primarily motivated by a desire to gain even further improvement in gas impedance performance.

Since beginning the use of SGC, there have been thirteen events on which the instrumentation stations above the first plug survived after detonation (See Table 2). Based on data from earlier events[2], it seems fair to assume that all thirteen of these deep plugs were challenged. Six involved the early detection of radiation above the deep plug including BARNWELL on which an early arrival of radiation was detected above the second plug. Consequently, early arrivals were observed on six of thirteen plugs.

In addition, radiation arrivals were detected at two successive stations adjacent to the cable bundle inside the deep plug on RHYOLITE, before being detected above the deep plug (see Figure 2c). These data indicate leakage through the deep SGC plug. It should be noted that, except for RHYOLITE, these data cannot be used to distinguish between flow paths around the plug or through the plug.

In summary, early arrivals of radiation were detected in the stemming column on six of thirteen events with SGC plugs, compared to five of eight with fines plugs. Consequently, the effectiveness of SGC appears to be about the same as fines for blocking the early flow of gas deep in the emplacement hole.

The deep SGC plug is also expected to provide a support platform for the stemming higher in the hole, should the stemming below this elevation be lost into the cavity. While none of the deep plugs failed as a stemming platform, it cannot be determined from available data whether a deep plug was challenged.

Plugs two to four (gas-impedance plugs, typically 20 feet in thickness)

The primary purpose of these plugs is to impede the flow of gas before cavity collapse (minutes to hours), should it somehow pass the deep plug. Ignoring BODIE and PANAMINT, where radiation arrivals appear to have been collapse-related (see Figures 2c and 3a), ten SGC gas-impedance plugs were challenged by early radiation arrivals (see Table 2). Five of the ten were bypassed within six minutes.

Figures 2d, 3b, 4 and 5 show radiation arrivals in the stemming columns of COSO and BARNWELL where radioactivity was observed above three gas impedance plugs before collapse.

Two events, BRISTOL and BODIE (see Figures 2d and 3a, and Table 1), involved sub–surface collapses to below one of the SGC gas-impedance plugs with corresponding negative pressure differentials. See Figures 6 and 7. The associated communication times across these plugs are 15 ± 10 and 50 ± 15 s, respectively.

Each of these plugs is also expected to provide a support platform for the stemming higher in the hole, should the stemming below this elevation be lost into an apical void at the top of a sub-surface subsidence chimney. Three events, BODIE, BARNWELL and BRISTOL (see Table 1 and Figures 2d and 3a) involved a sub-surface collapse to below one of these plugs. Each of these plugs performed as a stemming support platform.

Plug five (stemming platform, typically 40 feet in thickness)

The primary purpose of this plug is to provide a stemming support platform. This plug was challenged by sub-surface collapse on MONTELLO (see Table 1 and Figure 3b) where it performed as stemming platform.

This plug is also expected to impede the flow of gas up the stemming column, especially after a subsurface subsidence. Table 2 shows that on CORNUCOPIA (Figure 2c), RHYOLITE (see plug four–Figure 2c), COSO (Figure 2d), and BARNWELL (Figure 3b), this plug was challenged by radiation with none detected higher in the stemming column. However, it should also be noted that the driving pressure was essentially zero in each case.

Plug six (top plug, typically 40 feet in thickness)

The primary purpose of this plug is to provide a stemming support platform. For events in Yucca Flat, the top plug is placed partially within and partially below the surface casing where it is expected to act as a stemming support platform if sub-surface collapse extends to *above* this elevation. Since a near-surface collapse was not observed (see Figures 2c and 2d), this design feature was not rigorously tested. However, measurements of relative motion between the top plug and the surface casing were made on five events, CORNUCOPIA, SCHELLBOURNE, INGOT, PALISADE, and COSO. Data from three of these events (see Figure 8) indicate that relative displacements between the plug and surface casing began before collapse slap-down (when there would have been little differential force), suggesting these plugs might not have been reliable as support platforms had sub-surface collapse extended to above the bottom of the surface casing.

For events on the mesa, the top plug is emplaced in an uncased hole and is expected to provide a support platform when a subsurface collapse extends to above plug five. Table 1 and Figures 3a and 3b show that sub-surface subsidence extended to below the top plug on five mesa events, JEFFERSON, BARNWELL, BULLION, COMSTOCK, and HOYA. On HOYA and JEFFERSON, pressure and EXCORE data indicate the stemming below the top plug remained in place (bridged). Consequently, the top plug was not challenged on these two events. On BULLION, the stemming above the top plug was lost after about six hours and fifteen minutes. However, EXCORE and photographic data from re-entry suggest that a second collapse proceeded to above this plug at that time.

In summary, it appears that top plugs were challenged as stemming platforms on three mesa events (BARNWELL, BULLION, COMSTOCK), with successful performance in each case. No top plugs were challenged on Yucca Flat events, however the top plug and surface-casing displacement data suggest that these might have failed if challenged.

The top plug is also expected to impede the flow of gas into or around the surface casing[4]. None of these plugs were challenged by radiation. However, it seems safe to assume its performance as a gas block would have been similar to that observed for the deeper plugs.

Conclusions

SGC gas impedance plugs. The radiation and pressure time-of-arrival data indicate that a SGC plug is of benefit for impeding the flow of gas, with about the same reliability and effectiveness as that of a similarly placed fines plug. Data from RHYOLITE suggest the region of the cable bundle can provide a path for gas flow.

SGC stemming support platform plugs All SGC plugs appear to have performed as stemming platforms when challenged. However, relative motions between the top plug and the surface casing (in Yucca Flat) suggest that, if challenged, SGC plugs within the surface casing (as currently emplaced) may not provide reliable stemming support platforms.

The following table summarizes the information on those SGC plugs that were challenged by radiation and/or underlying stemming loss.

Plug#	Gas Impedance		Stemming Support	
	success[a]	challenge	success	challenge
1	6	13[b]	-	-
2-4	5	10	3	3
5	4	4	1	1
6	-	-	3	3
1-6	16[c]	27	7	7

a. No rapid bypass
b. Challenge radiation was observed on 7
c. Success rate for deep fines plugs was 3/8

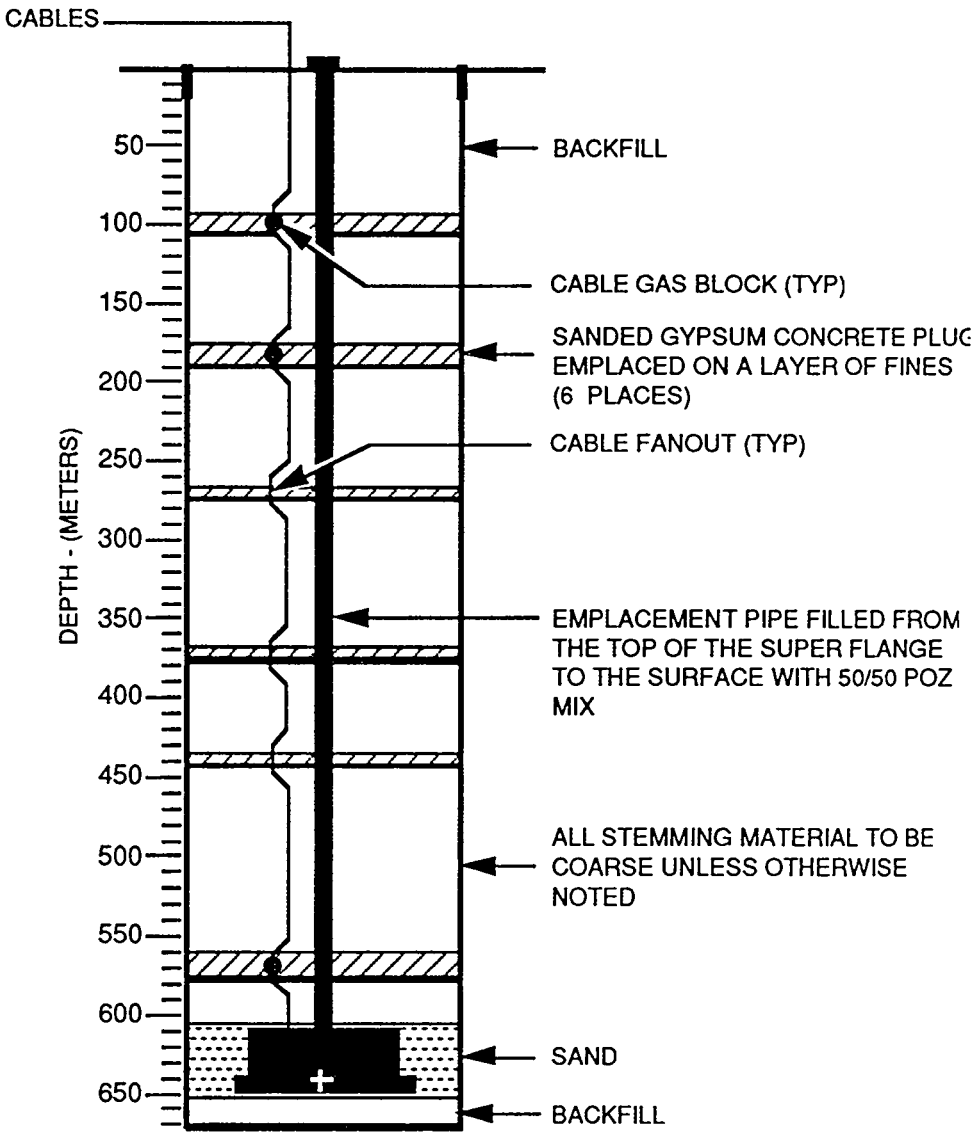


Figure 1a. Typical LLNL stemming plan using SGC plugs.

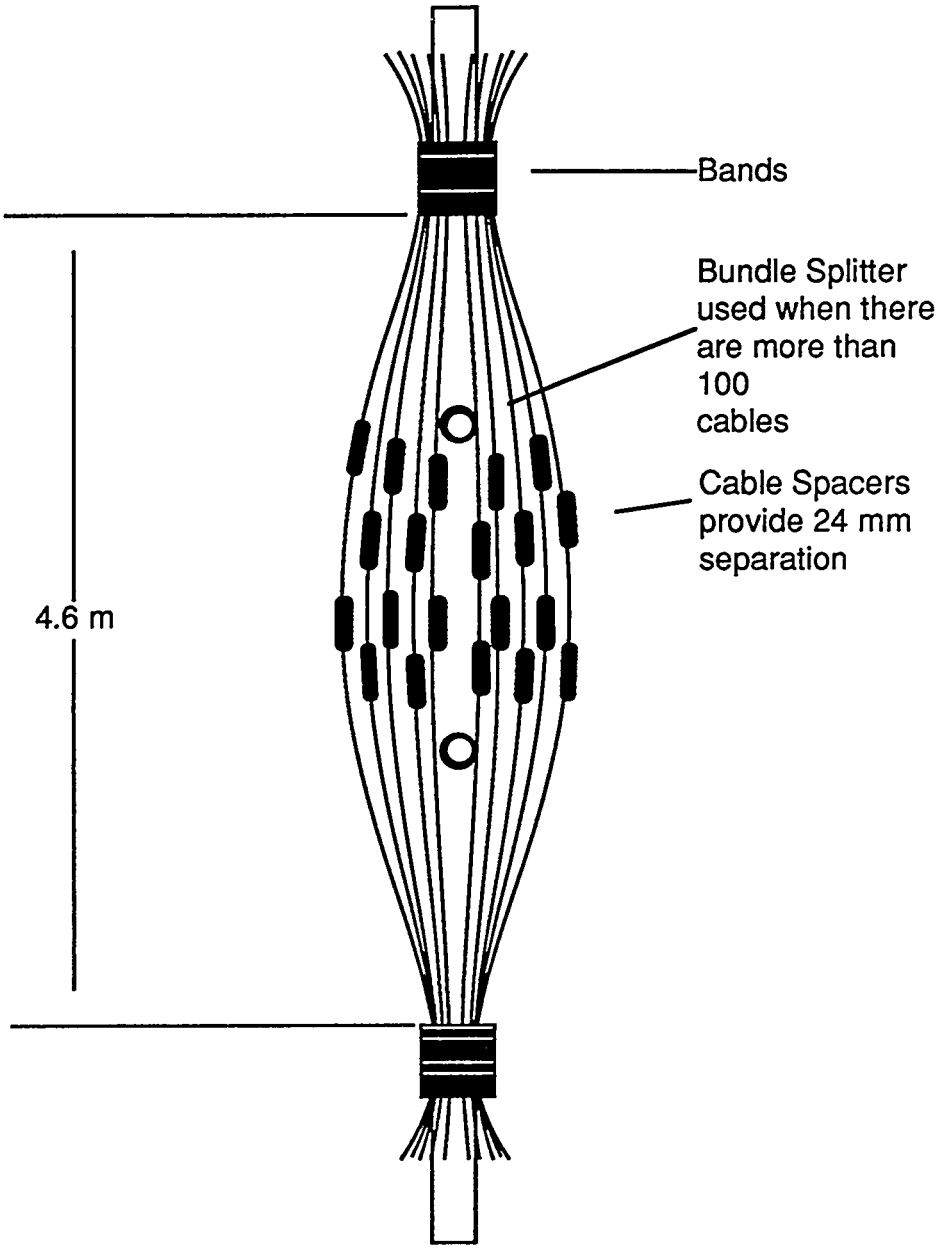


Figure 1b. Typical cable bundle fan-out geometry.

Event	Site	collapse time (hr, min)	depth to chimney (m)
PANAMINT	U2gb	0 hr, 19 min	below plug 2, 381 m
CORNUCOPIA	U2gas	9 hr, 0 min	surface
BORATE	U2ge	2 hr, 24 min	surface
SCHELLBOURNE	U2gf	31 hr, 0 min	surface
RHYOLITE	U2ey	0 hr, 57 min	below plug 1, 180 m
KAWICH	U2cu	1 hr, 10 min	surface
INGOT	U2gg	0 hr, 44 min	surface
METROPOLIS	U2gh	1 hr, 26 min	surface
BULLFROG	U4au	0 hr, 63 min	surface
PALISADE	U4at	0 hr, 49 min	surface
COSO	U4an	0 hr, 38 min	surface
BRISTOL	U4av	5 hr, 12 min	below plug 4, 225 m
GALENA	U9cv	0 hr, 17.5 min	surface
HAZEBROOK	U10bh	no collapse seen	
LABQUARK	U19an	3 hr, 52 min	surface
KEARSARGE	U19ax	5 hr, 22 min	above plug 6, 53 m
JEFFERSON	U20ai	9.0 hr	above plug 4, 190 m
BODIE	U20ap	11 hr, 48 min and 63 hr, 0 min	below plug 3, 347 m
COMSTOCK	U20ay	2 hr, 48 min	below plug 6, 143 m
CONTACT	U20aw	no collapse seen: EXCOR cable lost below plug 6 due to spall	
HORNITOS	U20bc	9 hr, 9 min	surface
BARNWELL	U20az	2 hr, 0 min	below plug 6, 175 m
BULLION	U20bd	0 hr, 52 min and 8 hr, 0 min	below plug 6, 105 m surface
TENABO	U20bb	no collapse seen	
MONTELLO	U20bf	4 hr, 9 min	below plug 5, 191 m
HOYA	U20be	1 hr, 35 min	below plug 6, 183 m

Table 1. LLNL events with SGC plugs and containment performance-related instrumentation.

event / site	pressure arrival	rad. arrival (depth)	rad. arrival (depth)	rad. arrival (depth)	rad. arrival (depth)	rad. arrival (depth)
PANAMINT U2gb [a] [post–collapse]	NI[b]	t = 1118 s (-381 m)	NA[c]	NA	NA	
CORNUCOPIA U2gas [a]	t <150 s, (-334)	t = ~60 s, (-280 m) t = 280 s, (-268 m)	t = 400 s (-232 m)	t = 750 s (-177 m)	NA	
RHYOLITE * U2ey [d]	t = 38 s (-185 m)	t <190 s, (-149 m)	t ~ 3600 s (-126 m)	t ~ 5000 s (-90 m)	NA	
KAWICH * U2cu	NI	NA	NA	NA	NA	NA
METROPOLIS U2gh	NI	NA	NA	NA	NA	NA
BULLFROG U4au	NI	NA	NA	NA	NA	NA
PALISADE * U4at	NI	NA	NA	NA	NA	NA
COSO * U4an	NI	t = 40 s, (-238 m)	t = 130 s, (-97 m)	t = 340 s, (-178 m)	t = 1200 s, (-99 m)	NA
BRISTOL U4av	NI	NA	NA	NA	NA	NA
GALENA * U9cv	NI	t = 315 s, (-220 m)	t = 360 s, (-185 m)	NA	NA	NA
HAZEBROOK * U10bh	NI	t = 21 s, (-152 m)	NA	NA		
BODIE U20ap [post–collapse]	NI	NA	t = 11.8 and 63 hours[e], (-347 m)	NA	NA	NA
BARNWELL U20az	NI	NI	t = 200 s, (-428 m)	t = 290 s, (-340 m)	t = 44 min, (-256 m)	NA
plug :	1	2	3	4	5	6

* Multiple explosion depths.

(a) Lightly shaded plugs are NOT composed of Sanded Gypsum Concrete.

(b) NI implies No Information: the required sensors were either not installed or were lost early.

(c) NA: Instrumented but No pre–collapse radiation Arrivals observed at this level.

(d) Radiation arrival seen within plug 1 at <100 s and depth of 175 m.

(e) Probably collapse–related radiation arrival.

Table 2. LLNL events (conducted since GOLDSTONE) with surviving performance-related instrumentation below plug 2 and/or an early radiation arrival. All radiation arrivals are indicated. Except for PANAMINT and BODIE, all initial arrivals occurred before collapse.

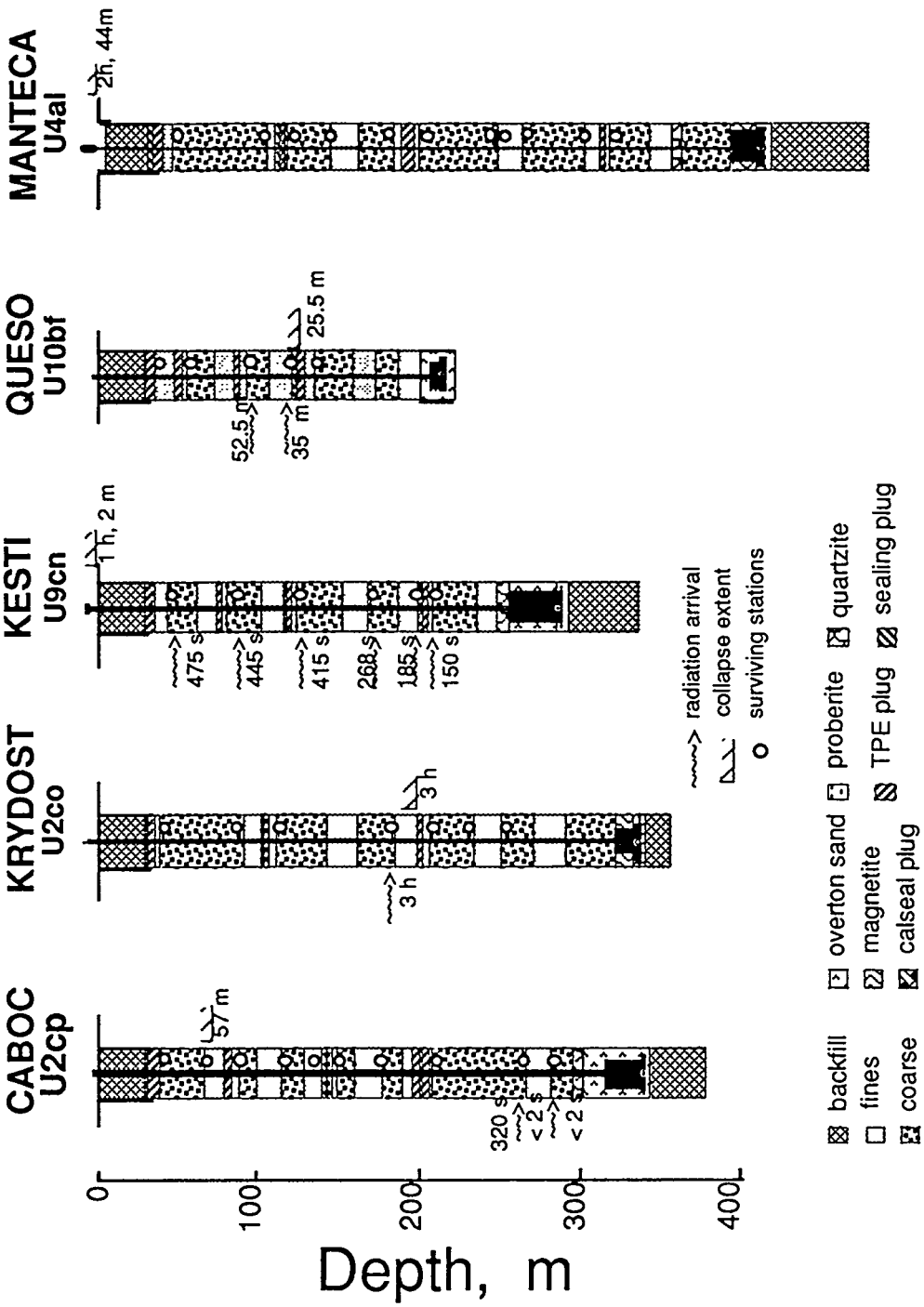


Figure 2a. Graphic representation of LLNL events in Yucca Flat with fines plugs and containment performance-related instrumentation. Radiation arrivals and overburden collapses are indicated. Open circles indicate positions of surviving radiation sensors.

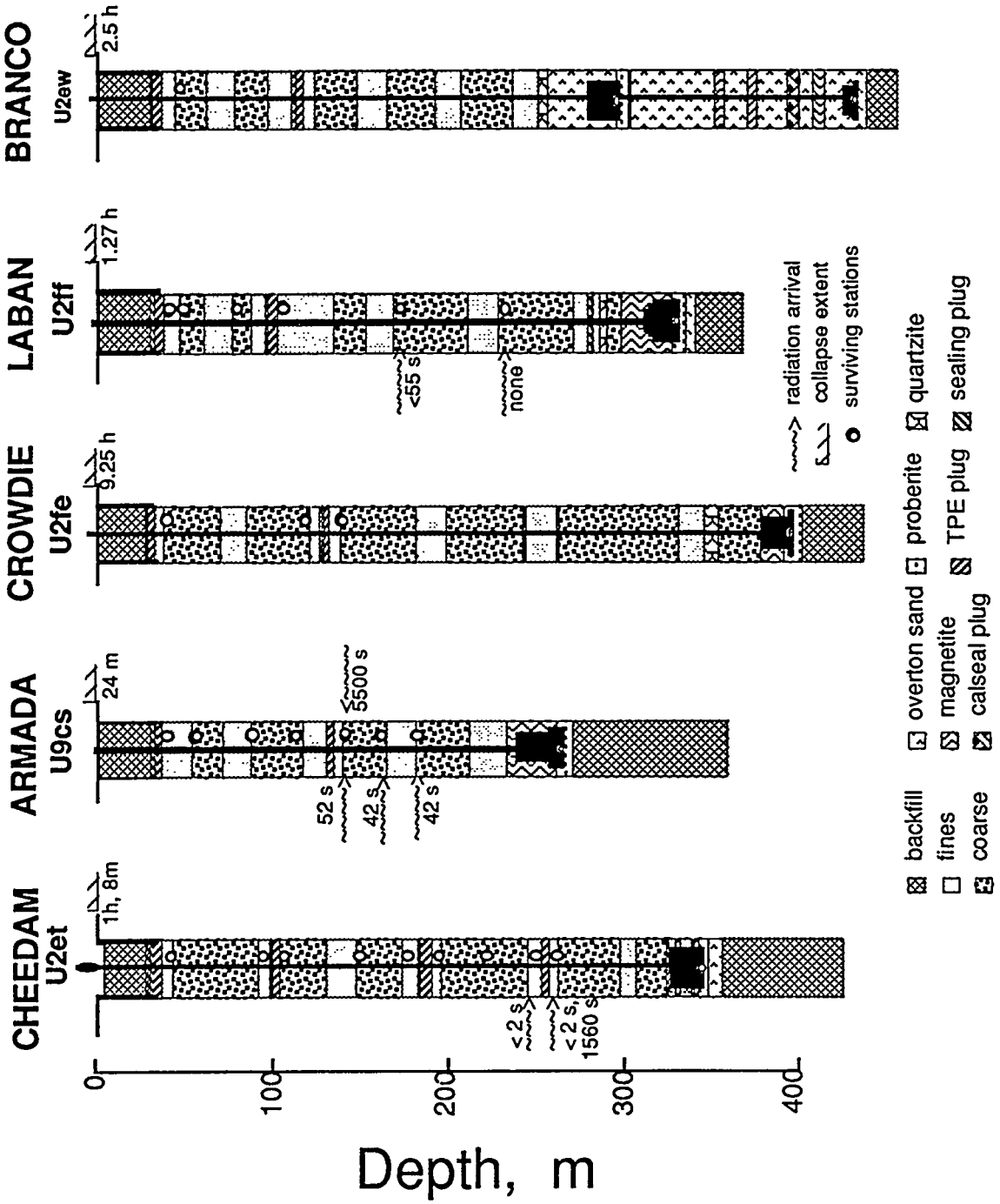


Figure 2b. Graphic representation of LLNL events in Yucca Flat with fines plugs and containment performance-related instrumentation (continued). Radiation arrivals and overburden collapses are indicated. Open circles indicate positions of surviving radiation sensors.

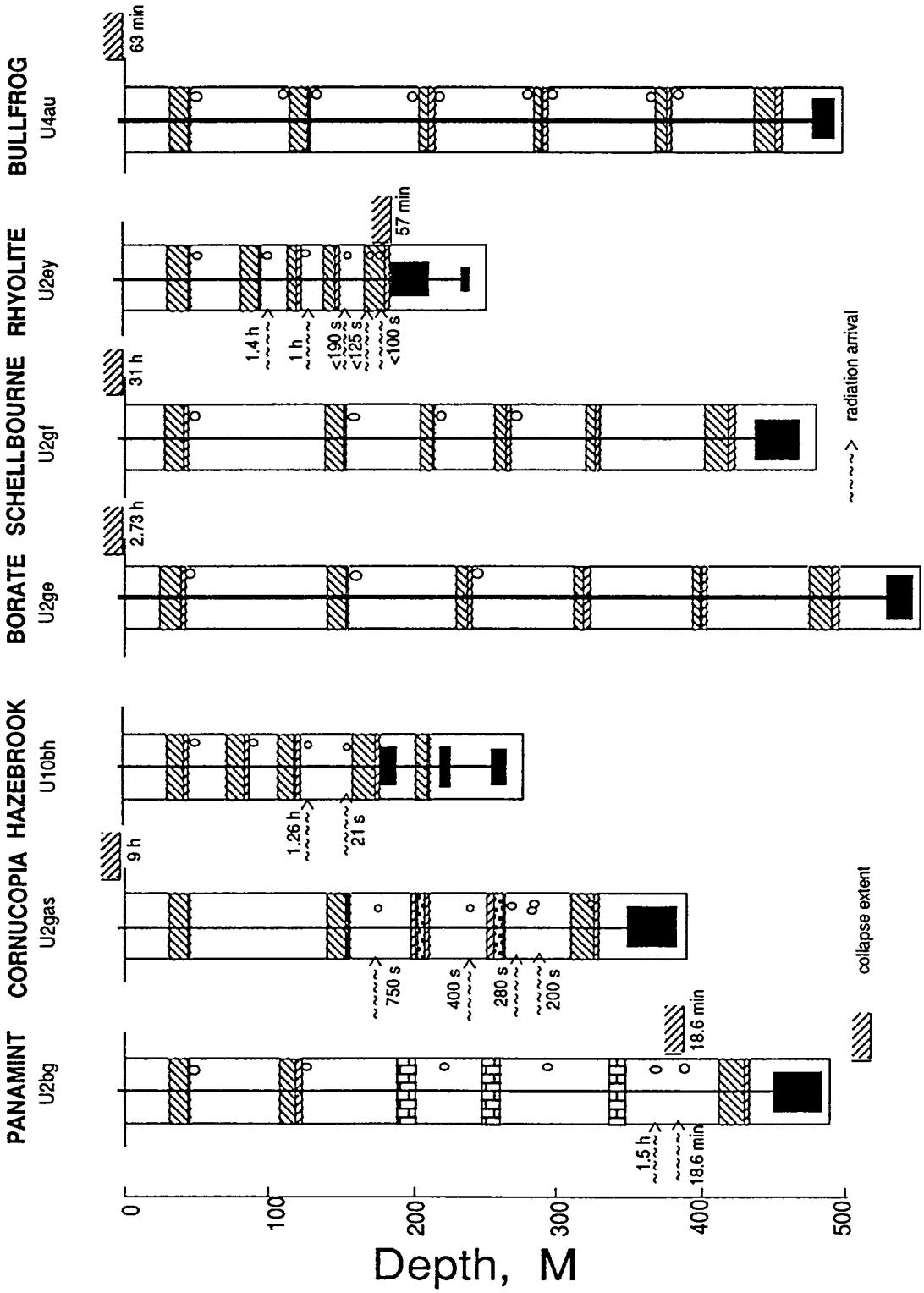


Figure 2c. Graphic representation of LLNL events in Yucca Flat with SGC plugs and containment performance-related instrumentation. Radiation arrivals and overburden collapses are indicated. Open circles indicate positions of surviving radiation sensors.

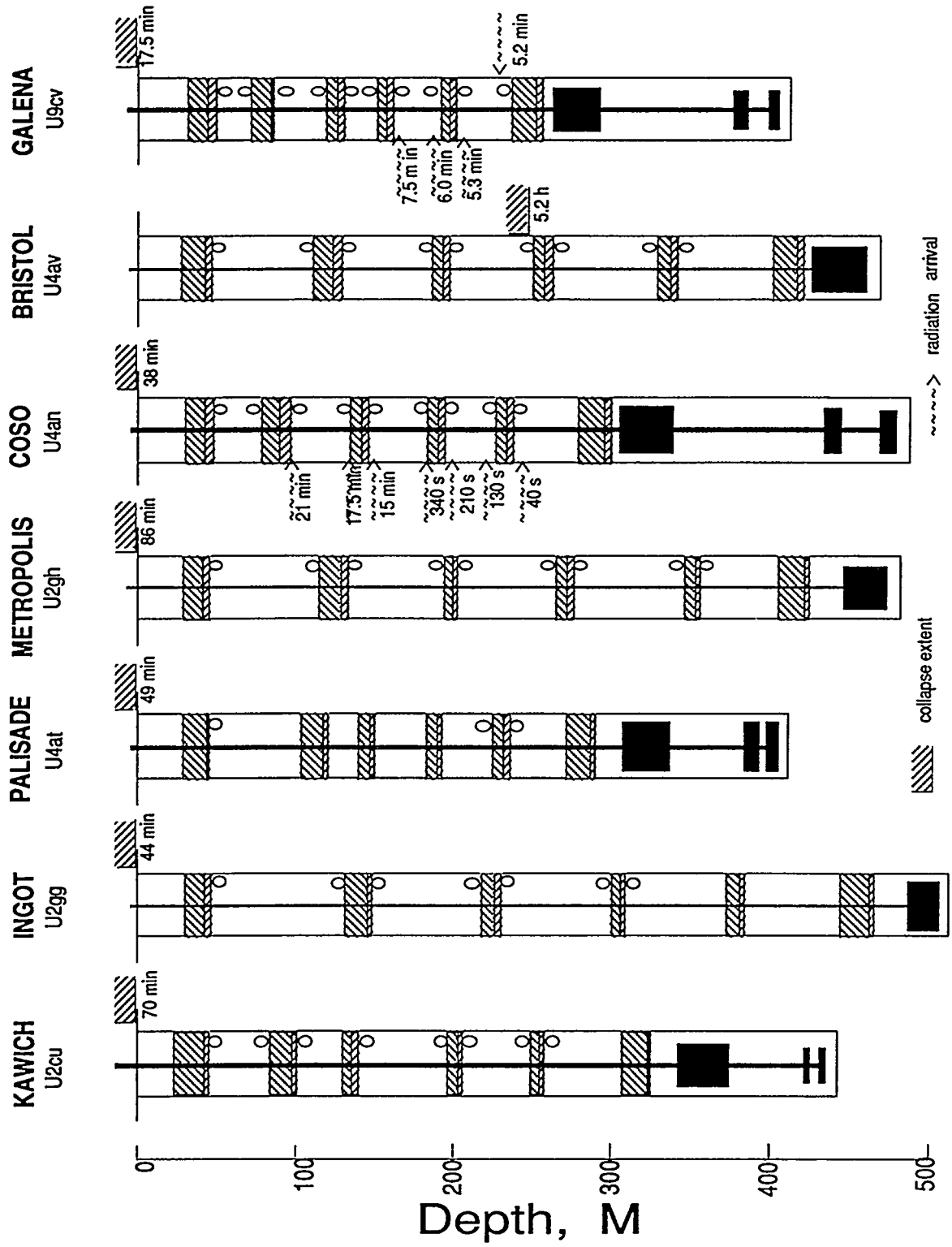


Figure 2d. Graphic representation of LLNL events in Yucca Flat with SGC plugs and containment performance-related instrumentation (continued). Radiation arrivals and overburden collapses are indicated. Open circles indicate positions of surviving radiation sensors.

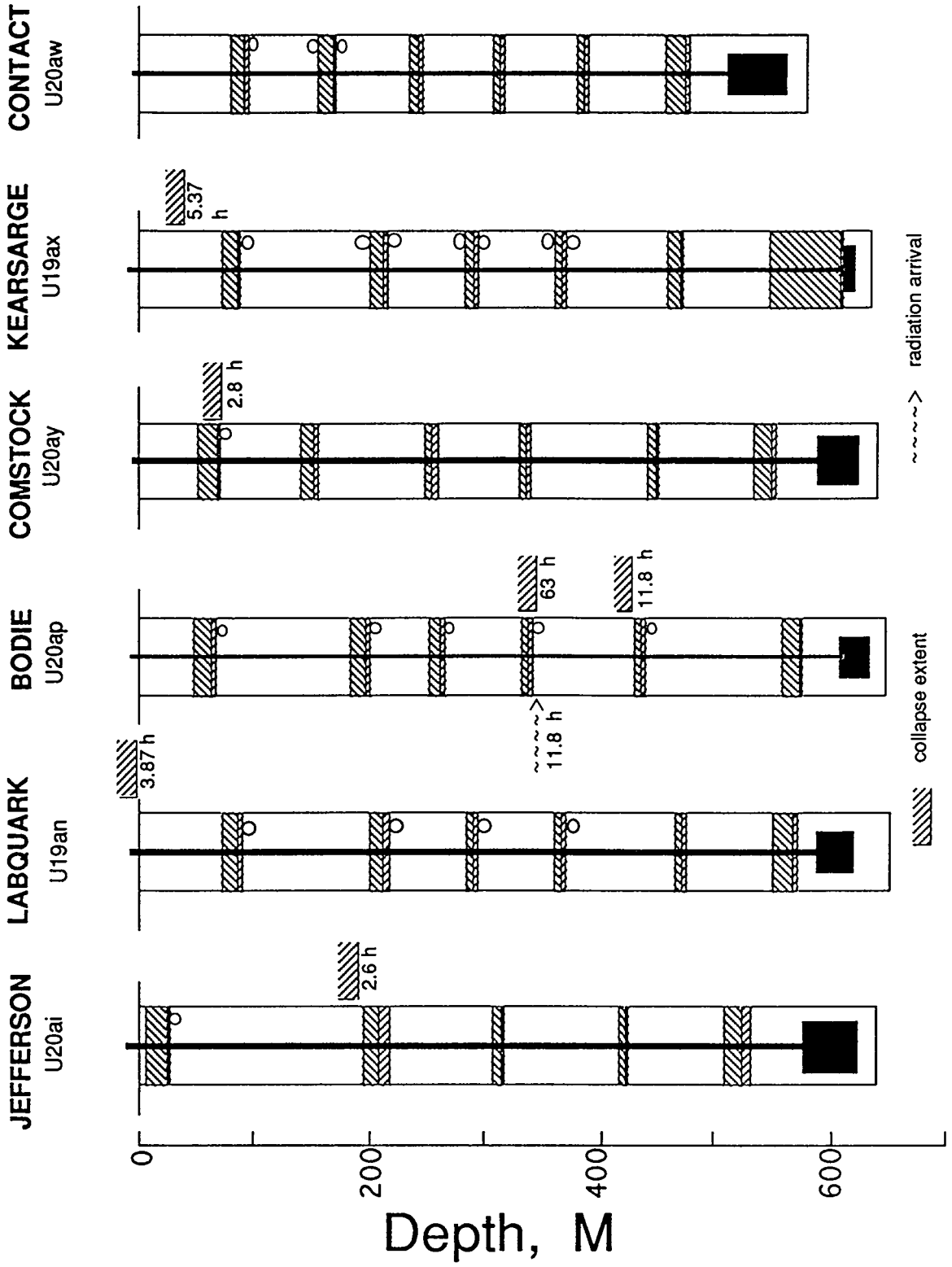


Figure 3a. Graphic representation of LLNL events on Pahute Mesa with SGC plugs and containment performance-related instrumentation. Radiation arrivals and overburden collapses are indicated. Open circles indicate positions of surviving radiation sensors.

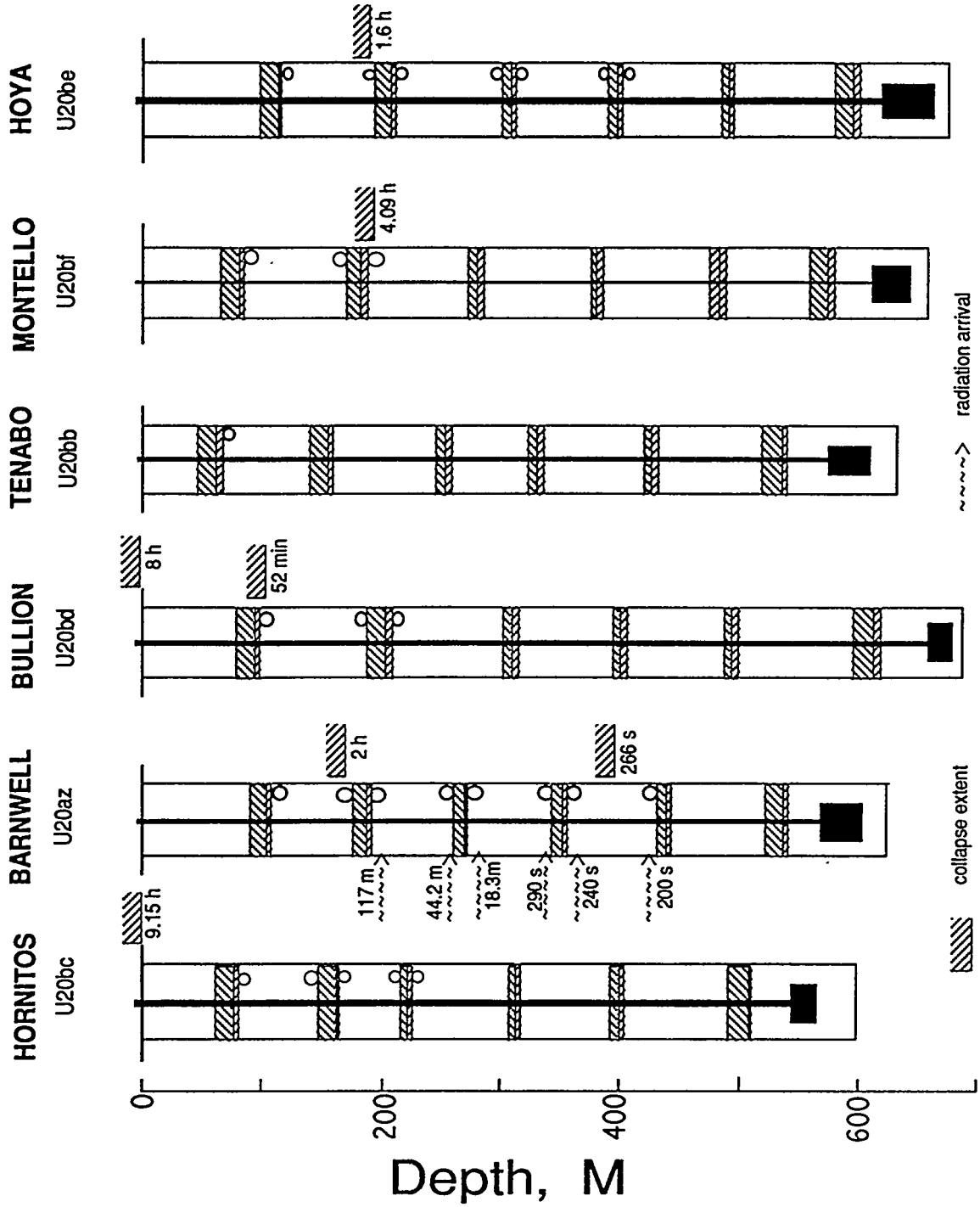


Figure 3b. Graphic representation of LLNL events on Pahute Mesa with SGC plugs and containment performance-related instrumentation (continued). Radiation arrivals and overburden collapses are indicated. Open circles indicate positions of surviving radiation sensors.

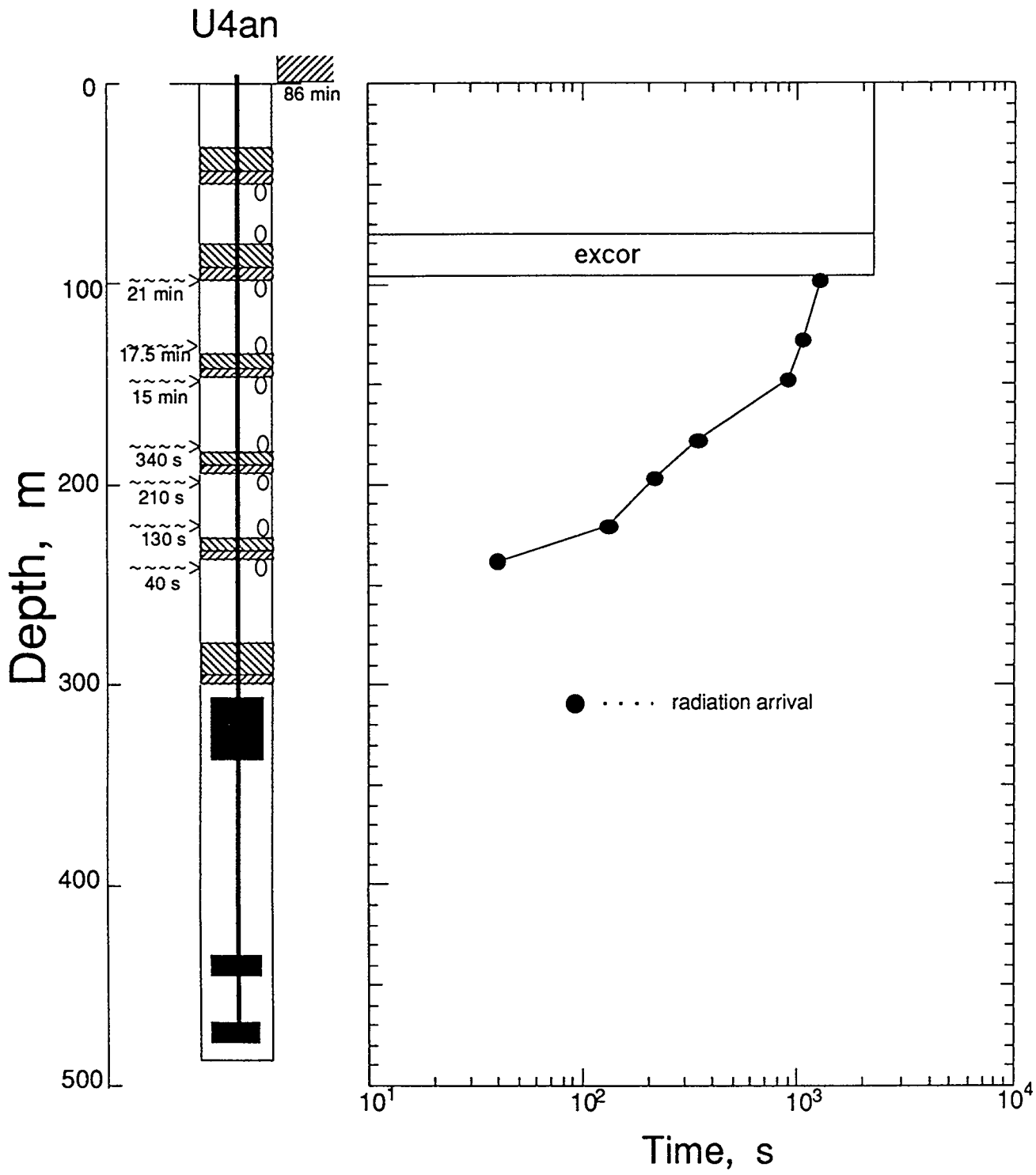


Figure 4. Observed radiation times of arrival versus range in the stemming column on the COSO event.

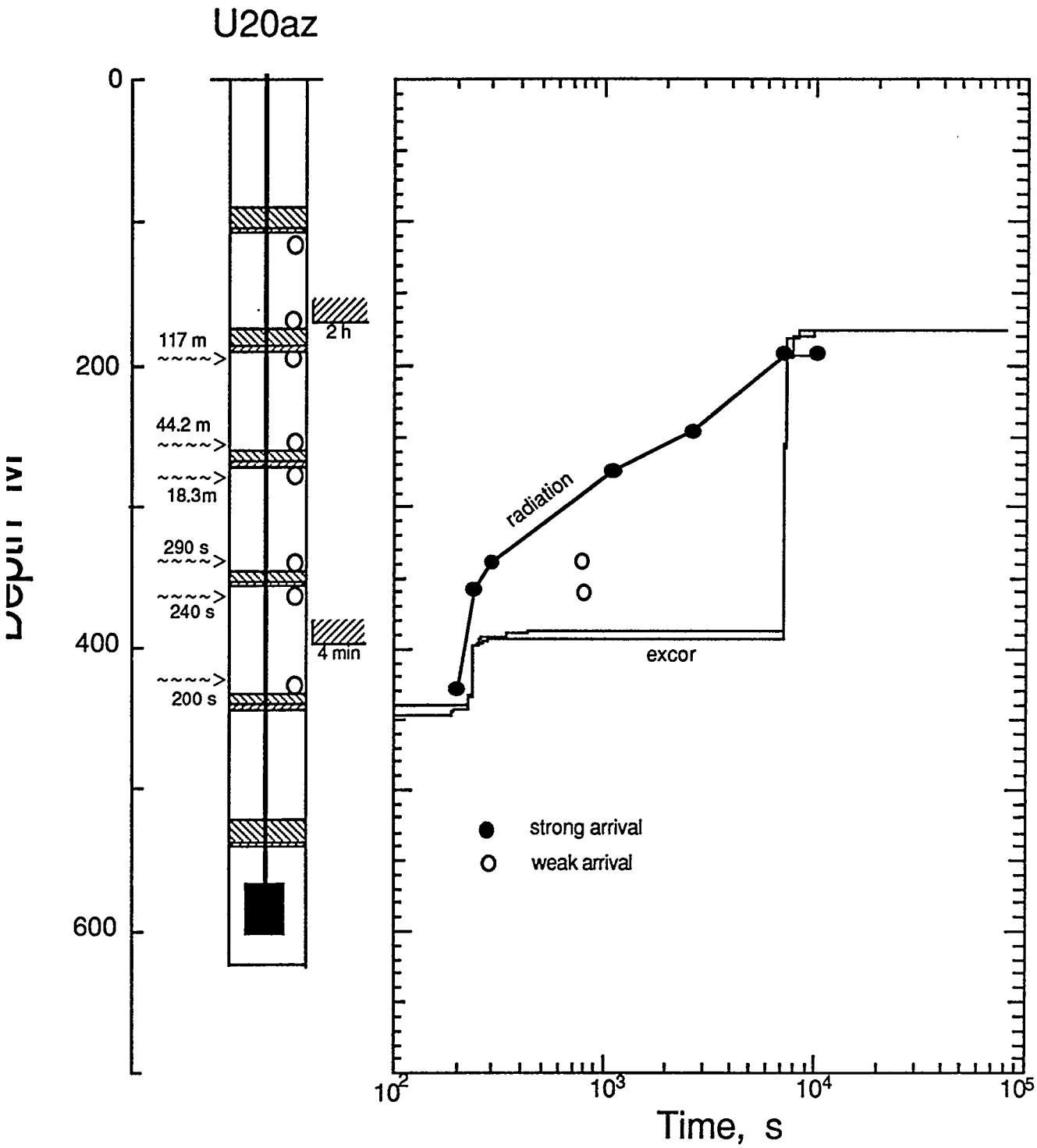


Figure 5. Observed radiation times of arrival versus range in the stemming column on the BARNWELL event.

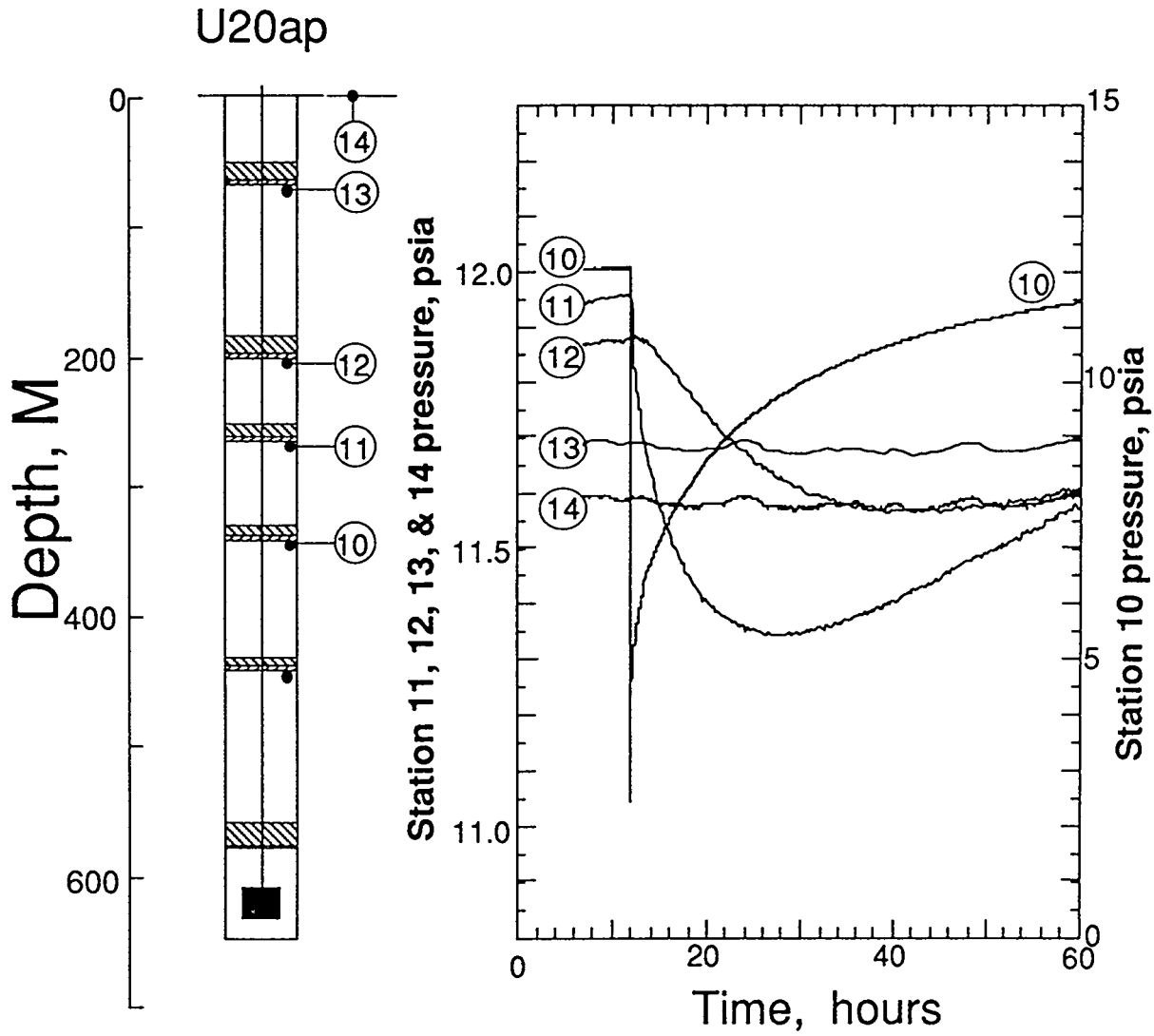


Figure 6. Negative pressure changes associated with sub-surface collapse on BODIE.

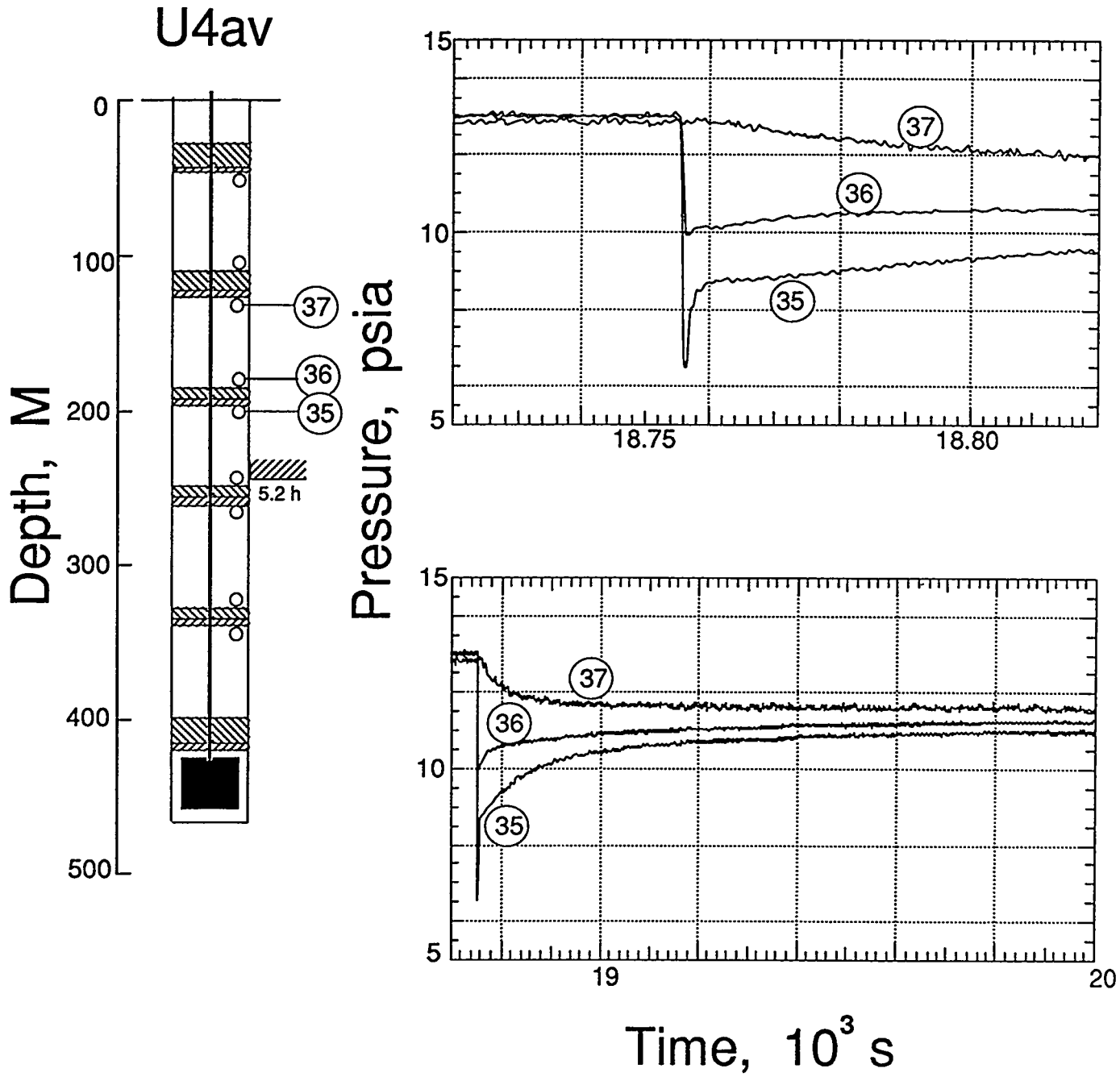


Figure 7. Negative pressure changes associated with sub-surface collapse on BRISTOL.

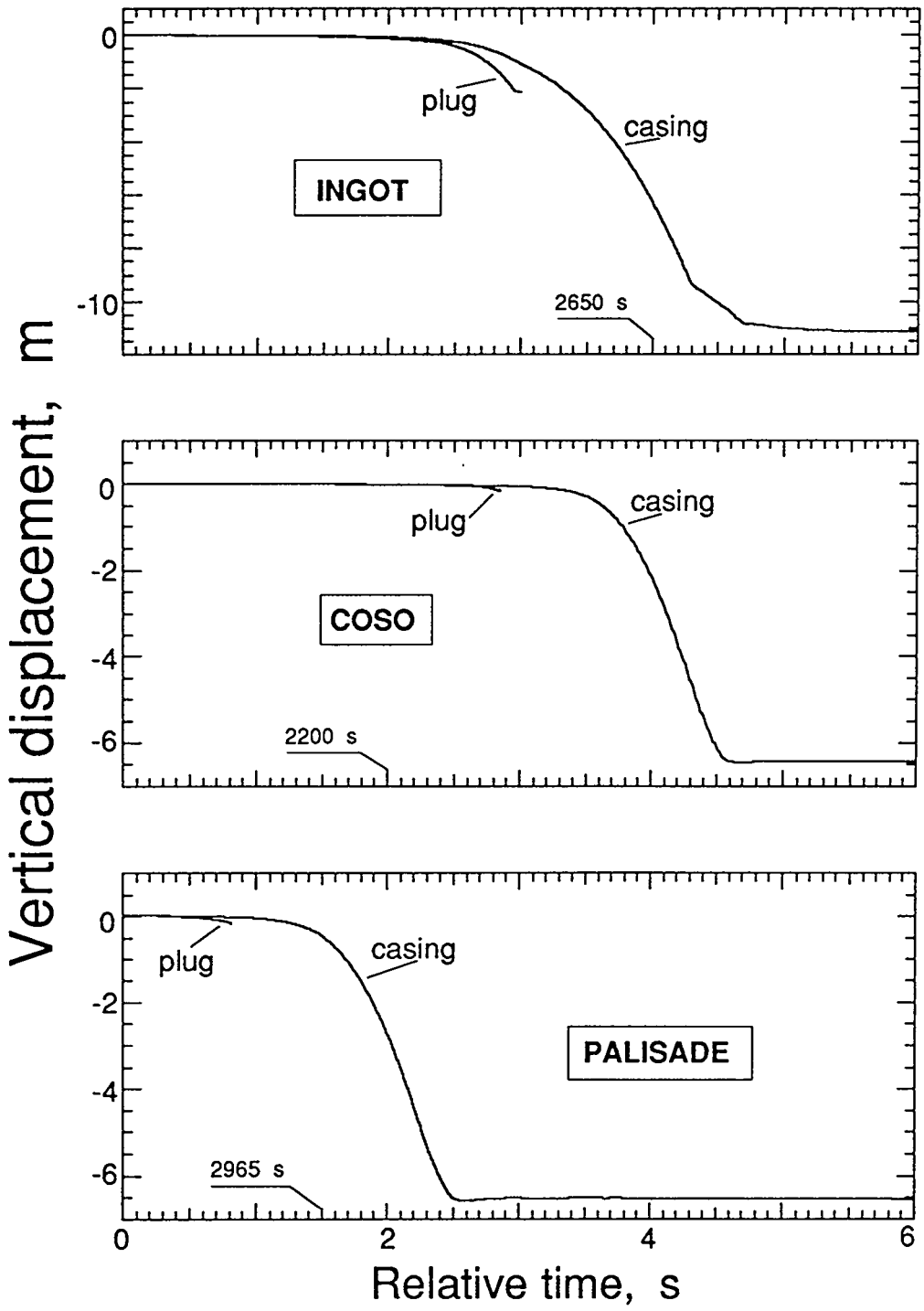


Figure 8. Vertical displacement histores of the top plug and the surface casing on INGOT, COSO, and PALISADE.

References:

1. Low levels of radiation resulting from the seepage of noble gasses through the geologic overburden media have been observed for some events on Pahute Mesa at times later than 24 hours after detonation. This behavior appears to be related to properties of the near–surface lithology and, due to level and lateness, is not considered to be a containment problem: [Erv Woodward, "Breathing on The Mesa", Fourth Symposium on Containment of Underground Nuclear Explosions, September 21–24, 1987; and Erv Woodward, "More About Breathing on the Mesa", Fifth Containment Symposium on Containment of Underground Nuclear Explosions, September 19–21, 1989.]

2. B. Hudson, "A Summary of Containment Diagnostics Data from Selected Events - 1975 Through 1979", March 26, 1980, UOPKL 80–13.

3. B. Hudson, C. Cordill, T. Stubbs, "AGRINI: Containment-Related Measurements and Conclusions", Lawrence Livermore National Laboratory, Livermore CA, UCRL-53725, April, 1989.

4. Gas flow around the surface casing was observed on the RIOLA event: [E. C. Woodward, "RIOLA Release Report", Lawrence Livermore National Laboratory, Livermore, CA, UCRL–53457, August 4, 1983]

Work performed under the auspices of the U.S. Department of Energy by the Lawrence Livermore National Laboratory under Contract ***W-7405-Eng-48.***

More RAMS Data for Selected LANL Events

Bruce C. Trent, X-4
and
Nancy L. Marusak, EES-5
Los Alamos National Laboratory
Los Alamos, NM 87545

ABSTRACT

The data presented at the Sixth Containment Symposium has been updated to provide additional records on measured pressure and radiation from downhole remote area monitoring station (RAMS) packages. The updates include, as before, complete stemming diagrams as well as the locations of all monitor stations. Data is provided for all tests conducted since the last symposium. The collection of this data will reside in an existing database management system which will enhance the flexibility for analysis and comparison of different RAMS package time-histories.

RECENT ADDITIONS TO THE DATABASE

Los Alamos National Laboratory has detonated four underground nuclear explosions since the last containment symposium. Data relevant to the performance of the stemming features were obtained in all four experiments. Radiation was detected in at least one RAMS package for two of the tests. As before, most of the effort has been directed towards presenting as much of the radiation and pressure data as possible, while the amenities, such as removing single spikes and filtering the data, have received a lower priority. In this respect the presentation of the data is equivalent to the previously published report (Trent and Marusak, 1991). The LEDOUX experience is documented in a separate report (Trent and Lowry, 1991).

Also in the spirit of the previous report, the data is presented for it's own sake, i.e., no attempt has been made to analyze the performance of any particular stemming feature as a result of the signals obtained from the RAMS. It should be noted, however, that each event was perfectly contained, in that no event-related radiation was ever detected at the surface, including late-time trace amounts associated with "atmospheric pumping" occasionally observed in connection with LLNL events.

The records presented in this report are generally similar in character to what has been observed previously, with the exception of the VICTORIA test. Here a very peculiar event occurred when a relative vacuum and an extremely high dose rate (> 70 kR/hr) were observed for nearly a minute at the deepest RAMS location. This was probably

associated with a complex combination of cavity collapse and stemming movement in the emplacement hole. Also, high radiation levels (> 4 kR/hr) were detected at the uppermost RAMS. Again, no radiation was detected at the surface. As a result of increased interest in the detection and the decay of radiation, the RAMS were monitored for over three days for VICTORIA and for over four days after the JUNCTION event. The radiation data presented in this report are summarized in tabular form.

Finally, the value of two separate recording teams should be mentioned. The data presented here is about equally split between coming from the Health Physics Policy and Programs Group (HS-12) and the Command, Control and Communications Group (J-8). While both organizations recorded all the relevant data, the different goals of each group resulted in a wide variety of sampling rates and data storage techniques. As a result, this report provides a more complete record of the post-shot stemming environment.

ACKNOWLEDGMENTS

As in the previous report, Richard Henderson of HS-12 (formally HSE-1) and Bob Fitzhugh of J-8 provided the data that appears in this report. This work was performed under the auspices of the U. S. Department of Energy.

REFERENCES

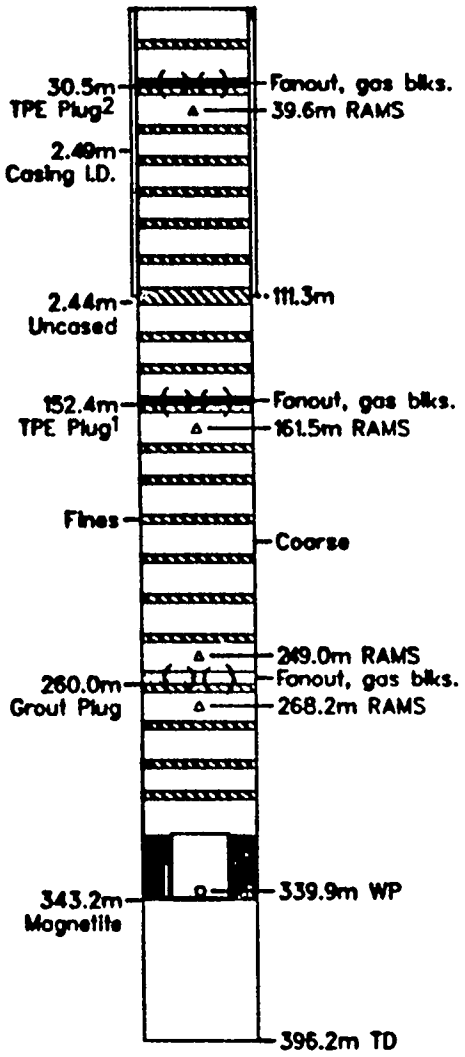
Trent, B. C. and N. L. Marusak, "RAMS Data for Selected LANL Events," 6th Symposium in Containment of Underground Nuclear Explosions, Reno, NV Sept. 23-27, 1991.

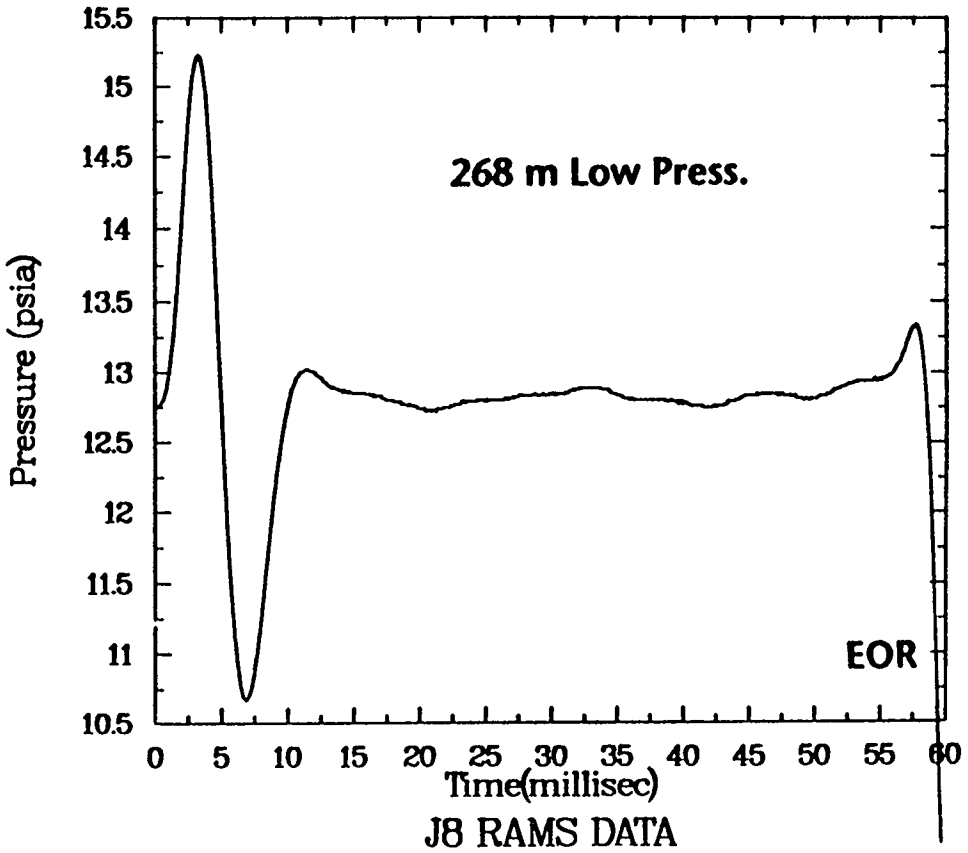
Trent, B. C. and Lowry, W. E., "Gas Flow Calculations for the LEDOUX Event," LA-CP-91-344, Proc. Sixth Symposium on Containment of Underground Nuclear Explosions, Reno, Nevada, September 24-27, 1991.

SUMMARY OF RADIATION DATA

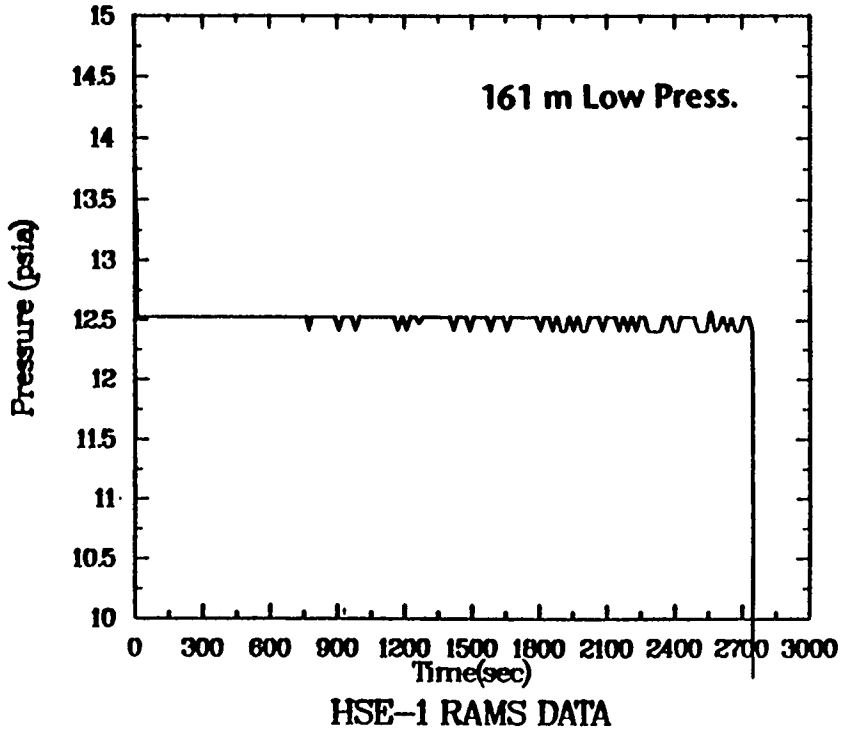
NAME	HOLE	DATE mmddyy	RAMS DEPTH (m)	TOA (sec)	MAX (R/h)	TMAX (sec)	EOR (sec)	COMMENTS
DIVIDER	U3ml	9/23/92	39.6				19000	Instrument still on line
			161.5				2766	Lost at collapse
			249.0				0.099	Instrument failure - ground shock
			268.2				0.055	Instrument failure - ground shock
VICTORIA	U3kv	6/19/92	113.1	1328	4311	1426	270300	
			192.3				7	Gauge lost early
			207.6	6	>74300	828	270300	Gauge saturated at peak
JUNCTION	U19bg	3/26/92	149.4				356700	Instrument still on line
			308.2				17100	Lost at collapse
LUBBOCK	U3mt	10/18/91	99.4				14977	Lost at collapse NOTE PROGRESS
			242.6				14929	Lost at collapse OF COLLAPSE
			264.0	1717	0.1954	11317	14893	Lost at collapse WITH DEPTH

Divider (U3ml)
9-23-92

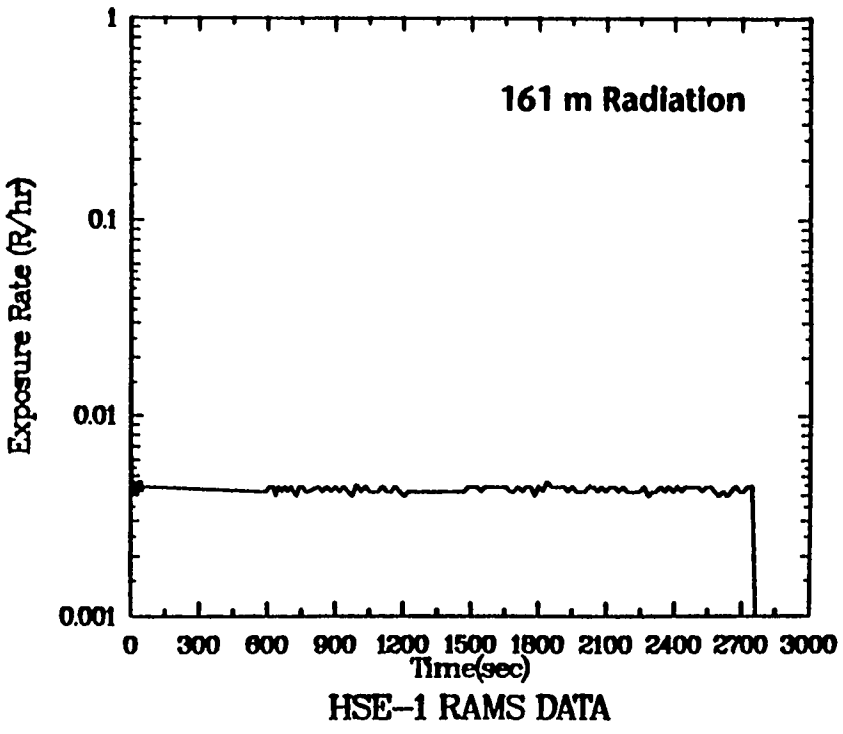




Divider (U3ml)
9-23-92
(cont.)

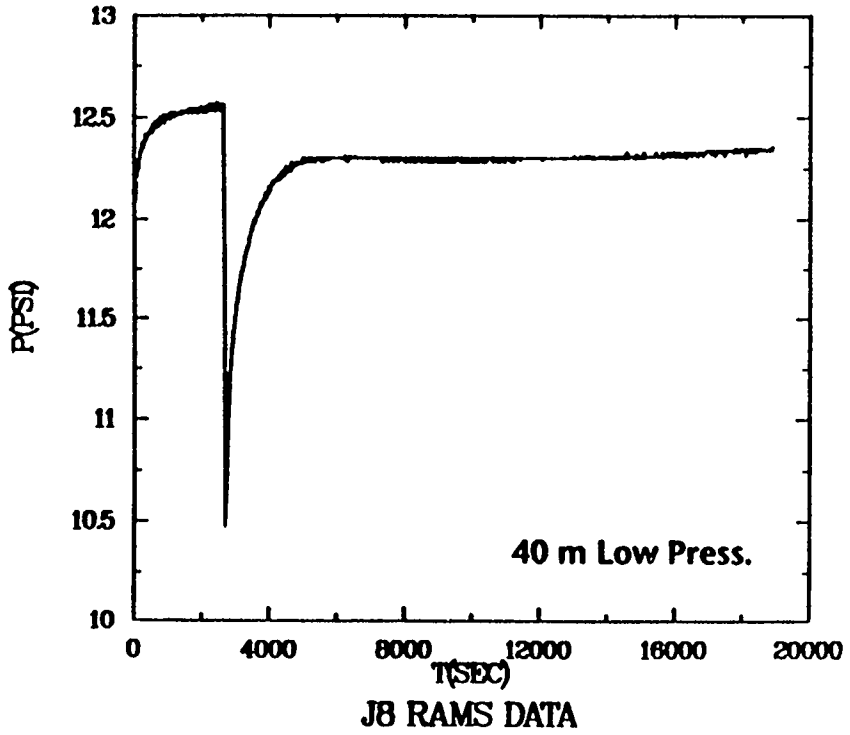


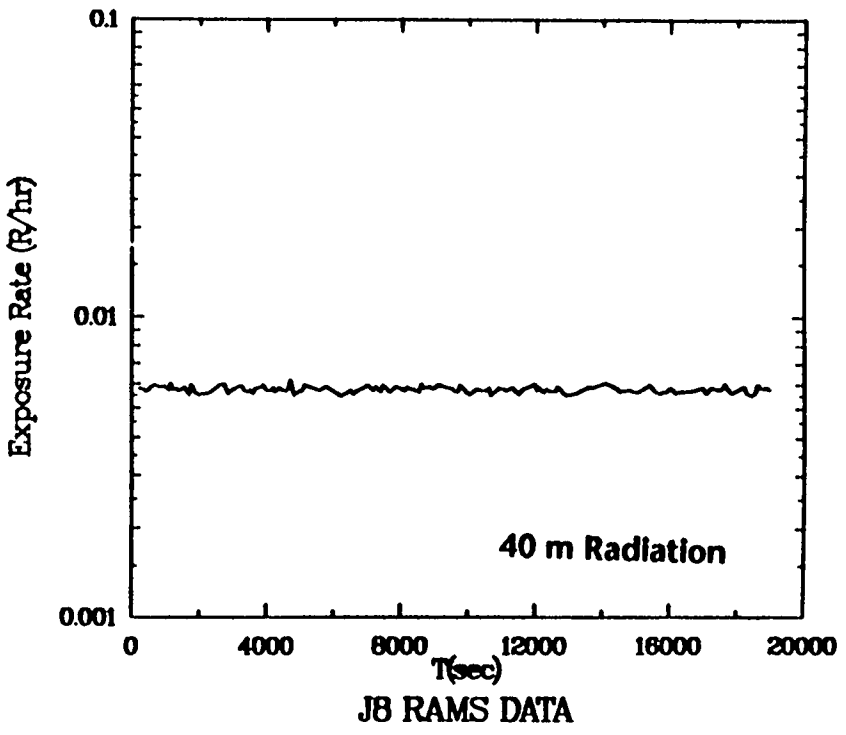
HSE–1 RAMS DATA



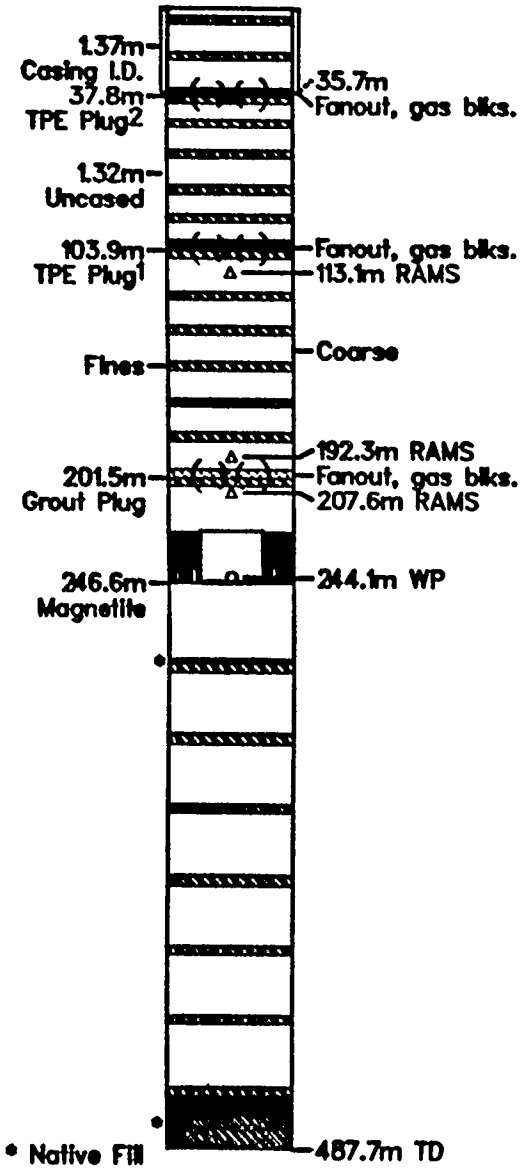
HSE–1 RAMS DATA

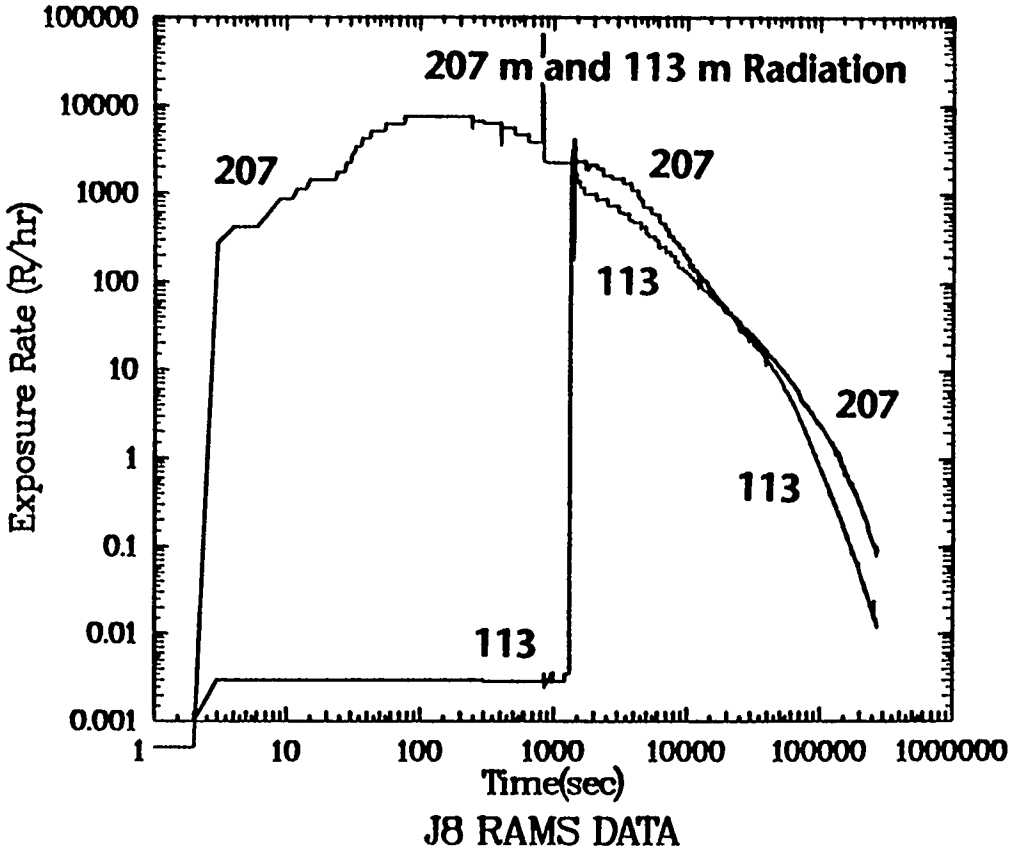
Divider (U3ml)
9-23-92
(cont.)





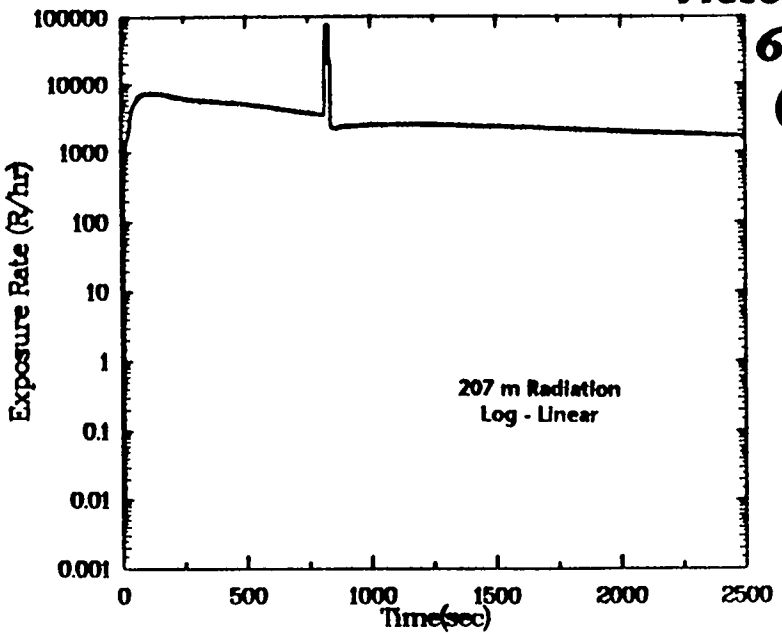
Victoria (U3kv)
6-19-92

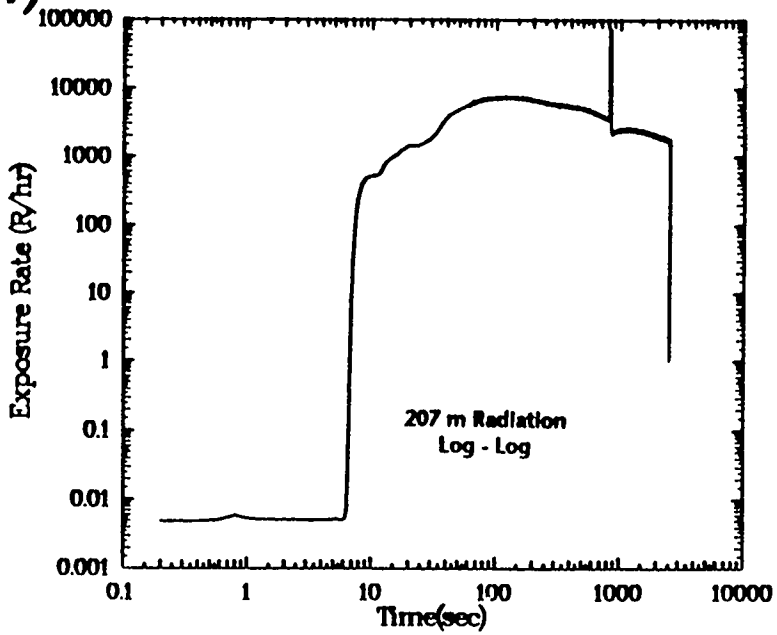


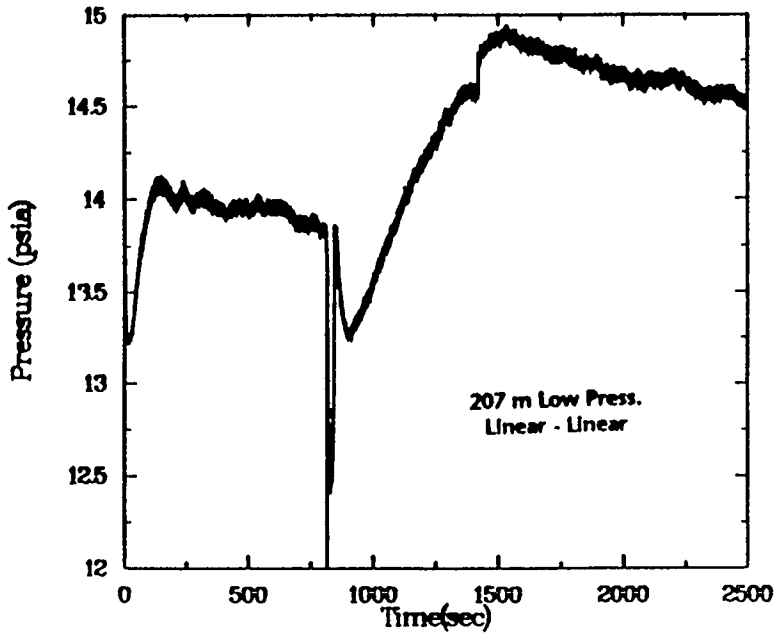


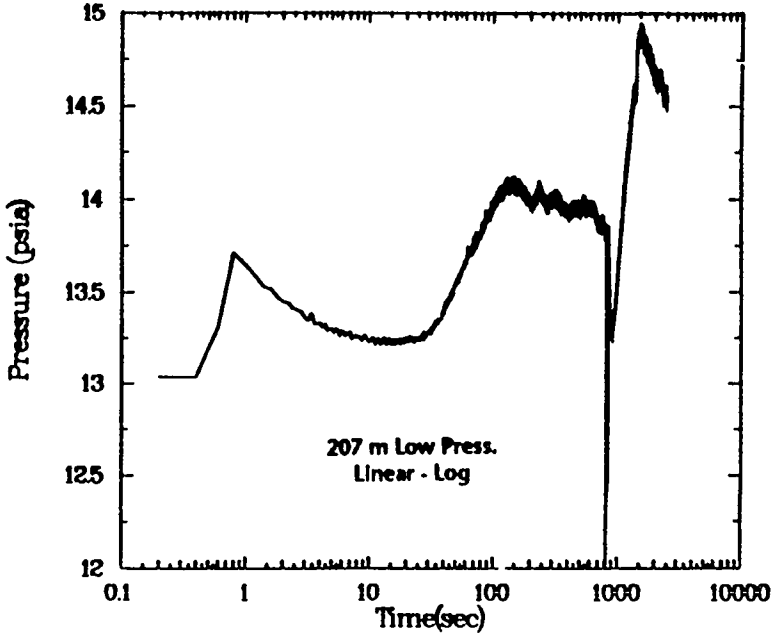
J8 RAMS DATA

Victoria (U3kv) 6-19-92 (cont.)

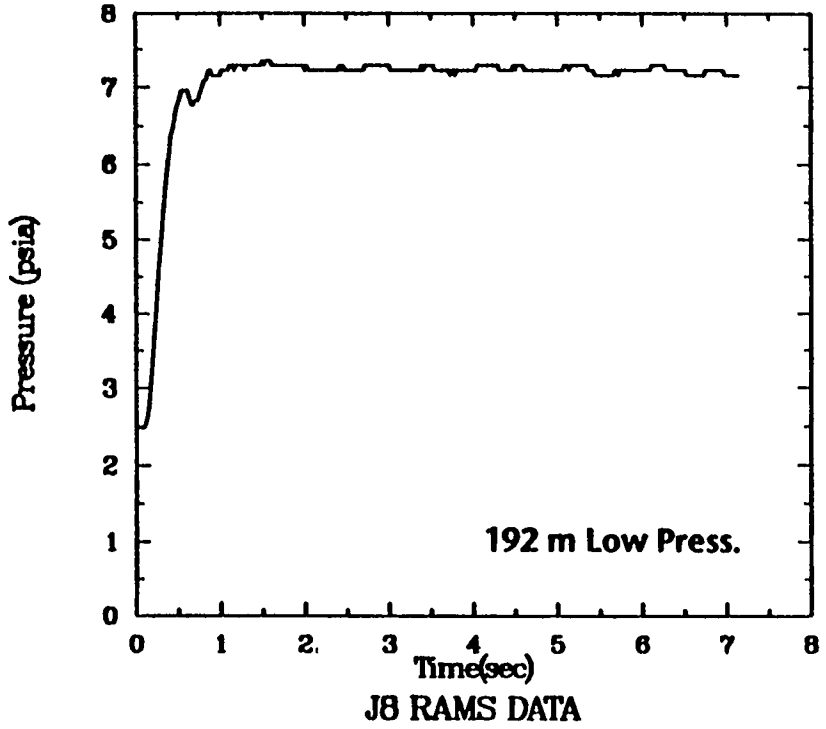


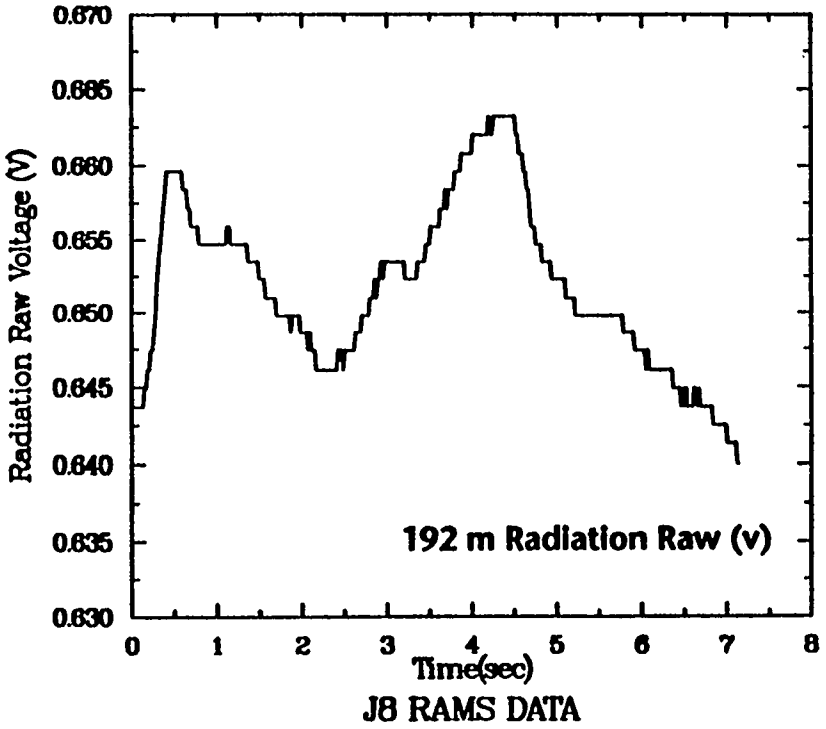




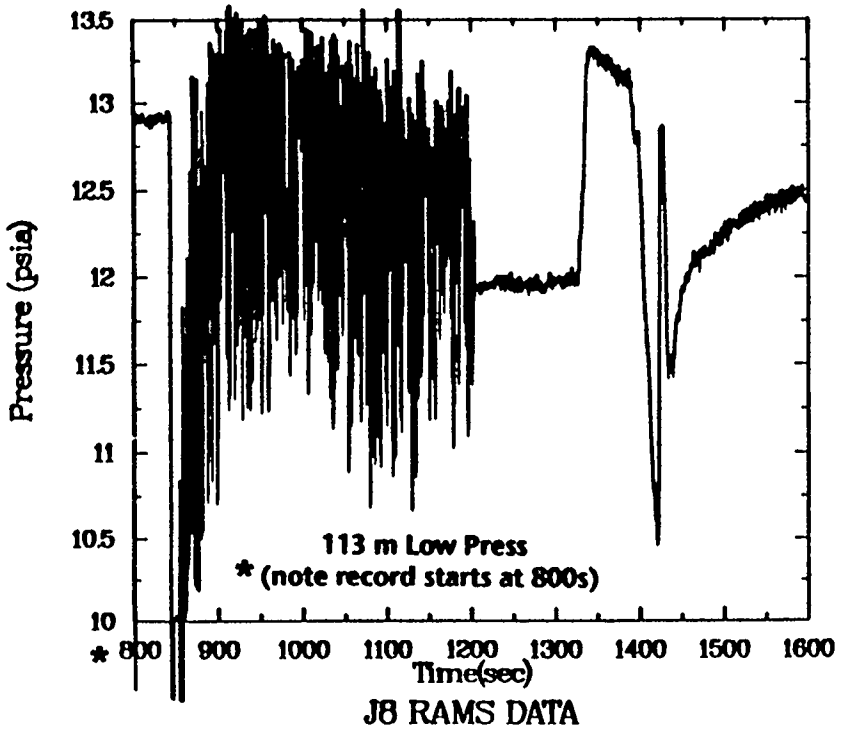


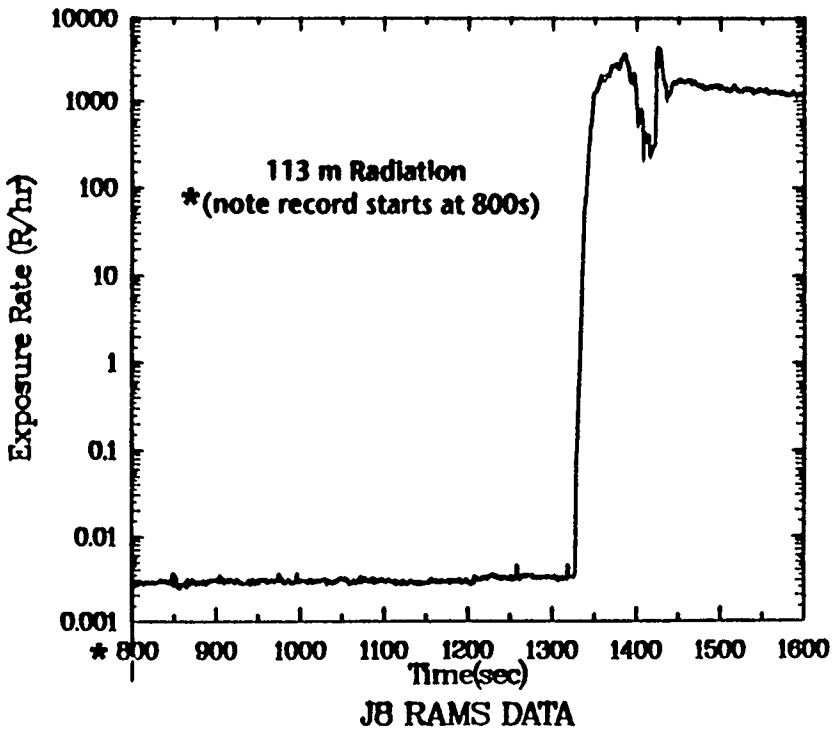
Victoria (U3kv)
6-19-92
(cont.)



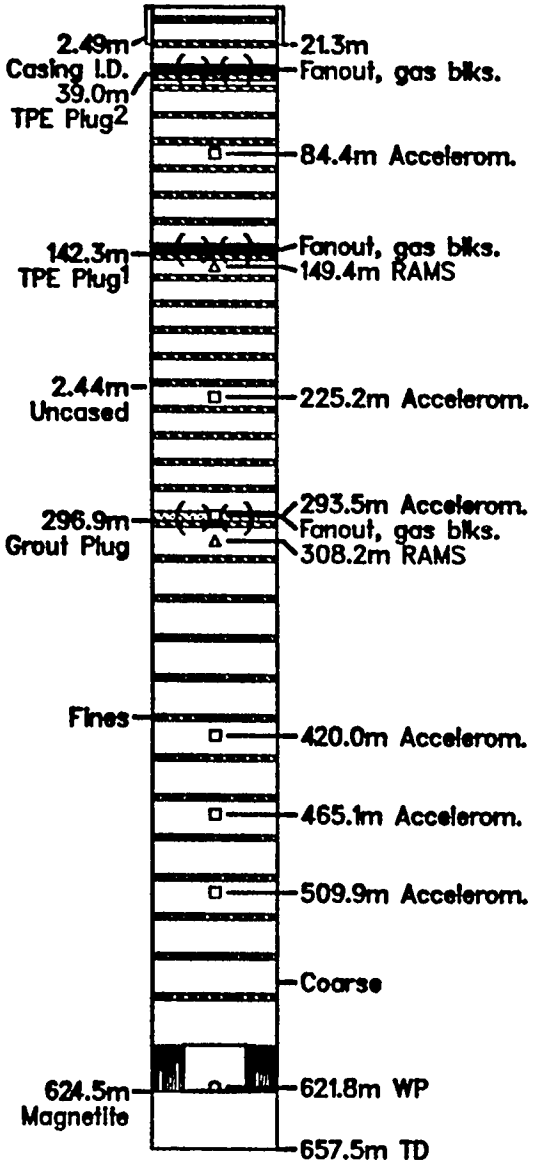


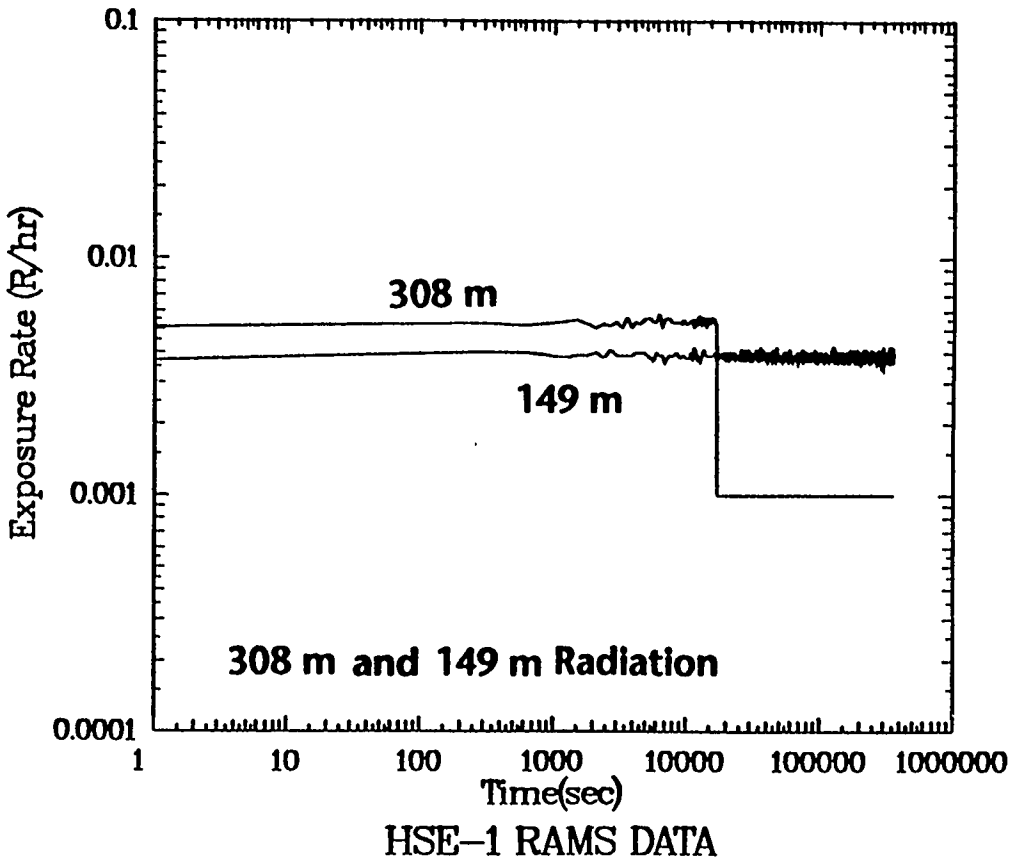
Victoria (U3kv)
6-19-92
(cont.)





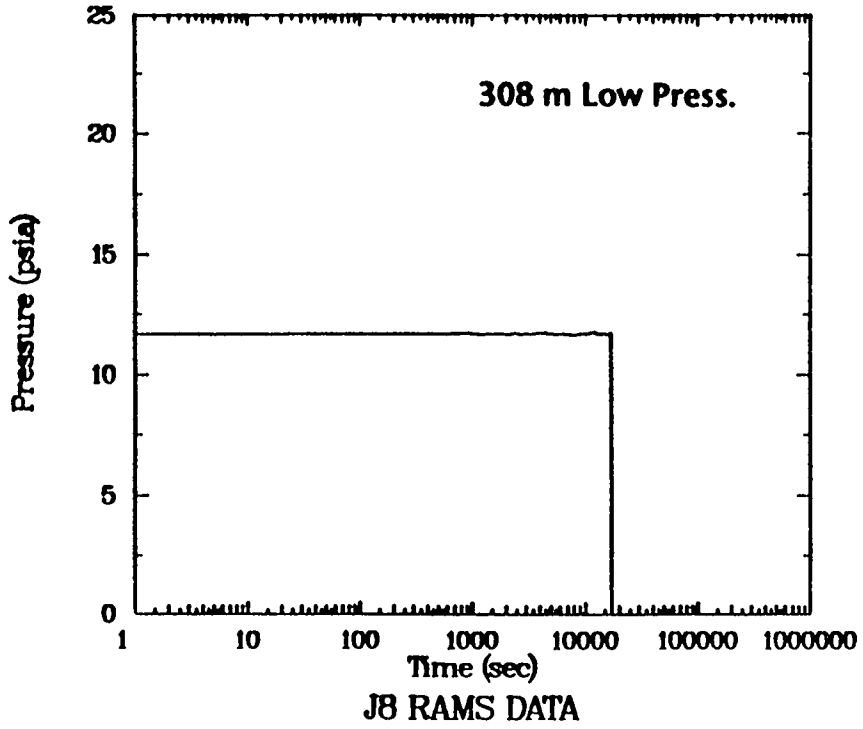
Junction (U19bg)
3-26-92

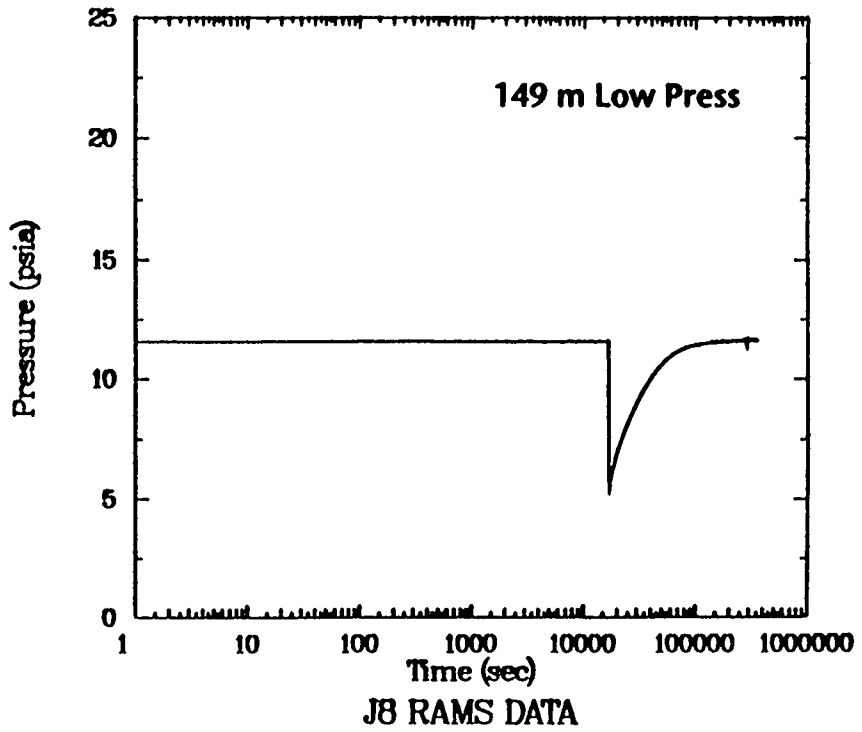




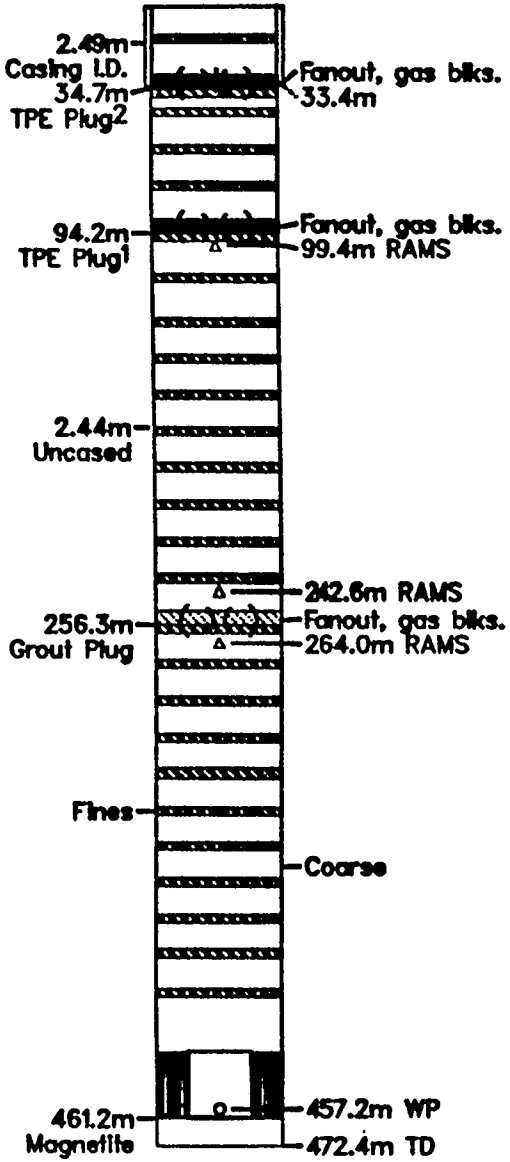
HSE–1 RAMS DATA

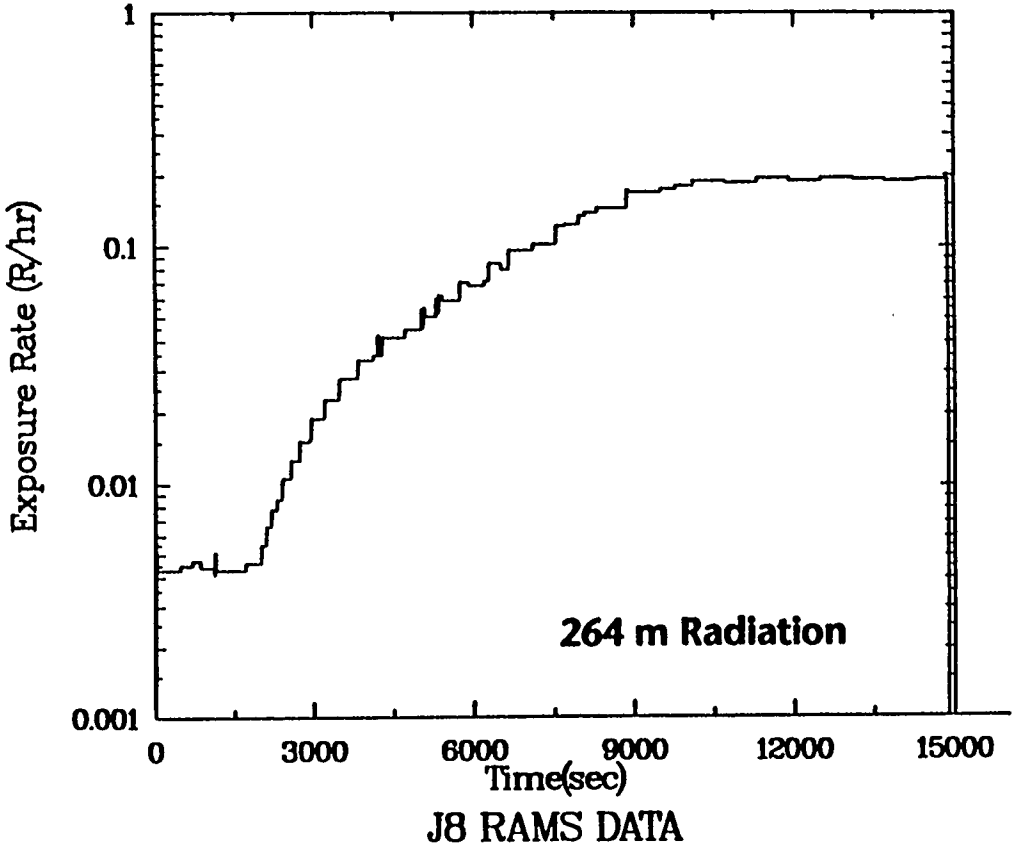
Junction (U19bg)
3-26-92
(cont.)





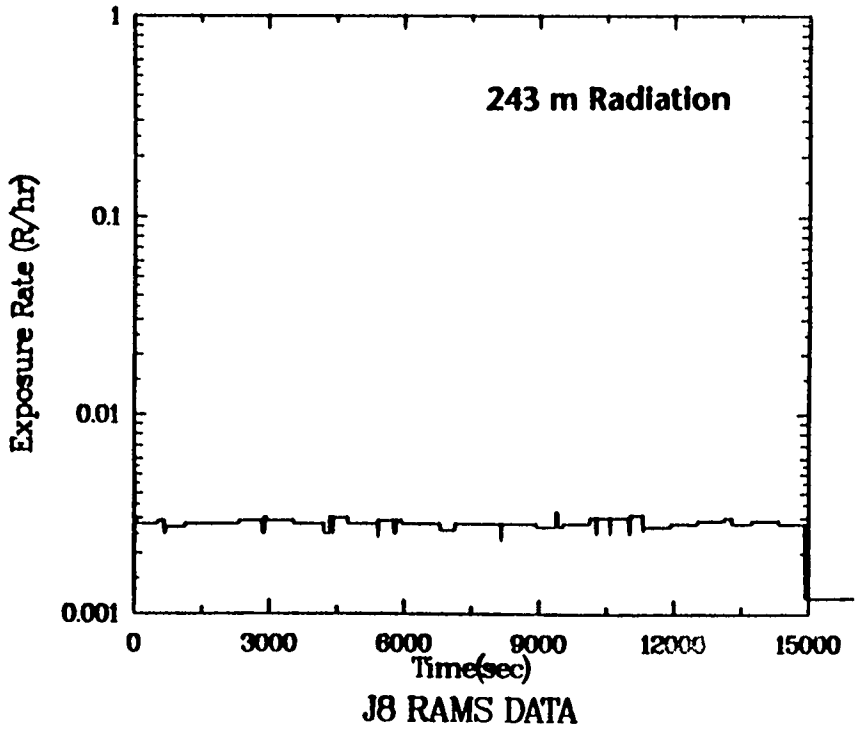
Lubbock (U3mt)
10-18-91

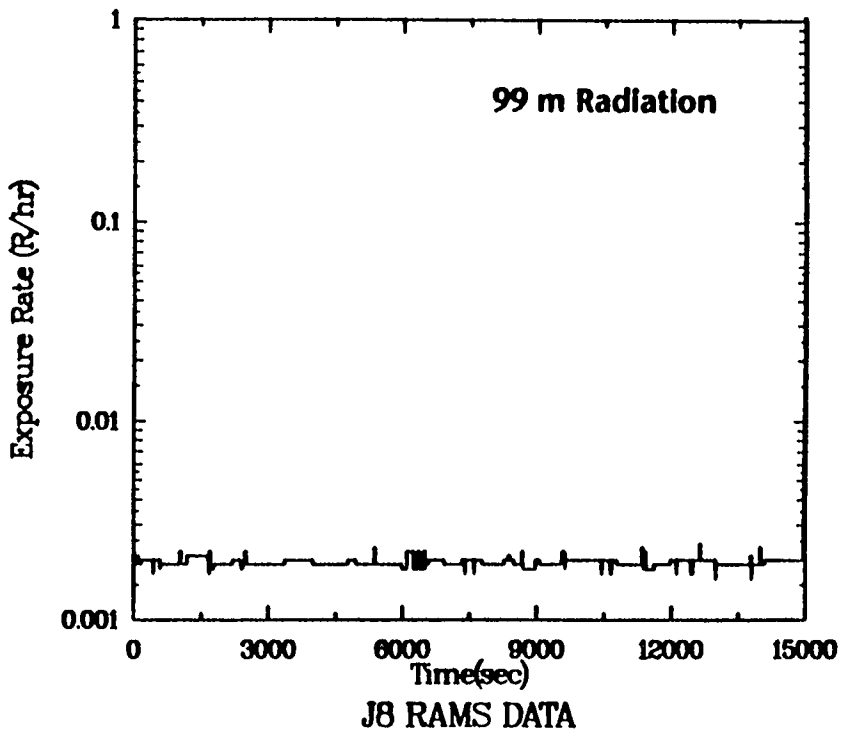




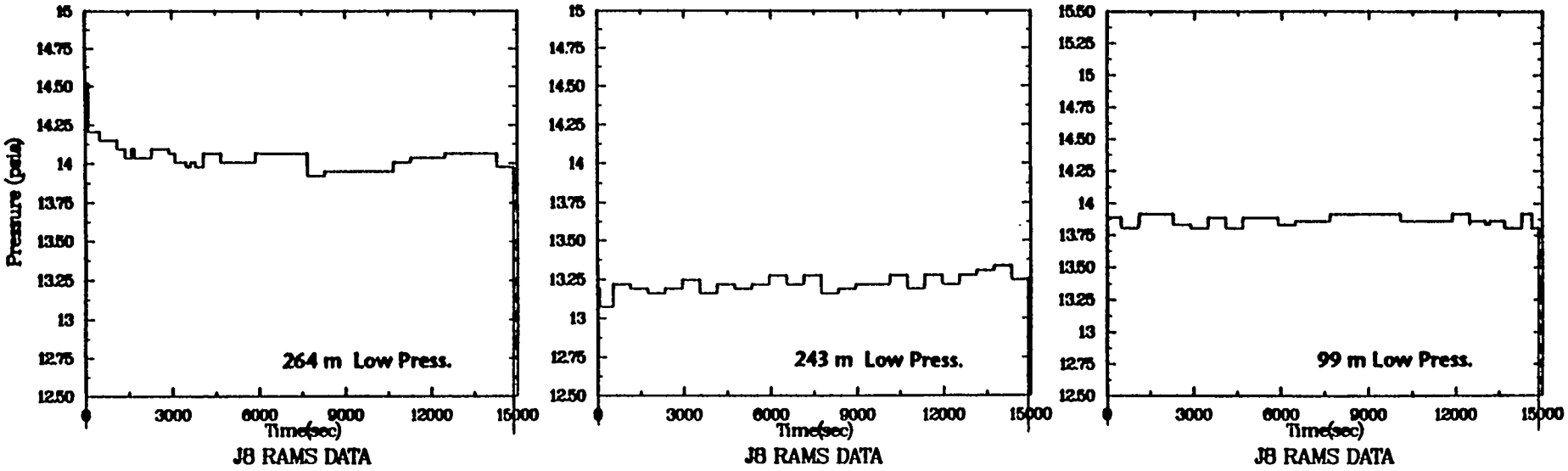
J8 RAMS DATA

Lubbock (U3mt)
10-18-91
(cont.)





Lubbock (U3mt)
10-18-91
(cont.)



Geophysics



IN SITU CONVERGENCE MEASUREMENTS AND INITIAL ANALYSIS FROM MINE-BY EXPERIMENTS IN U12P AND U12N TUNNELS AT THE NEVADA TEST SITE, NYE COUNTY, NEVADA

B. L. Harris-West, Defense Nuclear Agency
M. B. Fogel, SAIC/Pacifica Technology Division

ABSTRACT

Quantifying the tunnel convergence phenomenon (the relaxation or displacement that occurs around a newly mined drift) is important for understanding the character and stress field of the in situ medium. Both of these factors are instrumental in modeling containment and structure response, and in determining support requirements for construction. A new technique was used during continuous mining of drifts in two tunnel complexes in 1988-90 to actively measure and record when and where tunnel convergence occurred in relation to the mined face.

For the first experiment, an electromechanical gauge was installed at the collar of each of six holes drilled to varying depths perpendicular to the existing (Bypass) drift to measure displacement as mining proceeded by in the parallel (Main) drift. Over a four-day period in 1988, a 33.2-meter (109-foot) section of the U12p.03 Main drift was mined from 7.6 meters (25 feet) on the portal side of the first gauge anchor, located at the bottom of the hole, to more than 7.6 meters (25 feet) on the far side of the last gauge anchor. Data were recorded every 1 or 5 minutes, depending on the proximity of the face to the plane of the anchors. Longer term data were recorded every 2 hours for an additional 34 days.

It is commonly accepted that "stress relief" fracturing occurs at the mined face during or shortly after mining. Displacement-versus-distance plots of the data from the U12p.03 test indicated, however, that displacement began well before the face reached the plane of the measurement station. The plots also showed that the gauge anchor farthest from the Main rib (wall) measured about half the displacement of the closer anchors. The longer term data indicated continued relaxation, but at a slower rate, following the mine-by.

The U12p.03 experiment was simulated using a two-dimensional, quasi-static finite-element code that approximated the nominally rectangular drift with a circular cylinder and that assumed the rate of excavation was slow enough to allow for the maintenance of static equilibrium. Thus, the excavation process was represented in a single calculation by a partially mined tunnel. The initial computation was run using physical and mechanical properties measured on tuff samples from the U12p.03 site. Comparisons between the measured and computed displacements at different distances from the mined face and at different wall depths indicated that the field data did not follow the calculated response of an infinite cylinder of uniform material. Follow-up calculations using slightly different parameters indicated that the best match to the field data was achieved with a layered model and 25% reduction in the measured shear modulus. The calculational analysis showed that the experiment could be simulated numerically and may provide a sensitive measurement of the in situ shear modulus for the tuff in the vicinity of the tunnel.

Three additional mine-by experiments were conducted in the U12n.22 and U12p.04 drifts in 1989 and 1990, respectively. The configurations were very similar to that of the first test, but the geologic setting, overburden thickness, drift size and load history were somewhat different. Displacement-versus-distance plots of these data indicated an overall response similar to that of the U12p.03 experiment, with early initial displacement, smallest displacement for anchors at the greatest depth and continued relaxation following the mine-by. However, differences in the total magnitude of displacement, the location of the face when initial displacement occurred and the extent of divergence between data plots were observed and might be attributed to some variation(s) between the sites. No calculational analysis was done for any of the U12n.22 or U12p.04 data.

1.0 INTRODUCTION.

Quantifying tunnel convergence, that is, determining when, where and how much displacement occurs around a newly mined excavation, has long been an important goal of miners and tunnelers because of the clues that can be provided about the in situ rock's properties, stress condition and structural behavior under various load conditions. An understanding of the overall mechanical response of the rock mass has very specific applications in the Defense Nuclear Agency's (DNA's) program in terms of siting, characterization, containment, construction and structures performance.

Generally, it has been accepted that most displacement occurs at the face or heading either during or shortly after mining (Cummins and Given, 1973). As a result, most measuring devices, such as micrometer and tape extensometers, are passive gauges installed after mining has progressed past the area of interest. These devices provide questionable results and accuracy at best, and often cannot be recovered.

The purpose of this paper is to present the results of four experiments conducted in three pairs of drifts at the Nevada Test Site (NTS) using a new stress relaxation gauge (extensometer) capable of providing in situ, active measurements of displacement. The description of the experiment in the U12p.03 drifts is the most detailed and includes a calculational analysis. The U12n.22 and U12p.04 descriptions, on the other hand, simply summarize the data.

2.0 GENERAL GEOLOGY.

The mine-by experiments were conducted in the U12p and U12n tunnel complexes, located within Aqueduct Mesa and Rainier Mesa in the north-central part of the NTS. The drifts used were designated U12p.03, U12p.04 and U12n.22 (Figure 1) and were

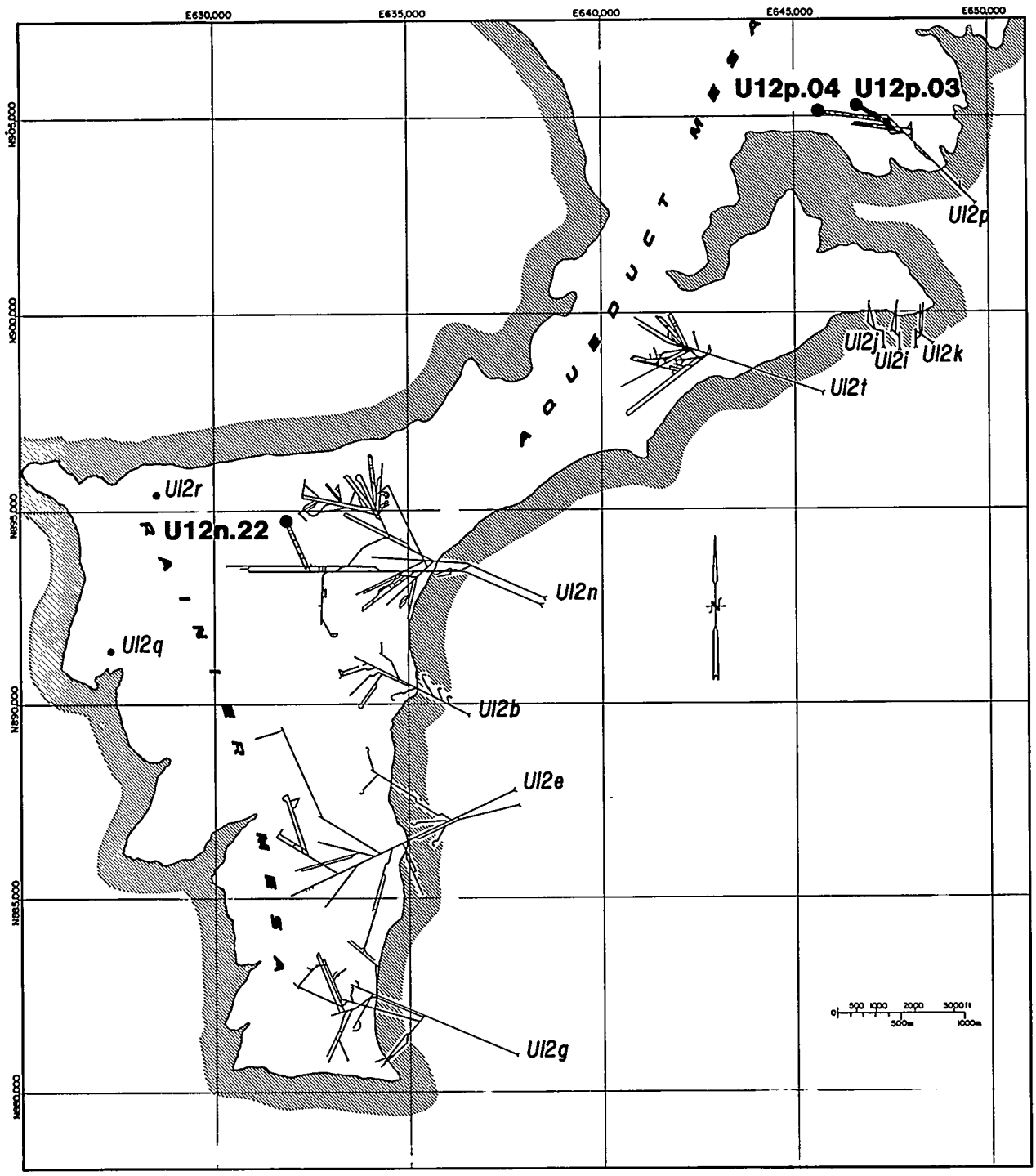


Figure 1. Reference map of Rainier and Aqueduct Mesas showing experiment locations. (Outline indicates topographic edge of the mesas. Tunnel portals not all at same elevation.)

excavated within the relatively flat-lying series of Tertiary-age volcanic rocks described by (Sargent and Orkild, 1973)[1]. The two drift pairs at U12p tunnel are very similar; both lie stratigraphically near the center of the Paintbrush Tuff at the same average depth (262 meters; 860 feet) and density (1.99 Mg/m^3; 124 lb/ft^3) of overburden. The U12n.22 site, on the other hand, lies almost 50% deeper in Rainier Mesa and 200 meters (656 feet) lower in the stratigraphic section within the bedded tuffs informally designated "Tunnel beds". Overburden density for the U12n.22 site is about 9% less than the U12p tunnel sites, reflecting the varying thicknesses of the overlying ash-fall and ash-flow units. The Miocene-age ash-fall tuffs at all four sites are pervasively zeolitized, with saturations measured in excess of 98%. However, only the U12n.22 drifts have visible fracture water and are considered "wet".

3.0 MINING METHOD.

The experiment sites were in typical DNA testbeds which consist of two paralliel drifts mined at different times. In all four investigations, the Bypass drift was mined prior to the Main drift using roadheader-type continuous mining machines. Some drill-and-blast mining was also done in the U12p.03 Main drift but not until the majority of the experiment was completed and the face was over 13.7 meters (45 feet) away from the site.

All drifts were nominally rectangular in cross section with only the upper corners rounded somewhat by the mining machines. Drift dimensions varied, depending on the testbed design. The Main drift averaged 3-meters by 3-meters (10-feet by 10-feet) at the U12p.03 site and 2.4-meters by 2.4-meters (8-feet by 8-feet) at the U12n.22 site. Of the two areas tested in the U12p.04 drifts, the first was mined to 4.9-meters by 4.9-meters (16-feet by 16-feet) initially and was later widened to 5.2-meters by 5.2-meters (17-feet by 17-feet). The second U12p.04 site had the same dimensions as the U12n.22 drifts.

4.0 GAUGE DESCRIPTION.

The electromechanical gauge (Figure 2) was designed and fabricated by Kaman Sciences Corporation (KSC) of Colorado Springs, Colorado, and provides direct positive (tension) and negative (compression) measurements by way of a calibrated potentiometer where 1 volt of electrical potential equals 0.025 meters (1 inch) of displacement (Secrist and Westlund, 1988). The gauge was designed for use in drifts or inside 76-mm (3-inch) diameter drill holes, but installation can be modified as needed to meet site-specific criteria. The system is simple, comprising off-the-shelf components that include gauges

---

1 A proposed revision of the stratigraphy for the Southwestern Nevada Volcanic Field has been presented (Sawyer, et al, 1989) but the 1973 designations are used in this paper, except where noted otherwise.

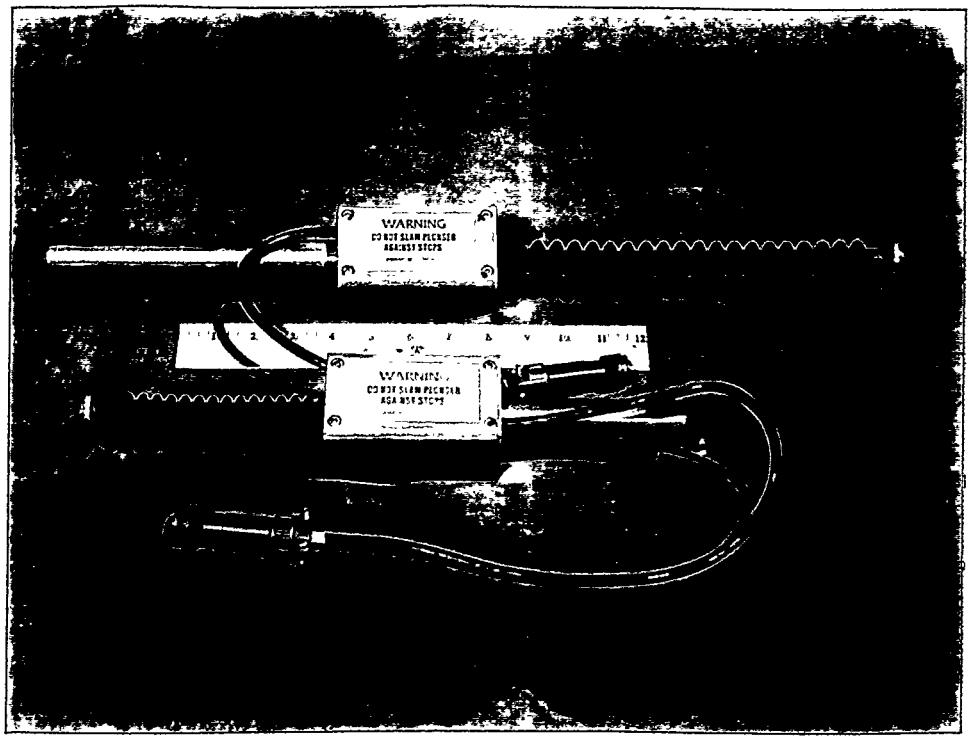


Figure 2. Photograph of stress relaxation gauges (extensometers) showing two plunger lengths. Gauge with the 0.15-meter (6-inch) stroke is used where the greatest displacement is expected; gauge with the 0.08-meter (3-inch) stroke is used where less displacement is expected.

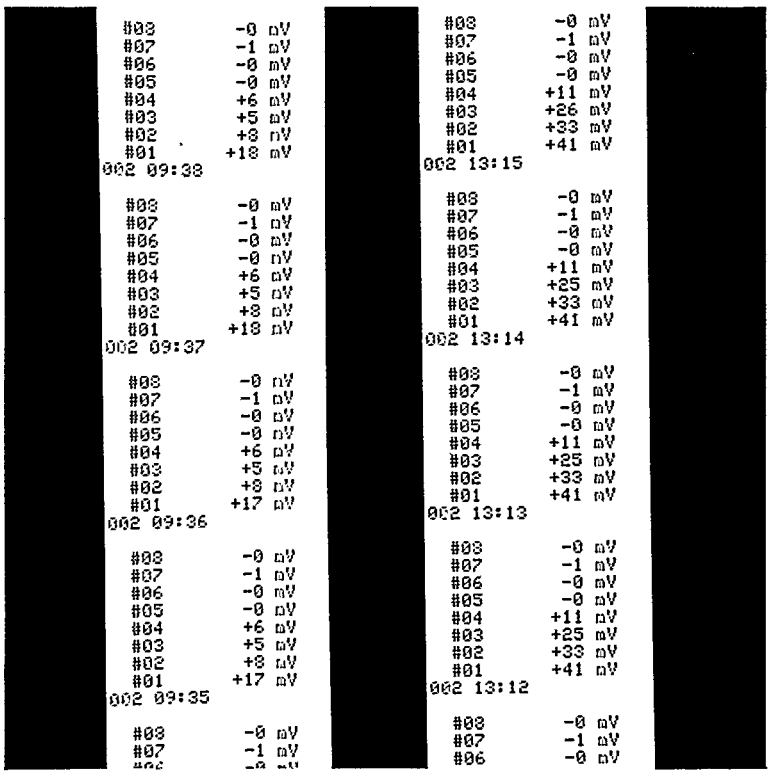


Figure 3. Photograph of typical 0.06-meter (2.25-inch) wide paper-tape records showing gauge number (#01-#08), tensional (+) displacement (millivolts), day (000), and time (00:00) on a 24-hour clock.

with a 0.08-meter (3-inch) or 0.15-meter (6-inch) stroke, six-conductor cables, a signal conditioner and a recorder. Data can be viewed constantly or recorded in increments that vary from 1 minute to 2 hours. Heat-sensitive paper tape was used as the recording medium here (Figure 3), but an electronic data logger could also be utilized.

5.0 EXPERIMENT CONFIGURATION.

The drill-hole method of installation was chosen to minimize interference with ongoing tunnel operations, and the gauges were placed at the collar rather than bottom of the holes to allow for recovery and subsequent reuse. For all four experiments, groups of four, six or eight 76-mm (3-inch) diameter holes were collared in the Bypass drift, drilled on 0.9-meter (3-foot) centers directly toward the planned Main drift at an inclination of minus 2%, and subsequently surveyed. Drill-hole depths varied from 17.4 to 27.1 meters (57 to 89 feet), depending on the design width of the pillar between the drifts. The bottoms of the holes were roughly 0.6 to 7.3 meters (2 to 24 feet; in multiples of 0.6 meters; 2 feet) away from the rib of the Main drift. The first 0.6 to 0.9 meters (2 to 3 feet) of the holes were reamed to 102 mm (4 inches) to allow installation of a stabilizing pipe and external support which would be bolted into the rock.

Several days prior to gauge installation, all test equipment and materials were moved underground to allow equilibration with the tunnel conditions at each site. As shown in Figure 4, sections of rebar were tack-welded together and run to the bottom of the holes, where the last 0.3 to 0.6 meters (1 to 2 feet) were anchored with grout. A packer near the bottom and wooden wedges near the collar were used to align the rebar with the half-compressed gauge plungers. Threaded bolts secured the gauges inside the stabilizing, protective pipes. Cables were routed from each gauge (Figure 5) to the recording system located in an unused side drift or alcove (Figure 6).

Data collection began when the mining machine in the Main drift was two to four tunnel diameters[2] on the portal side of the first gauge anchor, and continued until mining was well beyond three tunnel diameters on the far side of the last anchor. Displacement data were recorded on paper tape every 1 minute, 5 minutes, 1 hour or 2 hours depending on the distance or range of the mined face from the plane of the anchors. The times on the records were then correlated with detailed time/activity logs, prepared during the operation by mining inspectors and one of the authors, to produce a plot of displacement versus range for each gauge.

---

2 "Tunnel diameter", as used throughout, refers to the drift shape and dimensions explained in Section 3.0, and in no way indicates a perfectly round excavation.

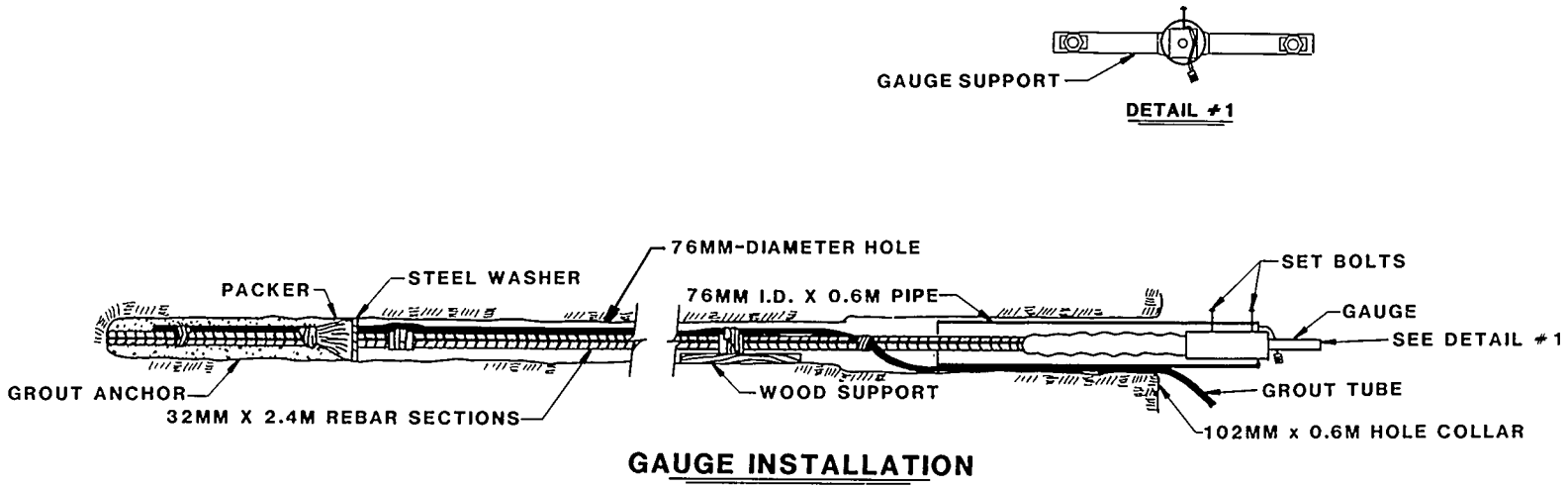


Figure 4. Schematic of typical installation in 76-mm (3-inch) diameter drill hole showing anchor, rebar and gauge locations, and one possible orientation for the external support.

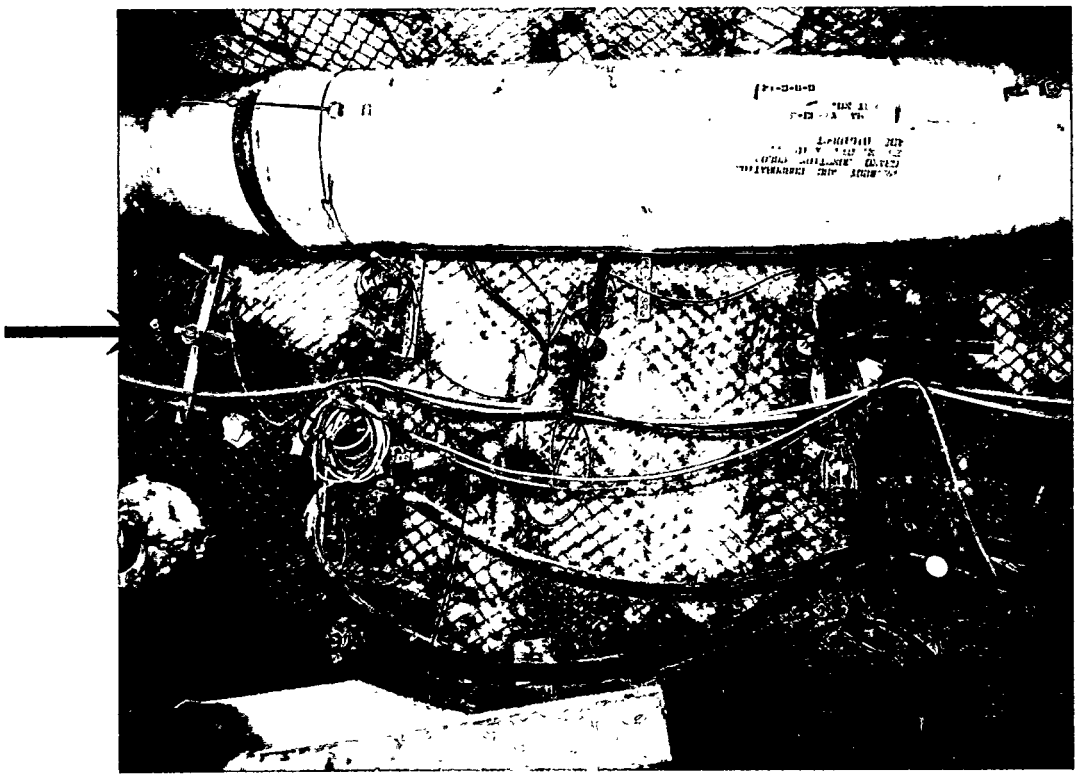


Figure 5. Photograph of installed gauges and supports at the collars of four holes (between arrows).

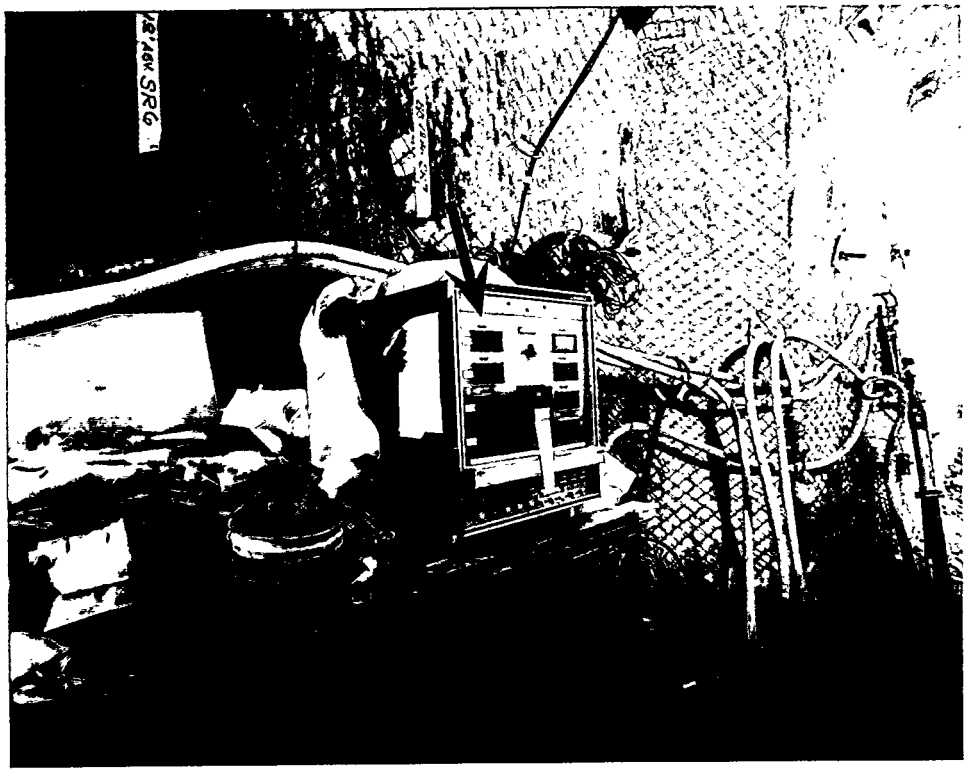


Figure 6. Photograph of recorder in small alcove. Visible are real-time display (arrow), paper-tape record (center), white brattice cloth (on top to minimize dust), and the general tunnel environment.

6.0 U12P.03 EXPERIMENT.

The first experiment was conducted in the U12p.03 drifts during June and July of 1988 at a depth beneath Aqueduct Mesa of 261.2 meters (857 feet). Overburden density, as calculated from measurements on core samples, was 1.99 Mg/m^3 (124 lb/ft^3). The dimensions of the Main drift were 3-meters by 3-meters (10-feet by 10-feet). A brief summary of the results was first presented during the Fifth Containment Symposium (Harris-West and Fogel, 1989).

6.1 Drill-Hole Details.

As shown in Figure 7, two groups of holes, consisting of one set of four separated by 4.3 meters (14 feet) from the second set of two, were collared 1.5 meters (5 feet) above the invert or floor between Construction Station (CS)[3] 9+75 and 10+02 in the left rib of the Bypass drift. The purpose of the second set was to provide redundancy and a check of the two anchors closest to the Main drift. The holes were designated SR-1, -4, -6 and -7 and were drilled to depths that varied from 16.2 to 20.4 meters (53 to 67 feet). The bottoms of the holes were 1.9, 0.7, 1.1, 5.0, 0.8 and 1.4 meters (6.1, 2.4, 3.5, 16.4, 2.5 and 4.4 feet), respectively, from the right rib of the planned Main drift. As-built survey data for the holes are listed in Appendix A.

All holes were drilled within the bottom meter of a massive, zeolitized, medium-grained calcalkaline ash-fall tuff with scattered silica nodules. This tuff is part of a series of alternating massive and thin-bedded units within the Paintbrush Tuff and is informally designated "MC-3". The beds dip a shallow 4.5 degrees toward the portal, and only one small fracture (which may affect gauge response) is projected to intersect SR-6 and SR-7. A tunnel-level geologic map of the experiment area is included in Appendix A.

6.2 Procedure.

Data collection began when mining in the Main drift was 7.6 meters (25 feet, or 2-1/2 tunnel diameters) on the portal side of the first anchor, SR-1, and proceeded as shown in Table 1.

Data were recorded manually on each of the remaining 34 days during drill-and-blast mining of another 9.4 meters (31 feet). On 21 July, the system and rebar were removed and the holes grouted closed.

---

3 Construction Stations (CS) are distances in feet from an underground point of reference and are used as measuring stations during construction and on design and as-built drawings.

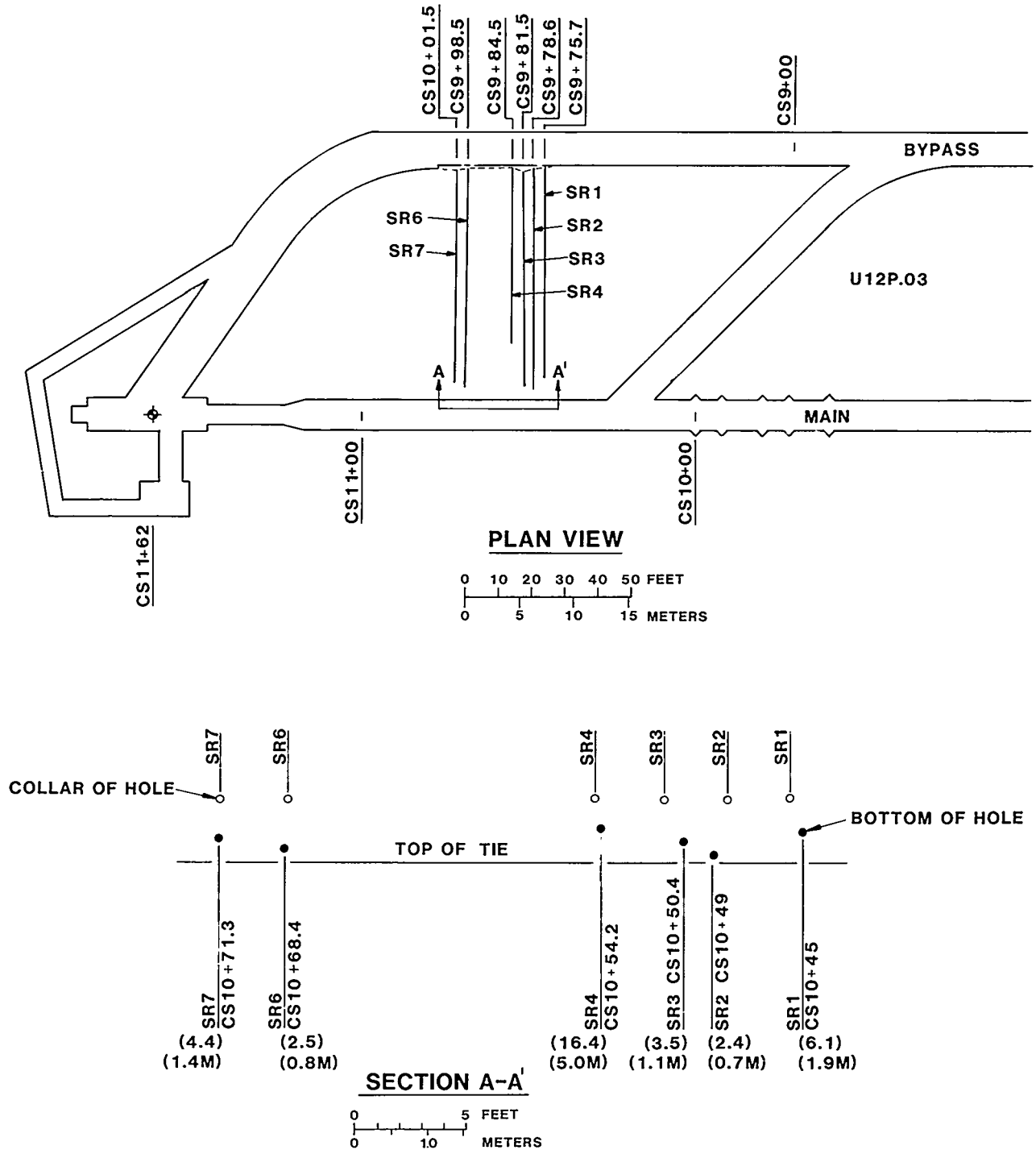


Figure 7. Plan view and cross section of drill holes U12p.03 SR 1-4, -6, and -7. Section A-A' shows position of hole collars and bottoms (anchors) relative to Main drift's "top of tie" (construction term for approximate tunnel grade and invert, as represented by a plane along the top of the railroad ties). Portal is to the right, off the figure.

Table 1. Mining and recording sequence in the U12p.03 Main drift.

Construction Stations	Mined Lengths (m/ft)	Dates	Mining Method	Recording Intervals
10+20 to 10+44	7.3/24.0	14-15 Jun	Roadheader	5 min
10+44 to 10+80.5	11.1/36.5	15-16 Jun	Roadheader	1 min
10+80.5 to 11+01	6.2/20.5	16 Jun	Roadheader	5 min
11+01 to 11+16.5	4.7/15.5	16 Jun	Roadheader	2 hrs
11+16.5 to 11+29	3.8/12.5	17 Jun	Drill/Blast	2 hrs

6.3 Results.

6.3.1 Field Data. All data for the 33.2-meter (109-foot) section of mining were plotted for each drill hole as functions of displacement (in thousandths of inches and millimeters, or millivolts) versus range (in feet and meters) from the mined face to the plane of the gauge anchors. The responses of SR-1 and SR-4 are shown on Figures 8 and 9 as examples of the variation in behavior for anchors closer to (1.9 meters; 6.1 feet) and farthest from (5.0 meters; 16.4 feet) the Main rib. Figure 10 is an overlay of data from all six gauges for a shorter 32-hour period when mining progressed from 9.1 meters (30 feet) on the portal side of SR-2 to 9.1 meters (30 feet) on the far side of all six anchors. Individual plots for all the gauges are included in Appendix A.

Overall, the plots indicate that for this experiment:

A. Displacement began 1/2 to 1-1/2 tunnel diameters before the mined face reached the plane of the gauge anchor locations.

B. Roughly 1/4 to 1/2 of the total displacement occurred before the face was opposite the anchors; and the majority of all displacement was completed within two tunnel diameters on the far side of each anchor.

C. The gauge anchor 5.0 meters (16.4 feet) from the Main rib (designated SR-4) moved roughly half the magnitude of and much sooner (almost three tunnel diameters) than the other five anchors.

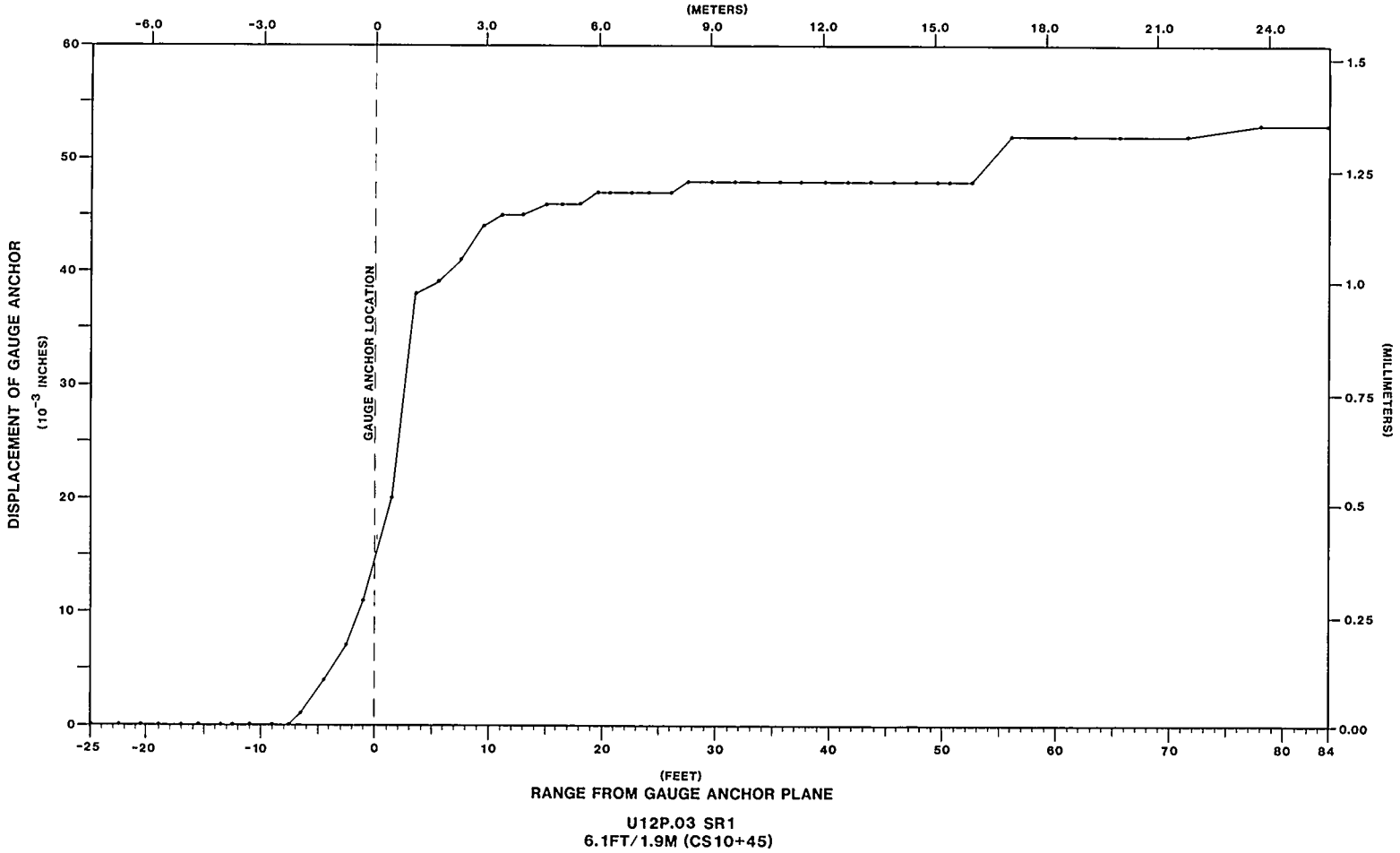


Figure 8. Plot of displacement versus range of the mined face to the plane of the gauge anchor for U12p.03 SR-1. Standoff distance between the anchor and Main rib is shown below the gauge number in feet and meters. Main drift Construction Station for the anchor is in parentheses.

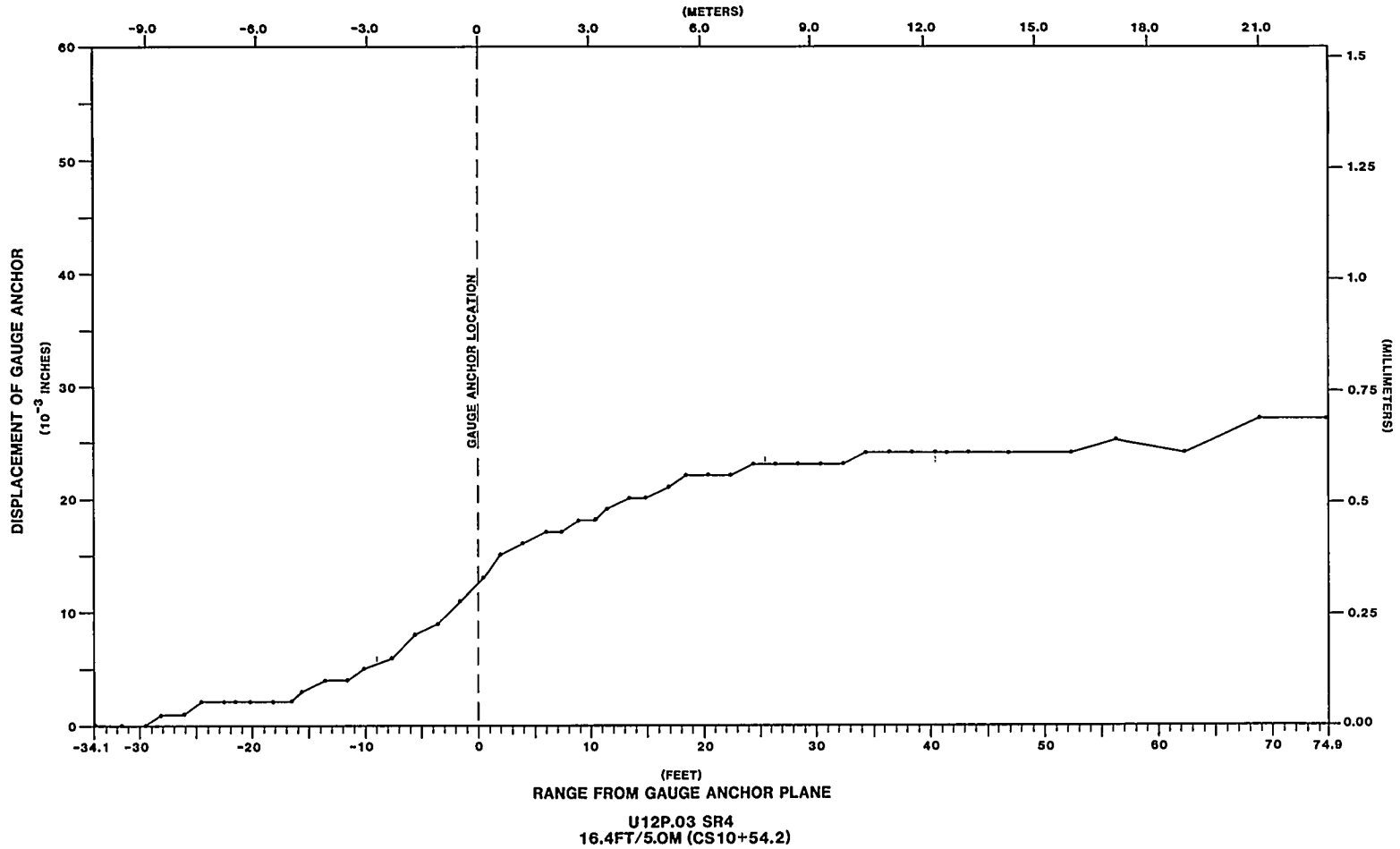


Figure 9. Plot of displacement versus range of the mined face to the plane of the gauge anchor for U12p.03 SR-4. Standoff distance between the anchor and Main rib is shown below the gauge number in feet and meters. Main drift Construction Station for the anchor is in parentheses.

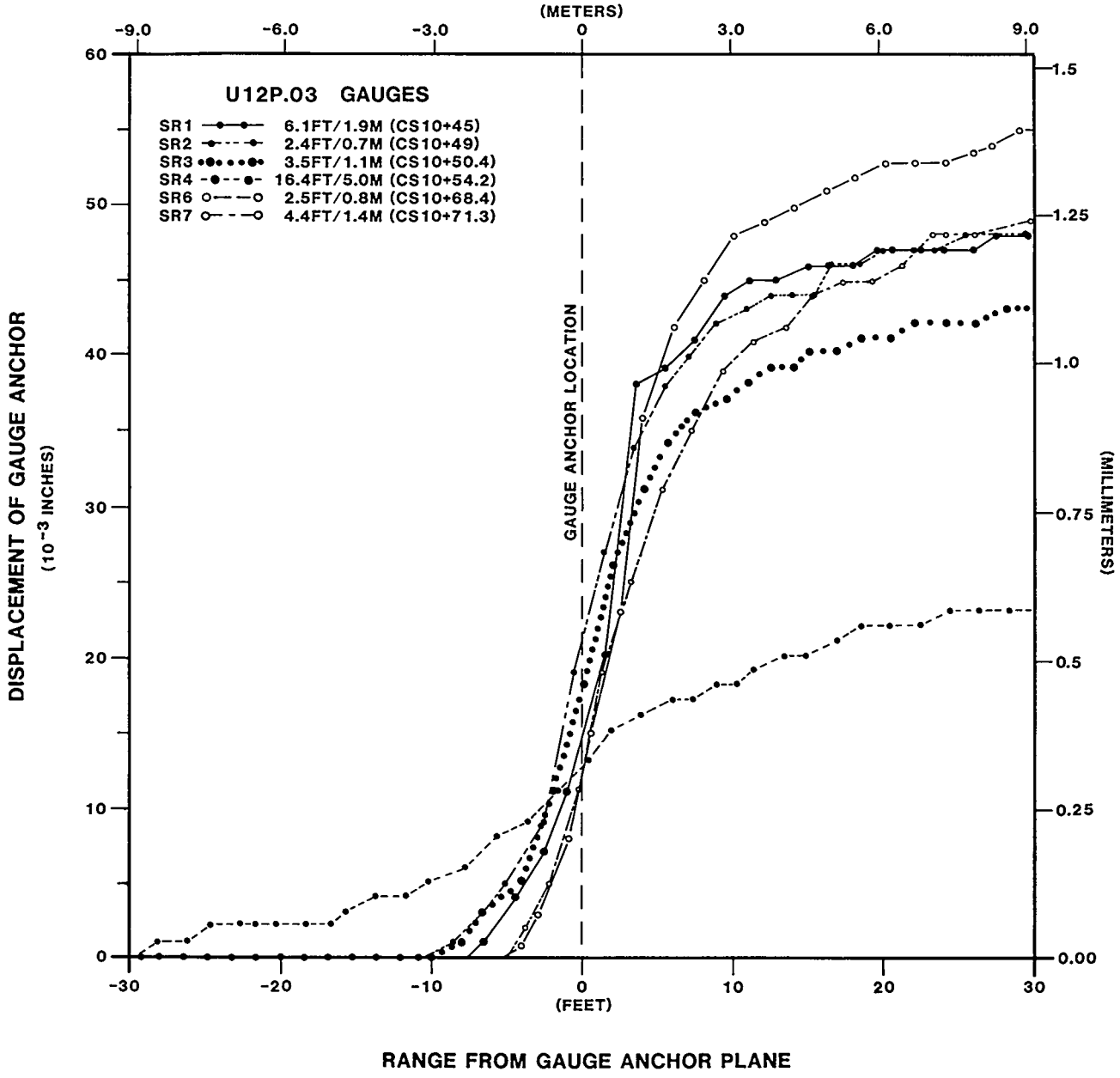


Figure 10. Overlay of displacement-versus-range plots for a short section of mining for U12p.03 SR 1-4, -6, and -7. Standoff distances between the anchors and Main rib are shown in feet and meters. Main drift Construction Stations for the anchors are in parentheses.

D. All gauges recorded continuing displacements, though at a slower rate, for the last 34 days of the experiment.

E. Gauge anchors located at similar distances from the Main rib, such as SR-2 and SR-6 at 0.7 and 0.8 meters (2.4 and 2.5 feet), did not respond exactly the same. One possible explanation is that the fractures near and projected to intersect SR-6 somehow delayed or masked initial displacement until the mined face was closer. Other possibilities are that the slight bend at the bottom of the SR-2 hole (as seen in the survey data) caused some angular component of displacement, or that the difference is simply normal variation.

6.3.2 Calculational Model. Information about the in situ response of tuffs at low stress levels can be deduced for a site when the overburden stress is known and measured displacements are available. Several two-dimensional, quasi-static finite-element calculations using the GRIFFIN code were conducted to extract this information (Fogel and Patch, 1992). The calculations represented the drift as a circular cylinder and the mining operation as a partially mined tunnel. The computations also assumed that the mining rate was slow enough to allow for the maintenance of static equilibrium. Conditions for the calculations included a grid length of 30.5 meters (100 feet) and stress of 0.1 Megapascal (1 bar) on an open tunnel surface. The possible effects of hole size, rebar stretch and temperature were ignored and later shown to be insignificant (Burgess, 1989).

The initial calculation was the simplest, using average shear modulus and crush-curve values measured on core samples from the U12p.03 site (Lupo and Klauber, 1987; Torres, 1988; Torres and Johnsson, 1988; 1989). The initial model predicted a decay rate of 1/radius (r^{-1}), but comparisons between the calculations (solid lines) and field data (dashed lines) indicated wide divergence, as shown on Figure 11.

An intermediate calculation was run using a 25% lower, but still reasonable, shear modulus of 2.4 Gigapascals (24 kilobars) in a uniform medium. The displacements were brought into closer agreement, but the attenuation rates still did not match those of the field data. The final model introduced layering into the calculation, which then provided the best match to the field data (Figure 12) and also seemed to explain the slow decay rate, $1/\text{radius}^{1/2}$ ($r^{-1/2}$), observed in the data. However, there is no evidence that the conditions used for the final calculation occur at the experiment site. Table 2 summarizes the values used in the three models.

Thus, the calculational analysis qualitatively verified the measured displacements and observations outlined previously in Section 6.3.1 and specifically showed:

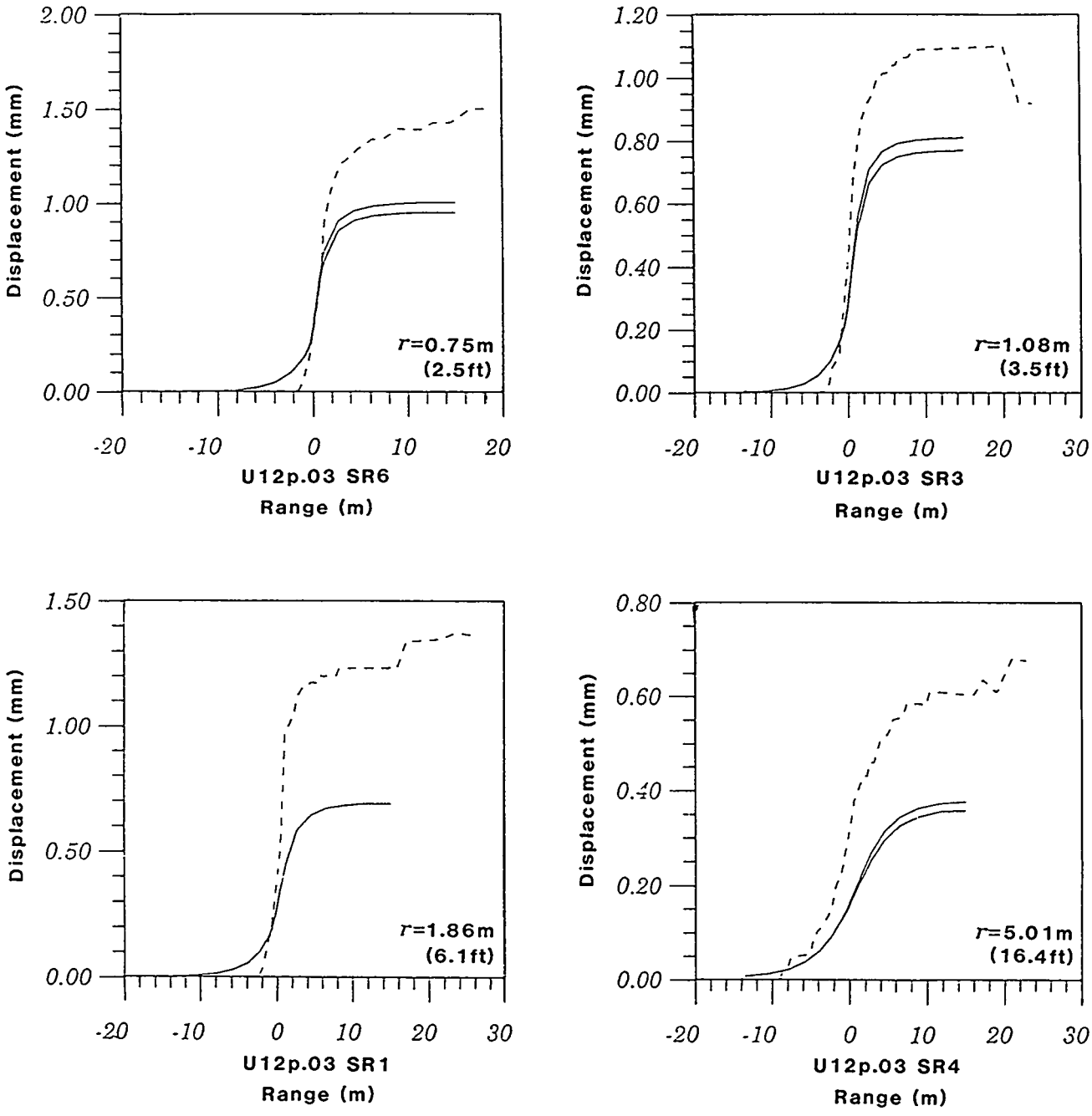


Figure 11. Comparison of computed (solid) and measured (dashed) displacements at four standoff distances (r, in meters and feet) from the U12p.03 Main rib. Shear modulus used in the calculation was 3.23 Gigapascals (32.3 kilobars).

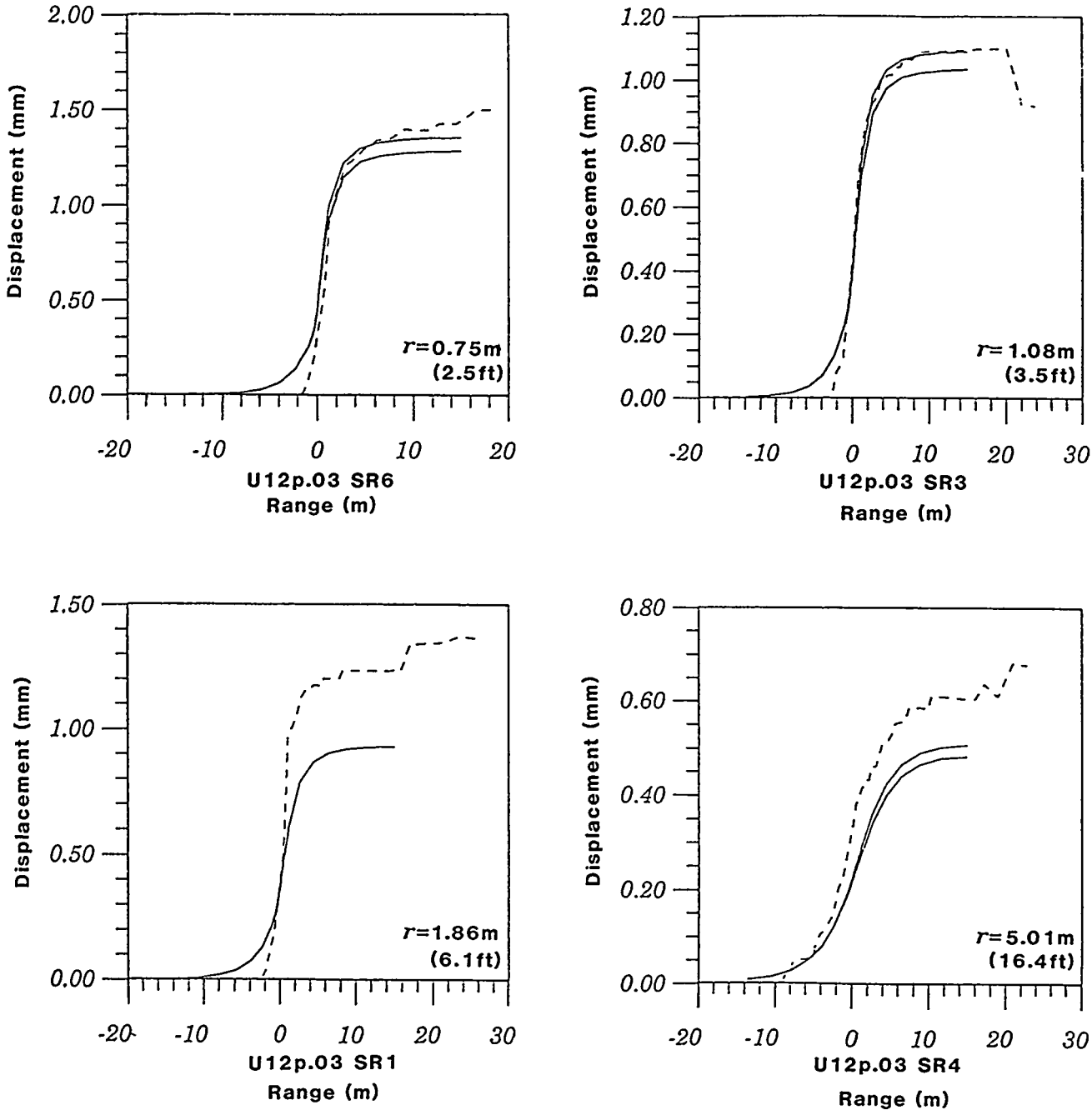


Figure 12. Comparison of computed (solid) and measured (dashed) displacements at four standoff distances (r, in meters and feet) from the U12p.03 Main rib. Shear modulus used in the calculation was 2.40 Gigapascals (24 kilobars).

Table 2. Parameters and values used for the initial, intermediate and final calculations for the U12p.03 experiment.

Parameter	Initial Model	Intermediate Model	Final (Layered) Model
Inside Tunnel Radius (m; ft)	1.4; 4.5	1.4; 4.5	1.7; 5.5
Outside Grid Radius (m; ft)	20; 65	20; 65	3/12; 10/40
Pre-Stress on Grid (MPa; bars)	6.0; 60	6.0; 60	5.37; 53.7
Shear Modulus (GPa; kb)	3.23; 32.3	2.4; 24	2.4/1.84; 24/18.4

A. The data did not follow the simplest response of a pressurized, infinite elastic cylinder of uniform material due to slower measured decay rates (an r^{-1} dependence was predicted, but a slower $r^{-1/2}$ rate was measured). In other words, the measured ultimate or total displacement at the anchor farthest from the Main rib was a greater fraction of the displacement at the nearest anchor than would be expected theoretically, assuming a uniform medium.

B. Computationally, initial displacements began sooner and represented a larger percentage of the total magnitude at the anchor location for the anchors farthest from the Main rib, than was measured.

C. The layered model with a 25% lower shear modulus provided the best match to the field data.

7.0 U12N.22 EXPERIMENT.

A second test of the gauges was conducted during mining of the U12n.22 drifts in March of 1989 at a depth beneath Rainier Mesa of 389.4 meters (1278 feet). Gauge installation was nearly identical to that of the first experiment. However, the calculated overburden density was lower (1.81 Mg/m^3; 113 lb/ft^3), the Main drift dimensions were smaller (2.4-meters by 2.4-meters; 8-feet by 8-feet) and the site was about 200 meters (656 feet) stratigraphically lower than in the U12p.03 area. The results of the experiment were originally reported by (Goodin, 1990).

7.1 Drill-Hole Details.

As shown in Figure 13, two groups of four holes, separated by 3.4 meters (11 feet), were collared 1.6 meters (5.2 feet) above the invert between CS 10+71 and 11+01 in the left rib of the Bypass drift. The holes were designated SR 9-16 and were drilled to depths that varied from 22.9 to 27.1 meters (75 to 89 feet). The bottoms of the holes ranged from 0.5 to 4.9 meters (1.7 to 16.0 feet) from the right rib of the planned Main drift.

All holes were drilled within "Tunnel beds Subunit 4J", a massive, zeolitized, medium- to coarse-grained calcalkaline ash-fall tuff with discontinuous, irregular lenses of coarse- to very coarse-grained peralkaline ash-fall tuff. The beds dip at a somewhat greater angle (14°) than in the U12p.03 area, and three steeply dipping, small displacement faults are projected to intersect the eight holes. A geologic map and drill-hole details are included in Appendix B.

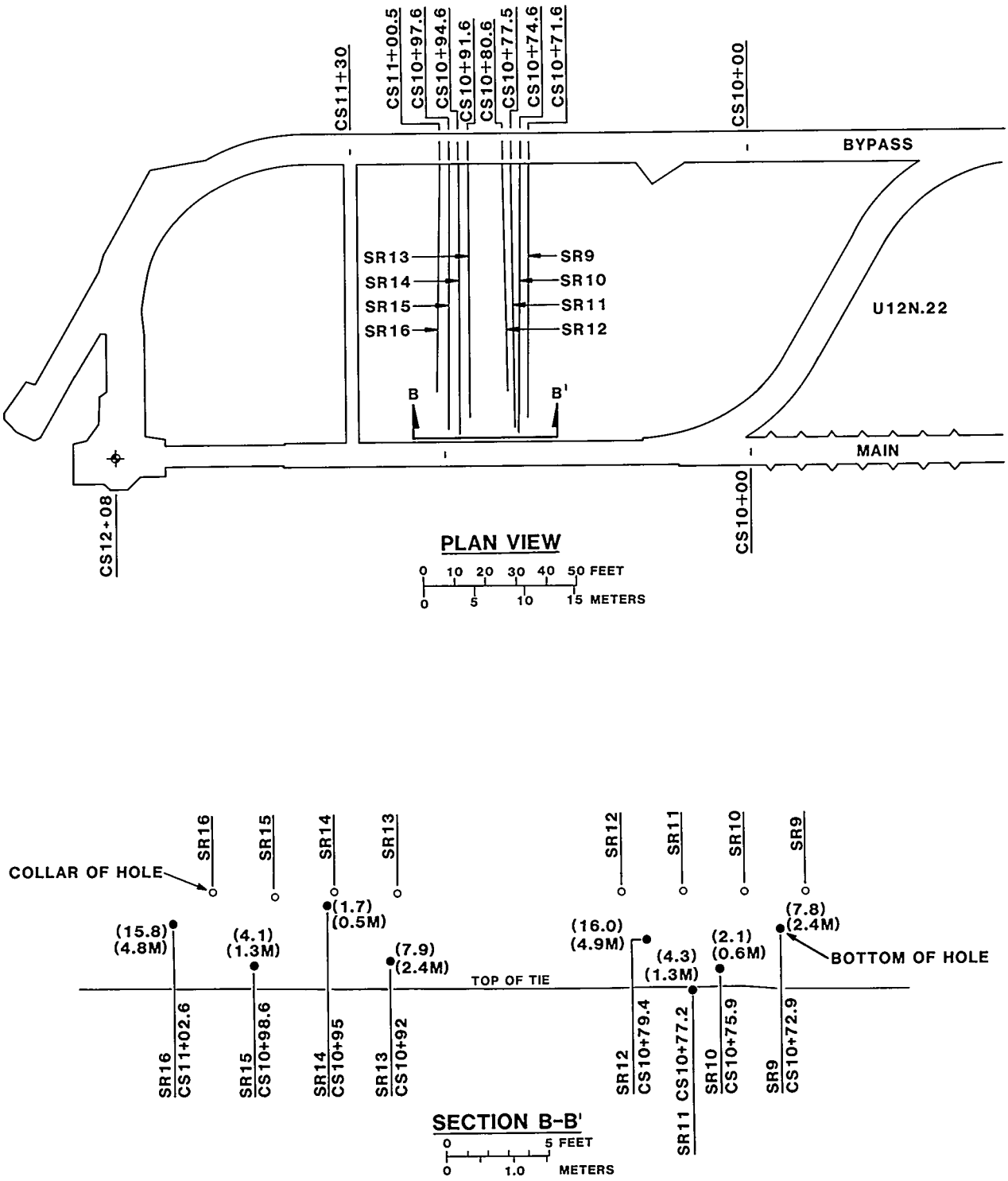
7.2 Procedure.

Data collection began on 6 March when mining in the Main drift was 10 meters (33 feet), or slightly more than four tunnel diameters, on the portal side of the first anchor, SR-9. Data were recorded every 1 or 5 minutes until 16 March when mining from CS 10+40 to 11+92 was completed. Longer term data were entered manually each day until 29 March when the system was removed and the holes grouted closed.

7.3 Results.

As with the U12p.03 experiment, data for the 46.3 meters (152 feet) of U12n.22 mining were plotted as displacement versus distance for all eight gauges (Figure 14). Three of the four gauges in the second set registered no displacement, possibly as a result of damage to the gauges prior to installation or the effects of other underground operations. The remaining five gauges (SR 9-12, -14) recorded a much flatter and more inconsistent response than the U12p.03 test, probably because of the greater overburden depth and somewhat different geology. The plots for this test indicate:

A. The magnitude of total displacement was roughly 1/5 that of the U12p.03 data, resulting in much flatter curves. Only the plot for SR-14 had a curve shape similar to those for U12p.03, with displacement increasing rapidly as the anchor was approached and passed, and then stabilizing at one tunnel diameter beyond the anchor.



NOTE: NUMBERS IN PARENTHESES ARE DISTANCE, IN FEET AND METERS, FROM MAIN RIB TO BOTTOM OF HOLE.

Figure 13. Plan view and cross section of drill holes U12n.22 SR 9-16. Section B-B' shows position of hole collars and bottoms (anchors) relative to Main drift's "top of tie" (construction term for approximate tunnel grade and invert, as represented by a plane along the top of the railroad ties). Portal is to the right, off the figure.

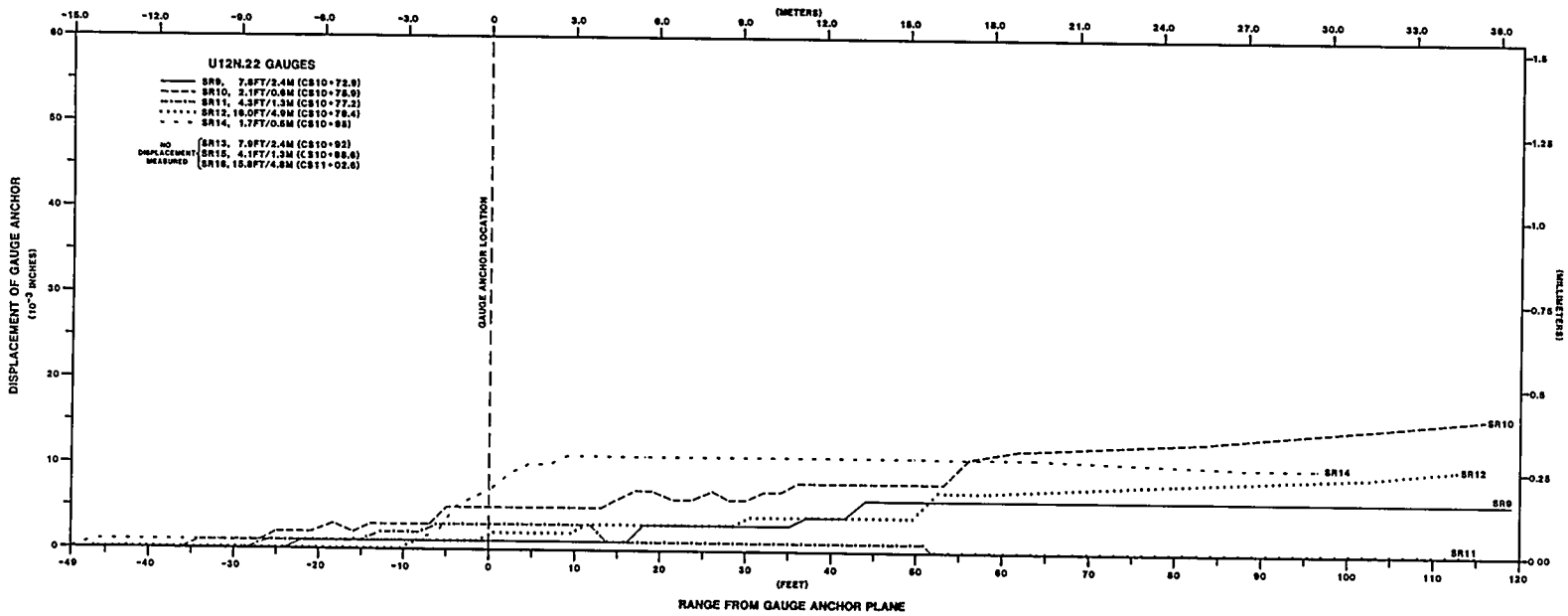


Figure 14. Overlay of displacement-versus-range plots for U12n.22 SR 9-16. Standoff distances between the anchors and Main rib are shown in feet and meters. Main drift Construction Stations for the anchors are in parentheses.

B. Displacement for four of the five gauges began more than three tunnel diameters before the mined face was opposite the anchor, which is earlier than the U12p.03 response. Specifically, SR-9 and -11 indicated that initial displacement occurred at three to 3-1/2 tunnel diameters from the anchor; and SR-10 and -14 began moving even earlier at four to six diameters from the anchor.

C. The gauge anchor located 4.9 meters (16 feet) from the Main rib (SR-12) began moving much later (one tunnel diameter) than the other four anchors, unlike the U12p.03 data where the farthest anchor moved earliest (three diameters). Also, the relationship between the magnitude of the SR-12 response and the other plots was not as consistent or obvious as that observed in the first test. Specifically, the magnitude recorded by SR-12 remained 1/3 to 1/2 lower than that for only one anchor (SR-10), but ranged both higher and lower than the other three anchors. This response differs from the U12p.03 test where the farthest anchor moved half the magnitude of all other anchors.

D. Roughly 1/6 to 1/3 of the total displacement for three anchors (SR-9, -10, -12) occurred before the face was opposite the anchors; and the majority of their displacement wasn't completed until the face was 4-1/2 to seven tunnel diameters on the far side of each anchor. Conversely, over 2/3 of the total displacement for the other two anchors occurred before the face was opposite the anchors.

E. All gauges recorded continuing displacements for the last 13 days of the experiment. However, there was no apparent consistency as to which anchors moved at faster or slower rates.

F. The one pair of gauge anchors located at similar distances from the Main rib did not respond exactly the same, as was the case for the U12p.03 test.

G. The response of SR-11, with a drop in values after the anchor was reached and passed, was unique for this data set.

8.0 U12P.04 EXPERIMENTS.

The most recent tests of the gauges were conducted during the first half of 1990 at two locations in the U12p.04 drifts of Aqueduct Mesa at depths of 260.6 and 263.8 meters (855 and 865 feet). Gauge installation was virtually identical to the previous experiments. The overall geologic setting at both U12p.04 locations was like that of the U12p.03 site, with identical overburden density, similar lithology and overburden thickness, and stratigraphic positions only 2 and 17 meters (6 and 56 feet) lower in the Paintbrush Tuff. Drift dimensions for the second U12p.04 location were 2.4-meters by 2.4-

meters (8-feet by 8-feet), as in the U12n.22 test. However, the first U12p.04 location was mined to 4.9-meters by 4.9-meters (16-feet by 16-feet) 27 February to 9 March and then expanded another 0.3 meters (1 foot) 27-29 March.

In addition to the large drift size, the first U12p.04 location was chosen so the anchors would be almost equidistant (70 and 75 meters; 229 and 246 feet) between two previous nuclear detonation points. The purpose was to supplement the observations of shock-induced effects documented during mining of the U12p.04 Bypass drift between the two points and which included: slabbing, offset or distorted bedding, low-angle fractures and reverse faults, and discontinuous seismic degradation (Hopkins and Baldwin, 1992).

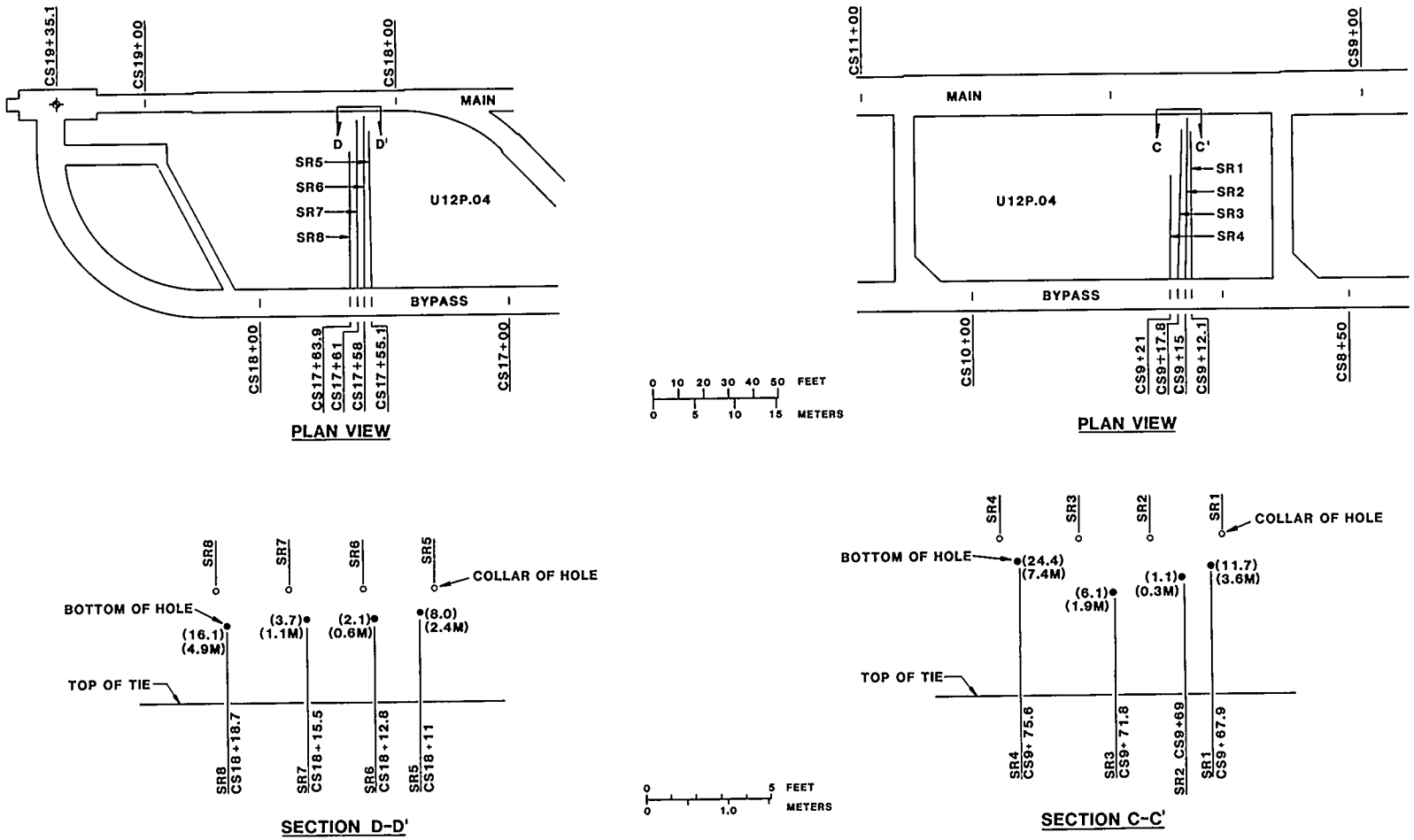
8.1 Drill-Hole Details.

The first group of four holes (SR 1-4) was collared 2.0 meters (6.6 feet) above the invert between CS 9+12 and 9+21 in the right rib of the Bypass drift. The holes were 12.5 to 18.9 meters (41 to 62 feet) deep and bottomed approximately 0.3 to 7.4 meters (1.1 to 24.4 feet) from the left rib of the planned Main drift. A second group of four holes (SR 5-8) was collared 2.2 meters (7.1 feet) above the invert between CS 17+55 and 17+64 in the same drift and were 16.5 to 21.0 meters (54 to 69 feet) deep. This second group was bottomed 0.6 to 4.9 meters (2.1 to 16.1 feet) from the Main drift. The locations of all eight holes are shown on Figure 15.

The SR 1-4 holes were drilled approximately 2 meters (6 feet) lower in the section than at the U12p.03 site within a sequence of thin- to thick-bedded, zeolitized calc-alkaline ash-fall tuffs that are interbedded with thin beds of reworked ash-fall tuffs and tuffaceous sandstone which vary in degree of silicification, argillization and zeolitization ("MC-2"). The beds dip 3.5 degrees toward the portal, and two steeply dipping, small displacement faults as well as several of the thin beds may intersect the holes. Most of holes SR 5-8 were drilled approximately 17 meters (56 feet) lower in the section than the U12p.03 site in the base of "MC-1", a massive bed of zeolitized, medium-grained, phenocryst-rich calcalkaline ash-fall tuff. The last few feet of all drill holes except SR-5 intersected a finer grained basal bed. The tuff beds dip 7 degrees toward the portal, and one fault is projected to intersect the bottom half of all holes (Hollon, 1992). Geology maps and drill-hole details are included in Appendix C.

8.2 Procedure.

Data collection for SR 1-4 began 27 February when mining of the Main drift was 11 meters (36 feet, or slightly more than two tunnel diameters) on the portal side of SR-1. Data were recorded every 5 minutes, 1 hour or 2 hours until 17 April when all mining from CS 9+32 to 12+05 was completed. Only data for the 4.9-meter (16-foot) diameter drift (CS 9+32 to 10+36) are presented in Section 8.3. Data for SR 5-8 were



NOTE: NUMBERS IN PARENTHESES INDICATE DISTANCE, IN FEET AND METERS, FROM LEFT RIB OF MAIN DRIFT TO BOTTOM OF HOLE.

Figure 15. Plan view and cross sections of drill holes U12p.04 SR 1-4 (right) and SR 5-8 (left). Sections C-C' and D-D' show position of hole collars and bottoms (anchors) relative to Main drift's "top of tie" (construction term for approximate tunnel grade and invert, as represented by a plane along the top of the railroad ties). Portal is to the right, off the figure.

recorded every 5 minutes or 1 hour beginning at CS 17+84 on 5 June when mining of the Main drift was 8.2 meters (27 feet, or almost 3-1/2 diameters) from SR-5. Data recording continued until mining reached CS 18+81 on 13 June and the system was removed.

8.3 Results.

Data for short segments of the U12p.04 mining were plotted as displacement versus range for all eight gauges, as in the two previous experiments. Figure 16 shows the response of SR 1-4 and focuses on the initial 31.7 meters (104 feet) of mining. Similarly, Figure 17 indicates the response of SR 5-8 for a 19.8-meter (65-foot) section of mining. Neither figure shows the longer term data.

Overall, the two U12p.04 plots are more like the U12p.03 data than those for U12n.22, as expected. However, total displacement, timing and the divergence between plots differ from the U12p.03 response, possibly because of the effects of drift size, geology or shock-conditioned material. The plots indicate that for these two experiments:

A. The curve shapes of SR 5-8 were similar to those in the U12p.03 test, but the magnitudes and timing differed. Specifically, displacement began earlier, at about two to 2-1/2 tunnel diameters before mining reached the anchors; roughly 1/2 or more of the total displacement occurred before the face was opposite the anchors; the majority of motion occurred within two diameters on the far side of each anchor; and total displacement was higher for the two anchors closest to the rib. Also, the deepest anchor (SR-8) moved earliest (three to 3-1/2 diameters) and had total displacements 13 to 27% below that of the other three anchors. Finally, the SR 5-8 plots are the first to indicate a direct relationship between anchor depth and total displacement, i.e., closest anchor moves the most and farthest anchor moves the least, as predicted in the original calculation in Section 6.3.2.

B. Displacements for SR 1-4 followed a similar pattern to SR 5-8 and the U12p.03 test, in that initial displacement occurred two tunnel diameters ahead of the mined face, and the majority of motion occurred within two diameters on the far side of the anchors. However, the magnitude of displacement for all four anchors averaged three to four times larger; over 90% of the total displacement for SR 1-3 occurred after the face was opposite the anchors; and displacement continued without any apparent stabilizing or flattening for a longer time than was observed in the experiments at U12p.03, U12n.22 and U12p.04 SR 5-8. Also, displacements for the deepest anchor (SR-4) began earliest (over two diameters), were over 1/4 complete before the face was opposite the anchor, and totalled 1/4 to 1/2 the magnitude of SR 1-3.

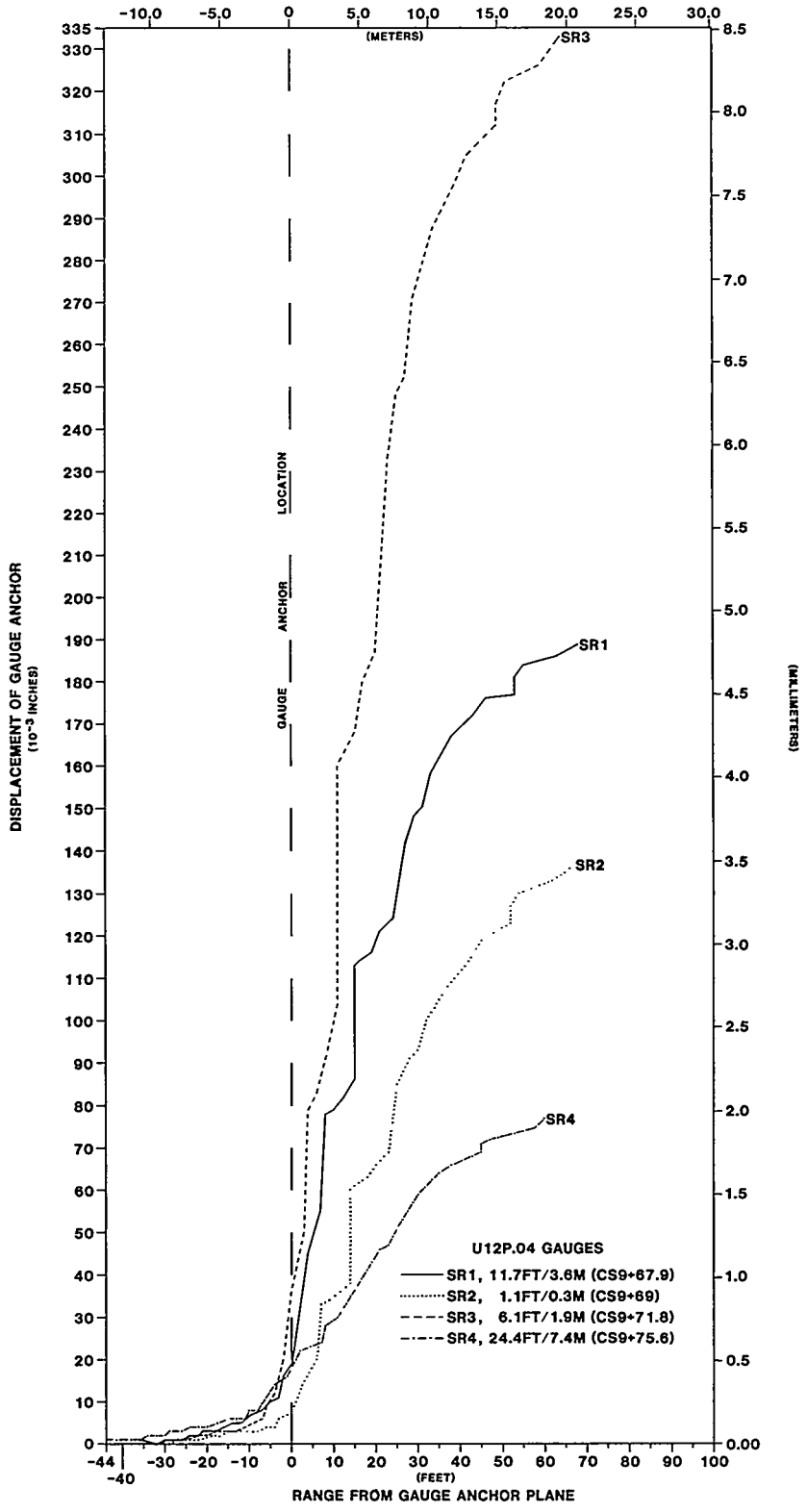


Figure 16. Overlay of displacement-versus-range plots for U12p.04 SR 1-4. Standoff distances between the anchors and Main rib are shown in feet and meters. Main drift Construction Stations for the anchors are in parentheses.

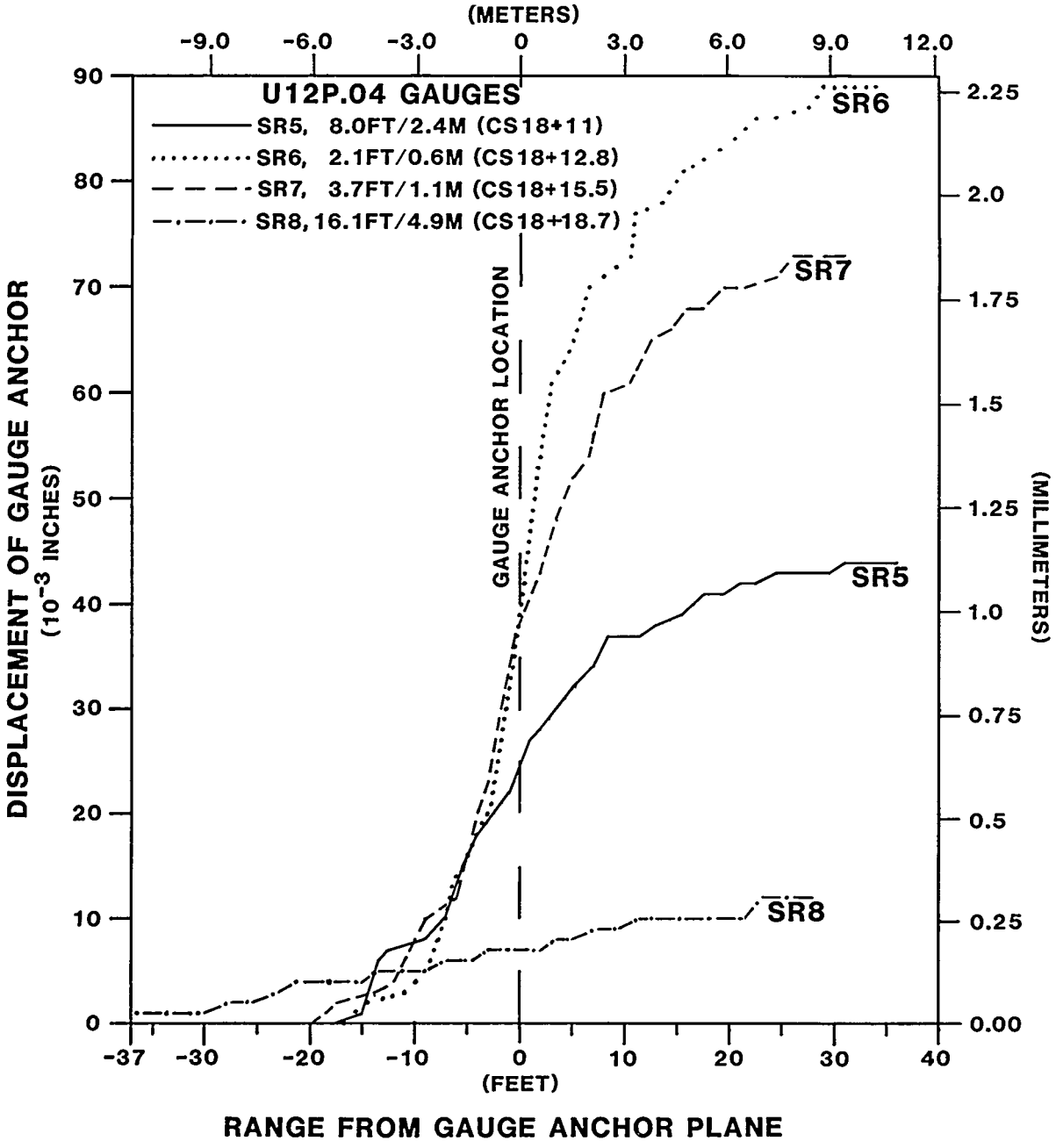


Figure 17. Overlay of displacement-versus-range plots for U12p.04 SR 5-8. Standoff distances between the anchors and Main rib are shown in feet and meters. Main drift Construction Stations for the anchors are in parentheses.

C. Detailed plots of the long-term records are not provided here, but the raw data indicate the SR 5-8 anchors continued to move at a much faster rate (doubling the magnitude in only 5 days) than in the two previous experiments. The SR 1-4 anchors also continued to move but at a reduced rate, similar to that observed in the U12p.03 test.

9.0 CONCLUDING REMARKS.

Four mine-by experiments, using KSC's recoverable stress-relaxation gauges (or extensometers), were sponsored by DNA and conducted in the U12p and U12n tunnel complexes of Aqueduct and Rainier Mesas at the NTS during 1988, 1989 and 1990. The gauges proved simple to use, when ample resources were available, and produced abundant real-time data that were easy to plot directly as displacement versus range.

It would not have been possible to obtain these high-quality, detailed data sets without the efforts of a good crew with an eye for detail. The ultimate success of these experiments was founded on straight drill holes, fully grouted anchors, careful gauge installation and detailed time/activity logs, in particular. Operational conditions that had a potential adverse impact included dust, occasional power outages, difficulty in resetting the recorder's clock and damage to the gauges during installation. These conditions can be overcome, however, with good people, a minimum of training and teamwork.

A general pattern was observed during the U12p.03 experiment which was repeated in the subsequent U12n.22 and U12p.04 tests: 1) initial displacement occurred well ahead of mining; 2) the anchor farthest from the rib measured less displacement than the other anchors; and 3) relaxation continued after the mine-by. Calculations for the U12p.03 data succeeded in simulating the response with the addition of layering to the model and a reasonable reduction in the measured shear modulus. No calculations have yet been done for the three additional tests, but it would be of interest to learn which adjustments to the original model may or may not be needed to provide the best match to these field data.

The distance from the face to the anchor when initial displacement occurred, the rate of rise (curve shape) up to and beyond the anchors, total magnitude and late-time rate of rise did vary from site to site. The three experiments sited at U12p tunnel were most alike in terms of overburden depth and overall geology, but different drift sizes, local geology (lithology and structure) and shock-induced effects may have contributed to the differences in the rates of rise and total displacement. The flat response observed in the U12n.22 data was the most striking compared to U12p tunnel, but seems more simply explained, at least in part, by the increased depth of overburden and different lithology.

In general, these experiments have shown that "stress relief" can begin more than three tunnel diameters ahead of the mined face in relatively soft volcanic rocks. Thus, standard devices for measuring tunnel convergence that are installed behind or adjacent to the face may not record all of the displacement that occurs ahead of mining. Finally, it appears the results of the experiments can be simulated calculationally.

ACKNOWLEDGEMENTS

The authors would like to acknowledge the work of the following people:

Joe LaComb (DNA) provided the impetus and approved the funding for the experiments, and persistently supported the completion of this paper. Dale Secrist, Dick Westlund and Ted Tetman (KSC) designed and fabricated the gauges, and trained NTS personnel in installation and recording procedures at the U12p.03 site. Reynolds Electrical and Engineering Company personnel drilled the holes and assisted as needed, Raytheon Services Nevada (RSN) inspectors installed the anchors, and John Whipple (EG&G Energy Measurements) connected the gauges and recorder at the U12n.22 and U12p.04 sites. RSN personnel also provided time/activity logs, operational support and the geologic maps. Chuck Caldwell (RSN) drew the majority of the illustrations. Johnson Controls provided photographs and camera-ready copies of the drawings. Debbie Kilb (SAIC) performed the calculations. Dan Patch (SAIC), Byron Ristvet (DNA), and especially Margaret Baldwin and Dean Townsend (RSN) provided valuable comments and suggestions. TSgt Cheryl Gygi-Gowan (DNA) provided word processing of the text, and Linda Haley (RSN) refined the final document.

REFERENCES

Burgess, D. N., "MISSION CYBER and DISKO ELM Geotechnical Investigations", BDM International, Redlands, CA, Technical Report 88-009-01, pp. 92-100 and 281-285, 5 June 1989.

Cummins, A. B., and I. A. Given, "Time-Dependent Properties, In Situ Rock", in Elements of Soil and Rock Mechanics, Society of Mining Engineers Mining Engineering Handbook, Vol. 1, pp. 6-26 to 6-28, 1973.

Fogel, M. B., and D. F. Patch, "Mineby Analyses", SAIC/Pacifica Technology Division, San Diego, CA, 2 September 1992 (unpublished letter to B. L. Harris-West).

Goodin, S. W., "MINERAL QUARRY Extensometer Results", Defense Nuclear Agency, Mercury, NV, 6 February 1990 (unpublished memorandum to J. W. LaComb).

Harris-West, B. L., and M. B. Fogel, "In Situ Stress Relief Measurements and Initial Analysis from a Mineby in U12p Tunnel", presented at the 5th Symposium on Containment of Underground Nuclear Explosions, Santa Barbara, CA, 19-21 September 1989.

Hollon, D. M., "Geology of Extensometer Holes U12p.04 SR#5-8", Raytheon Services Nevada (formerly Fenix and Scisson of Nevada), Mercury, NV, GEO-1039, 22 August 1990 (unpublished memorandum to B. L. Harris-West).

Hopkins, S. P., and M. J. Baldwin, "Observations in the U12p.04 Drifts of Probable Shock Effects from the MISSION CYBER and DISKO ELM Events", Raytheon Services Nevada, Mercury, NV, GEO-1394, 18 August 1992 (unpublished report to B. L. Harris-West).

Lupo, J., and W. Klauber, "Physical and Mechanical Characterization of Tuff from UE12p#4", TerraTek Research, Salt Lake City, UT, TR 87-94, June 1987.

Sargent, K. A., and P. P. Orkild, "Geologic Map of the Wheelbarrow Peak-Rainier Mesa Area, Nye County, Nevada", U. S. Geological Survey, Denver, CO, Miscellaneous Geologic Investigations Map I-754, 1973.

Secrist, A. D., and W. L. Westlund, "A Proposal for a Rock Stress Relief Gauge", Kaman Sciences Corporation, Colorado Springs, CO, P613X-8002, 2 May 1988 (proprietary proposal to J. W. LaComb).

Torres, G., "Characterization of Tuff from Vertical Drill Hole UE12p#4 with Emphasis on Material from 813.6 - 1777.8 Feet", TerraTek Inc., Salt Lake City, UT, TR 89-36, October 1988.

Torres, G., and R. Johnsson, "Characterization of Tuff from Drill Hole U12p.03 GI-1", TerraTek Inc., Salt Lake City, UT, TR 89-43, November 1988.

Torres, G., and R. Johnsson, "Characterization of Tuff from Drill Hole U12p.03 IH-2", TerraTek Inc., Salt Lake City, UT, TR 89-65, January 1989.

Warren, R. G., D. A. Sawyer, and H. R. Covington, "Revised Volcanic Stratigraphy of the Southwestern Nevada Volcanic Field", presented at the 5th Symposium on Containment of Underground Nuclear Explosions, Santa Barbara, CA, 19-21 September 1989.

APPENDIX A

DATA FOR U12P.03 EXPERIMENT

TABLE A-1. As-built survey data for drill holes U12p.03 SR 1-4, -6, and -7.

FIGURE A-1. Tunnel-level geology map for drill holes U12p.03 SR 1-4, -6, and -7.

FIGURES A-2 - A-5. Long-term displacement-versus-range plots for U12p.03 SR-2, -3, -6, and -7.

FIGURES A-6 - A-11. Short-term displacement-versus-range plots for U12p.03 SR-1, -4, -6, and -7.

Data provided by Raytheon Services Nevada

Table A-1. As-built survey data for drill holes U12p.03 SR 1-4, -6 and -7[1].
(Measurements in meters, except where noted otherwise)

				COLLAR OF HOLE				BOTTOM OF HOLE				
DRILL HOLE	BEARING	ANGLE	TOTAL DEPTH	BYPASS STATION[2]	COORDINATES	ELEVATION	VERTICAL DISTANCE TO BYPASS TOP OF TIE[3]	MAIN STATION[2]	COORDINATES	ELEVATION	VERTICAL DISTANCE TO MAIN TOP OF TIE	HORIZONTAL DISTANCE TO RIB OF MAIN DRIFT
U12p.03 SR-1	S31°28'W	-1°24'	19.2	9+75.7	N275,916 E197,141	1682.3	1.1 (0.9)	10+45	N275,900 E197,131	1681.8	0.4	1.86
U12p.03 SR-2	S32°09'W	-2°10'	20.3[4] (18.3)	9+78.6	N275,916 E197,141	1682.3	1.1 (1.0)	10+49	N275,899 E197,129	1681.5	0.1	0.74
U12p.03 SR-3	S30°58'W	-1°41'	19.7	9+81.5	N275,917 E197,139	1682.3	1.0 (0.9)	10+50.4	N275,900 E197,129	1681.7	0.3	1.08
U12p.03 SR-4	S31°28'W	-1°23'	16.1	9+84.5	N275,917 E197,139	1682.3	1.1 (0.9)	10+54.2	N275,904 E197,130	1681.9	0.5	5.01
U12p.03 SR-6	S31°46'W	-1°53'	20.4	9+98.5	N275,920 E197,135	1682.3	1.0 (0.9)	10+68.4	N275,902 E197,124	1681.6	0.2	0.75
U12p.03 SR-7	S31°44'W	-1°33'	19.7	10+01.5	N275,920 E197,134	1682.3	1.0 (0.9)	10+71.3	N275,903 E197,124	1681.8	0.3	1.35

1 Survey target was 0.03 meters above invert of each 76-mm-diameter hole.

2 Indicates Construction Station, measured in feet. (Subtract 69.8 feet from station in Main drift to get equivalent station in Bypass drift.)

3 Number in parentheses is vertical distance to top of tie in Main drift.

4 Total depth projected from surveyed depth in parentheses.

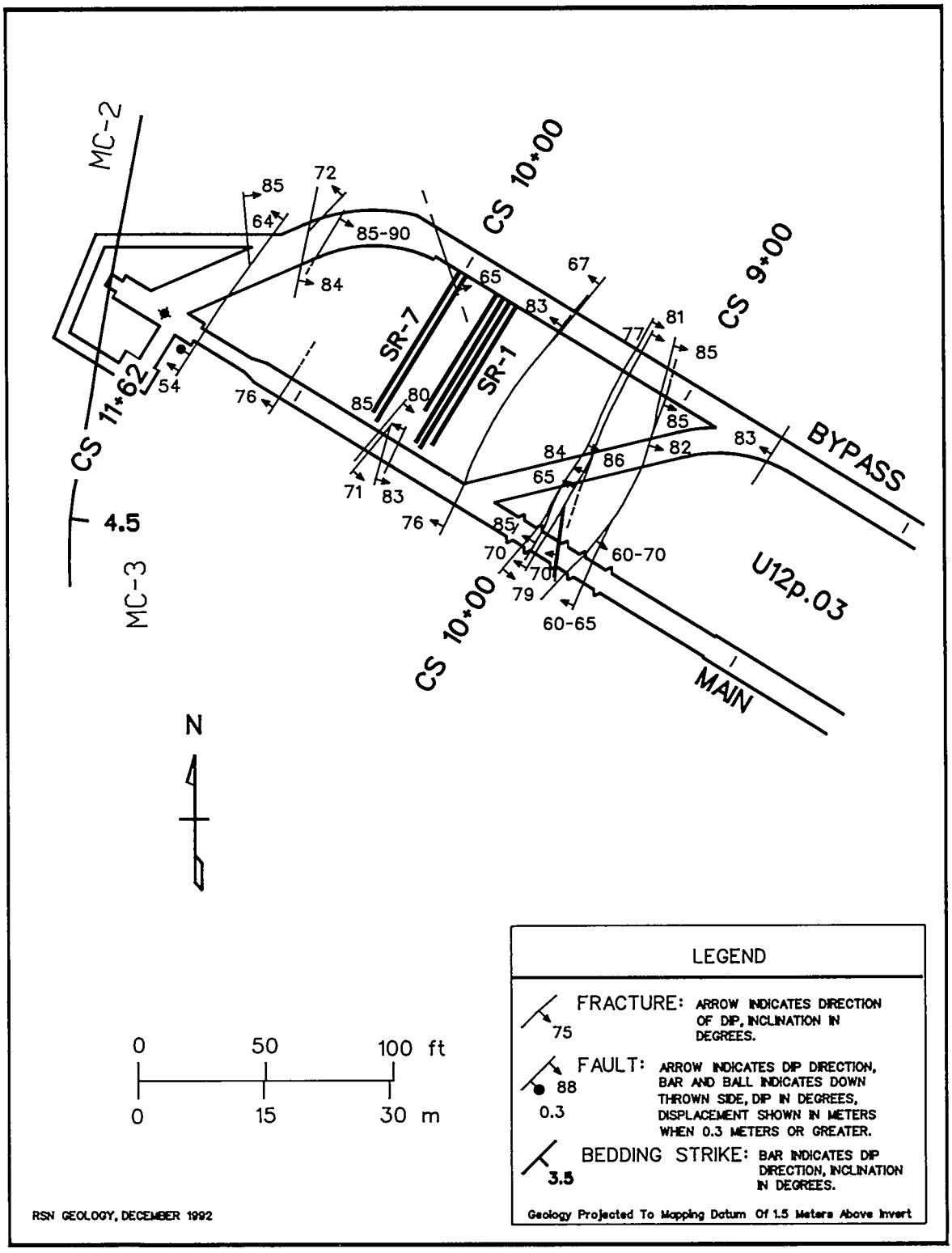


Figure A-1. Tunnel-level geology map for drill holes U12p.03 SR 1-4, -6, and -7.

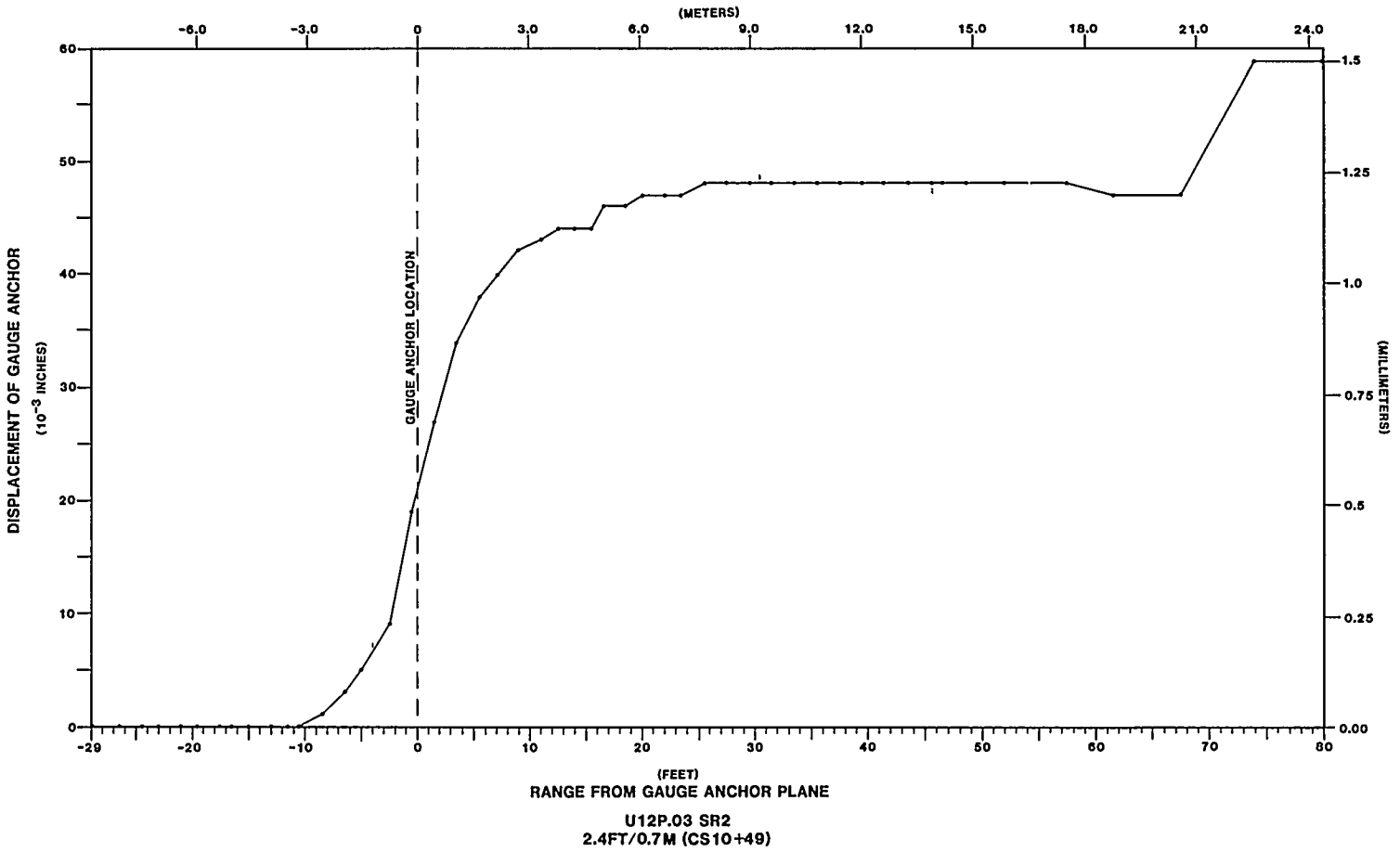


Figure A-2. Long-term displacement-versus-range plot for U12p.03 SR-2.

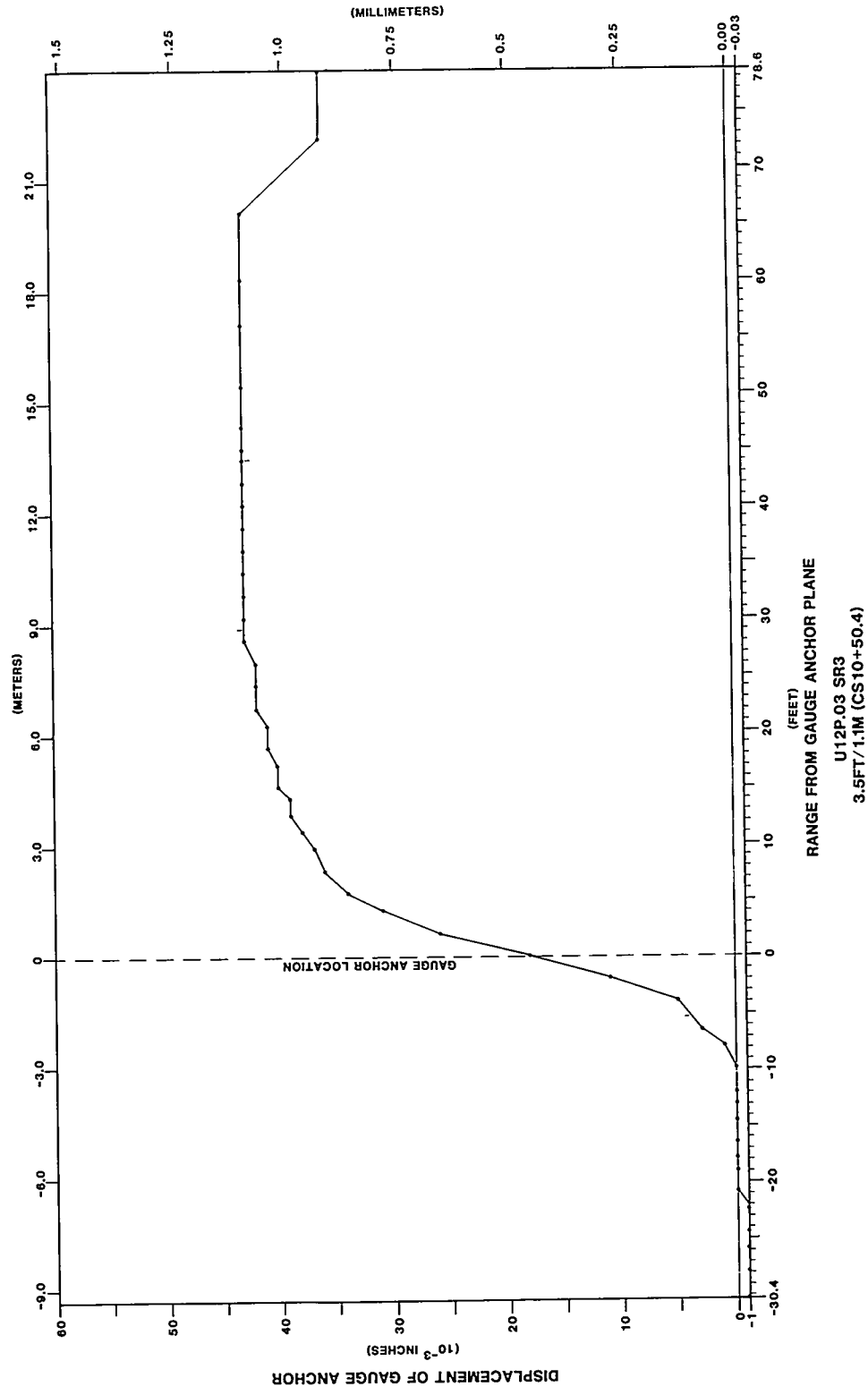


Figure A-3. Long-term displacement-versus-range plot for U12p.03 SR-3.

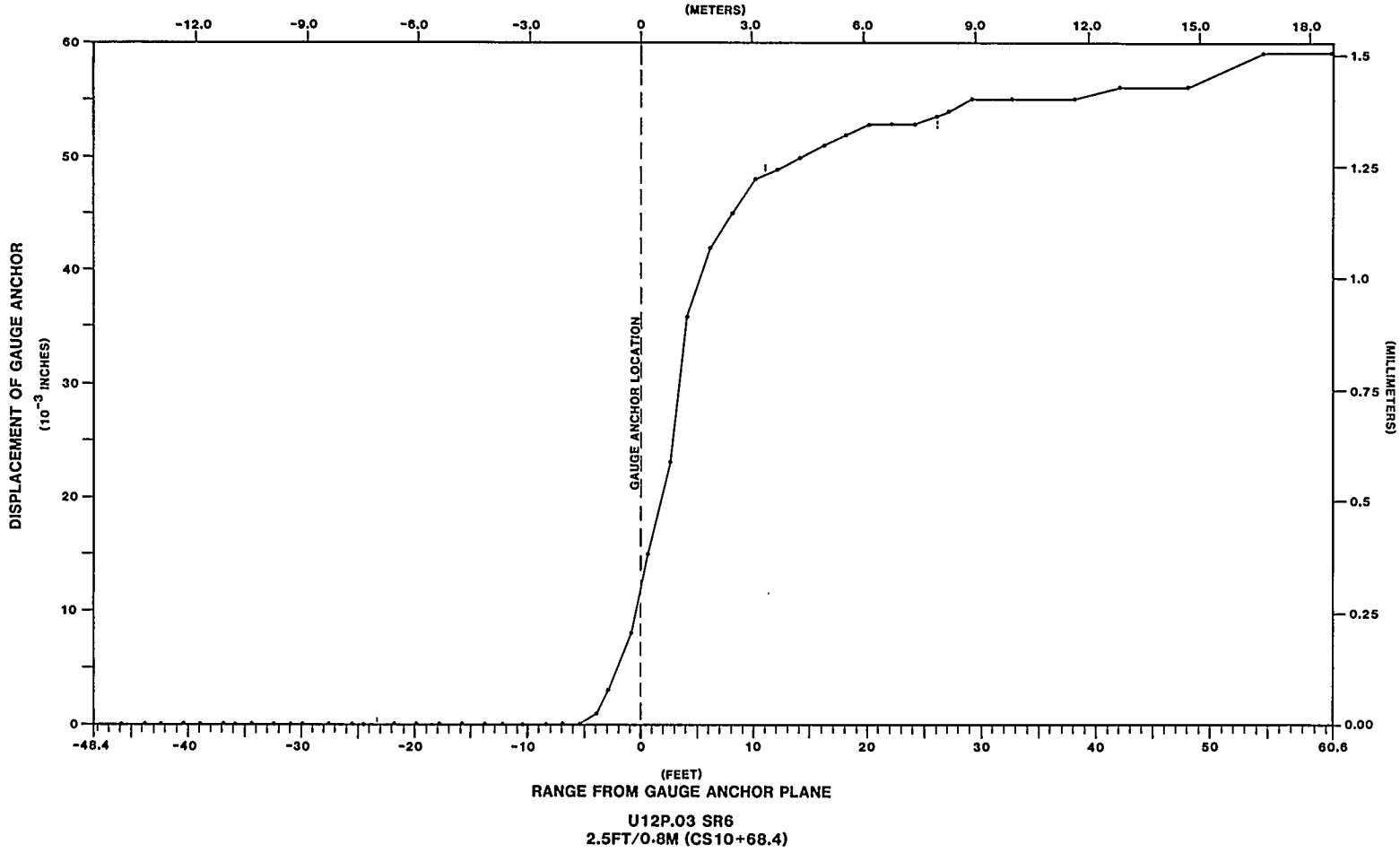


Figure A-4. Long-term displacement-versus-range plot for U12p.03 SR-6.

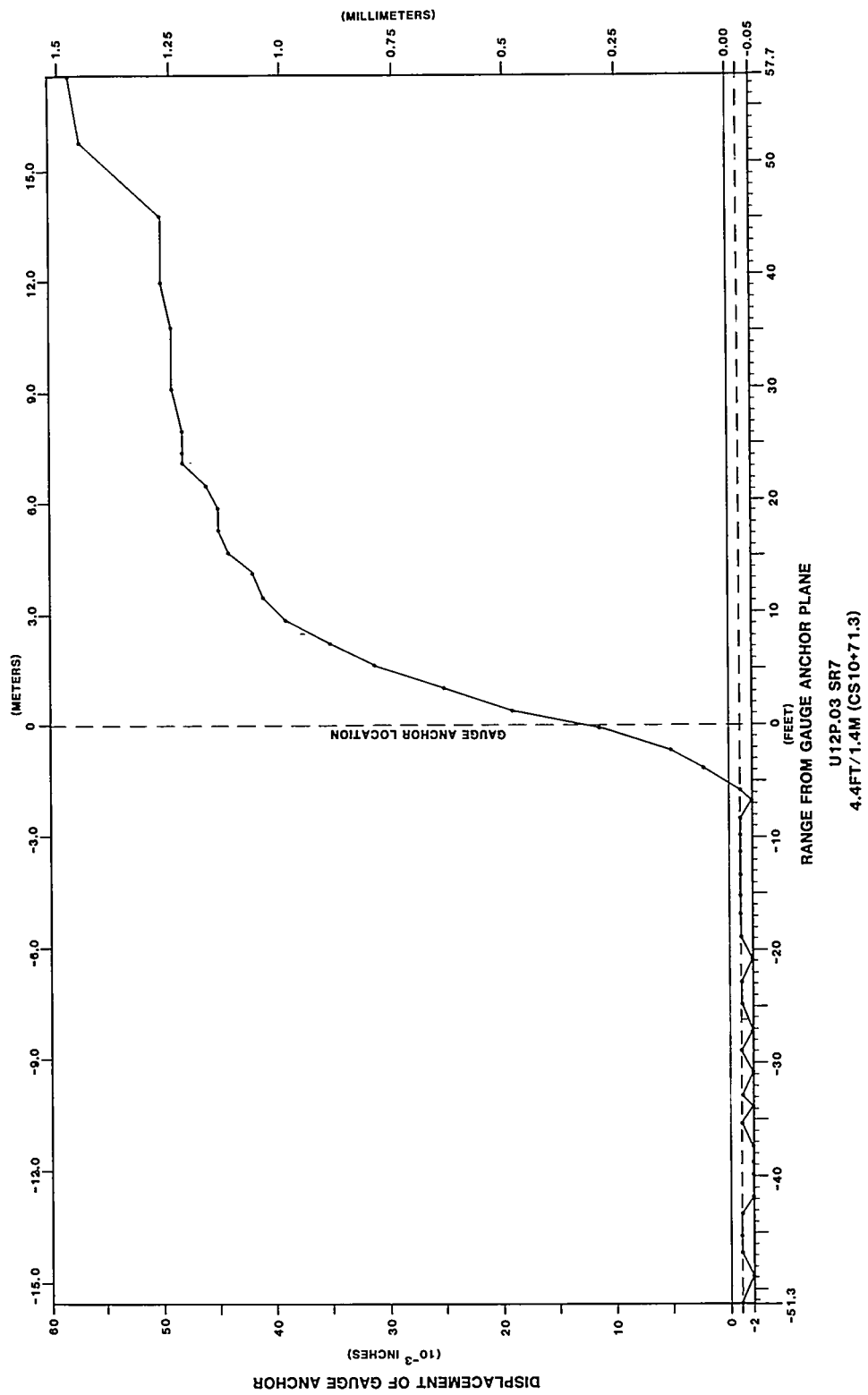


Figure A-5. Long-term displacement-versus-range plot for U12p.03 SR-7.

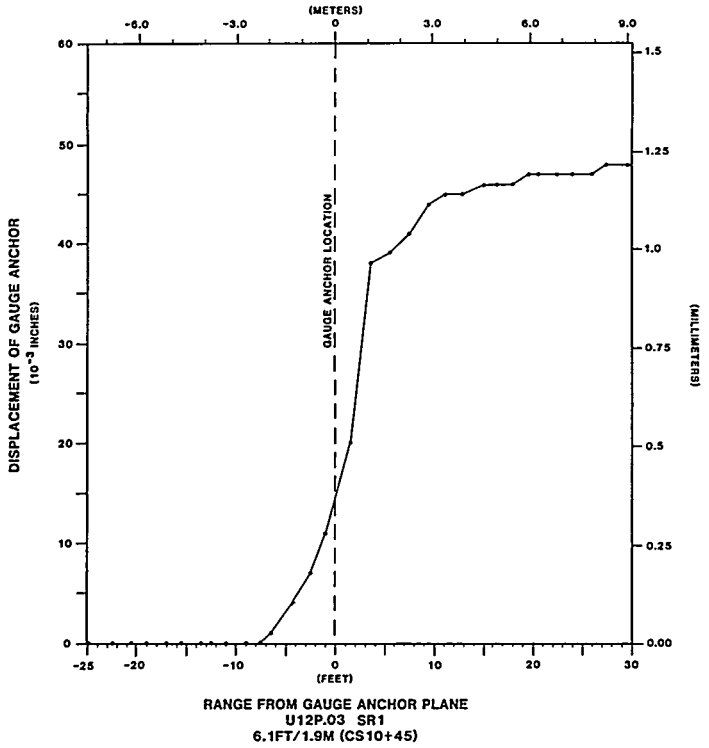


Figure A-6. Short-term displacement-versus-range plot for U12p.03 SR-1.

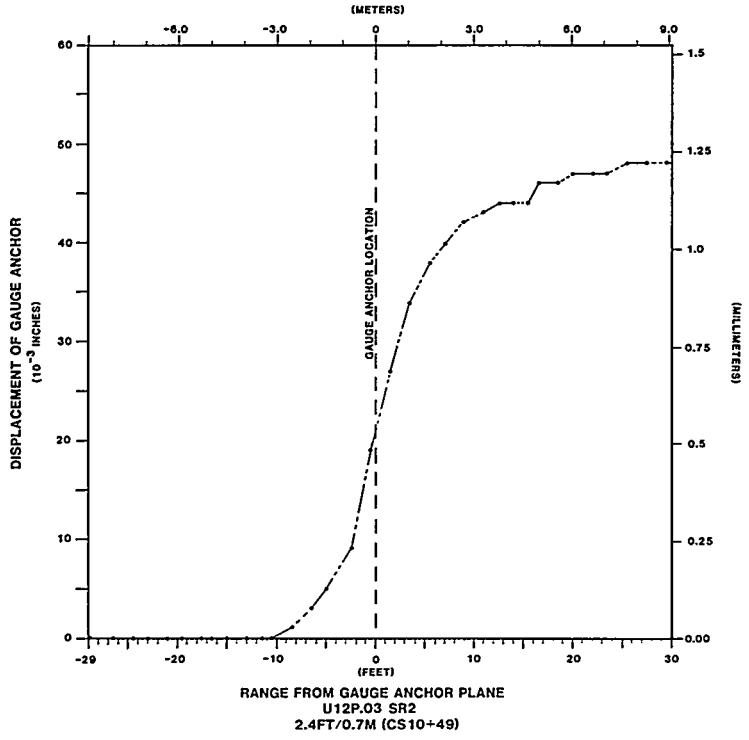


Figure A-7. Short-term displacement-versus-range plot for U12p.03 SR-2.

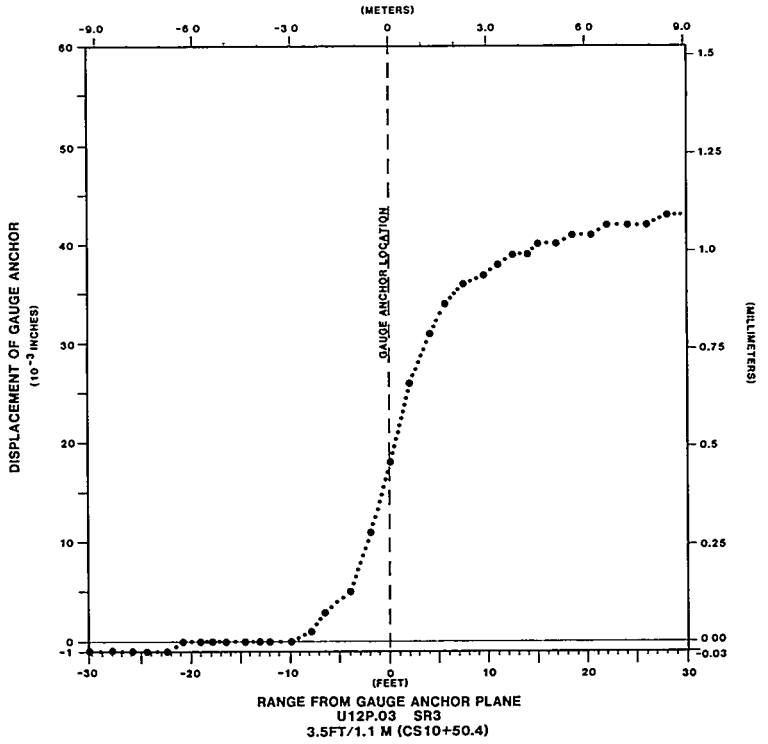


Figure A-8. Short-term displacement-versus-range plot for U12p.03 SR-3.

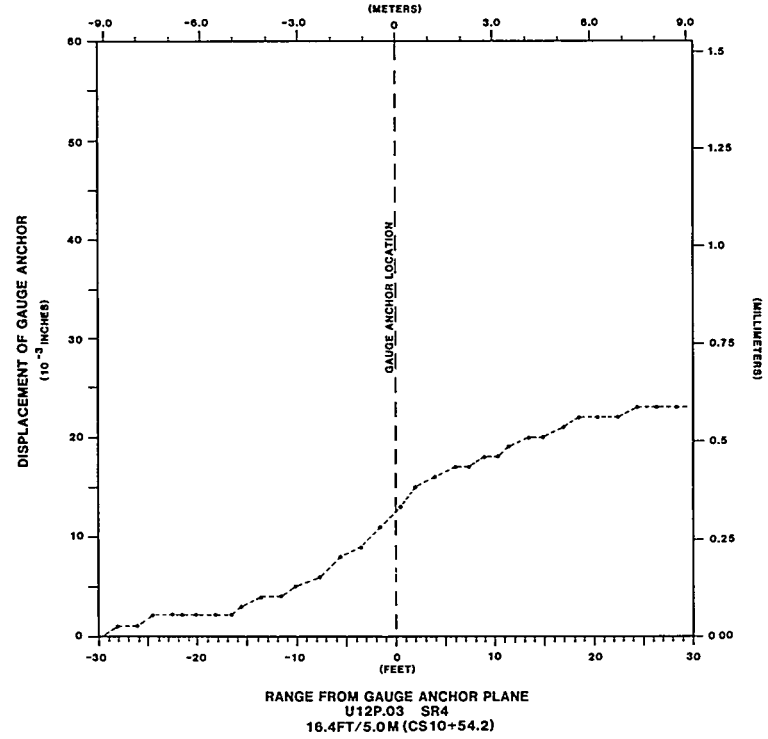


Figure A-9. Short-term displacement-versus-range plot for U12p.03 SR-4.

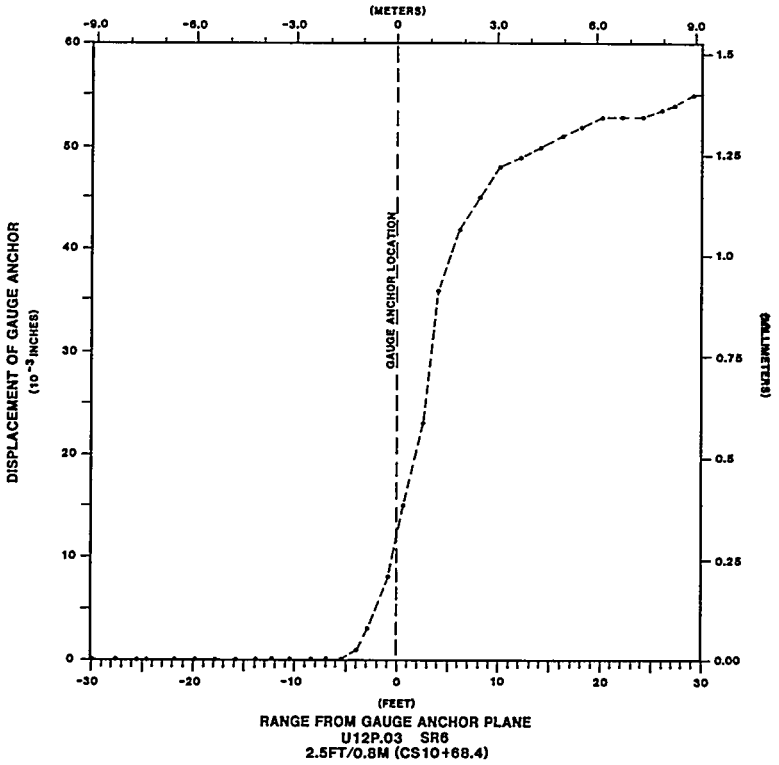


Figure A-10. Short-term displacement-versus-range plot for U12p.03 SR-6.

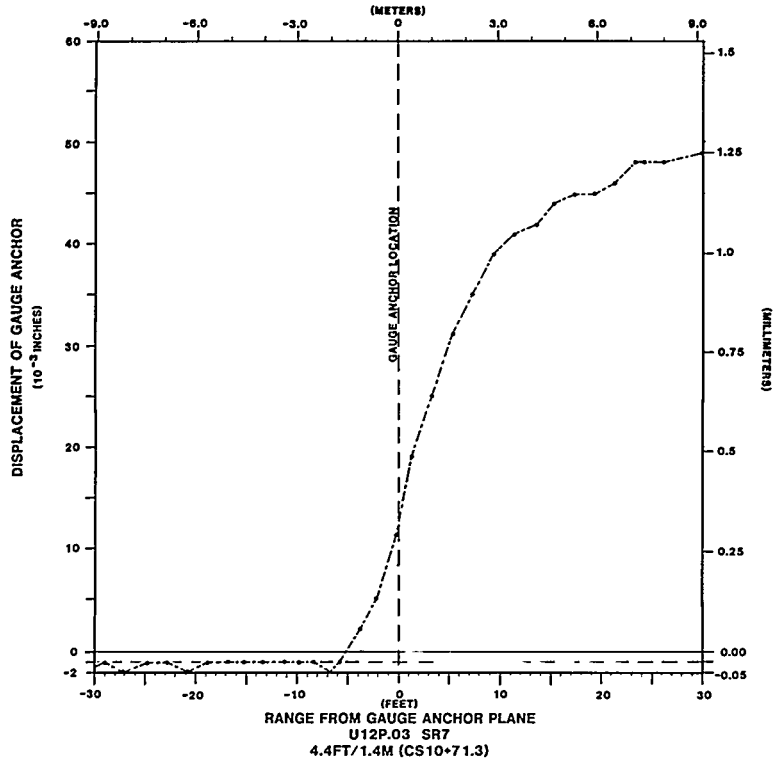


Figure A-11. Short-term displacement-versus-range plot for U12p.03 SR-7.

APPENDIX B

DATA FOR U12N.22 EXPERIMENT

TABLE B-1. As-built survey data for drill holes U12n.22 SR 9-16.

FIGURE B-1. Tunnel-level geology map for drill holes U12n.22 SR 9-16.

Data provided by Raytheon Services Nevada

Table B-1. As-built survey data for drill holes U12n.22 SR 9-16[1].
(Measurements in meters, except where noted otherwise)

				COLLAR OF HOLE				BOTTOM OF HOLE				
DRILL HOLE	BEARING	ANGLE	TOTAL DEPTH[2]	BYPASS STATION[3]	COORDINATES	ELEVATION	VERTICAL DISTANCE TO BYPASS TOP OF TIE[4]	MAIN STATION[3]	COORDINATES	ELEVATION	VERTICAL DISTANCE TO MAIN TOP OF TIE	HORIZONTAL DISTANCE TO RIB OF MAIN DRIFT
U12n.22 SR-9	S65°22'W	-1°12'	25.4 (19.5)	10+71.6	N272,647 E192,601	1854.0	1.6 (1.4)	10+72.9	N272,637 E192,578	1853.5	0.9	2.36
U12n.22 SR-10	S65°16'W	-2°19'	27.1 (15.7)	10+74.6	N272,648 E192,601	1854.0	1.6 (1.4)	10+75.9	N272,637 E192,576	1852.9	0.3	0.63
U12n.22 SR-11	S64°14'W	-3°11'	26.5 (11.3)	10+77.5	N272,649 E192,601	1854.0	1.6 (1.4)	10+77.2	N272,637 E192,577	1852.6	0.1	1.30
U12n.22 SR-12	S63°34'W	-1°53'	22.7 (21.0)	10+80.6	N272,650 E192,600	1854.1	1.6 (1.4)	10+79.4	N272,639 E192,580	1853.3	0.7	4.87
U12n.22 SR-13	S64°45'W	-2°16'	25.3 (19.6)	10+91.6	N272,653 E192,599	1854.1	1.6 (1.4)	10+92	N272,642 E192,576	1853.0	0.4	2.42
U12n.22 SR-14	S64°46'W	-0°21'	27.0 (19.4)	10+94.6	N272,653 E192,598	1854.1	1.6 (1.4)	10+95	N272,642 E192,574	1853.9	1.2	0.50
U12n.22 SR-15	S65°12'W	-2°08'	26.4 (18.7)	10+97.6	N272,654 E192,598	1854.0	1.5 (1.4)	10+98.6	N272,643 E192,574	1853.0	0.3	1.26
U12n.22 SR-16	S66°03'W	-1°07'	22.8 (22.3)	11+00.5	N272,655 E192,597	1854.1	1.6 (1.4)	11+02.6	N272,64o E192,577	1853.6	1.0	4.81

1 Survey target was 0.02 meters above invert of each 76-mm-diameter hole.

2 Total depths projected from surveyed depths in parentheses.

3 Indicates Construction Station, measured in feet. (Stations in Main drift are the same as those in Bypass drift.)

4 Number in parentheses is vertical distance to top of tie in Main drift.

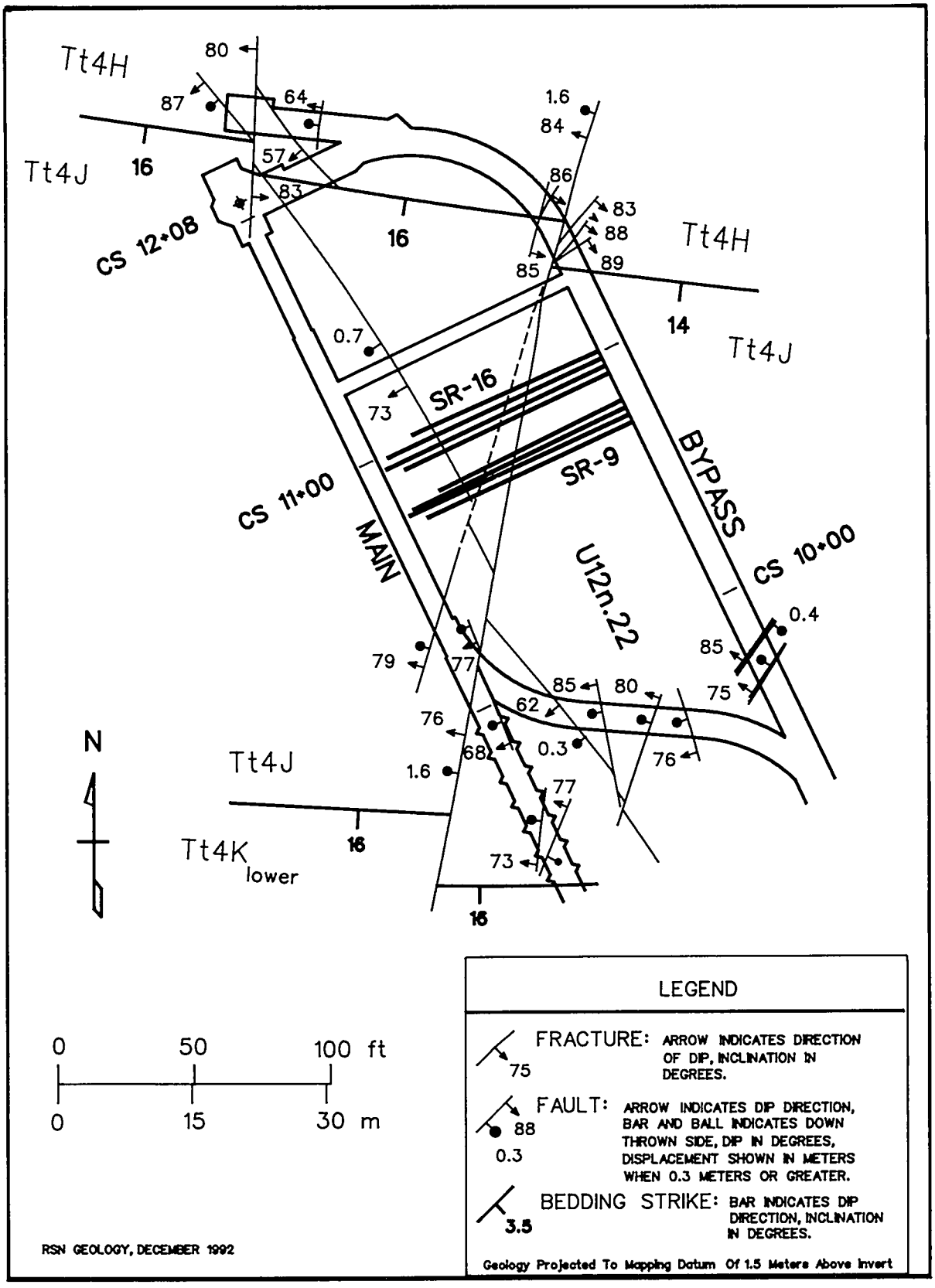


Figure B-1. Tunnel-level geology map for drill holes U12n.22 SR 9-16.

APPENDIX C

DATA FOR U12P.04 EXPERIMENTS

TABLE C-1. As-built survey data for drill holes U12p.04 SR 1-8.

FIGURE C-1. Tunnel-level geology map for drill holes U12p.04 SR 1-4.

FIGURE C-2. Tunnel-level geology map for drill holes U12p.04 SR 5-8.

Data provided by Raytheon Services Nevada

Table C-1. As-built survey data for drill holes U12p.04 SR 1-8[1].
(Measurements in meters, except where noted otherwise)

				COLLAR OF HOLE				BOTTOM OF HOLE				
DRILL HOLE	BEARING	ANGLE	TOTAL DEPTH[2]	BYPASS STATION[3]	COORDINATES	ELEVATION	VERTICAL DISTANCE TO BYPASS TOP OF TIE[4]	MAIN STATION[3]	COORDINATES	ELEVATION	VERTICAL DISTANCE TO MAIN TOP OF TIE	HORIZONTAL DISTANCE TO RIB OF MAIN DRIFT
U12p.04 SR-1	N07°11'E	-1°19'	16.2 (15.8)	9+12.1	N275,834 E197,075	1683.7	2.1 (1.9)	9+67.9	N275,850 E197,077	1683.4	1.6	3.58
U12p.04 SR-2	N08°48'E	-1°23'	19.6 (16.4)	9+15	N275,834 E197,074	1683.7	2.0 (1.9)	9+69	N275,854 E197,077	1683.2	1.4	0.32
U12p.04 SR-3	N09°01'E	-2°04'	18.0 (15.8)	9+17.8	N275,834 E197,073	1683.7	2.0 (1.9)	9+71.8	N275,852 E197,076	1683.1	1.3	1.86
U12p.04 SR-4	N08°40'E	-1°15'	12.5 (12.1)	9+21	N275,834 E197,072	1683.7	2.0 (1.9)	9+75.6	N275,847 E197,074	1683.4	1.6	7.43
U12p.04 SR-5	N07°10'E	-0°51'	19.1 (16.8)	17+55.1	N275,868 E196,820	1684.8	2.2 (1.4)	18+11	N275,887 E196,822	1684.5	1.1	2.44
U12p.04 SR-6	N08°05'E	-0°58'	20.9 (15.2)	17+58	N275,868 E196,819	1684.8	2.2 (1.4)	18+12.8	N275,889 E196,822	1684.5	1.0	0.63
U12p.04 SR-7	N08°22'E	-1°	20.4 (16.7)	17+61	N275,868 E196,818	1684.8	2.2 (1.4)	18+15.5	N275,889 E196,821	1684.5	1.0	1.12
U12p.04 SR-8	N08°16'E	-1°26'	16.6 (16.1)	17+63.9	N275,869 E196,817	1684.8	2.2 (1.4)	18+18.7	N275,885 E196,820	1684.4	0.9	4.92

[1] Survey target was 0.02 meters above invert of each 76-mm-diameter hole.

[2] Total depth projected from surveyed depth in parentheses.

[3] Indicates Construction Station, measured in feet. (Subtract 55.28 feet from station in Main drift to get equivalent station in Bypass drift.)

[4] Number in parentheses is vertical distance to top of tie in Main drift.

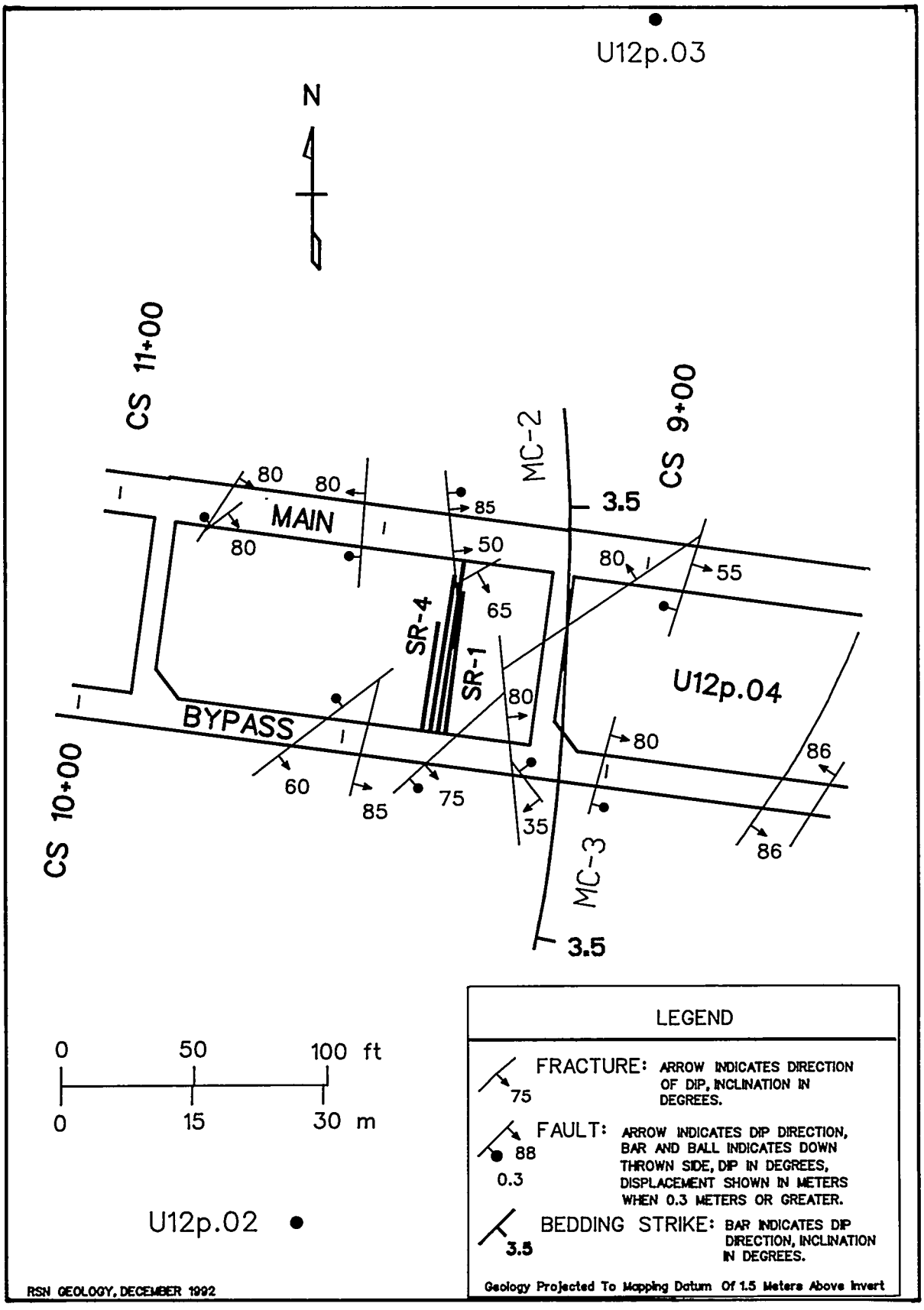


Figure C-1. Tunnel-level geology map for drill holes U12p.04 SR 1-4.

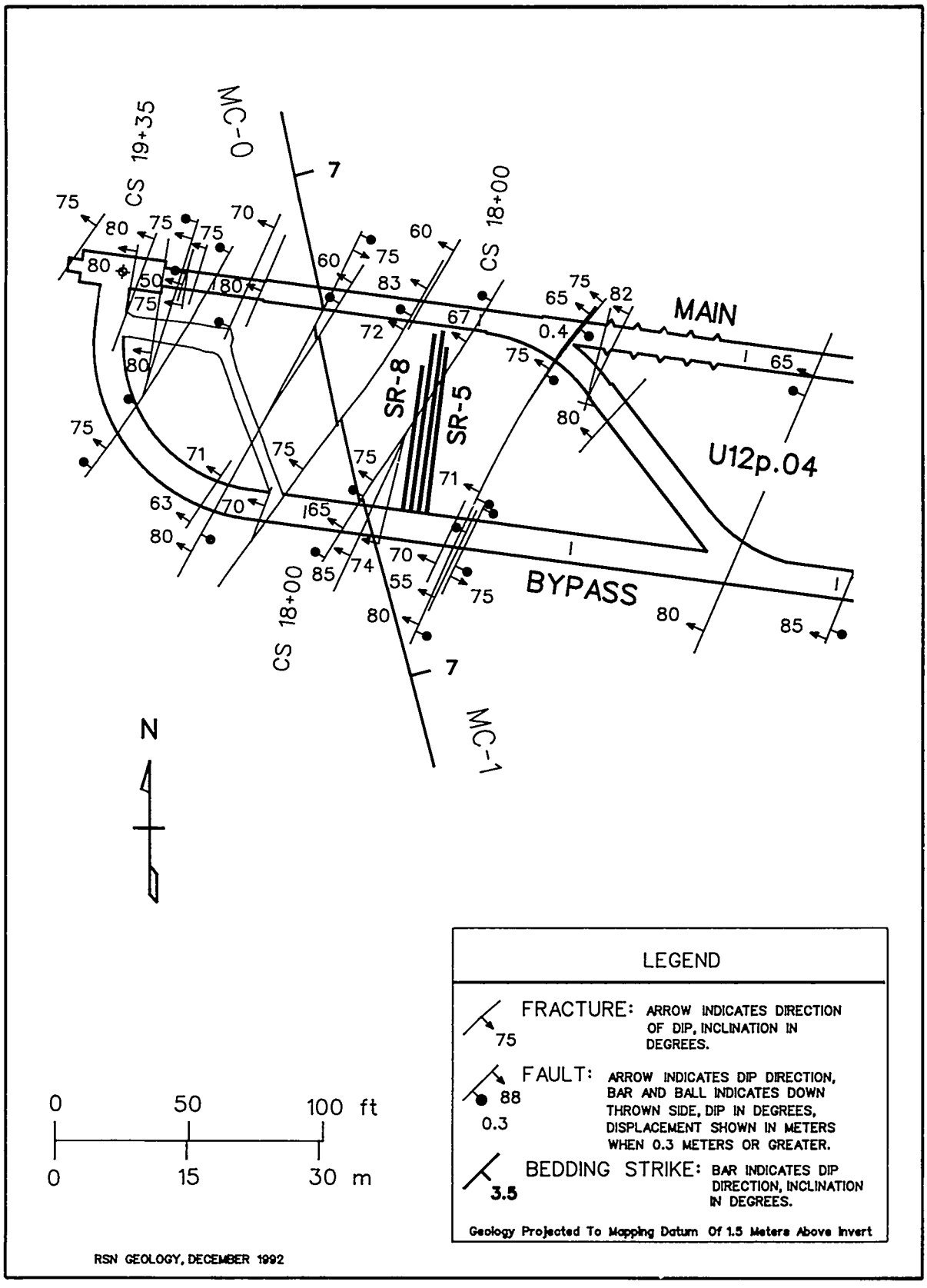


Figure C-2. Tunnel-level geology map for drill holes U12p.04 SR 5-8.

USE OF A SIMPLE CONSTITUTIVE MODEL FOR VOLCANIC ROCKS OF THE SOUTHWESTERN NEVADA VOLCANIC FIELD FOR THE DETERMINATION OF HUGONIOTS IN TESTING MEDIA OF THE NEVADA TEST SITE

Bart Olinger, J. N. Fritz, R. G. Warren, and S. J. Chipera
Los Alamos National Laboratory, Groups M-6, M-7 and EES-1

ABSTRACT

Our analysis of the known chemical and physical characteristics of Tertiary volcanic rocks of the southwestern Nevada volcanic field (SWNVF) indicates that rock alteration is the most important geologic consideration for shock-wave propagation. Volcanic rock chemistry is unusually consistent within the SWNVF as rhyolite, so chemical variation among and within volcanic units does not appear to significantly affect shock wave character. The three common alterations (vitric, devitrified, and zeolitic) appear to have consistent mineral assemblages throughout the SWNVF, and therefore each alteration type shows consistent physical properties throughout the SWNVF. In addition to alteration, porosity and degree of water saturation are important factors for shock-wave propagation. Rock porosity is strongly related to its lithology (e.g., lava, welded tuff), and degree of saturation is generally related to proximity to the water table.

We obtained large samples from well-characterized vitric, devitrified, and zeolitic zones of the Topopah Spring Tuff, a rhyolitic, phenocryst-poor unit of the SWNVF. We measured shock-wave compression in each of these samples using explosive-driven systems that compared shock velocities in the rock samples with velocities in aluminum standards. Measurements have been repeated, artificially varying degrees of saturation and porosity to include the *in situ* range observed in subsurface of the Nevada Test Site (NTS), located within the SWNVF. From these results, we provide Gruneisen parameters that allow calculation of Hugoniots for each alteration type to include the *in situ* range of saturation and porosity observed in Tertiary volcanic rocks of NTS subsurface.

Our preliminary interpretation of results from these experiments suggests that use of our results and knowledge of the rock lithology, porosity, and alteration should allow calculation of Hugoniots for most tests conducted in Tertiary volcanic rocks. Hugoniots (shock-wave equations-of-state) calculated from the constants that we provide should be generally applicable to predict shock-wave behavior for future tests, or to model previous tests.

PURPOSE AND SCOPE OF PAPER

The U. S. and Russia have agreed by treaty to verify yields of each others' underground nuclear tests by the CORRTEX method. The CORRTEX yield, determined by measuring the velocity of the shock wave in a nearby satellite hole, was initially assumed to be largely independent of the geologic medium. However, experience has demonstrated that this assumption is invalid, and very different shock-wave velocities have been measured in different geologic media where yields are accurately known. The purpose of our work has been to define geologic parameters that might influence shock-wave propagation, and to experimentally evaluate the importance of these parameters.

The scope of our work is to provide a method to model the shock-wave character of all past, present, and future tests in volcanic rocks of the southwestern Nevada volcanic field (SWNVF) of the Nevada Test Site (NTS), based on the yield and a knowledge of the appropriate geologic parameters. In the initial portion of the paper we examine pertinent chemical and mineralogical data available for volcanic rocks of the SWNVF to choose appropriate rock types (geologic parameters) for shock-wave experiments. In the final portion we report and discuss the results of experiments to determine shock-wave equations of state for these rock types.

DESCRIPTION OF ROCKS OF SWNVF

In this paper, we consider only shock wave characteristics for underground nuclear tests conducted in Tertiary volcanic rocks of the SWNVF. Rocks exposed within the NTS and surrounding regions of the SWNVF (Figure 1)

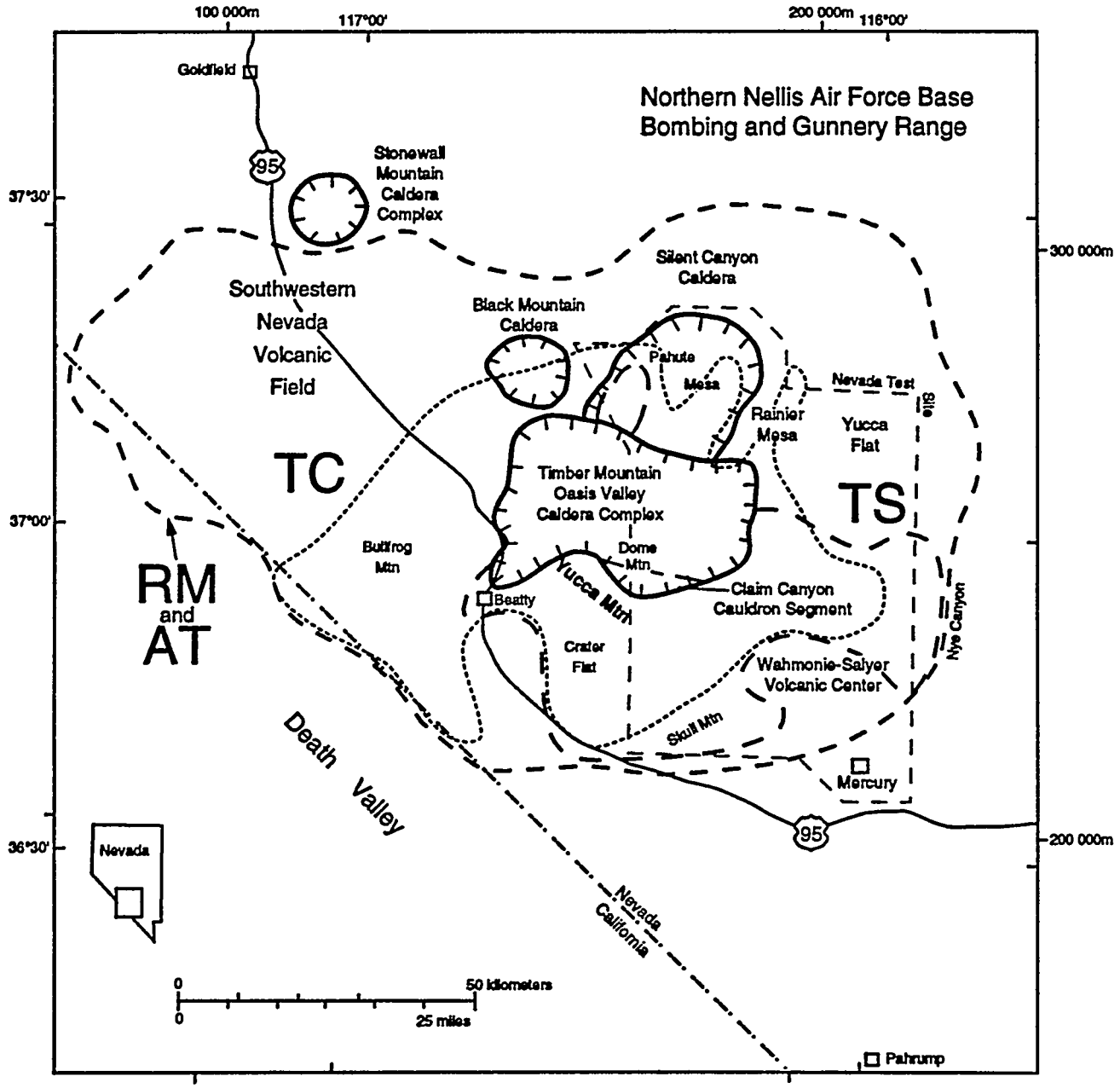


Figure 1. Location of southwestern Nevada volcanic field (SWNVF), defined by the approximate limits of large-volume ash flow sheets and location of Stonewall Mountain caldera complex. Large-volume sheets are Ammonia Tanks (AT), Rainier Mesa (RM), Tiva Canyon (TC) and Topopah Spring (TS) Tuffs.

are primarily 1) Quaternary and Tertiary alluvium, 2) Tertiary volcanic rocks largely erupted during the Miocene epoch 11 to 15 million years ago, and 3) pre-Tertiary plutonic and sedimentary rocks. Subsurface nuclear tests have been conducted in all these rocks, primarily at Pahute Mesa and Yucca Flat. These other rock types are so different from Tertiary volcanic rocks that it is unlikely that our results can be directly applied to such testing media of the SWNVF.

Characteristics of volcanic rocks discussed below that might influence shock-wave propagation are their chemistry, primary and secondary mineralogy, lithology, alteration, porosity, and saturation. We do not discuss the nature of fractures or permeability of volcanic rocks of the SWNVF because there is no reason to believe that these characteristics might affect their shock-wave character.

CHEMISTRY AND PRIMARY MINERALOGY

Volcanic rocks of the SWNVF are dominately enriched in silica and alkalis, and poor in calcium, magnesium, and iron relative to common volcanic rocks, and classify mostly as rhyolites (Figure 2). All of the approximately 200 rhyolitic units within the SWNVF consist of rhyolitic glass or its alterated chemical equivalent, and variable amounts of primary (phenocryst) minerals. Volcanic glasses have virtually identical compositions for all rhyolitic units of the SWNVF (Table 1, Figure 3); therefore chemical differences among units of the SWNVF are related primarily to differences in their phenocryst abundances. However, phenocryst abundances are typically low (Figure 4), accounting for the restricted chemical range for units of the SWNVF (Figure 2). The dominance of relatively phenocryst-poor rhyolite within the SWNVF is unique within the western U. S. (see descriptions of other volcanic fields by Swanson et al., 1989; Best et al., 1989; Lipman, 1989; Bonnichsen et al., 1989; Ratte et al., 1989; and Elston et al., 1976).

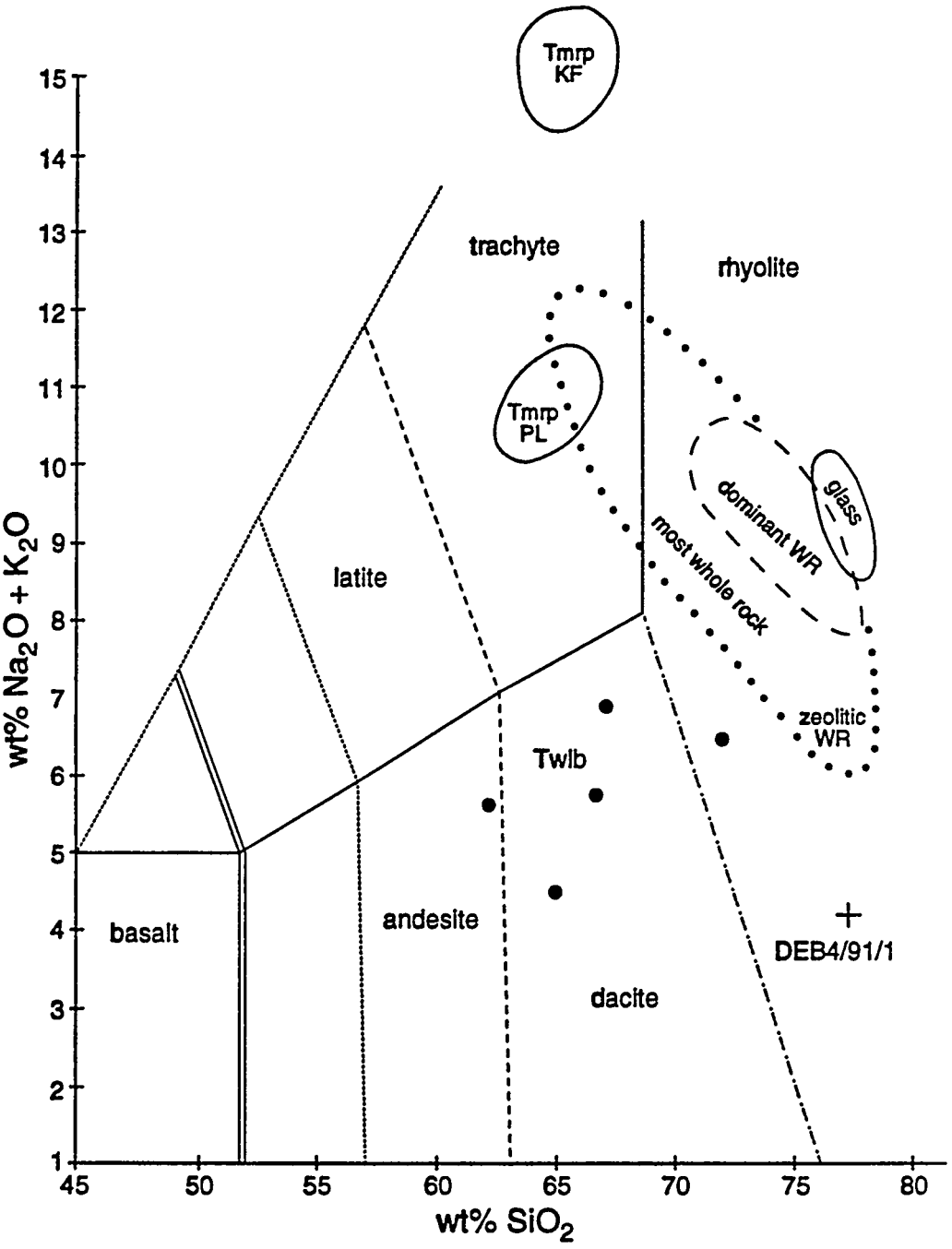


Figure 2. Fields for total alkalis versus silica for volcanic rocks of SWNVF, normalized water-free. Rock names as defined by Le Bas et al. (1986). Phenocrysts of mafic-poor Rainier Mesa Tuff (Tmrp) include 4% quartz, 4% sanidine (KF), and 2% plagioclase (PL) of composition shown. DEB4/91/1 is zeolitic sample tested for shock-wave character. Individual analyses shown for tuff of Wahmonie Flat (Twlb). Analyses from database of R. G. Warren.

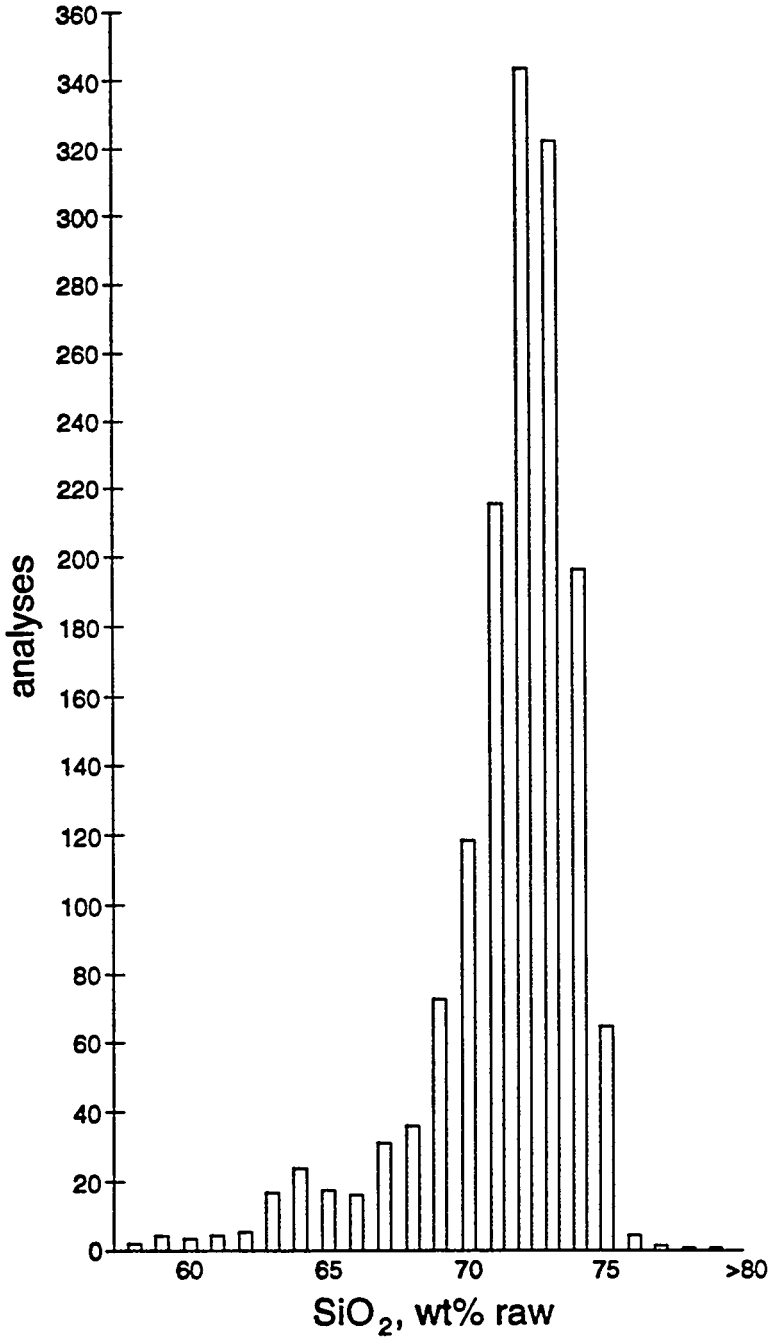


Figure 3. Bargraph of silica for 1493 analyses of glasses in volcanic rocks of the SWNVF, not normalized water-free. Analyses that do not fall within the dominant cluster of points at about 73% silica are over-represented rock types. Analyses from database of R. G. Warren.

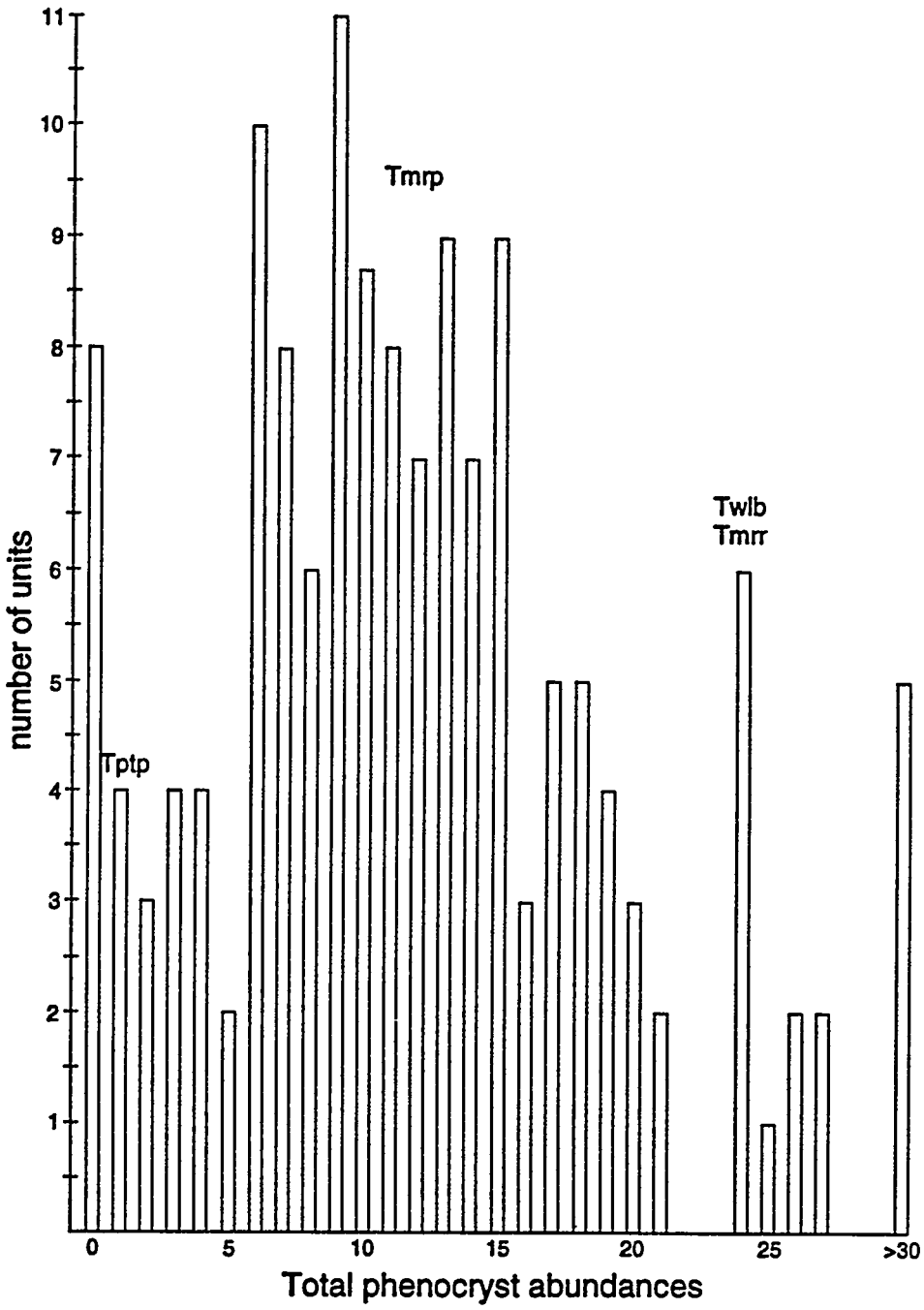


Figure 4. Bargraph of mean total phenocryst abundances of volcanic units of the SWNVF. Symbols are: crystal-poor Topopah Spring Tuff (Tptp), mafic-rich Rainier Mesa Tuff (Tmrr), mafic-poor Rainier Mesa Tuff (Tmrp), tuff of Wahmonie Flat (Twlb).

Table 1. Statistical summary for 1493 analyses of volcanic glasses of the SWNVF

All values are wt% by electron microprobe. Total includes additional minor elements; difference from 100% primarily due to H_2O (not analyzed). Analyses for total Fe only, reported as Fe_2O_3T. Analyses primarily from Warren et al. (1989) and unpublished analyses by R. G. Warren. SEM is standard error of mean.

oxide	minimum	maximum	median	mean	σ	SEM
SiO_2	58.81	79.20	72.53	71.98	2.67	0.07
Al_2O_3	7.23	16.30	11.70	11.94	1.05	0.03
Fe_2O_3T	0.11	6.01	0.78	1.02	0.78	0.02
CaO	0.00	4.28	0.39	0.47	0.43	0.01
Na_2O	0.82	6.11	3.53	3.62	0.66	0.02
K_2O	0.62	7.60	4.97	4.95	0.73	0.02
total	88.08	99.76	94.50	94.34	1.78	0.05

The importance of the unique character of the SWNVF as dominant phenocryst-poor rhyolite is to provide an unusually uniform chemistry throughout the volcanic pile (Byers et al., 1976; Broxton et al., 1989; Figure 2). Because chemical variation among and within rhyolitic volcanic units of the SWNVF is generally small, it is probably a minor factor in the variation of shock-wave characteristics among nuclear tests. We have selected samples of crystal-poor Topopah Spring Tuff for our tests that typically contain less than 1% phenocrysts and about 77% SiO_2; zeolitic sample DEB4/91/1 contains 77.5% SiO_2 on a water-free basis (Broxton et al., in press). These samples represent typical rhyolites that have hosted most nuclear tests in volcanic rock, but at the same time these phenocryst-poor rocks were selected to maximize chemical contrast with phenocryst-rich rocks that may have hosted some tests. Although small volumes of non-rhyolitic rocks occur throughout the SWNVF, including basalts in subsurface of both Yucca Flat and Pahute Mesa testing areas, geologic

media within two cavity radii for nearly all nuclear tests in volcanic rock have been rhyolite. The most likely non-rhyolitic rocks within past testing environments are probably those of tuff of Wahmonie Flat, which occurs as zeolitic bedded tuff up to 50 m thick within Yucca Flat subsurface (Drellack and Thompson, 1990). Tuff of Wahmonie Flat within Yucca Flat subsurface is typically dacite (Figure 2) that is phenocryst-rich (Figure 4).

SECONDARY MINERALOGY AND ALTERATION

Because rocks of the SWNVF are phenocryst-poor, the secondary mineral assemblage (alteration) dominates the mineral assemblage and determines the physical character of the rocks. Therefore the secondary mineral assemblages probably controls the shock-wave character of tests at the NTS in volcanic rock. Under most conditions, most phenocryst minerals remain unaltered in volcanic rocks of the SWNVF, but rhyolitic magma originally erupted transforms into three common secondary mineral assemblages: it may 1) chill to rhyolitic glass, 2) crystallize at relatively high temperature to a submicroscopic assemblage that consists of about 35% quartz and 65% feldspar, or 3) crystallize at relatively low temperature to a submicroscopic assemblage that consists of zeolite and associated minerals. The terms to describe these alteration processes and their secondary mineral assemblages are vitric, devitrified, and zeolitic alteration, respectively. The primary low temperature zeolites (clinoptilolite and mordenite) originally formed in rhyolites of the SWNVF may be transformed later by increased alteration to the zeolite analcime, and under still more severe (albitic) alteration conditions into the secondary feldspars albite and adularia (Broxton et al., 1987). Additional types of alteration may dominate under unusual conditions; the best known is argillic (clay) alteration, which played a major role in the BANEBERRY release (Glenn et al., 1981). Thick sequences of volcanic rock generally exhibit alteration that is exclusively one of the three major types. Alteration types are occasionally mixed, most commonly in thin zones between zones of thick, uniform alteration type, and particularly in lavas. Although alteration does not occur under closed chemical conditions (especially for zeolitic alteration), differences in the dominant constituents, SiO_2 and Al_2O_3, are very small among the three major alteration types (Broxton et al., 1987 and 1986).

To assess the consistency of secondary mineral assemblages for each type of alteration, we examined quantitative X-ray diffraction (XRD) mineral analyses for samples from five drill holes at Yucca Mountain (Bish and Chipera, 1989). Each of these holes has been continuously or extensively cored and studied, and logs that define alteration zones (ALTN) are available for each hole in the GEODES Containment database. Figure 5 shows mineral assemblages determined by XRD and alteration zones for one of these holes. To simplify comparisons, we combined abundances for minerals that probably respond in similar manner to a shock wave: the silica polymorphs quartz, cristobalite, and tridymite were combined as total silica, and the zeolites clinoptilolite, mordenite, and analcime were combined with opal-CT as total zeolite. Opal-CT indicates opal with short-range crystal structure, which is distinguishable by XRD from amorphous opal-A. Opal-CT from Yucca Mountain drill holes contains about 6% H_2O, assuming that differences in analytical totals from 100% is due to structural H_2O (based on 7 unpublished analyses by F. A. Caporuscio for USW G-1 and 1 unpublished analysis by D. E. Broxton for USW G-2). Because of the structural water, we assume that opal-CT will respond to shock waves more like a zeolite, which generally contains 10-20% H_2O (Broxton et al., 1986), rather than as an anhydrous silica polymorph.

Mineral abundances represented in Figure 6 were obtained from a wide range in depth and from several major stratigraphic units, demonstrating that the mineralogy for a particular type of alteration is largely independent of depth, stratigraphic unit, and location within the Yucca Mountain area. Based on these comparisons, we combined analyses from all five drill holes. The results, summarized in Figure 7 and Table 2, demonstrate a consistency in mineral abundances for each type of alteration, and significant differences in mineral abundances among alterations. From these results, we might expect possibly significant differences in shock-wave character between rocks with different alteration, but not between rocks with the same alteration. We selected samples for our shock-wave experiments as typical of the three major types of alteration: vitric, devitrified, and zeolitic (Table 3).

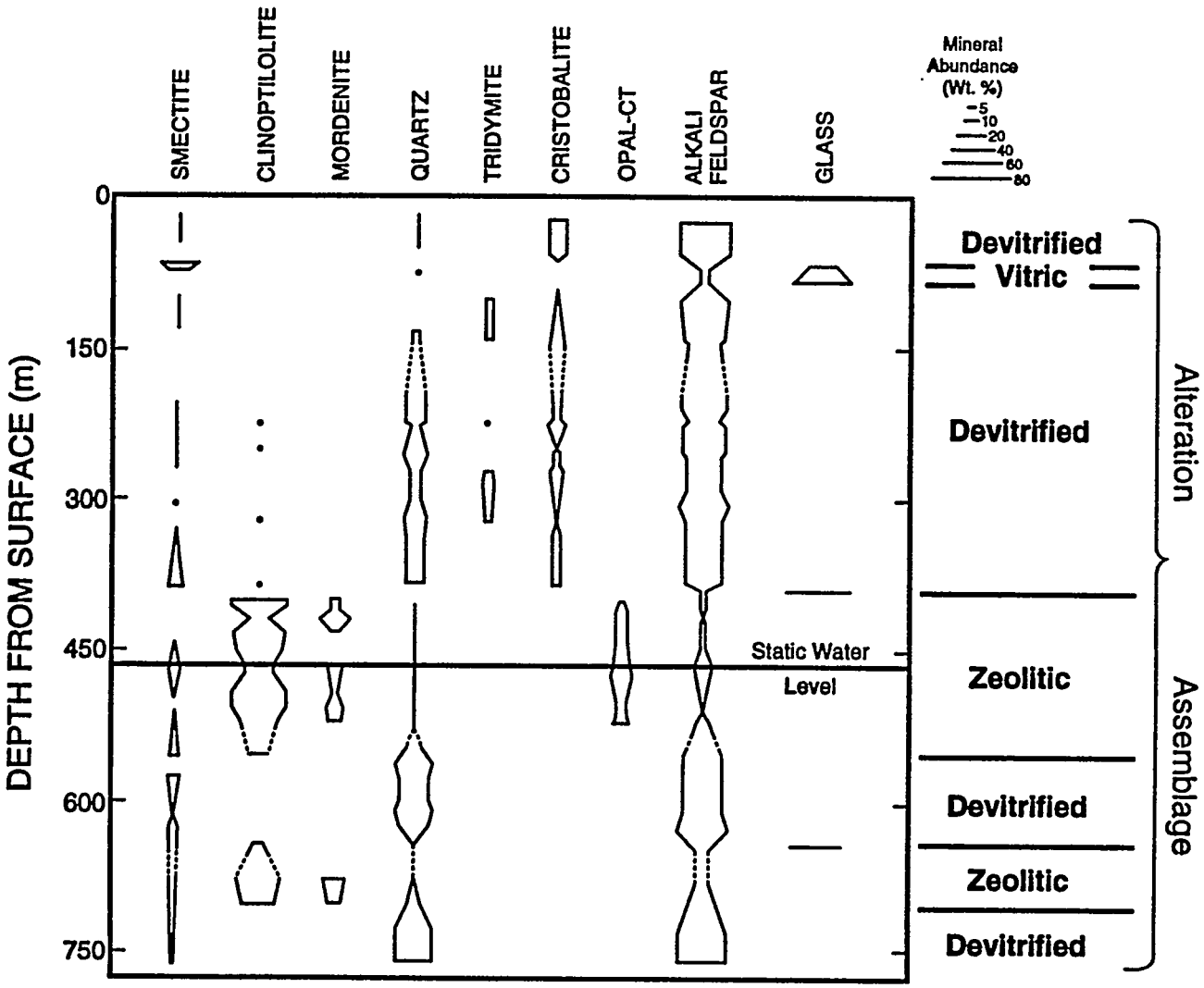


Figure 5. "Pagoda" diagram showing mineral abundances by XRD and alteration zones for Yucca Mountain drill hole UE-25a1. Modified from Bish and Chipera (1989).

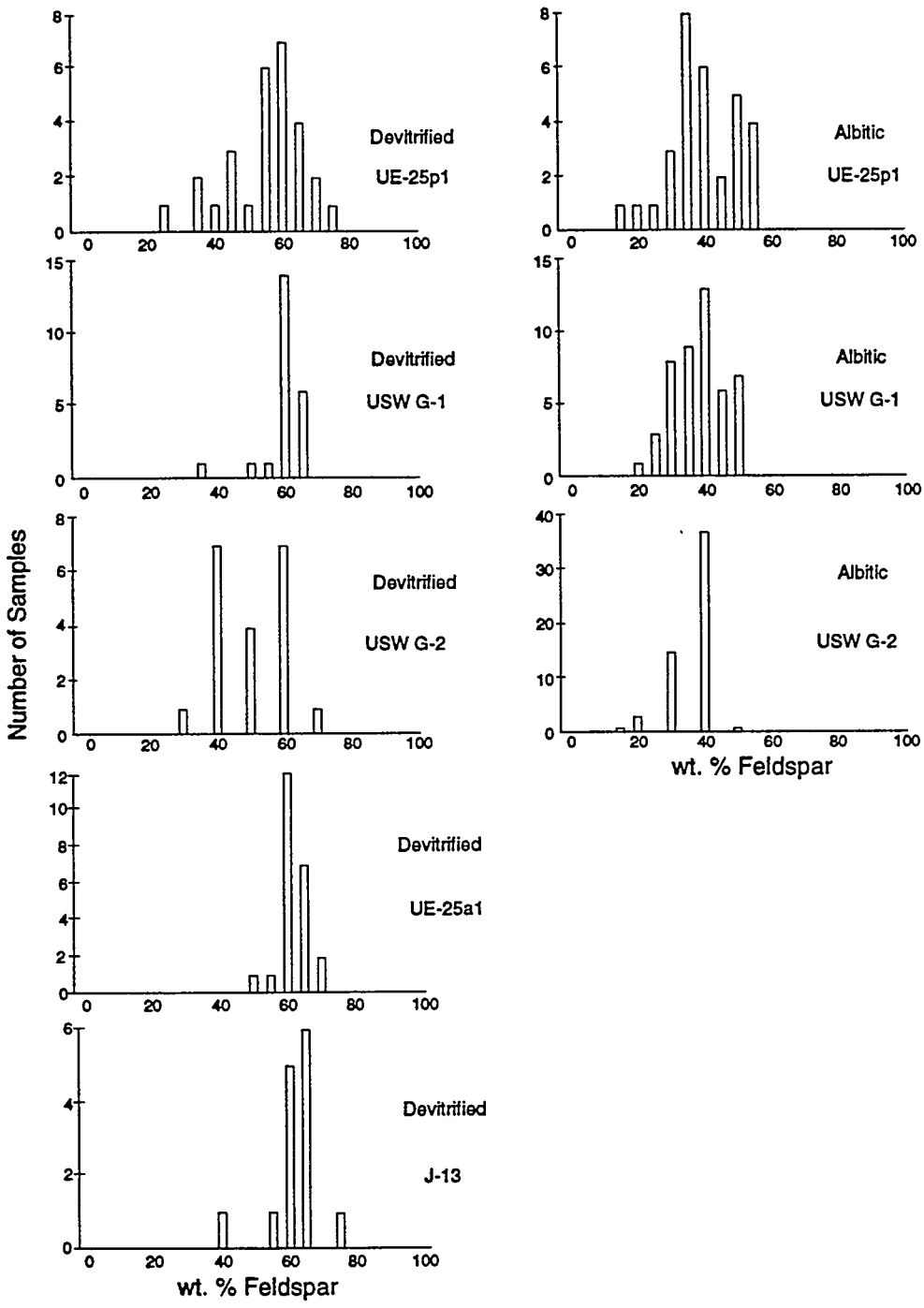


Figure 6. Bargraphs comparing wt% feldspar from XRD analyses by Bish and Chipera (1989) for devitrified and for albitic rocks among drill holes of the Yucca Mountain area.

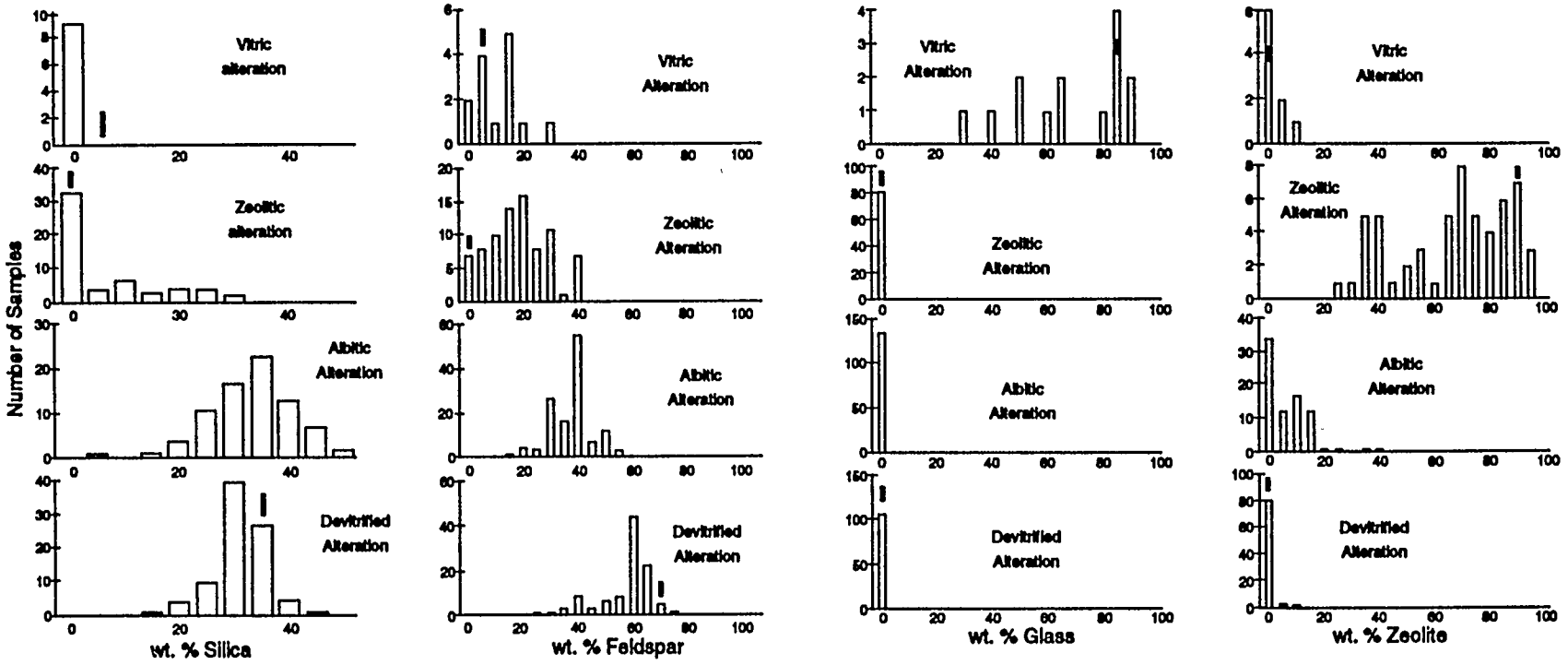


Figure 7. Bargraphs comparing mineral abundances from XRD analyses by Bish and Chipera (1989) for common alterations of the Yucca Mountain area. Narrow solid bars represent samples tested for shock-wave characteristics (Table 3). See text for minerals combined as silica and as zeolite. Wide range in mineral abundances for zeolitic alteration results from significant differences in mineral assemblages among the zeolites (clinoptilolite, analcime, and mordenite; see Table 3).

Table 2. Statistical summary of mineral abundances for common alteration types

Data are wt%, from Bish and Chipera (1989), combined for the five drill holes at Yucca Mountain shown in Figure 6. See text for definition of silica and total zeolite. SEM is standard error of mean. Number of feldspar and glass analyses for each alteration is *n1*; number of silica and total zeolite analyses is *n2*. Symbol is for ALTN log of Los Alamos GEODES Containment database (Winterkamp et al., 1985).

Alteration	sym-bol	Feldspar			Glass		Silica			Total zeolite	
		n1	mean	SEM	mean	SEM	n2	mean	SEM	mean	SEM
vitric	GL	14	12	2	70	6	9	1	0	3	1
clinoptilolite	ZC	59	18	1	0	0	47	6	1	73	3
mordenite	ZM	15	26	2	0	0	6	14	5	57	7
analcime	ZA	7	29	2	0	0	4	31	2	36	4
devitrified	D	106	59	1	0	0	86	33	0	1	0
vapor phase	VP	45	54	2	0	0	27	31	1	0	0
albitic	AB	136	39	1	0	0	79	35	1	8	1

Table 3. XRD analyses of samples tested for shock-wave characteristics

Analyses by internal standard method, following procedures in Bish and Chipera (1989)

	DEB10/90/3	DEB10/90/1	DEB4/91/1-M6
Alteration	vitric	devitrified	zeolitic
Smectite		tr	--
Clinoptilolite	--	--	72 ± 6
Chabazite?	--	--	3 ± 1
Quartz	--	12 ± 1	2 ± 1
Cristobalite	5 ± 1	23 ± 2	--
Opal-CT	--	--	17 ± 3
Feldspar	8 ± 1	69 ± 8	--
Mica	1 ± 1	tr	--
Hematite	--	tr	--
Glass	86 ± 2	--	--
Total	100 ± 3	104 ± 8	94 ± 7

LITHOLOGY AND POROSITY

Four general types of lithology are common in volcanic rocks: ash-flow cooling units, bedded tuffs, lavas, and volcanoclastic rocks. These lithologies are defined in the GEODES Containment database (Winterkamp et al., 1985) by the log LITH. Ash-flow cooling units are typically zonal, with interiors most strongly compacted and therefore least porous (Smith, 1960). Lavas are also zonal, although often in a more complex manner. Volcanoclastic rocks include laharic debris flows, such as those of the Salyer member of the Wahmonie Formation (Salyer Formation of Poole et al., 1965), and caldera collapse breccias penetrated by deep drill holes in the Pahute Mesa testing area. They are unimportant in the testing environment, lithologically complex, and are not further considered. Bedded and associated nonwelded tuffs of the SWNVF are most often associated with lavas, forming precursor tuff cones that the lavas generally filled.

Lithology strongly controls alteration and porosity, and therefore strongly controls the expected shock-wave characteristics of volcanic rocks. Table 4 shows idealized zonal relations between lithology, alteration, and porosity. Interior zones may disappear with increasing distance from source, or may never be formed. Although the relations in Table 4 are idealized, data inconsistent with Table 4 should be viewed with suspicion. For example, a sample description as "nonwelded and devitrified tuff" is probably erroneous, and a porosity of 20% for a "densely welded tuff" indicates an error or a very unusual sample (perhaps highly fractured in a fault zone). We selected samples for our shock-wave experiments to obtain those with the lowest possible porosities, because we can reconstitute samples with relatively high porosities, but those with porosities less than 20% must be obtained naturally.

Table 4. Typical porosities (%) for idealized lithologies and alterations

Porosities are in vol%. Depths are in percent of total unit thickness.
No entry for porosity indicates rocks not observed or very rare

		Ash-flow cooling unit			
lithology	**GEODES symbol**	**idealized depth**	**vitric porosity**	**zeolitic porosity**	**devitrified porosity**
nonwelded[a]	NWT, B[a]	0-10	30-50	30-50[b]	
partially welded	PWT	10-20	15-30		15-30[c]
moderately welded	MWT	20-70	10-20		10-20
densely welded	DWT	70-75	5-10		5-10
vitrophyric	VT	75-80	0-5		0-5
partly-densely welded		80-82	5-30		5-30
nonwelded[a]	NWT, B[a]	82-100	30-50	30-50	

		Lava flow cooling unit			
lithology	**GEODES symbol**	**idealized depth**	**vitric porosity**	**zeolitic porosity**	**devitrified porosity**
pumiceous lava	PL	0-20	30-50	30-50	
lava (interior)	L	20-90	5-30		5-30
lava (vitrophyre)	L	90-95	0-5		0-5
flow breccia	FB	95-100	5-30		5-30

a Bedded tuffs are not ordinarily part of an ash-flow cooling unit, but have similar character as shown.
b Zeolitic nonwelded tuffs are often misidentified as partially welded.
c Devitrified partially welded tuffs are usually vapor phase (GEODES symbol VP).

EQUATIONS OF STATE FOR RHYOLITIC VOLCANIC ROCKS OF THE SWNVF

The properties important to understand the response of the three alteration types of rhyolite of the SWNVF to shock waves are the equations-of-state and the influences of porosity and saturation. We introduce the equations of state by assuming that the shock wave pressure-time profile remains steady as it passes through rock material, allowing application of the Rankine-Hugoniot equations. These relate pressure (P), internal energy (E), and specific volume (V) behind the shock wave to those in front in terms of the shock-wave velocity (u_S) and particle (mass) velocity behind the shock front (u_p). These equations express the conservation of mass, momentum, and energy:

$$u_s V = (u_s - u_p) V_0 \quad (1)$$

$$P = u_s u_p / V_0 \quad (2)$$

$$E - E_0 = u_p^2/2 \quad (3)$$

The zero subscript refers to the initial state. Another form of Eq. 3 is the Hugoniot energy equation:

$$E - E_0 = P(V_0 - V)/2 \tag{4}$$

Any pair of variables can represent the shock wave equation of state or Hugoniot of the material. One pair of variables, the shock and particle velocity, is particularly important for describing experimental results. For most materials, equations-of-state can be described by a linear equation relating these two velocities :

$$u_s = c_0 + su_p \tag{5}$$

When determining the Hugoniot of a mixture of two substances, A and B, a simple mixing model is used:

$$V_{A+B}(P) = X_A V_A(P) + X_B V_B(P) \tag{6}$$

Where X_A and X_B are the mass fractions of A and B.

In order to calculate the equations of state for other porosities, and to calculate the velocities of the release waves, the Gruneisen parameter, γ, must be determined for each of the three alteration types:

$$\gamma/V = (\partial P/\partial E)_V \tag{7}$$

The Gruneisen parameter can be determined from the difference in pressure needed to achieve the same shock-compressed volume, V, starting with two different initial volumes, V_{01} and V_{02}, of the same material:

$$\gamma/V = \frac{2(P_2 - P_1)}{P_2(V_{02} - V) - P_1(V_{01} - V)} \tag{8}$$

The pressure is greater for the larger initial volume because the change in internal energy is greater for porous samples. This same relation, rearranged, can be used to calculate Hugoniots for various porosities based on the Gruneisen parameters that we have determined, and a measured

Hugoniot for a given initial volume. With mixtures, the resulting Gruneisen parameter can be calculated from the component parameters:

$$V/\gamma = X_A V_A/\gamma + X_B V_B/\gamma \qquad (9)$$

For the shock compression of most solids, γ/V has been found to be nearly constant within resolution of the data.

For complex mixtures, such as these rocks, Eq. 8 would be exactly applicable if the phase compositions were the same for both porosities. However, the high-density sample will be at a lower pressure and lower temperature than the low-density sample. These different conditions will probably produce different, and unknown phase compositions. We apply Eq. 8 because we have no better model to calculate Hugoniots for rocks having different porosities. The Gruneisen parameter that we determine for each rock type is used only for calculating Hugoniots at different porosities; it is not a true thermodynamic property of that rock as defined in Eq. 7.

SAMPLE PREPARATION

Samples of vitric, devitrified, and zeolitic rhyolite described in previous sections were cut into wafers designated TfVit01, TfDeV01, and TfZeo01, respectively. In an effort to obtain off-Hugoniot measurements, the vitric and devitrified samples were ground to 88Im particle size, and 100 parts by weight were added to 5 parts by weight vinyl acetate binder dissolved in acetone. The slurry was dried and the resulting powder pressed to 10,000 psi in a 1 inch diameter cylinder, producing relatively high-porosity samples 4.5 mm thick. The higher porosity of these samples, designated TfVit02, TfDeV02, results in shock loci in a hotter P,V region than those from samples in their natural state. Because TfZeo01 already had a relatively high porosity, and our experience indicated that we would be unable to decrease this mechanically, we shocked TfZeo01 dry, with voids air-filled. In order to determine P,V relations for zeolitic material in a cooler region, another wafer of zeolitic tuff that we designated TfZeo02 was shocked in a water-saturated condition. Table 5 summarizes densities and porosities measured for the samples.

Table 5. Densities and porosities of samples of rhyolitic volcanic rock tested for shock-wave characteristics

Laboratory number	Bulk Density (kg/m^3)	Grain Density (kg/m^3)	Porosity (%)
	DEB10/90/3 (Vitric)		
TfVit01	2347	2354	0.5
TfVit02	1600	2252	29
	DEB10/90/1-M6 (devitrified)		
TfDeV01	2360	2501	5.5
TfDeV02	1650	2376	31
	DEB4/91/1-M6 (Zeolitic)		
TfZeo01	1424	1929	26
TfZeo02	1540	2078	26

EXPERIMENTAL TECHNIQUES

Two techniques were used to determine the equations-of-state. Both use flash gaps (i.e., thin gaps filled with argon and/or xenon that flash when shocked) to indicate the arrival of shock waves through a sample or standard material.

In the first technique, accurately measured blocks of rock samples are mounted on a plate of standard material whose equation-of-state is well defined. On this plate are also mounted blocks of the plate material. A streak camera measures the time differences between the shock wave breaking through the plate and through the blocks. These differences determine the shock velocity in both the standard material and samples. These shock velocities uniquely determine the particle velocity in the samples. The initial density of the sample and its particle velocity determine the pressure and volume to which the sample was shock compressed. We refer to points obtained in this manner as base-plate (BP) points (Figure 8).

In the second technique, accurately measured blocks of rock samples are mounted **into** a plate of standard material whose equation-of-state is well

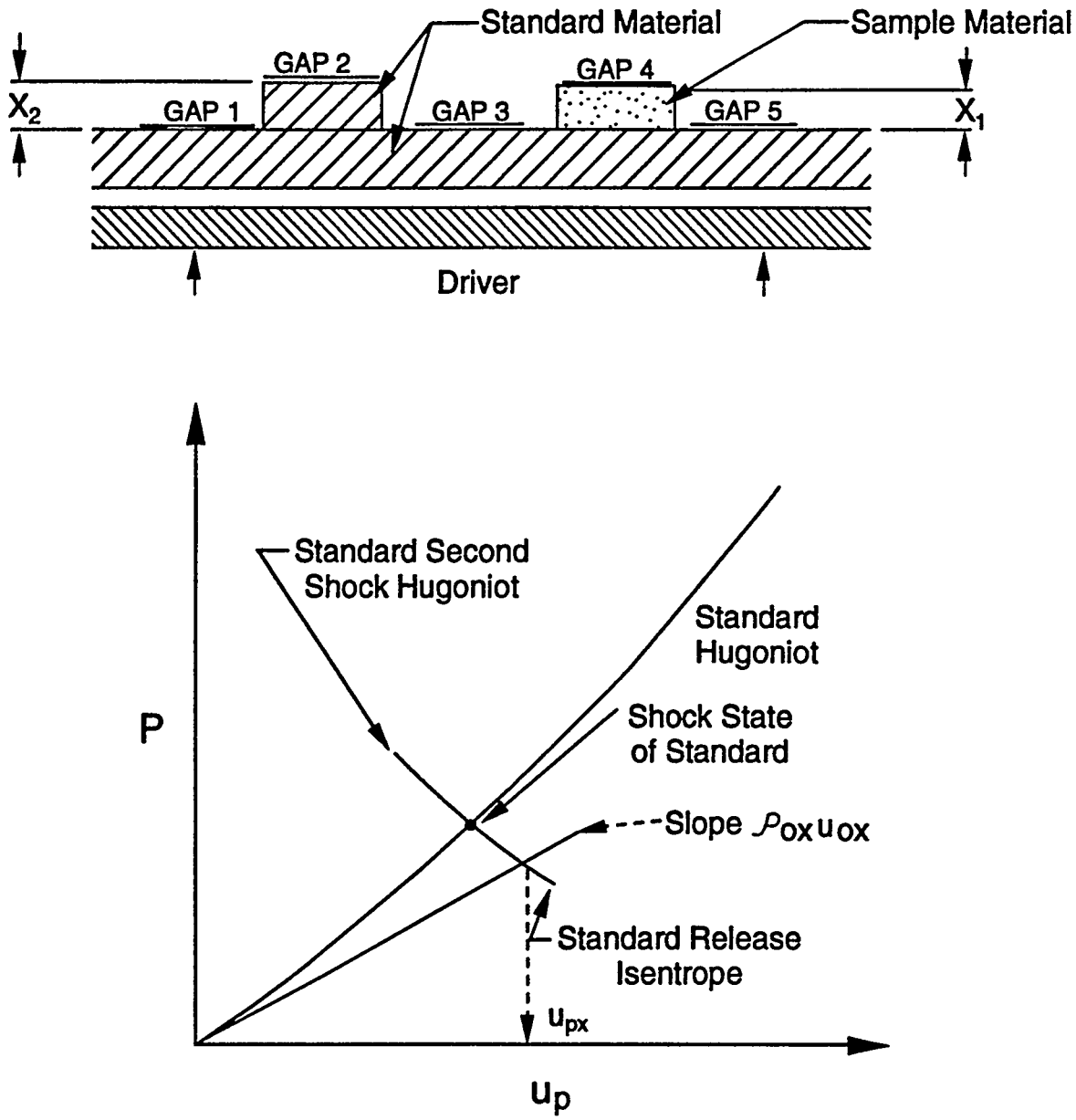


Figure 8. The standard Base-Plate technique for determining Hugoniots. Measurement of u_s in the standard determines the standard curve configuration in P, u_p. Then the intersection of the Rayleigh line with the appropriate branch of the standard cross curve determines the Hugoniot point for the sample.

defined. A plate of another standard material, called a driver plate, is explosively accelerated and impacts the sample plate. The velocity of this plate is determined from steps machined into the standard plate. A streak camera measures the time differences between the shock wave passing through the standard plate and through the samples in the standard plate can be determined. From the driver-plate velocity, the shock velocity and pressure in the standard plate can be determined. Combining this velocity with the differential velocity between standard and sample provides the shock velocity of the sample. These shock velocities and the driver plate velocity determine the particle velocities in the samples. Points obtained in this manner are direct-impact Hugoniot (DIH) points (Figure 9).

Results: Equations of state for devitrified, vitric, and zeolitic rhyolite

Results are provided in Table 6 and shown in Figures 10 to 12. The u_s,u_p data for both devitrified (TfDeV01) and vitric (TfVit01) samples can be fit with two line segments, shown as solid and dashed lines in Figure 11. This indicates the occurrence of phase transitions typical for the constituent minerals of volcanic rocks as described by McQueen et al. (1967). The lower pressure segment, below $u_p = 2.3$ mm/μs, is a pressure-volume region where many minerals in rhyolitic material transform into high-pressure stable structures. Above $u_p = 2.3$ mm/μs (P = 30 GPa), the u_s,u_p data appear linear, as found by McQueen et al. (1967). In this study we will compare data only in this high-pressure region to determine values for the Gruneisen parameter.

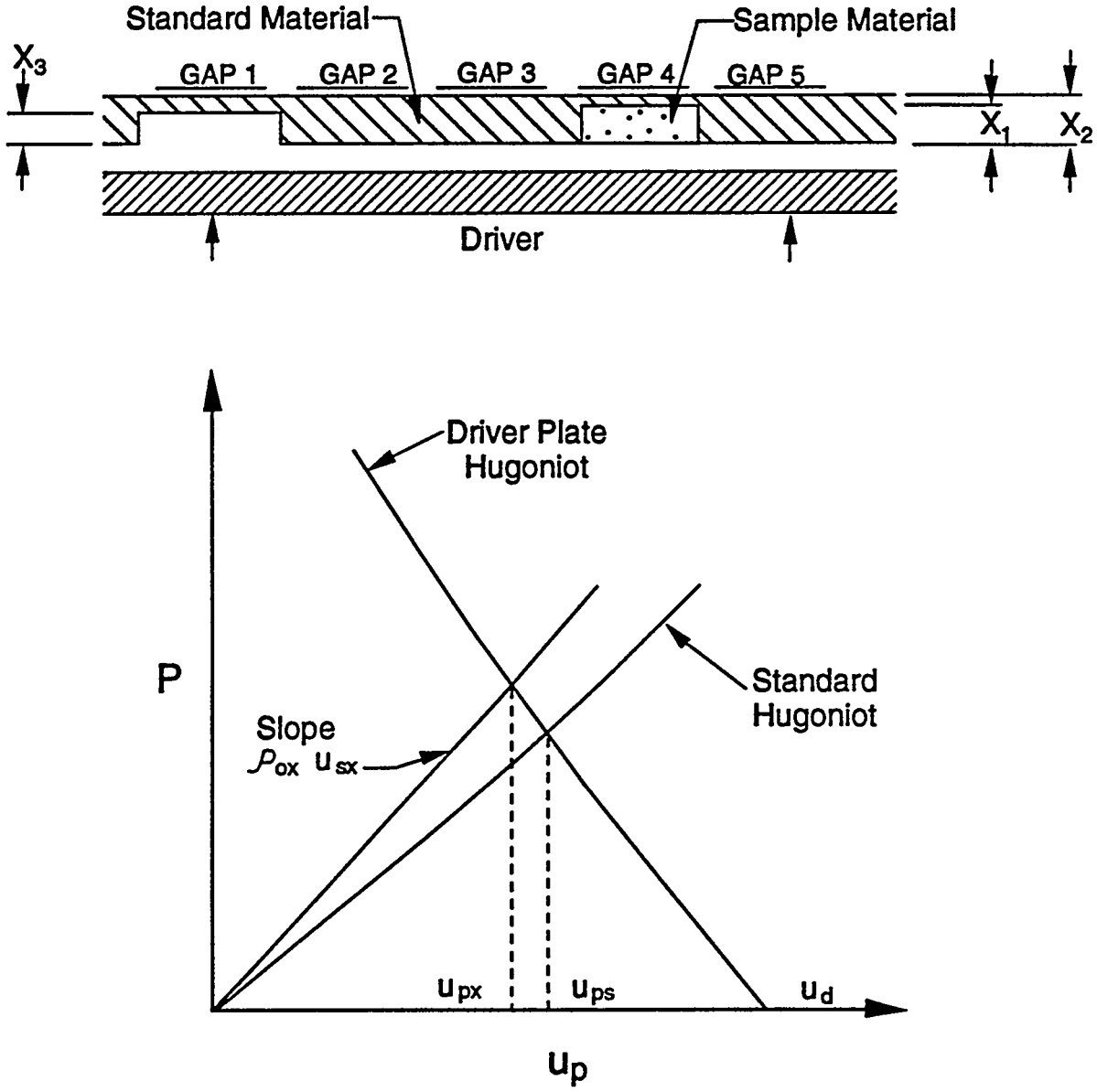


Figure 9. The standard Direct-impact Hugoniot technique. The advantage of the technique is that it only uses the Hugoniot of the driver which is directly measured.

Table 6. Hugoniot values for samples of rhyolitic volcanic rock

Measurements by base-plate method except where "D" follows ρ_0 to indicate direct impact hugoniot method. Uncertainties (1σ) are calculated from estimated standard errors for length and time measurements. Estimates of error from other sources have not been included, so uncertainties provided here are minimum values.

ρ_0 (kg/m^3)	u_p (m/s)	u_s (m/s)	P (GPa)	ρ (kg/m^3)
	TfDeV01 devitrified low porosity			
2361	1582±13	5054±11	18.88	3437
2356	1599±13	4912±14	18.51	3493
2359	2065±36	5315±22	25.89	3858
2359	2075±36	5241±32	25.65	3904
2361	2295±29	5399±22	29.26	4107
2356	2302±29	5368±16	29.11	4124
2404D	2330±15	5526±17	30.96	4158
2375D	2337±15	5512±17	30.60	4124
2356D	2342±15	5500±19	30.35	4103
2419D	2463±25	5736±29	34.17	4239
2371D	2482±26	5639±17	33.18	4234
2342D	2484±26	5680±17	33.04	4162
2417D	3116±38	6778±20	51.06	4474
2381D	3133±38	6705±18	50.01	4469
2351D	3138±38	6735±26	49.69	4402
2405D	3740±32	7924±27	71.27	4554
2382D	3751±32	7896±27	70.56	4538
2351D	3766±32	7852±22	69.52	4518

Table 6. Hugoniot values for samples of rhyolitic volcanic rock, continued

ρ_0 (kg/m^3)	u_p (m/s)	u_s (m/s)	P (GPa)	ρ (kg/m^3)
	TfDeV02 devitrified high porosity			
1654	2641±48	4846±10	21.17	3634
1656	2644±48	4814±10	21.08	3674
1657	3204±11	5661±13	30.05	3817
1653	3219±11	5578±17	29.68	3908
1654	3705±16	6562±15	40.22	3799
1655	3708±16	6541±14	40.14	3822
1652	4100±2	7162±17	48.52	3864
1668	4102±2	7085±18	48.47	3961
1650	4448±44	7742±16	56.82	3879
1640	4462±44	7708±22	56.41	3894
	TfVit01 vitric low porosity			
2342	1607±13	4878±11	18.35	3492
2335	1607±13	4890±10	18.35	3477
2338	2092±36	5159±11	25.24	3933
2338	2093±36	5155±10	25.22	3936
2342	2303±29	5389±11	29.07	4090
2335	2309±29	5368±11	28.93	4097
2356D	2323±15	5720±18	31.31	3968
2358D	2327±15	5677±17	31.15	3995
2365D	2329±15	5635±18	31.03	4031
2367D	2464±26	5847±19	34.11	4091
2357D	2467±26	5838±19	33.95	4083
2354D	2471±26	5807±18	33.77	4097
2366D	3124±38	6841±23	50.56	4354
2354D	3124±38	6872±18	50.55	4317
2358D	3139±38	6710±17	49.67	4431
2365D	3750±32	7962±22	70.61	4470
2356D	3755±32	7938±32	70.23	4471
2359D	3758±32	7905±18	70.06	4495

Table 6. Hugoniot values for samples of rhyolitic volcanic rock, continued

ρ_0 (kg/m^3)	u_p (m/s)	u_s (m/s)	P (GPa)	ρ (kg/m^3)
	TfVit02 vitric high porosity			
1597	2666±49	4836±10	20.59	3560
1602	2668±49	4808±9	20.55	3600
1596	3242±11	5626±15	29.11	3767
1599	3246±11	5590±18	29.01	3813
1603	3743±16	6529±18	39.18	3757
1606	3753±16	6455±15	38.91	3837
1613	4139±2	7097±16	47.38	3870
1603	4140±2	7137±17	47.37	3817
1603	4489±44	7725±15	55.58	3826
1604	4506±44	7618±16	55.06	3926
	TfZeo01 zeolitic unsaturated			
1478	1341±58	2682±16	5.32	2956
1362	1368±60	2613±7	4.87	2858
1439	1944±15	4098±8	11.46	2737
1387	2006±15	3696±24	10.28	3033
1427	2502±42	4518±10	16.12	3197
1419	2504±42	4528±10	16.09	3174
1474D	2584±17	4834±16	18.41	3166
1357D	2616±17	4769±12	16.93	3006
1299D	2625±17	4835±32	16.50	2843
1591D	2695±28	5197±52	22.28	3305
1439D	2759±34	4670±11	18.53	3515
1387D	2773±34	4737±15	18.22	3345
1355	2777±28	4886±32	18.38	3139
1299	2785±29	4976±36	18.01	2952
1529D	3438±42	6202±62	32.60	3431
1383D	3506±42	5990±23	29.04	3334
1358D	3513±43	6014±44	28.68	3264
1533D	4127±35	7351±60	46.49	3494
1389D	4213±36	7082±44	41.45	3429
1357D	4230±36	7049±31	40.46	3393

Table 6. Hugoniot values for samples of rhyolitic volcanic rock, continued

ρ_0 (kg/m^3)	u_p (m/s)	u_s (m/s)	P (GPa)	ρ (kg/m^3)
		TfZeo02 zeolitic saturated		
1781	2494±47	5517±13	24.51	3251
1800	2507±47	5370±13	24.23	3376
1810	3029±10	6292±24	34.50	3491
1790	3067±10	6107±43	33.52	3596
1820	3510±15	7155±22	45.71	3573
1788	3540±15	7087±38	44.85	3572
1808	3888±2	7812±18	54.91	3599
1778	3920±2	7738±18	53.93	3603
1792	4227±43	8434±24	63.89	3592
1791	4246±43	8321±34	63.28	3657

Fitting the data in Table 6 (shown in Figure 11), the Hugoniot fit for high-pressure data from devitrified, low porosity rock (TfDev01) is:

$$u_s = 1.513 + 1.691u_p \text{ , } V_0 = 0.4214 \text{ cm}^3/\text{g} \qquad (10)$$

Devitrified, high porosity rock samples (TfDev02) include 4.8% mass fraction admixed vinyl acetate, with an unknown Hugoniot, which must be computationally removed to determine the Gruneisen parameter for devitrified rock. Because the mass fraction is small, we assume that substituting the Hugoniot of a similar plastic, PMMA, will not introduce significant error into the computation. The Hugoniot for PMMA above 30 GPa (Marsh, 1980) is:

$$u_s = 3.0 + 1.321u_p \text{ , } V_0 = 0.8432 \text{ cm}^3/\text{g} \qquad (11)$$

Combining eqs. 10 and 11, the Hugoniot for the devitrified rock-vinyl acetate mixture is:

$$u_s = 1.614 + 1.652u_p \text{ , } V_0 = 0.4415 \text{ cm}^3/\text{g} \qquad (12)$$

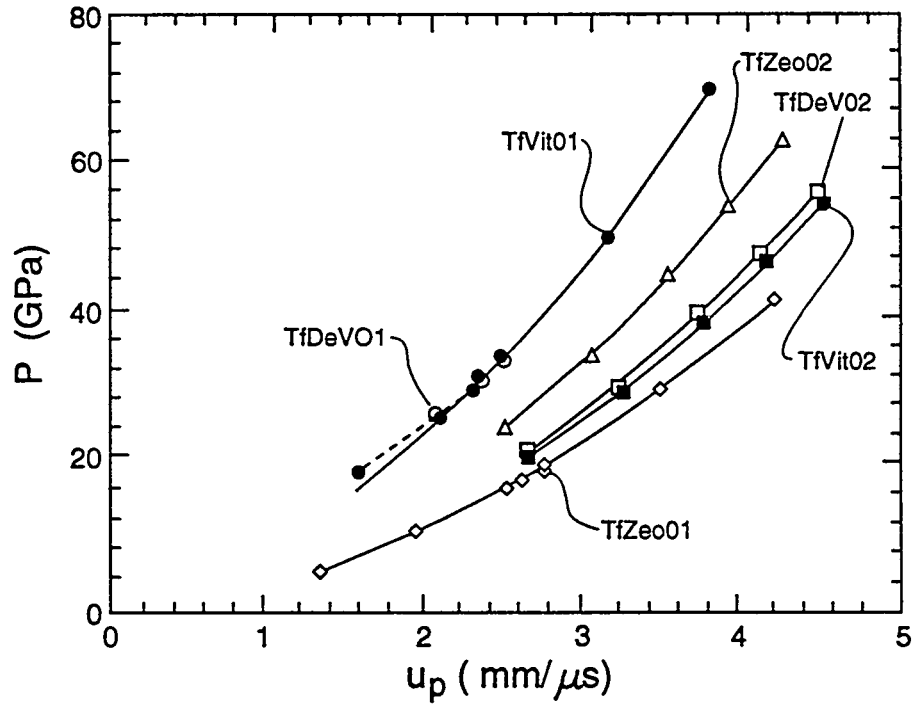


Figure 10. $P(u_p)$ Hugoniots for vitric, devitrified, and zeolitic rhyolite. Solid lines are the c_0, s linear fits for $u_s(u_p)$. The dotted line indicates the typical deviation from the high pressure phase that occurs for most rocks.

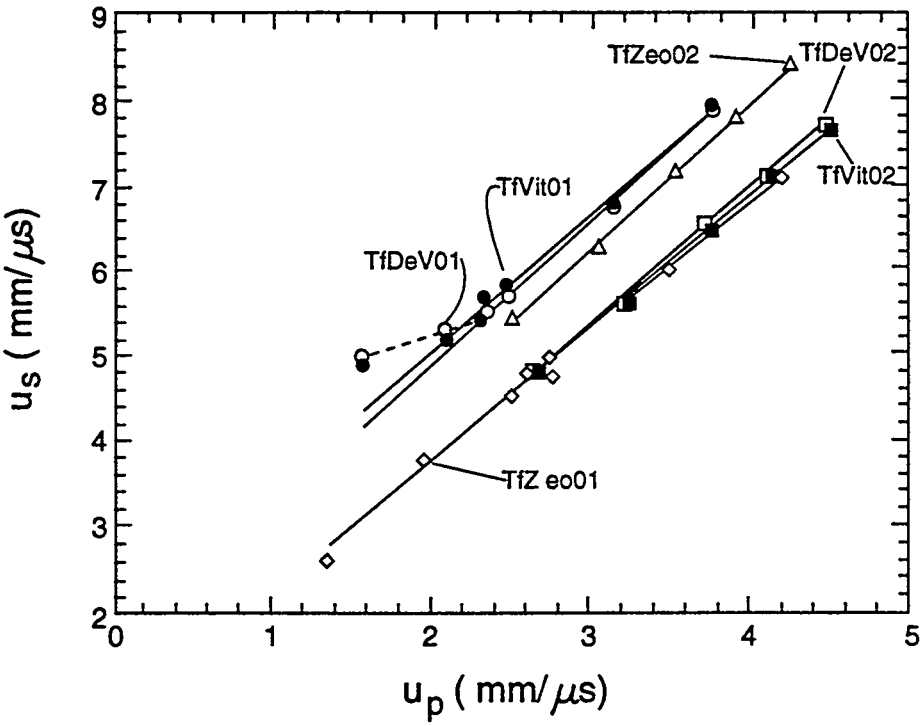


Figure 11. $u_s(u_p)$ Hugoniots for vitric, devitrified, and zeolitic rhyolite.

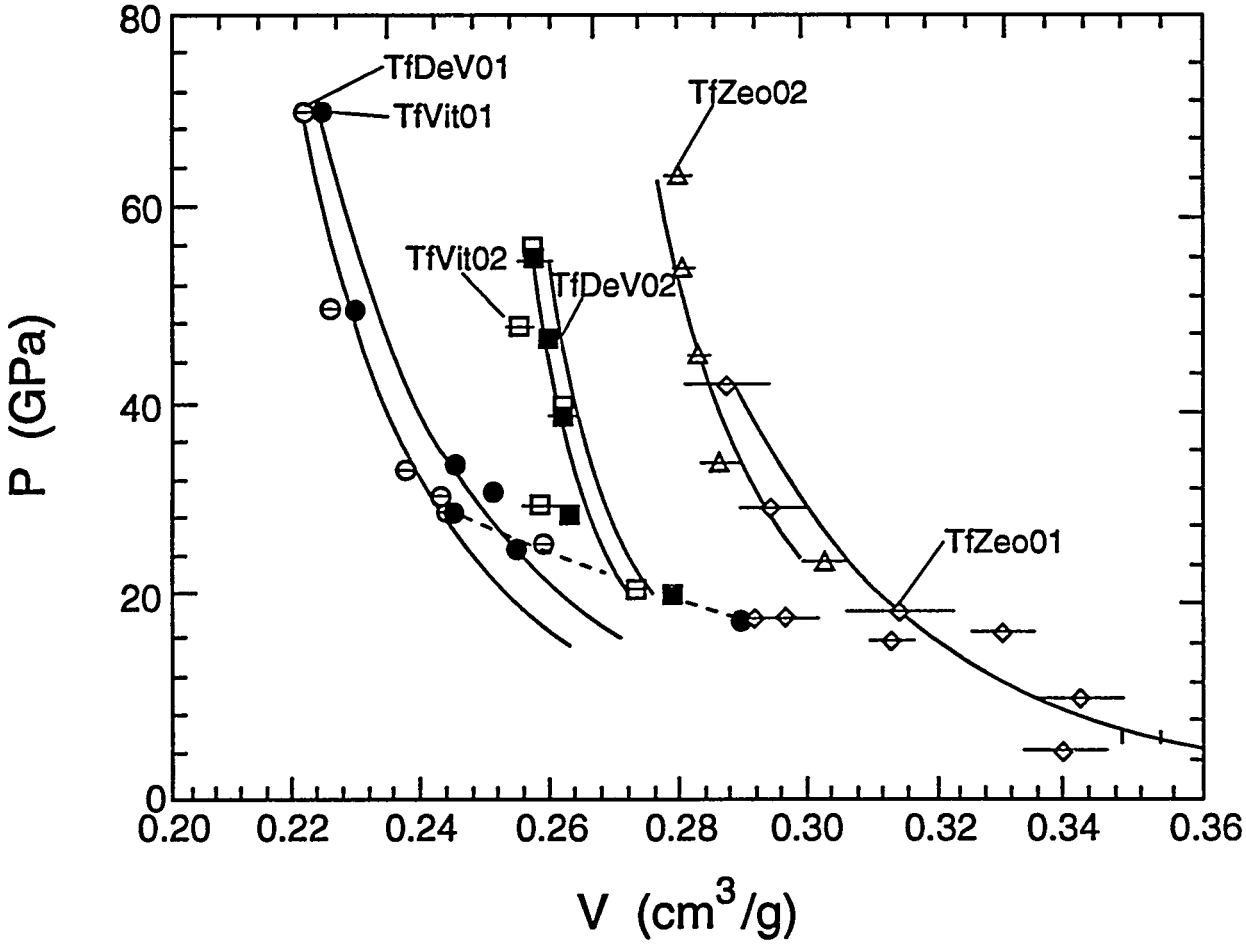


Figure 12. P(V) Hugoniots for vitric, devitrified, and zeolitic rhyolite.

The smallest volumes achieved when shock compressing the devitrified, high porosity rock samples (TfDev02) were about 0.257 cm^3/g. The largest volumes reached at the low end of the high-pressure linear fit were about 0.243 cm^3/g. Therefore, to determine the Gruneisen parameter, we must extrapolate the high pressure Hugoniot to lower pressures where we have no data.

Pressures for devitrified, low porosity rock (TfDev01) were calculated from the Hugoniot for the volumes with the six highest pressures for devitrified, high porosity rock (TfDev02). Using Eq. (8), an average value for γ/V of devitrified rock-vinyl acetate mixture is 3.8 ± 0.3. Assuming that vinyl acetate has the same γ as PMMA, then γ/V for devitrified rhyolite is 4.3 ± 0.3.

A similar analysis of data from Table 6 (shown in Figure 11) is used for vitric rhyolite. The Hugoniot for the high-pressure phase of vitric, low porosity rock (TfVit01) is:

$$u_s = 1.769 + 1.633u_p \, , \, V_0 = 0.4250 \text{ cm}^3/\text{g} \qquad (13)$$

The Hugoniot for the vitric rock-vinyl acetate mixture is:

$$u_s = 1.898 + 1.583u_p \, , \, V_0 = 0.4451 \text{ cm}^3/\text{g} \qquad (14)$$

The resulting γ/V for vitric rhyolite is 3.4 ± 0.4.

The fully water-saturated zeolitic samples (TfZeo02) yielded a Hugoniot:

$$u_s = 1.097 + 1.709u_p \, , \, V_0 = 0.556 \text{ cm}^3/\text{g} \qquad (15)$$

High-pressure shock compression of water is described by the Hugoniot (Marsh, 1980):

$$u_s = 2.638 + 1.270u_p \, , \quad V_0 = 1.001 \text{ cm}^3/\text{g} \qquad (16)$$

Subtracting out the pore water for each datum, saturated zeolitic samples (TfZeo02) yielded a Hugoniot for unsaturated zeolitic rhyolite:

$$u_s = 0.607 + 1.923u_p \text{ , } V_0 = 0.482 \text{ cm}^3/\text{g} \qquad (17)$$

Comparing pressures from this Hugoniot for volumes determined from the shock compression of unsaturated zeolitic rhyolite (TfZeo01), γ/V for zeolitic rhyolite is 4.6 ± 0.4.

SUMMARY AND CONCLUSIONS

We have considered the chemistry, primary and secondary mineralogy, and lithologies of testing media within Tertiary volcanic rocks of the NTS, and conclude that the most significant differences within this environment with respect to shock-wave characteristics are defined by three distinctive rock alterations: vitric, devitrified, and zeolitic. Rocks with these alterations consist mostly of rhyolitic volcanic glass, feldspar and quartz, and zeolite, respectively. Each type of alteration is defined by an assemblage of minerals with a restricted range in abundances; therefore, **accurate** recognition of alteration type yields the probable mineral assemblage. The variety of lithologies exhibited in generally zonal fashion is also important, controlling the porosity. In typical geologic media, both alteration and lithology can be confidently recognized in hand sample with a binocular microscope by an experienced geologist. Alteration is even better determined by thin section petrography, and best by XRD, but lithology is generally best determined by simple hand sample inspection. Often, the primary limitation is by the nature of the sample. Cuttings often misrepresent alteration and may be inadequate to determine lithology. If it is important to accurately characterize both lithology and alteration, then core samples may be essential. In summary, simple qualitative descriptions of rock lithology and alteration can provide suprisingly accurate estimates of parameters important for prediction of shock-wave character, although these descriptions may be limited both by the quality of samples available and by the skill of the geologist that describes the rock.

We have experimentally determined Hugoniots for low-porosity vitric, devitrified, and zeolitic rhyolite of the SWNVF. In addition, we have determined the values of γ/V for each of these rock types. Combining these results, Hugoniots can be calculated for rocks of various porosities using Eq. (8), and these Hugoniots can be combined with the Hugoniot for water, Eq. (16), to calculate Hugoniots for various saturations using the mixing model of Eq. (6). Finally, knowledge of these Hugoniots and the values for γ/V permits the calculation of the overtaking release wave velocity, C, where $\eta = 1 - V/V_0$:

$$c/u_s = V/V_o\left[\frac{(1-s\eta) - (\gamma/v)\, V_o\, s\eta^2}{1-s\eta}\right]^{1/2} \qquad (18)$$

This work provides an integrated geologic and physics model to compute shock wave characteristics for the testing medium of Tertiary volcanic rocks of the SWNVF. This model can be applied even where physical property data from samples are unavailable, as long as accurate descriptions of rock alteration and lithology are available, and reasonable estimates for water saturation can be made. Although there can be no substitute for direct measurement of Hugoniots, there are countless nuclear tests where such measurements are unavailable, and calculational modeling offers the only approach for understanding shock-wave effects.

Acknowledgments

This work is supported by the United States Department of Energy under Contract 7405-ENG-36. We wish to acknowledge the help of Conception Gomez, Dennis Price, and Dennis Shampine in preparing and conducting the shock wave measurements. We greatly appreciate the administrative and moral support of Jack W. House, Ward L. Hawkins, and Wayne A. Morris of the Earth and Environmental Sciences Division at Los Alamos National Laboratory.

References

Best, M. G., E. H. Christiansen, A. L. Dieno, G. S. Gromme, E. H. McKee, and D. C. Noble, "Eocene through Miocene volcanism in the Great Basin of the western United States", in *Field excursions to volcanic terranes in the Western United States, Volume II: Cascades and Intermountain West*, C. E. Chapin and Z. Zidek, eds, **N. M. Bur. Mines Min. Res. Memoir 47**, Socorro N. M., pp. 91-133, 1989.

Bish, D. L., and S. J. Chipera, "Revised mineralogic summary of Yucca Mountain, Nevada," **Los Alamos National Laboratory Report LA-11497-MS**, 68 pp., March 1989.

Bonnichsen, B., R. L. Christiansen, L. A. Morgan, F. J. Moye, W. R. Hackett, W. H. Leeman, N. Honjo, M. D. Jenks, and M. M. Godchaux, "Silicic volcanic rocks in the Snake River Plain-Yellowstone Plateau", in *Field excursions to volcanic terranes in the Western United States, Volume II: Cascades and Intermountain West*, C. E. Chapin and Z. Zidek, eds, **N. M. Bur. Mines Min. Res. Memoir 47**, Socorro N. M., pp. 135-182, 1989.

Broxton, D. E., S. J. Chipera, F. M. Byers, Jr., and C. A. Rautman, "Geologic evaluation of six nonwelded tuff sites in the vicinity of Yucca Mountain, Nevada for a surface-based test facility for the Yucca Mountain project", **Los Alamos National Laboratory Report**, *in press.*

Broxton, D. E., R. G. Warren, F. M. Byers, and R. B. Scott, "Chemical and mineralogic trends within the Timber Mountain-Oasis Valley caldera complex, Nevada: evidence for multiple cycles of chemical evolution in a long-lived silicic magma system", **J. Geophys. Res.,** Vol. 94, No. B5, p. 5961-5985, 10 May 1989.

Broxton, D. E., D. L. Bish, and R. G. Warren, "Distribution and chemistry of diagenetic minerals at Yucca Mountain, Nye County, Nevada", **Clays and Clay Minerals**, Vol. 35, No. 2, p. 89-110, 1987.

Broxton, D. E., R. G. Warren, R. C. Hagan, and G. Luedemann, "Chemistry of Diagenetically Altered Tuffs at a Potential Nuclear Waste Repository, Yucca Mountain, Nye County, Nevada", **Los Alamos National Laboratory Report LA-10802-MS**, 160 pp., October 1986.

Byers, F. M., Jr., W. J. Carr, P. P. Orkild, W. D. Quinlivan, and K. A. Sargent, Volcanic suites and related cauldrons of Timber Mountain-Oasis Valley caldera complex, southern Nevada, **U. S. Geol. Survey Prof. Paper 919**, 70 pp., 1976.

Drellack, S. L., and P. H. Thompson, "Selected stratigraphic data for drill holes in LANL use areas of Yucca Flat, NTS", **DOE/NV/10322-39**, July 1990.

Elston, W. E., R. C. Rhodes, P. J. Coney, and E. G. Deal, "Progress report on the Mogollon Plateau volcanic field, southwestern New Mexico, No. 3 - Surface expression of a pluton", in *Cenozoic volcanism in southwestern New Mexico*, W. E. Elston and S. A. Northrop, eds, **N. M. Geol. Soc Special Publication No. 5**, pp. 3-28, 1976.

Glenn, H. D., J. T. Rambo, and R. W. Terhune, "Calculational examination of the Baneberry event - addendum", **Lawrence Livermore National Laboratory Report UCRL-53164**, 71 pp., June 1981.

Le Bas, M. J., R. W. Le Maitre, A. Streckeisen, and B. Zanettin, A chemical classification of volcanic rocks based on the total alkali-silica diagram, **Jour. Petrol.**, Vol. 27, part 3, pp. 745-750, 1986.

Lipman, P. W., compiler, "Oligocene-Miocene San Juan volcanic field, Colorado", in *Field excursions to volcanic terranes in the Western United States, Volume I: Southern Rocky Mountain Region*, C. E. Chapin and Z. Zidek, eds, **N. M. Bur. Mines Min. Res. Memoir 47**, Socorro N. M., pp. 303-380, 1989.

Marsh, S. P., ed., **LASL Shock Hugoniot Data**, University of California Press, Berkeley, CA, 1980, 658 p.

McQueen, R. G., S. P. Marsh, and J. N. Fritz, "Hugoniot Equation of States of Twelve Rocks", **J. Geophys. Res.**, Vol 72, No. 20 p. 4999-5036, October 1967.

Poole, F. G., D. P. Elston, and W. J. Carr, Geologic map of the Cane Spring quadrangle, Nye County, Nevada, **U.S. Geol. Surv. Map GQ-455**, 1965.

Ratte, J. C., S. M. Cather, C. E. Chapin, W. A. Duffield, W. E. Elston, and W. C. McIntosh, "Eocene-Miocene Mogollon-Datil volcanic field, New Mexico", in *Field excursions to volcanic terranes in the Western United States, Volume I: Southern Rocky Mountain Region*, C. E. Chapin and Z. Zidek, eds, **N. M. Bur. Mines Min. Res. Memoir 47**, Socorro N. M., pp. 43-119, 1989.

Smith, R. L., Zones and zonal variations in welded ash flows, **U. S. Geol. Survey Prof. Paper 354-F**, p. 149-159, 1960.

Swanson, D. A., K. A. Cameron, R. C. Evarts, R. T. Pringle, and J. A. Vance, "Cenozoic volcanism in the Cascade Range and Columbia Plateau, southern Washington", in *Field excursions to volcanic terranes in the Western United States, Volume II: Cascades and Intermountain West*, C. E. Chapin and Z. Zidek, eds, **N. M. Bur. Mines Min. Res. Memoir 47**, Socorro N. M., pp. 1-50, 1989.

Warren, R. G., F. M. Byers, Jr., D. E. Broxton, S. H. Freeman, and R. C. Hagan, "Phenocryst abundances and glass and phenocryst compositions as indicators of magmatic environments of large-volume ash-flow sheets in southwestern Nevada", **J. Geophys. Res.**, Vol. 94, No. B5, p. 5987-6020, 10 May 1989.

Winterkamp, J. L., J. R. Neergaard, C. F. Mills, and C. A. Watson, "Geoscience data evaluation system", *Proceedings of the Third Symposium on Containment of Underground Nuclear Explosions*, **Lawrence Livermore National Laboratory, CONF-850953, Vol. 2**, p. 141-156, September 1985.

A COMPARISON OF THE MOISTURE GAUGE AND THE NEUTRON LOG IN AIR-FILLED HOLES AT NTS

Joseph R Hearst and Richard C. Carlson
Lawrence Livermore National Laboratory
P.O. Box 808, Livermore CA 94551

Two methods are commonly used to measure water content of geologic materials by neutron diffusion. One is used mostly in agricultural, mining and civil engineering areas and is called a moisture gauge. The other is used principally in petroleum and mineral exploration, and is called a neutron log. Both are used at NTS, the moisture gauge principally in tunnels, the neutron log in vertical drilled holes. There is little communication between the two industrial groups, and the measurement instruments have evolved with very different operational characteristics, and one important physics difference, the source to detector spacing. The moisture gauge has a very short, 0-6 cm, spacing, with little internal shielding, and count increases with water. In contrast, the neutron log has a long spacing, 30-50 cm, substantial internal shielding, and exhibits decreasing count with increasing water. Because of its short spacing the moisture gauge gives better bed resolution than the neutron log. Because its count increases with water, the moisture gauge is more strongly affected by water in the borehole, especially in dry formations. In these conditions the neutron log is the method of choice. In air-filled holes, if source size or logging time is not a constraint, the relative sensitivity of the two tools to water is determined by the relative strengths of borehole effects as fluid, holesize, or tool-wall gap. If source size is a constraint for safety reasons, the short spacing provides higher countrates for a given detector efficiency and thus better relative precision in determining the true count. If source size is limited because of detector or electronics saturation, the short spacing will be better at high water content, while the long spacing will be better at low water content. In any case the short spacing may have an advantage because it can make better contact with the hole wall and it can be more easily corrected for gap. We currently use the long spacing tool in vertical holes at NTS because that is the only tool available from logging contractors. Since we are most concerned with high water contents, the short spacing tool could prove to be better.

INTRODUCTION

Neutron diffusion has been used for many years to measure the water content of geologic materials. A large literature describing the technique has evolved. But in fact two methods, each with its own literature, have come into use. Many years ago workers in different industries made independent decisions to use different methods. The instrument used in soil science, agriculture, and construction is called a moisture gauge. The moisture gauge is often used in tunnels at NTS, and in the Yucca Mountain Project (Buscheck et al, 1991.) The instrument used in the petroleum industry and to some extent in the mining industry, is called a neutron log. A modified version of the neutron log is routinely used in vertical holes at NTS (Axelrod and Hearst, 1984.) The two methods exhibit very different operational characteristics, and, in addition, one important physics difference: the source to detector spacing.

The physics difference between the two methods is illustrated by Figure 1 (Tittman, 1956), which shows a simple calculation of the thermal neutron flux as a function of distance from a fast-neutron source. On the left side of the plot, the flux increases with increasing water content; on the right side the flux decreases with increasing water content. Moisture gauges use short source-detector spacings (the left side). Neutron logs use long source-detector spacings (the right side).

Many users of each method are almost unaware of the other method, and they are certainly unaware of its capabilities. It is unfortunate that with all the possible design choices, within each industry the tools of the various manufacturers are remarkably similar. This gives the user only two choices for an instrument best suited to the task at hand. This paper compares the two methods and suggests ways in which their virtues could be combined. The result may surprise users of both methods.

Since the two methods use somewhat different terminologies, some quantities need to be specified for this paper:

1. Water content is expressed in volume percent, and it is assumed that this is equivalent to the volume percent of fresh water, or the "hydrogen index." (It should be kept in mind that all neutron tools measure total hydrogen content, and hydrogen is present in many rocks and soils in forms other than free water.)

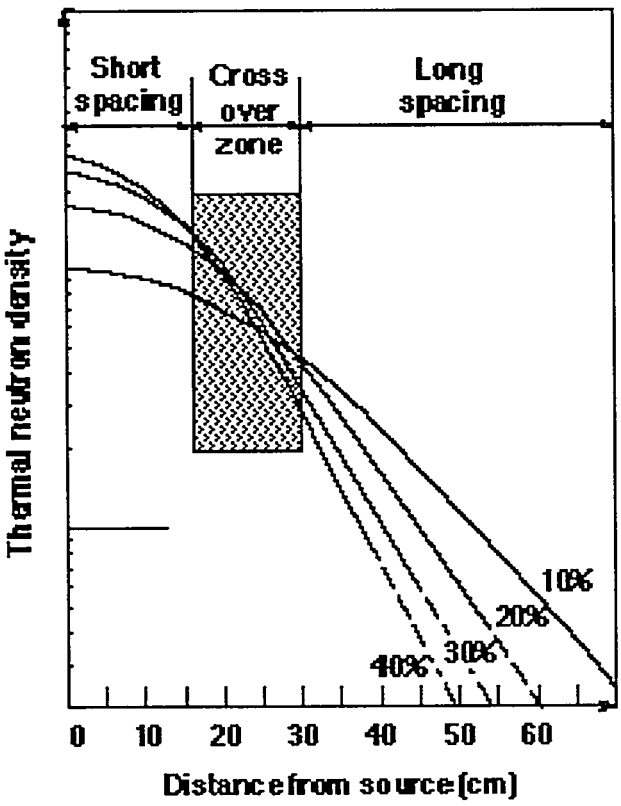


Figure 1. Thermal neutron density for a point source of Ra-Be neutrons in infinite formations with different water content. These curves were calculated using age theory, which is known to apply poorly to hydrogenous media. Thus they must be used as qualitative guides only. (Tittman, 1956)

2. We define the radius of investigation as the distance into the formation beyond which, if all material were removed, there would be no more than a 10% change in the neutron count rate.

3. A "tool" is the sensor portion of the instrument system used to make the water content measurements.

4. We define the source-detector spacing as the distance from the center of the source to the center of the detector. Note that detector lengths differ significantly from tool to tool.

5. We define the sensitivity as the change in the neutron count rate caused by a given change in water content.

To compare tools with greatly different count rates, it is convenient to express the sensitivity of a tool as

$$S = \frac{dc/dw}{(c_{max} - c_{min})/2}$$

where c is the count rate, w is the volume percent water, and c_{max} and c_{min} are the maximum and minimum values of the count rates over the range of water contents desired to be measured. (In practice, since different tools are calibrated over different ranges of water content, it is convenient to choose the range of water content to be the same for all tools being compared, and determine c_{max} and c_{min} from each tool's response curve.) Then, if all count rates are normalized by dividing by $(c_{max} - c_{min})/2$, the sensitivity as defined will simply be the slope of the plot of count rate vs water content.

Since the slope of the count rate vs water content plot for the neutron log is opposite in sign from that of the moisture gauge, all plots for the neutron log have been inverted. Thus the plotted sensitivities are comparable. We shall discuss the sensitivities as if they were the same sign.

THE MOISTURE GAUGE

A good general reference for the moisture gauge is *Neutron Moisture Gauges*, published by the International Atomic Energy Agency (1970). (It should be noted that some authors refer to the moisture gauge as a "moisture probe," "moisture meter," or occasionally even "neutron log.") The source-detector spacing of a moisture gauge is generally between zero (the source is a ring around the center of the detector) and 6 cm or so. The detector is designed for thermal neutrons. Figure 2 shows that the spacing strongly affects the sensitivity of the measurement, in agreement with Tittman's (1956) calculation. Calibrations above 40% water content are not shown in this figure. but it is evident in Figure 1 that the moisture gauge must lose sensitivity and become nonlinear at some water content above 40% (Preiss and Grant, 1964).

The tool is usually designed to either lie on the ground surface or be a close fit in a small-diameter (approx. 5 cm) tubing-lined borehole. The source is usually very weak (approx. 50 mCi AmBe or PuBe), and the tool is hand-held while being placed on the surface or lowered into the borehole. In a hole, the tool is lowered to different depths, and a measurement lasting tens of seconds is made at each depth.

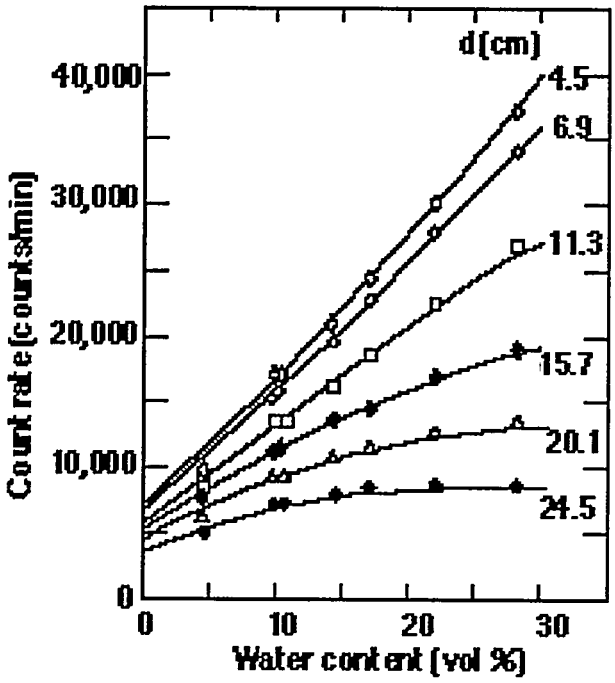


Figure 2. Effect of source-detector distance *d* on the calibration curve for a sub-surface neutron moisture probe with a short (1.25 cm long, 2.5 cm diameter ^{6}Li glass) detector situated at different distances from the source. (Olgaard and Haahr, 1967).

Because of the close fit, the borehole fluid and the gap between the borehole wall and the tool are usually irrelevant. However, experiments in boreholes significantly larger than the tool diameter have shown that placing the tool centered or decentralized in an air-filled hole 12 to 15 cm in diameter does not affect its sensitivity (Tyler, 1988; Klenke and Flint, 1991). On the other hand, because the count rate increases with water content, filling the hole with hydrogenous material, or even lining it with a thin layer of hydrogenous material, greatly reduces sensitivity (Tittman, 1956, Klenke and Flint, 1991; Goncalves et al., 1992).

The radius of investigation of any neutron tool depends on the water content. In the case of the moisture gauge, different investigators report different radii of investigation for tools with approximately the same source-detector spacing, depending on the design of their experiments. The most plausible values appear to range from about 20 cm for 5% water to about 14 cm for 32% water (Silvestri et al, 1991; Nyhan et al., 1983).

THE NEUTRON LOG

A good general reference for the neutron log is *Well Logging for Earth Scientists* by Ellis (1987) or *Well Logging for Physical Properties* by Hearst and Nelson (1984). The neutron log often has two detectors: a long-spaced one, with a source-detector spacing of 55 to 65 cm, and a short-spaced one, with a source-detector spacing on the order of 40 cm, which is used to correct the long-spaced data for borehole effects. If a two-detector tool is used, the detectors are generally designed for thermal neutrons, and the count rate is therefore perturbed by materials with a high capture cross section. If a single detector is used, it is generally surrounded by a thermal-neutron absorber such as cadmium so that mostly epithermal neutrons are counted, and the perturbation caused by absorbers is reduced.

The tool is generally run in uncased holes significantly larger than the tool diameter. It has a housing designed to resist formation fluid pressures as high as 150 MPa. It is commonly pulled up the hole at a speed of about 20 m/min, for distances on the order of km, and consequently the source is fairly large, often several curies.

Because the tool is smaller than the hole, its data are significantly perturbed by borehole diameter, rugosity, and fluid. The correction procedure developed by industry for the two-detector tool, which uses the ratio of counts in the two detectors, is designed for holes filled with hydrogenous liquid, and it is not satisfactory for use in dry holes (Alger et al., 1972). It is possible to correct the data from the long-spaced detector for these perturbations (Axelrod and Hearst, 1984). Consequently, we shall only discuss a single-detector tool in the remainder of this paper.

Sherman and Locke (1975) performed an elegant experiment that showed that the radius of investigation of both single- and two-detector thermal and epithermal neutron logs for water contents of both 22 and 35 vol% is about 18 to about 25 cm, depending on the design of the tool. This radius is somewhat larger than the radius for the moisture gauge. Note that the volume of investigation of the neutron log is markedly larger than that of the moisture gauge because of the much greater source-detector distance.

RELATIVE SENSITIVITIES

A good way to compare the moisture gauge and the neutron log is to compare their normalized sensitivities to water. Figure 3a shows sensitivity, as defined earlier, for different moisture gauges under various conditions. Although the absolute count rates vary greatly with differences in conditions, the sensitivities are essentially the same.

Figure 3b shows a similar plot for a single-detector epithermal neutron log in a water-filled and an air-filled

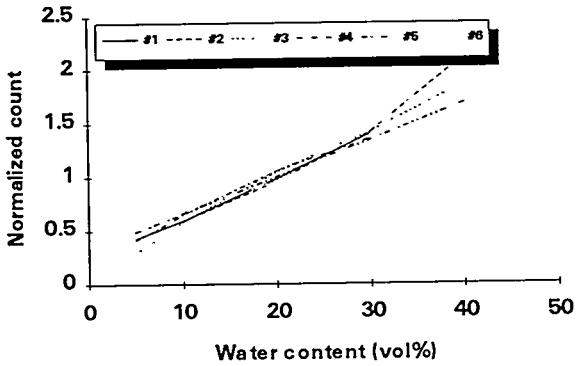


Figure 3a. Normalized count rate for moisture gauges: #1, 4.5-cm spacing 3 cm-dia gauge in tight-fitting hole (Olgaard and Haahr, 1967); #2, 5-cm spacing, surface gauge (IAEA, 1970); #3, 14-cm spacing 5.25 cm dia gauge in 7.5 cm tube (van Bavel et al, 1954); #4, zero spacing, 3.8-cm-diam gauge centered in 14-cm-diam casing (Tyler, 1988); #5, 8-cm spacing 3.8-cm-diam gauge sidewalled in 12.8-cm-diam casing (Klenke and Flint, 1991); #6, 5-cm-spacing, surface gauge with 0.038 cm Cd shield (Preiss and Grant, 1964). Normalization extrema at 10% and 30%.

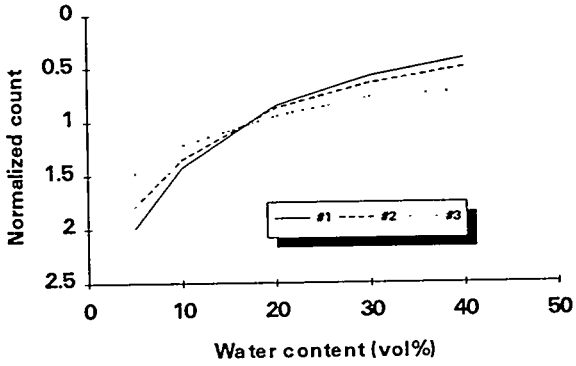


Figure 3b. Normalized count rate for sidewalled neutron logs: #1, Epithermal neutron log in 20-cm water-filled hole (Tittman et al., 1966); #2, epithermal neutron log in 20-cm air-filled hole (Tittman et al, 1966); #3, thermal-neutron gamma-ray log in 15-cm-diam water-filled hole (Tittman, 1956). Normalization extrema at 10% and 30%.

hole, and a thermal neutron log (with a gamma-ray detector, because data for single detectors of two-detector tools are not available in the literature) in a water-filled hole. Note that the thermal log is less sensitive than the epithermal log. Since that tool uses a gamma-ray detector, this difference in sensitivity does not necessarily indicate that a neutron log based on a single thermal-neutron detector would be less sensitive than an epithermal log.

It is clear that the epithermal neutron log is significantly more sensitive than the thermal moisture gauge at water contents below about 20%, and that the moisture gauge is significantly more sensitive than the neutron log at water contents above about 30%. For example, the slope for a moisture gauge in an air-filled hole (van Bavel et al., 1954) is about 0.038. For a neutron log in an air-filled hole between 5% and 10% water (Tittman et al., 1966), the slope is about 0.11. Between 30% and 40% water, it is about 0.016. Evidently the neutron log is at least twice as sensitive as the moisture gauge in the 5 to 10% range and half as sensitive in the 30 to 40% range.

The observable quantity for these tools is the number of neutrons detected by the detector over a specific time interval: the count rate. The precision expected in the measurement of the water content then depends on the precision of the measurement of the count rate, the relative change in count rate that is caused by a given change in water content, and changes in the count rate due to perturbations other than water content. In principle, with any of these tools one can select a source strength and/or counting time large enough that the relative error in determining the true count rate is insignificant. In that case, the difference in sensitivity is unimportant. Adequate precision can be obtained with either tool. Frequently, however, the maximum count rate is limited in two distinct ways. If the source must be very small, higher counts will be seen with the moisture gauge, and thus its precision will be better. If the count rate is limited by detector or electronics saturation, then the sensitivity is a useful way to compare different tools.

For any tool that depends on neutron transport through the formation, when both water content and bulk density are zero, no neutrons are returned to the detector, and so the count rate must also be zero. Consequently, at some combination of low values of density and water content the neutron log must have a maximum count rate. Below those values its count rate must decrease with decreasing water content, and it will behave like a moisture gauge. For example, we test tools for leakage through the shielding by suspending them in air. The count rate under those conditions is very small.

PERTURBATIONS

The literature (IAEA, 1970, for example) recommends that a moisture gauge be calibrated for each

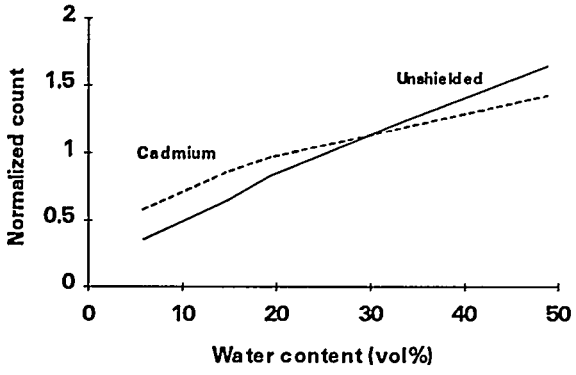


Figure 4a. Normalized count rate for an 8-cm-spacing moisture gauge in a 2.4-m hole in the NTS neutron calibrator, with and without cadmium shield. Normalization extrema 6 to 49%.

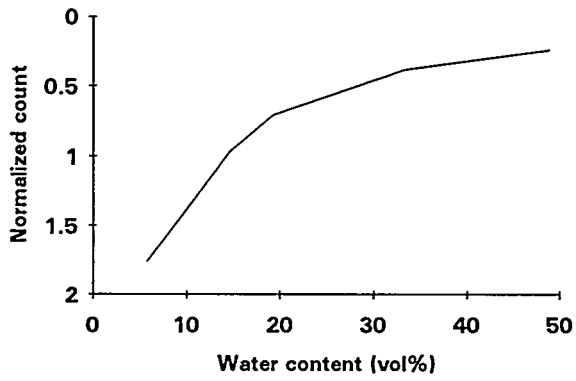


Figure 4b. Normalized count rate for a collimated 43-cm spacing epithermal neutron log in a 2.4-m hole in the NTS neutron calibrator. Normalization extrema 6 to 49%

specific soil in which it is used. Normally three properties of the formation cause perturbations in the neutron count rate: elements with high neutron-absorption cross sections, bulk density, and hydrogen that is not associated with free water. In addition, the count rate can be affected by changes in the size of the borehole and by gaps between the tool and the wall of the borehole.

The effect of non-pore water is independent of the type of tool, and some corrections can be made by measuring the non-pore water content of samples of the formation by heating to high temperatures or using nuclear magnetic resonance (McKague et al., 1992).

The effect of high-cross-section elements can be reduced by shielding the thermal-neutron detector with a shell of a thermal-neutron absorber such as cadmium (Preiss and Grant, 1964). This procedure, however, can affect the sensitivity of the tool.

The effect of the other perturbations in small boreholes is discussed in the literature, but each discussion refers to a specific tool. It would be useful to compare the magnitudes of each effect on the moisture gauge and the neutron log, to help users select a tool for a specific application. Therefore we compared the effects of bulk density and sonde-wall gap on a moisture gauge and a neutron log in the Nevada Test Site (NTS) neutron log calibrator. We also used calibrator data to investigate the effect of the cadmium shield.

The calibrator consists of two cylindrical aluminum shells, each 2.4 m inside diameter, 4.8 m outside diameter, and 2.3 m high. Each cylinder is divided into six 60° segments, and each segment is filled with a different mixture of silica sand, alumina, aluminum hydrate, and water. The mixtures are chosen to provide desired values of density and effective water content. Aluminum casings 30 and 5 cm in diameter pass vertically through each segment. In this experiment five cells, all having a bulk density of approximately 1.4 g/cm^3, were used to create a constant-density calibration curve. Water contents were 5.8%, 14.6%, 19.3%, 33.4%, and 48.9%. Then two other cells, with different bulk densities but the same water content as two of the first five, were used to investigate the density effect.

To reduce hole-size effects, the neutron log tools used at NTS are in most cases surrounded by polyethylene shields except where the tool contacted the wall of the hole. The shields are roughly elliptical in cross section, with the minor axis normal to the wall of the hole, and each tool is inserted into a cylindrical hole tangent to the circumference of its shield. For the 2.4-m hole, the major axis is about 45 cm and the minor axis about 22 cm.

Figure 4a shows the sensitivity of a moisture gauge in the 2.4 m central hole, with and without a 0.079-cm cadmium shield. This shield has twice the thickness of the shield used by Preiss and Grant (1964), for which the sensitivity is shown in Fig. 3a, and the same thickness as the shield in our commercial epithermal neutron log. The sensitivity of the unshielded tool agrees with those shown in Figure 3a. The 0.079-cm cadmium shield substantially reduces the sensitivity of the gauge to the point that it is not much more sensitive than the neutron log at high water content. Evidently, although a 0.038-cm cadmium shield

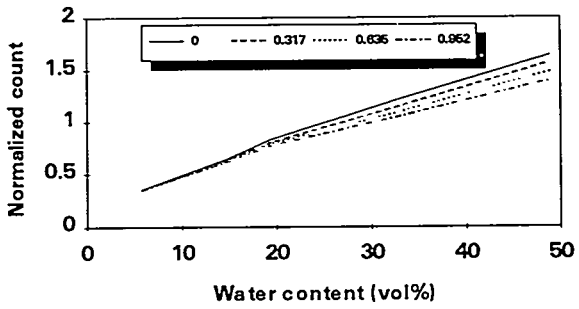


Figure 5a: Normalized count rate for an 8-cm-spacing moisture gauge in a 2.4 m hole in the NTS calibrator at different gaps between the tool and the wall of the hole. The legend shows the gap in cm. Normalization extrema 6 to 49%

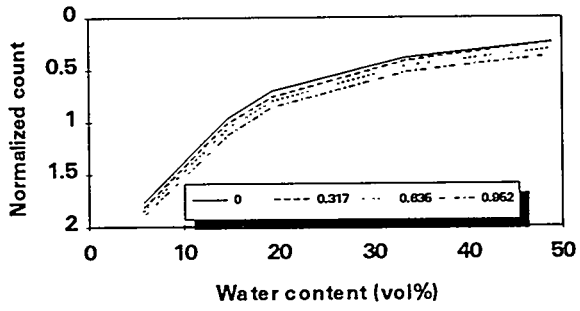


Figure 5b. Normalized count rate for a collimated epithermal neutron log in the NTS calibrator at different gaps between the tool and the wall of the hole. The legend shows the gap in cm. Normalization extrema 6 to 49%.

does not significantly affect the sensitivity, doubling the thickness does. We have no data on the effect of cadmium thickness on reduction of the effect of high absorption cross-section elements. Figure 4b is a similar plot of a neutron log, with a built-in 0.079 cm cadmium shield, again in the 2.4-m-diameter central hole. The sensitivity of this tool agrees with those seen in Figure 3b. Each tool was forced against the wall of the hole.

The simplest way to compare the effects of other perturbations among tools is to calculate the water content that would be obtained using a standard calibration curve, such as those in Figure 4, with and without the perturbation, and then compare the derivative of the calculated water content with respect to the size of the perturbation.

Effect of density

The effect of bulk density on a moisture gauge in a small-diameter hole is discussed by Couchat (no date), cited in IAEA (1970). No hole size or gauge type is stated. Couchat found that a change in bulk density of 0.4 g/cm^3 changed the apparent water content by about 4 vol% at water content values of both 20 vol% and about 35 vol%. This change gives a derivative of 10 vol% water per g/cm^3. The effect of density on an epithermal neutron log in a 30-cm hole is similar to the effect seen in the 2.4-m hole, discussed below (Axelrod and Hearst, 1984.).

In our tests in the 2.4-m hole, we used two cells with densities higher than those used to obtain the curves in Figure 4. One had a bulk density of 1.88 g/cm^3 and water content of 20.3% to compare with the cell of bulk density of 1.34 g/cm^3 and water content of 19.3%. The other had a bulk density of 2.44 g/cm^3 and water content of 32.9% to compare with the cell of bulk density of 1.34 g/cm^3 and water content of 33.4%. We found that the density effect was a function of water content and was approximately the same for the moisture gauge and the neutron log. The derivative is about 5 vol% per g/cm^3 at 20 vol% water and 15 vol% per g/cm^3 at 33 vol% water. It is, of course, feasible to correct the water content for the effect of density using data from a density log (Axelrod and Hearst, 1984). In fact, some moisture gauges include density logs, and automatic, in-field, corrections could easily be developed.

Effect of borehole size

Abeele (1979) observed the effect of hole size from 5.1 to 10.2 cm on a centralized moisture gauge and found it to vary from 0.07 vol% per cm at 5 vol% water to 1.2 vol% per cm at 27 vol% water. Tittman et al. (1966) obtained similar results for a decentralized neutron log over a larger range of hole sizes: 0.08 vol% per cm at 5 vol% water to 1.1 vol% per cm at 30 vol% water.

Effect of tool-wall gap

In small air-filled holes, data are sparse for both tools. Abeele (1979) states that the count rate of a 5-cm-dia moisture gauge does not depend on whether a tool is centered or eccentered in an air-filled hole up to 10.2 cm in diameter. Tyler (1988) suggests that an effect is observed in a 14-cm hole. The effect of gap on an epithermal neutron log in a 30-cm hole is similar to that in the 2.4-m hole discussed below (Axelrod and Hearst, 1984).

Figure 5 shows the effects of gap on the moisture gauge and the neutron log in the 2.4-m hole in the NTS calibrator. For the moisture gauge the effect is negligible at 10 vol% water and becomes as high as 0.8 vol% per cm at 40 vol% water. For the neutron log, the effect is somewhat larger: 0.2 vol% per cm at 10 vol% water and 1 vol% per cm at 40 vol% water. For either tool, it is possible to measure the gap and apply a correction if desired (Axelrod and Hearst, 1984).

DISCUSSION

The petroleum industry has, quite justifiably, used the neutron log because the moisture gauge is overwhelmed by hydrogenous fluids in fairly large, liquid-filled holes, which are normal in petroleum wells. It is clear that the neutron log is the appropriate method for any hole filled with hydrogenous fluid unless the tool is a tight fit in the hole.

At NTS, however, we commonly use neutron diffusion to measure water content from air-filled boreholes. The effects of perturbations are similar for the two tools. The effects of density and borehole size are about the same for the two methods and so need not be considered. The moisture gauge is affected somewhat less by the gap between the tool and the wall of the hole than the neutron log and, because it is much shorter than the neutron log, the gap is likely to be smaller. This difference, however, is not usually a major consideration. The remaining choice then concerns the sensitivity, because the more-sensitive tool can be used with a smaller source or run at a higher logging speed.

If a smaller radius of investigation is desired, the moisture gauge is the tool of choice in high-water-content formations (but note that even the moisture gauge loses sensitivity above about 40 vol% water). If a large volume of investigation (with its consequent poor depth resolution) is acceptable, the neutron log is the tool of choice for low-water-content formations. If the entire range of water content is expected, the moisture gauge will give better thin-bed resolution and a smaller overall numerical uncertainty, whereas the neutron log will give a smaller overall fractional uncertainty.

It is not practical to run a conventional moisture gauge in a deep hole because its cable is so short, it is not watertight, and its source is so small that it must be operated at fixed stations. It is also impractical to use the logging winch, the many-km-long cable, and the heavy pressure casing of a neutron log in short holes. It would not be difficult to produce moisture gauges with long spacings or neutron logs with short spacings. (Some laboratory tools have already been built with variable spacings; such tools might also be commercially feasible.) Then we could choose the spacing on the basis of bed-thickness resolution and sensitivity to water, without being constrained by operating characteristics such as source size, logging speed, cable length, or the need for a winch with depth-drive mechanism.

ACKNOWLEDGMENT

This work was performed under the auspices of the U.S. Department of Energy by the Lawrence Livermore National Laboratory under Contract W-7405-ENG-48. The work was supported by the LLNL Nuclear Test Containment Program.

REFERENCES

Abeele, W. V. (1979) The Influence of Access Hole Parameters on Neutron Moisture Probe Readings, Los Alamos National Laboratory, Los Alamos, N. M., LA-8094-MS.

Alger, R. P., Locke, S., Nagel, W. A., and Sherman, H. (1972) The Dual-Spacing Neutron Log - CNL, *Jour. Pet. Tech.* 24, 1073-1083.

ASTM (1988), Standard Test Method for Water Content of Soil and Rock in Place by Nuclear Methods (Shallow Depth), Annual Book of ASTM Standards, American Society for Testing and Materials, Philadelphia, PA, . 411-415.

Axelrod, M. C., and Hearst, J. R (1984) Calibration of a Neutron Log in Partially Saturated Media IV: Effects of Sonde-wall Gap, *Proc. Soc. Prof. Well Log Analysts 25th Annual Symposium*, New Orleans, June 10-13. Paper Q.

Belknap, W. B., Dewan, J. T., Kirkpatrick, C. V., Mott, W. E., Pearson, A. J., and Rabson, W. R. (1960), API Calibration Facility for Nuclear Logs, Am. Petr. Inst. Drilling Production, . 289

Buscheck, T., Carlson, R., Daily, W., Lee, K., Lin, W., Mao, N., Ramirez, A., Ueng, T., Wang, H. and Watwood, D. (1991), Prototype Engineered Barrier System Field Test (PEBSFT) Final Report, Lawrence Livermore National Laboratory, Livermore CA, UCRL-ID-106159.

Couchat, P. (no date), The Neutron Method for Measuring Soil Moisture, CEA Report 3298.

Ellis, D. V. (1987), Well Logging for Earth Scientists. Elsevier, New York.

Goncalves, I. F., Salgado, J. and Carvalho, F. G. (1992)., Calibration of a neutron moisture gauge by Monte-Carlo Simulation. *Nuc. Geophys.* 6, 371-381.

Hearst, J. R, and Nelson, P. H., (1984) Well Logging for Physical Properties, McGraw-Hill, New York.

IAEA (International Atomic Energy Agency) (1970), Neutron Moisture Gauges, Technical Report Series 112, Vienna.

Klenke, J. M., and Flint, A. L. (1991), Collimated Neutron Probe for Soil Water Content Measurements. *Soil Science Society of America Jour*, 55, 916-923.

McKague, H. L., Hearst, J. R, Ward, R. L., and Burkhard, N. R. (1992), Nuclear Magnetic Resonance Determination of the Nonpore Water Content of Zeolitic Tuffs and its Application to Correction of Epithermal-neutron-derived Water Content *Nuc. Geoph.* 6, 359-366.

Nyhan, J. W., Drennon, B. J., Rodgers, J. C., and Abeele, W. V. (1983), Spatial Resolution of Soil Water Content by Three Neutron Moisture Gauges. Los Alamos National Laboratory, Los Alamos N. M., LA-UR-83-2863.

Olgaard, P. L., and Haahr, V. (1967), Comparative Experimental and Theoretical Investigations of the DM Neutron Moisture Meter Probe. *Nuclear Engineering and Design* 5, 311-324.

Preiss, K., and Grant, P. J. (1964), The Optimization of a Neutron Scattering Water Content Gauge for Soils and Concretes, *Jour. Sci. Instrum.* 41, 548-551.

Sherman, H., and Locke, S. (1975), Effect of Porosity on Depth of Investigation of Neutron and Density Sondes, Society of Petroleum Engineers Paper SPE-5510.

Silvestri, V., Sarkis, G., Bekkouche, N., Soulie, M., and Tabib, C., (1991), Laboratory and Field Calibration of a Neutron Depth Moisture Gauge for Use in High Water Content Soils, *Geotechnical Testing Journal, GTJODJ*, 14, 64-70.

Tittman, J. (1956), Radiation Logging, in *Fundamentals of Logging, University of Kansas Petroleum Engineering Conference,* University of Kansas, April 2-3.

Tittman, J., Sherman, H., Nagel, W. L., and Alger, R. P. (1966) The Sidewall Epithermal Neutron Porosity Log, *Jour. Pet. Tech.* 18, 1351-1362.

Tyler, S. W., (1988), Neutron Moisture Meter Calibration in Large Diameter Boreholes. *Soil Society of America Jour.* 52, 890-893.

van Bavel, C. H. M., Hood, E. E., and Underwood, N. (1954), Vertical Resolution in the Neutron Method for Measuring Soil Moisture, *Trans. Am. Geophysical Union* 35, 595-600.

MAXIMUM LIKELIHOOD BOREHOLE CORRECTIONS FOR DUAL-DETECTOR DENSITY LOGS

RICHARD C. CARLSON

Lawrence Livermore National Laboratory, P. O. Box 808, Livermore, CA 94551

ABSTRACT

Dual-detector density logs have been used in the petroleum industry for years. The tool was designed with a second detector to allow compensation for the effect of a layer of mudcake between the tool and the formation being measured. The compensation algorithm commonly used calculates the correction to apply to the density measured by the long-spaced detector as proportional to the difference in the densities measured by the two detectors. The coefficient of proportionality is determined from experimental data taken with the tool in a fluid-filled hole of 15 to 40 cm diameter, with uniform thickness sheets of various materials simulating the mudcake. In applying this technology for the Containment program at the Department of Energy Nevada Test Site (NTS) we have discovered two problems. First, we frequently log in air-filled holes much larger than 40 cm. Correlations between the corrected data and the amount of correction applied suggest that the standard algorithm undercorrects in these circumstances. Second, the gap, or layer, is rarely uniform with depth or vertical position on the face of the tool. We have found that when the source end of the tool makes better contact with the wall than the detector end, the standard algorithms will undercorrect the data. When the reverse is true, the algorithm can overcorrect the data. We have developed a method to determine the proper amount of correction dynamically. No experimental data on the gap effect are needed as long as the two detectors are calibrated to read the proper density when the gap is zero. The method assumes that the form of the equation used in the standard algorithm is correct, but uses the variation of the two density signals with depth to determine the appropriate value of the coefficient, assuming true density varies more slowly than the gap effects. Essentially, at each depth point we use that value of the coefficient which would produce the smoothest density over a short depth interval of the log centered at the depth of interest. A least squares method which assumes both axes of the fit have significant noise is used. Ironically, the expression used is simpler than the standard one which assumes no error in the independent variable. This new, maximum likelihood, method appears to work better than the standard method in both fluid and air-filled holes where the borehole wall is rough and no mudcake is present. It cannot, however, correct for a uniform mudcake or air gap, and so complements but does not replace the standard method.

INTRODUCTION

Dual-detector density logs were introduced to the logging industry nearly 30 years ago (Wahl, et al, 1964). The tool was designed with a second detector to allow compensation for the effect of a layer of mudcake or drilling fluid between the tool and the formation being measured. The original paper recognized that the compensation method required the layer or fluid-filled gap to be uniform or the tool to be parallel to the borehole wall, and would over or undercorrect if this was not the case. The amount of correction to apply to the apparent long-spacing density was derived from the count rates of the two detectors using an undisclosed algorithm which did not depend on bulk formation density. The algorithm was derived from laboratory measurements of tool response where formation density and the thickness and density of the layer were known. It was shown to be accurate for corrections less than .1 gm/cc, with formation density dependent errors becoming significant beyond that point. It was emphasized that individual measurement of layer thickness and density was not required to correct logging data.

In applying this technology for the Containment program at the Department of Energy Nevada Test Site (NTS) the problems described above are particularly severe. Because the holes are air-filled, the density contrast between the layer and formation is almost double that seen in mud-filled holes. In addition, the historical coefficients determining the magnitude of the correction are only readily available for mud or water-filled holes of 150 to 400 mm diameter, while we must log holes as large as 4 m in diameter. Because the holes are drilled in weak tuffs and alluviums they are rugose, and the gap, or layer, is rarely uniform with depth or vertical position on the face of the tool. The tool cannot be parallel to the wall because some part of the tool is almost always in contact since the face of

the tool is pushed against the wall. The tool can ride up the hole with the source end in contact, the (far) detector end in contact, or some point in between. Note that a layer of mudcake between the tool and the borehole wall is equivalent to a gap filled with a material of mudcake density. In the balance of this paper we will refer to all such space between the tool and wall as a gap, defining the particular density only when needed.

Figure 1 shows corrected density and the amount of correction applied on a industry standard compensated density log in a large water-filled hole with no mudcake. It illustrates the type of logging results which ultimately led to development of the current method. Since one would not expect the true formation density to be influenced by the degree to which the tool fails to make contact with the wall, a strong correlation of the correction curve with the corrected density curve suggests over-correction. By the same argument, the anti-correlation observed in Figure 1 suggests undercorrection.

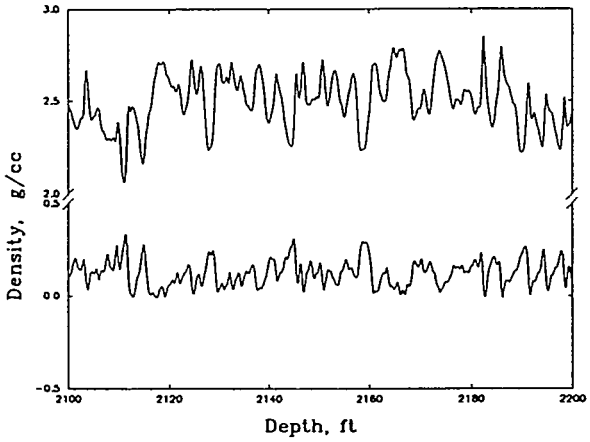


Figure 1. Corrected density and the amount of correction from a large water-filled hole with rough walls, using the standard method.

The two detectors can be calibrated to read the same density when in contact , i.e., when the gap has zero thickness, and more recent correction algorithms are written in terms of the apparent densities seen by the two detectors instead of the count rates observed (Tittman, 1986). An equation of the form:

$$\rho_t = \rho_l + \alpha(\rho_l - \rho_s) \qquad 1)$$

is commonly used, where ρ_t is the true density, ρ_l and ρ_s are the long and short detector apparent densities, and α is the coefficient of proportionality (Ellis, 1987).

In Figure 2 we plot short-spaced, long-spaced, and corrected densities at the same scale, versus depth, using the standard algorithm. The formation in this interval is strong and should have a fairly uniform density with a value near the peak values seen in the figure. Those peak values, of course, are the locations where the long and short-spaced densities agree, and no correction is needed. Note that where the long-spaced density dips, the short-spaced data does also, and more vigorously. The dips in the corrected density at these locations is an indication that more correction is needed there.

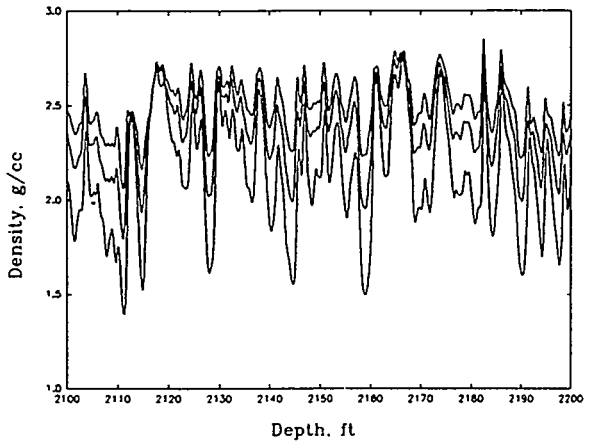


Figure 2. The corrected density of Figure 1, along with the associated long and short-spaced apparent densities (upper, middle, and lower curves respectively).

Figure 3 shows data from a gap test of a commercial two-detector sonde on blocks of known density, and with a radius of curvature of 220 mm. The

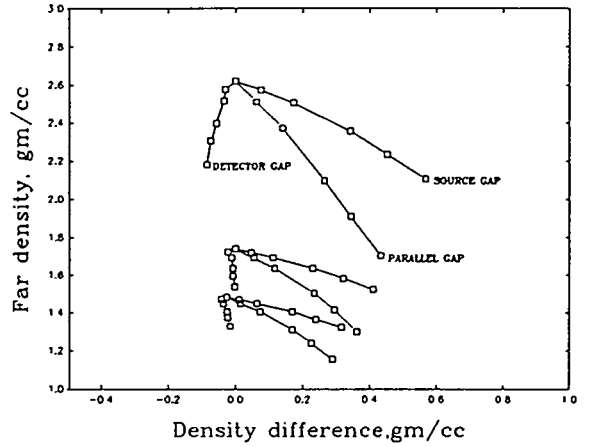


Figure 3. Data from a gap test of a commercial two-detector density tool on blocks of known density and 220 mm radius of curvature.

electron densities of the blocks are 1.48, 1.74, and 2.62 gm/cc. On each block the count rates of the two detectors were recorded with the sonde in contact, and with 6, 13, 19 and 25-mm shims inserted between the sonde and the block. The shims were inserted in three separate ways, at the source end of the sonde, at the far detector end of the sonde and at both ends equally. These are identified in the figure only for the 2.62 density block, since the data sets for the three blocks are similar in shape. The countrates were calibrated to density by a semilog fit of the zero-gap counts to the known block densities. In the figure the long spaced density is plotted versus the difference in density seen by the two detectors. The degree to which each set of data points can be fit with a straight line is an indicator of the validity of Eq. 1) at any particular formation density. The different slopes for the data from the different blocks (identified by their intercept with the ρ_l axis) shows that the value of α in Eq. 1) varies with formation density. It is also apparent that if the source end is in contact on a flat surface, the gap at the detector end affects both detectors' density readings by nearly the same amount, i.e.,ρ_l-ρ_s=0, so no correction would be applied by Eq 1) even though correction is needed. On the other hand, a gap at the source end with the detector end in contact would be overcorrected by the standard approach.

Figure 4 shows the data of Figure 2 plotted in the manner of Figure 3. The short-spaced data are shifted in depth by .125 feet to align them with the long-spaced data. The data are clearly structured and amenable to fitting by Eq 1). One can even see a non-linearity in the data which suggests possibilities for further improvement. The entire 100-foot interval is shown here, so some of the spread is because of changing formation density.

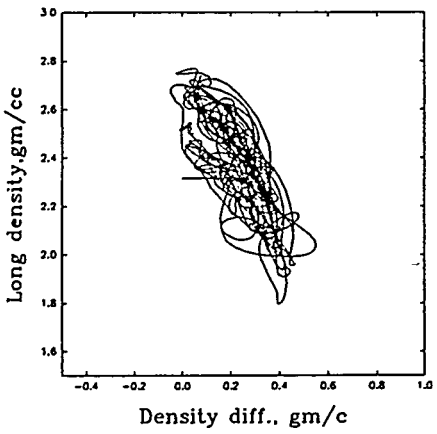


Figure 4. Long spaced density of Figure 2 versus the difference between long and short-spaced densities. The full 100-foot interval is shown.

The foregoing discussion shows that the proportionality coefficient in the two-detector algorithm changes with the mode of contact and formation density and therefore can vary with depth in the hole. We have developed a method to determine the coefficient dynamically. The method assumes the same model described above in Eq 1) but does not require parallelism. It uses the variation of the two density signals with depth to determine the value of the coefficient most consistent with that model, assuming true density varies more slowly than the gap effects. We call this method maximum-likelihood compensation (MLC) because, essentially, this is a maximum likelihood (for Gaussian distributions, least squares) fitting process.

THEORY

Almost all standard least square fitting routines assign all error to the dependent, or y axis. This is equivalent to minimizing the sum of the squares of the **vertical** distance of each point from the fitted line, and these routines may not perform properly if both axes of the fit have significant noise. This assumption is much more important than one might at first suppose, because the value determined for the fitted slope can vary greatly depending on the choice made. The choice is particularly important when the variance of the data points from the fitted line is large, but because there are a large number of points, the expected error of the fit is relatively small. There is ample discussion of this problem in the literature on statistical theory, but little in the applied journals (Rock and Duffy, 1986), which is perhaps why most of us usually assume all error in the y, or dependent, data, even though errors can be very large. We derive a solution as follows:

If we have a data set of x and y values which fits a model of the form:

$$y=\alpha x+b$$

with no error, then the slope can be calculated as:

$$\alpha=\sigma_y/\sigma_x,$$

where σ_y and σ_x are the standard deviations of y and x. If, instead, we have a data set:

$$x=\mathbf{x}+\varepsilon_x$$
$$y=\mathbf{y}+\varepsilon_y$$

where the x and y have errors ε_x and ε_y, independent of the true values **x** and **y** respectively, the calculated standard

deviation will be related to the standard deviation of the true values and the standard deviation of the errors, by:

$$\sigma_x^2=\sigma_{\mathbf{x}}^2+\sigma_{\varepsilon_x}^2$$
$$\sigma_y^2=\sigma_{\mathbf{y}}^2+\sigma_{\varepsilon_y}^2$$

We can now solve for the standard deviations of the true values of **x** and **y** and calculate the slope, α:

$$\alpha=\frac{\sqrt{\sigma_y^2-\sigma_{\varepsilon y}^2}}{\sqrt{\sigma_x^2-\sigma_{\varepsilon x}^2}}=\frac{\sqrt{1-\frac{\sigma_{\varepsilon y}^2}{\sigma_y^2}}}{\sqrt{1-\frac{\sigma_{\varepsilon x}^2}{\sigma_x^2}}}\bullet\frac{\sigma_y}{\sigma_x}=\frac{R_y}{R_x}\bullet\frac{\sigma_y}{\sigma_x} \qquad 2)$$

Where R_y is the standard "coefficient of correlation" or "goodness of fit" parameter and R_x is its analog for errors in x. The sign of α must be the same as sign of the cross-correlation of x and y, in our case always positive.

This solution reduces to standard least squares when $\varepsilon_x=0$, although in that case we can solve for, rather than estimate, ε_y. It also agrees with a result published elsewhere (Miller, 1986) which allocates the expected errors to the x and y axes via a parameter λ which defines their ratio. The slope can then be determined without specifying ε_y or ε_x. The form of equation 2), however, suggests a symmetry not mentioned by Miller; that if we assume the x and y errors are equal when scaled by the x and y standard deviations, or ranges, i.e.:

$$\frac{\sigma_{\varepsilon_y}}{\sigma_y}=\frac{\sigma_{\varepsilon_x}}{\sigma_x}$$

then R_y is equal to R_x, and the ratio reduces to 1.0, regardless of the specific values of ε_y or ε_x. This then is an implicit assumption of the current method, since we calculate the slope as:

$$\alpha=\frac{\sigma_y}{\sigma_x} \qquad 3)$$

APPLICATION

Using Eq. 3), where the y axis is the long-spaced density and the x axis is the density difference between the two detectors, and calculating the standard deviations over the 4 ft of data surrounding each depth of interest, produces α as a function of depth as shown in Figure 5. This varying α is then used in Eq. 1) with the long and short-spaced density data in a point-by-point fashion to obtain a corrected density. Figure 6 is the analog of Figure 2, done by the new method for comparison. Note that the dips in

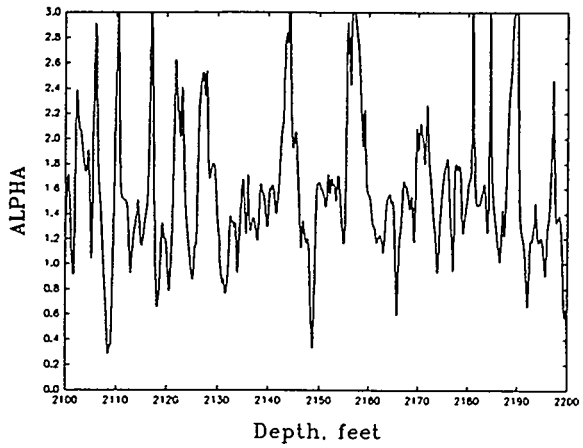


Figure 5. The correction coefficient, α, for the data of Figure 2, determined by the MLC method.

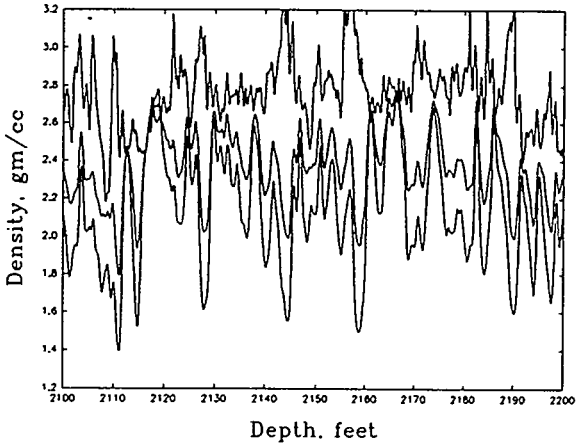


Figure 6. Long and short-spaced density of Figure 2 with the corrected density from MLC (middle, lower, and upper curves respectively).

density have been removed, and the result is more uniform in depth, riding the peaks of the uncorrected densities as it should. There are a few high density excursions, e.g., at 2144 and 2156 feet, apparently due to the non-linearity noted in Figure 4. The fitting windows at these locations contain no low values for the density difference, lying entirely in the right half of the data of the figure, beyond the bend in the data trend. Extrapolating this data past the bend to the vertical axis would produce overcorrection. We expect to improve this by using a non-linear model in place of Eq. 1). Note that this is a difficult case, with high formation density and rough wall, and requires corrections

as large as 1.0 gm./cc, well beyond the 0.1 gm/cc range over which the standard algorithm is considered applicable

Figure 7 shows an example from a 17.5-inch air-filled hole with an interesting gap problem we have seen several times. The density tool used is again an industry standard two-detector tool. Because of the drilling methods or hardware used, the hole follows a helical path with a pitch of about 10 m. This produces a sinusoidal gap variation. The figure overlays the density produced by the standard algorithm on the logging truck with the MLC corrected density. Also shown is the standard correction curve from the logging truck. Both the logging company curves show the 10-m oscillations, but the MLC curve does not, tracking the peaks of the logging company density data and producing a more uniform curve.

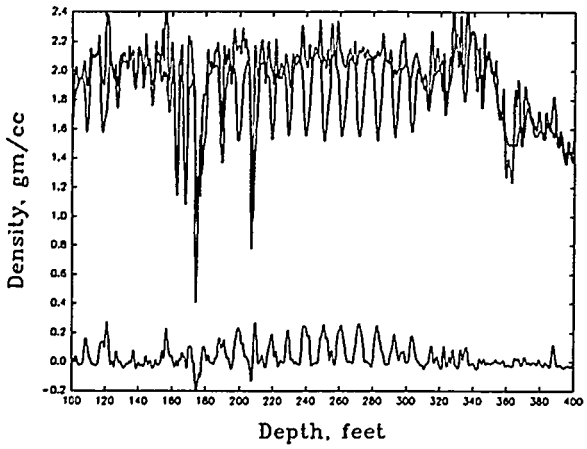


Figure 7. MLC corrected density, logger corrected density and logger correction curve (upper, middle and lower curves respectively), for a 17.5" air-filled hole.

CONCLUSIONS

The MLC method appears to be superior to the standard method in the cases examined so far, and is especially recommended where strong correlations are observed between the standard corrected density and its associated correction curve. The standard method relies on expensive experimental data to determine the value of α and the conditions under which the data are taken may not match the downhole environment. A major strength of the MLC method is that it allows α to vary with depth to suit downhole conditions. The method doesn't care what causes the perturbations to ρ_l and ρ_s, only that they occur proportionately. So if gap varies with depth due to borehole roughness or a varying angle from parallelism the MLC method can correct appropriately. It cannot, on the other hand, correct for a constant gap, or a constant deviation from parallelism. Thus in smooth, liquid-filled holes with uniform mudcake, the standard method may work better than MLC, if the value of α is appropriate. In rougher holes with no mudcake, either air or liquid filled, the MLC method may be better. Neither method can work if the gap occurs predominantly at the detector end, for that case gap measurement devices are needed.

In applying this method plots like Figure 3 should be examined to be sure the long and short-spaced densities approach equality at their peaks. Their failure to do so generally indicates improper calibration or an unusual downhole situation such as a glob of mud lodged over one of the detector ports in an air-filled hole. The long and short-spaced densities required are not normally shown on the log, but the data, at least in the form of count rates, are usually available on tape and the associated calibration data can generally be found in the heading/calibration data on the log. We recommend requesting this data from the logger, if only for Q/A purposes. The calibration must be such that the two detectors would read the same when in full contact with the wall in the downhole environment expected (holesize, mud weight, etc.). The log analyst must also ensure that the two detector curves register in depth, as the loggers do not always do this with sufficient accuracy.

We consider the MLC method to be of very general applicability, with this application to two-detector density a first example of its usefulness. While it is common to do statistical fits on data sets to determine underlying structure, e.g., the various cross-plots done by log analysts, we are not aware of efforts to do so in a sliding window, obtaining a fit which can vary with position in the data set. We expect to apply this method to other log types such as neutron and sonic, as well as between log types to infer rock properties not directly measured by the separate logs.

ACKNOWLEDGMENT

This work was performed under the auspices of the U. S. Department of Energy by the Lawrence Livermore National Laboratory under Contract W-7405-ENG-48. The work was supported by the LLNL Nuclear Test Containment Program.

REFERENCES

Ellis, Darwin V., (1987), Well Logging for Earth Scientists, Elsevier, New York.

Miller, Rupert G. (1986), Beyond ANOVA, Basics of Applied Statistics, John Wiley & Sons, New York.

Rock, N., M., S., and Duffy, T., R. (1986), Regres: A Fortran Program To Calculate Nonparametric and "Structural" Parametric Solutions to Bivariate Regression Equations, *Computers & Geosciences,* Vol. 12, No. 6, pp. 807-818, Pergammon Journals Ltd., Great Britain.

Tittman Jay (1986), Geophysical Well Logging, Excerpted from Methods in Experimental Physics, *Geophysics*, Vol. 24, Academic Press, Orlando, Florida.

Wahl, J. S., and Tittman, J., The Dual Spacing Density Log, Society of Petroleum Engineers Paper SPE-989.

An *In-Situ* Check of the Epithermal Neutron Log Calibration

Norman R. Burkhard
Lawrence Livermore National Laboratory
L-221, P.O. Box 808, Livermore, CA 94551-0808

Abstract

The epithermal neutron log is used to measure the water content of the formation. The large hole epithermal neutron sonde (ENS) that we utilize at the Nevada Test Site (NTS) has been calibrated in the Hydrogen Content Test Facility (HCTF). These calibrations are used to correct the measured neutron count rate for the effects of tool stand-off and density. For sometime, the suspicion has existed that the water contents that are calculated from the ENS data are too large. Hole U2gj represented a unique opportunity to check the validity of the ENS calibration under realistic logging conditions; a portion of the hole had been cemented and re-drilled and then logged. The cements have a known water content and can be used as an *in-situ* calibration check. I found that the water contents from the log data after processing with the existing calibrations are consistent with these known cement water contents. In addition, the study indicates that the raw neutron data might be more appropriately smoothed by using a median smoother rather than the currently utilized mean smoother.

Introduction

The epithermal neutron log measures the total hydrogen content of the formation; the water content of the formation is calculated from the total hydrogen content. The large hole epithermal neutron sonde (ENS) that we utilize at the Nevada Test Site (NTS) has been calibrated in the Hydrogen Content Test Facility (HCTF) [1]. These calibrations are used to both convert the measured neutron count rate to water content and correct the measured neutron count rate for the effects of tool stand-off and formation density. For sometime, the suspicion has existed that the water contents that are calculated from the ENS data are too large. This suspicion is particularly strong when the measured water contents exceed about 20 wt % or 40 vol %. The implication is that the corrections that have been derived from the HCTF calibration data are, for some reason, not correct in a real logging situation.

Several hypotheses have been formulated to explain why the calibrations may not be correct. The calibrations are done in a static configuration with fixed standoffs with the sonde parallel to the calibrator's hole wall; the standoffs represent gaps between the logging sonde and the hole wall. However, the ENS is moving while counting is taking place in the real logging situation. Because of the size and geometry of the ENS logging sonde, the sonde is not always parallel to the hole wall since the tool is moving across a very rough hole wall. A real drill hole is not a right circular cylinder! While the gap between the sonde and the hole wall can be determined quite accurately in the calibration process, the gap between the sonde and the hole wall in a realistic logging situation is very difficult to determine. The gap cannot be measured at the neutron detector itself because the gap measuring device would interfere with the detection of the neutrons. Hence, the gap is measured at both ends of the sonde on the log. During processing, these gap measurements are combined with some assumptions about ENS tool behavior in order to derive a gap to be used to correct the raw neutron counts for tool standoff. The calibration data are also taken with the sonde stationary and the epithermal neutrons are counted for long time intervals to reduce the counting statistics errors. In the real logging situation, the sonde is not stationary; the ENS is run dynamically at logging speeds at about 30 ft/min (~0.15 m/s).

The LLNL hole U2gj provided us with the unique opportunity to determine whether the suspicions about the log were correct. Extensive caving occurred in U2gj during the drilling process. The portion of the hole that experienced this extensive caving was cemented and then redrilled. The hole was logged in normal manner after the drilling operation was completed. As the LLNL site geophysicist for U2gj, I had the normal log processing conducted for this site. In this process, the data from the cemented zone is removed (gapped out) from the log since it is not representative of the formation. Sometime later after considerable debate about the validity of ENS data in general, it occurred to me that the U2gj cement zone represented a unique opportunity.

The U2gj cement zone could be used to check *in-situ* the calibration of the ENS log if several conditions were meet. The cement after drilling needed to have an annular thickness which exceeded the depth of investigation of the ENS log. The cement zone needed to be sufficiently long to eliminate "end effects". The cement zone needed to have regions of distinctly different water content. The cement zone's roughness (rugosity) needed to be similar to rugosity of drill hole elsewhere so that gap measurements in the cement zone would have the same characteristics as the gap measurements in the rest of the drill hole.

The Cement Zone in U2gj

While drilling hole U2gj to a total depth of 1697 ft (517.2 m) during February, 1991, hole sloughing occurred several times. A caliper tool was run and a hole enlargement which exceeded the measurement limits of the caliper tool spanning the depth range 1340 ft to 1380 ft was discovered. After backfilling the hole to 1378 ft., the hole was cemented in six stages using Redi-Mix cement, Type II cement, and HPNS-3 grout. A small quantity of Type II cement was used to complete a 3 ft stage that first used 3240 ft^3 of HPNS-3 cement and was topped of with 162 ft^3 Type II cement. I have ignored the presence of the Type II cement in the analysis that I have conducted. The hole was redrilled and another caliper log was obtained. However, I do not know if the void that existed and was filled with cement was symmetric with respect to the original centerline of the hole. I also do not know if the drill bit upon redrilling followed the original centerline of the hole. Therefore, I cannot know what the exact thickness of the cement might actually be at any particular depth and orientation in the hole. However, if I assume that the void that was filled is circular symmetric and that the redrilling followed the original centerline in the hole, the thickness of the cement in all stages exceeds 25 inches (~63 cm) and for a significant portion of the hole exceeds 125 inches (~317 cm) (Figure 1).

The water contents of each cement type can be calculated from the mix formulas used for the U2gj cementing job. The water contents calculated from the mix formulas of HPNS-3 grout and the U2gj Redi Mix was 64 and 36 vol %, respectively (see Appendix 1). These calculated water contents ignore any evaporization losses, ignore any water loss to the surrounding formation, and ignore changes in volume percentage water content due to contraction of the cement or grout. Contractions of these cements are on the order of 2 vol % or less; a 2 vol % contraction would increase the water content in volume percent by less than this amount. Since drill holes are typically very humid and the cemented zone is very thick, it seems reasonable to assume that significant volumes of water were not lost to evaporization or into the formation. I cannot, however, demonstrate this. Therefore, I estimate that the error in the volume percent is about 3 vol % and that therefore, the water contents of the HPNS-3 and the U2gj Redi-Mix are 64±3 and 36±3 vol %, respectively.

The depth of investigation of the ENS log is a function of both the water content and density of the formation. The depth of investigation of the ENS log for moderate to high water contents is in the range of 20 to 50 cm (~8-20 inches) [2]. This depth is less than the thickness of the cement that would remain after the cement zone was redrilled, if I assume that the void that was filled is circular symmetric and that the redrilling followed the original centerline in the hole (void is

not a one-sided directional break-out). If regions exist where the cement might not thick enough so that the logging sonde "saw" the native formation, the measured water contents would generally be less than the estimated cement water contents because the water contents of the cements are in general higher than the water contents of the native formation. The log itself can therefore be used to partially determine whether the cement behind the logging sonde is thick enough to avoid the effects of the formation.

The caliper log shows that the characteristics of the rugosity of the redrilled cemented portion is essentially the same as the characteristics of the rest of the drill hole (Figure 2). I assume that the logging tool's dynamic behavior in the cement region would therefore be on average the same as anywhere else in the hole. The measured proximities would have the same statistical variation.

The characteristics of the cemented zone (annular thickness, length, water contents, and rugosity) make this region of the hole an ideal location to conduct an *in-situ* check of the calibration of the ENS tool that was determined in the HCTF.

Results

Figure 3 shows the ENS log after processing with the LLNL techniques with and without a gap correction. The gap correction itself is a function of the neutron count rate, density, and gap. Superimposed on Figure 3 are the cemented regions where the cement values are known to be 64 and 36 vol %. The log water contents agree quite well with the high water contents in the cement zones *if a gap correction is performed.* Environmental or borehole effects typically make the epithermal neutron log read low. My first conclusion is that ENS log agrees quite well with the cement zone's high water contents. Proximity corrections for gap (tool standoff from the borehole wall) are clearly needed; otherwise, the log values would be too low.

The exact boundaries between the HPNS-3 and Redi-Mix cements and the cement-native formation are a little uncertain. Well loggers and drillers do not always use a common datum to reference the depths that they measure in the hole. This can often lead to a depth differences of up to 5 ft. In hole U2gj, this might be the case since the boundaries of higher water content from the drilling log for the cement zones do not exactly coincide with water content measurements from the ENS log. In addition, the blue-line log has the notation: "Log was recorded off depth. Log played back at correct depth." However, correct depth is really unknown; all that is known is the depth of the casing. If this was done, it appears as though the log is still off on the order of 2-

3 ft. Additional evidence of a potential discrepancy can be seen most clearly in the Rainier Mesa vitrophyre boulder region of the alluvium. As Figure 4 suggests, the ENS logger's depths disagree by about 3-4 ft with depths determined from a fisheye camera log run in the hole that was. Overall, I believe that the boundaries are uncertain by 2-5 ft.

Closer examination of the ENS log, however, indicates that gap corrections are sometimes applied that may not properly represent the logging tool sensor's standoff from the borehole. For example, in Figure 3, between 1340 and 1350 ft depths, the three largest water contents (at depths of approximately 1341.4, 1345.5, and 1348.5 ft) have a large gap at their respective depths but *the neutron count rate data shows almost no effect of a gap* . One could conclude that a gap correction was being made when the logging tool's sensor was not off or as far off the borehole wall as the proximity traces would indicate. In addition, Figure 3 shows that the gap corrected log has more and higher amplitude excursions in water content than does the uncorrected log over a similar depth interval.

I tried to reduce or eliminate this problem by preprocessing the proximity and neutron count rate data. I tried various forms of median filtering and in general found that the extreme points tended to be removed from the processed log. No analytical justification was discovered to justify using median smoothing. A median smoother tends to remove extreme values (data outliers). Since the ENS logging sonde neutron source to detector distance is approximately 3 ft long and therefore in some sense averages the formation properties across approximately a 3 ft interval, I decided to illustrate the advantages that extremal removal with a 3 ft median smoother on the proximity and neutron count rate data would have on the final processed log.

Figures 5 and 6 show the raw and 3 ft median smoothed data for the neutron count rate and proximity data, respectively. Figure 7 shows the ENS log in the cement region processed with the median smoothed count rate and proximity data and the ENS log with the standard LLNL processing. Note that the extreme values in the 1340-1350 ft range are gone and that in general, the spikiness of the processed log has been greatly reduced.

The figures tend to support the conclusion that gap corrections are sometimes being made when they are not warranted. Our measurements of the gap are not made at the sensing element of the tool, but rather at both ends with an average gap being applied in the processing to represent the logging sonde's standoff. In fact, Figure 6 supports the hypothesis that the logging sonde is on average at least 0.1 inches off the borehole wall.

I believe that a better method of measuring or calculating the actual logging sensor standoff from the borehole wall is desirable. 3 ft median smoothing as a preprocessing step may eliminate part of the problem; however, this "fix" is purely empirical.

Conclusions

The U2gj cement zones represent a unique opportunity to verify the *in-situ* performance of the ENS log in actual logging conditions. The U2gj ENS log processed using the standard LLNL ENS log processing algorithm utilizing the the calibrations from the HCTF agrees quite well with high water contents observed in cement zones. Gap (proximity) corrections are necessary to obtain good agreement with the cement water values. I conclude that there is no evidence that high water contents that have been previously measured (and sometime suspected as being too high) in other boreholes are suspect.

However, the current method of measuring gap appears to result in gap corrections sometimes being made when in fact no gap corrections may really be warranted. Preprocessing of the neutron count rate and proximity data with a median smoother appears to help reduce this effect. However, an improved method for proximity measurement could eliminate the problem of overcorrection and would negate my suggestion for preprocessing by median filtering.

Acknowledgements

The work was performed under the auspices of the U.S. Department of Energy by the Lawrence Livermore National Laboratory under Contract W-7405-ENG-48. This work was supported by the Nuclear Test Containment Program.

References

1. Axelrod, M. C. and J. R Hearst, Calibration of a Neutron Log in Partially Saturated Media IV: Effects of Sonde-Wall Gap, SPWLA Twenty-Fifth Annual Logging Symposium, June 10-13, 1984.
2. Hearst, J. R and P. H. Nelson, Well Logging for Physical Properties, McGraw-Hill Book Company, New York, NY, 1985.

Appendix 1

U2gj Cement Formulations
and the
Water Contents of U2gj Cements

U2gj Redi-Mix Specifications per Cubic Yard Mix		HPNS-3 Specifications per Cubic Foot Mix	
Cement:	360.0 lbs.	Type II Cement:	35.0 lbs
Sand:	2540.0 lbs.	Bentonite:	5.0 lbs
Water:	609.0 lbs.	Barite:	38.53 lbs
		D-19:	0.04 lbs
		Water:	40.0 lbs
Totals:	3509.0 lbs/cubic yard		118.57 lbs/cubic foot
Water Content:	36.2 Volume %		64.2 Volume %

The following relationships were used to obtain Volume % water content:

0.99823 kg/l = density of water at 20 °C

1 lb = 0.45359237 kg

1 Cubic foot = 28.316847 liters

1 Cubic yard = 764.55486 liters

Figure 1. U2gj caliper log from 1300-1400 ft showing five stages of HPNS-3 cement and one stage of U2gj Redi-Mix cement. The diameters of the cemented zones were determined by assuming that the cement-filled voids were circularly symmetric and that redrilling followed the centerline of the borehole.

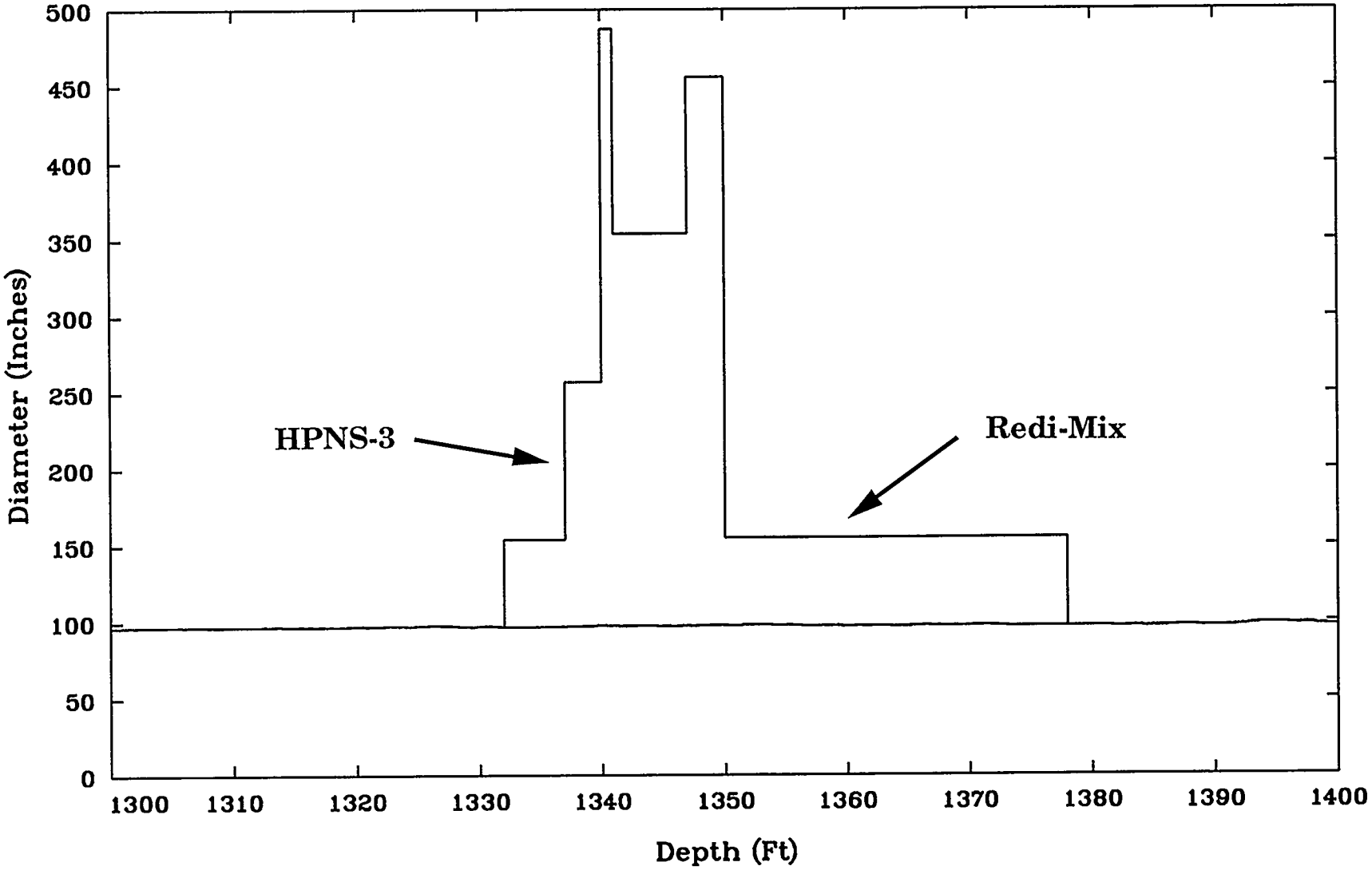
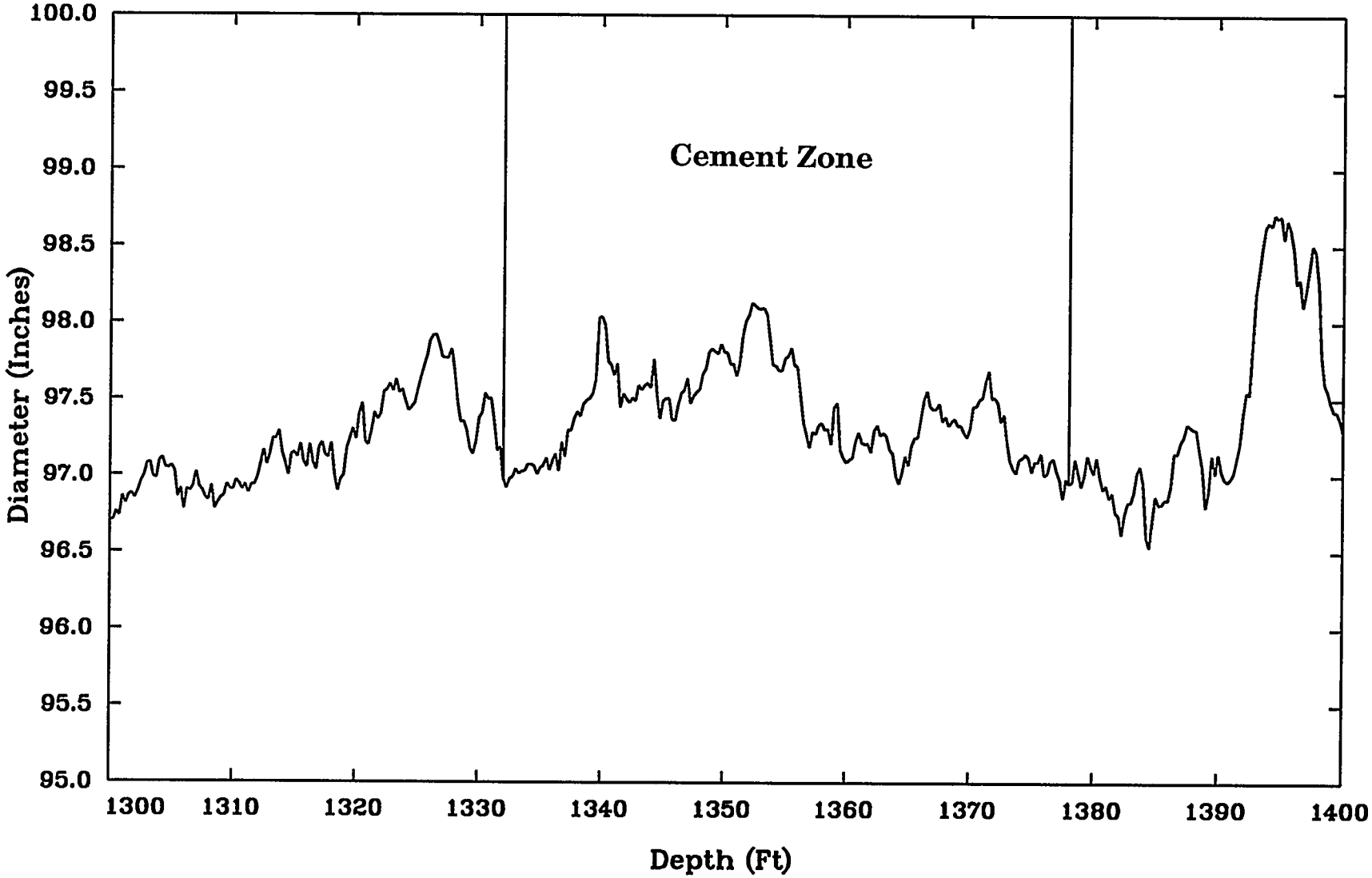


Figure 2. U2gj caliper log after redrilling the cemented zone (1332-1378 ft). The characteristics of the borehole rugosity in the cement zone appear to be the same as the borehole rugosity elsewhere in the borehole.



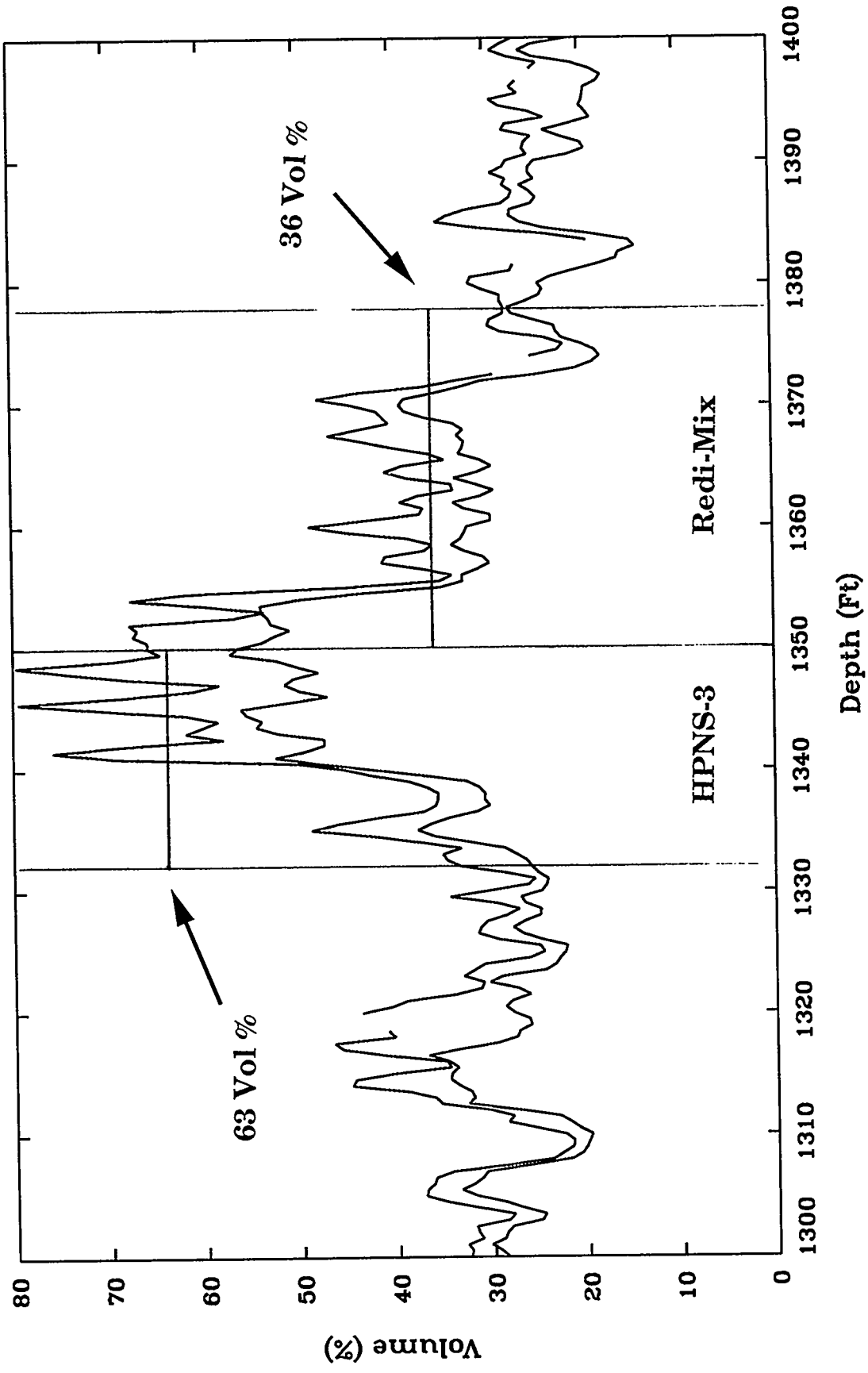


Figure 3. U2gj ENS log processed with and without gap correction. Note that the gap correction is necessary in order to match the high water contents in the cement zones.

Figure 4. U2gj ENS log in the region of the U2gj vitrophyric boulder in the alluvium. The regions of the extremely low water contents are the vitrophyric boulder. Note that there is an apparent depth shift of between 2-5 ft between the ENS log and the boulder depth as determined by the fisheye camera log.

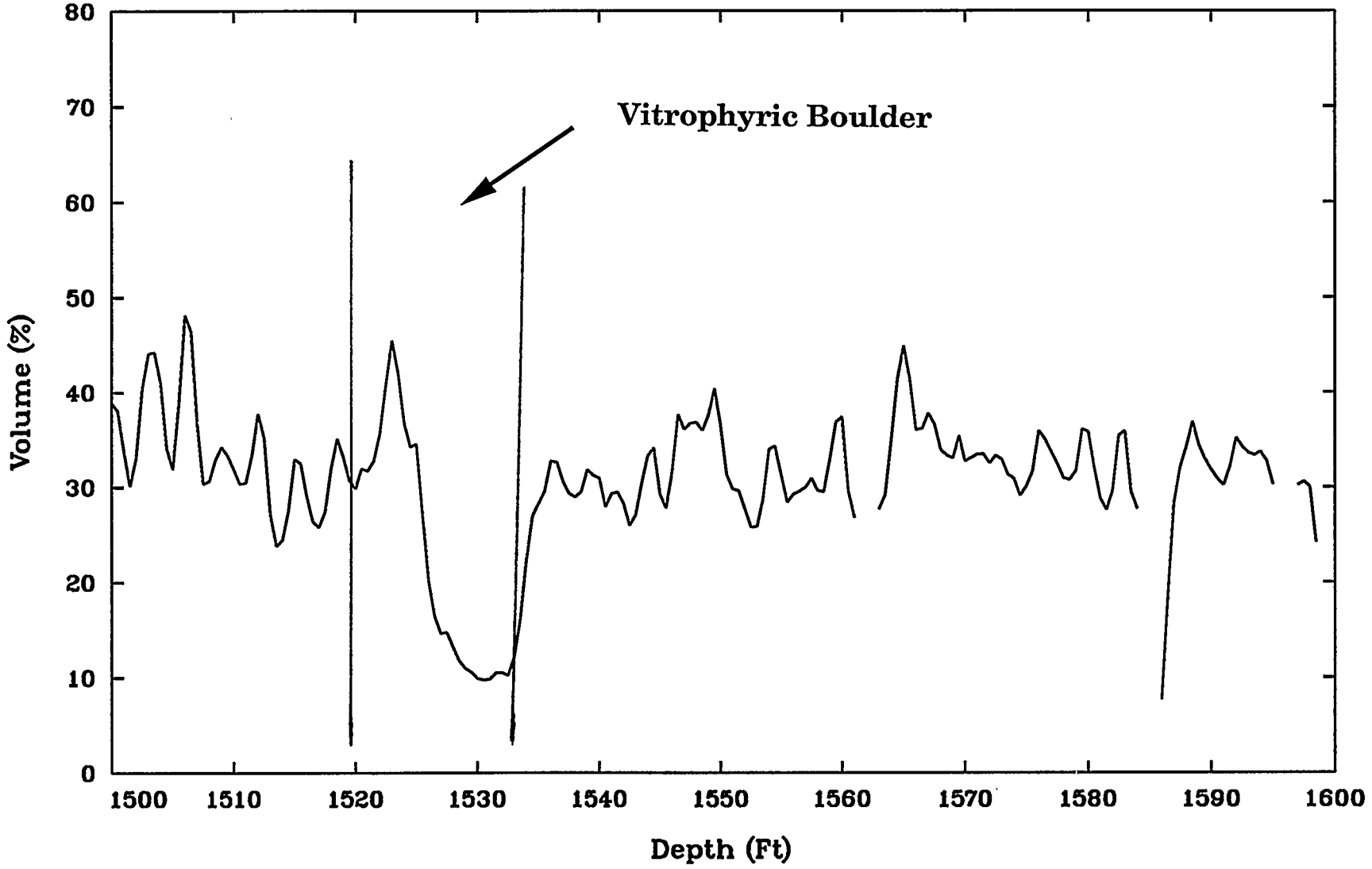


Figure 5. U2gj ENS neutron count rate data. The count rate data is shown as gathered (raw field data) and after smoothing with a 3 ft median smoother.

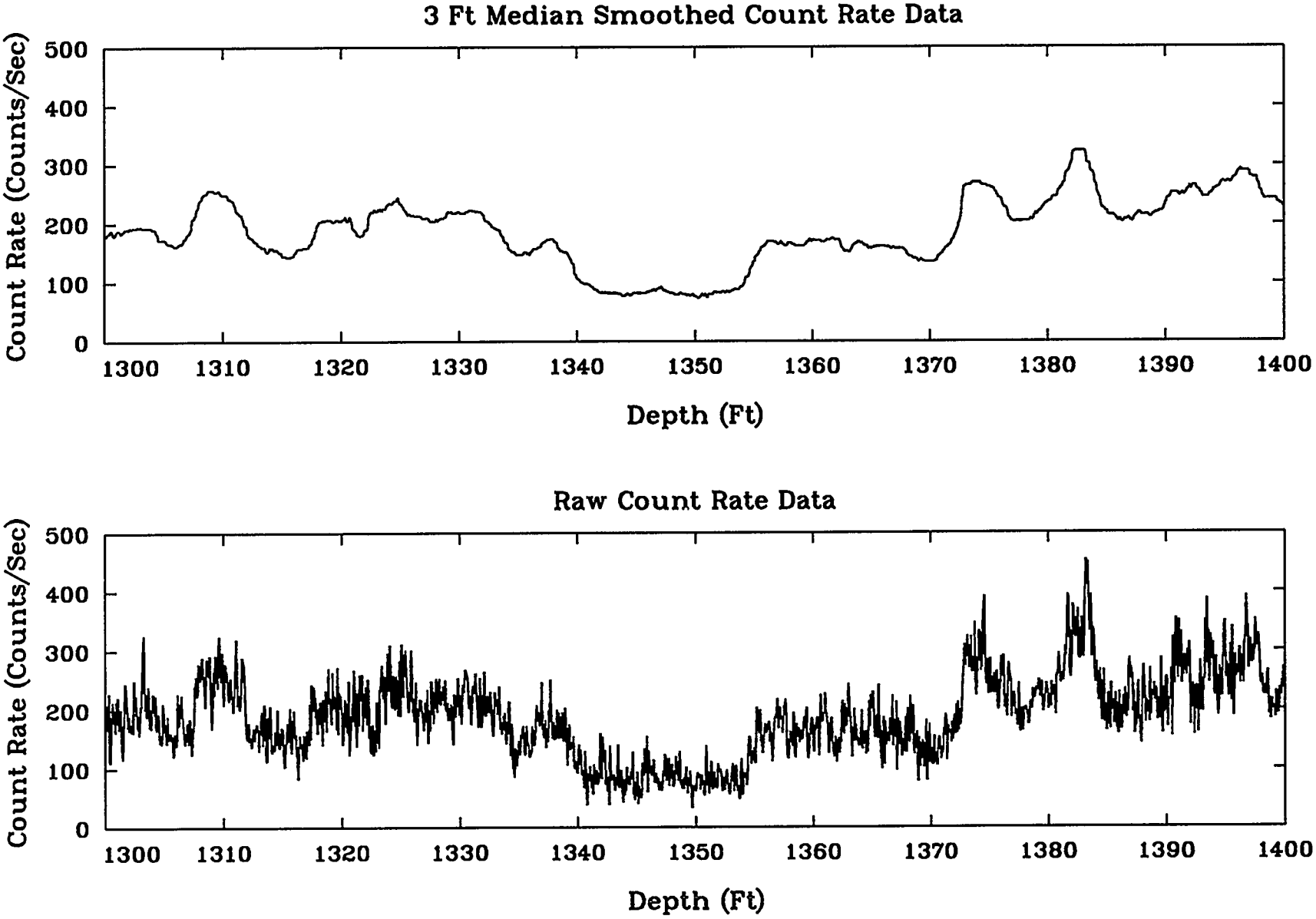


Figure 6. U2gj ENS proximity traces. Normal LLNL processing averages the upper and lower proximity traces and corrects the count rate data using this average proximity. The 3 ft median smoothed average proximity trace was calculated from this average proximity trace.

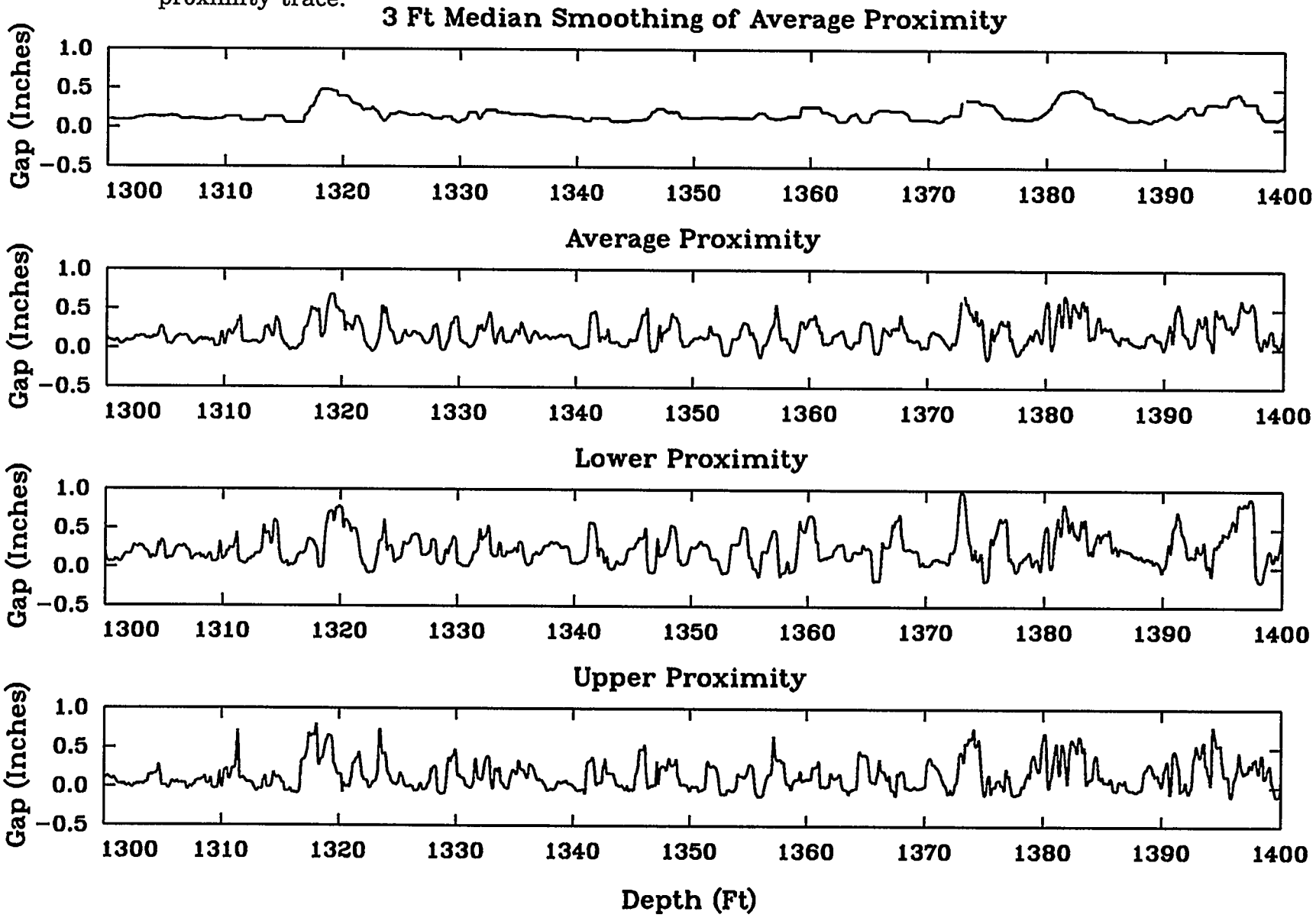
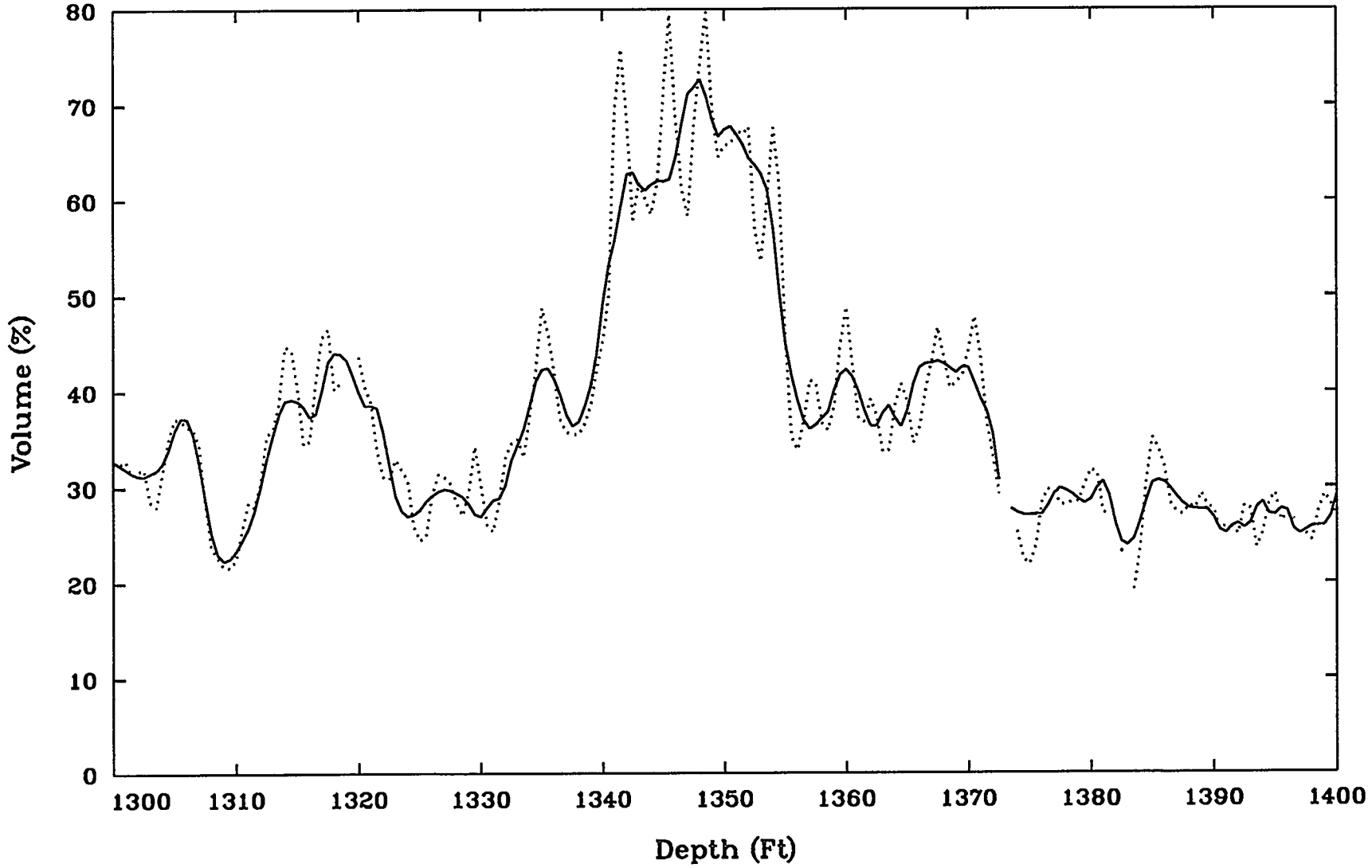


Figure 7. U2gj ENS log processed with the standard proximity traces and with the 3 ft median smoothed proximity and count rate traces. The solid line is the 3 ft median smoothed water content; the dotted line is the water content from standard processing.



Geosciences and Weapons Destruction



Soil Mounds at the Nevada Test Site: Natural or Nuclear?

M. N. Garcia and H. R. Covington
U.S. Geological Survey, P.O. Box 25046, Denver, CO 80225

Abstract

Pahute Mesa occupies the northwest portion of the Nevada Test Site (NTS) and ranges in elevation from about 1760 to 2230 m. It is composed of welded ash-flow tuffs and rhyolite lavas. Soil mounds have been observed in the field and on aerial photographs of the mesa that were taken prior- and subsequent-to subsurface nuclear testing. The mounds are commonly composed of loose, unstratified sediment and are surrounded by gravel at their bases. They range from 3 to 6 m in diameter, are generally less than 1 m in height, and are hemispherical. The mounds are most abundant on flat mesa surfaces, and they have not been observed on slopes greater than 15 degrees or in areas where the soil is sufficiently thick to support trees. Preliminary photogrammetric maps of the mesa show that the mounds form on mesa ridges where thin surficial material overlies thin welded ash-flow tuffs. No mounds have been observed on thick welded ash-flow tuffs or on rhyolite lavas.

The origin of the mounds may be due in part to three natural causes: the burrowing of small animals along natural and nuclear-induced fractures, vegetation serving as traps for eolian sediment, and frost action. A fourth factor may be seismicity. A seismic explanation has been suggested for the origin of similar mounds in Washington State. The seismic explanation suggests that the mounds in Washington State formed where ground shaking affected unconsolidated fine sediments on a relatively rigid planar substratum. It is unclear whether the mound formation on Pahute Mesa coincided with either natural or nuclear-induced seismicity. Soil mounds have been observed on some aerial photographs that predate subsurface nuclear testing. Currently, studies are in progress to determine if mound shape and distribution have changed as a result of subsurface nuclear testing.

WATER-LEVEL MAP OF EASTERN PAHUTE MESA AND VICINITY, NEVADA TEST SITE, NYE COUNTY NEVADA *

O'HAGAN, Mike D., IT Corporation, 4330 South Valley View, Suite 114, Las Vegas, Nevada, 89103-4047

A water-level contour map of Eastern Pahute mesa and vicinity, Nevada Test Site, Nye County, Nevada was constructed using water levels measured in seventy-three drill holes. The water level map supports previous conceptualizations of ground-water movement beneath eastern Pahute Mesa.

The drill holes were emplaced in volcanic rocks of the Silent Canyon Caldera complex, the Timber Mountain caldera and adjacent areas. Depth-to-water measurements range from 852 to 2,336 feet below land surface. Water-level altitudes range from 4,904 feet in the eastern part to 4,190 feet in the southeastern part of the map area. Within the Silent Canyon Caldera complex a northeast to southwest ground-water flow direction is indicated by the water-level contours.

A north-south lateral ground-water flow barrier is located coincident with the western boundary of the Silent Canyon caldera complex. The barrier is defined on the basis of a steep hydraulic gradient resulting in higher water levels measured in drill holes located west of the caldera complex. West of the barrier, a north-south ground-water flow direction is indicated by the water-level contours.

Anomalously high water levels in the eastern, central and southwestern map area are identified. The anomalous water levels may represent perched or semiperched conditions. Alternatively, The anomalous water levels may indicate transient perturbations of the ground-water system caused by underground nuclear testing.

* Map project conducted under the auspices of the U.S. Geological Survey.

Groundwater Levels from Well and Test-Hole Data, Yucca Flat, Nevada Test Site, Nye County, Nevada, 1959–91

G. S. Hale and D. A. Trudeau
U.S. Geological Survey, Water Resources Division, 6770 South Paradise Road, Las Vegas, NV 89119

Abstract

Groundwater levels at the Nevada Test Site, 65 miles northwest of Las Vegas, Nevada, have been affected by underground nuclear testing. Water-level data collected from wells and test holes during April 1959 through December 1991 in the Yucca Flat area are being evaluated by the U.S. Geological Survey, in cooperation with U.S. Department of Energy for their nuclear-test and environmental-assessment planning. These water-level data are being used to construct a water-table-altitude map by evaluating the location of wells and test holes, water-level measurements, the location of the contact between Paleozoic and Cenozoic rocks at the water table, and the generalized hydrostratigraphic (Paleozoic or Cenozoic) unit contributing water at each well or test hole. This information updates the map by Doty and Thordarson (1983), *Water table in rocks of Cenozoic and Paleozoic Age, 1980, Yucca Flat, Nevada Test Site, Nevada,* U. S. Geological Survey Water-Resources Investigations Report 83-4067. Within the Ceno-zoic rock of central Yucca Flat, the number of delineated groundwater mounds and the areal extent of mounding have increased since 1980. Generally, groundwater altitudes are higher in the Cenozoic rock of central Yucca Flat than in the underlying and adjacent Paleozoic carbonate rock. A more precise interpretation of groundwater flow in Yucca Flat is limited by sparse 1991 data, composite water-level data (the well or test hole is open to more than one hydrostratigraphic unit within saturated Paleozoic and Cenozoic rock), and the effects of nuclear testing on water levels. These limitations prevent an accurate interpretation of groundwater flow direction within Yucca Flat.

An Electromagnetic Hole Separation Survey Tool

H. C. Goldwire, Jr.
Lawrence Livermore National Laboratory, P.O. Box 808, Livermore, CA 94551

Abstract

We describe an electromagnetic survey tool developed by others, which can be used to accurately determine the offset distances between various points in nearby emplacement holes or adits (e.g., the satellite hole offset from an emplacement hole at the device horizon in a vertical geometry emplacement). The technique was demonstrated on a vertical event at the Nevada Test Site. The basic theory of operation, sample data, and analyzed results will be presented and compared to results obtained by conventional survey means.

DESTRUCTION OF CHEMICAL WEAPONS BY UNDERGROUND NUCLEAR EXPLOSIONS

Benoit Morel and Stephen Black
Carnegie Mellon University

Introduction

After several decades, the negotiation of a ban on production, possession and use of chemical weapons, was completed in Geneva this summer. An important provision of the treaty is that the parties have ten years to destroy the chemical warfare agents and chemical weapons deployed on their territories. In contrast to the frenzy of other post-cold war demilitarization efforts, chemical weapons destruction presents significant unresolved technical and economic problems to a large number of states. Specific solutions may not be universally accepted because of technical, economic, and societal differences. In particular, the use of underground nuclear detonations was dismissed in the West but is being examined by Russian scientists.[1]

The destruction of chemical weapons is more difficult and more expensive than their manufacture. In addition to their extreme toxicity, the high explosive bursting charge contained in many of the munitions adds a significant degree of difficulty. There have been many suggestions for industrial scale destruction of chemical weapons. The cost, difficulty and efficiency of these approaches vary, but none seem ideal.[2]

Currently two methods of large scale stockpile disposal have been investigated. Detoxification and incineration both have significant drawbacks. The detoxification of chemical warfare agents through chemical action is not as complicated as the total destruction of the agent. But detoxification alone is not a satisfactory solution to the disposal of chemical weapon as it is easy to resynthesize the original CW agent from the detoxification waste products. The only reliable way to destroy effectively the most toxic chemical warfare agents (nerve agents) is to utilize a process which irreversibly breaks the molecules' most resilient bond (Phosphorus-Methyl).[3] Because of the high activation energy of this bond a highly energetic reaction such as incineration is required. But these processes come at a high price and current technology is not perceived as environmentally sound.[4] Furthermore the destruction rate of these processes would be very small compared to the size of the arsenals to be destroyed.

Peaceful nuclear explosions have been advocated as the most cost effective or "rational" approach to chemical weapon destruction.[5] The two most visible advantages of this approach are that given the physical conditions created by a nuclear explosion large

quantities of chemical agent can be completely atomized in an instant. Also there would be no need to dismantle live munitions, which is the most delicate and expensive phase of chemical warhead destruction. Yet for reasons primarily political in nature nuclear destruction of chemical weapons is not perceived as a suitable option for the United States arsenal. One reason is the opposition by the U.S. government to the concept of peaceful nuclear explosions because of the possibility that countries could legitimately develop nuclear weapon disguised as peaceful nuclear device which would undermine nuclear non-proliferation. Also public perception of the risks of nuclear detonations would create formidable opposition.

What is not suitable for the U.S. however may be the most rational solution for other countries, in particular Russia. Russia has inherited a huge arsenal of chemical warfare munitions - estimated at around 50,000 tons. Furthermore it is in principle bound by the bilateral accord of January 1990 (U.S. and U.S.S.R.) to destroy half of its arsenal by the end of the decade and all but 5000 agent tons by the year 2003. The existing Russian program for the destruction of its chemical arsenal is meeting a variety of obstacles. Given the cost of building environmentally safe destruction facilities, the dire conditions of the Russian economy, and the fact that Russia must also reduce its nuclear arsenal, the nuclear destruction of its chemical stockpile is an attractive possibility.

Before the use of nuclear devices for the destruction of chemical weapons can be recommended, a closer look at the technical aspect of this approach is crucial. An underground explosion whose purpose is to destroy chemical weapons differs considerably from an underground nuclear test. Consequently, expertise that has developed in predicting detonation effects and in maintaining radioactive containment may not all transfer to CW destruction shots. Much of the current understanding of detonation and containment phenomenology was originally developed on a trial and error basis. Although there are significant differences, experience gained thru underground weapon tests provides a good starting point for assessing the effects and containment of CW destruction explosions.

The dynamics of a "tamped" underground detonation are reasonably well understood.[6 7 8] A certain amount of rock in the immediate vicinity of the nuclear device is vaporized (roughly 70 tons of material per kiloton of yield).[9] This results in the creation of a cavity containing compressed gas at very high temperature. The energy communicated to the rock surrounding the cavity leads first to its fracture and, as the shock wave abates, to the generation of an elastic deformation propagating as a seismic wave. Once the cavity has reached its maximum diameter it recompresses under the effect of an elastic rebound. The cavity diameter shrinks until the hoop stress generated by radial convergence approaches the compressive strength of the rock. At the end of this dynamic phase, which lasts from

50 to 80 milliseconds, the cavity has reached a metastable equilibrium between various forces: the high pressure gas inside, lithostatic pressure from the over burden, and compressive hoop stress. The rebound creates a "containment cage" of fractured rock surrounding the cavity in which compressive hoop stress is at its maximum. The containment cage thickness is typically 60m / $kT^{1/3}$. The cavity created by a tamped explosion has a diameter of roughly 12-16m / $kT^{1/3}$. That means that a 100 kT explosion would create a cavity diameter of 56-74 meters with a containment cage diameter of 300 meters.[10]

The containment cage usually prevents the release of radioactive contaminants by reducing the two prime channels of contaminant seepage: diffusion through the surrounding rock and flow through natural or explosion induced fissures. Contaminant seepage should not be confused with "venting" which is the formation of a direct channel to the surface which allows a prompt release of hot gases carrying radioactive products. While venting is a concern before every underground explosion the precautions needed to avoid this type of catastrophic release are reasonably well understood. Over the years the methodology developed to ensure containment and avoid seepage has proven to be quite effective. It is based on the use of rules of thumb to determine the depth of underground explosions for a given yield. The rule is 400 feet / $kT^{1/3}$ or 133m / $kT^{1/3}$. This means that a 100 kT device should be detonated at a depth of roughly 600m. However, the destruction of chemical warfare agents will lead to the creation of much larger quantities and different species of noncondensible gas. This could increase the danger of late time seepage. A tamped detonation primarily produces CO_2 while a CW destruction shot would create significant amounts of lighter noncondensible gasses like H_2 or CH_4. Because gaseous diffusion is effected by the mass of the mobile contaminant this may also require a larger depth of burial factor.

Of further concern is the fact that underground nuclear explosions for chemical weapons destruction could produce more hydrofracturing than tamped explosions. Hydrofractures are cracks through which contaminants can migrate and possibly reach the surface. Gas and particulate transport through these fractures, when they exist, is by far the dominant contaminant transport mechanism. The size of a given crack is dependent on a balance between compressive stress in the fractured material and the gas pressure propagating the crack.[11] A decrease in compressive stress or an increase in cavity pressure will increase the size and extent of hydrofractures. The explosion of a nuclear device in a cavity filled with chemical weapons will unavoidably correspond to a "partially decoupled" explosion.[12] An explosion is said to be decoupled when a significant part of the released energy is not communicated to the rock. The creation of the containment cage is dependent

on the compressive hoop stress created by cavity rebound. The shock wave from a decoupled detonation does not increase residual compressive hoop stresses so no containment cage is created. Thus in a partially decoupled explosion a weaker containment cage is created.[13] The nuclear destruction of chemical weapons will lead to a partially decoupled explosion, because the cavity has to be large enough to accommodate the chemical munitions, and a portion of the explosive energy is used to vaporize the weapons. As a result the detonation will not generate as effective a containment cage as a tamped explosion. Furthermore it will produce more noncondensible gas, therefore increasing the cavity gas pressure. Also, the cavity contents will remain gaseous for a longer period giving the fracture a longer growth time.

For all these reasons a more detailed investigation of the physics and chemistry of the processes involved in the nuclear destruction of chemical weapons is of the essence.

Example: CW Destruction with a 100 kT nuclear device

To calibrate our assessment we assume that a nuclear device of 100 kT is used to destroy chemical weapons. Furthermore, let us assume first that it is used to destroy artillery shells charged with the nerve agent Sarin. Only one fifth of the munition mass is actual chemical agent, the rest is assumed to be iron. All our estimates can easily be generalized to other yield and situations.

The mass of munitions to be destroyed must be carefully scaled to the yield of the explosion in such a way that there is no possibility of any agent surviving the initial energy release. To make sure that all the chemical warfare agent is thoroughly destroyed we utilize the rule of thumb that a 100 kT detonation will vaporize roughly 7000 tones of surrounding material. From this rule we can make the conservative assumption that 5000 tons of chemical shells can be destroyed by a 100kT device.

1000 tons of chemical agent per detonation is not a large quantity considering the total amount that needs to be destroyed. However it would be imprudent to recommend destroying a larger quantity with the same yield as not all of what is to be destroyed would be reliably vaporized.

At the end of the dynamic phase, after the rebound creating the containment cage, 7000 tons of gas will be trapped in the cavity where according to another rule of thumb, 35% of the energy remains.[14] The vaporization of 4,000 tons of iron requires roughly 8 kT of energy. If approximately 20 kT is used to heat up the gas trapped in this cavity, it should reach a temperature around 10,000 ^{o}K. Assuming that the cavity contents behave approximately like a perfect gas, its pressure is multiplied by 35. The pressure and temperature at the end of the dynamic phase should not significantly differ between a

tamped explosion and a CW destruction detonation, since in both cases one expects that the cavity contains 7 kT of gas at 10,000 °K. If at room temperature this gas had a pressure between one and three atmospheres, at the end of the dynamic phase the cavity pressure should be between 40 and 100 atmospheres. However, the gas composition of the cavity will be markedly different in the two cases. Given that the 5000 tons of chemical munitions containing the nerve agent Sarin ($C_4FH_{10}O_2P$) and 2000 tons of granite at 15% water content (1700 tons of SiO_2 mixed with 300 tons of H_2O) were vaporized we should expect to find in the cavity at the end of the dynamic phase:

1. $1x10^8$ moles of 'H' + $5.9x10^7$ 'O' + $2.8x10^7$ 'C' + $7.1x\ 10^7$ 'Fe' + $7x\ 10^6$ 'F' + $7x\ 10^6$ 'P' + $3.3x10^7$ 'Si'.

This amounts to about: 110 tons of hydrogen, 944 tons of oxygen, 336 tons of carbon, 3962 tons of iron, 133 tons of fluorine, 217 tons of phosphorus and 927 tons of silicon. This can be compared with a tamped explosion of similar yield which would instead produce: 2797 tons of silicon, 4088 tons of oxygen and 116 tons of hydrogen.

Upon cooling a number of reactions will take place which are unique to a CW destruction detonation. By examining the thermodynamics of specific reactions the relative yields of end-products can be gauged. The following is a list of several possible reactions, their free energy change at standard temperature and pressure, and the approximate temperature below which the chemical equilibrium begins to favor the products. While pressure effects are omitted they will serve to drive the equilibrium toward the products side.

Reaction	ΔG(kJ/mol)	Equilibrium Temperature(°K)
$3Fe(g) + 4O(g) \rightarrow Fe_3O_4(s)$	-3011	4165
$2Fe(g) + 3O(g) \rightarrow Fe_2O_3(s)$	-2149	4000
$C(g) + 4H(g) \rightarrow CH_4(g)$	-1536	3854
$C(g) + 2O(g) \rightarrow CO_2(g)$	-1527	6034
$C(g) + 2H(g) \rightarrow C(s,gr) + H_2(g)$	-1079	4598
$2H(g) + O(g) \rightarrow H_2O(g)$	-865	4579

In both types of detonations the amount of hydrogen generated is basically the same. But in a tamped shot far more oxygen is created which can recombine during cooling with the hydrogen to make steam or water. Whereas the atomization of chemical weapons leads to the generation of large quantities of iron and carbon which will avidly wash away the oxygen and leave the hydrogen either to become gaseous hydrogen or recombine with the remaining carbon to give rise to light noncondensible hydrocarbons like

methane. The appearance of substantial quantities of light noncondensibles in the cavity changes the conditions for transport of gas and radioactive contaminants after the explosion.

The transport of gas mixtures in a porous media can be studied with the "Dusty Gas Model."[15] In the dusty gas model the porous medium (the "dust") is treated as one of the components of the gas mixture. In our case the dominate effect responsible for the gas transport is the pressure gradient (∇p). Under a pressure gradient, the different components of a gas mixture travel at different velocities. This phenomenon is similar to that used in gas chromatography to separate sample components. The flux of each component depends on the composition of the whole mixture. The Stefan-Maxwell equations relates the fluxes $\mathbf{J_i}$ (expressed as a number of particles or molecules per unit of time and area) of the different mobile components to the gradient of pressure.

Dividing the gaseous mixture into a light and heavy component, the equations describing the transport of this two component mixture become:

$$(n_H/nE_{LH})(\mathbf{J_L}/n_L - \mathbf{J_H}/n_H) + (1/E_{LK})(\mathbf{J_L}/n_L) = -\nabla \ln(p)$$

$$(n_L/nE_{HL})(\mathbf{J_H}/n_H - \mathbf{J_L}/n_L) + (1/E_{HK})(\mathbf{J_H}/n_H) = -\nabla \ln(p)$$

Where n_H, n_L and n are the number of molecules of the light and heavy components and the total number of molecules of gas. $\mathbf{J_L}$ and $\mathbf{J_H}$ are the molecular fluxes of both components. E_{LH} (assumed to be equal to E_{HL}) is a diffusion coefficient which describes the relative diffusivity properties of the two components in the porous medium. E_{LH} depends on the porosity properties of the medium and on the viscosity of the gas mixture. E_{LK} and E_{HK} are related to the Knudsen diffusion coefficients and also depend on the porosity of the medium and on the viscosity of the gas mixture.

The medium in which we apply these equations is highly non-homogeneous in the sense that its porosity varies widely with location. The viscosity properties of the gas mixture vary with changes in its composition due to the cooling of the mixture and associated chemical changes. For these reasons and others we can extract only qualitative, but important, information from their use.

Of special relevance is the mass dependance of the diffusion coefficients, particularly when the mass of the light component is significantly smaller than the mass of the heavier constituents ($m_L << m_H$). When T is the temperature of the mixture, E_{LH} and

E_{LK} are proportional to $(T/m_L)^{1/2}$, but E_{HK} is proportional to $(T/m_H)^{1/2}$. After some simple manipulations, when $m_L << m_H$ one gets:

$$\mathbf{J}_L/n_L = -\{E_{LK}/[1+(n_H/n)(E_{LK}/E_{HL})]\}\ \nabla \ln(p)$$

and:

$$\mathbf{J}_H/n_H = -E_{HK}\left\{1+\frac{(n_L/n)(E_{LK}/E_{HL})}{[1+(n_H/n)(E_{LK}/E_{HL})]}\right\}\ \nabla \ln(p)$$

One obvious message of the Stefan-Maxwell equations is that the flow $\mathbf{J}_L$ of the lightest component of the mixture is roughly inversely proportional to the square root of m_L. This implies that the fluxes of the light components tend to be enhanced. If the lightest component is hydrogen instead of CO_2, everything else being equal, the flux of hydrogen will be four times larger than the flux of CO_2. Radioactive products are either gaseous (Krypton^{85}, Tritium, and Tritinated methane) or particulate. The mass of these radioactive contaminants are much larger than most of the noncondensables. As a result the gradient of pressure tends to generate a smaller flow for them than for the lighter gases. However the generation of large quantities of molecular hydrogen or other light species could lead to an enhanced flux of the heavier radioactive components through the rock surrounding the cavity. The equation for the flux of the heavier component suggest that it will be enhanced by the presence of the lighter component in proportion to the quantity n_L/n of the lighter component.

If all other conditions are held constant the effect of producing significant quantities of light noncondensible gasses could increase by 20% to 40% the flux of the radioactive contaminants. A way to avoid radioactive surface contamination would be to increase the depth at which the explosion takes place by a similar proportion. This is not a simple solution as increased emplacement depth comes at a significant cost. Also there is a constraint place on burial depth by the location of the water table.

Also the assumption "all the other conditions being equal" is very questionable here. The fact that when there are chemical weapons in the cavity, the explosion is partially decoupled adds to the problem. As we saw, the explosion could lead to greater hydrofracturing through which the contaminated gas mixture can migrate more easily. Fractures and rubblized rock are the dominant pathways for underground gas flows.[16]

The results would be somewhat but not very different if we had assumed that large batches of bulk chemical warfare agent had been put in the cavity, instead of chemical warheads. The first difference would be the absence of iron. This would have the advantage of avoiding iron fixation of oxygen But in this case far more hydrogen would be produced thus eliminating the benefit of more available oxygen. Methane would become the major light noncondensible. Methane is eight times more massive than hydrogen, but there would be far more of it. The problem with seepage would be similar but somewhat worse than the artillery shell example.

Policy Implications

Is the destruction of chemical weapons through underground nuclear explosions unsafe and unadvisable? Such a conclusion does not necessarily follow from our findings. However our considerations show unambiguously that the presence of chemical weapons changes the physics and the chemistry of the explosion and its containment. We show that the rules of thumb currently used to determine the depth of underground nuclear explosions do not bring the same level of safety if applied to nuclear explosions in the presence of chemical weapons.

Although we did not attempt any estimate, past experience with gaseous radionuclide seepage suggests that the danger represented by some marginal seepage may be limited. In fact, each boiling water reactor power station in the U.S. releases nearly 25,000 curies of Krypton^{85}, and hundreds of curies of Tritium each year. And while particulate transport occurs to a much lesser extent its effects are much more dangerous. It remains that it would be imprudent to declare nuclear destruction of chemical weapons a safe approach given the present state of understanding.

One major lesson of this work is also that the quantity of chemical weapons which can be confidently destroyed by one nuclear explosion is not so large (around 50 tons per kiloton of yield). The fact that the cavity will have to be large enough to contain the chemical weapons, and deep enough to avoid seepage, suggests that this approach may not be as cost effective as originally envisioned. However there are still two areas of superiority for nuclear destruction over alternative approaches. PNE destruction is significantly faster than any other process and because munitions are emplaced as-is there is no need for a costly and dangerous disassembly step.

Furthermore PNE for CW destruction must be compared with the alternatives which also tend to be expensive, complicated and somewhat polluting. The conclusion may be that the nuclear destruction of chemical weapons is probably not as attractive as it may have looked superficially, not as clean or cost effective. Yet it may still be the most

appropriate approach for a country like Russia which has many nuclear weapons to get rid of, a very large chemical arsenal, and which is bound by treaty to destroy its arsenal in a limited amount of amount of time.

---

1. Black S., B. Morel, "Rational Disposal of Chemical Weapons." *Nature*, 360, 17 December 1992. pp. 621-2.
2. U.S. Department of the Army, "Chemical Agent and Munition Disposal; Summary of the U.S. Army Experience," Office of the Program Manager for Chemical Demilitarization, Aberdeen Proving Ground, MD, September 1987.
3. Black S., B. Morel, P. Zapf, "Verification of the Chemical Convention." *Nature*, 351, 13 June 1991. p. 515-6.
4. Picardi, Alfred et al. "Alternative Technologies for the Detoxification of Chemical Weapons: an Information Document." (Greenpeace, Washington D.C., 5/91)
5. I.A. Andryushin, Yu. A. Trutnov, and A.K. Chernyshev. "Report on Some Aspects of Creation of Nuclear Explosion Technology for Destruction of Toxic and Hazardous Materials and Waste Products." (Arzamas 16, 1992).
6. "The Containment of Underground Nuclear Explosions", U.S. Congress, Office of Technological Assessment, 1988, p. 53.
7. G.W. Johnson, G.H. Higgins, C.E. Violet, *Underground nuclear detonations*, Journal of Geophysical research, **64** (1959), p. 1457.
8. R.W. Terhune, H.D. Glenn, D.E. Burton, H.L. Hague, J.T. Rambo, *Numerical Simulation of the Baneberry event*, Nuclear technology, **46** (1979), p.159.
9. R. Duff, *The Feasibility of Chemical Munition Disposal Using Nuclear Explosions*, technical report prepared for Defense Nuclear agency, DNA-TR-81-205, November 1982, p. 26.
10. Terhune et al.
11. T.D. Kunkle, B.J. Travis. *Hydrofracture From a Growing Cavity*. Los Alamos National Laboratory LA-UR-82-2308, 1981.
12. D.W. Patterson. *Nuclear Decoupling, Full and Partial*, Journal of Geophysical Research, **71**, (1966), p.3427. R.F. Herst, G.C. Werth, D.L. Springer, *Use of large cavities to reduce seismic waves from underground explosions*, Journal of Geophysical Research, 66 (1961), p.959. A.L. Latter, R.E. Lelevier, E.A. Martinelli, W.G. McMillan, *A Method of Concealing Underground Explosions*, Journal of Geophysical Research, 66 (1961), p. 943.
13. L.A. Glenn, *Energy Density Effects on Seismic Decoupling*, Lawrence Livermore National Laboratory, UCRL-JC-109393, 1992.
14. Duff, p. 10.
15. Mason E.A. , A.P. Malinauskas. "*Gas Transport in Porous Media: The Dusty Gas Model*", (Elsevier, Amsterdam, Oxford, New-York) 1983, p.71.
16. N.R. Burkhard, J.R. Hearst, E.W. Peterson, R.H. Nilson, K.H. Lie: "*Containment of Cavity Gas in Fractured or Rubblized Emplacement Media*", Lawrence Livermore National Laboratory, UCRL-100953, DE90 001054, 1989.

Recycled Recyclable